Measurement of Differential Cross Sections and Spin Density Matrix Elements along with a Partial Wave Analysis for $\gamma p \to p\omega$ using CLAS at Jefferson Lab

by

Mike Williams

A dissertation submitted in partial fulfillment of the requirements
for the degree of

Doctor of Philosophy

in the Department of Physics

Carnegie Mellon University

November 29, 2007

Abstract

This work presents measurements of differential cross sections, $d\sigma/d\cos\theta_{CM}^{\omega}$, and spin density matrix elements, $\rho_{MM'}^{0}$, for the reaction $\gamma p \to p\omega$ in the energy range 1.72 GeV$< \sqrt{s} <$2.84 GeV. The data were collected at Jefferson Lab, using the CLAS detector, as part of the $g11a$ run period in 2004. Our $\rho_{MM'}^{0}$ measurements vastly increase the precision of the world's data and extend the large angle measurements by over 400 MeV in $\sqrt{s}$. Our data confirms that for $\sqrt{s} < 2.1$ GeV, the forward angle (small $|t|$) production amplitude is dominated by t-channel π^{0} exchange. At higher energies, existing non-resonant models do a poor job of describing our data. In particular, u-channel models fail to reproduce our highest energy backwards $\rho_{MM'}^{0}$ measurements.

A *mass-independent* partial wave analysis has also been performed. Near threshold, the dominant resonance contributions extracted are the **** $F_{15}(1680)$ and *** $D_{13}(1700)$. Together with the t-channel π^{0} exchange, these three waves provide a remarkably good description of our differential cross section and spin density matrix element measurements for $\sqrt{s} < 2$ GeV. Strong, but not conclusive, evidence for the **** $G_{17}(2190)$ has also been extracted. Improved non-resonant models may be necessary to irrefutably show whether this state contributes to ω photoproduction. Evidence for *missing resonances* is suggestive, but inconclusive without theoretical input.

Preface

This thesis represents the combined effort of a number of people. For this reason, I have chosen to write it in first person plural; however, in the preface and the acknowledgments that follow, I will be speaking solely about my research experience and the people in my life who have made undertaking and completing this work possible. Thus, these sections will be written in first person singular. The research presented in this thesis is not an exhaustive list of the work I've done while a graduate student at Carnegie Mellon University. I have restricted its content to the work that specifically involves partial wave analysis, the CLAS $g11a$ run period and the $\gamma p \rightarrow p\omega$ channel. In this section, mostly for posterity, I will give a brief overview of my research experience at CMU.

I began working for the *Medium Energy Experimental Physics Group* in the spring of 2002. The first project I worked on involved testing gas compositions for the straw tube chamber in the (proposed) GlueX detector. I spent most of the next year learning quantum field theory and basic partial wave analysis techniques, along with finishing my required course work and qualifying exams. In the summer of 2003, I began developing a kinematic fitter for the CLAS detector. I had initially planned on analyzing the CLAS $g1c$ dataset for my thesis research. Thus, the original version of the covariance matrix was tuned for that run period. I completed work on the kinematic fitter in the fall of 2003 [1]. I then wrote the first version of a generalized CLAS analysis software package which incorporated the kinematic fitting routine.

In the summer of 2003, the CLAS collaboration published evidence for the $\Theta^+(1540)$ pentaquark state from the $g2a$ run period [2]. Upon completing the kinematic fitter, I applied it to the pentaquark data. The *peak-like* structure proved not to be robust [3, 4, 5]. This work was one of several motivating factors for producing a higher statistics dataset, labeled $g10a$, to convincingly resolve this issue. The collaboration decided to wait for the results of this new experiment to make any firm public statements, *ie* I was not allowed to present my work outside of the CLAS collaboration; however, from this point forward, all CLAS pentaquark talks were required to include the statement: *Further analysis has led to reduced significance in the peak*. My null result was eventually confirmed by $g10a$ [6].

In the spring of 2004, I returned to my $g1c$ analysis and, with the help of CMU undergraduate Doug Applegate, derived tagger and momentum corrections using the kinematic fitter [7]. The tagger corrections possessed an interesting structure, later understood to be a sag in the support rods of the hodoscope [8]. At this point in time, I had completed four quantum field theory courses and a general relativity course. I began to question the utility of using the non-relativistic Helicity formalism in a partial wave analysis of a channel which (almost certainly) had s-,t- and u-channel contributions. I was also convinced that any additional computational complexity introduced by using a covariant framework could be overcome with proper coding. The next three months were spent developing software capable of calculating almost any covariant amplitude while maintaining an API which closely resembled the hand-written formulas. The strict performance requirements, along with the API goals of this project forced me to greatly improve my programming skills. I then applied the knowledge that I had gained into translation of a PWA software package, written by Matt Bellis, into pure *high-performance* C++. Upon completing these projects, I next derived all of the covariant amplitudes and partial wave analysis formulas found in chapters 5 and 6.

In the summer of 2004, a higher statistics version of $g1c$, labeled $g11a$, was run to investigate another possible pentaquark observation. My work on the $g2a$ data had led to a collaboration mandate that any new pentaquark results must be robust under kinematic fitting to be cleared for publication. That November, the $g11a$ spokespersons, Marco Battaglieri and Raffaella De Vita, invited me to the *Instituto Nationale di Fisica Nucleare* (INFN) in Genova, Italy to tune the kinematic fitter for $g11a$. After a short time working with the data, I decided to switch my thesis research to the $g11a$ data set (I didn't know it at the time, but Curtis and Matt had already discussed this change). The $+ + -$ skim of the data was approximately 11 TB. We wanted to keep it live on disk at CMU due to the large number of separate analyses which planned to use this new data set. At that time, there was only 800 GB of disk space available on the Medium Energy Group's raid array for data storage. Doug and I spent the spring of 2005 writing software that allowed us to compress $g11a$ down to 600 GB and $g1c$ down to 60 GB (it now fits on an iPod). Next, I recalculated the tagger and momentum corrections (originally done for $g1c$) for $g11a$.

In the fall of 2005, I updated my generalized CLAS analysis software package, now renamed COBRA, to better handle the diverse analyses underway at CMU. Most of the next year was spent working closely with Matt Bellis, Zeb Krahn and Doug Applegate at CMU, along with other CLAS collaborators at JLab and the INFN, performing systematic studies of the $g11a$ data [9]. Most of this work, though not all of it, is detailed in Chapter 4. Also during this time, Matt, Zeb and I began working on a partial wave analysis of the $\gamma p \to p\eta$ and $\gamma p \to p\eta'$ channels using data from $g11a$. Matt and I also continued work on his previous $g1c$ $\gamma p \to p\pi^+\pi^-$ PWA. In the spring of 2006, we decided to expand our program to include final states with strangeness. Thus, Matt and I began working with Mike McCracken and Biblap Dey on the $\gamma p \to K^+\Lambda$ and $\gamma p \to K^+\Sigma^0$ channels, also using data from $g11a$.

By the summer of 2006, it was clear that the original version of our partial wave analysis software lacked the generality necessary to handle all of the channels now included in our group's PWA program. For this reason, I decided to completely rewrite the entire package from the ground up. The new software dealt with all of the known issues which had plagued the previous version, and has also handled many unforeseen difficulties since. By that fall, most of our systematic studies of $g11a$ were complete and I had produced $\gamma p \to p\omega$ differential cross sections which were in good agreement with the world's data. At this time, we also had obtained preliminary $p\eta$ and $p\eta'$ PWA results. It wasn't long until the $K^+\Lambda$ and $K^+\Sigma^0$ analyses were producing differential cross sections and preliminary PWA results as well.

With all of the other CMU partial wave analyses on firm ground, I was now free to focus on my thesis channel, $\gamma p \to p\omega$. The spring and early summer of 2007 were mainly devoted to the spin density matrix element measurements. This is when Curtis and I worked out the *probabilistic* background subtraction method found near the end of Chapter 3 [10]. It was also at this time that I began writing my thesis. All of the measurements presented in this document, both the differential cross section and spin density matrix elements, were completed by July 2007. I next turned my efforts towards performing a partial wave analysis of the $\gamma p \to p\omega$ channel. The work that I had put into ensuring the PWA software was general enough for all of the other CMU analyses paid off when I began working on my own channel. For the first time in years, my primary focus was on physics and not software development. Within about three months, I had obtained very promising preliminary partial wave analysis results. I then began diverting more of my time into writing this document, while still continuing to work towards completing the PWA. In the fall of 2007, I also began working closely with USC professor, and current CLAS collaboration chair, Dave Tedeschi on setting up a partial wave analysis of the $\gamma p \to p\phi$ channel using $g11a$ data. This work is still ongoing. The last month or so has been almost entirely dedicated to writing this thesis.

Acknowledgments

First off, I would like to thank Mario Lemieux for coming out of retirement as I was applying to graduate schools. This was my prime motivation for coming to CMU.

None of this work would have been possible without the guidance of my adviser, Curtis Meyer, who I also wish to thank for providing me with great freedom to pursue my ideas. I would like to thank Reinhard Schumacher, Brian Quinn, Gregg Franklin and Richard Jones for serving on my thesis committee and providing many helpful suggestions. I would also like to thank Reinhard for knowing everything there is to know about the CLAS detector, and imparting a small fraction of that knowledge to me. My discussions with Doug Applegate helped broaden my knowledge of computer science and provided me with some insight into what happens at CMU outside of the physics department.

I can not thank enough my office-mate Matt Bellis for the many productive discussions which have greatly improved the quality of this work. I also want to thank my primary study partner for the qualifying exam and most of my classes, Adam Lichtl, for his help and (more importantly) enthusiasm during some very very long work days.

I am indebted to professors Anis Maize, John Smetanka and Michael Botsko for all of their help, guidance and instruction during my undergraduate years. My study partners (and friends) Kip Boggs and Suman Chakrabarti made the work required to obtain degrees in both mathematics and physics much less painful. I would also like to thank my high school physics teacher, Michael Chovanec, for sparking my initial interest in this field of study.

There are also a number of people who I'd like to thank for *non-physics* reasons. First and foremost, I need to acknowledge the support of my family, especially my parents and my brother Erik. I would like to thank my mom for proof-reading this thesis. My two best friends, Tim and Ken, have been providing much needed distractions from work/school for most of my life. Finally, surviving graduate school would not have been possible without the camaraderie (*ie* numerous discussions at work, or in bars, about sports, music, etc. along with endless *you-tubing*) of Matt Bellis, Zeb Krahn, Mike McCracken, Kei Moriya, Ryan Dickson, Seamus Riordan, Ryan Booth, Brian Vernarsky and Alex Eggeman.

Contents

Chapter 1

Introduction and Overview

The principle question for which this work seeks to provide insight is: *What is happening inside of a nucleon?* Nucleons are known to be composite particles, *ie* they are made up of smaller constituents. Thus, they can be excited into unstable higher energy states. Quantum mechanics dictates that only a discreet subset of the continuum of higher energy states are allowed to be occupied. Collectively, these states are known as the *spectrum* of the nucleon. Studying the spectra of composite systems has yielded a number of great scientific discoveries. The spectrum of chemical elements, now grouped into the periodic table, inspired the concept of the atom, and atomic spectroscopy led to the development of quantum mechanics. The quantum numbers and energies, or masses, of the states that make up the nucleon spectrum are determined by the underlying physics of the system. Thus, understanding the nucleon spectrum is an important step towards answering the *principle* question proposed above.

The theory believed to govern the physics inside of the nucleon is known as Quantum Chromodynamics, or QCD. It is a highly non-linear theory which can not be solved analytically. For this reason, a first principles description of the nucleon spectrum is not yet possible; however, models which provide approximations to the full theory are available and predict the existence of many more excited nucleon states than have been observed experimentally. This dilemma is referred to as the *missing baryons* problem, and is the prime motivation for our analysis. One way to excite a nucleon is to *strike* it with a high energy photon. The photon and proton can combine to form an excited nucleon state. This state will then propagate for a very short time ($\sim 10^{-23}$ s) before decaying (possibly indirectly) to a ground state nucleon (a proton or neutron) and at least one other particle. Our work involves studying these types of events. Specifically, we are analyzing the reaction $\gamma p \rightarrow p \omega$, where γ denotes the high energy photon and p denotes a proton. The ω is an electrically neutral spin-1 isoscalar *meson* (a quark-antiquark object) with a mass of 782.59 MeV/c^2. The main properties of the ω are listed in Table 1.1. In this thesis, we will measure the differential cross section and ω spin density matrix elements for ~ 2000 ($\sqrt{s}, \theta_{CM}^{\omega}$) points (Chapter 7), then examine the production mechanisms by performing a *partial wave analysis* (Chapter 8). In this chapter, we will give a broad overview of QCD and the missing baryons problem. Previous measurements and analyses of $\gamma p \rightarrow p \omega$ will also be discussed.

1.1 QCD: Quantum Chromodynamics

Quantum Chromodynamics is the theory of the strong nuclear force, one of the four *fundamental* forces of physics along with electromagnetism, gravity and the weak nuclear force. QCD describes the interactions between *quarks* and *gluons*, the constituents of all strongly interacting subatomic particles (protons, neutrons, π's, ω's,...). Quarks are (currently believed to be) fundamental particles, *ie* they are not made up of smaller particles. The name originates (indirectly) from the the

J^P	Q	I	M(MeV/c^2)	Γ_{tot}(MeV)	$\Gamma_{\pi^+\pi^-\pi^0}/\Gamma_{tot}$	$\Gamma_{\pi^0\gamma}/\Gamma_{tot}$	$\Gamma_{\pi^+\pi^-}/\Gamma_{tot}$
1^-	0	0	782.59 ± 0.11	8.49 ± 0.08	$89.1 \pm 0.7\%$	$8.92 \pm 0.28\%$	$1.70 \pm 0.27\%$

Table 1.1: Properties of the ω meson. J^P: spin-parity, Q: electric charge, I: isospin, M: mass, Γ_{tot}: full width, $\Gamma_{\pi^+\pi^-\pi^0}$: $\omega \to \pi^+\pi^-\pi^0$ decay width, $\Gamma_{\pi^0\gamma}$: $\omega \to \pi^0\gamma$ decay width, $\Gamma_{\pi^+\pi^-}$: $\omega \to \pi^+\pi^-$ decay width. Only the three largest decay modes are listed, for a complete listing see the PDG [11].

phrase "Three quarks for Muster Mark" from the James Joyce novel *Finnegan's Wake* [12]. Quarks come in six different types, or *flavors*, each having its own antiparticle or antiquark. QCD has three types of charge as opposed to the single type found in electromagnetism (electric charge), referred to as red, green and blue which are collectively called *color charge* — hence the name of the theory. Each quark carries a color charge (red, green or blue) and also an electric charge. Antiquarks have the opposite color charge of quarks, referred to as anti-red, anti-green and anti-blue, along with the opposite electric charge. Table 1.2 summarizes the properties of the six flavors of quarks.

In the theory of Quantum Electrodynamics (QED), the electromagnetic force is mediated by massless vector bosons known as photons. In QCD, the strong nuclear force is also mediated by massless vector bosons, referred to as gluons — which *glue* the nucleon together. Unlike the photon in QED, the gluon carries the charge of QCD (color charge). Therefore, the theory of QCD consists of three basic types of interactions: (1) a quark emitting(absorbing) a gluon; (2) a gluon emitting(absorbing) a gluon; (3) direct interaction between two gluons. The presence of the latter two make the equations of QCD nonlinear and impossible to solve analytically. This complication has led to the development of a number of techniques for obtaining approximate solutions to the full theory. At very high energies, the strong force becomes weaker and perturbative techniques can be applied (pQCD); however, at *medium energies*, typically a few GeV (*eg* inside of a proton), QCD remains an enigmatic theory in need of more quantitative testing.

1.2   Spectroscopy

Spectroscopy is the study of interactions between matter and radiation. As discussed above, atomic spectroscopy played a key role in developing and understanding the theory of quantum mechanics. Studying atomic spectra also provided inspiration for a number of other important concepts, some of which later became integral components of QED. In this section, we will examine how measuring atomic spectra helped lay the foundations of modern physics. From this past success, a template will be constructed and applied to the excited nucleon spectrum. Finally, some of the aspects which make studying the nucleon spectrum such a difficult task will be discussed.

Name	Symbol	Charge(e)	Mass(MeV/c^2)
Up	u	$+2/3$	$1.5 - 3.0$
Down	d	$-1/3$	$3 - 7$
Strange	s	$-1/3$	95 ± 25
Charm	c	$+2/3$	1250 ± 90
Bottom	b	$-1/3$	4200 ± 70
Top	t	$+2/3$	$1.725 \pm 0.023 \times 10^5$

Table 1.2: Properties of the six flavors of quarks [11].
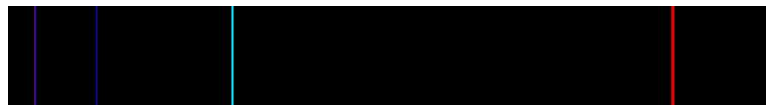
Figure 1.1: Visible emission spectrum for Hydrogen.

1.2.1 Atomic Spectroscopy

Atomic spectroscopy involves measuring the spectra of photons (light) emitted by atoms. During the latter half of the 19th century, large amounts of atomic spectral data were collected. Figure 1.1 shows an example of the visible emission spectrum for Hydrogen. Notice that only a discrete subset of wavelengths from the continuous spectrum are emitted. This fact puzzled physicists for decades until 1913 when Niels Bohr proposed his quantum theory of atomic Hydrogen which stated that electrons could only exist in a discrete set of orbits around the nucleus. When an electron jumps(falls) from one orbit to another, a single *quantum* of light (a photon) is absorbed(emitted). Bohr's model was able to explain the discreteness of the experimental spectral data and played an integral role in the development of the theory of quantum mechanics.

Studying atomic spectra also led Wolfgang Pauli to formulate the *Pauli Exclusion Principle*, which states that no two electrons can occupy the same quantum state at the same time. Pauli's theory led to the concept of intrinsic angular momentum, or *spin*, one of the most important components of Quantum Electrodynamics — the most successful theory in all of science. Thus, measuring atomic spectra provided physicists with a window into the inner workings of the atom. Interpreting this data, which took nearly half of a century, led to the development of a theory which (we currently believe) provides a complete understanding of electromagnetism. All of this work was done to answer the question: *What is happening inside of an atom?* We are trying to answer a very similar question: *What is happening inside of a nucleon?* As is often the case in science, we look towards past successes for guidance in our current pursuits.

The steps followed by experimental physicists, beginning over a century ago, to obtain the information necessary to understand the atom were:

- Excite atoms.

- Detect the radiation (photons) as they transition to more stable states.

- Map out the spectra.

Interpreting this information played a key role in the development of quantum mechanics and eventually QED. To follow this road map when studying the nucleon we should:

- Excite nucleons.

- Detect the radiation (photons,π's,ω's,...) as they transition to more stable states.

- Map out the spectra.

This is exactly the approach that we are taking; however, unlike the atom, which can be excited using domestic electricity (this is how fluorescent lights work), exciting a nucleon requires a large particle accelerator. Detecting the radiation emitted by atoms can be performed using a diffraction grating and, if the light is in the visible spectrum, ones eyes. Detecting the radiation emitted by nucleons requires complicated multi-component detector systems. These are just two of the hurdles that make mapping out the nucleon spectrum a difficult endeavor.
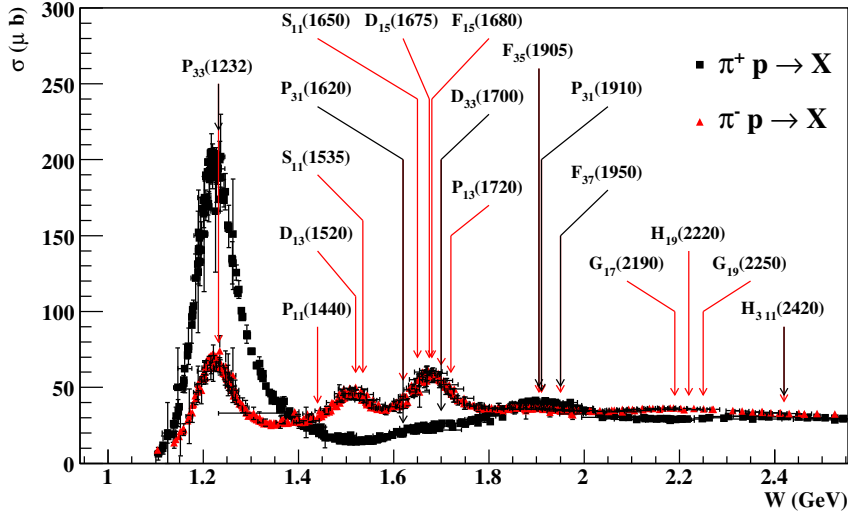
Figure 1.2: Nucleon resonances which have obtained a **** rating from the PDG [11]. The notation is $L_{2I2J}(M)$, where I is the isospin, J is the spin, L is the orbital angular momentum for the decay $X \to \pi p$ and M is the mass in (MeV/c^2). There are also six *** states which are not shown here.

1.2.2   Baryon Spectroscopy

Baryon spectroscopy — a *baryon* is an object made of three (constituent) quarks, such as a proton or neutron — is a very difficult field of study. As discussed in the previous section, performing an experiment to measure the spectrum requires a particle accelerator and a complex detector system. Interpreting the data is also quite difficult. According to the *Heisenberg Uncertainty Principle*, the energy of any unstable quantum state is spread over the range

$$\Delta E \approx \hbar/\tau, \tag{1.1}$$

where τ is the mean lifetime of the state. Therefore, atomic spectral lines are not infinitely sharp. Their widths are inversely proportional to the lifetimes of the excited states; however, the broadening of these lines is often small compared to their separation. Thus, the spectra are still easily identifiable (see Figure 1.1). The mean lifetimes of excited nucleons (known as resonances) are very small, typically $\sim 10^{-23}$ s, resulting in very large uncertainties in their energies causing the states to overlap. Advanced analysis techniques are required to overcome this complication.

The first baryon spectroscopy experiments were run in the 1960's using beams of pions (a *meson* made of a quark and antiquark). Figure 1.2 shows the *cross sections* (a concept discussed in Section 7.2) for $\pi p \to X$ along with all of the nucleon resonances which have obtained a **** (highest possible) rating from the PDG [11]. There are also six *** states listed in the PDG which are not shown in Figure 1.2. The severe overlap of the states makes it impossible to simply use the energy for identification. The quantum numbers of each nucleon resonance determine the angular distribution of its decay products. Thus, by measuring these decay distributions, as a function of energy, it is possible to identify nucleon resonance states. Of course, this is a quantum mechanical system, so interference effects must be taken into account. The technique used to extract the nucleon resonances is known as *partial wave analysis* and will be discussed in chapters 5, 6 and 8.

1.3 The Missing Baryons Problem

As mentioned at the beginning of this chapter, the ω is an isoscalar. Thus, the $p\omega$ final state only couples to resonances with $I = 1/2$, known as N^* states. From this point forward, we will restrict our discussion to these states, ignoring the $I = 3/2$ Δ^* states. There are ten N^* states with a **** PDG rating (see Figure 1.2) along with three *** rated states. By simply using the quark degrees of freedom, assuming that the nucleon is a three quark object, the number of states expected to exist is much higher than the number observed experimentally. This is known as the *missing baryons problem*, and is the prime motivation for our analysis. Inevitably, one is led to two possible conclusions: (1) the *missing* states exist but have not yet been observed experimentally; (2) the *missing* states simply do not exist. Both of these possibilities will be examined in this section. In Section 1.1, we noted that at the energies found inside of a nucleon, perturbative methods can not be used to obtain approximate solutions to QCD. Thus, pQCD can not be used to calculate the nucleon spectrum. In this section, we will examine the nucleon spectrum obtained using the two most prominent techniques for performing QCD calculations in this energy regime.

1.3.1 The Constituent Quark Model

In the *Constituent Quark Model* (CQM), the relevant degrees of freedom are in the valence quarks. The gluonic degrees of freedom are not excited. Table 1.3 shows the predicted N^* spectrum obtained from the CQM calculations of Capstick and Roberts [13]. The ratio of predicted to observed states is $\sim 4 : 1$. This particular model includes a number of relativistic effects, but the calculations are not carried out in a fully covariant framework. There are also a number of approximations regarding QCD which must be made to perform these types of calculations. Quark models still have some deficiencies and could be further refined; however, this is unlikely to reduce the number of predicted states [13]. Thus, further refinement of these models is not likely to resolve this issue. Below we present two possible solutions, within the Constituent Quark Model, to the missing baryons problem.

The Diquark Model

One possible solution to the missing baryons problem involves introducing the concept of a *diquark*, a system consisting of two tightly bound quarks, first proposed by Lichtenberg in 1968 [14]. The three-quark system is then replaced with a quark-diquark system when modeling the baryon. This approach reduces the number of effective degrees of freedom, which decreases the number of predicted states. Many of the states absent in the diquark model are not observed experimentally; however, there is currently no evidence from deep inelastic scattering to support the existence of any diquark clustering inside the baryon.

$N\pi$ Couplings

Another possibility, first proposed by Koniuk and Isgur in 1980 [15], suggests that the missing states may not couple strongly to the $N\pi$ system, which makes up the bulk of the existing scattering data. In fact, there are currently no **** resonant states which do not have a **** coupling to $N\pi$. If an N^* state exists but couples weakly to $N\pi$, then it would most likely not have been observed by the previous experiments. A number of the missing states in the CQM are predicted to have very small $N\pi$ branching fractions, suggesting that experiments need to be run which do not involve the $N\pi$ system. Measuring the reaction $\gamma p \to p\omega$ is one such experiment. We also note here that Capstick [16] predicts a number of the missing N^* resonances do have fairly strong couplings to γp and $p\omega$. Thus, experimental measurements in this channel, and other non-$N\pi$ channels, are needed to truly test these theories.

J^P	M_{CQM}	M_{PDG}	Rating	J^P	M_{CQM}	M_{PDG}	Rating
$1/2^-$	1460	1535	****	$1/2^+$	1540	1440	****
$1/2^-$	1535	1650	****	$1/2^+$	1770	1710	***
$1/2^-$	1945	2090	*	$1/2^+$	1880		
$1/2^-$	2030			$1/2^+$	1975		
$1/2^-$	2070			$1/2^+$	2065	2100	*
$1/2^-$	2145			$1/2^+$	2210		
$1/2^-$	2195						
$3/2^-$	1495	1520	****	$3/2^+$	1795	1720	****
$3/2^-$	1625	1700	***	$3/2^+$	1870		
$3/2^-$	1960	2080	**	$3/2^+$	1910		
$3/2^-$	2055			$3/2^+$	1950		
$3/2^-$	2095			$3/2^+$	2030		
$3/2^-$	2165						
$3/2^-$	2180						
$5/2^-$	1630	1675	****	$5/2^+$	1770	1680	****
$5/2^-$	2080			$5/2^+$	1980	2000	**
$5/2^-$	2095	2200	**	$5/2^+$	1995		
$5/2^-$	2180						
$5/2^-$	2235						
$5/2^-$	2260						
$5/2^-$	2295						
$5/2^-$	2305						
$7/2^-$	2090	2190	****	$7/2^+$	2000	1990	**
$7/2^-$	2205			$7/2^+$	2390		
$7/2^-$	2255			$7/2^+$	2410		
$7/2^-$	2305			$7/2^+$	2455		
$7/2^-$	2355						
$9/2^-$	2215	2250	****	$9/2^+$	2345	2220	****
$11/2^-$	2600	2600	***				
$11/2^-$	2670						
$11/2^-$	2700						
$11/2^-$	2770						
$13/2^-$	2715						

Table 1.3: Constituent Quark Model predictions for the N^* spectrum from Capstick and Roberts [13]. All masses, M_{CQM} and M_{PDG}, are in units of MeV/c^2. The ratio of predicted to observed states is $\sim 4 : 1$.

1.3.2 Lattice QCD

Lattice QCD (LQCD) is the study of quantum chromodynamics on a space-time that has been discretized onto a lattice. Over the past several decades, LQCD has developed into a powerful method for calculating quantities in the non-perturbative regime of QCD. Formulating QCD on a discrete, as opposed to a continuous, space-time facilitates studying the theory by simulation on a computer. The behavior of the continuum theory can be recovered by performing simulations using increasingly large lattices, while also decreasing the lattice spacing. Discretization also naturally introduces an ultraviolet cutoff of the order of the inverse of the lattice spacing $(1/a)$, which regularizes the theory [17].

Discretizing QCD is performed by defining quark field variables on the sites of a hypercubic space-time lattice. To preserve gauge invariance, parallel transporters (representing the gauge degrees of freedom) are introduced on the links. Since the Lie group of QCD is $SU(3)$, this means that there is a 3×3 special unitary matrix defined on each link. Additionally, the time variable is analytically continued (Wick rotated) to imaginary time, replacing the Minkowski metric with a Euclidean one. This transforms the oscillatory time evolution operator into an exponential damping operator

$$e^{iH(t-t')} \rightarrow e^{-a_\tau H}, \tag{1.2}$$

where H is the Hamiltonian of the theory and a_τ is the temporal lattice spacing. This permits the use of computational techniques developed in the field of statistical mechanics [18].

The spectrum can be accessed by considering the two-point function, or *correlator*, of an interpolating operator $\bar{\mathcal{O}}$ [17]

$$C(\tau) \equiv \langle \mathcal{O}(\tau)\bar{\mathcal{O}}(0) \rangle. \tag{1.3}$$

If the lattice is sufficiently large temporally, then $C(\tau)$ is effectively the amplitude for the Euclidean propagation of the state created by the action of $\bar{\mathcal{O}}$ on the vacuum

$$C(\tau) = \langle 0|\mathcal{O}e^{-H\tau}\bar{\mathcal{O}}|0 \rangle. \tag{1.4}$$

The correlator can be decomposed into its spectral components by inserting the complete set of energy states $|k\rangle$:

$$C(\tau) \quad = \quad \langle 0|\mathcal{O}\sum_{k=0}^{\infty}|k\rangle\langle k|e^{-H\tau}\bar{\mathcal{O}}|0\rangle \tag{1.5a}$$

$$= \quad \sum_{k=1}^{\infty}|\langle k|\bar{\mathcal{O}}|k\rangle|^2 e^{-E_k\tau}, \tag{1.5b}$$

using the choice $\langle 0|\bar{\mathcal{O}}|0\rangle = 0$. For large time separations τ, the correlator is dominated by the lowest energy state accessible by applying $\bar{\mathcal{O}}$ to the vacuum. Thus, operator design is a crucial component of extracting the spectrum. Operators must be constructed to maximally overlap the states $|k\rangle$ of interest with minimal overlap of all other modes.

The correlators are calculated using the Monte Carlo technique resulting in an uncertainty at each τ. To prevent this *noise* from masking the signals, two types of smearing are performed which replace the site variables with weighted local spatial averages. Quark field smearing reduces the coupling of the operators $\bar{\mathcal{O}}$ to the contaminating short-wavelength modes. Gauge link smearing attenuates the noise in the operators themselves [17]. What we've presented here is a simplified overview of how to calculate the QCD spectrum on the lattice. There are a number of difficulties which must be overcome to cleanly extract the excited states. For example, the operator $\bar{\mathcal{O}}$ in (1.4) can be replaced by a basis of operators to define a *correlator matrix*. Diagonalizing this matrix facilitates extraction of multiple excited states. These topics are discussed in detail in [19].

J	1/2	3/2	5/2	7/2	9/2	11/2	13/2
$n_{G_1}^J$	1	0	0	1	1	1	1
n_H^J	0	1	1	1	2	2	2
$n_{G_1}^J$	0	0	1	1	0	1	2

Table 1.4: Degeneracies in the spinorial irreducible representations (irreps) of the double octahedral group, O^D, of continuum spin-J states under discrete lattice rotations. While there are an infinite number of continuum spin-J states, there are only three spinorial irreps of the lattice rotation group. Thus, continuum spin-J states appear as degenerate levels in one or more channels on the lattice [18].

The spin of a state, J, determines how it transforms under continuum rotations. Connecting lattice states to continuum states of total angular momentum J requires an examination of rotations on a discretized lattice. The group of discrete rotations of a cube, a subgroup of the continuum rotation group $SO(3)$, is known as the octahedral crystal point group, O. In the continuum, the rotational group of half-integral spin states is $SU(2)$. Since $SU(2)$ is a double cover of $SO(3)$, a double cover of O is needed for the discrete case as well. This is obtained by augmenting O with an additional generator of 2π rotations about any axis which is distinct from the identity element, the resulting group is referred to as the double octahedral group, O^D. The spinorial (baryonic) irreducible representations (irreps) of O^D are the two-dimensional irreps G_1 and G_2 along with the four-dimensional irrep H. Table 1.4 shows the mapping of continuum spin-J states to lattice degeneracies in the irreps of O^D. Thus, a two-dimensional spin-1/2 state maps directly into a two-dimensional G_1 lattice state, while a four-dimensional spin-3/2 state maps directly into a four-dimensional H lattice state. A six-dimensional spin-5/2 state transforms like a tensor product of a two-dimensional G_2 state and a four-dimensional H state, both with the same mass. Thus, the presence of a pair of degenerate states, in these two channels on the lattice, is the signature of a spin-5/2 continuum state [18].

Parity is the same on the lattice as it is for the continuum. The LQCD convention is to denote even parity g and odd parity u. Therefore, the final set of irreps are G_{1g}, H_g, G_{2g} for even parity states and G_{1u}, H_u, G_{2u} for odd parity states. Figure 1.3(a) shows the nucleon spectrum obtained by Lichtl et al [19] using 200 quenched $12^3 \times 48$ anisotropic lattice configurations with parameters $a_s \sim 0.1$ fm, $a_s/a_\tau \sim 0.3$ and $m_\pi \sim 700$ MeV (the lower the pion mass, the more cpu intensive the calculation). The quenched approximation neglects the effects of quark loop diagrams, or equivalently, the effects of the dynamical sea quarks. Figure 1.3(b) shows the experimentally observed nucleon spectrum projected onto the irreps of the lattice. Even though this study was performed under the quenched approximation and at an unphysically high pion mass, there are several encouraging features present in Figure 1.3. The single low-lying state in the G_{1g} channel corresponds to the proton (recall from Table 1.4 that a $J = 1/2$ continuum state corresponds to a single G_1 state on the lattice). The lattice is also able to (qualitatively) reproduce the low-lying band of odd parity states seen in the experimental spectrum.

The lattice formulation of QCD is an extremely powerful method for performing calculations in the non-perturbative regime. The work of [19] represents tremendous progress towards calculating the resonance spectrum of QCD from first principles. Improved LQCD calculations are currently underway. These calculations are unquenched and are using multiple volumes and pion masses to help determine the systematic effects of the lattice parameters. Though LQCD has not yet reached a stage where it can make a statement about the *missing barons problem*, accurate calculations of the QCD nucleon spectrum should be obtainable from the lattice in the near future. At that time, experimental measurements of the spectrum will be able to provide a true quantitative test of QCD in the non-perturbative regime.
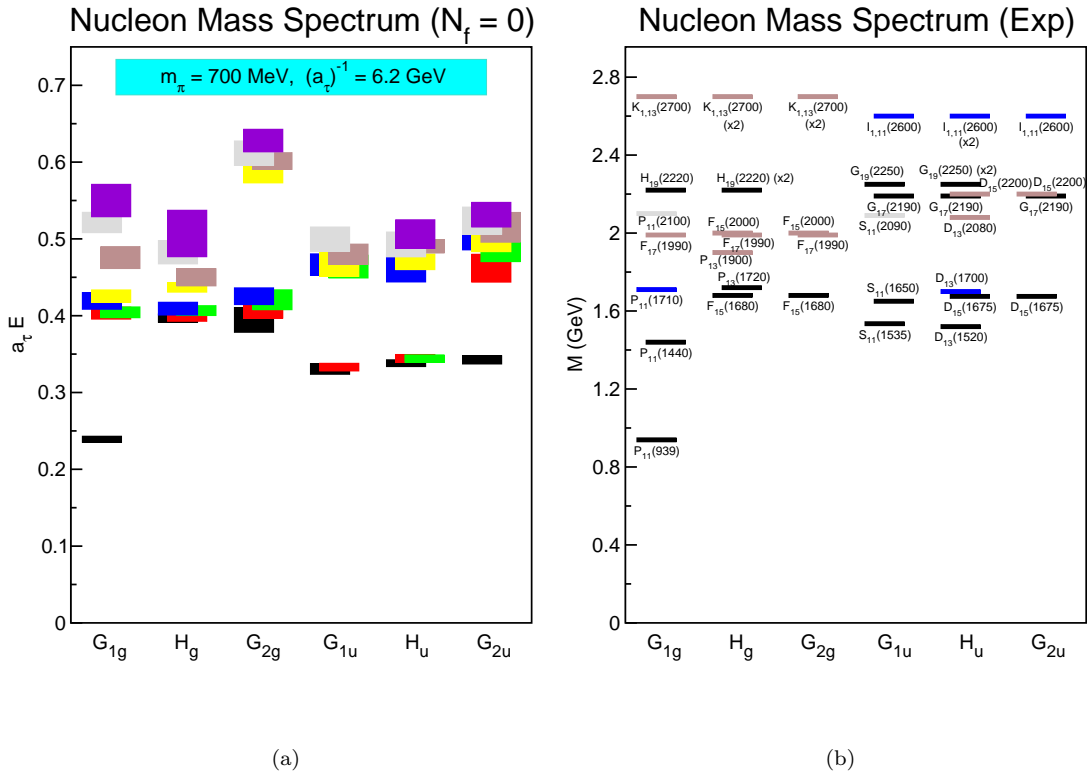
Figure 1.3: Nucleon spectra [19]. (a) Predicted from 200 quenched $12^3 \times 48$ lattice configurations using the anisotropic Wilson action with $a_s \sim 0.1$ fm, $a_s/a_\tau \sim 0.3$ and $m_\pi \sim 700$ MeV. The vertical heights of the boxes indicate the statistical uncertainties. (b) Determined by experiment, with PDG ratings ****(black), ***(blue), **(light brown) and * (light gray), projected onto the irreducible representations of the lattice. A more detailed discussion, including a comparison of the two spectra, is given in the text.

1.4 Physical Observables in Vector Meson Photoproduction

A complete description of ω photoproduction requires $2 \times 2 \times 2 \times 3 = 24$ complex helicity amplitudes; however, parity invariance reduces the number of independent amplitudes to 12. Thus, there are 23 independent real numbers needed to completely describe the reaction $\gamma p \to p\omega$ (the overall phase is irrelevant). Using *bilinear helicity products*, the number of observables is found to be $12^2 = 144$. Clearly, there is a lot of redundant information in these observables. Unlike the pseudoscalar case, a complete description of the vector meson photoproduction amplitudes can not be obtained using only single and double spin observables. Triple and quadruple spin observables are required to perform a complete ω photoproduction experiment [20]. In this analysis, we have measured the differential cross section and three spin density matrix elements at ~ 2000 $(\sqrt{s}, \theta_{CM}^{\omega})$ points (see Chapter 7). The remaining 19 observables required to *complete* the measurement are only obtainable using a polarized beam and/or target and/or a recoil proton polarization measurement (probably not feasible in the near future). Even without a full experimental determination of all 12 complex helicity amplitudes, it is possible to extract useful dynamical information for ω photoproduction from the subset of observables presented in this work.

1.5 Previous $\gamma p \to p\omega$ Measurements

While ω photoproduction has been studied for more than 40 years, recent advances in accelerator and detector technologies have greatly improved the quality of the world's data in this reaction. The first modern experiment to study this channel was SAPHIR, which published mostly forward angle differential cross sections in 1998 [21]. These results were followed by CLAS [22] and SAPHIR [23] (with higher statistics and better kinematic coverage than their 1998 publication), both of which published results in 2003. In this section, we will examine previous $\gamma p \to p\omega$ measurements made in the energy regime in which our analysis was performed, 1.72 GeV $< \sqrt{s} <$ 2.84 GeV.

1.5.1 Pre-CLAS/SAPHIR

In the 1970's and early 1980's, ω photoproduction experiments were run at SLAC and Daresbury. In 1973, Ballam et al [24] published differential cross section and spin density matrix element measurements at $E_\gamma = 2.8$ GeV using data collected at SLAC. The data were obtained by exposing a hydrogen bubble chamber to monochromatic photons from the SLAC backscattered laser beam. In 1984 (Barber et al [25]) and 1977 (Clift et al [26]), the LAMP2 group measured differential cross sections and spin density matrix elements using data collected at the NINA electron synchrotron located at Daresbury, Warrington, UK. The detector consisted of a tagging system, multi-wire proportional chambers and a lead glass calorimeter. The 1984 measurements were only at very forward angles, while the 1977 results were only at very backwards angles.

Figure 1.4 shows the differential cross sections from each of these experiments. There is almost no data in the transverse direction. The forward angle data are in decent agreement. The large peak in this region is typical of a t-channel production mechanism. The backwards angle data have an interesting *dip* near $\cos\theta_{CM}^{\omega} \sim -0.95$. At this energy, this corresponds to the value of u where the non-degenerate Regge nucleon propagator contains a node. Unfortunately, no other experimental data exists at these kinematics to confirm this interesting feature of the cross section. Figure 1.5 shows the spin density matrix elements, $\rho_{MM'}^0$, from these experiments. Only forward angle results were published. Extracting $\rho_{MM'}^0$ elements requires examining the orientation of the ω decay plane with respect to the scattering plane — a three-dimensional problem. Thus, the statistical uncertainties are much larger for this set of measurements. These results provided a good first step towards understanding ω photoproduction; however, more precision and more transverse data would be necessary to truly investigate the production mechanisms at these energies.
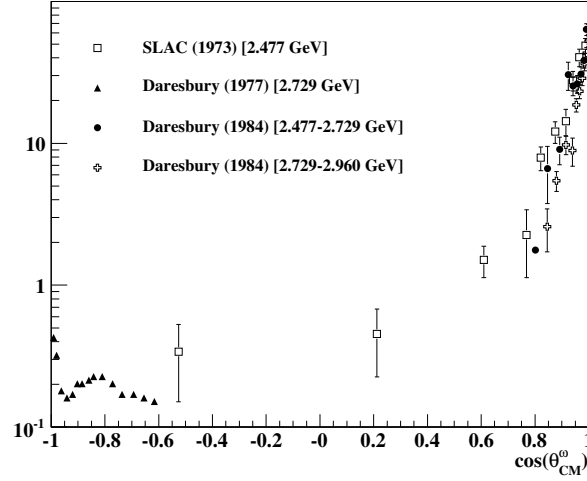
Figure 1.4: $\frac{d\sigma}{d\cos\theta^\omega_{CM}}(\mu b)$ vs $\cos\theta^\omega_{CM}$: Differential cross sections published by SLAC in 1973 [24] and Daresbury in 1977 [26] and 1984 [25]. The Daresbury 1977 points have no error bars (the points were extracted from a PDF image).
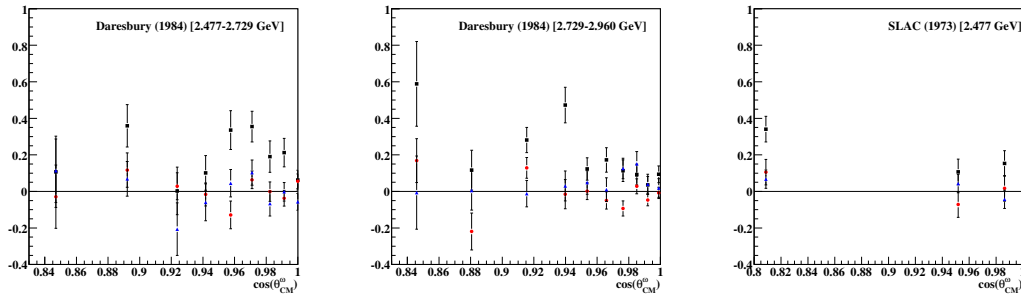
Figure 1.5: Spin density matrix elements, in the Adair frame, vs $\cos\theta^\omega_{CM}$: (a),(b) Daresbury [25], (c) SLAC [24]. The black squares are ρ^0_{00}, the red circles are ρ^0_{1-1} and the blue triangles are $Re(\rho^0_{10})$.
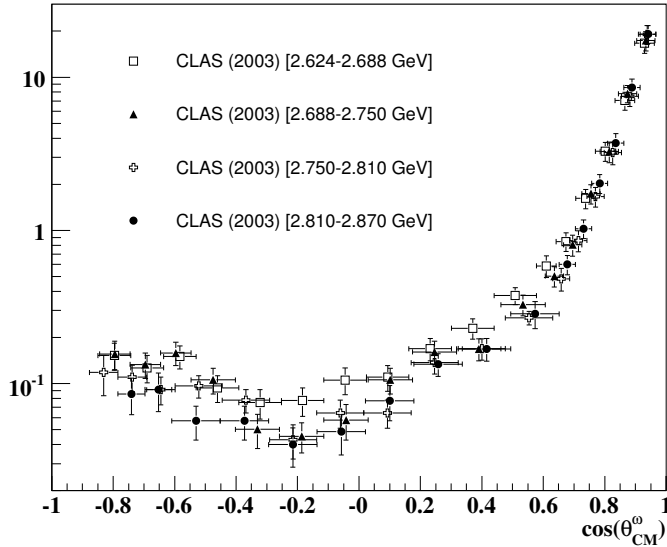
Figure 1.6: $\frac{d\sigma}{d\cos\theta^{\omega}_{CM}}(\mu b)$ vs $\cos\theta^{\omega}_{CM}$: Differential cross sections published by CLAS in 2003 [22].

1.5.2   CLAS 2003

In January 2003, the CLAS collaboration (Battaglieri et al [22]) published differential cross section measurements for $\gamma p \rightarrow p\omega$ in the energy range 2.624 GeV $\leq \sqrt{s} \leq$ 2.87 GeV. Thus, these results overlap those of SLAC [24] and Daresbury [25] discussed in the previous section. The CLAS measurements, shown in Figure 1.6, greatly increased the precision of the world's cross section data in the transverse direction; however, no spin density matrix element results were published. The CLAS detector, which was also used in our analysis, is discussed in detail in Chapter 2.

1.5.3   SAPHIR 2003

In October 2003, the SAPHIR collaboration (Barth et al [23]) published differential cross section and spin density matrix element measurements for $\gamma p \rightarrow p\omega$ in the energy range from threshold up to $\sqrt{s} = 2.4$ GeV. These results greatly increased the precision and kinematic coverage of the 1998 publication [21]. The SAPHIR detector is a large acceptance spectrometer located at the Bonn electron stretcher ring ELSA. The accepted solid angle is $\sim 0.6 \times 4\pi$ Sr — due to pieces of the magnetic poles. Photons are produced from the ELSA electron beam via bremsstrahlung radiation. Their energies are determined using a tagging system, which is also used (along with a photon veto counter) to measure the photon flux. Drift chambers are utilized to track charged particles which are bent in a magnetic field, providing momentum determination and a scintillator wall provides time-of-flight information used to determine particle identification. The SAPHIR differential cross sections, shown in Figure 1.7, were the first high precision measurements in this energy range. The (nearly) complete kinematic coverage also provided a first look at the near threshold transverse cross section, which is suggestive of resonance production. The SAPHIR collaboration also made spin density matrix element measurements in both the Helicity and Gottfried-Jackson frames (see Appendix A). These results, shown in Figure 1.8, were the first ever published in this energy regime. Polarization information is vitally important for determining production mechanisms; more precise measurements at these energies are needed.
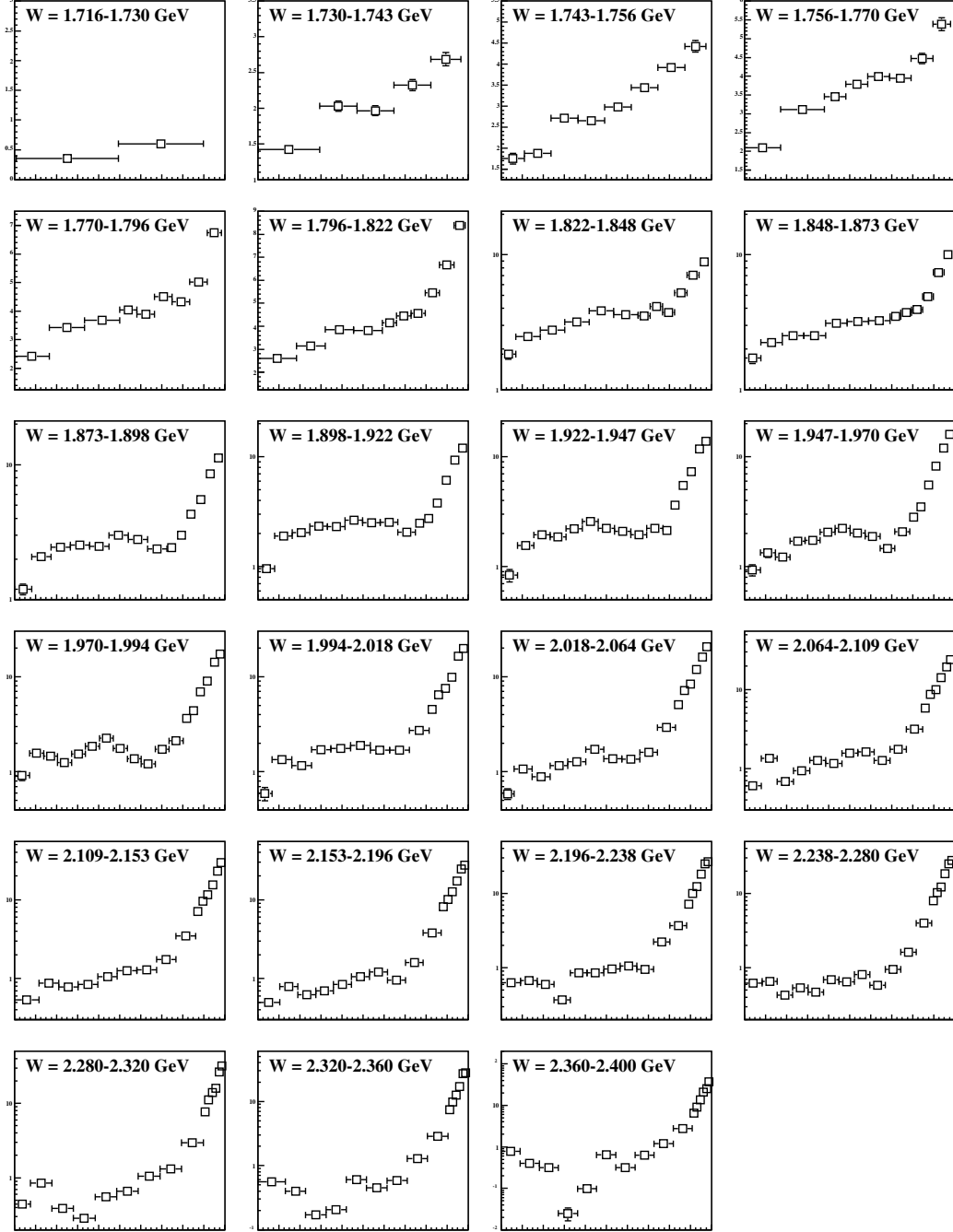
Figure 1.7: $\frac{d\sigma}{d\cos\theta^{\omega}_{CM}}(\mu b)$ vs $\cos\theta^{\omega}_{CM}$: Differential cross sections published by SAPHIR in 2003 [23].
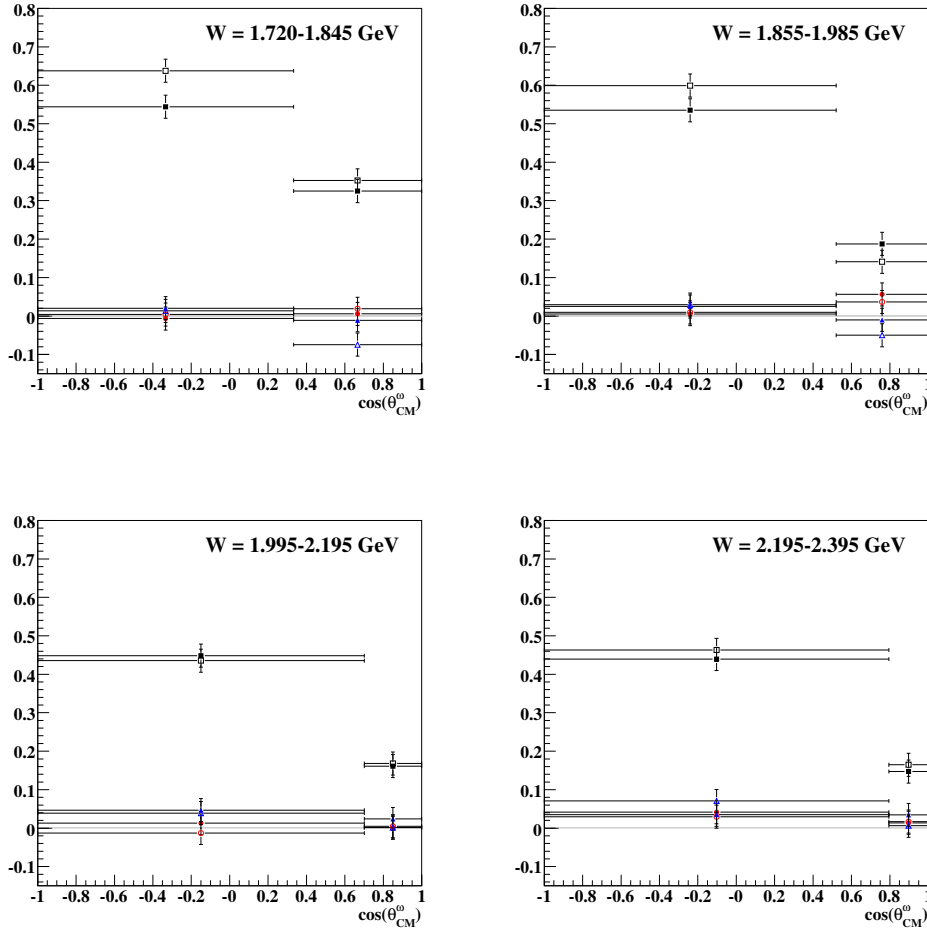
Figure 1.8: Spin density matrix elements, in the Adair frame, vs $\cos\theta^{\omega}_{CM}$ from SAPHIR [23]: The black squares are ρ^0_{00} fit in the (filled) Helicity and (open) Gottfried-Jackson frames. The red circles are ρ^0_{1-1} fit in the (filled) Helicity and (open) Gottfried-Jackson frames. The blue triangles are $Re(\rho^0_{10})$ fit in the (filled) Helicity and (open) Gottfried-Jackson frames.

1.6 Previous $\gamma p \to p\omega$ Partial Wave Analyses

In recent years, several attempts to extract resonant contributions to ω photoproduction have been made. All of the authors agree that the forward cross section is dominated by t-channel π^0 exchange. Most of the work done on this channel was fit to the 1998 SAPHIR data [21], which consisted only of moderately forward differential cross sections. In 2001, Zhao [27] used an effective quark model Lagrangian approach and found the dominant resonance contributions to be from the $P_{13}(1720)$ and $F_{15}(1680)$. Also in 2001, Oh, Titov and Lee [28] used the resonance parameters from the quark model calculations of [13] and extracted strong contributions from a $P_{13}(1910)$ (a *missing* state) and the $D_{13}(2080)$ (a ** state). The next year, Titov and Lee [29] applied an effective Lagrangian approach and found the dominant resonant contributions near threshold to be from the $D_{13}(1520)$ and $F_{15}(1680)$. Also in 2002, Penner and Mosel [30] used a coupled channel approach and extracted dominant $P_{11}(1710)$ and $D_{13}(1900)$ (a *missing* state) contributions.

A more recent analysis by Penner and Mosel [31] is the only work to fit the SAPHIR 2003 results [23], which include (very coarse) spin density matrix element measurements. The $P_{11}(1710)$ and $D_{13}(1900)$ resonances, found to be dominant in their previous analysis, are still present but with reduced significance. The newer analysis finds the dominant contributions to be from the $D_{15}(1675)$ and $F_{15}(1680)$. They also find a small contribution from a missing $F_{15}(1946)$ state. Clearly, inclusion of the spin density matrix measurements, $\rho^0_{MM'}$, has a significant impact on the extracted resonances. Penner and Mosel note [31]: *Since the $\rho_{\lambda\lambda'}$ put strong constraints on the $\gamma p \to p\omega$ reaction mechanism there is urgent need for precise measurements of the spin density matrix in more narrow energy bins to pin down the reaction picture.* This also calls into question how much faith should be placed in the resonances extracted by these analyses. The spin density matrix element measurements presented in this work, which include ~ 2000 ($\sqrt{s}, \theta^\omega_{CM}$) points (see Chapter 7) are ~ 250 times more precise than those used in [31]. Thus, our partial wave analysis (see Chapter 8) will be the first in this channel to benefit from high precision polarization information.

1.7 Summary

A lot of work has been performed over the past 40+ years on ω photoproduction; however, the lack of precise polarization information has made it difficult to determine the nature of the production mechanisms. Our measurements (presented in Chapter 7 of this thesis), which include differential cross section and spin density matrix element results in ~ 2000 ($\sqrt{s}, \theta^\omega_{CM}$) bins, represent the first high precision polarization measurements for $\gamma p \to p\omega$. The recent progress of Lattice QCD towards calculating the nucleon spectrum from first principles will soon make it possible to quantitatively test Quantum Chromodynamics in the non-perturbative regime. Therefore, the experimental nucleon spectrum must be solidified. Recent efforts to explain the missing baryons problem suggest that previously unobserved nucleon resonance states may contribute to ω photoproduction. Thus, it is imperative that the resonance contributions to this channel be extracted. Our efforts in this area are presented in Chapter 8.

Chapter 2

Jefferson Lab, CEBAF and the CLAS detector

The data used in our analysis were taken as part of the $g11a$ run period during the summer of 2004 at the Thomas Jefferson National Accelerator Facility (TJNAF), also referred to as Jefferson Laboratory or JLAB, in Newport News, Virginia. There are currently three experimental halls at JLAB, denoted as A, B and C, along with the CEBAF electron accelerator, a free-electron laser and a number of other research and manufacturing facilities. An aerial view of the lab is shown in Figure 2.1. The $g11a$ run period — part of experiment E04021, *Spectroscopy of Excited Baryons with CLAS: Search for Ground and First Excited States* — was conducted in Hall B. The goal of the experiment was to carry out a high statistics search for the Θ^+ pentaquark state [32]; however, the experiment also provided high statistics datasets for a number of other final states, including $p\omega$. The run conditions called for a photon beam incident on a proton target. Producing a photon beam required use of both the CEBAF accelerator and the photon tagging system located in Hall B. The proton target was actually Hydrogen, kept in its liquid state by a cryogenic system.

The detector used for $g11a$ was the CEBAF Large Acceptance Spectrometer (CLAS) which was housed in Hall B. CLAS is optimized for the detection of multi-particle final states. The large acceptance of the CLAS detector, along with the continuous nature of the CEBAF electron beam and the quality of the Hall B data acquisition system (capable of recoding over 1 TB of data each day) led to production of the world's largest multi-particle dataset in the energy range 1.55 GeV $< \sqrt{s} < 2.84$ GeV. In this chapter, we will discuss in detail the CEBAF accelerator, CLAS detector and several other hardware devices which played key roles during $g11a$.

2.1 CEBAF: Continuous Electron Beam Accelerator Facility

The Continuous Electron Beam Accelerator Facility (CEBAF) delivers electron beams to the three experimental halls at Jefferson Lab. The major advancement first employed at CEBAF was providing the acceleration gradient using superconducting radio frequency (RF) cavities. Prior to CEBAF, copper RF cavities had been used. The resistivity of the copper caused the cavities to heat up during use which, in turn, required significant cooling time between beam spills. Superconducting cavities are non-resistive, allowing CEBAF to obtain a 100% duty factor. The continuous delivery of electrons permits quick acquisition of high statistics datasets even at low current (often required by coincidence experiments). A schematic which displays the major accelerator components is shown in Figure 2.2.
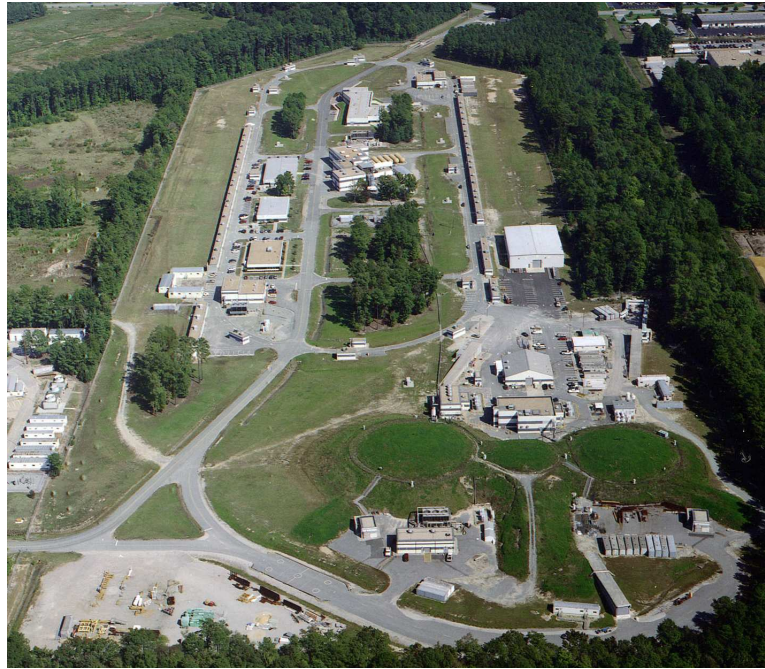
Figure 2.1: An aerial view of the Thomas Jefferson National Accelerator Facility (TJNAF), also referred to as JLAB. Image Source: [33].
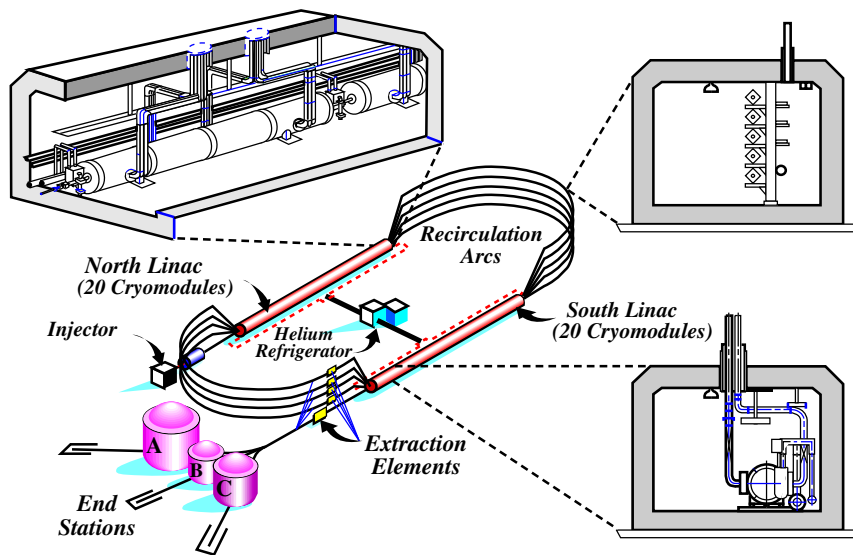

Figure 2.2: Schematic diagram of the Continuous Electron Beam Accelerator Facility (CEBAF). The electron beam, which begins its first orbit at the injector, is accelerated by the two LINACs to a maximum energy of 6 GeV. The beam can make up to 5 orbits, or passes, prior to being directed towards one of the experimental halls (A, B or C). Image Source: [34].
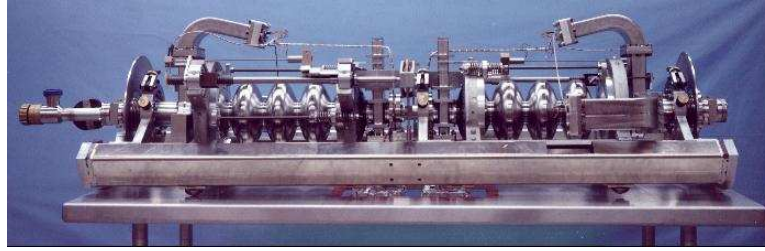
Figure 2.3: A pair of CEBAF's superconducting RF cavities, shown here with support hardware and beam pipe. Image Source: [33].

Production of the CEBAF electron beam begins at the injector. The electrons are obtained by illuminating a GaAs photocathode with pulsed lasers. The laser pulses are fixed temporally such that each experimental hall receives electron bunches every 2 ns. After extraction from the photo-cathode, 2 1/4 superconducting RF cavities are used to accelerate the electrons to 45 MeV [35]. The injector system then employs an optical chopper to cleanly separate the bunches prior to sending them to CEBAF's recirculating linear accelerators (LINACs).

The recirculating LINACs each contain 168 superconducting RF Niobium cavities. Figure 2.3 shows a picture of a RF cavity assembly. Each cavity is immersed in liquid Helium and cooled to -271°C, the temperature at which it becomes superconducting. The acceleration gradient for the electron beam is provided by setting up radio frequency standing waves in the cavities. The standing waves were kept in phase with the electron bunches resulting in a continuous positive electric force on each bunch as it passed through a cavity (see Figure 2.4). CEBAF has two such LINACs located along the *straightaways* of the 7/8 mile *racetrack* course. Each LINAC is capable of providing 600 MeV of acceleration, although there are plans to nearly double this in a few years. The LINACs are connected by nine recirculating arcs, allowing the beam to make up to five passes through each LINAC, obtaining a maximum energy of $\sim$ 6 GeV, prior to extraction by the experimental halls. Extraction of the beam by the halls is performed using RF separator cavities. Each hall can choose to extract the beam after any number of passes (not exceeding the maximum number of five), giving the halls control over their energy. We also note here that while any number of halls could run at the maximum energy, no two halls could run with the same lower energy [35]. After extraction, each beam pulse was then directed towards either Hall A, B or C.
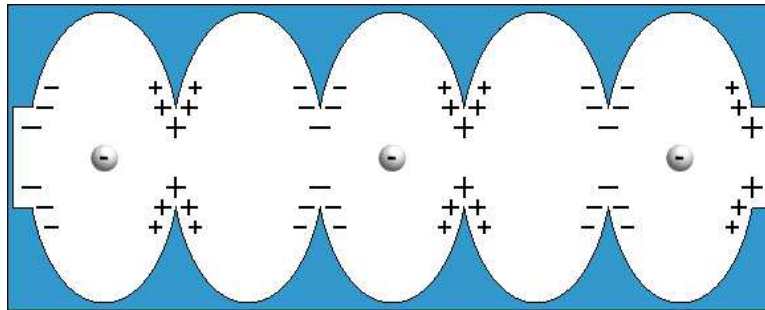

Figure 2.4: The acceleration gradient was provided by establishing standing waves tuned such that an electron always experienced a positive electric force while propagating through the cavity [36].
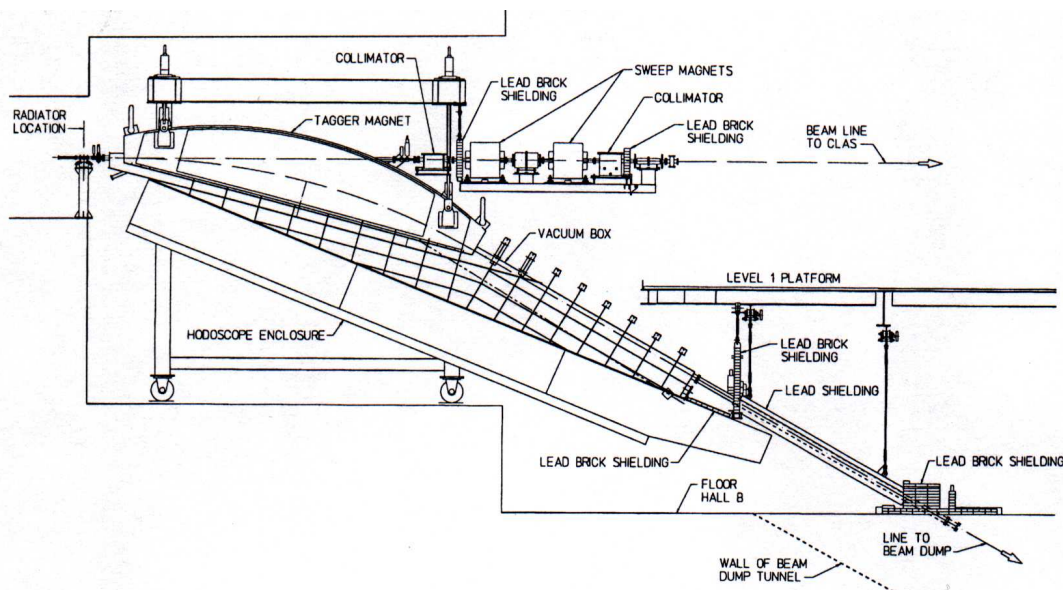
Figure 2.5: The Hall B photon tagging system. The main components include the radiator, magnetic spectrometer and collimators. Image Source: [37].

2.2 The Photon Tagger

Converting the CEBAF electron beam into a photon beam is handled by the Hall B tagging system, a schematic diagram of which is shown in Figure 2.5. When the electron beam interacts with a gold foil radiator, photons are produced via bremsstrahlung radiation. The high atomic number of gold helps reduce contamination of photons produced by electron-electron scattering. A radiator of thickness 10^{-4} radiation lengths was used during $g11a$ production runs, while a much thiner radiator was used during *normalization* runs. After passing through the radiator, the beam was a mixture of non-interacting electrons, recoil electrons and photons. A dipole magnetic field was then used to sweep the electrons out of the beam, allowing the photons to proceed towards the CLAS target. The magnetic field directed the recoil electrons towards the two hodoscope planes, each made of overlapping arrays of scintillators, of the tagger spectrometer.

The first scintillator plane, referred to as the E-plane, was used to determine the momentum of the recoiling electrons. It consisted of 384 paddles that were 20 cm long, 4 mm thick and from 6 to 18 mm wide. The paddles were arranged in an overlapping fashion, increasing the number of logical paddles to 767. The trajectory followed by an electron in the magnetic field is governed by its momentum. Thus, by determining which paddle an electron passed through, we can calculate its momentum. The momentum of the recoil electron can then be used to obtain the energy of the photon. The energy resolution of the E-plane is 0.1% of the incident electron beam energy. The second scintillator plane, referred to as the T-plane, was used to make accurate timing measurements of the recoiling electrons. This plane was comprised of 61 paddles that were each 2 cm thick. The added thickness of these paddles allowed for a timing resolution of 110 ps. The spectrometer was able to tag photons ranging from 20–95% of the incident electron beam energy. Figure 2.6 shows a schematic diagram of the tagger spectrometer.
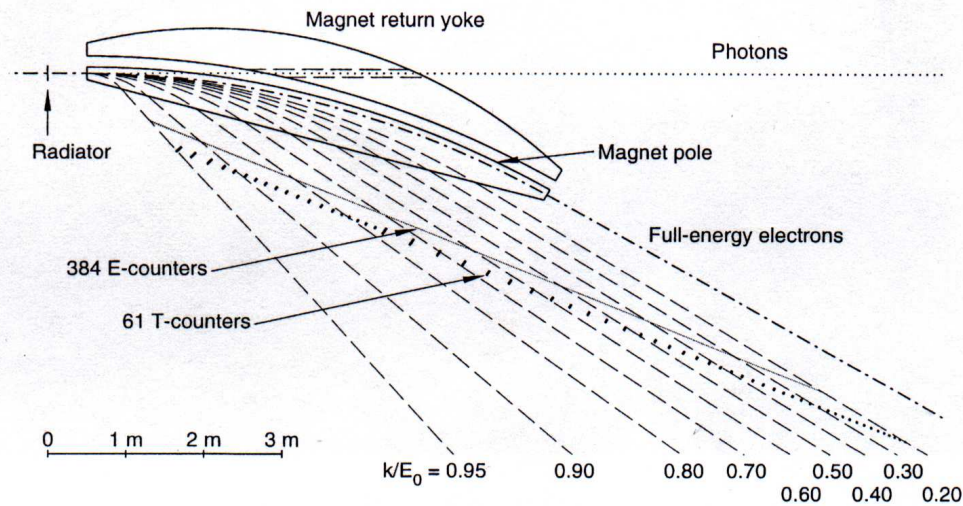
Figure 2.6: Schematic diagram of the tagger spectrometer. The dashed lines show the trajectories followed by recoil electrons of various fractional energies. Both hodoscope scintillator planes, the E- and T-planes, are accurately depicted geometrically and with the correct segmentation. Image Source: [37].

The signals produced by the scintillator paddles were read out using photomultiplier tubes (PMTs). The T-counter PMT signals, which satisfied a discriminator, were sent to the *Master OR* (MOR) and an array of FASTBUS TDCs. The MOR is an important part of the $g11a$ trigger, discussed in Section 2.5. The TDC array was used to extract the timing information from the T-counters and also to count the total number of hits registered in the tagger for use during normalization calculations. This timing information was used to correctly associate photons with events in the CLAS detector. The E-counter PMT signals were also sent through a discriminator and then forwarded to a multi-hit TDC. The timing signals from both the E- and T-counters were written into the data stream and used during offline analysis to establish coincidence between paddles, *ie* used to determine which sets of signals corresponded to an electron passing through the two planes of the tagger spectrometer. Figure 2.7 shows a schematic diagram of the front-end electronics of the Hall B tagging system.

The Hall B tagging system is also used (during offline analyses) to determine the event *start time*. The timing resolution of the tagger is good enough to identify which RF beam bucket each photon is associated with. The RF signal obtained from the accelerator is the most accurate timing information available in the entire experiment. The event vertex time — or time at which all the final state particles produced in the interaction were at the same point in space, referred to as the event vertex — is calculated by propagating (temporally) the RF time from the radiator to the event interaction vertex.

The final pieces of the tagging system are the collimators. In order to trim the beam halos, the photon beam is passed through two collimators prior to arriving at the CLAS cryotarget. Sweeping magnets were placed between the two collimators to remove any charged particles created by interactions of photons with the first collimator. More detailed information on the Hall B tagging system can be found in [37].
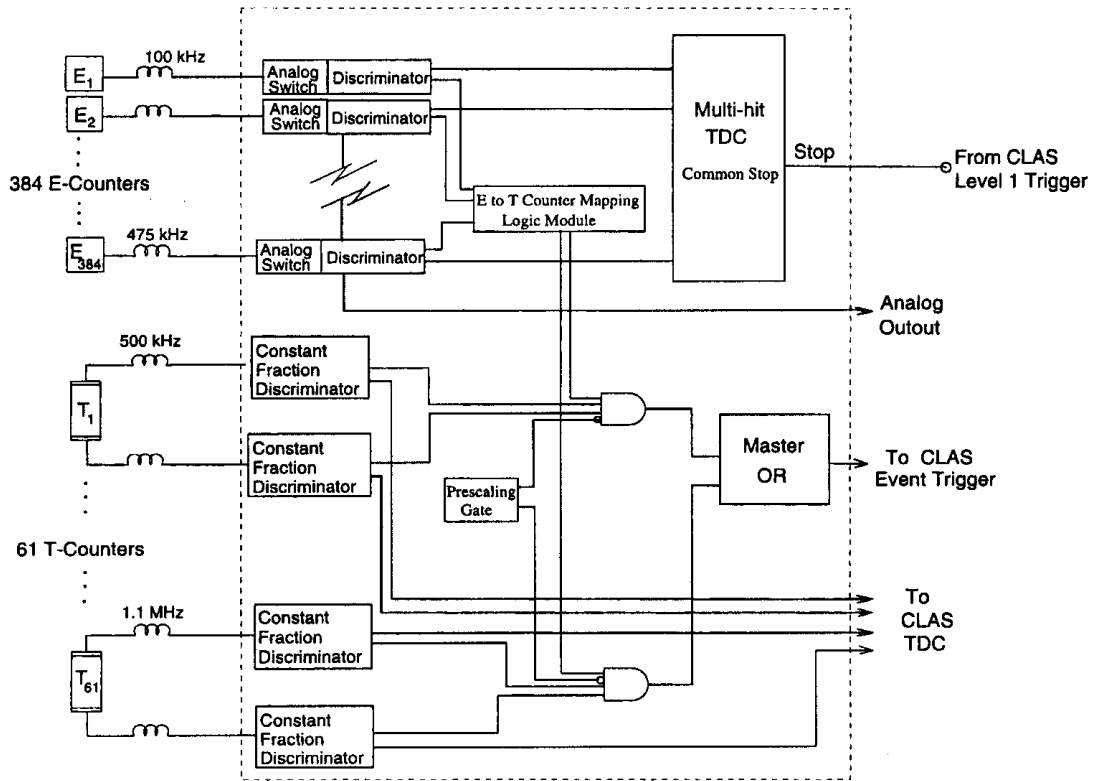
Figure 2.7: Schematic diagram of the readout electronics of the Hall B photon tagging system. Image Source: [37].

Figure 2.8: Photograph of the CLAS detector taken during a maintenance period for which the time-of-flight scintillator walls, forward region Cerenkov counters and electromagnetic calorimeters were pulled away from the interior detector elements. Image Source: [33].

2.3   The CLAS Detector

The CEBAF Large Acceptance Spectrometer (CLAS) was used to detect particles produced by interactions of the photon beam with the cryogenic target located near the center of the CLAS detector. The main CLAS subsystems are the start counter, drift chambers, time-of-flight scintillators, along with Cerenkov counters and electromagnetic calorimeters in the forward region. The latter two forward region detector elements were not used in our analysis and will not be discussed here. Our analysis did not incorporate the start counter; however, it was used in the $g11a$ trigger. The drift chambers were used to track charged particles, which were bent by a superconducting toroidal magnetic, as they traveled through the detector. By reconstructing a particle's flight path, we were able to determine its momentum. The time-of-flight scintillator walls were used for particle identification purposes. In this section, we will discuss in detail the detector subsystems which played vital roles in our analysis.

2.3.1   Cryotarget

Target cells with a variety of shapes and sizes have been employed by experiments using the CLAS detector. The $g11a$ target cell, which was cylindrical in shape, was constructed out of Kapton by CLAS technician Steve Christo. The cell was 40 cm long with a radius of 2 cm. A picture of the cell is shown in Figure 2.10. A number of different target materials have also been used during CLAS experiments. The target material used during the $g11a$ experiment was liquid Hydrogen. Approximately once per hour, the temperature and pressure of the target were measured and recorded. In Section 4.4, these measurements will be used to calculate the density of the liquid Hydrogen — an important quantity necessary to extract *cross section* measurements.
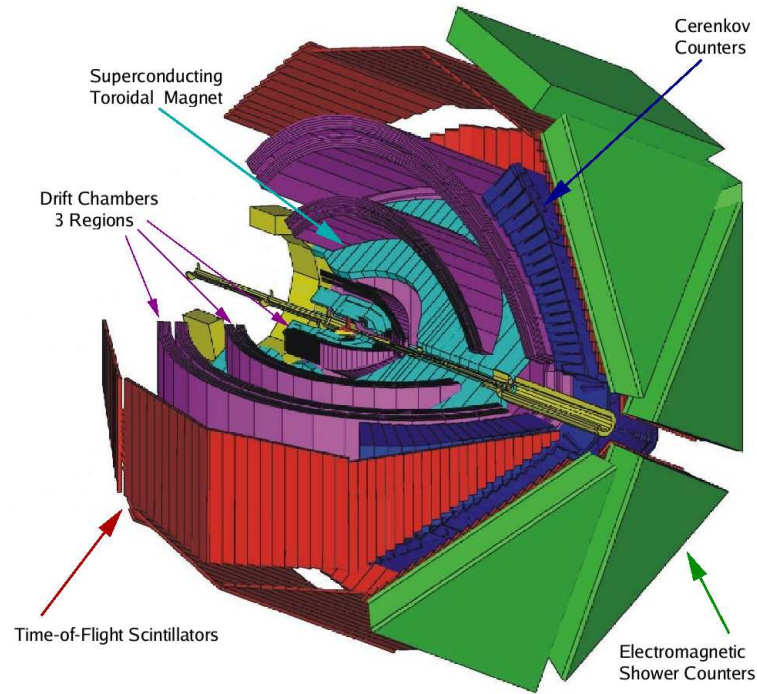
Figure 2.9: Schematic of the CLAS detector showing all of the major subsystems. The detector, which is approximately 8 m in diameter, is housed in experimental Hall B at Jefferson Lab. Image Source: [38].

Figure 2.10: Target cell used during the $g11a$ run period. Image Source: [39].
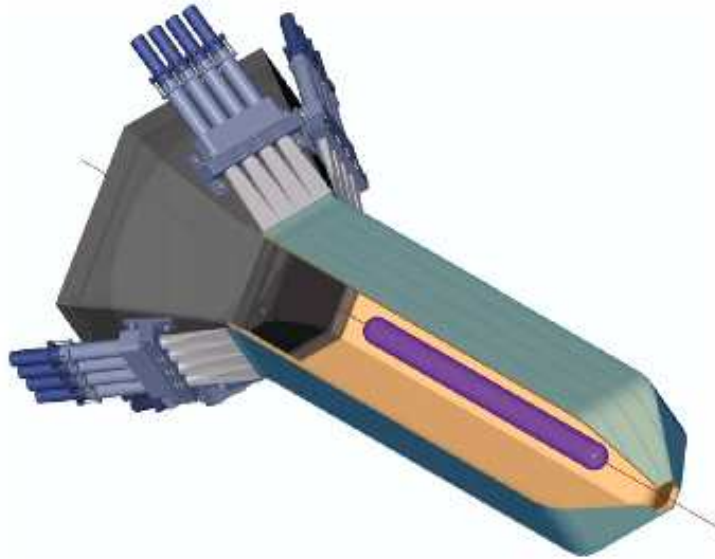
Figure 2.11: Schematic diagram of the new CLAS start counter installed just prior to running $g11a$. Image Source: [40].

2.3.2   Start Counter

A new start counter was installed for the $g11a$ run period. Like the CLAS detector itself, the start counter is divide into six sectors each with four scintillator paddles (see Figure 2.11). The timing resolution of the new CLAS start counter is ~ 400 ps. Though we did not incorporate the timing information obtained from the start counter in our analysis, it was included in the Level 1 trigger during $g11a$. More information on this detector element, including details on its construction, can be found in [40].

2.3.3   Superconducting Toroidal Magnet

The superconducting toroidal magnet is a vital piece of the CLAS detector. The field generated by the magnet caused charged particles to travel along non-linear paths through the drift chambers. A tracking system, discussed in the next section, was used to determine the trajectory followed by each particle. Given knowledge of the strength and direction of the magnetic field, the trajectory of the particle could be used to determine its momentum. Figure 2.12 shows a picture of the bare torus coils during construction of the CLAS detector.

The magnet utilized six kidney-shaped superconducting coils, each separated in the azimuthal direction by 60° to generate its toroidal field. The *normal field* configuration, used during $g11a$, bends negatively charged particles in towards the beam pipe and positively charged particles away from the beam pipe. The peak current the magnet can support is 3861 A, resulting in a maximum field strength of 3.5 T; however, during the $g11a$ run period, the current was limited to about half the maximum, 1920 A. Running at higher currents provides better momentum resolution but decreases the detector's acceptance for negative particles. Given the physics goals of $g11a$, it was decided that running at a lower current was the optimal choice. During operation, the magnet was cooled down to 4.4 K using liquid Helium obtained from the central CEBAF refrigerator [41].

Figure 2.12: The coils of the CLAS toroidal magnet prior to installation of the rest of the detector subsystems. Image Source: [33].
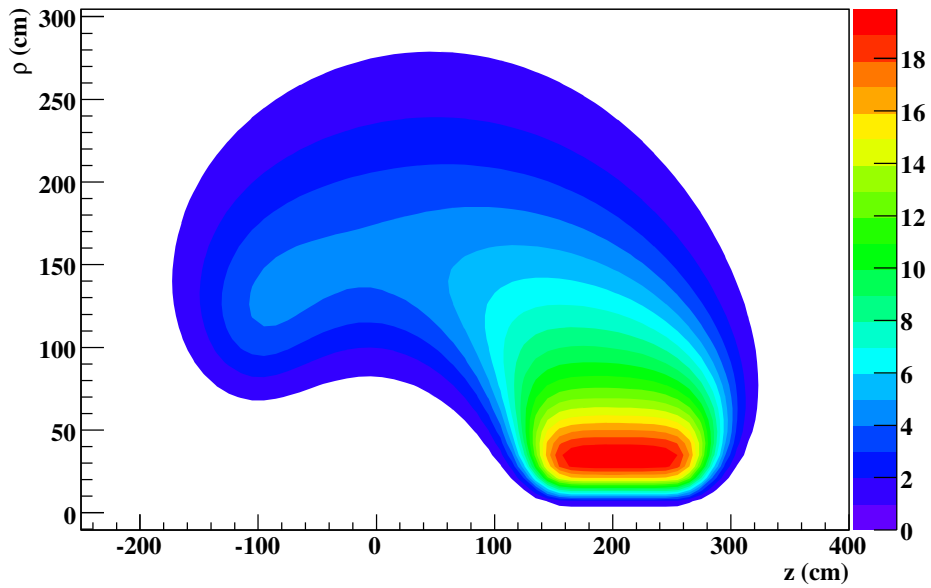

Figure 2.13: Strength of the CLAS magnetic field, at the azimuthal center of a sector, when running with the $g11a$ current setting (kG) vs radial distance from the beam line (cm) and the beam line coordinate z (cm). For $g11a$, the center of the 40 cm long target was placed at $z = -10$ cm.
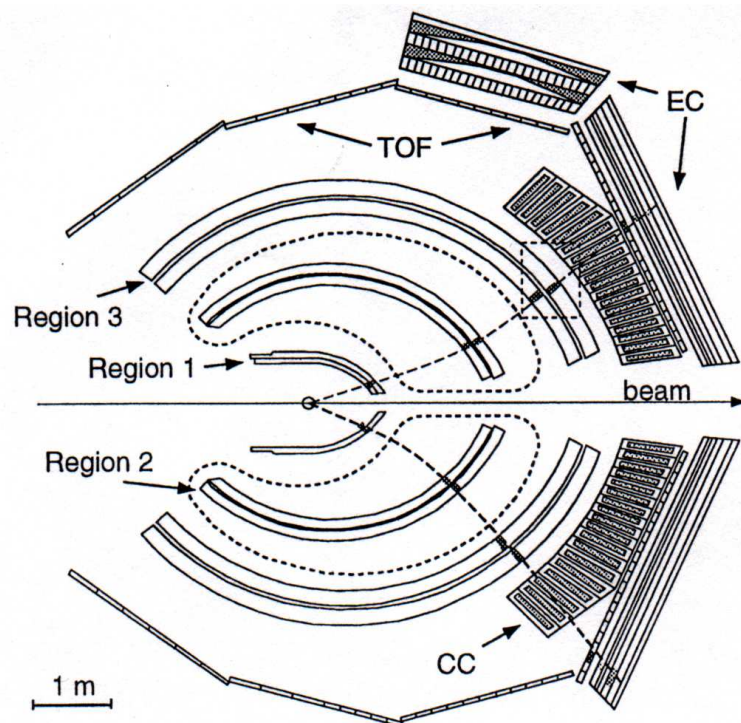
Figure 2.14: Cut away diagram of CLAS showing the relative positions of the detector subsystems. The kidney shaped dashed lines outline the location of the toroidal magnet coils. Image Source: [42].

2.3.4   Drift Chambers

As mentioned in the previous section, determining the momentum of charged particles was performed by tracking the particles as they traveled through the field generated by the toroidal magnet. The charged particles were tracked using three separate drift chamber regions. Region 1 was located inside the torus coils, a region where the magnetic field was weak. Region 2 was mounted directly to the magnet's cryostats. Thus, Region 2 occupied the space where the magnetic field was the strongest. Region 3 was positioned outside of the torus coils, another region possessing a weak magnetic field. Figure 2.14 shows a cut-away diagram of the CLAS detector. The positions of the three drift chamber regions, relative to the torus coils, are visible on the diagram.

Each of the drift chamber regions was divided into two *superlayers*, one with axially oriented wires (relative to the magnetic field direction) and one with wires oriented at a 6° stereo angle. Each superlayer typically consisted of six layers of hexagonal drift cells arranged such that neighboring layers were offset by half a cell width. Each cell had a 20 μm gold-plated tungsten sense wire located at its center surrounded by six 140 μm gold-plated aluminum alloy field wires. The sense wire possessed a positive potential, while the field wires were kept at a negative high voltage. Signals from the sense wires were passed to preamplifiers, then to amplifier discriminator boards (ADBs) and finally to TDCs to obtain the timing information. The drift gas mixture was chosen to be 90% Argon and 10% CO_2, due to its ionization properties and because it is non-flammable. More information pertaining to the CLAS drift chambers is given in [42, 43, 44, 45].
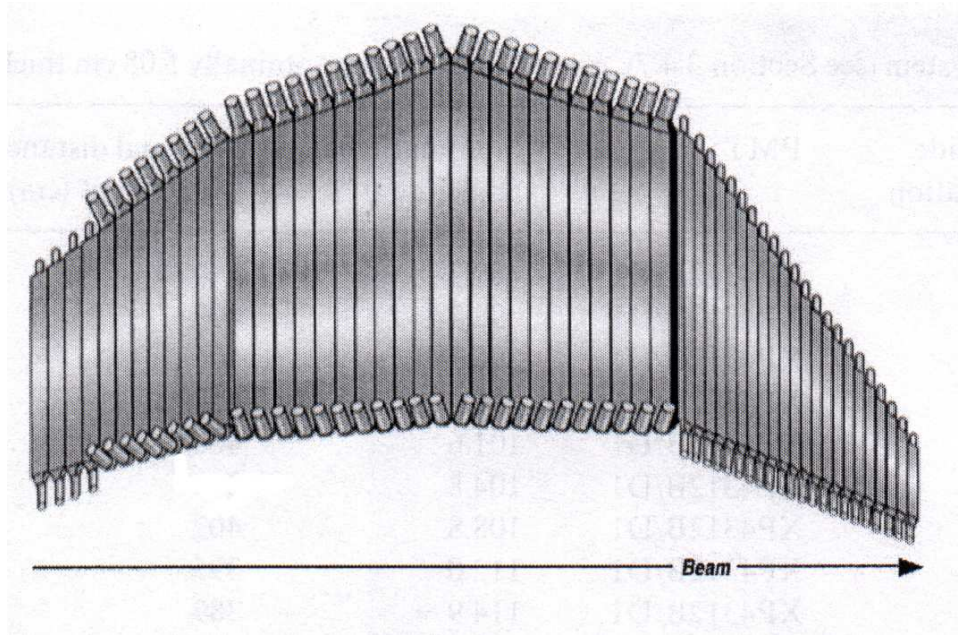
Figure 2.15: Diagram of the time-of-flight (TOF) scintillator shell from one CLAS sector. Image Source: [46].

2.3.5 Time-of-Flight Scintillators

The outer shell of the CLAS detector was comprised of six segmented scintillator walls, one for each sector, located approximately four meters from the cryotarget. The scintillator wall in each sector had four panels and a total of 57 bars of varying lengths and widths (see Figure 2.15). To provide 100% detection efficiency of minimum ionizing particles, each bar was made 2 inches thick. The signals from the scintillators were collected via photo-multiplier tubes (PMTs) mounted at each end of the bars. The timing resolution was 80–160 ps, depending on the length of the bar (longer bars had worse resolution). The time-of-flight (TOF) scintillator shell was used in the Level 1 trigger (see Section 2.5) and also in our analysis to perform particle identification. A more detailed description of the TOF system, construction and performance, is given in [46].

2.4 Beamline Devices

A number of beamline devices were used in Hall B during $g11a$. Devices placed upstream from the CLAS detector were used to monitor the quality of the beam. These included beam position monitors (BPMs), harps and devices which measured the current of the beam. Downstream devices, such as the total absorption shower counter (TASC), pair spectrometer (PS) and pair counter (PC), were used to measure the photon flux. The TASC was used by *gflux* [47] — the standard CLAS photon flux calculation method — to obtain the *tagging ratio* of the T-counters. It consisted of four lead glass blocks, with 100% photon detection efficiency, each instrumented with a phototube. The TASC could provide an absolute measurement of the photon flux, but only if the beam current was less than 100 pA [37]. Thus, low current *normalization runs* were taken periodically so that the flux calculated by the tagger could be calibrated against the TASC.

2.5   Triggering and Data Acquisition

Each detector subsystem had its own electronics package to monitor its components and collect signals. The presence of a signal in a single detector element did not necessarily mean that a physics event had been detected. A number of unwanted sources could produce signals, such as cosmic radiation passing through a detector element, electronic noise, etc. It was the job of the *trigger* to determine which sets of signals constituted a physics event. Once this decision had been made, the data acquisition system (DAQ) collected the signals and wrote them to magnetic tape for future *offline* analysis. At the time $g11a$ was run, the DAQ was capable of running at ~ 5 kHz.

The $g11a$ trigger required coincidence between the tagger Master OR (MOR) and the CLAS Level 1 trigger. The entire tagger focal plane was kept on and recorded data; however, only the first 40 (highest energy) tagger T-counters were enabled in the trigger. For an individual CLAS sector to satisfy the Level 1 trigger, a signal was required from any of the 4 start counter paddles and any of the 48 TOF paddles within a coincidence window of 150 ns. The Level 1 trigger, as a whole, was only passed if at least two CLAS sectors satisfied the above conditions. The final requirement for the $g11a$ trigger was a coincidence between the tagger MOR and the start counter OR within a timing window of 15 ns [48].

2.6   Summary

Prior to performing our analysis, we required an experiment to be run which could produce, observe and record $\gamma p \to p\omega$ events. Production of the desired events employed the photon beam generated (indirectly) by the CEBAF accelerator and the CLAS cryogenic liquid Hydrogen target. The events were observed by the various components of the CLAS detector and recored by the data acquisition system. At this stage of the $g11a$ experiment, we had $\sim$21 TB of electronic signals stored on magnetic tape. In the next few chapters, we will detail the process of converting this *raw* information into physics observables.

Chapter 3

Event Selection

The $g11a$ dataset was collected from May 17th to July 29th in 2004 by the CLAS collaboration. A total of ~ 20 billion triggers and 21 TB of data were recorded. The next step in the analysis procedure is known as *cooking*. This is when the information recorded from the various detector subsystems is converted into a form suitable for physics analysis. During cooking, each detector subsystem (drift chambers, photon tagger, RF, etc.) was calibrated. The cooking of the $g11a$ dataset was performed by Maurizio Ungaro and is documented in [49]. This chapter deals with our data analysis efforts which began after the cooking phase had been completed.

From this large dataset, we want to select events of the type $\gamma p \to p\omega$. The ω decays strongly, so we must identify it through its decay products. In particular, we chose the $\omega \to \pi^+\pi^-\pi^0$ decay mode — which has an $\sim 89\%$ branching fraction — for our analysis. The CLAS detector is not optimized for neutral particle detection, thus we reconstructed the π^0 through conservation of energy and momentum. All other final state particles were required to be detected. This led us to begin our analysis on the $++-$ skim. This skim consisted only of events with at least two positively charged tracks and at least one negatively charged track. This chapter details all of the steps involved in our event selection procedure.

3.1   Excluded Runs

Data taking during the $g11a$ run period was grouped into *runs*, each of which consisted of $\sim 10\text{M}$ events. The $g11a$ run period includes CLAS runs 43490 to 44133. Runs 43490 to 44107 were taken with electron beam energy 4.019 GeV, while for runs 44108 to 44133 the energy was 5.021 GeV. To avoid any possible systematic differences between the two sets of runs, we have chosen to use only the 4.019 GeV data. These runs make up the bulk of the dataset, thus the addition of the 5.021 GeV data would provide almost no reduction in our statistical uncertainties. The set of runs from 43490 to 43525 were *commissioning* runs. These runs were taken for diagnostic reasons and were not meant to be used for physics analysis. Thus, we also excluded these runs.

There are also several other runs which we have been excluded from our analysis. Runs 43675, 43676, 43777, 43778 and 44013 were taken with different trigger configurations than the standard production trigger. There were documented drift chambers problems that occurred during runs 43981 and 43982. Also, a data acquisition problem occurred during runs 43989 to 43991. Run 43558 was found to have an unusually low normalized ω yield. Finally, an unknown computer error occurred while skimming run 43871. These twelve runs have all been excluded from our analysis. Table 3.1 summarizes the cooked runs which we have chosen to exclude.

Run	Description
43490-43525	Commissioning Runs
43558	Abnormal Normalized ω Yield
43675-43676	Different Trigger Configuration
43777-43778	Different Trigger Configuration
43871	Data Processing Error
43981-43982	Logbook Lists DC Problems
43989-43991	Logbook Lists DAQ Problems
44013	Different Trigger Configuration
44108-44133	5.021 GeV Beam Energy

Table 3.1: $g11a$ cooked runs which have been excluded from our analysis.

3.2   Kinematic Fitting Formulas

In this section, we present formulas used to perform all kinematic fits found in this chapter. Kinematic fitting will be used not only for improving the data by enforcing energy and momentum conservation, but also for deriving tagger and momentum corrections. The extensive use of this technique warrants the detailed description presented below.

3.2.1   Least Squares Fitting with Lagrange Multipliers

Kinematic fitting utilizes the method of *least squares*, first described by Carl Friedrich Gauss in the early 19th century. This method seeks to determine the values of the unknown quantities of a model by minimizing the sum of the squares of the residuals — differences between the measured and predicted values.

When performing a least squares fit with a set of constraint equations, each equation could be used to reduce the number of fit quantities. One could then proceed with a smaller set of fit quantities. Rather than take this approach, we chose to use Lagrange multipliers, allowing us to treat each of the unknowns equally. This section follows directly from the work of [50].

First we set up our notation. The m unknown parameters are denoted $\vec{x}$, the n measurable quantities are $\vec{y}$. The actual measured quantities and their errors are the n-vectors $\vec{\eta}$ and $\vec{\epsilon}$ respectively. Therefore,

$$\vec{\eta} = \vec{y} + \vec{\epsilon}. \tag{3.1}$$

The vectors $\vec{x}$ and $\vec{y}$ are related by the r constraint functions

$$f_k(\vec{x}, \vec{y}) = 0, \qquad k = 1, 2, ..., r. \tag{3.2}$$

We denote the first approximation of the unknowns $\vec{x}_0$. We take $\vec{y}_0 = \vec{\eta}$ and require the constraint functions to be approximately linear near $(\vec{x}_0, \vec{y}_0)$.

We then Taylor expand, to first order, the constraint functions in this region

$$f_k(\vec{x}, \vec{y}) \approx f_k(\vec{x}_0, \vec{y}_0) + \sum_i^m \left(\frac{\partial f_k}{\partial x_i} \right) (\vec{x}_0, \vec{y}_0)(x^i - x_0^i) + \sum_i^n \left(\frac{\partial f_k}{\partial y_i} \right) (\vec{x}_0, \vec{y}_0)(y^i - y_0^i). \tag{3.3}$$

It is then convenient to introduce the matrices

$$a_{ij} = \left(\frac{\partial f_i}{\partial x_j}\right)(\vec{x}_0, \vec{y}_0), \qquad A = \begin{pmatrix} a_{1,1} & a_{1,2} & \cdots & a_{1,m} \\ a_{2,1} & a_{2,2} & \cdots & a_{2,m} \\ \vdots & \vdots & \ddots & \vdots \\ a_{r,1} & a_{r,2} & \cdots & a_{r,m} \end{pmatrix}, \tag{3.4}$$

$$b_{ij} = \left(\frac{\partial f_i}{\partial y_j}\right)(\vec{x}_0, \vec{y}_0), \qquad B = \begin{pmatrix} b_{1,1} & b_{1,2} & \cdots & b_{1,n} \\ b_{2,1} & b_{2,2} & \cdots & b_{2,n} \\ \vdots & \vdots & \ddots & \vdots \\ b_{r,1} & b_{r,2} & \cdots & b_{r,n} \end{pmatrix}, \tag{3.5}$$

the vector of constraint equations

$$\vec{c} = \begin{pmatrix} f_1(\vec{x}_0, \vec{y}_0) \\ f_2(\vec{x}_0, \vec{y}_0) \\ \vdots \\ f_r(\vec{x}_0, \vec{y}_0) \end{pmatrix}, \tag{3.6}$$

and the differential vectors

$$\vec{\xi} = \vec{x} - \vec{x}_0, \tag{3.7}$$

$$\vec{\delta} = \vec{y} - \vec{y}_0. \tag{3.8}$$

We can then rewrite (3.3) as

$$A\vec{\xi} + B\vec{\delta} + \vec{c} = 0. \tag{3.9}$$

The minimization quantity is then given by $\vec{\delta}^T C_\eta^{-1} \vec{\delta}$, where C_η is the covariance matrix of the measured quantities. In the special case of independent measurements, $\vec{\delta}^T C_\eta^{-1} \vec{\delta}$ takes on the familiar form of $\sum_{j=1}^{n} \epsilon_j^2 / \sigma_j^2$.

We now introduce the Lagrangian

$$L = \vec{\delta}^T C_\eta^{-1} \vec{\delta} + 2\vec{\mu}^T \left(A\vec{\xi} + B\vec{\delta} + \vec{c}\right), \tag{3.10}$$

where $\vec{\mu}$ is the r-vector of Lagrangian multipliers. Using the fact that $\vec{\delta}$ and $\vec{\xi}$ are independent variables, setting the total differential of L to zero yields

$$\frac{\partial L}{\partial \delta_i} = \frac{\partial L}{\partial \xi_i} = 0. \tag{3.11}$$

Substituting the solutions to (3.11) into (3.9) gives

$$\vec{\xi} = -\left(A^T C_B A\right)^{-1} A^T C_B \vec{c} \tag{3.12}$$

$$\vec{\delta} = -C_\eta B^T C_B \left(\vec{c} - A\vec{\xi}\right), \tag{3.13}$$

where $C_B = (B C_\eta B^T)^{-1}$. The least squares estimates for the parameters $\vec{x}$ and improved measurements $\vec{y}$ are then

$$\vec{x} = \vec{x}_0 + \vec{\xi} \tag{3.14}$$

$$\vec{y} = \vec{y}_0 + \vec{\delta}. \tag{3.15}$$

When the constraint equations are nonlinear, these results should be considered as better approximations and the process should be iterated.

The estimates of the measurement errors are the n-vector

$$\vec{\epsilon} = \vec{\eta} - \vec{y}, \tag{3.16}$$

where $\vec{y}$ are the improved measurements obtained from the final iteration and $\vec{\eta}$ are the measured values. If the errors are normally distributed and the constraint functions are sufficiently linear near $(\vec{x}_0, \vec{y}_0)$, then $\vec{\epsilon}^T C_\eta^{-1} \vec{\epsilon}$ follows a χ^2 distribution with $r - m$ degrees of freedom.

Finally, we can use propagation of errors to write the covariance matrix for the improved measurements as

$$C_y = C_\eta - C_\eta B^T C_B B C_\eta + C_\eta B^T C_B A (A^T C_B A)^{-1} A^T C_B B C_\eta, \tag{3.17}$$

and the covariance matrix for the parameters as

$$C_x = (A^T C_B A)^{-1}. \tag{3.18}$$

3.2.2   Confidence Levels and Pull Distributions

The primary measure of the *goodness of fit* for the least squares method is the *confidence level*

$$CL = \int_{\chi^2}^{\infty} f(z; n) dz, \tag{3.19}$$

where $f(z; n)$ is the χ^2 probability density function with n degrees of freedom. It is a measure of the probability that a χ^2 from the theoretical distribution is greater than the χ^2 obtained from the fit.

For a dataset consisting entirely of events which satisfy the fit hypothesis with normally distributed errors, the confidence level distribution is flat on $(0, 1]$. Background events — events that do not satisfy the fit hypothesis — have small confidence levels. Cutting events with a low confidence level provides a controlled way to eliminate the majority of the background events while losing a well defined amount of the signal.

To effectively use the confidence level to cut background, a good understanding of each fit quantity's errors is necessary. The quality of the error estimation can be examined using the *pull distributions* or *stretch functions*. The pull of the ith fit quantity is defined as [51]

$$z_i = \frac{\epsilon_i}{\sigma(\epsilon_i)}, \tag{3.20}$$

where $\epsilon_i = \eta_i - y_i$ with standard deviation σ_{ϵ_i}. The pulls are written using $\vec{\epsilon}$ since it is the only quantity for which the true mean value of each measurement is known. We can then rewrite the ith pull as

$$z_i = \frac{\eta_i - y_i}{\sqrt{\sigma^2(\eta_i) - \sigma^2(y_i)}}. \tag{3.21}$$

The z_i's should be normally distributed about zero with $\sigma = 1$. A systematic error in the measured quantity η_i, can be seen as an overall shift in the distribution of the corresponding z_i away from zero. Similarly, if the error of η_i has been consistently overestimated (underestimated), then the corresponding pull distribution will be too narrow (broad).
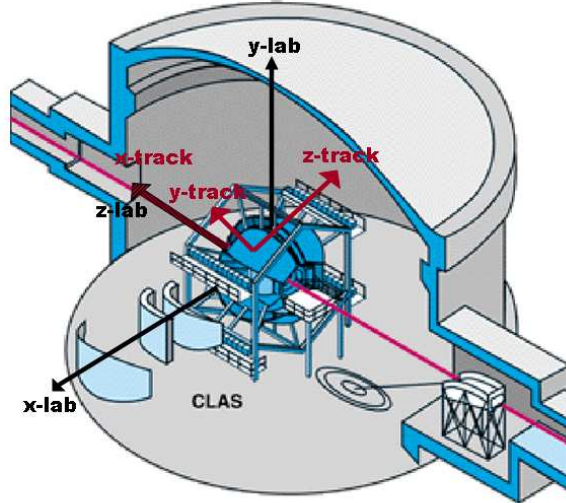
Figure 3.1: The lab coordinate system along with the tracking coordinates for sector 2 [33].

3.2.3 CLAS Tracking Parameters

There are three main coordinate systems defined for the CLAS detector: the *lab* system, the *sector* system and the *tracking* system. The lab system is used for physics analysis. It defines the z_{lab}-axis as the direction of the beam line, the x_{lab}-axis passes through the center of sector 1 and the y_{lab}-axis points vertically upwards (between sectors 2 and 3). The sector system was not used in this analysis and will not be discussed here.

Track reconstruction in CLAS is carried out in a sector-dependent tracking coordinate system. The tracking coordinates in each sector are defined such that the x_{track}-axis lies along the beam line, the y_{track}-axis passes through the center of the sector and the z_{track}-axis is aligned with the average magnetic field direction in that sector (see Figure 3.1). Therefore, the tracking coordinates are related to the lab coordinates by

$$\left(\begin{array}{c} x_{track} \\ y_{track} \\ z_{track} \end{array} \right) = \left(\begin{array}{c} z_{lab} \\ cos(\alpha)x_{lab} + sin(\alpha)y_{lab} \\ -sin(\alpha)x_{lab} + cos(\alpha)y_{lab} \end{array} \right), \tag{3.22}$$

where $\alpha = \frac{\pi}{3}(N_{sector} - 1)$.

The track momenta are reconstructed in terms of the charge to momentum magnitude ratio q/p, the dipolar angle relative to the sector's (x_{track}, y_{track}) plane λ, and the angle in the sector's (x_{track}, y_{track}) plane relative to the x_{track}-axis ϕ.

The momentum in the lab frame can be written using the tracking parameters as [52]

$$\left(\begin{array}{c} p_{x_{lab}} \\ p_{y_{lab}} \\ p_{z_{lab}} \end{array} \right) = \left(\begin{array}{c} p(cos(\lambda)sin(\phi)cos(\alpha) - sin(\lambda)sin(\alpha)) \\ p(cos(\lambda)sin(\phi)sin(\alpha) + sin(\lambda)cos(\alpha)) \\ p\,cos(\lambda)cos(\phi) \end{array} \right). \tag{3.23}$$

All kinematic fitting and momentum corrections will be done using the track reconstruction parameters — except p will be used instead of q/p.

3.3   Energy and Momentum Corrections

This section documents the energy and momentum corrections used to improve the data. Both the tagger and momentum corrections were derived using the $\gamma p \rightarrow p\pi^+\pi^-$ channel and the kinematic fitting procedure. When calculating these corrections, we are only concerned with whether the events used were actually $p\pi^+\pi^-$. Losing *good* events has no effect on the results. Thus, for this specific stage of the analysis, the standard CLAS particle identification scheme (which is strict enough to ensure that background leakage from misidentified particles is negligible) will be used.

The procedure used to calculate the tagger and momentum corrections is as follows. First we obtain the tagger corrections. These corrections are then applied when obtaining the momentum corrections; however, the presence of a systematic offset in the momenta — the magnitude of the momentum for high momentum particles for example — could affect the tagger corrections (since they are performed first). Thus, we have adopted an iterative approach. For each iteration, we apply the previous iteration's momentum corrections, then calculate the tagger correction. Next, we apply the new tagger correction and recalculate the momentum corrections. In the sections below, we document the procedure used during a single iteration. All plots shown are from the final iteration.

3.3.1   Energy Loss Corrections

The momentum vectors of the proton, π^+ and π^- were each corrected for energy lost as they passed through material in the detector. Charged particles, excluding electrons, at CLAS energies lose energy in matter primarily through atomic excitation and ionization [11]. Corrections were made to account for energy lost in the target material (liquid Hydrogen) and walls, the beam pipe, the start counter and the air gap located between the start counter and the Region 1 drift chambers. The corrections were applied by the *eloss* software package written by Eugene Pasyuk for the CLAS detector [53].

3.3.2   Tagger Corrections

Alignment issues in the photon tagger's focal plane were first discovered in 2003 [54, 7, 8]. This leads to an inaccurate photon energy constructed from the raw tagger information. We can obtain an empirical correction for this effect using the $p\pi^+\pi^-$ channel.

We begin by selecting events with only one proton, π^+ and π^- with no other charged tracks reconstructed. We then apply energy loss corrections and the previous iteration's momentum corrections to all three final state particles. The event is then kinetically fit to the hypothesis $(\gamma)p \rightarrow p\pi^+\pi^-$, ignoring the measured photon energy. Only events with a confidence level greater than 10% are used to determine the corrections.

For each event, the kinematic fit estimate for the tagger energy correction is

$$\Delta E_\gamma = E_\gamma^{kfit} - E_\gamma^{meas}. \tag{3.24}$$

The corrections are binned in tagger E-counter (see Figure 3.2(a)) and from each bin we extract the Gaussian mean (see Figure 3.2(b)). Then, for each $g11a$ run we also calculate the beam offset B_r (see Figure 3.2(c)).

Thus, for an event from run r with a photon from E-counter e, the correction applied to the photon energy is

$$\Delta E_{\gamma,e,r} = \Delta E_{\gamma,e} + B_r, \tag{3.25}$$

where $\Delta E_{\gamma,e}$ is the Gaussian mean for E-counter e.
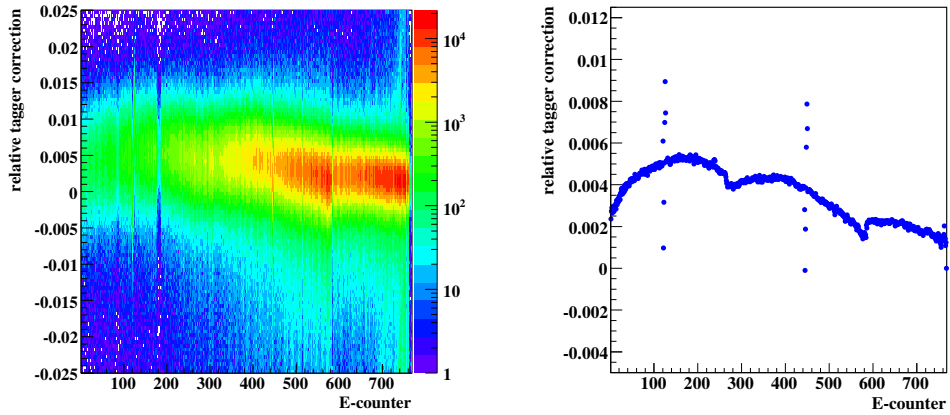
(a)

(b)
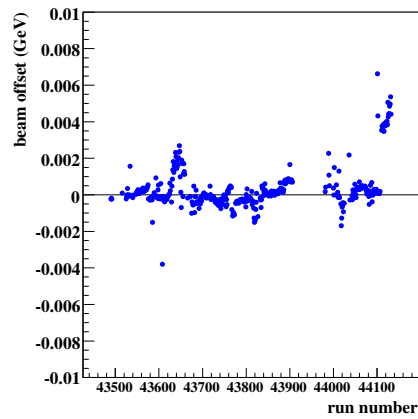
(c)

Figure 3.2: Tagger Corrections: (a) $\Delta E_\gamma / E_{beam}$ vs E-counter for $(\gamma)p \rightarrow p\pi^+\pi^-$ events. (b) Gaussian mean extracted for each E-counter from (a). The two sets of six E-counter corrections which do not fall on the curve are the result of swapped cables during data taking [55]. (c) beam offset (GeV) vs run number.

3.3.3   Momentum Corrections

Discrepancies in the toroidal magnetic field map and/or in the drift chamber survey information can lead to inaccuracies in the reconstructed momenta. As we did for the tagger, we can again use the inclusive $\gamma p \to p\pi^+\pi^-$ channel to empirically obtain corrections for the reconstructed momenta.

We again begin by selecting events with only one proton, π^+ and π^- with no other charged tracks reconstructed. We then apply energy loss corrections to all three final state particles and the previous iteration's tagger corrections. Next, the event is kinematically fit to the hypotheses $\gamma p \to p\pi^+(\pi^-)$, $\gamma p \to p(\pi^+)\pi^-$ and $\gamma p \to (p)\pi^+\pi^-$. Using the notation of Section 3.2.1, each fit has its vector of measured quantities $\vec{y}^T = (p_{i1}, \lambda_{i1}, \phi_{i1}, p_{i2}, \lambda_{i2}, \phi_{i2})$ and vector of parameters $\vec{x} = (p_x, \lambda_x, \phi_x)$ where $i1, i2$ denote the *included* particles and x denotes the *excluded* particle for each fit. Only fits whose confidence levels are greater than 10% are used for determining the corrections.

The kinematic fit estimate for the corrections to the tracking parameters are then

$$
\begin{align}
\Delta p_x &= p_x^{kfit} - p_x^{meas} \tag{3.26a}\\
\Delta \lambda_x &= \lambda_x^{kfit} - \lambda_x^{meas} \tag{3.26b}\\
\Delta \phi_x &= \phi_x^{kfit} - \phi_x^{meas}, \tag{3.26c}
\end{align}
$$

where $x = (p, \pi^+, \pi^-)$ is the *excluded* particle. For example, Δp_p is obtained using p_p^{kfit} from the kinematic fit to $\gamma p \to (p)\pi^+\pi^-$, whereas Δp_{π^-} is obtained using $p_{\pi^-}^{kfit}$ from the fit to $\gamma p \to p\pi^+(\pi^-)$, etc.

Each of the quantities defined in (3.26) is, in principle, a function of the particle's momentum magnitude p, orientation (θ, ϕ) in the lab coordinates , CLAS sector number and charge. Thus, to obtain our momentum corrections, we have divided each of the 6 CLAS sectors into 180 (θ, ϕ) bins. A correction is then obtained for the quantities (3.26) as a polynomial function of p, in each bin, for both charges. The binning in each sector and charge is the same. The azimuthal angle ϕ is divided into twelve 5° bins in each θ bin. The polar angle θ is divided into nine 5° bins for $\theta\epsilon[5°, 50°)$, four 10° bins for $\theta\epsilon[50°, 90°)$ and two 25° bins for $\theta\epsilon[90°, 140°)$.

In each bin, we build the histograms ΔX_q vs. p_q where X_q denotes the quantities (3.26) for both charges. The momentum magnitude p is binned in equal sized $1/p$ bins, since the tracking is done in terms of q/p. The Gaussian means are extracted for each p bin and fit to a polynomial function of p. Figure 3.3 shows an example of this process in a single $(sector, \theta, \phi)$ bin for Δp. The size of the corrections in this particular $(sector, \theta, \phi)$ bin are atypically large. Most bins have much smaller, if not negligible, momentum corrections. This particular bin was chosen, out of the 1080 bins, for two reasons. First, the size of the corrections aids in illustrating how the process works. Second, the corrections in this bin are clearly indicative of detector misalignment. Notice that at higher momenta $\Delta p_+(p) \approx -\Delta p_-(p)$. Thus, the correction to the tracking quantity q/p is independent of which way the track bends. The same process is followed to obtain the corrections $\Delta\lambda$ and $\Delta\phi$.

Figure 3.4 shows the size of the corrections for all detected protons and π's in the $++-$ skim for run 43582. The corrections to the magnitude of the momenta are generally less than 10 MeV/c (see Figures 3.4(a) and (d)). The corrections to the tracking angles are typically on the order of a few milliradians (see Figures 3.4(b),(c),(e),(f)).

(a)

(b)

(c)

(d)
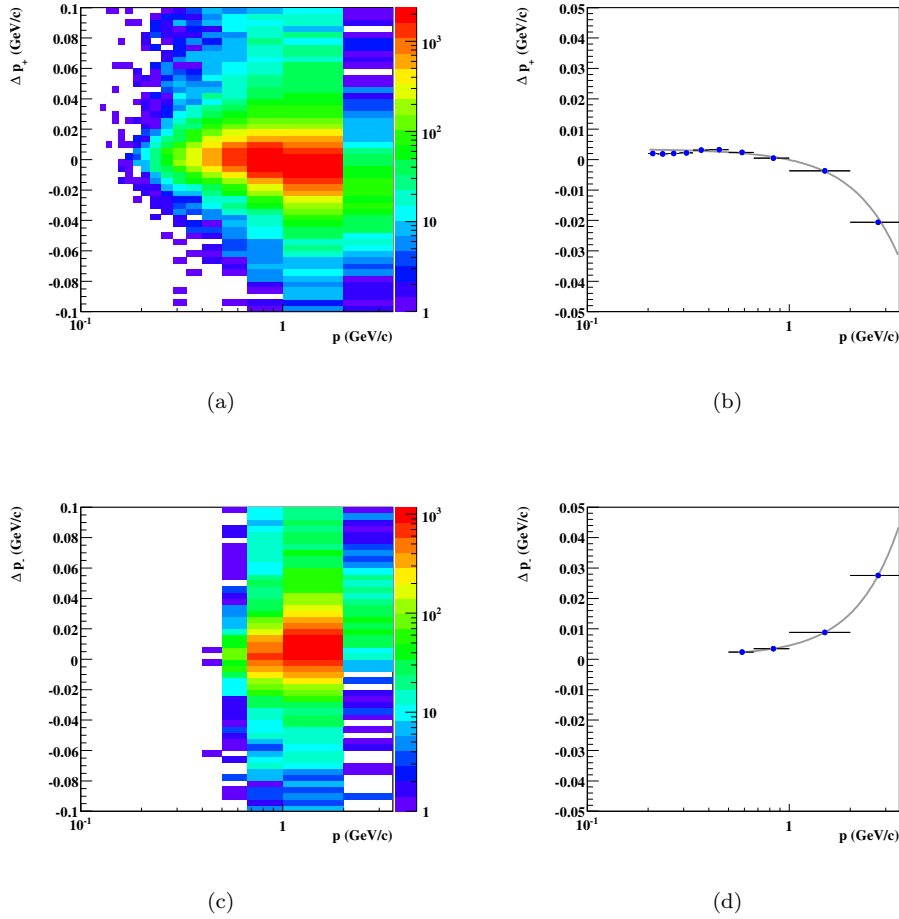
Figure 3.3: Momentum Corrections: Example bin: Sector 1, $\theta\epsilon(20°, 25°)$, $\phi\epsilon(-15°, -10°)$: (a) $\Delta p(\text{GeV/c})$ vs. $p(\text{GeV/c})$ for positively charged particles in this $(sector, \theta, \phi)$ bin. (b) Gaussian mean extracted for each p bin from (a). The line is from a polynomial fit which is used as the correction to p. (c) $\Delta p(\text{GeV/c})$ vs. $p(\text{GeV/c})$ for negatively charged particles in this $(sector, \theta, \phi)$ bin. The lack of events with $p < 0.5$ GeV/c is an artifact of the detector acceptance. (d) Gaussian mean extracted for each p bin from (c). The line is from a polynomial fit which is used as the correction to p. The size of the corrections in this particular $(sector, \theta, \phi)$ bin are atypically large, which aids in displaying how the corrections are obtained. Most bins have much smaller, if not negligible, momentum corrections.
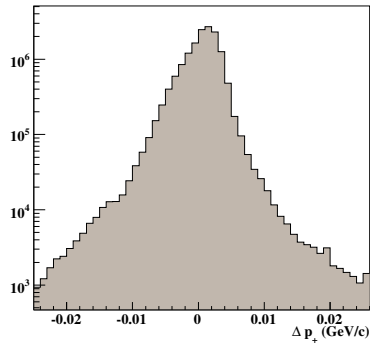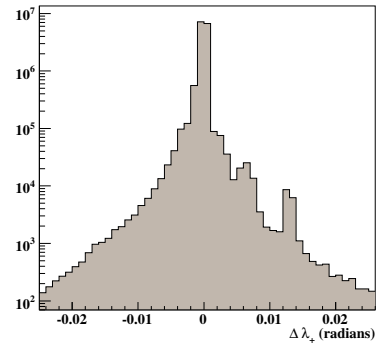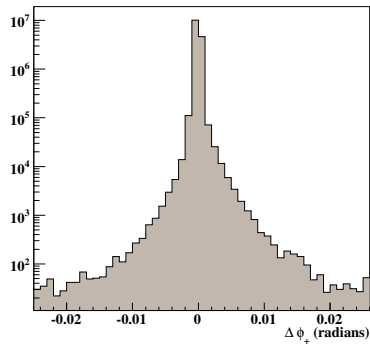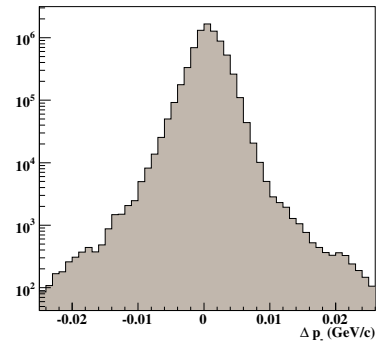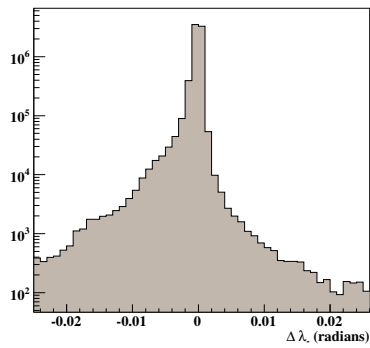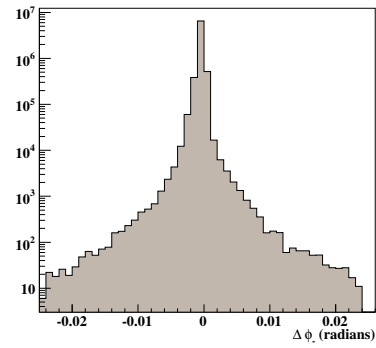
Figure 3.4: Momentum corrections for all protons and pions in the $++-$ skim for run 43582. Corrections for positively charged particles are shown in (a) $\Delta p(\text{GeV/c})$, (b) $\Delta\lambda(\text{radians})$ and (c) $\Delta\phi(\text{radians})$. Corrections for negatively charged particles are shown in (d) $\Delta p(\text{GeV/c})$, (e) $\Delta\lambda(\text{radians})$ and (f) $\Delta\phi(\text{radians})$. Note that the majority of the corrections are small.
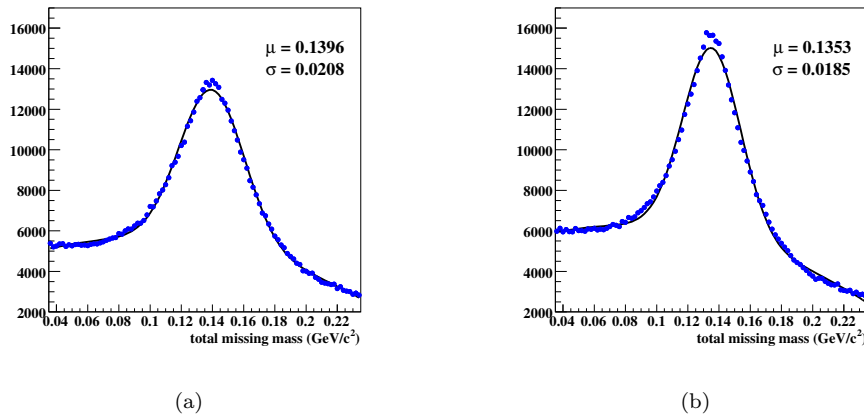
Figure 3.5: Total missing mass off $\gamma p \rightarrow p\pi^+\pi^-(\pi^0)$: (a) As measured by CLAS. The line represents a Gaussian plus 2nd order polynomial fit to the distribution. The Gaussian mean and width — μ and σ — extracted from this fit are shown on the plot. (b) With energy loss, tagger and momentum corrections applied. The fit is the same as in (a). Notice that the peak position, relative to the PDG π^0 mass, and width improve when applying the corrections.

3.3.4 Effectiveness

To check the effectiveness of our corrections, as they apply to the $p\omega$ channel, we'll examine the total missing mass distribution for the $\gamma p \rightarrow p\pi^+\pi^-(\pi^0)$ channel. Only two event selection criteria are applied during this check. First, we require at least one proton, π^+ and π^- are detected. We then consider all $\gamma p\pi^+\pi^-$ combinations such that $|dt_x| < 2ns$ (where dt_x is the difference between the photon vertex time and the start counter vertex time for particle x) for at least one of the detected final state particles. The total missing mass distribution using energy and momenta as measured by CLAS is shown in Figure 3.5(a). Fitting this distribution to a Gaussian plus 2nd order polynomial yields a peak of mass 139.6 MeV/c^2 and width 20.8 MeV/c^2. Applying all the corrections described in this section — energy loss, tagger and momentum corrections — yields the distribution shown in Figure 3.5(b). The peak mass and width extracted in this case are 135.3 MeV/c^2 and 18.5 MeV/c^2 respectively. The PDG reports the mass of the π^0 as 134.98 MeV/c^2. Thus, applying our corrections has improved the peak mass from $\Delta m_{\pi^0} = 4.62$ MeV/c^2 to $\Delta m_{\pi^0} = 0.3$ MeV/c^2 and reduced the width by 11%.

3.4 The Kinematic Covariance Matrix

To effectively use the confidence level from a kinematic fit to select events from a desired topology, the covariance matrix must be well understood. This section details the methods we used to obtain an empirical parameterization of the g11a covariance matrix.

3.4.1   Tagged Photon Errors

Each of the 384 E-counter paddles in the tagger has an energy resolution of $r = 0.001 E_{beam}$ [37]. Assuming equal acceptance along the length of each paddle yields

$$\sigma_{E_\gamma}^2 = \frac{1}{2r} \int_{-r}^{r} E^2 dE = \frac{r^2}{3}. \tag{3.27}$$

Therefore, for the $E_{beam} = 4.019$ GeV runs (which is all we are using) $\sigma_{E_\gamma} = 2.32$ MeV.

3.4.2   Charged Particle Errors

To obtain the covariance matrix for charged particles, we follow a similar approach to what was done in calculating the momentum corrections. We select events with only one proton, π^+, and π^- with no other reconstructed tracks. We then apply the energy loss, tagger and momentum corrections from Section 3.3. Next, the event is kinematically fit to the hypotheses $\gamma p \to p\pi^+(\pi^-)$, $\gamma p \to p(\pi^+)\pi^-$ and $\gamma p \to (p)\pi^+\pi^-$. Only fits with confidence levels greater than 10% were used for determining the resolution errors.

The kinematic fit estimate for the inaccuracy in the measurement of the tracking parameters is given in (3.26). The variance of these quantities is given by

$$\sigma_{\Delta X}^2 = \sigma_X^2 + \sigma_{kfit}^2, \tag{3.28}$$

where σ_{kfit} is the kinematic fit error on the parameter X and σ_X is the detector resolution error that we are trying to calculate.

Each σ_X is, in principle, a function of the particle's momentum magnitude p, orientation (θ, ϕ) in the lab coordinates, CLAS sector number, charge and mass. During this study, we found that any resolution dependence on the azimuthal angle ϕ is negligible. Thus, to obtain our resolution errors, we have divided each of the 6 CLAS sectors into 15 θ bins , the binning is the same as in Section 3.3.3. The resolution error for the tracking quantities p, λ, ϕ is then obtained — as a polynomial function of p — in each bin for each particle type (proton,π^+,π^-).

Momentum Errors

Errors in determining the magnitude of the momentum of a charged particle at the interaction vertex come from: (1) tracking errors which led to inaccuracies in the reconstructed momenta; (2) energy loss errors which led to inaccuracies in propagating the measured momenta back to the interaction vertex.

The tracking errors arise from limitations in the detector itself — the spatial resolution of the drift chambers, performance of the track reconstruction code, etc. These errors are calculated during cooking; however, the error calculations depend on knowledge of what the resolution of the detector components are. For this reason, we write the resolution uncertainty as

$$\sigma_{res} = C_{res} \sigma_{track}, \tag{3.29}$$

where σ_{track} is the error reported by the tracking code and C_{res} is a scaling parameter, to be fit in each bin, which empirically accounts for inaccurate knowledge of the component resolutions.

The energy loss corrections applied by *eloss* are simply the mean energy loss. For moderately relativistic particles, the width of the energy loss distribution can be written as [56]

$$\sigma_{eloss}^2 = C_{eloss} \frac{\gamma^2(1 - \beta^2/2)}{\beta^2}, \tag{3.30}$$

where C_{eloss} is a scaling parameter, to be fit in each bin, which depends on the properties and amount of material traversed by the particle. Notice that (3.30) diverges as $\beta \to 1$ (the equation is only valid for moderately relativistic particles). We chose to eliminate this divergence by simply rewriting (3.30) as

$$\sigma_{eloss}^2 = C_{eloss} \times \left\{ \begin{array}{ll} \frac{\gamma^2(1-\beta^2/2)}{\beta^2}, & \text{if } \beta < 0.765 \\ 2.914, & \text{if } \beta \geq 0.765 \end{array} \right\}, \tag{3.31}$$

where $\beta = 0.765$ is at the minimum of (3.30) and 2.914 is simply (3.30) evaluated at $\beta = 0.765$. This *ad hoc* choice forces the function and its derivative to be continuous.

The total error is then

$$\sigma_p^2 = \sigma_{res}^2 + \sigma_{eloss}^2. \tag{3.32}$$

An example of this procedure is shown in Figure 3.6(a) for protons in sector 1 and $\theta \epsilon (20°, 25°)$. The functional form provides a good fit of the resolution , excluding the lowest momentum point; protons below 350 MeV/c were excluded from the resolution study and our analysis (see Section 3.7.2). This process was carried out in each θ bin in each sector for each particle type to obtain σ_p.

Tracking Angle Errors

Errors in determining the tracking angles of a charged particle at the interaction vertex come from: (1) tracking errors which led to inaccuracies in the reconstructed angles; (2) multiple scattering errors which led to differences between the the measured angles and the angles at the interaction vertex. Thus, the uncertainties on the tracking angles can be written as

$$\sigma_x^2 = (C_{res}\sigma_{track})^2 + \left(\frac{C_{ms}}{\beta p} \right)^2, \tag{3.33}$$

where x is either λ or ϕ, σ_{track} is the error reported by the tracking code and C_{res}, C_{ms} are scaling parameters to be fit in each bin. C_{res} empirically accounts for any inaccuracies which may exist in the knowledge of the detector resolution. The second term in (3.33) parameterizes the multiple scattering contribution to the resolution error. C_{ms} depends on the properties and amount of material traversed by the particle.

An example is shown in Figure 3.6(b) and (c) for protons in sector 1 with $\theta \epsilon (20°, 25°)$. Clearly, the fits are quite good. This process was carried out in each θ bin in each sector for each particle type to obtain σ_λ and σ_ϕ.

Off-Diagonal Elements

Off-diagonal elements in the covariance matrix come from correlations between different tracking parameters. We assume that all correlations occur from tracking, not from energy loss or multiple scattering. Thus, we write all off-diagonal elements of the covariance matrix as

$$\sigma_{xy}^2 = C_{res}^x C_{res}^y \sigma_{xy}^{track}, \tag{3.34}$$

where $C_{res}^{x,y}$ are the scale parameters and σ_{xy}^{track} is the covariance matrix element reported by the tracking code for tracking quantities x, y. We have now empirically calculated all elements of the kinematic covariance matrix.
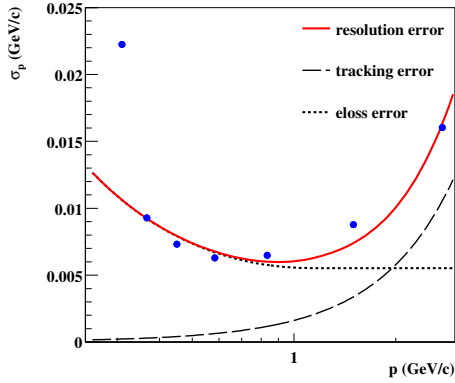
(a)
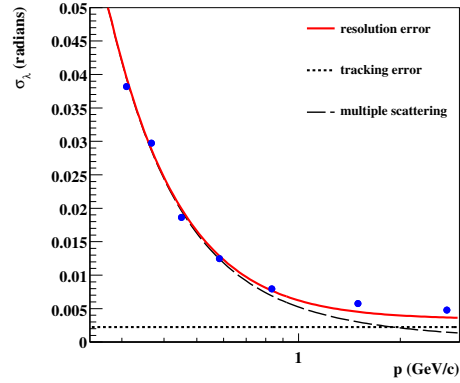
(b)
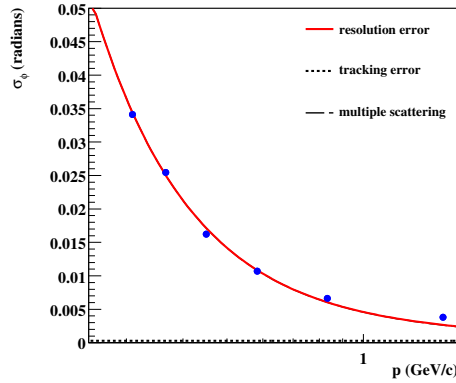
(c)

Figure 3.6: Proton Errors: Sector 1, $\theta\epsilon(20°, 25°)$: (a) $\sigma_p(\text{GeV/c})$ vs $p(\text{GeV/c})$ for protons in this $(sector, \theta)$ bin. The blue circles are the points extracted from the kinematic fits, the dashed line represents the tracking error only, the dotted line represents the energy loss error only and the solid red line shows the total error. (b) $\sigma_\lambda(\text{radians})$ vs $p(\text{GeV/c})$ for protons in this $(sector, \theta)$ bin. The blue circles are the points extracted from the kinematic fits, the dotted line represents the tracking error only, the dashed line represents the multiple scattering error only and the solid red line shows the total error. (c) $\sigma_\phi(\text{radians})$ vs $p(\text{GeV/c})$ for protons in this $(sector, \theta)$ bin. Notation same as in (b).
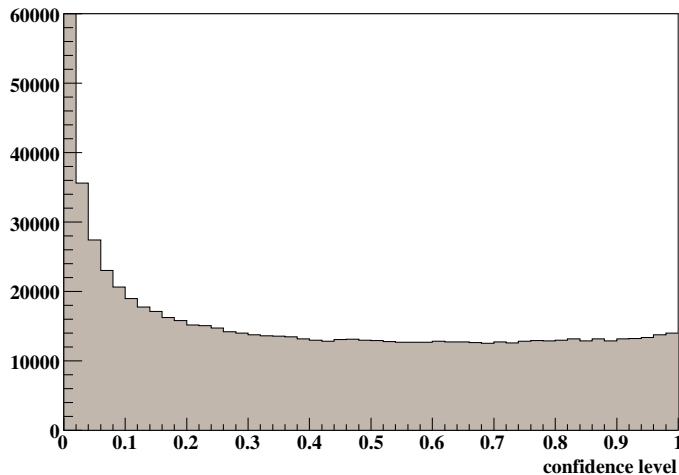
Figure 3.7: $4C$ confidence level for $\gamma p \to p\pi^+\pi^-$ events from run 43582

3.4.3 Pulls and Confidence Level Checks

We can examine the quality of the covariance matrix using the pull and confidence level distributions from the $4C$ kinematic fit of $\gamma p \to p\pi^+\pi^-$. For this study, we again use all events from run 43582 which satisfy the same selection criteria as in Section 3.3.3. The confidence level distribution for all such events is shown in Figure 3.7. The distribution is quite flat. The pull distributions for this fit are shown in Figure 3.8. The Gaussian means and widths are listed in Table 3.2. Recall that each of these distributions should have zero mean and width of one. The agreement of the extracted values with these ideal values is very good.

The quality of the global confidence level and pull distributions is excellent; however, we require more than just global agreement. To check the quality of the confidence level in all kinematic regions, we consider the *normalized slope* of the distribution

$$\bar{a} = \frac{a}{a/2 + b}, \tag{3.35}$$

where a is the slope and b is the intercept obtained by fitting the confidence level distribution to a linear function. Figures 3.9(a) and (b) show examples of confidence level distributions and their respective normalized slopes. Below, we will examine how to use this quantity to estimate signal loss.

To get a better handle on this quantity, we generated $\gamma p \to p\pi^+\pi^-$ Monte Carlo events with three different resolutions. All three were kinematically fit using the same covariance matrix. Next, the normalized slopes were extracted from each kinematic region. Figure 3.9(c) shows the signal kept by a 10% confidence level cut relative to a perfectly flat distribution. The width of the distribution makes it difficult to quantitatively set a tolerance; however, the region of $[-0.5, 0.5]$ is safely within a few percent of the ideal distribution. Thus, if all kinematic regions yield normalized slopes in this range we can consider the covariance matrix to be acceptable.

Figure 3.10 shows the normalized slope extracted in $(p, \cos\theta)$ bins for each particle type for the data events used in this study. Notice that all kinematic regions (excluding edge bins with low statistics) have $|\bar{a}| < 0.5$. Thus, we conclude that the covariance matrix is acceptable.
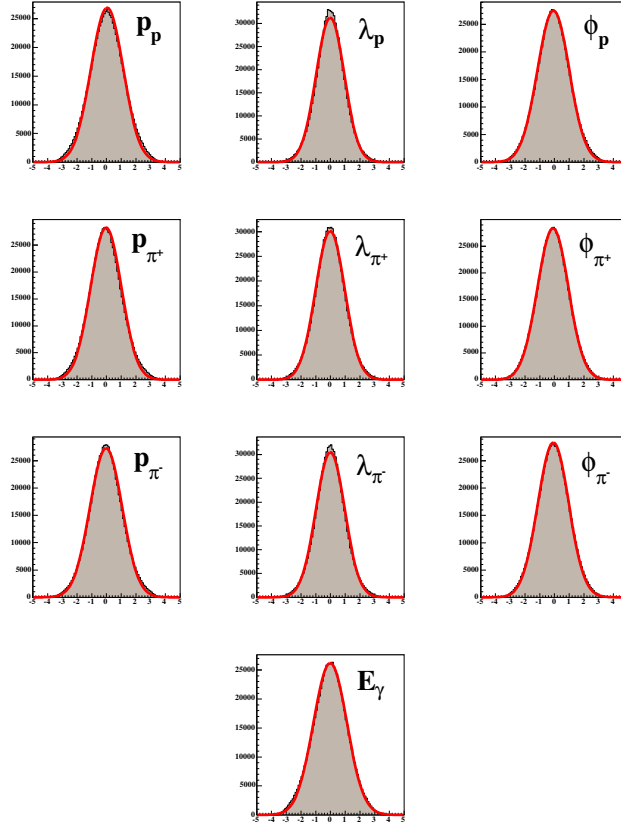
Figure 3.8: Pull distributions obtained from a $4C$ kinematic fit of $\gamma p \rightarrow p\pi^+\pi^-$ for events from run 43582. The lines represent a Gaussian fit to each distribution. See Table 3.2 for the means and widths extracted from these fits.

Quantity	μ	σ
p_p	0.040	1.091
λ_p	-0.018	0.951
ϕ_p	-0.073	1.081
$p_{\pi+}$	-0.033	1.043
$\lambda_{\pi+}$	-0.020	0.987
$\phi_{\pi+}$	-0.101	1.050
$p_{\pi-}$	-0.030	1.086
$\lambda_{\pi-}$	-0.008	0.975
$\phi_{\pi-}$	-0.076	1.048
E_γ	-0.020	1.133

Table 3.2: Gaussian means and widths for the pull distributions from a $4C$ kinematic fit of $\gamma p \rightarrow p\pi^+\pi^-$ for events from run 43582. The distributions are shown in Figure 3.8

(a)

(b)
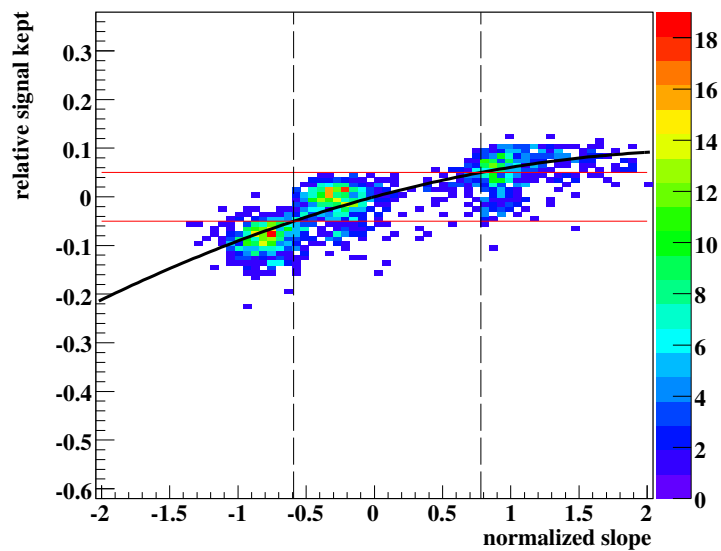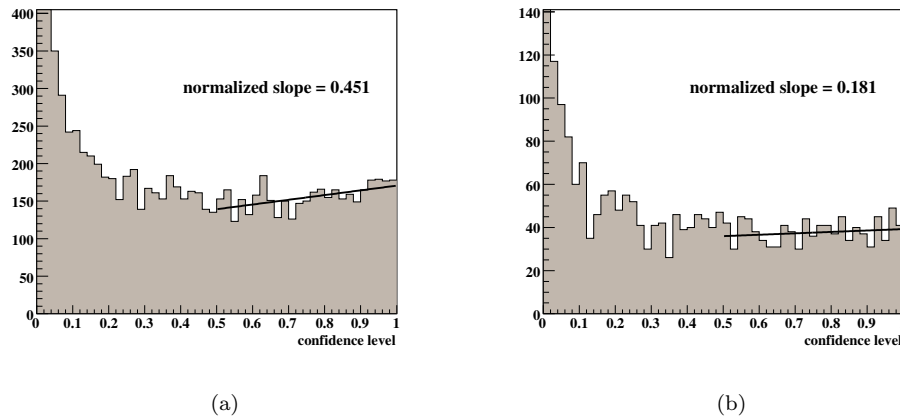
(c)

Figure 3.9: Normalized slopes from confidence level distributions: (a) Example confidence level distribution and its normalized slope extracted by fitting the distribution in the range $(0.5, 1)$ to a linear function. (b) Another example — see (a). (c) Signal kept relative to a perfectly flat distribution vs extracted normalized slope. Monte Carlo was thrown using three different degrees of smearing with each being fit using the same covariance matrix. In each kinematic region, the normalized slope was extracted. The solid black line is a 2nd order polynomial fit to the data. The solid (horizontal) red lines show $\pm 5\%$ and the vertical dashed lines indicate where the polynomial fit intersects the $\pm 5\%$ lines. The width of the distribution makes it difficult to quantitatively set a tolerance on the slope; however, the region of $[-0.5, 0.5]$ is safely within a few percent of the flat distribution. Thus, if all kinematic regions yield normalized slopes in this range we can consider the covariance matrix to be acceptable.

(a)

(b)

(c)
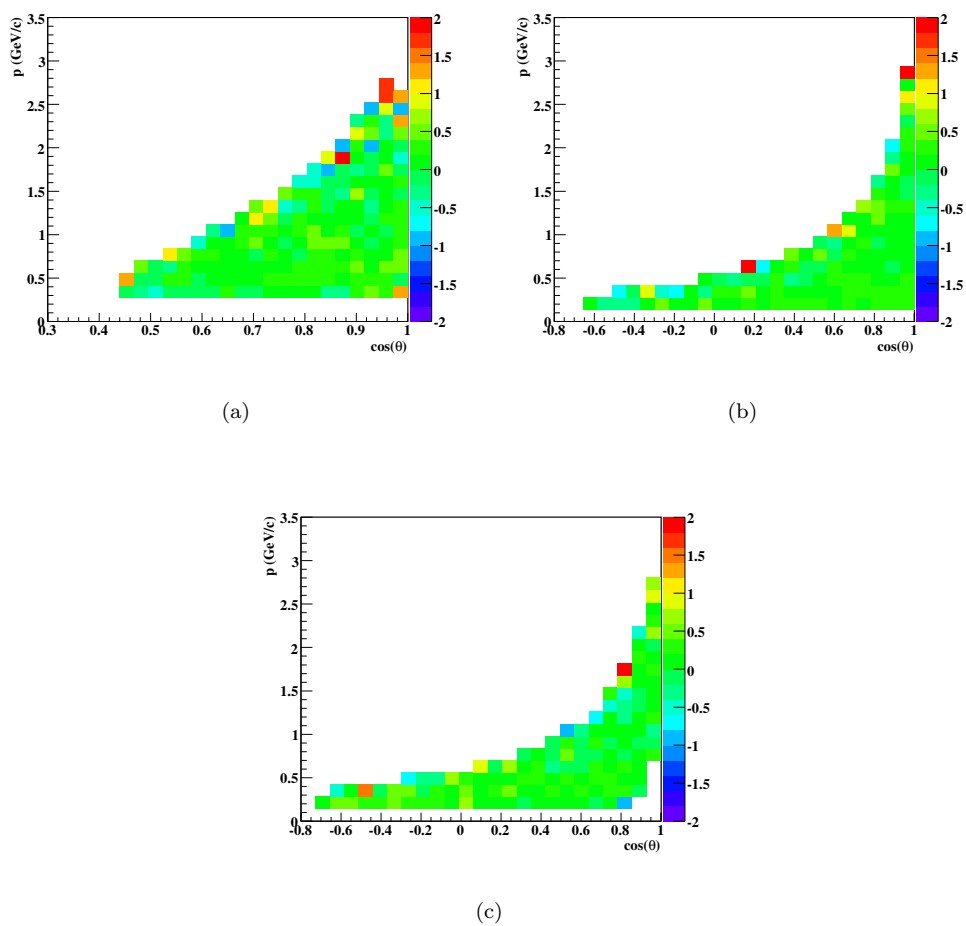
Figure 3.10: Confidence Level Checks: Normalized confidence level slope vs $p(\text{GeV/c})$ and $\cos\theta$ for: (a) proton (b) π^+ (c) π^-. Notice that — excluding edge bins with low statistics — all kinematic regions have $|\bar{a}| < 0.5$. We can now consider the covariance matrix to be acceptable.

(a) (b)
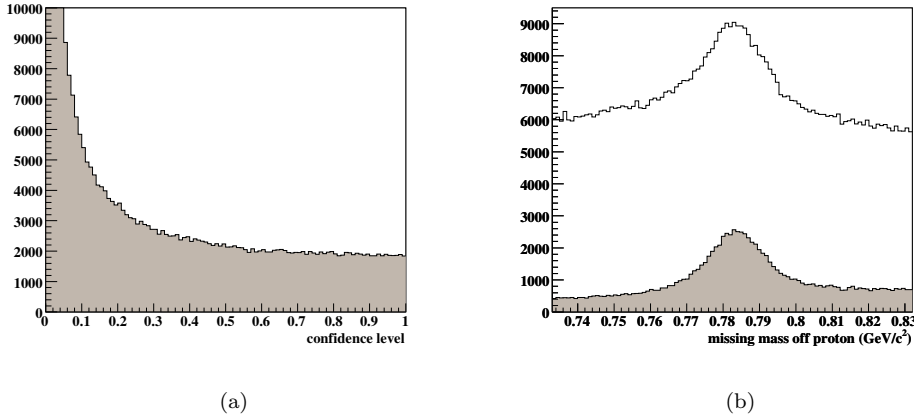
Figure 3.11: (a) Confidence Level for the $1C$ kinematic fit of $\gamma p \rightarrow p\pi^+\pi^-(\pi^0)$ for events from run 43582. The large bleed through from background events up to ~ 0.5 is mainly due to the lack of any particle identification cuts at this stage. (b) Missing mass off the Proton (GeV/c^2): The unshaded histogram is all events from run 43582. The gray shaded histogram is just events that pass a 10% confidence level cut. Clearly the background is greatly reduced.

3.5 Kinematic Fit of $\gamma p \rightarrow p\pi^+\pi^-(\pi^0)$

Now that we've built and tested the covariance matrix, we can proceed to fitting $\gamma p \rightarrow p\pi^+\pi^-(\pi^0)$. At this stage of the analysis, we apply only two very loose cuts: (1) we require that the total missing mass be within 300 MeV/c^2 of the π^0 mass; (2) we require that the missing mass off the proton be within 150 MeV/c^2 of the ω mass. No particle identification or photon timing cuts have been applied.

Figure 3.11(a) shows the confidence level distribution obtained from this fit for all $++-$ events in run 43582. After about 0.5 the distribution is quite flat. The large background bleed through is mainly due to the lack of any particle identification cuts at this stage. Figure 3.11(b) shows the effect of a 10% confidence level cut on the missing mass off the proton distribution. Clearly the background is greatly reduced.

Some signal is also lost when making the confidence level cut. If the errors were truly Gaussian and we had tuned the covariance matrix perfectly, the 10% confidence level cut would cut 10% of the signal; this is the definition of a confidence level. Energy loss and multiple scattering produce a small number of *hard scatters* — scattering off the nucleus rather than the electrons — which do not have Gaussian errors. Thus, these events fall outside of the assumptions used to calculate the confidence level. This causes the actual amount of signal loss to be higher than the nominal 10%.

In principle, this could be accounted for when calculating the confidence level. The χ^2 probability density function could be replaced by a pdf that takes into account the distortions made to the error distributions by the hard scatter events; however, if the Monte Carlo models this effect properly, reproducing the number and distribution of hard scattering events, then we can safely choose to ignore it. We will show in Section 4.2 that this is in fact the case. The Monte Carlo properly handles the hard scattering events, allowing us to ignore this effect in the data.

3.6   Particle Identification

In the previous section, we used the confidence level obtained from a kinematic fit to the missing π^0 hypothesis to greatly reduce the number of background events. The next step in event selection is particle identification (PID). The kinematic fit only utilizes kinematic information. Particle identification will allow us to also incorporate timing information to improve event selection. The events used in this study will be those from the previous section that pass the 10% confidence level cut.

The PID method we use involves making hypotheses as to whether a positively charged track is a proton or a π^+. All negatively charged tracks are assumed to be pions. We can judge the quality of a hypothesis by examining the quantity

$$\Delta tof = tof_{meas} - tof_{calc}, \tag{3.36}$$

where tof_{meas} is the measured time-of-flight and tof_{calc} is the time-of-flight calculated for the current hypothesis. The measured tof is

$$tof_{meas} = t_{SC} - t_{\gamma}, \tag{3.37}$$

where t_{SC} is the time at which the particle struck the CLAS TOF scintillators and t_{γ} is the time at which the photon was at the interaction vertex. The calculated time-of-flight is given by

$$tof_{calc} = \frac{L}{c}\sqrt{1 + \left(\frac{m}{p}\right)^2}, \tag{3.38}$$

where L is the path length from the target to the scintillator, c is the speed of light, m is the hypothesized mass and p is the magnitude of the momentum. Clearly, the closer Δtof is to zero the more confidence there is in the hypothesis.

Figure 3.12 shows Δtof for the particle that passed the kinematic fit under the π^+ hypothesis vs Δtof for the particle that passed the kinematic fit under the proton hypothesis. The region near $(0, 0)$ contains events where both particles are good matches to their respective PID hypotheses. The clusters of events around $(\pm 2, \pm 2)$, $(\pm 4, \pm 4)$, etc., are due to photons associated with the wrong RF bucket. Recall from Chapter 2 that the accelerator delivers bunches of elections to Hall B every 2 ns. The black lines, resembling an iron cross, indicate the timing cut that we impose (events outside the cross are cut). These cuts are meant to be very loose so as not to cut any signal. Any additional background will be separated from the signal as described in Section 3.9.

Figure 3.13 shows the effects of our particle identification cut. The events that fail our PID cut contain no visible amount of signal. To place an upper limit on the value of the signal loss we do the following. First, we extract the fit number of signal and background events in a region around the peak. The boundaries of this region are marked in Figure 3.13 by the vertical dashed lines. The values obtained are 30982.7 signal and 6940.43 background events. Next, we count the actual number of cut events in this same region, which is 7183. We can then use the method of Feldman and Cousins [57] to obtain an upper limit on the number of signal events lost.

The Feldman-Cousins method utilizes *confidence intervals* to place upper and lower limits on measured quantities. A confidence interval, for a confidence level CL, is the range of a measured quantity that has probability CL of containing the true value of the quantity. What makes the Feldman-Cousins method unique is its method for determining the endpoints of the interval using likelihood ratios, for more details see [57]. Applying this method — assuming events originating from a Poisson distribution and using a 95% confidence level — we obtain an upper limit of 392.57 signal events lost or about 1.3% of the total signal in this region. This number will be used as the uncertainty in our PID scheme.
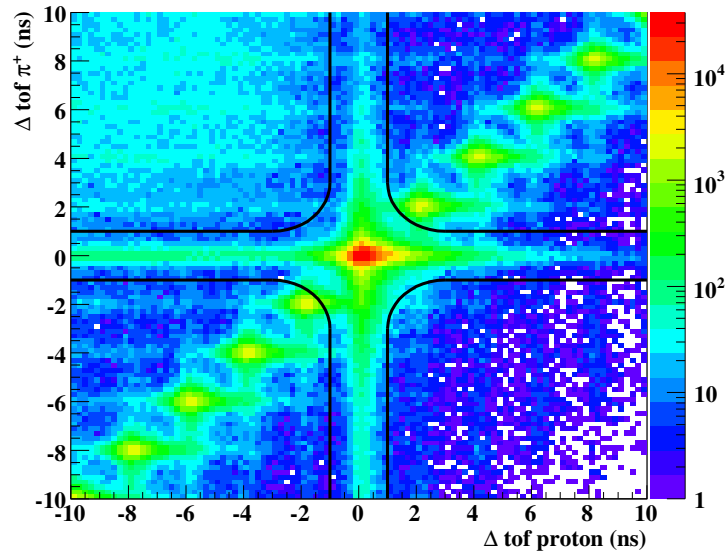
Figure 3.12: Δtof_{π^+}(ns) vs Δtof_p(ns): Particle identification cut for all $\gamma p \to p\pi^+\pi^-(\pi^0)$ events passing a 10% confidence level cut for run 43582. The clusters of events around $(\pm 2, \pm 2)$, $(\pm 4, \pm 4)$, etc. are due to photons associated with the wrong RF bucket. The black lines indicate our timing cuts.
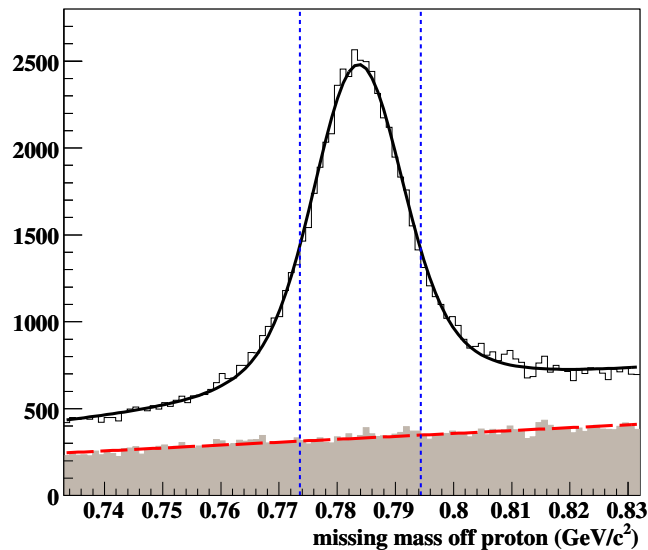

Figure 3.13: Missing mass off the proton for all $\gamma p \to p\pi^+\pi^-(\pi^0)$ events passing a 10% confidence level cut from run 43582. The shaded histogram contains all events cut by our PID cut. The method of Feldman and Cousins was applied to obtain an upper limit of 1.3% signal loss — see text for details.
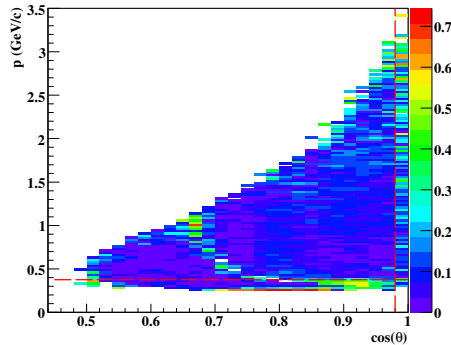
Figure 3.14: Acceptance asymmetry defined in (3.39) vs $p(\mathrm{GeV/c})$ and $\cos\theta$ for protons in Matt Bellis' acceptance study. The curved band of large asymmetries is the result of a bad TOF counter. The vertical dashed line at $\cos\theta = 0.985$ shows a hard fiducial cut placed on all tracks. The horizontal dashed line at $p = 375$ MeV/c indicates our low momentum proton cut. See text for more details.

3.7   Detector Performance Cuts

Another set of necessary cuts has to do with detector performance. If there are certain detector elements or regions that have deficiencies that aren't well enough understood to be modeled in the Monte Carlo, they must be removed from the analysis. This section describes three of these types of cuts that are performed in our analysis.

3.7.1   Minimum Proton Momentum Cut

Low momentum protons are difficult to model in CLAS. They lose a lot of energy as they pass through material in the detector. This not only affects the accuracy of the energy loss corrections, but also causes problems when modeling the acceptance.

Matt Bellis, a post-doctoral researcher at CMU, performed a study that compared the acceptance of the data and Monte Carlo, both of which were calculated empirically using the $\gamma p \to p\pi^+\pi^-$ channel. For example, the acceptance of the proton can be determined by selecting events for which a π^+ and π^- were detected. The event is then kinematically fit to the desired topology. If the event passes, the data is examined to see if it contains a proton in the correct CLAS sector. Using a large enough sample of events, the acceptance of each particle type can be calculated in each kinematic region of the detector.

To examine the results of this study, we define the acceptance asymmetry,

$$A = \frac{|\mathcal{A}_{data} - \mathcal{A}_{mc}|}{\mathcal{A}_{data} + \mathcal{A}_{mc}}, \tag{3.39}$$

where A_{data}, A_{mc} are the acceptances of the data and Monte Carlo respectively. Ideally this quantity should be zero. Figure 3.14 shows A for protons *vs* momentum and $\cos\theta$. In most areas, the agreement between data and Monte Carlo is quite good — A is close to zero. Two regions where problems are evident are forward tracks and low momentum tracks. The former is discussed below, the latter are removed by simply cutting all protons with magnitude of momentum less than 375 MeV/c.

(a)   (b)
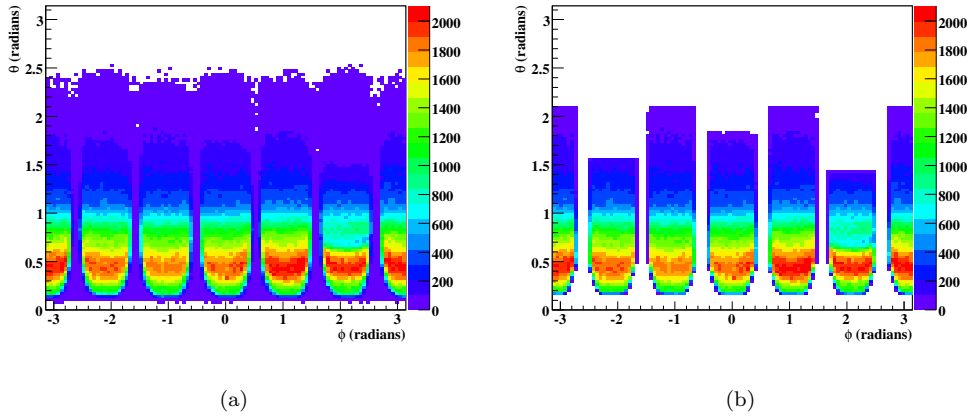
Figure 3.15: θ(radians) vs ϕ(radians): (a) All tracks in run 43582. (b) Tracks in 43582 which pass our fiducial volume cuts. The effects of the fiducial cuts are most dramatic at the sector boundaries and in the forward direction where the torus coils occupy a larger fraction of the solid angle. See text for more details.

3.7.2 Fiducial Volume Cuts

The acceptance study discussed in the previous section was also used to determine fiducial volume cuts — regions of the detector that aren't well modeled and need to be removed from the analysis. Figure 3.15 shows the results of these cuts. The magnetic field varies rapidly close to the torus coils making these regions difficult to model. Thus, any particle whose trajectory is near a torus coil is removed from our analysis. This cut is most dramatic in the forward region, where the coils occupy a larger amount of the solid angle. There is also a hard cut in the forward direction at $\cos\theta = 0.985$ and a sector-dependent cut in the backwards direction.

3.7.3 TOF Paddle Knock Outs

Another necessary cut involved removing or *knocking out* problematic time-of-flight paddles. These paddles were identified by examining occupancy plots of both the data and Monte Carlo. All paddles with noticeable discrepancies for pions and/or protons were flagged as problematic. Table 3.3 lists the paddles in each sector which we have removed from our analysis.

Sector	Knocked Out Paddles
1	18,26,27,33
2	none
3	11,24,25
4	26
5	20,23
6	25,30,34

Table 3.3: Time-of-flight paddles removed from our analysis.
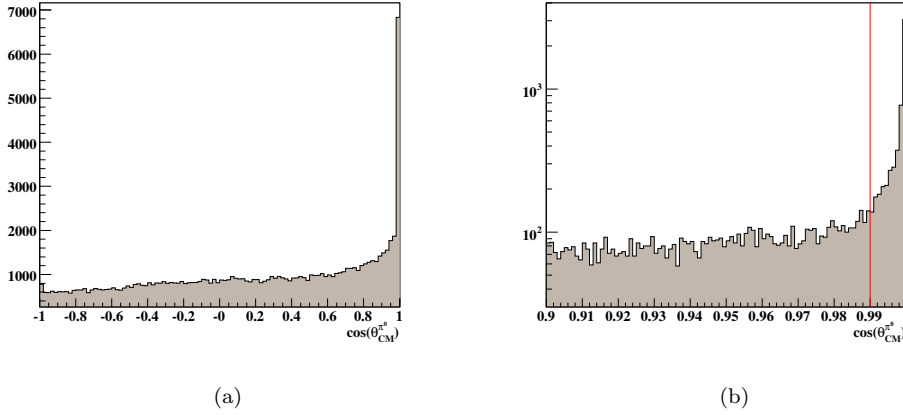
Figure 3.16: $\cos\theta_{CM}^{\pi^0}$: (a) All events in run 43582 which pass a 10% confidence level cut from the 1C fit. There is clearly an unphysical spike in the distribution near 1. (b) Same as (a) except zoomed in on the forward region (note the log scale). The red line indicates the location of our cut.

3.8 The $\cos\theta_{CM}^{\pi^0}$ Distribution

The channel $\gamma p \to p\pi^+\pi^-$ has a significantly larger cross section than $\gamma p \to p\pi^+\pi^-(\pi^0)$. This fact, coupled with the relatively small difference in the missing masses of the two channels, makes $p\pi^+\pi^-$ leakage into our $p\pi^+\pi^-(\pi^0)$ sample a cause for concern. In this section, we consider the possibility of $p\pi^+\pi^-$ leakage resulting from selection of the wrong photon.

To eliminate any leakage from the $\gamma p \to p\pi^+\pi^-$ channel, we need to identify a characteristic of these types of events that can be used to separate them out of our $p\pi^+\pi^-(\pi^0)$ sample. First, consider a $\gamma p \to p\pi^+\pi^-$ event that was produced in the detector. Our analysis procedure will attempt to reconstruct a π^0 from the missing momentum, $\vec{p}_{miss}$. Since the event produced was actually a $p\pi^+\pi^-$ event, the missing transverse momentum measured should be approximately zero, regardless of whether the correct photon has been found. Thus, the momentum vector of the reconstructed π^0 must point (approximately) along the beam direction, $\vec{p}_{miss} \approx \pm|\vec{p}_{miss}|\hat{z}$.

Also, the addition of the extra pion will cause the center-of-mass energy of the final state to increase, due to the additional mass of the π^0. The photon selected would then have to have a higher energy than the photon which actually caused the event to balance out this additional energy in the initial state. This would then lead to extra momentum in the positive $\hat{z}$ direction, in any frame, since we define $\hat{z}$ as the beam direction. Thus, since the missing momentum measured using the correct photon is approximately zero, $\vec{p}_{miss}$ constructed using the higher energy photon must point in the positive $\hat{z}$ direction. Therefore, we expect any leakage of $\gamma p \to p\pi^+\pi^-$, caused by selecting the incorrect photon, into $\gamma p \to p\pi^+\pi^-(\pi^0)$ to result in an excess of events with $\cos\theta_{\pi^0} \approx +1$.

Figure 3.16 shows the $\cos\theta_{CM}^{\pi^0}$ distribution for all events in run 43582 which pass a 10% confidence level cut when fit to $\gamma p \to p\pi^+\pi^-(\pi^0)$. The excess events in the forward direction are quite pronounced. To eliminate this leakage, we cut out all events with $\cos\theta_{CM}^{\pi^0} > 0.99$.

3.9 Signal-Background Separation

Separating *background* events — all non-ω events — from signal events is typically done using the *side-band subtraction* method. In this approach, events from outside the signal region are subtracted from those inside the signal region to remove the background from the distribution; however, this method isn't well suited for multi-dimensional problems. Our channel, $\gamma p \to p\omega \to p\pi^+\pi^-\pi^0$ has four relevant kinematic variables in each $\sqrt{s}$ bin (excluding $m_{3\pi}$). We chose to use the set containing the ω production angle $\cos\theta_{CM}^{\omega}$, the decay helicity angles $\cos\theta_{HEL}$ and ϕ_{HEL} (the choice of which frame to use for the decay angles is not important) and the quantity

$$\lambda \propto |\vec{p}_{\pi^+} \times \vec{p}_{\pi^-}|^2, \tag{3.40}$$

where the pion momenta are measured in the ω rest frame. We note here that a general three body decay, such as $\omega \to \pi^+\pi^-\pi^0$ has five independent kinematic variables which describe an event. Above, we only chose to use three. This is sufficient for our analysis since the ω decay amplitude (described in Section 6.4) is only sensitive to the three variables listed above. The multi-dimensionality of this problem has led us to develop a more powerful method than side-band subtraction to separate the background from our signal.

Our partial wave analysis is event based, so it would be advantageous if we could assign each event a *signal probability*. This could then be used to weight the event's contribution to the likelihood during fitting. It could also be used to weight the event's contribution to any distribution, *ie* when measuring differential cross sections, spin density matrix elements, etc. In this way, we could *subtract* the background without resorting to using events outside the signal region. This section details the procedure we've developed to perform this type of event-based signal-background separation.

3.9.1 Obtaining Q-values

Consider a dataset made up of N events (a $\sqrt{s}$ bin for example) where each event has kinematic variables $\vec{\xi}_i = (cos\theta_{CM i}^{\omega}, \cos\theta_{HEL_i}, \phi_{HEL_i}, \lambda_i)$ and invariant mass of the 3π system m_i. The dataset is made up of both signal and background events. The signal distribution is given by the function

$$S(m, \vec{\xi}) = F_s(\vec{\xi})V(m, \mu, \sigma, \Gamma), \tag{3.41}$$

where

$$V(m, \mu, \sigma, \Gamma) = \frac{1}{\sqrt{2\pi}\sigma} Real\left[w\left(\frac{1}{2\sqrt{\sigma}}(m - \mu) + i\frac{\Gamma}{2\sqrt{2}\sigma}\right)\right], \tag{3.42}$$

is the convolution of a Gaussian of width σ and a non-relativistic Breit-Wigner of width Γ with mean μ, known as a *Voigtian* ($w(z)$ is the complex error function) and $F_s(\xi)$ is the unknown kinematic dependence of the signal distribution. The background distribution is given by $B(m, \xi)$, the functional form is not known. If it were known, we wouldn't need to do any of this.

The aim of this procedure is, for each event, to determine the signal weight factor Q_i, or equivalently, the background weight factor $1 - Q_i$. We first need to define a metric for the space spanned by $\vec{\xi}$. We chose to use δ_{ij}/r_i^2, where $\vec{r} = (2, 2, 2\pi, 1)$ are the ranges of $\vec{\xi}$, so that the *distance* between any two events, d_{ij}, is given by

$$d_{ij}^2 = \sum_{k=1}^{4}\left[\frac{\xi_k^i - \xi_k^j}{r_k}\right]^2. \tag{3.43}$$

Then, for each event, with kinematics $\vec{\xi}_0$ and mass m_0, we find the closest N_c events according to (3.43) (we chose to use $N_c = 100$). These N_c events occupy a very small region around $\vec{\xi}_0$, thus we can approximate the signal and background functions of each event as

$$S(m_i, \vec{\xi}_i) = F_s(\vec{\xi}_0)V(m_i, \mu, \sigma, \Gamma) \approx A \cdot V(m_i, \mu, \sigma, \Gamma), \tag{3.44}$$

$$B(m_i, \vec{\xi}_i) = B(m_i, \vec{\xi}_0) \approx am_i + b, \tag{3.45}$$

where A, a, b are parameters to be determined. The linear approximation of the mass dependence of the background is validated by the small regions of phase space which we are examining. Not only are we selecting events occupying a very small amount of the available phase space, but the ω mass region also only accounts for a fraction of the range of the 3π invariant mass.

For each event, we then fit the N_c closest events using the unbinned maximum likelihood method to obtain the parameters $\vec{\eta} = (A, a, b)$ and the corresponding covariance matrix C_η. Using the results of the fit, the expected number of signal and background events, denoted as s_i and b_i respectively, can be calculated at m_0 and the Q-factor written as

$$Q_i = \frac{s_i}{s_i + b_i}. \tag{3.46}$$

This Q-factor can then be used to effectively subtract out the background.

3.9.2   Error Estimation

We also need to be able to extract the uncertainties on the individual Q-factors and then combine these to obtain the errors on measurable quantities. We can use the covariance matrix, C_η, for the fit parameters, $\vec{\eta}$, from each event's fit to write the error on Q as

$$\sigma_Q^2 = \sum_{ij} \frac{\partial Q}{\partial \eta_i}(C_\eta^{-1})_{ij}\frac{\partial Q}{\partial \eta_j}. \tag{3.47}$$

To make any measurement, we need to bin the data. Consider a bin with N events. The procedure employed to obtain the Q-values leads to highly correlated results between each event and its N_c nearest neighbors. Thus, adding the N individual errors in quadrature would clearly underestimate the total error. We then choose to write the error on extracting the number of signal events as

$$\sigma_{signal} = \sum_i^N \sigma_{Q_i}, \tag{3.48}$$

which assumes 100% corelation. This assumption is an overestimate of the error. The statistical error on the number of events is then added to (3.48) to obtain the total error

$$\sigma_N^2 = N_{signal} + \sigma_{signal}^2, \tag{3.49}$$

where

$$N_{signal} = \sum_i^N Q_i, \tag{3.50}$$

is the total number of signal events extracted in the bin.
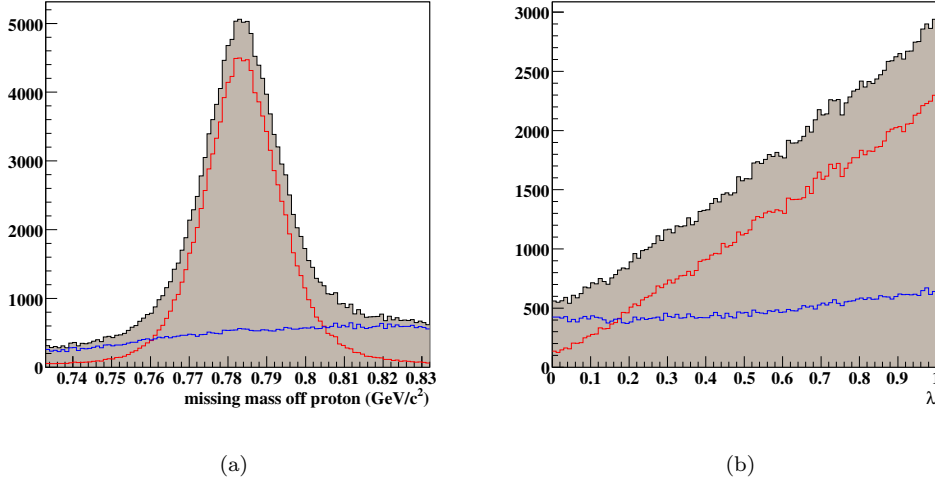
(a)

(b)
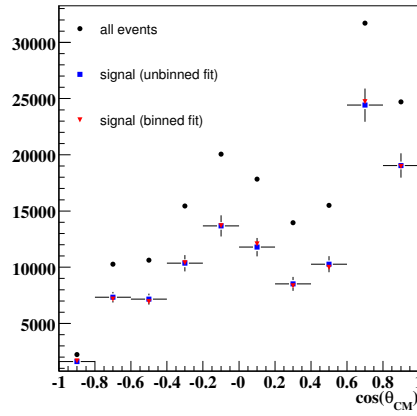
(c)

Figure 3.17: Signal-Background separation in the $\sqrt{s} = 2.205$ GeV bin: (a) Missing mass off the proton (GeV/c²): The shaded histogram is all the data in this bin. The red line is each data event weighted by its Q-value (signal). The blue line is each event weighted by $1 - Q$ (background). (b) λ (defined in (3.40)): Notation is the same as (a). (c) Events vs $\cos \theta_{CM}^{\omega}$: The black circles are the events, the blue squares are the signal extracted using the unbinned fitting method described in this section, the red triangles are the signal extracted by simply binning the data in $\cos \theta_{CM}$, then fitting each bin to a Voigtian plus a linear background. The agreement between the two methods, in the binning angle, is excellent.
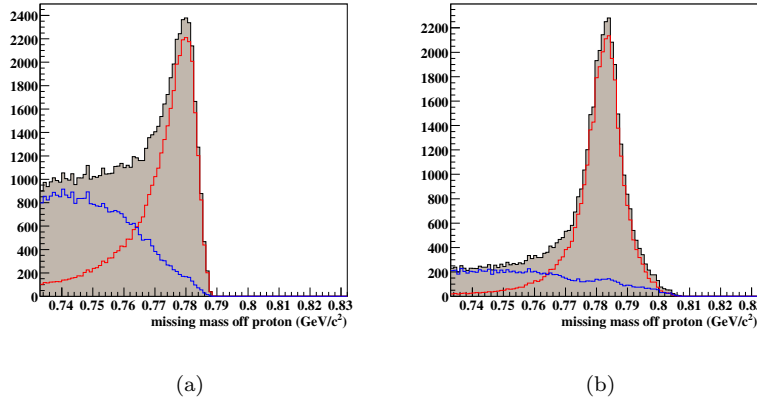
Figure 3.18: Signal-Background separation extrapolated to near-threshold bins. Missing mass off the proton (GeV/c^2): (a) $\sqrt{s} = 1.735$ GeV. (b) $\sqrt{s} = 1.755$ GeV. Notation as in Figure 3.17(a),(b).

3.9.3   Applying the Procedure

Figure 3.17(a) shows the global signal-background separation as a function of the $\pi^+\pi^-\pi^0$ mass from the $\sqrt{s} = 2.205$ GeV bin. The background estimation appears to be quite reasonable. Notice that even though the background shape in each small kinematic region was approximated as linear, the global background parameterization deviates from this shape. The quantity λ, defined in (3.40), provides us with an interesting way to test our procedure. The ω decay amplitude is proportional to λ (see Section 6.4). Thus, the number of signal events should be proportional to λ. Figure 3.17(b) shows the global signal-background separation as a function of λ. The extracted signal is found to be proportional to λ, even though this was not enforced by the fits.

We can also compare projections of the signal-background separation to a more traditional binned fit approach. Figure 3.17(c) shows a comparison between extracting signal events by binning the data in $\cos\theta^{\omega}_{CM}$, then fitting each bin to a Voigtian plus linear background and extracting the signal using (3.50). The agreement between the two methods, in the angle used to bin the data, is excellent. We re-emphasize here that simply fitting to 1-D projections of the data is not sufficient. The kinematic correlations must be preserved, which is why this technique was developed. This method of separating signal from background has proven to be very robust.

3.9.4   Near Threshold Bins

A problem arises in $\sqrt{s}$ bins near ω threshold. The CLAS detector has very limited (if any) acceptance for events on the high side of the ω mass peak, since these events correspond to lower momentum protons. With only one side of the peak, it is not possible to extract the shape of the background. Thus, for bins with $\sqrt{s} < 1.77$ GeV, we must extrapolate the Q-values from the closest bins where a reliable separation can occur. For each event in a near-threshold bin, the closest event, as defined by (3.43), from each bin in the range 1.775 GeV $\leq \sqrt{s} \leq$ 1.895 GeV is identified. The $\sqrt{s}$ dependence of the Q-values of these points is extracted using a χ^2 fit to a 2nd order polynomial. This polynomial is then evaluated at the near-threshold bin's $\sqrt{s}$ to determine the event's Q-value and error. Figure 3.18 shows the global signal-background separation in two near-threshold bins. The background parameterizations are quite reasonable.
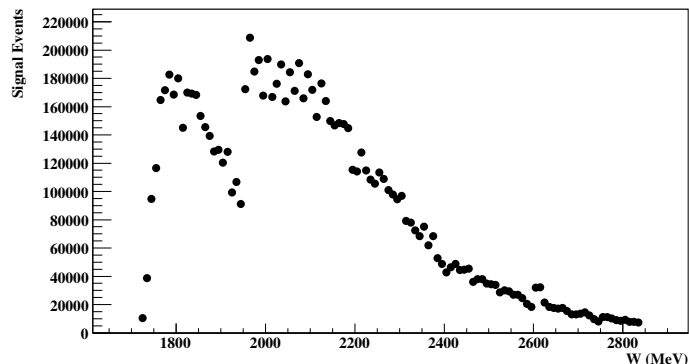
Figure 3.19: Number of signal events, extracted using the method discussed in Section 3.9, after all cuts detailed in this chapter vs W (MeV). The total number of signal events integrated over all energies is ~ 10.1 million. The discontinuity near $W \sim 1950$ MeV is an artifact of the $g11a$ trigger, see Section 2.5 for details.

3.10 Summary

Prior to analyzing the $\gamma p \to p\omega$ channel, we used inclusive $\gamma p \to p\pi^+\pi^-$ events to develop energy and momentum corrections for the $g11a$ run period. This channel was also employed to tune the kinematic covariance matrix specifically for $g11a$. Starting from a skim containing all events from the $g11a$ run period in which at least two positive and at least one negative track were detected, we began developing a set of cuts to select out $\gamma p \to p\omega$ events. All of these cuts were described in detail in this chapter. To separate ω from non-ω events, we developed an event-based technique which properly handles all kinematic correlations. Figure 3.19 shows the number of signal events extracted using the method described in Section 3.9, after applying all cuts detailed in this chapter, in each $\sqrt{s}$ bin. The total number of $\gamma p \to p\omega$ events, after applying all of the cuts described in this chapter, integrated over all $\sqrt{s}$ is ~ 10.1 million.

Chapter 4

Acceptance and Normalization

In the previous chapter, we discussed how we select $p\omega$ events from the data measured by the CLAS detector. To extract the physics produced in the detector, we now need to account for inefficiencies in our analysis resulting in lost events. These can arise in the detector itself or in the software used to process the raw detector information. The probability that an event of a given kinematics will be kept by the analysis is known as the *acceptance*. Once our detector acceptance has been accounted for, we then must *normalize* the data to convert the number of events detected into the probability for which the events were produced. Normalization includes things such as the number of target particles, the total number of photons which were incident on the target, the fraction of time which the detector was ready to record an event, etc. This chapter covers our acceptance calculation along with determinations of all normalization factors.

4.1 Detector Simulation

4.1.1 GSIM

The basis of our acceptance calculation was the CLAS GSIM package. GSIM is a GEANT based simulation of the CLAS detector and is the collaboration's standard simulation package [58]. We generated a total of 200 million $\gamma p \rightarrow p\omega \rightarrow p\pi^+\pi^-\pi^0$ events across all $\sqrt{s}$ bins. The E_γ distribution was thrown such that each bin would have $\sim 100,000$ accepted events after all cuts. In all other kinematic variables the events were thrown according to $p\omega$ and $\omega \rightarrow \pi^+\pi^-\pi^0$ phase space. The Breit-Wigner width of the ω was included in the generation.

After generation, the events were processed by GSIM. GSIM propagated each of the particle tracks from the event vertex through the CLAS detector resulting in a simulated set of detector signals for each track. GSIM simulates any particle decays that may occur, along with energy loss and multiple scattering effects caused by interactions of the particles with material in the CLAS detector. The GSIM output was then processed by a CLAS software package known as GPP which *smears* the detector signals to more accurately reflect the actual resolution. The scintillator times are smeared according to the length of the scintillator. GPP allows the user to specify the degree of smearing via a parameter which we set to 0.5. GPP also smears the drift chamber time signals according to the distance of closest approach (DOCA). We found that by simply smearing these times we weren't able to completely match the resolution in all regions of the detector. So we chose to apply minimal smearing — the GPP parameters for each DC region were set to 1.0 — at this step. The next section contains details on an empirical smearing algorithm which we developed to better match the resolution in all regions of the detector.

(a)   (b)
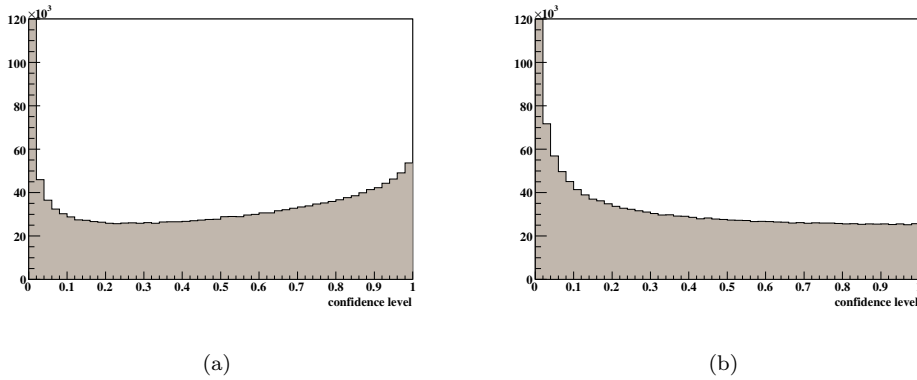
Figure 4.1: $4C$ confidence level for $\gamma p \to p\pi^+\pi^-$ events from Monte Carlo. (a) Events obtained from GSIM and GPP. Clearly the resolution does not match the data. (b) With additional smearing applied from our study. The global agreement with the data resolution is quite good.

At this stage, the Monte Carlo is in the form of raw data obtained from the detector. Next, it was cooked and skimmed with the same analysis software used on the $g11a$ data. It is vitally important that the exact same versions of the software are used on the Monte Carlo as the data. This ensures that any inefficiencies are reflected the same way in both.

4.1.2 Momentum Smearing

In Section 3.4, we used the normalized slope of the confidence level from a $4C$ kinematic fit to $\gamma p \to p\pi^+\pi^-$ to evaluate the quality of our covariance matrix. We can use the same approach here to examine the quality of our Monte Carlo resolution. The resolution of the Monte Carlo should be the same as the data in all kinematic regions.

Figure 4.1(a) shows the confidence level distribution for all events in this study. At this stage, the resolution is that obtained from GSIM and GPP using the parameters from the previous section. Clearly, the resolution of the Monte Carlo is better than the data globally. Figures 4.2(a),(c),(e) show the normalized slope, $\bar{a}$, extracted in $(p, \cos\theta)$ bins for each particle type. Notice that in every kinematic region $|\bar{a}| > 0.5$ — recall in Section 3.4 we required $|\bar{a}| < 0.5$ in all kinematic regions for the data. Thus, without additional smearing, the Monte Carlo resolution does not match the data anywhere.

Smearing the tracking angles was performed by sampling from a Gaussian distribution with mean λ, ϕ — the reported value of the tracking angles — and width $1.85\sigma_{track}$, where σ_{track} is the resolution obtained from the tracking code. Smearing of the magnitude of the momentum was done in the same (p, θ) binning used to determine the momentum corrections in Section 3.3.3. The average value of the smearing was ~ 2 MeV/c. Figure 4.1(b) shows the confidence level distribution for all events in this study after applying the additional smearing. The global confidence level is now flat, suggesting the global resolution is in agreement with the data. Figures 4.2(b),(d),(f) show the normalized slope extracted in $(p, \cos\theta)$ bins for each particle type with the additional smearing applied. Notice that in every kinematic region, we now have $|\bar{a}| < 0.5$. Therefore, the Monte Carlo resolution now matches that of the data in all kinematic regions.
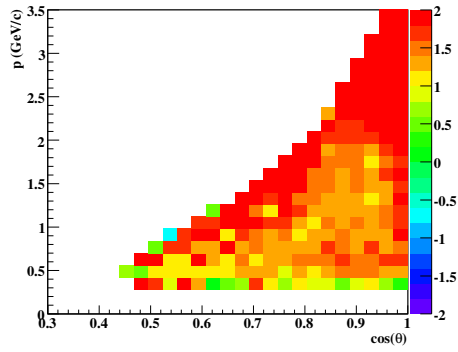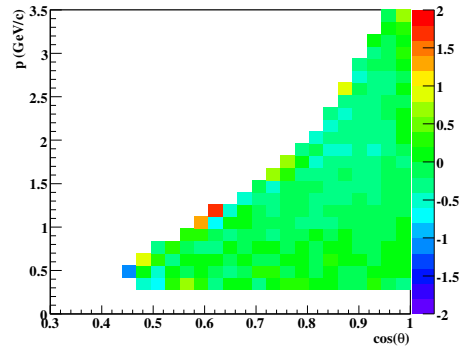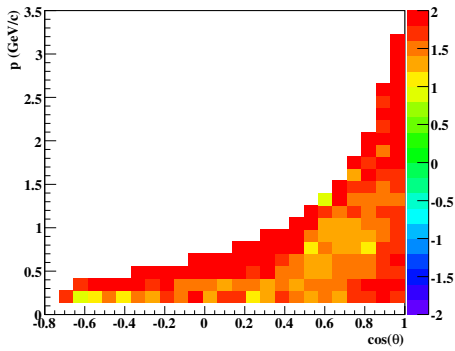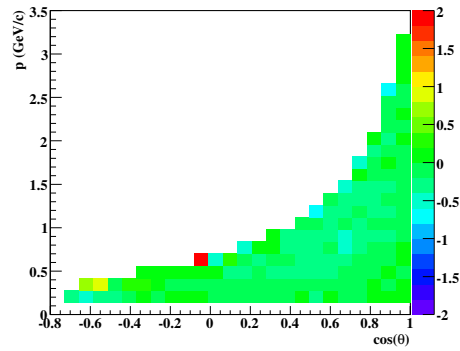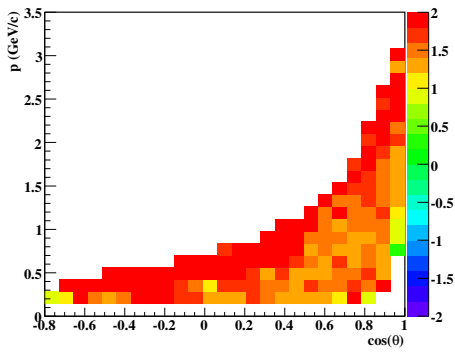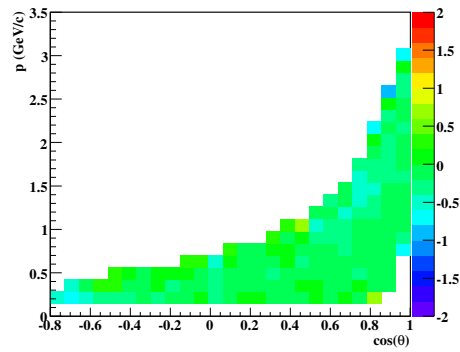
Figure 4.2: Confidence Level Checks: Normalized confidence level slope, $\bar{a}$, vs $p(GeV/c)$ vs $\cos\theta$ for: (a) proton (b) proton with smearing (c) π^+ (d) π^+ with smearing (e) π^- (f) π^- with smearing. Recall that for the data, all kinematic regions had $|\bar{a}| < 0.5$. After smearing, all kinematic regions in the Monte Carlo also fall in this range.

4.1.3 Trigger Simulation

The details of the $g11a$ trigger are discussed in Section 2.5. For this section, we only need to note that at least two charged tracks were required. Possible trigger inefficiencies were first noticed by the Genova group [48]. They saw a discrepancy between differential cross sections of $\gamma p \to p\omega$ using the two topologies $\gamma p \to p\pi^+(\pi^-\pi^0)$ and $\gamma p \to p\pi^+\pi^-(\pi^0)$. They chose to correct for this effect by applying a global scale factor to the two track topology. The cause for the trigger inefficiency was not determined.

To correct for the trigger inefficiency, Zeb Krahn, a graduate student at CMU, did a study which utilized the *trigger word* written into the data stream during the run. This word contains information on which sectors met the trigger conditions for each event. His study used $\gamma p \to p\pi^+\pi^-$ events and required all three tracks be detected. Since only two tracks are required in the trigger to keep the event, one can look for events of this type where a third particle was tracked through a sector but the trigger word doesn't record that sector as having met the trigger conditions. In this way, Zeb was able to build a map of the trigger efficiency for each particle type as a function of sector, time-of-flight counter and ϕ (azimuthal angle).

Figure 4.3 shows the trigger efficiency maps for sector 1 for each particle type. For most TOF-counters and at most angles, the efficiency is high — close to 1. But there are distinct features which are clearly noticeable. For example, both pion trigger maps show deficiencies in paddles 12 and 13 around azimuthal angles of $15°$ and $-15°$ respectively. The TOF-counters are equipped with a photo-multiplier tube on each end. For a paddle to fire the trigger, at least one of its PMTs must record a pulse above a predefined threshold. Thus, if the threshold of one of the PMTs is set too high, then attenuation of the light produced by the particle when it interacts with the scintillator is most likely to lead to an inefficiency at $\pm15°$.

To check the validity of the maps, we looked at $\gamma p \to p\pi^-(\pi^+)$ events from run 43582. We required that the π^+ not be detected to enhance any trigger inefficiencies. Figure 4.4(a) shows the π^- trigger map for Sector 1. Figure 4.4(b) shows the π^- yield in Sector 1 from events in run 43582 which pass a 10% confidence level cut when kinematically fit to $\gamma p \to p\pi^-(\pi^+)$. The yields are normalized such that each TOF-counter bin has a maximum of 1. The distinct features of the trigger map are clearly visible in the yield plot as well. For example, there are noticeable depletions in the yields of paddles 12 and 13 around the azimuthal angles where inefficiencies can be seen in the trigger map. In fact, every distinct inefficiency of the trigger map has a corresponding area of depletion in the yield plot. It isn't possible to determine quantitatively the quality of the map from just this study; however, we can conclude that, at least qualitatively, the maps are valid.

Since we require that at least three charged particles be reconstructed in all events used in our analysis, the effects of the trigger inefficiency are small; however, it is still important to account for this effect. We implement the trigger inefficiency as follows. For each particle, we throw a random number, sampled uniformly from $(0, 1)$. If that number is less than or equal to the trigger efficiency for that track, then the track is considered to have fired the trigger in its sector. We do this for each particle detected in the event. If at least two sectors fire the trigger, then the event is kept. Otherwise, we cut the event from the Monte Carlo. In this way, we can reproduce the trigger inefficiency in our detector simulation.

Figure 4.5 shows the effect of the trigger simulator on $\gamma p \to p\omega \to p\pi^+\pi^-(\pi^0)$ in two $\sqrt{s}$ bins. The overall effect is, on average, about 5%. In the higher energy bins, each TOF-counter maps onto a larger region of $\cos\theta_{CM}^\omega$. Thus, the individual paddle inefficiencies become more apparent; however, the correction is still less than 10%.

(a)

(b)

(c)
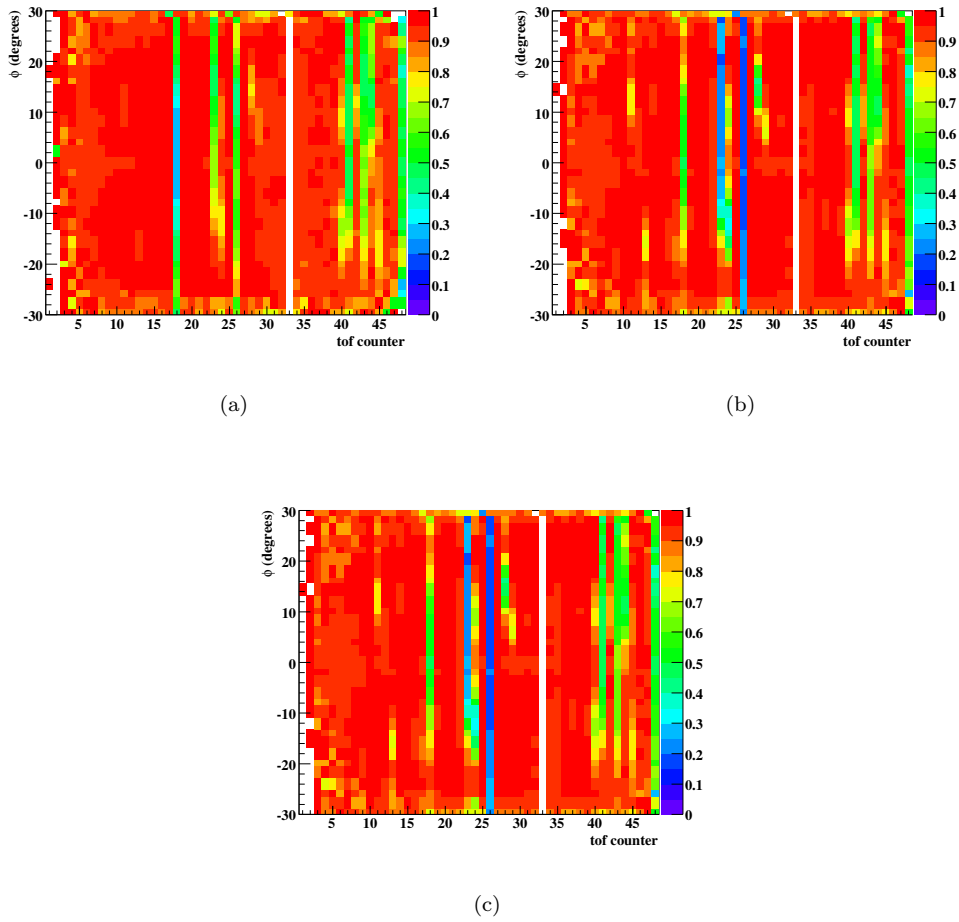
Figure 4.3: Trigger efficiency vs ϕ(degrees) and TOF-counter for Sector 1: (a) proton (b) π^+ (c) π^-.
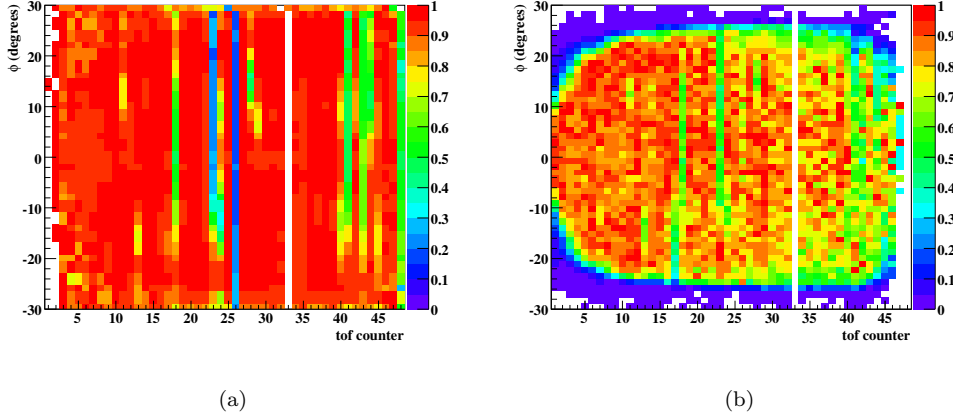
Figure 4.4: (a) π^- trigger efficiency vs ϕ(degrees) and TOF-counter for Sector 1 as determined by our study using the trigger word. (b) π^- yield — normalized such that each TOF-counter bin has a maximum of 1 — vs ϕ(degrees) and TOF-counter for Sector 1 from $\gamma p \to p\pi^-(\pi^+)$ events from run 43582. Notice that the trigger inefficiencies map directly onto depletions in the yield.
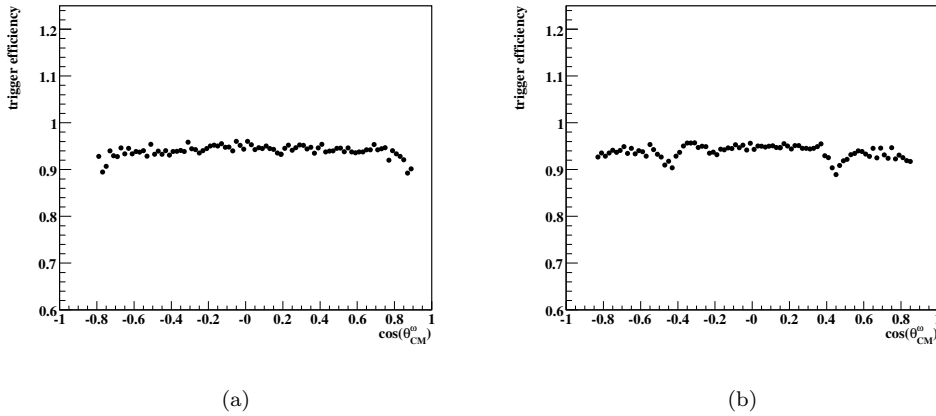
Figure 4.5: Trigger efficiency vs $\cos\theta_{CM}^\omega$: (a) Low energy, $\sqrt{s} = 1.805$ GeV, bin. (b) High energy, $\sqrt{s} = 2.705$ GeV, bin. Each shows the ratio of events kept after running our trigger simulator. The overall effect on $\gamma p \to p\pi^+\pi^-(\pi^0)$ is about 5%. In the higher energy bins, each TOF-counter maps onto a larger range of $\cos\theta_{CM}^\omega$. Thus, the individual inefficient counters are more visible at higher energies.
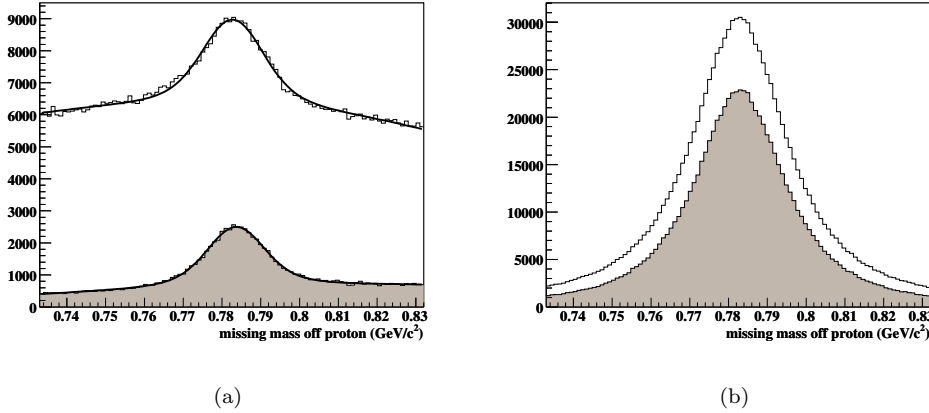
Figure 4.6: Missing mass off the proton (GeV/c^2): (a) The unshaded histogram is all events from run 43582. The gray shaded histogram is just events passing a 10% $1C$ confidence level cut. No PID cuts were placed on the data at this point. The lines represent the Voigtian plus polynomial background used to extract the number of signal events. (b) Same as (a) but for Monte Carlo.

4.2 Kinematic Fit of $\gamma p \to p\pi^+\pi^-(\pi^0)$

In Section 4.1.2 we showed that, after momentum smearing, we can use the same covariance matrix for both the data and Monte Carlo. Recall in Section 3.5 we discussed the topic of non-Gaussian errors. Energy loss and multiple scattering produce a small number of *hard scatters* — scattering off the nucleus rather than the electrons. These events do not follow a Gaussian distribution. Thus, they fall outside the assumptions used to calculate the confidence level. If the Monte Carlo handles this properly, then the same fraction of events will be cut in both the data and Monte Carlo and we can ignore the effect.

Figure 4.6(a) shows the ω mass peak obtained from events from the $++-$ skim in run 43582. The unshaded histogram contains all the events (the cuts used in the skim are detailed in Section 3.5), while the shaded histogram contains only the events which pass a 10% confidence level cut when kinematically fit to $\gamma p \to p\pi^+\pi^-(\pi^0)$. The number of signal events can be extracted by fitting both distributions to a Voigtian plus a fourth degree polynomial. The 10% confidence level cut keeps 66.90% of the signal events. For the Monte Carlo, we can simply count how many events are kept when applying the confidence level cut. This number turns out to be almost identical to what was kept in the data, 66.91%.

At first glance, the amount of signal kept might seem low; however, recall that for this study we haven't applied any other cuts — including particle identification, which also tends to cut events with hard scatters. Even our very loose PID cuts 6% of the signal, the standard CLAS PID schemes would cut much more. To compare our confidence level cut to the more traditional missing mass cuts, we fit the missing π^0 peak in the Monte Carlo to a Gaussian. The width of the peak extracted from this fit was 20.2 MeV/c^2. Making a 2.5σ cut on the Monte Carlo leaves 66.6%. Thus, our 10% confidence level cut leaves us with (globally) the same number of events as the more traditional 2.5σ missing mass cut.

4.3 Systematic Study of the Acceptance

To obtain an estimate of how well we know our acceptance, we performed a sector dependent study in several $\sqrt{s}$ bins. In each bin, we extracted the acceptance corrected yields for each sector, tagging the sector according to proton detection, since this directly maps onto the ω production quantities $\cos\theta_{CM}^{\omega}$ and t. Each sector has its own acceptance, due to the various sector dependent inefficiencies such as knocked out TOF-counters, drift chamber holes, etc.; however, if we have properly accounted for these problems, then we should extract the same acceptance corrected yield from each sector (within statistical errors).

Figure 4.7 shows the yields extracted for each CLAS sector from the $\sqrt{s} = 2.005$ GeV bin. The TOF-counter knock outs and fiducial cuts are very prominent when examining each sector independently. The error bars include the signal-background separation error, along with the statistical error on the number of signal events and the number of accepted Monte Carlo events. Figure 4.8 shows the acceptance corrected yields in the same $\sqrt{s}$ bin. Notice that even though the extracted yields are quite different, our acceptance correction does a good job of bringing each of the sectors' corrected yields into alignment.

Figure 4.9 shows the ratio of each sector's acceptance corrected yield to the six sector mean value in each $\cos\theta_{CM}^{\omega}$ bin. There is no clear $\cos\theta_{CM}^{\omega}$ dependence in this bin or any of the other bins used in this study. Thus, we conclude that any acceptance errors are (approximately) independent of $\cos\theta_{CM}^{\omega}$ or t. Recall that the error bars include the signal-background extraction errors along with the statistical errors on the number of signal and Monte Carlo events. If these errors are sufficient, then we expect

$$\sum_{c,s}\Theta(\sigma_{c,s}^2 - (y_{c,s} - \mu_c)^2) \approx 0.68N, \tag{4.1}$$

where s denotes the sector, c is the $\cos\theta_{CM}^{\omega}$ bin, $\sigma_{c,s}$ is the error (as described above), $y_{c,s}$ is the acceptance corrected yield, μ_c is the mean value of the corrected yield, Θ is the Heaviside step function and N is the number of $(sector, \cos\theta_{CM}^{\omega})$ bins.

In this bin, only 52.8% of the points lie within one σ of the mean value — a good indicator that some additional error, from our acceptance calculation, needs to be included. Recall that there is no evidence for any $\cos\theta_{CM}^{\omega}$ dependence in the additional error. Thus, to estimate the acceptance error, we require

$$\sum_{c,s}\Theta(\sigma_{c,s}^2 + (\sigma_{acc}y_{c,s})^2 - (y_{c,s} - \mu_c)^2) \approx 0.68N \tag{4.2}$$

where σ_{acc} is the relative error on the acceptance corrected yield due to the acceptance calculation. For this bin, the value obtained is $\sigma_{acc} \approx 5\%$.

This procedure was carried out in five $\sqrt{s}$ bins. Figure 4.10 shows the values obtained for σ_{acc} in each of the bins used in this study. There is a gradual increase in the size of the acceptance error with increasing $\sqrt{s}$, which is not surprising. Using these results, we can parameterize the acceptance error as a function of center-of-mass energy

$$\sigma_{acc}(\sqrt{s}) = 0.0217\sqrt{s} + 0.002791. \tag{4.3}$$

The value of σ_{acc} ranges from 4.02% at $p\omega$ threshold up to 6.43% in our highest energy bin. In each of the $\sqrt{s}$ bins used in our analysis, we will include a relative error of $\sigma_{acc}(\sqrt{s})$ to account for any (relative) inaccuracies in our acceptance calculations.
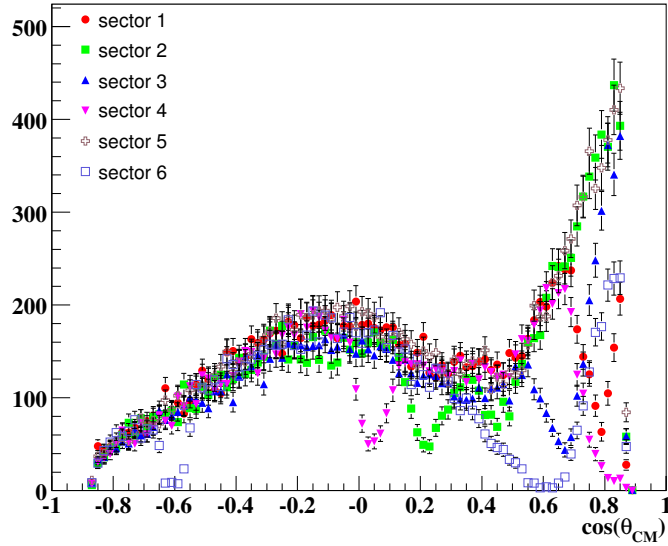
Figure 4.7: Data yields in the $\sqrt{s} = 2.005$ GeV bin for each sector vs $\cos \theta^{\omega}_{CM}$. The dips correspond to time-of-flight paddles which have been removed from our analysis.
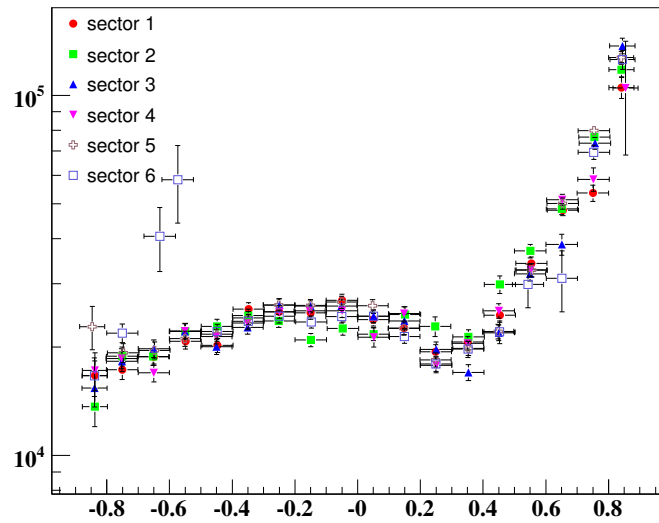

Figure 4.8: Acceptance corrected yields in the $\sqrt{s} = 2.005$ GeV bin for each sector vs $\cos \theta^{\omega}_{CM}$.
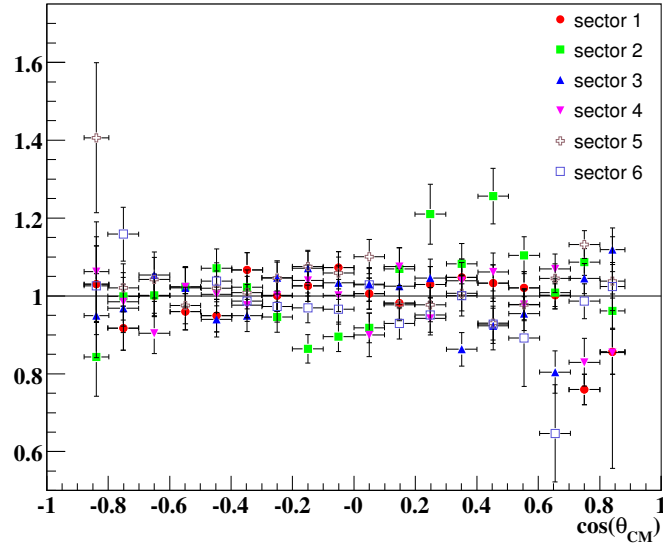
Figure 4.9: Ratio of each sector's acceptance corrected yield to the six sector mean vs $\cos\theta^{\omega}_{CM}$ from the $\sqrt{s} = 2.005$ GeV bin.
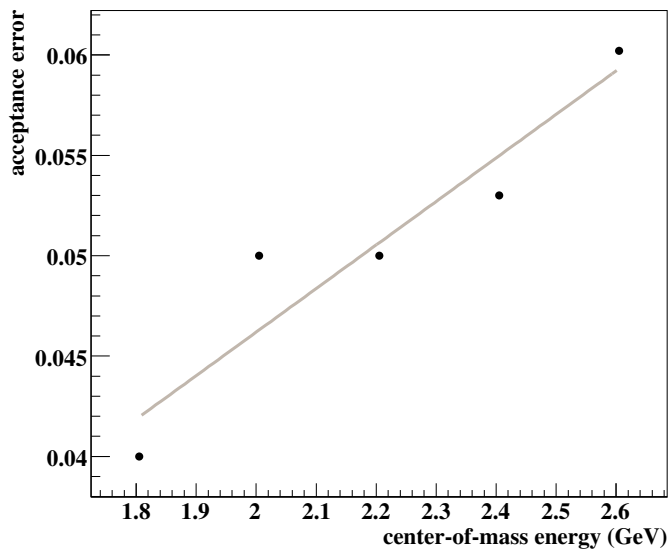

Figure 4.10: Acceptance errors vs $\sqrt{s}$ (GeV).
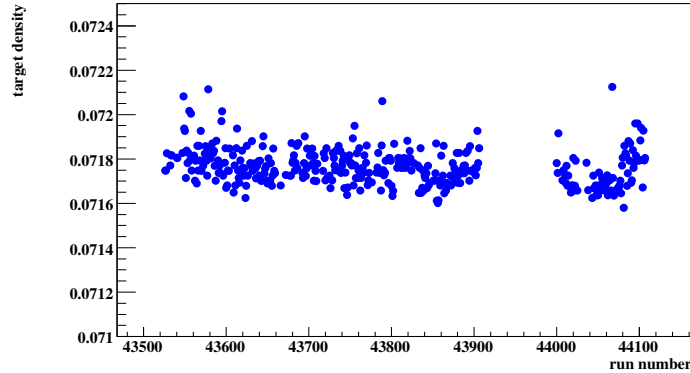
Figure 4.11: Target Density $\left(\frac{g}{cm^3}\right)$ vs Run Number: Density of liquid H_2 in the CLAS cryotarget as calculated from the temperature and pressure measured at the beginning of each run.

4.4 Target Density

Determining the density of liquid H_2 in the CLAS cryotarget is a necessary step towards calculating cross sections. Here we follow [59] and write the density as

$$\rho = a_1 T^2 + a_2 P + a_3, \tag{4.4}$$

where T is the temperature, P is the pressure and a_1, a_2, a_3 are constants given in Table 4.4.

The temperature and pressure of the cryotarget are measured at the beginning of each CLAS run. Using (4.4), along with these temperature and pressure measurements, we can calculate the density of the liquid H_2 for each run used in our analysis (this is shown in Figure 4.11). The mean value is obtained as

$$\bar{\rho} = \frac{1}{N_{run}} \sum_r \rho_r = 0.07177 \frac{g}{cm^3}, \tag{4.5}$$

and the variance is found to be

$$\sigma^2 = \frac{1}{N_{run} - 1} \sum_r (\rho_r - \bar{\rho})^2 = 6.776 \times 10^{-9} \frac{g^2}{cm^6}. \tag{4.6}$$

Thus, the relative fluctuations in the target density are only about 0.1%.

Parameter	Value
a_1	$-2.89 \times 10^{-5} \frac{g}{cm^3 K^2}$
a_2	$1.0 \times 10^{-7} \frac{g}{cm^3 mbar}$
a_3	$8.249 \times 10^{-2} \frac{g}{cm^3}$

Table 4.1: Parameters used to calculate the density of liquid H_2 [59].

4.5 Photon Normalization

Another important piece of the cross section calculation is determining the total number of photons, or photon flux, incident on the target. It is also standard in CLAS analyses to include the detector *live time* at this stage. The live time accounts for the fraction of the running time when the detector was ready to record data. This section details both of these calculations.

4.5.1 gflux

The standard CLAS normalization technique is the *gflux* method, developed by James Ball and Eugen Pasyuk at Arizona State University. A detailed description of the method can be found in [47]. The gflux method was used to determine the photon flux associated with each tagger T-counter for each $g11a$ run. The basic idea of the method is to use the rate at which electrons hit a given T-counter in a specified time window to obtain the number of electrons which hit the T-counter. This number is then adjusted to account for the detector live time. Thus, as this point gflux has determined the number of electrons which hit each tagger T-counter during the time when the detector was ready to record data. To convert this number into the number of photons which were incident on the target, we simply need to account for the number of photons which are lost between the tagger and the target. This factor is T-counter dependent and is generally about a 10% loss. The final step, for our analysis, is to rebin the T-counter flux according to E-counter and then finally to $\sqrt{s}$ bin.

4.5.2 Live Time Corrections

A *current dependent* normalization issue was first noticed by the Genova group [60]. To examine this effect, we selected four $g11a$ runs with different electron beam currents. Table 4.2 lists the runs selected for this study, along with their currents. These particular runs were chosen because they each have good agreement between the requested current (as recorded in the electronic log book) and the measured current (as recorded at some point during the run). For each run, we calculate the normalized ω yield using events containing a photon which struck any of the first 40 T-counters, the counters used in the trigger. The reason for excluding the lower energy events will become clear in the next section. Figure 4.12(a) shows the normalized ω yield extracted from each of the runs in this study *vs* beam current. It is clear that the normalized yield decreases significantly as the current increases.

To further investigate this problem, we must first look at how the detector live time is calculated. During photon runs, the live time is calculated using the scaler clocks. The *run-gated* clock measures the time during which the experiment is running. Thus, the run-gated clock simply provides a highly

Run	Current (Log Book)	Current (Database)
43532	30 nA	30.0419 nA
43582	60 nA	59.4842 nA
44106	65 nA	64.7637 nA
43626	70 nA	72.6400 nA

Table 4.2: Runs used for the live time study. The *Log Book* current is the requested current as recorded in the electronic log book. The *Database* current is the current measured during the run.
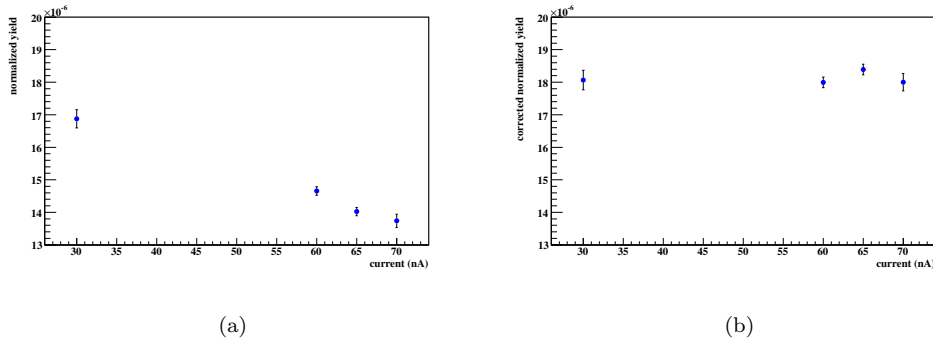
Figure 4.12: Normalized yield vs current (nA). (a) Normalization as obtained using gflux. Notice the strong current dependence. (b) Normalization obtained from gflux with the correction derived in this section. The correction does a good job of removing the current dependence.

precise measurement of the length of time elapsed during data taking. The *busy-gated* clock measures the time during which the data acquisition system is prepared to record an event. The ratio

$$LT_{clocks} = \frac{T_{busy-gated}^{clock}}{T_{run-gated}^{clock}}, \qquad (4.7)$$

is then a measure of the detector live time. This method is the one used by gflux, and thus, the one used to produce the normalized yields in Figure 4.12(a). Figure 4.13(a) shows the live time fraction *vs* beam current.

For photon runs, the scaler clocks provide the most precise measurement of the live time; however, we can also calculate the live time using the Faraday cup — a downstream device used during electron runs to measure the total current. During a photon run, the Faraday cup essentially measures electronic noise. Thus, the rates are low making its measurements less precise. That being said, there still shouldn't be any systematic difference between the live times measured by the clocks and the Faraday cup. Figure 4.13(b) shows the ratio of the Faraday cup and clock live times. The current dependence is quite strong. In fact, the ratio of the live times is nearly linear with beam current.

Figure 4.13(c) shows the ratio of the Faraday cup live time to the square of the clock live time *vs* beam current. The ratio is fairly close to one at all currents. In our analysis, we do not have access to the Faraday cup live time for each run; however, we do have access to the clock live times. If we assume that the Faraday cup live time is the accurate one, then we can approximate the correction to our normalized yields by replacing the clock live time by its square. Figure 4.12(b) shows the normalized ω yields, for the four runs used in this study, using the *corrected* live time as described above. The current dependence seen previously has now been removed.

Of course, the question still remains as to why this correction works. Unfortunately, the answer will probably never be known. The piece of hardware responsible for this measurement was replaced after the g11a run period. This discrepancy between the Faraday cup and clock live times appears to only exist in the runs taken in 2004. Both earlier and later runs show no signs of any live time discrepancies.
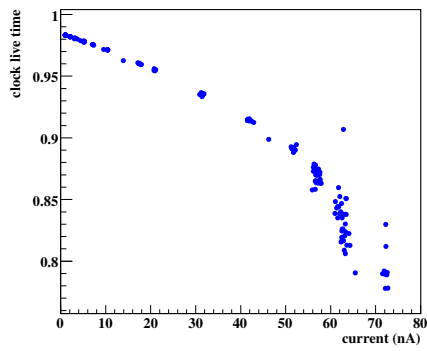
(a)
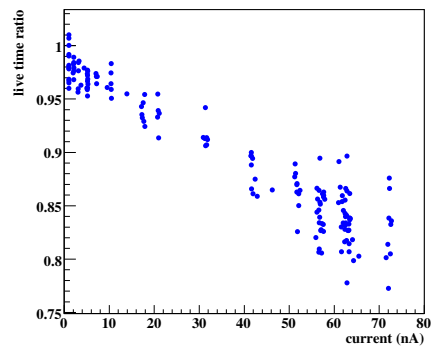
(b)
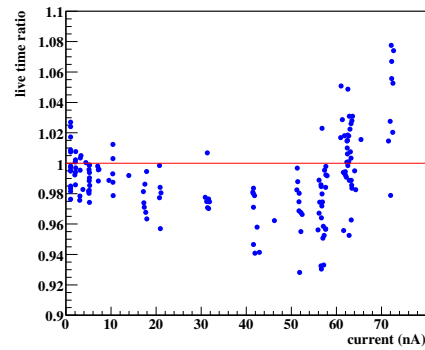
(c)

Figure 4.13: Live time study: (a) Clock live time vs current(nA). (b) LT_{FCUP}/LT_{CLOCK}: Faraday cup live time divided by clock live time vs current(nA). Notice the linear current dependence. (c) LT_{FCUP}/LT_{CLOCK}^2: Faraday cup live time divided by the square of the clock live time vs current(nA). The ratio is close to one at all currents.

4.5.3 Un-Triggered T-Counter Corrections

As discussed in Section 2.5, only the first 40 tagger T-counters were included in the $g11a$ trigger. Thus, events caused by photons associated with electrons hitting counters 41-60 could only be written into the data stream if a separate electron hit one of the first 40 T-counters during the trigger time window. The gflux software does not take the trigger configuration into account when calculating the photon flux. It simply uses the rates on each of the T-counters. Therefore, we must provide a correction to the normalization for the T-counters not included in the trigger.

The Poisson probability for observing n events in the time interval τ is given by

$$P(n) = \frac{(R\tau)^n}{n!} e^{-R\tau}, \tag{4.8}$$

where R is the rate at which the events occur. The probability that no photons hit any of the first 40 T-counters in this time interval is then

$$P_0 = \prod_{t=1}^{40} P(0) = e^{-\sum_{t=1}^{40} R_t \tau}. \tag{4.9}$$

Thus, the probability that at least one photon does hit any of the first 40 T-counters is

$$P_{trig} = 1 - P_0 = 1 - e^{-\sum_{t=1}^{40} R_t \tau}. \tag{4.10}$$

We didn't have direct access to the T-counter rates R_t; however, we were able to calculate the average rate for each T-counter using the flux. The flux from each run can be converted into a rate by dividing by the total amount of live time recorded for the run, along with using the inverse of the factors used by gflux to convert the T-counter hits into the number of photons at the target. The average rate for all runs for each T-counter was then obtained as the weighted average — weighting by number of events in good trip intervals — of the individual rates from each run. For the runs used in our analysis, (4.10) yields a trigger probability of $P_{trig} = 0.46669$.

The run dependent tagger correction discussed in Section 3.3.2 means that for each run the trigger cuts off at a slightly different photon energy. The average value is $E_\gamma \sim 1.57$ GeV or $\sqrt{s} \sim 1.956$ GeV. Therefore, we must scale our normalization factors by $1/P_{trig} = 2.143$ for all bins with energies lower than this cutoff.

Figure 4.14(a) shows the normalized ω yield in each $\sqrt{s}$ bin using the flux as reported by gflux. The red line indicates the (approximate) position of the lowest energy T-counter used in the trigger. The necessity of a correction is quite obvious. Figure 4.14(b) shows the normalized ω yields after applying the normalization correction derived in this section. The correction appears to work quite well. The bin which contains the trigger cutoff, $\sqrt{s} = 1.955$ GeV, does not line up with the rest of the bins, as expected, and will be removed from any cross section measurements. Figure 4.14(c) shows the only other $\sqrt{s}$ bins which show a discrepancy in normalized yield. The yields in bins $\sqrt{s} = 2.735$ GeV and $\sqrt{s} = 2.745$ GeV are abnormally low. It is unclear why this is the case, so these bins will also be removed from cross section measurements.
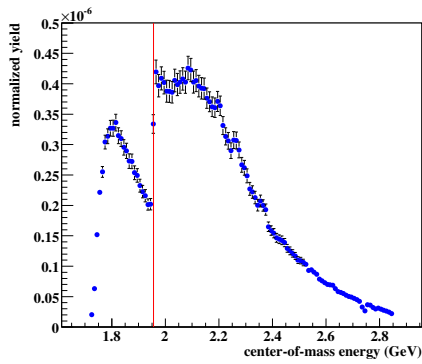
(a)
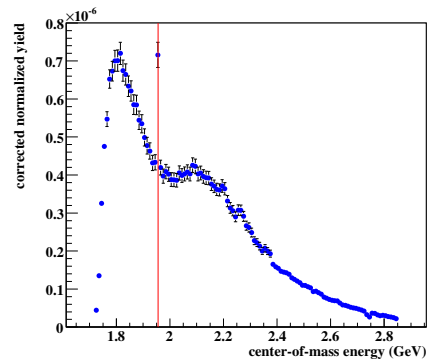
(b)
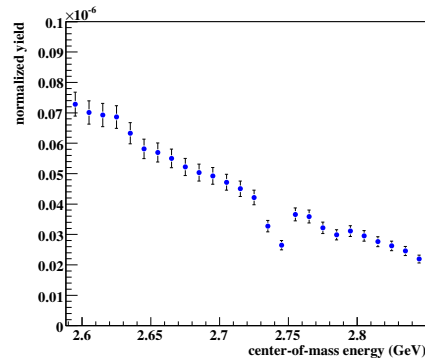
(c)

Figure 4.14: Normalized yield vs $\sqrt{s}$ (GeV): (a) Using normalization as obtained from gflux. (b) gflux normalization with the correction derived in this section. (c) Normalized yield discrepancy in bins $\sqrt{s} = 2.735$ GeV and $\sqrt{s} = 2.745$ GeV.
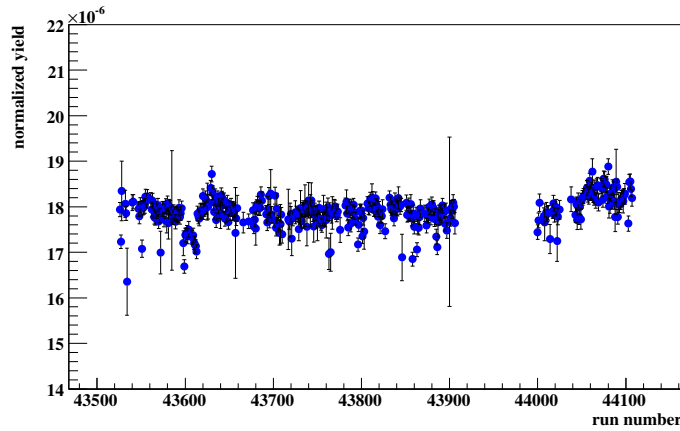
Figure 4.15: Normalized ω Yield vs Run Number: Total ω yield (integrated over all $\sqrt{s}$ used in the $g11a$ trigger) divided by the measured flux for each run used in our analysis. See the text for more details on the yield and error calculations. The normalized yield is quite stable across the entire set of runs used in our analysis. The standard deviation is only $\sim 1.8\%$.

4.6 Stability of the Normalized ω Yield

To check the quality of the normalization calculations and corrections detailed in the previous sections, we can examine the stability of the normalized ω yield from run to run. For each run used in our analysis, we extract the total normalized ω yield as

$$\mathcal{N} = \sum_b \frac{Y_b}{\mathcal{F}_b}, \tag{4.11}$$

where Y_b and $\mathcal{F}_b$ are the ω yield and corrected flux for each $\sqrt{s}$ bin in the run. The errors on each normalized yield can be obtained using

$$\sigma_{\mathcal{N}}^2 = \sum_b \frac{Y_b + \sigma_b^2}{\mathcal{F}_b^2}, \tag{4.12}$$

where σ_b is the error on the extracted ω yield Y_b in each bin. Thus, these errors include the error associated with signal-background separation, along with the statistical errors associated with the number of signal events in each bin.

Figure 4.15 shows the total normalized ω yield vs CLAS run number. It is very stable across the entire set of runs used in our analysis. The mean value of the total normalized yield is obtained by performing a χ^2 fit yielding $\bar{\mathcal{N}} = 1.790 \times 10^{-5}$. The variance is then found to be

$$\sigma^2 = \frac{1}{N_{run} - 1} \sum_r (\mathcal{N}_r - \bar{\mathcal{N}})^2 = 1.060 \times 10^{-13}, \tag{4.13}$$

or $\sigma/\mathcal{N} \sim 1.8\%$. This number will be used as the relative error on our normalization, which includes the photon flux calculation and the target density.

4.7 Summary

The basis of our acceptance calculation was a GEANT based simulation of the CLAS detector. Using inclusive $\gamma p \rightarrow p\pi^+\pi^-$ events, we developed a smearing algorithm to better match the resolution of the simulated detector to that achieved during the $g11a$ run period. The same channel was also used to obtain the efficiency of the $g11a$ trigger, which was then incorporated into the simulation. Data taken with different beam currents were used to detect and account for an error in the detector live time calculation. The tagger T-counter rates, along with the size of the $g11a$ trigger timing window, were used to obtain a correction to the photon flux for T-counters which were not included in the $g11a$ trigger. The result of these corrections was a normalized ω yield which varies by less than 2% from run to run.

Chapter 5

Partial Wave Analysis Formulas and MINUIT

The goal of our partial wave analysis is to look for nucleon resonance contributions in the $\gamma p \to p\omega$ channel. To limit theoretical model dependence, we divide our data into 10 MeV $\sqrt{s}$ bins. This allows us to avoid enforcing energy dependent shapes onto our resonant amplitudes. It is important to keep this fact in mind while reading this chapter. Whether it be event based likelihood fits or χ^2 fits to differential cross sections, the formulas written below, except when explicitly stated otherwise, are intended to describe data from a single narrow $\sqrt{s}$ bin. This chapter discusses in detail the methods used to perform all of our partial wave analysis fits, including the algorithm used by the CERNLIB software package MINUIT when determining the best parameter set.

5.1 Notation

In all of the work that follows, p_i, p_f, q and k will be used for the initial proton, final proton, ω and photon 4-momenta. The z-axis in the overall CM frame, defined by $\hat{k}$, is used as the angular momentum quantization axis. We denote particle spin projections as m_x and particle masses as w_x for any particle x. The Mandelstam variables are defined as

$$
\begin{align}
s &= (p_i + k)^2 = (p_f + q)^2 \tag{5.1a} \\
t &= (q - k)^2 = (p_i - p_f)^2 \tag{5.1b} \\
u &= (p_i - q)^2 = (p_f - k)^2. \tag{5.1c}
\end{align}
$$

The fit parameters are denoted as $\vec{x}$. The set of all independent kinematic variables will be X and the Lorentz invariant phase space element $d\Phi(X) = \phi(X)dX$. The detector acceptance is given by $\eta(X)$. The Lorentz invariant transition amplitude, $\mathcal{M}$, which takes γp to $p\pi^+\pi^-\pi^0$, can be written as

$$
|\mathcal{M}(\vec{x}, X)|^2 = \sum_{m_i, m_\gamma, m_f} |\sum_a \alpha_a(\vec{x}, X) \mathcal{A}^a_{m_i, m_\gamma, m_f}(X)|^2, \tag{5.2}
$$

where $\mathcal{A}^a_{m_i, m_\gamma, m_f}$ are the known pieces of the partial wave amplitudes, α_a are complex functions built from the fit parameters (and possibly the kinematic variables X) and m_i, m_γ, m_f are the initial proton, incident photon and final proton spin projections respectively. The form of the partial wave amplitudes will be covered in Chapter 6, for now they can just be thought of as complex functions of X.

When performing χ^2 fits to differential cross sections, the ω will be treated as a final state particle. In this case, $\mathcal{M}$ is the transition amplitude from $\gamma p \to p\omega$ and the ω decay is ignored. This leads to (5.2) taking on the slightly modified form

$$|\mathcal{M}(\vec{x}, X)|^2 = \sum_{m_i, m_\gamma, m_f, m_\omega} |\sum_a \alpha_a(\vec{x}, X) \mathcal{A}^a_{m_i, m_\gamma, m_f, m_\omega}(X)|^2, \tag{5.3}$$

to account for the polarization of the ω.

5.2 Extended Maximum Likelihood Method

This section details the formulas necessary for performing *event-based* fits. This term is used to describe fits where no binning, except in $\sqrt{s}$, is done. The work detailed in this section is based on that of Chung [61]; however, the normalizations we have developed differ from his work.

The goal is to find estimators $\hat{x}$ for the set of parameters $\vec{x}$ in a $\sqrt{s}$ bin with n detected events. We begin by defining the likelihood function as

$$\mathcal{L} = \left(\frac{\bar{n}^n}{n!} e^{-\bar{n}}\right) \prod_i^n \mathcal{P}(\vec{x}, X_i), \tag{5.4}$$

where the term in parentheses is the Poisson probability of obtaining n events given the expected number is $\bar{n}$ (the calculation of which is discussed in the next section), X_i represents the kinematics of event i, and $\mathcal{P}(\vec{x}, X)$ is the probability density function.

The probability density for an event with acceptance $\eta(X_i)$, phase space element $\phi(X_i)$ and Lorentz invariant transition amplitude $\mathcal{M}(\vec{x}, X_i)$ is

$$\mathcal{P}(\vec{x}, X_i) = \frac{|\mathcal{M}(\vec{x}, X_i)|^2 \eta(X_i) \phi(X_i)}{\mathcal{N}(\vec{x})}, \tag{5.5}$$

where $\mathcal{N}(\vec{x})$ is defined such that the p.d.f. is properly normalized

$$\int \mathcal{P}(\vec{x}, X) dX = 1. \tag{5.6}$$

From left to right, (5.5) accounts for the relative strength of the transition amplitude, the detection probability and the available phase space for the i-th event. The estimators $\hat{x}$ are then found by maximizing $\mathcal{L}$.

5.2.1 Normalization

To maximize the likelihood, we need to be able to calculate the expected number of events $\bar{n}$. We begin by introducing the concept of a *cross section*. A cross section for a reaction, in our case $\gamma p \to p\omega$, is defined as the transition rate per unit incident flux per target particle [56]. For photoproduction, the cross section σ can be defined in terms of measurable quantities as

$$\sigma = \frac{N}{\mathcal{F} \rho_{target} \ell_{target} N_A / A_{target}}, \tag{5.7}$$

where N is the number of scattering events, $\mathcal{F}$ is the incident photon flux, ρ_{target}, ℓ_{target} and A_{target} are the target density, length and atomic weight and, N_A is Avogadro's number.

The cross section, in any $\sqrt{s}$ bin, can also be related to the transition amplitude $\mathcal{M}$ by [11]

$$\sigma = \frac{1}{4}\frac{(2\pi)^4}{2(s - w_p^2)} \int |\mathcal{M}(\vec{x}, X)|^2 d\Phi(X), \tag{5.8}$$

where the factor of $1/4$ comes from averaging over the initial spin states. Thus, for a given set of parameters $\vec{x}$, (5.7) and (5.8) can be used to get the number of expected scattering events as

$$N = (\mathcal{F}\rho_{target}\ell_{target}N_A/A_{target})\frac{(2\pi)^4}{8(s - w_p^2)} \int |\mathcal{M}(\vec{x}, X)|^2 d\Phi(X). \tag{5.9}$$

To obtain the expected number of data events $\bar{n}$, we simply need to account for the detector acceptance in (5.9):

$$\bar{n} = (\mathcal{F}\rho_{target}\ell_{target}N_A/A_{target})\frac{(2\pi)^4}{8(s - w_p^2)} \int |\mathcal{M}(\vec{x}, X)|^2 \eta(X) d\Phi(X). \tag{5.10}$$

The integral in (5.10) must be done numerically due to the lack of an analytic expression for the detector acceptance $\eta(X)$. The numerical integration is done using the *Monte Carlo* technique.

We begin by randomly generating N_{raw} events according to $\gamma p \to p\omega$, $\omega \to \pi^+\pi^-\pi^0$ phase space for CM energy $\sqrt{s}$. The integral can then be approximated by

$$\int |\mathcal{M}(\vec{x}, X)|^2 \eta(X) d\Phi(X) \approx \frac{\int d\Phi(X)}{N_{raw}} \sum_i^{N_{raw}} |\mathcal{M}(\vec{x}, X_i)|^2 \eta(X_i). \tag{5.11}$$

To obtain the values of $\eta(X_i)$, each event is run through a GEANT based detector simulation package, discussed in detail in Section 4.1. This procedure simulates the acceptance of the detector by rejecting events that would not have survived to be part of the data analysis. Thus, for each event, the acceptance factor is $\eta(X_i) = 0$ or 1. We denote the number of Monte Carlo events which are accepted as N_{acc}. We can then rewrite (5.11) as

$$\int |\mathcal{M}(\vec{x}, X)|^2 \eta(X) d\Phi(X) \approx \frac{\int d\Phi(X)}{N_{raw}} \sum_i^{N_{acc}} |\mathcal{M}(\vec{x}, X_i)|^2. \tag{5.12}$$

Notice that (5.12) requires the value of the phase space integral $\int d\Phi(X)$. In our analysis, we factor the size of the $\omega \to \pi^+\pi^-\pi^0$ phase space into the ω decay amplitude (see Section 6.4). Thus, here we need only compute the $p\omega$ phase space integral value:

$$\begin{aligned}
\int d\Phi(X) &= \int \delta^4(p_i + k - p_f - q)\frac{d^3\vec{p_f}}{(2\pi)^3 2E_f}\frac{d^3\vec{q}}{(2\pi)^3 2E_\omega} \\
&= \frac{1}{4(2\pi)^6}\int \delta(\sqrt{s} - E_f - E_\omega)\frac{|\vec{p_f}|^2 d\Omega}{E_f E_\omega} \\
&= \frac{1}{4(2\pi)^6}\int \frac{|\vec{p_f}| d\Omega}{\sqrt{s}} \\
&= \frac{\left[(s - (w_p + w_\omega)^2)(s - (w_p - w_\omega)^2)\right]^{1/2}}{8(2\pi)^5 s}, \tag{5.13}
\end{aligned}$$

where we've made use of the identity $\delta(f(x)) = \delta(x - x_0)/|f'(x_0)|$ with x_0 being the root of $f(x)$.

Using (5.12) and (5.13), (5.10) can be rewritten as

$$\bar{n} \approx \frac{\mathcal{S}(s)}{N_{raw}} \sum_{i}^{N_{acc}} |\mathcal{M}(\vec{x}, X_i)|^2, \tag{5.14}$$

where

$$\mathcal{S}(s) = \frac{\mathcal{F}\rho_{target}\ell_{target}N_A}{A_{target}} \frac{\left[(s - (w_p + w_\omega)^2)(s - (w_p - w_\omega)^2)\right]^{1/2}}{64\pi s(s - w_p^2)}. \tag{5.15}$$

We conclude this section by extracting the total cross section given a set of estimators $\hat{x}$. By removing the detector acceptance from (5.11) and using (5.13), we can write

$$\int |\mathcal{M}(\hat{x}, X)|^2 d\Phi(X) \approx \frac{\left[(s - (w_p + w_\omega)^2)(s - (w_p - w_\omega)^2)\right]^{1/2}}{8(2\pi)^5 s} \frac{1}{N_{raw}} \sum_{i}^{N_{raw}} |\mathcal{M}(\hat{x}, X_i)|^2. \tag{5.16}$$

Then, using (5.8) the total cross section is given by

$$\sigma = \frac{\left[(s - (w_p + w_\omega)^2)(s - (w_p - w_\omega)^2)\right]^{1/2}}{64\pi s(s - w_p^2)} \frac{1}{N_{raw}} \sum_{i}^{N_{raw}} |\mathcal{M}(\hat{x}, X_i)|^2. \tag{5.17}$$

5.2.2 Log Likelihood

Since the natural logarithm is a monotonically increasing function, we're assured that the estimators which minimize $-\ln\mathcal{L}$ will also maximize $\mathcal{L}$. From (5.4) we can write the *log likelihood* as

$$-\ln\mathcal{L} = -n\ln\bar{n} + \ln n! + \bar{n} - \sum_{i}^{n} \ln\mathcal{P}(\vec{x}, X_i). \tag{5.18}$$

Using (5.10) and (5.6), we can write the probability density scale factor $\mathcal{N}(\vec{x})$ as

$$\mathcal{N}(\vec{x}) = \mathcal{C}(s)\bar{n}, \tag{5.19}$$

where

$$\mathcal{C}(s) = \frac{8(s - w_p^2)}{(2\pi)^4} \frac{A_{target}}{\mathcal{F}\rho_{target}\ell_{target}N_A}. \tag{5.20}$$

The log likelihood then becomes

$$-\ln\mathcal{L} = -\sum_{i}^{n} \ln |\mathcal{M}(\vec{x}, X_i)|^2 \eta(X_i)\phi(X_i) + \bar{n} + \ln n! + n\ln\mathcal{C}(s). \tag{5.21}$$

We're not actually interested in the value of $-\ln\mathcal{L}$, just that it's been minimized. Thus, we can drop all terms in (5.21) which do not depend on the parameters $\vec{x}$:

$$-\ln\mathcal{L} = -\sum_{i}^{n} \ln |\mathcal{M}(\vec{x}, X_i)|^2 + \bar{n} + const. \tag{5.22}$$

Finally, using (5.14) we can rewrite (5.22) as

$$-\ln\mathcal{L} = -\sum_{i}^{n} \ln |\mathcal{M}(\vec{x}, X_i)|^2 + \frac{\mathcal{S}(s)}{N_{raw}} \sum_{i}^{N_{acc}} |\mathcal{M}(\vec{x}, X_i)|^2 + const. \tag{5.23}$$

We'll end this section by examining the expected number of events $\bar{n}$ for the parameter estimators $\hat{x}$. Assume that a suitable set of parameters has been found that maximize $\mathcal{L}$. Then, define the set of functions $\{\alpha'\}$ such that

$$\alpha_a(\hat{x}, X) = c \cdot \alpha'_a(\hat{x}, X) \tag{5.24}$$

where c is a constant independent of X. Using (5.2), we can define

$$\begin{aligned}
|\mathcal{M}'(\vec{x}, X)|^2 &= \sum_{m_i, m_\gamma, m_f} |\sum_a \alpha'_a(\vec{x}, X)\mathcal{A}_a(X)|^2 \\
&= \frac{1}{c^2}|\mathcal{M}(\vec{x}, X)|^2. \tag{5.25}
\end{aligned}$$

For the estimators $\hat{x}$,

$$\begin{aligned}
\frac{\partial}{\partial c^2} \ln \mathcal{L} &= \frac{\partial}{\partial c^2}\left(\sum_i^n \ln c^2 |\mathcal{M}'(\hat{x}, X_i)|^2 - \frac{\mathcal{S}(s)}{N_{raw}} \sum_i^{N_{acc}} c^2 |\mathcal{M}'(\hat{x}, X_i)|^2 \right) \tag{5.26a} \\
&= \frac{n}{c^2} - \frac{\bar{n}}{c^2} \tag{5.26b} \\
&= 0. \tag{5.26c}
\end{aligned}$$

Therefore, the best estimate for $\bar{n}$ is n — as expected.

5.2.3   Handling Background

In the $\gamma p \to p\omega$ channel, there is no way to separate non-ω $p\pi^+\pi^-\pi^0$ events from the signal events. We assume that the processes involved in producing these non-ω events do not interfere with the $\gamma p \to p\omega$ amplitudes. This assumption is justified by the large mean distance traveled by the ω prior to its decay ~ 20 fm, relative to the length scale of the strong interaction ~ 1 fm. We also note that the quality of the fits of our data to a Voigtian plus linear background (see Section 3.9) also suggest that interference effects are negligible.

In this section, we assume that we are able to obtain a Q-value for each data event which gives the likelihood that the event is truly a $p\omega$ event. The technique used to obtain these values is described in Section 3.9. To account for this *background*, we can rewrite (5.23) as

$$-\ln \mathcal{L} = -\sum_i^n Q_i \ln |\mathcal{M}(\vec{x}, X_i)|^2 + \frac{\mathcal{S}(s)}{N_{raw}} \sum_i^{N_{acc}} |\mathcal{M}(\vec{x}, X_i)|^2 + const, \tag{5.27}$$

where Q_i is the Q-value for event i. Thus, the Q-value for each event is used to weight the event's contribution to the log likelihood.

5.3   The Method of Least Squares

There are certain times when it is advantageous to perform fits to binned data. These fits are much faster — fitting to ~ 20 data points as opposed to $\sim 100,000+$ events — than the event based fits; however, they are working from less information which provides somewhat less confidence in their results. These fits are used for two main purposes. First, when an amplitude(s) has an $\alpha(\vec{x}, X)$ which is known to be a function of X. These can be extracted using the event-based fit; however, for technical reasons the fits are extremely cpu intensive and it is more convenient in this case to

fit to binned data. Secondly, fitting to binned data can be used to guide our event-based fits. We can quickly scan regions of the data and test whether certain waves appear to contribute at a level which warrants further investigation in an event-based fit. We can also use the binned fitting to obtain good starting values for the event-based fit, saving cpu time.

We want to find estimators $\hat{x}$ for our set of parameters $\vec{x}$ in a $\sqrt{s}$ bin with n data points. We choose to bin the data in t and use the differential cross section $\frac{d\sigma}{dt}$ as the quantity to fit to. The estimators are then found by minimizing

$$\chi^2 = \sum_i^n \frac{(\frac{d\sigma_i}{dt} - \frac{d\sigma}{dt}(\vec{x}, X_i))^2}{\sigma_i^2}, \tag{5.28}$$

where $\frac{d\sigma_i}{dt}$, σ_i are the measured differential cross section and its error for point i, X_i are the kinematic variables at the bin center, and

$$\frac{d\sigma}{dt}(\vec{x}, X) \propto |\mathcal{M}(\vec{x}, X)|^2, \tag{5.29}$$

is the differential cross section built from the partial waves and fit parameters.

To calculate $\frac{d\sigma}{dt}(\vec{x}, X)$, we begin by rewriting (5.8) as

$$d\sigma = \frac{1}{4} \frac{(2\pi)^4}{2(s - w_p^2)} |\mathcal{M}(\vec{x}, X)|^2 d\Phi(X). \tag{5.30}$$

From (5.13),

$$d\Phi(X) = \frac{1}{4(2\pi)^6} \frac{|\vec{p}_f| d\Omega}{\sqrt{s}}. \tag{5.31}$$

Then, using $dt = \frac{s - w_p^2}{\sqrt{s}} |\vec{p}_f| d\cos(\theta_{CM})$

$$d\Phi(X) = \frac{dt}{(2\pi)^5 4(s - w_p^2)}, \tag{5.32}$$

and

$$\frac{d\sigma}{dt}(\vec{x}, X) = \frac{|\mathcal{M}(\vec{x}, X)|^2}{64\pi(s - w_p^2)^2}. \tag{5.33}$$

5.4 MINUIT

The CERNLIB package MINUIT is used to minimize $-\ln \mathcal{L}$. MINUIT was written by Fred James while at CERN in the late 1960's. It has been revised several times over the years with the most extensive revision coming in 1989. The current package is written entirely in FORTRAN 77 [62]. MINUIT's main field of usage is in statistical analysis of experimental physics data; however, it is also used in other fields as well.

5.4.1 MIGRAD and the DFP Algorithm

The minimization algorithm we use is called MIGRAD. It uses a variation of the Davidon-Fletcher-Powell (DFP) variable metric method (VMM). This method is suited for minimizing a function $F(\vec{x})$ of n variables $\vec{x}^T = (x_1, x_2, \ldots, x_n)$ where the gradient vector $\nabla_x F = \vec{g}(\vec{x})$ can be obtained explicitly, but the Hessian G ($G_{ij} = \partial^2 F / \partial x_i \partial x_j$) can not [63].

The DFP method uses an iterative approach to minimizing $F(\vec{x})$. Each iteration starts at some point $\vec{x}$ with gradient $\vec{g}(\vec{x})$. The goal is to find another point, $\vec{y}$, for which $F(\vec{y}) < F(\vec{x})$. This procedure is then repeated until the convergence criteria, $\delta F \equiv F(\vec{x}) - F(\vec{y}) < tolerance$, is met. The main feature of the DFP method is that an approximation to G^{-1}, denoted H, is kept and updated at each iteration. There are two formulas for updating H which arise in the DFP method:

$$
H_y \;\; = \;\; H_x + \frac{\vec{\delta}\vec{\delta}^T}{\vec{\delta}^T\vec{\gamma}} - \frac{H_x\vec{\gamma}\vec{\gamma}^T H_x}{\vec{\gamma}^T H_x \vec{\gamma}} \tag{5.34}
$$

$$
H_y \;\; = \;\; \left(1 - \frac{\vec{\delta}\vec{\gamma}^T}{\vec{\delta}^T\vec{\gamma}}\right) H_x \left(1 - \frac{\vec{\gamma}\vec{\delta}^T}{\vec{\gamma}^T\vec{\delta}}\right) + \frac{\vec{\delta}\vec{\delta}^T}{\vec{\delta}^T\vec{\gamma}}, \tag{5.35}
$$

where H_y is the Hessian to be used at $\vec{y}$, H_x is the Hessian at $\vec{x}$ (current position), $\vec{\delta} = \vec{y} - \vec{x}$ and $\vec{\gamma} = \vec{g}(\vec{y}) - \vec{g}(\vec{x})$.

Both (5.34) and (5.35) can, under certain circumstances, cause the minimization process to diverge. In particular, updating H_y using only (5.34) is more likely to lead to singularities than (5.35); however, updating using only (5.35) is more likely to cause H_y to become unbounded. This lead Fletcher to develop what is referred to as the *switching* method. This method tests the criteria $\vec{\delta}^T\vec{\gamma} \leq \vec{\gamma}^T H_x \vec{\gamma}$ during each iteration. If *true*, then the updating scheme (5.35) is used, otherwise H_y is updated using (5.34).

To determine the correction to the current position $\vec{\delta}$, we first define the *direction of search* as $\vec{s} = - H_x \vec{g}(\vec{x})$. Then,

$$
\vec{\delta} = \alpha\vec{s} = -\alpha H_x \vec{g}(\vec{x}), \tag{5.36}
$$

where α minimizes $F(\vec{x} + \alpha\vec{s})$. This method of minimizing F along the *direction of search* is known as *linear searching*. From $\vec{\delta}$, $\vec{y}$ is easily obtained as $\vec{y} = \vec{x} + \vec{\delta}$ and we can proceed to the next iteration if $F(\vec{y})$ doesn't meet the convergence criteria. For more information on the DFP method see [63] and the references within.

5.4.2   Derivatives of the Log Likelihood

The MIGRAD routine, since it uses the DFP method, requires accurate knowledge of the gradient vector. For our specific case, (5.27) implies we need to supply MIGRAD with

$$
\frac{\partial(-\ln\mathcal{L})}{\partial x_j} = \frac{\partial}{\partial x_j}\left(-\sum_i^n Q_i \ln|\mathcal{M}(\vec{x}, X_i)|^2 + \frac{\mathcal{S}(s)}{N_{raw}}\sum_i^{N_{acc}}|\mathcal{M}(\vec{x}, X_i)|^2\right) \tag{5.37}
$$

for each parameter x_j. The only term in (5.37) that depends on $\vec{x}$ is $|\mathcal{M}|^2$. Thus, (5.37) becomes

$$
\frac{\partial(-\ln\mathcal{L})}{\partial x_j} = -\sum_i^n Q_i \left(\frac{1}{|\mathcal{M}(\vec{x}, X_i)|^2}\frac{\partial|\mathcal{M}(\vec{x}, X_i)|^2}{\partial x_j}\right) + \frac{\mathcal{S}(s)}{N_{raw}}\sum_i^{N_{acc}}\frac{\partial|\mathcal{M}(\vec{x}, X_i)|^2}{\partial x_j}. \tag{5.38}
$$

Using (5.2), we can write $\partial|\mathcal{M}(\vec{x}, X_i)|^2/\partial x_j$ as

$$
\frac{\partial|\mathcal{M}(\vec{x}, X_i)|^2}{\partial x_j} \;\; = \;\; \frac{\partial}{\partial x_j}\left(\sum_{m_i, m_\gamma, m_f}|\sum_a \alpha_a(\vec{x}, X_i)\mathcal{A}_a(X_i)|^2\right)
$$

$$
= \;\; \sum_{m_i, m_\gamma, m_f} 2Re\left(\sum_a \frac{\partial\alpha_a(\vec{x}, X_i)}{\partial x_j}\mathcal{A}_a(X_i)\sum_{a'}(\alpha_{a'}(\vec{x}, X_i)\mathcal{A}_{a'}(X_i))^*\right). \tag{5.39}
$$

5.4.3 Derivatives of χ^2

As in the log likelihood case in the previous section, for the least squares fits we also need to supply MIGRAD with

$$\frac{\partial \chi^2}{\partial x_j} = \frac{\partial}{\partial x_j} \left(\sum_i^n \frac{(\frac{d\sigma_i}{dt} - \frac{d\sigma}{dt}(\vec{x}, X_i))^2}{\sigma_i^2} \right) \tag{5.40}$$

for each parameter x_j. The only term in (5.40) that depends on $\vec{x}$ is $\frac{d\sigma}{dt}(\vec{x}, X)$. Thus,

$$\frac{\partial \chi^2}{\partial x_j} = \sum_i^n \frac{2}{\sigma_i^2} \left(\frac{d\sigma}{dt}(\vec{x}, X_i) - \frac{d\sigma_i}{dt} \right) \frac{\partial}{\partial x_j} \frac{d\sigma}{dt}(\vec{x}, X), \tag{5.41}$$

where

$$\frac{\partial}{\partial x_j} \frac{d\sigma}{dt}(\vec{x}, X) = \frac{1}{64\pi(s - w_p^2)^2} \frac{\partial |\mathcal{M}(\vec{x}, X)|^2}{\partial x_j}, \tag{5.42}$$

and $\partial |\mathcal{M}(\vec{x}, X)|^2 / \partial x_j$ is defined in (5.39).

5.4.4 HESSE and the Covariance Matrix

The HESSE routine calculates the matrix of second derivatives of the *log likelihood* with respect to the parameters and inverts it to obtain the covariance matrix. The second derivatives are calculated using the method of finite differences (*ie* numerically). The technique of using the inverse of the matrix of second derivatives relies on the assumption that the curvature at the minimum follows a parabolic shape. Though this is typically not the case, it should (in most cases) be a decent approximation.

5.5 Coupling Multiple Datasets

There are times when it is necessary to couple multiple datasets, for our case multiple $\sqrt{s}$ bins, into a single fit. This is done to constrain the estimators $\hat{x}$, or some subset of them, to be the same for each of the coupled datasets. This is easily accomplished by minimizing

$$\psi = \sum_d^{N_d} \psi_d, \tag{5.43}$$

where ψ_d is the minimization quantity, χ^2 or $-\ln \mathcal{L}$, for dataset d and N_d is the number of coupled datasets. Then, the derivatives of the parameters $\vec{x}$ are just

$$\frac{\partial \psi}{\partial x_j} = \sum_d^{N_d} \frac{\partial \psi_d}{\partial x_j}. \tag{5.44}$$

5.6 Summary

The unbinned extended maximum likelihood method has been described in detail. This method has been employed to perform all fits discussed in subsequent chapters. We have developed a normalization scheme which permits the direct use of physics couplings as fit parameters, making it much easier to incorporate amplitudes from theoretical models into our partial wave analysis fits. The signal Q-values, obtained using the method of Section 3.9, have been incorporated into the likelihood formalism. The CERNLIB package MINUIT, which was used to determine the estimators for our fit parameters, was also discussed in detail in this chapter.

Chapter 6

Partial Wave Amplitudes

In the previous chapter, we discussed how to perform fits using partial wave amplitudes. Now we need to construct those amplitudes. The first half of this chapter is a detailed overview of the formalism which is based on the work of W. Rarita and J. Schwinger [64]. It utilizes a covariant framework and all amplitudes are required to be Lorentz invariants. This allows us to evaluate all amplitudes in the same frame (we choose the overall center-of-mass frame), and greatly reduces the amount of bookkeeping that needs to be done to properly deal with final state particles with spin. After laying out the formalism, the amplitudes will be constructed. Notation in this chapter is the same as that defined in Section 5.1.

6.1 Integral Spin Formalism

In this section, we will construct the polarization tensors for relativistic integral spin particles. The technique used will be to embed each spin-J system, with $(2J + 1)$ independent elements, into the higher dimension space of rank-J tensors, with 4^J independent elements. Supplementary conditions, known as the Rarita-Schwinger conditions [64], will then be needed to reduce the number of independent elements to the proper number. The reason for using this embedding process is that the transformation properties of the spin-J system become those of the rank-J tensor. Thus, coupling the spin-J system to any 4-momenta or other spin tensors (including the half-integral spin tensors discussed below) to form a Lorentz scalar becomes a straight forward process.

6.1.1 Spin-1 Polarization 4-Vectors

Massive Particles

We want to construct the polarization vector for a massive spin-1 particle with momentum p, mass w and canonical spin projection m. The constraint equation

$$p_\mu \epsilon^\mu(p, m) = 0 \tag{6.1}$$

reduces the number of independent components of the 4-vector to 3 — the correct number for a spin-1 state. In the particle's rest frame, (6.1) implies that the energy component is 0. The spatial components are then chosen to be the eigenvectors of the S^2 and S_z angular momentum operators:

$$\vec{\epsilon}(\pm 1) = \mp \frac{1}{\sqrt{2}}(1, \pm i, 0), \qquad \vec{\epsilon}(0) = (0, 0, 1). \tag{6.2}$$

Thus, in the particle's rest frame, $\epsilon^\mu(p, m)$ transforms under spatial rotations as

$$R^\mu{}_\nu(\alpha, \beta, \gamma)\epsilon^\nu(p, m) \xrightarrow[rf]{} R_{ij}(\alpha, \beta, \gamma)\epsilon_j(m) = \sum_{m'} D^{(1)}_{m'm}(\alpha, \beta, \gamma)\epsilon_i(m'), \tag{6.3}$$

where $R_{ij}(\alpha, \beta, \gamma)$ is the rotation matrix for Euler angles α, β and γ. To get the polarization 4-vector in any arbitrary frame, we simply boost it from the rest-frame

$$\epsilon^\mu(p, m) = \Lambda^\mu{}_\nu(p)\epsilon^\nu(p_{rf}, m), \tag{6.4}$$

where $\Lambda^\mu{}_\nu(p)$ performs the Lorentz transformation that boosts p_{rf} to p. The spin-1 projection operator is defined as

$$P^{(1)}_{\mu\nu}(p) = \sum_m \epsilon_\mu(p, m)\epsilon^*_\nu(p, m) = -g_{\mu\nu} + \frac{p_\mu p_\nu}{w^2} \equiv -\tilde{g}_{\mu\nu}. \tag{6.5}$$

When $P^{(1)}_{\mu\nu}(p)$ is contracted with an arbitrary 4-vector y^ν, the resulting 4-vector $\tilde{y}_\mu = P^{(1)}_{\mu\nu}(p)y^\nu$ is orthogonal to p. Therefore, it projects any 4-vector into the space spanned by the spin-1 states.

Photons

Since the photon doesn't have a rest frame, we can't build its polarization 4-vectors in the same way as for the massive case. To construct the photon polarization 4-vectors, we begin by considering

$$A \equiv A^\mu \epsilon_\mu(k, m), \tag{6.6}$$

where A is the Lorentz invariant amplitude for some process $\gamma X \to Y$. Under the gauge transformation $\epsilon_\mu \to \epsilon_\mu + \lambda k_\mu$, (6.6) becomes

$$A^\mu \epsilon_\mu(k, m) \to A^\mu(\epsilon_\mu + \lambda k_\mu) = A + \lambda A^\mu k_\mu. \tag{6.7}$$

Therefore, gauge invariance requires $A^\mu k_\mu = 0$ (known as the Ward Identity). If we require

$$k^\mu \epsilon_\mu(k, m) = 0, \tag{6.8}$$

then only the gauge invariant piece of A^μ, the component orthogonal to k, will contribute to A once we've chosen a gauge in which to work. We choose the Coulomb gauge:

$$\vec{k} \cdot \vec{\epsilon} = 0. \tag{6.9}$$

Equations (6.8) and (6.9) reduce the number of independent elements of ϵ_μ to 2, corresponding to helicities ± 1. As an example, consider a photon with $\vec{k} = k\hat{z}$. Equations (6.8) and (6.9) require $\epsilon_0 = \epsilon_3 = 0$. We can then write the photon polarization vectors as

$$\epsilon^\mu(k\hat{z}, \pm 1) = \mp \frac{1}{\sqrt{2}}(0, 1, \pm i, 0). \tag{6.10}$$

6.1.2 Spin-2 (and higher) Polarization Tensors

The spin-2 polarization tensors are constructed from the spin-1 polarization 4-vectors as [65]

$$\epsilon_{\mu\nu}(p, m) = \sum_{m_1, m_2} (1m_1 1m_2 | 2m)\epsilon_\mu(p, m_1)\epsilon_\nu(p, m_2), \tag{6.11}$$

where $(1m_1 1m_2 | 2m)$ is the Clebsch-Gordon coefficient coupling two spin-1 states to a spin-2 state. The transformation properties of the spin-1 states (6.3) along with the properties of the D-functions can be used to show that, in the particle's rest frame, $\epsilon_{\mu\nu}(p, m)$ does transform under spatial rotations as a spin-2 state:

$$R^\mu{}_\rho R^\nu{}_\pi \epsilon_{\mu\nu}(p, m) \xrightarrow{rf} R_{ik}R_{jl}\epsilon_{kl}(m) = \sum_{m'} D^{(2)}_{m'm}(R)\epsilon_{ij}(m'). \tag{6.12}$$

A general 2nd rank tensor has 16 independent elements; however, a spin-2 state only has 5 ($m_z = \pm 2, \pm 1, 0$). The Rarita-Schwinger conditions

$$
\begin{align}
p^\mu \epsilon_{\mu\nu}(p, m) &= 0 \tag{6.13a} \\
\epsilon_{\mu\nu}(p, m) &= \epsilon_{\nu\mu}(p, m) \tag{6.13b} \\
g^{\mu\nu} \epsilon_{\mu\nu}(p, m) &= 0, \tag{6.13c}
\end{align}
$$

which follow directly from (6.11) and (6.1), reduce the number of independent elements to 5. The spin-2 projection operator is defined as [65]

$$
\begin{align}
P^{(2)}_{\mu_1\mu_2\nu_1\nu_2}(p) &= \sum_m \epsilon_{\mu_1\mu_2}(p, m)\epsilon^*_{\nu_1\nu_2}(p, m) \tag{6.14a} \\
&= \frac{1}{2}(\tilde{g}_{\mu_1\nu_1}\tilde{g}_{\mu_2\nu_2} + \tilde{g}_{\mu_1\nu_2}\tilde{g}_{\mu_2\nu_1}) - \frac{1}{3}\tilde{g}_{\mu_1\mu_2}\tilde{g}_{\nu_1\nu_2}, \tag{6.14b}
\end{align}
$$

where $\tilde{g}_{\mu\nu}$ is defined in (6.5). When $P^{(2)}_{\mu_1\mu_2\nu_1\nu_2}(p)$ is contracted with an arbitrary 2nd rank tensor, the resulting tensor satisfies the spin-2 Rarita-Schwinger conditions (6.13). Therefore, it projects any 2nd rank tensor into the space spanned by the pure spin-2 states.

The technique used to build the spin-2 states can now be generalized to arbitrary integer spin-J. The spin-J state is described by a rank-J polarization tensor given by [65]

$$
\epsilon_{\mu_1\mu_2\ldots\mu_J}(p, m) = \sum_{m_{J-1}, m_1} ((J-1)m_{J-1}1m_1|Jm)\epsilon_{\mu_1\mu_2\ldots\mu_{J-1}}(p, m_{J-1})\epsilon_{\mu_J}(p, m_1). \tag{6.15}
$$

Therefore, using the spin-1 and spin-2 states, the spin-3 states can be built using (6.15). Then, the spin-1 and spin-3 states, along with (6.15), give the spin-4 states, and so on up to any spin-J. The rotational properties of the spin-1 states (6.3) along with the properties of the D-functions can be used to show that, in the particle's rest frame, $\epsilon_{\mu_1\mu_2\ldots\mu_J}(p, m)$ does transform under spatial rotations as a spin-J state:

$$
R^{\mu_1}{}_{\nu_1} \ldots R^{\mu_n}{}_{\nu_n} \epsilon^{\nu_1\ldots\ldots\nu_J}(p, m) \xrightarrow[rf]{} R_{i_1 j_1} \ldots R_{i_J j_J} \epsilon_{j_1\ldots j_J}(m) = \sum_{m'} D^{(J)}_{m'm}(R)\epsilon_{i_1\ldots i_J}(m'). \tag{6.16}
$$

The Rarita-Schwinger conditions for integer spin-J are

$$
\begin{align}
p^{\mu_i} \epsilon_{\mu_1\mu_2\ldots\mu_i\ldots\mu_J}(p, m) &= 0 \tag{6.17a} \\
\epsilon_{\mu_1\mu_2\ldots\mu_i\ldots\mu_j\ldots\mu_J}(p, m) &= \epsilon_{\mu_1\mu_2\ldots\mu_j\ldots\mu_i\ldots\mu_J}(p, m) \tag{6.17b} \\
g^{\mu_i\mu_j} \epsilon_{\mu_1\mu_2\ldots\mu_i\ldots\mu_j\ldots\mu_J}(p, m) &= 0, \tag{6.17c}
\end{align}
$$

for any μ_i, μ_j, and reduce the number of independent elements from 4^J to $(2J+1)$. The spin-J projection operator can then be defined as

$$
P^{(J)}_{\mu_1\mu_2\ldots\mu_J\nu_1\nu_2\ldots\nu_J}(p) = \sum_m \epsilon_{\mu_1\mu_2\ldots\mu_J}(p, m)\epsilon^*_{\nu_1\nu_2\ldots\nu_J}(p, m), \tag{6.18}
$$

and simply projects out the piece of an arbitrary rank-J tensor that satisfies the Rarita-Schwinger conditions for spin-J, (6.17). Thus, it projects any rank-J tensor into the space spanned by the states of pure spin-J.

We can also use a similar technique to build spin-J projection operators whose rank is not $2J$. These operators will be useful when writing N^* photoproduction amplitudes using the multipole formalism. We start by constructing a state with spin-J and rank r, $r - 2 \leq J < r$

$$\epsilon^J_{\mu_1 \mu_2 \dots \mu_r}(p, m) = \sum_{m_{r-1}, m_1} ((r-1)m_{r-1} 1 m_1 | Jm) \epsilon_{\mu_1 \mu_2 \dots \mu_{r-1}}(p, m_{r-1}) \epsilon_{\mu_r}(p, m_1). \tag{6.19}$$

We can then form the projection operator as before

$$P^{(J)}_{\mu_1 \mu_2 \dots \mu_r \nu_1 \nu_2 \dots \nu_r}(p) = \sum_m \epsilon^J_{\mu_1 \mu_2 \dots \mu_r}(p, m) \epsilon^{J*}_{\nu_1 \nu_2 \dots \nu_r}(p, m). \tag{6.20}$$

6.2 Half-Integral Spin Formalism

We now need to construct the polarization spinors for relativistic half-integer spin particles. We will use the 4-component spinor formalism of Dirac for spin-1/2. The polarization tensors from the previous section will be coupled to the relativistic spin-1/2 spinors to form spinors of higher half-integral spin.

6.2.1 Spin-1/2 Dirac Spinors

The Dirac formalism uses a 4-component spinor, $u(p, m)$, to describe the polarization of a spin-1/2 particle; however, a spin-1/2 particle only has 2 independent elements ($m = \pm\frac{1}{2}$). The Dirac equation, which in momentum space is written as

$$(\gamma^\mu p_\mu - w)u(p, m) = 0, \tag{6.21}$$

where the 4 x 4 matrices γ^μ satisfy

$$\gamma^\mu \gamma^\nu + \gamma^\nu \gamma^\mu = 2g^{\mu\nu}, \tag{6.22}$$

reduces the number of independent components of $u(p, m)$ to two. Choosing the following representation in 2 x 2 block form for the γ matrices:

$$\gamma^0 = \begin{pmatrix} 1 & 0 \\ 0 & -1 \end{pmatrix} \tag{6.23a}$$

$$\gamma^i = \begin{pmatrix} 0 & \sigma_i \\ -\sigma_i & 0 \end{pmatrix}, \tag{6.23b}$$

where σ_i are the Pauli matrices, the Dirac equation in the particle's rest frame is

$$\begin{pmatrix} 0 & 0 \\ 0 & -2w \end{pmatrix} u(p_{rf}, m) = 0. \tag{6.24}$$

Therefore, the lower 2 components of $u(p_{rf}, m)$ are zero. Thus, the 4 component spinor takes the form

$$u(p_{rf}, m) = 2w \begin{pmatrix} \chi(m) \\ 0 \end{pmatrix}, \tag{6.25}$$

where

$$\chi(+\frac{1}{2}) = \begin{pmatrix} 1 \\ 0 \end{pmatrix}, \quad \chi(-\frac{1}{2}) = \begin{pmatrix} 0 \\ 1 \end{pmatrix}, \tag{6.26}$$

are the non-relativistic 2-component spinors. Under spatial rotations in the rest frame, $u(p_{rf}, m)$ transforms as

$$\Lambda_{\frac{1}{2}}(R)u(p, m) \xrightarrow[rf]{} 2wR_{ij}\chi_j(m) = 2w \sum_{m'} D^{(\frac{1}{2})}_{m'm}(R)\chi(m'). \tag{6.27}$$

Table 6.1: Transformation properties of $\bar{u}\Gamma u$.

Γ	Transforms As
1	scalar
γ^5	pseudo-scalar
γ^μ	vector
$\gamma^\mu\gamma^5$	pseudo-vector
$\gamma^\mu\gamma^\nu$	tensor

To get the 4-component spinor in any arbitrary frame, we simply boost it from the rest frame yielding [66]

$$u(p,m) = \Lambda_{\frac{1}{2}}(p)u(p_{rf},m) = \sqrt{E+w}\left(\begin{array}{c}\chi(m) \\ \frac{\vec{\sigma}\cdot\vec{p}}{E+w}\chi(m)\end{array}\right),\tag{6.28}$$

where $\Lambda_{\frac{1}{2}}(p)$ is the boost operator that takes a spin-1/2 particle from p_{rf} to p.

When writing out amplitudes, we often need to multiply two Dirac spinors together to form a Lorentz scalar. The first guess at how to do this might be $u^\dagger u$, but under a Lorentz transformation this becomes $u^\dagger\Lambda_{\frac{1}{2}}^\dagger\Lambda_{\frac{1}{2}}u$ and, since $\Lambda_{\frac{1}{2}}$ isn't unitary, this doesn't produce a scalar [66]. If we define

$$\bar{u} \equiv u^\dagger\gamma^0,\tag{6.29}$$

which transforms as $\bar{u} \to \bar{u}\Lambda_{\frac{1}{2}}^{-1}$, then $\bar{u}u$ is a Lorentz scalar. We can now define the spin-1/2 projection operator as

$$P^{(\frac{1}{2})}(p) = \frac{1}{2w}\sum_m u(p,m)\bar{u}(p,m) = \frac{1}{2w}(\gamma^\mu p_\mu + w).\tag{6.30}$$

When $P^{(\frac{1}{2})}(p)$ operates on an arbitrary spinor Π, it projects out the piece that is a solution to the Dirac equation with 4-momentum p:

$$(\gamma^\mu p_\mu - w)P^{(\frac{1}{2})}(p)\Pi = \frac{1}{2w}(p^2 - w^2)\Pi = 0.\tag{6.31}$$

Therefore, Π has been projected into the space spanned by $u(p,m)$ $(m = \pm\frac{1}{2})$.

Here we introduce one more important point before moving on to higher half-integer spins. The γ matrices have the following property: [66]

$$\Lambda_{\frac{1}{2}}^{-1}\gamma^\mu\Lambda_{\frac{1}{2}} = \Lambda^\mu{}_\nu\gamma^\nu.\tag{6.32}$$

So the combination $\bar{u}\gamma^\mu u$ transforms under Lorentz transformations as

$$\bar{u}\gamma^\mu u \to \bar{u}\Lambda_{\frac{1}{2}}^{-1}\gamma^\mu\Lambda_{\frac{1}{2}}u = \Lambda^\mu{}_\nu\bar{u}\gamma^\nu u.\tag{6.33}$$

Therefore, $\bar{u}\gamma^\mu u$ transforms like a 4-vector. Thus, even though the μ-index on γ^μ isn't a true 4-vector index, we can safely treat it as one when contracting a γ matrix with any tensor. Using property (6.32), it's also easy to derive the transformation properties of $\bar{u}\Gamma u$ found in Table (6.1), where we also introduce an additional γ matrix, $\gamma^5 \equiv i\gamma^0\gamma^1\gamma^2\gamma^3$.

6.2.2 Spin-3/2 (and higher) Dirac Spinor-Tensors

Now that we've constructed polarization tensors for any integer spin-n and spin-1/2 spinors, we can couple them to build a spinor-tensor for any half-integer spin-J, where $J = n+1/2$, according to [65]

$$u_{\mu_1\mu_2......\mu_n}(p,m) = \sum_{m_n m_{\frac{1}{2}}} (nm_n\frac{1}{2}m_{\frac{1}{2}}|Jm)\epsilon_{\mu_1\mu_2......\mu_n}(p,m_n)u(p,m_{\frac{1}{2}}), \tag{6.34}$$

where $\epsilon_{\mu_1\mu_2......\mu_n}(p,m_n)$ is the spin-n polarization tensor defined in (6.15). The rotational transformation properties (6.27) and (6.16), along with the properties of the D-functions, can be used to show that, in the particle's rest frame, $u_{\mu_1\mu_2......\mu_n}(p,m)$ transforms as a spin-J state under spatial rotations

$$R^{\mu_1}{}_{\nu_1}\ldots R^{\mu_n}{}_{\nu_n}u^{\nu_1......\nu_n}(p,m)\xrightarrow[rf]{}R_{i_1j_1}\ldots R_{i_nj_n}u_{j_1...j_n}(m) = \sum_{m'} D^{(J)}_{m'm}(R)u_{i_1...i_n}(m'). \tag{6.35}$$

A general 4-component spinor of n-th rank tensors has 4^{n+1} independent elements, but a spin-J state only has $(2J+1)$. The Rarita-Schwinger conditions which follow from (6.34) are [64]

$$
\begin{align}
(\gamma^\mu p_\mu - w)u_{\mu_1\mu_2......\mu_n}(p,m) &= 0 \tag{6.36a}\\
u_{\mu_1\mu_2...\mu_i...\mu_j...\mu_n}(p,m) &= u_{\mu_1\mu_2...\mu_j...\mu_i...\mu_n}(p,m) \tag{6.36b}\\
p^{\mu_i}u_{\mu_1\mu_2...\mu_i...\mu_n}(p,m) &= 0 \tag{6.36c}\\
\gamma^{\mu_i}u_{\mu_1\mu_2...\mu_i...\mu_n}(p,m) &= 0 \tag{6.36d}\\
g^{\mu_i\mu_j}u_{\mu_1\mu_2...\mu_i...\mu_j...\mu_n}(p,m) &= 0, \tag{6.36e}
\end{align}
$$

and reduce the number of independent elements to $(2J+1)$. Of the 5 Rarita-Schwinger conditions, all but (6.36d) follow directly from the properties of $\epsilon_{\mu_1\mu_2......\mu_n}(p,m_n)$ and $u(p,m_{\frac{1}{2}})$. Property (6.36d) can be understood by considering the Dirac equation of the spinor $\gamma^5\gamma^{\mu_i}v_{\mu_1\mu_2...\mu_i...\mu_n}(p,m)$, where

$$v_{\mu_1\mu_2...\mu_i...\mu_n} = \epsilon_{\mu_1\mu_2......\mu_n} \otimes u. \tag{6.37}$$

Clearly v satisfies all of the Rarita-Schwinger conditions except (6.36d). It then follows that

$$
\begin{align}
(\gamma^\nu p_\nu - w)\gamma^5\gamma^{\mu_i}v_{\mu_1\mu_2...\mu_i...\mu_n}(p,m) &= \gamma^5(\gamma^{\mu_i}(\gamma^\nu p_\nu - w) - 2p^{\mu_i})v_{\mu_1\mu_2...\mu_i...\mu_n}(p,m) \tag{6.38a}\\
&= \gamma^5\gamma^{\mu_i}(\gamma^\nu p_\nu - w)v_{\mu_1\mu_2...\mu_i...\mu_n}(p,m) \tag{6.38b}\\
&= 0. \tag{6.38c}
\end{align}
$$

Therefore, $\gamma^5\gamma^{\mu_i}v_{\mu_1\mu_2...\mu_i...\mu_n}(p,m)$ satisfies the Rarita-Schwinger conditions (except (6.36d)) for a spin-$(J-1)$ state (since v was built from a tensor product of a spin-n and spin-1/2 state, it has both spin-$(n+1/2)$ and spin-$(n-1/2)$ components). So (6.36d) must hold for a state of pure spin-J, which we've insured through the use of the Clebsch-Gordon coefficients in (6.34).

The spin-$J = n + 1/2$ projection operator can be written as

$$P^{(J)}_{\mu_1\mu_2...\mu_n\nu_1\nu_2...\nu_n}(p) = \frac{1}{2w}\sum_m u_{\mu_1\mu_2......\mu_n}(p,m)\bar{u}_{\nu_1\nu_2......\nu_n}(p,m) \tag{6.39}$$

When $P^{(J)}_{\mu_1\mu_2...\mu_n\nu_1\nu_2...\nu_n}(p)$ operates on an arbitrary 4-component spinor of rank-n tensors, it projects out the piece that satisfies the Rarita-Schwinger conditions (6.36) for spin-J. Thus, it projects any 4-component spinor of rank-n tensors into the space spanned by the states of pure spin-J.

As an example, the spin-3/2 projection operator is [65]

$$P^{(\frac{3}{2})}_{\mu\nu}(P) = P^{(\frac{1}{2})}(P)\left(\tilde{g}_{\mu\nu} - \frac{1}{3}\tilde{g}_{\mu\alpha}\gamma^\alpha\tilde{g}_{\nu\beta}\gamma^\beta\right). \tag{6.40}$$

Notice that the 2nd term in (6.40) enforces (6.36d). It follows directly from the arguments above concerning this Rarita-Schwinger condition that the spin-1/2 projection operator in rank-2 space is

$$P^{(\frac{1}{2})}_{\mu\nu}(P) = P^{(\frac{1}{2})}(P)\frac{1}{3}\tilde{g}_{\mu\alpha}\gamma^\alpha\tilde{g}_{\nu\beta}\gamma^\beta. \tag{6.41}$$

Both (6.40) and (6.41) will be used heavily in all of our s-channel amplitudes.

6.3   Orbital Angular Momentum Tensors

We now look at how to couple two particles to a state of pure orbital angular momentum ℓ. Let the momenta of the 2 particles be p_a and p_b, then define $P = p_a + p_b$ and $p_{ab} = \frac{1}{2}(p_a - p_b)$ to be the total and relative momentum respectively. A state of pure orbital angular momentum can be constructed out of the measured momenta using the integer spin projection operators $P^{(\ell)}_{\mu_1\mu_2...\mu_\ell\nu_1\nu_2...\nu_\ell}(P)$, defined in equation (6.18). This is done by building a rank-ℓ tensor out of the relative momentum $p^{\nu_1}_{ab}p^{\nu_2}_{ab}\ldots p^{\nu_\ell}_{ab}$, then projecting it to a state of pure spin-ℓ which yields

$$L^{(\ell)}_{\mu_1\mu_2...\mu_\ell}(p_{ab}) = (-)^\ell P^{(\ell)}_{\mu_1\mu_2...\mu_\ell\nu_1\nu_2...\nu_\ell}(P)p^{\nu_1}_{ab}p^{\nu_2}_{ab}\ldots p^{\nu_\ell}_{ab}. \tag{6.42}$$

The properties of the integer spin projection operators guarantee that the states $L^{(\ell)}_{\mu_1\mu_2...\mu_\ell}(p_{ab})$ satisfy the Rarita-Schwinger conditions

$$P^{\mu_i}L^{(\ell)}_{\mu_1\mu_2...\mu_i...\mu_\ell}(p_{ab}) \quad = \quad 0 \tag{6.43a}$$

$$L^{(\ell)}_{\mu_1\mu_2...\mu_i...\mu_j...\mu_\ell}(p_{ab}) \quad = \quad L^{(\ell)}_{\mu_1\mu_2...\mu_j...\mu_i...\mu_\ell}(p_{ab}) \tag{6.43b}$$

$$g^{\mu_i\mu_j}L^{(\ell)}_{\mu_1\mu_2...\mu_i...\mu_j...\mu_\ell}(p_{ab}) \quad = \quad 0, \tag{6.43c}$$

for any μ_i, μ_j, which insures that they have $(2\ell+1)$ independent elements. The states of pure orbital angular momentum for $\ell = 0, 1, 2, 3$ are [67]

$$L^{(0)}(p_{ab}) \quad = \quad 1 \tag{6.44a}$$
$$L^{(1)}_\mu(p_{ab}) \quad = \quad \tilde{p}^{ab}_\mu \tag{6.44b}$$

$$L^{(2)}_{\mu_1\mu_2}(p_{ab}) \quad = \quad \tilde{p}^{ab}_{\mu_1}\tilde{p}^{ab}_{\mu_2} - \frac{1}{3}\tilde{p}^2_{ab}\tilde{g}_{\mu_1\mu_2} \tag{6.44c}$$

$$L^{(3)}_{\mu_1\mu_2\mu_3}(p_{ab}) \quad = \quad \tilde{p}^{ab}_{\mu_1}\tilde{p}^{ab}_{\mu_2}\tilde{p}^{ab}_{\mu_3} - \frac{1}{5}\tilde{p}^2_{ab}(\tilde{g}_{\mu_1\mu_2}\tilde{p}^{ab}_{\mu_3} + \tilde{g}_{\mu_1\mu_3}\tilde{p}^{ab}_{\mu_2} + \tilde{g}_{\mu_2\mu_3}\tilde{p}^{ab}_{\mu_1}), \tag{6.44d}$$

where $\tilde{g}_{\mu_1\mu_2} = g_{\mu_1\mu_2} - \frac{P_{\mu_1}P_{\mu_2}}{P^2}$ and $\tilde{p}^{ab}_\mu = \tilde{g}_{\mu\nu}p^\nu_{ab}$.

In the previous sections, we made a point to demonstrate that the rotational properties of the spin-J states were the same as in *traditional* non-relativistic quantum mechanics. We can draw a similar connection in this case. Consider the inner product of the $\ell = 2$ orbital tensor with a state of pure $m = 2$ in the rest frame of the system

$$L^{(2)}_{\mu\nu}(p_{ab})\epsilon^{\mu\nu}(P, +2) \quad \xrightarrow{rf} \quad (\vec{p}_{ab}\cdot\vec{\epsilon}(+))(\vec{p}_{ab}\cdot\vec{\epsilon}(+)) - \frac{1}{3}|\vec{p}_{ab}|^2(\vec{\epsilon}(+)\cdot\vec{\epsilon}(+))$$

$$= \quad (p\sin(\theta)e^{i\phi})^2 \propto p^2 Y^2_2(\theta, \phi). \tag{6.45}$$

Thus, the non-relativistic quantum mechanical solution, up to an energy dependent scale factor, is again preserved in the rest frame of the system.

6.4 $\omega \to \pi^+\pi^-\pi^0$ Amplitude

Now we want to construct the amplitude for $\omega \to \pi^+\pi^-\pi^0$. Let's first consider isospin. The ω is an iso-scalar, while the three π's are iso-vectors. There is only one way to form an iso-scalar from three iso-vectors that conserves isospin: $(\vec{I}_{\pi^+} \times \vec{I}_{\pi^-}) \cdot \vec{I}_{\pi^0}$ (which is fully anti-symmetric in the three π's). Using the convention $\vec{I}_{\pi^+} = -\frac{1}{\sqrt{2}}(1, i, 0)$, $\vec{I}_{\pi^-} = \frac{1}{\sqrt{2}}(1, -i, 0)$ and $\vec{I}_{\pi^0} = (0, 0, 1)$ gives

$$(\vec{I}_{\pi^+} \times \vec{I}_{\pi^-}) \cdot \vec{I}_{\pi^0} = i. \tag{6.46}$$

Thus, isospin conservation just contributes an overall phase factor to the amplitude. If we now consider just spin and parity, the decay can be written as $\omega(1^-) \to \pi^+(0^-)\pi^-(0^-)\pi^0(0^-)$. The 3π system has negative intrinsic parity and spin-0. Therefore, the angular dependent piece describing the 3π system must have $\ell = 1$ and positive parity (a two particle system with $\ell = 1$ must have negative parity; however, a three particle system can have either parity depending on how the orbital angular momenta are coupled). We can write the amplitude as

$$A_{\omega \to \pi^+\pi^-\pi^0} = N\left((\vec{I}_{\pi^+} \times \vec{I}_{\pi^0}) \cdot \vec{I}_{\pi^-}\right) \epsilon_{\mu\nu\alpha\beta} p^\nu_{\pi^+} p^\alpha_{\pi^-} p^\beta_{\pi^0} \epsilon^\mu(q, m_\omega), \tag{6.47}$$

which is totally symmetric in the 3 π's ($\epsilon_{\mu\nu\alpha\beta}$ is the totally anti-symmetric Levi-Civita tensor). N is a normalization factor defined such that

$$\int |A_{\omega \to \pi^+\pi^-\pi^0}|^2 d\Phi_{3\pi} = 1. \tag{6.48}$$

The mean path of the ω prior to its decay is ~ 20 fm. For the CLAS detector to track the decay π^+ and π^- (which is required for any event used in our analysis) the ω must decay prior to traveling ~ 1 m. Thus, all ω's produced do decay inside the detector. The normalization condition (6.48) enforces this at the amplitude level.

The quantity $\epsilon_{\mu\nu\alpha\beta} p^\nu_{\pi^+} p^\alpha_{\pi^-} p^\beta_{\pi^0}$ can be rewritten as $\epsilon_{\mu\nu\alpha\beta} p^\nu_{\pi^+} p^\alpha_{\pi^-} q^\beta$ using conservation of 4-momentum. In the ω rest frame, (6.47) simplifies to

$$
\begin{aligned}
A_{\omega \to \pi^+\pi^-\pi^0} &= iN\epsilon_{\mu\nu\alpha0} p^\nu_{\pi^+} p^\alpha_{\pi^-} w_\omega \epsilon^\mu(q, m_\omega) & (6.49\text{a}) \\
&= iNw_\omega \epsilon^i(q, m_\omega) \epsilon_{ijk} p^j_{\pi^+} p^k_{\pi^-} & (6.49\text{b}) \\
&= iNw_\omega (\vec{p}_{\pi^+} \times \vec{p}_{\pi^-}) \cdot \vec{\epsilon}(q, m_\omega), & (6.49\text{c})
\end{aligned}
$$

where w_ω is the mass of the ω. Performing an incoherent sum over the polarizations of the ω yields

$$\sum_{m_\omega} |A_{\omega \to \pi^+\pi^-\pi^0}|^2 \propto |\vec{p}_{\pi^+} \times \vec{p}_{\pi^-}|^2, \tag{6.50}$$

where the π momenta are measured in the ω rest frame ((6.50) agrees with the result obtained by Zemach using a non-relativistic tensor approach [68]). We also define the following useful quantity for the ω decay:

$$\omega^\mu(p_{\pi^+}, p_{\pi^-}, p_{\pi^0}) = NP^{(1)\mu\sigma}(q)\epsilon_{\sigma\nu\alpha\beta} p^\nu_{\pi^+} p^\alpha_{\pi^-} p^\beta_{\pi^0}. \tag{6.51}$$

Note that we are not using a Breit-Wigner propagator for the ω. Our Monte Carlo has the natural width of the ω built in. In the following sections, we will define amplitudes for $\gamma p \to p\omega$ via various processes. In each of these, the ω will be represented by a factor of $\epsilon^*_\mu(q, m_\omega)$. To add the $\omega \to 3\pi$ decay to any of these amplitudes, we simply need to replace $\epsilon^*_\mu(q, m_\omega)$ with ω_μ defined in (6.51).

6.5   Non-Resonant Amplitudes

6.5.1 t-channel 0^- Exchange

To build the pseudo-scalar meson exchange amplitude, we first write the necessary effective Lagrangians:

$$\mathcal{L}_{\phi pp} = -ig_{\phi pp}\bar{\psi}\gamma^5\psi\phi \tag{6.52a}$$

$$\mathcal{L}_{\gamma\phi\omega} = e\frac{g_{\gamma\phi\omega}}{w_\omega}\epsilon^{\mu\nu\alpha\beta}\partial_\mu\omega_\nu\partial_\alpha A_\beta\phi, \tag{6.52b}$$

where ϕ, A_μ and ψ denote the pseudo-scalar, photon and proton fields respectively. From these Lagrangians, we can write the pseudo-scalar exchange amplitude as

$$A_{\gamma p\to p\omega}^{0^- ex(bare)} = -ieg_{\phi pp}\frac{g_{\gamma\phi\omega}}{w_\omega}\bar{u}(p_f,m_f)\gamma^5 u(p_i,m_i)\frac{1}{t-m_\phi^2}\epsilon^{\mu\nu\alpha\beta}q_\mu\epsilon_\nu^*(q,m_\omega)k_\alpha\epsilon_\beta(k,m_\gamma). \tag{6.53}$$

To account for the finite size of the particles, we follow [28] and apply monopole form factors to each vertex

$$A_{\gamma p\to p\omega}^{0^- ex} = F(t,m_\phi,\Lambda_{\gamma\phi\omega})F(t,m_\phi,\Lambda_{\phi pp})A_{\gamma p\to p\omega}^{0^- ex(bare)}, \tag{6.54}$$

where

$$F(t,m,\Lambda) = \frac{\Lambda^2 - m^2}{\Lambda^2 - t} \tag{6.55}$$

and Λ is the cutoff mass for the interaction. The values of the coupling constants and cutoffs will be given in Section 8.1.

6.5.2 t-channel Pomeron Exchange

At very high energies, ω photoproduction is known to be dominated by diffractive processes (*ie* Pomeron exchange). Here we follow Oh, Titov and Lee and write the amplitude as [28]

$$A_{\gamma p\to p\omega}^{pomeron} = R(s,t)\bar{u}(p_f,m_f)\epsilon_\mu^*(q,m_\omega)(k_\alpha\gamma^\alpha g^{\mu\nu} - k^\mu\gamma^\nu)\epsilon_\nu(k,m_\gamma)u(p_i,m_i), \tag{6.56}$$

where $R(s,t)$ is a Regge parameterization of the form

$$R(s,t) = C_\omega F_1(t)F_\omega(t)\left(\frac{s}{s_0}\right)^{\alpha_P(t)-1}e^{-\frac{i\pi}{2}(\alpha_P(t)-1)}. \tag{6.57}$$

The Pomeron trajectory is $\alpha_P(t) = 1.08 + 0.25t$. $F_1(t)$ is the isoscalar electromagnetic form factor of the nucleon and is given by

$$F_1(t) = \frac{4m_p^2 - 2.8t}{(4m_p^2 - t)(1 - t/t_0)^2}, \tag{6.58}$$

where $t_0 = 0.7 GeV^2$. $F_\omega(t)$ is the form factor for the ω-photon-Pomeron vertex and is given by

$$F_\omega(t) = \frac{1}{1 - t/w_\omega^2}\frac{2\mu_0^2}{2\mu_0^2 + w_\omega^2 - t}. \tag{6.59}$$

The strength factor $C_\omega = 12e\beta_0^2/f_\omega$ parameters, along with μ_0, are determined by fitting all total cross section data available for the ω, ρ and ϕ mesons. This fixes $\mu_0^2 = 1.1 GeV^2$, $\beta_0 = 2.05 GeV^{-1}$ and $s_0 = 4 GeV^2$.

6.5.3 t-channel σ Exchange

The σ exchange amplitude can be constructed from the effective Lagrangians:

$$\begin{align}
\mathcal{L}_{\sigma pp} &= g_{\sigma pp}\bar{\psi}\psi\sigma \tag{6.60a}\\
\mathcal{L}_{\gamma\sigma\omega} &= ew_\omega g_{\gamma\sigma\omega}\omega_\mu A^\mu\sigma, \tag{6.60b}
\end{align}$$

where σ, A_μ and ψ denote the σ, photon and proton fields respectively, yielding the amplitude

$$A_{\gamma p\to p\omega}^{\sigma-ex(bare)} = \frac{ew_\omega g_{\sigma pp}g_{\gamma\sigma\omega}}{t-w_\sigma^2}\bar{u}(p_f,m_f)u(p_i,m_i)\epsilon_\mu^*\epsilon^\mu(k,m_\gamma). \tag{6.61}$$

To restore gauge invariance (current conservation), Sibirstev et al [69] made the slight modification

$$A_{\gamma p\to p\omega}^{\sigma-ex(bare)} = \frac{ew_\omega g_{\sigma pp}g_{\gamma\sigma\omega}}{t-w_\sigma^2}\bar{u}(p_f,m_f)u(p_i,m_i)\epsilon_\mu^*\left(g^{\mu\nu}-\frac{k^\mu q^\nu}{k\cdot q}\right)\epsilon_\nu(k,m_\gamma), \tag{6.62}$$

As in the pseudoscalar case, monopole form factors are added to account for the finite size of the particles:

$$A_{\gamma p\to p\omega}^{\sigma-ex} = F(t,m_\sigma,\Lambda_{\gamma\phi\omega})F(t,m_\sigma,\Lambda_{\phi pp})A_{\gamma p\to p\omega}^{\sigma^-ex(bare)}. \tag{6.63}$$

The values of the coupling constants and cutoffs can be found in [69].

6.5.4 Direct and Crossed Nucleon Exchange

To build the proton exchange amplitudes, we first write the appropriate effective Lagrangians:

$$\begin{align}
\mathcal{L}_{\gamma pp} &= -e\bar{\psi}(\gamma^\mu-\frac{\kappa_p}{2m_p}\sigma^{\mu\nu}\partial_\nu)A_\mu\psi \tag{6.64a}\\
\mathcal{L}_{\omega pp} &= -g_{\omega pp}\bar{\psi}(\gamma^\mu-\frac{\kappa_\omega}{2m_p}\sigma^{\mu\nu}\partial_\nu)\omega_\mu\psi. \tag{6.64b}
\end{align}$$

From these Lagrangians we can construct proton exchange amplitudes via s- and u-channel as

$$\begin{align}
A_{\gamma p\to p\omega}^u &= eg_{\omega pp}\bar{u}(p_f,m_f)\Gamma_\nu^\gamma(k)\epsilon^\nu(k,m_\gamma)\frac{(p_i-q)\cdot\gamma+m_p}{u-m_p^2}\Gamma_\mu^\omega(q)\epsilon^{*\mu}(q,m_\omega)u(p_i,m_i) \tag{6.65}\\
A_{\gamma p\to p\omega}^s &= eg_{\omega pp}\bar{u}(p_f,m_f)\Gamma_\mu^\omega(q)\epsilon^{*\mu}(q,m_\omega)\frac{(p_i+k)\cdot\gamma+m_p}{s-m_p^2}\Gamma_\nu^\gamma(k)\epsilon^\nu(k,m_\gamma)u(p_i,m_i), \tag{6.66}
\end{align}$$

where

$$\begin{align}
\Gamma_\mu^\omega(q) &= \gamma_\mu-i\frac{\kappa_\omega}{2M_p}\sigma_{\mu\alpha}q^\alpha-\frac{k_\mu(q\cdot\gamma)}{k\cdot q} \tag{6.67}\\
\Gamma_\nu^\gamma(k) &= \gamma_\mu+i\frac{\kappa_p}{2M_p}\sigma_{\nu\beta}k^\beta-\frac{q_\nu(k\cdot\gamma)}{k\cdot q}. \tag{6.68}
\end{align}$$

The last term in each of the above expressions was added by Oh, Titov and Lee to restore gauge invariance (current conservation) [28]. The couplings at the γpp vertex are $e=\sqrt{4\pi/137}$ and $\kappa_p=1.79$. The ωpp couplings will be specified in Section 8.1. It is also necessary to account for the finite size of the particles by including form factors. There are several prescriptions for this found in the literature. In Section 8.1, we will discuss two different approaches to handling this issue and provide comparisons of both models to our data.

6.6   Resonant Amplitudes

6.6.1 $J^P \to p\omega$ Amplitudes

Here we consider a baryon with spin-parity J^P, 4-momentum P and spin projection M decaying to $p\omega$. Since the ω is an iso-scalar, $p\omega$ only couples to J^P states with $I = \frac{1}{2}$. Thus, J^P must be an N^* state and isospin will only contribute a factor of 1 at this vertex (thus we'll ignore it). The work presented in this section loosely follows that of Anisovich [67] (there are some important differences).

J^P **States with** $P = (-)^{J-\frac{1}{2}}$ $\left(\frac{1}{2}^+, \frac{3}{2}^-, \frac{5}{2}^+ \ldots \right)$

First, consider $J^P = \frac{1}{2}^+$ which decays to $p\omega$ in P-wave only. The $p\omega$ system can be coupled to either $s = \frac{1}{2}$ or $s = \frac{3}{2}$. Therefore, there are 2 independent amplitudes for the decay of $J^P = \frac{1}{2}^+ \to p\omega$ which we can write as

$$A^{\ell=1,s=\frac{1}{2},\frac{3}{2}}_{\frac{1}{2}^+ \to p\omega} = \bar{u}(p_f, m_f)\epsilon^{*\mu}(q, m_\omega)P^{(s)}_{\mu\nu}(P)L^{(1)\nu}(p_{p\omega})u(P, M). \tag{6.69}$$

We can then generalize (6.69) to construct the amplitudes for $J = \ell - \frac{1}{2}$ states

$$A^{\ell=J+\frac{1}{2},s=\frac{1}{2},\frac{3}{2}}_{J^P \to p\omega} = \bar{u}(p_f, m_f)\epsilon^{*\mu}(q, m_\omega)P^{(s)}_{\mu\nu}(P)L^{(\ell)\nu\mu_1\mu_2\ldots\mu_{\ell-1}}(p_{p\omega})u_{\mu_1\mu_2\ldots\mu_{\ell-1}}(P, M). \tag{6.70}$$

Therefore, (6.70) can be used to obtain amplitudes for $\frac{1}{2}^+ \to p\omega$ in P-wave, $\frac{3}{2}^- \to p\omega$ in D-wave, $\frac{5}{2}^+ \to p\omega$ in F-wave, etc.

To build the remaining amplitudes for these states, we first consider $\frac{3}{2}^- \to p\omega$ in S-wave. The $p\omega$ system must couple to $s = \frac{3}{2}$, so there's only 1 amplitude which can be written as

$$A^{\ell=0,s=\frac{3}{2}}_{\frac{3}{2}^- \to p\omega} = \bar{u}(p_f, m_f)\epsilon^{*\mu}(q, m_\omega)u_\mu(P, M), \tag{6.71}$$

which can be generalized for $J = \ell + \frac{3}{2}$ states to

$$A^{\ell=J-\frac{3}{2},s=\frac{3}{2}}_{J^P \to p\omega} = \bar{u}(p_f, m_f)\epsilon^*_\nu(q, m_\omega)L^{(\ell)}_{\mu_1\mu_2\ldots\mu_\ell}u^{\nu\mu_1\mu_2\ldots\mu_\ell}(P, M). \tag{6.72}$$

Therefore, (6.72) can be used to obtain amplitudes for $\frac{3}{2}^- \to p\omega$ in S-wave, $\frac{5}{2}^+ \to p\omega$ in P-wave, $\frac{7}{2}^- \to p\omega$ in D-wave, etc. Thus, (6.70) and (6.72) together yield all of the $J^P \to p\omega$ amplitudes for the $P = (-)^{J-\frac{1}{2}}$ states.

J^P **States with** $P = (-)^{J+\frac{1}{2}}$ $\left(\frac{1}{2}^-, \frac{3}{2}^+, \frac{5}{2}^- \ldots \right)$

For the remaining J^P states, first consider $\frac{1}{2}^- \to p\omega$ which can proceed in either S-wave (with $s = \frac{1}{2}$) or D-wave (with $s = \frac{3}{2}$). Therefore, there are two amplitudes for this process which can be written as

$$A^{\ell=0,s=\frac{1}{2}}_{\frac{1}{2}^- \to p\omega} = \bar{u}(p_f, m_f)\epsilon^*_\mu(q, m_\omega)\gamma^\mu\gamma^5 u(P, M) \tag{6.73}$$

$$A^{\ell=2,s=\frac{3}{2}}_{\frac{1}{2}^- \to p\omega} = \bar{u}(p_f, m_f)\epsilon^*_\mu(q, m_\omega)L^{(2)\mu\nu}(p_{p\omega})\gamma_\nu\gamma^5 u(P, M), \tag{6.74}$$

where γ^5 has been added to conserve parity.

Next we consider $\frac{3}{2}^+ \to p\omega$ where the $p\omega$ system can be in either P-wave (with $s = \frac{3}{2}$ or $s = \frac{1}{2}$) or F-wave (with $s = \frac{3}{2}$). The amplitudes for the P-wave decay can be written as

$$A^{\ell=1,s=\frac{1}{2}}_{\frac{3}{2}^+ \to p\omega} = \bar{u}(p_f, m_f)\epsilon^{*\mu}(q, m_\omega)P^{(s)}_{\mu\nu}(P)\gamma^\nu\gamma^5 L^{(1)}_\alpha u^\alpha(P, M) \tag{6.75a}$$

$$A^{\ell=1,s=\frac{3}{2}}_{\frac{3}{2}^+ \to p\omega} = \bar{u}(p_f, m_f)\epsilon^{*\mu}(q, m_\omega)P^{(s)}_{\mu\nu}(P)\gamma^\alpha\gamma^5 L^{(1)}_\alpha u^\nu(P, M), \tag{6.75b}$$

which can be generalized for $J = \ell + \frac{1}{2}$ to

$$A^{\ell=J-\frac{1}{2},s=\frac{1}{2}}_{J^P \to p\omega} = \bar{u}(p_f, m_f)\epsilon^{*\mu}(q, m_\omega)P^{(s)}_{\mu\nu}(P)\gamma^\nu\gamma^5 L^{(\ell)\alpha_1\alpha_2...\alpha_\ell}(p_{p\omega})u_{\alpha_1\alpha_2...\alpha_\ell}(P) \tag{6.76a}$$

$$A^{\ell=J-\frac{1}{2},s=\frac{3}{2}}_{J^P \to p\omega} = \bar{u}(p_f, m_f)\epsilon^*_\mu(q, m_\omega)P^{(s)\mu\nu}(P)\gamma_{\alpha_1}\gamma^5 L^{(\ell)\alpha_1\alpha_2...\alpha_\ell}(p_{p\omega})u_{\nu\alpha_2...\alpha_\ell}(P). \tag{6.76b}$$

The F-wave decay of the $\frac{3}{2}^+$ to $p\omega$ has amplitude:

$$A^{\ell=3,s=\frac{3}{2}}_{\frac{3}{2}^+ \to p\omega} = \bar{u}(p_f, m_f)\epsilon^{*\nu}(q, m_\omega)L^{(3)}_{\mu\nu\alpha}(p_{p\omega})\gamma^\alpha\gamma^5 u^\mu(P, M), \tag{6.77}$$

which can be generalized for $J = \ell - \frac{3}{2}$ to

$$A^{\ell=J+\frac{3}{2},s=\frac{3}{2}}_{J^P \to p\omega} = \bar{u}(p_f, m_f)\epsilon^{*\mu_1}(q, m_\omega)L^{(\ell)}_{\mu_1\mu_2...\mu_\ell}(p_{p\omega})\gamma^{\mu_2}\gamma^5 u^{\mu_3...\mu_\ell}(P, M). \tag{6.78}$$

Therefore, (6.76a) and (6.78) can be used to obtain all of the $J^P \to p\omega$ amplitudes for the $P = (-)^{J+\frac{1}{2}}$ states.

6.6.2 $\gamma p \to J^P$ Amplitudes

In this section, we'll construct amplitudes for photoproduction of a Baryon with spin-parity J^P off a proton target. In the previous sections, amplitudes were constructed in terms of specific $L - S$ states; however, the presence of a real photon in these amplitudes makes $L - S$ states not the best choice. As an example, consider $\gamma p \to \frac{1}{2}^-$. To conserve parity and angular momentum, the γp system must be in either $\ell = 0$ or 2. This leads to two Lorentz invariant amplitudes, which can be written as

$$A^{\ell=0}_{\gamma p \to \frac{1}{2}^-} = \bar{u}(P, M)\gamma^\mu\gamma^5 u(p_i, m_i)\epsilon_\mu(k, m_\gamma) \tag{6.79a}$$

$$A^{\ell=2}_{\gamma p \to \frac{1}{2}^-} = \bar{u}(P, M)L^{(2)}_{\mu\nu}(p_{p\gamma})\gamma^\mu\gamma^5 u(i_p, m_i)\epsilon^\nu(k, m_\gamma), \tag{6.79b}$$

which are both Dirac scalars, Lorentz scalars and conserve parity. Notice that $A^{\ell=2}_{\gamma p \to \frac{1}{2}^-}$ can be reduced to

$$\bar{u}L^{(2)}_{\mu\nu}(p_{p\gamma})\gamma^\mu\gamma^5 u\epsilon^\nu = \bar{u}(\tilde{p}^{p\gamma}_\mu\tilde{p}^{p\gamma}_\nu - \frac{1}{3}\tilde{p}^2_{p\gamma}\tilde{g}_{\mu\nu})\gamma^\mu\gamma^5 u\epsilon^\nu \tag{6.80a}$$

$$= \bar{u}(-\frac{1}{3}\tilde{p}^2_{p\gamma}\epsilon_\mu)\gamma^\mu\gamma^5 u \tag{6.80b}$$

$$= -\frac{1}{3}\tilde{p}^2_{p\gamma}A^0_{\gamma p \to \frac{1}{2}^-}, \tag{6.80c}$$

using $\tilde{p}^\mu_{p\gamma}\epsilon_\mu = 0$ and $\tilde{g}_{\mu\nu}\epsilon^\nu = \epsilon_\mu$ for a real photon. Since we bin in $\sqrt{s}$, there is no way to distinguish between $A^{\ell=0}_{\gamma p \to \frac{1}{2}^-}$ and $A^{\ell=2}_{\gamma p \to \frac{1}{2}^-}$. So, instead of writing the $\gamma p \to J^P$ amplitudes in terms of $L - S$ states, we'll switch to using multipoles where the number of ways of coupling the states matches the number of angularly independent amplitudes.

In the multipole representation, the spin of the photon is coupled to the orbital angular momentum of the γp system ℓ to form a state of definite spin-parity j^p. This j^p state is then coupled to the proton to form a state of definite total J^P. The real photon only has $m_\gamma = \pm 1$ states and ℓ only contributes from its $m_\ell = 0$ state (in the J^P rest frame, where ℓ is defined, the quantization axis is chosen to be $\hat{p}_\gamma$, since the physical states of γ are helicity states, therefore $\ell_z = 0$), thus, $m_j = \pm 1$ and $j \neq 0$. Two classes of multipoles are defined, *electric* states are those with $p = (-)^j$, while *magnetic* states have $p = (-)^{j+1}$. Thus, the states $1^-, 2^+, \ldots$ are given the designation $E1, E2, \ldots$ and the states $1^+, 2^-, \ldots$ are called $M1, M2, \ldots$ (there are no 0 states).

J^P **States with** $P = (-)^{J+\frac{1}{2}}$ $\left(\frac{1}{2}^-, \frac{3}{2}^+, \frac{5}{2}^- \ldots \right)$

Let's return to $\gamma p \to \frac{1}{2}^-$ where $\ell = 0$ or 2. We can couple the photon to $\ell = 0$ to get $j^p = 1^-$ and to $\ell = 2$ to get $1^-, 2^-, 3^-$. But only the 1^- state can then be coupled to the proton to get $J^P = \frac{1}{2}^-$. Thus, $J^P = \frac{1}{2}^-$ only couples to the $E1$ multipole with amplitude

$$A^{mp=1^-}_{\gamma p \to \frac{1}{2}^-} = \bar{u}(P, M) \gamma^\mu \gamma^5 u(p_i, m_i) \left(P^{(1)}_{\mu\nu}(P) \epsilon^\nu(k, m_\gamma) \right), \tag{6.81}$$

which reduces to

$$A^{mp=1^-}_{\gamma p \to \frac{1}{2}^-} = \bar{u}(P, M) \gamma^\mu \gamma^5 u(p_i, m_i) \epsilon_\mu(k, m_\gamma). \tag{6.82}$$

Now we move on to $A_{\gamma p \to \frac{3}{2}^+}$. The reaction $\gamma p \to \frac{3}{2}^+$ can proceed with the γp system in P-wave or F-wave. The photon couples to $\ell = 1$ giving $j^p = 1^+, 2^+$ and to $\ell = 3$ giving $j^p = 2^+, 3^+, 4^+$; however, only the 1^+ and 2^+ states can couple with the proton to get $J^P = \frac{3}{2}^+$. Thus, $J^P = \frac{3}{2}^+$ couples to the $E2$ and $M1$ multipoles, which can both be built with $\ell = 1$ according to

$$A^{mp=j^+}_{\gamma p \to \frac{3}{2}^+} = \bar{u}^\mu(P, M) \gamma^\nu \gamma^5 P^{(j)}_{\mu\nu\alpha\beta}(P) L^{(1)\alpha}(p_{p\gamma}) \epsilon^\beta(k, m_\gamma) u(p_i, m_i), \tag{6.83}$$

where $j = 1, 2$. This can then be generalized for any of the $P = (-)^{J+\frac{1}{2}}$ states $(J > \frac{1}{2})$. Each J^P will couple to 2 multipoles (1 electric and 1 magnetic) with the following amplitudes:

$$A^{mp=j^p}_{\gamma p \to J^P} = \bar{u}^{\mu_1\mu_2\ldots\mu_\ell}(P, M) \gamma^\nu \gamma^5 P^{(j)}_{\mu_1\mu_2\ldots\mu_\ell\nu\alpha_1\alpha_2\ldots\alpha_\ell\beta}(P) L^{(\ell)\alpha_1\alpha_2\ldots\alpha_\ell}(p_{p\gamma}) \epsilon^\beta(k, m_\gamma) u(p_i, m_i), \tag{6.84}$$

where $j = J - \frac{1}{2}, J + \frac{1}{2}, p = (-)^{J+\frac{1}{2}}$ and $\ell = J - \frac{1}{2}$.

J^P **States with** $P = (-)^{J-\frac{1}{2}}$ $\left(\frac{1}{2}^+, \frac{3}{2}^-, \frac{5}{2}^+ \ldots \right)$

Now we want to write out the multipole amplitudes for the photoproduction of the states with $P = (-)^{J-\frac{1}{2}}$. We start with $\gamma p \to \frac{1}{2}^+$ where $\ell = 1$ is the only possibility. The photon couples to $\ell = 1$ giving $j^p = 1^+, 2^+$ but only the 1^+ state can couple with the proton to obtain $J^P = \frac{1}{2}^+$, thus only the $M1$ multipole will contribute. We can write this amplitude as

$$A^{mp=1^+}_{\gamma p \to \frac{1}{2}^+} = \bar{u}(P, M) \gamma^\alpha L^{(1)}_\alpha(p_{p\gamma}) \gamma^\mu \epsilon_\mu(k, m_\gamma) u(p_i, m_i). \tag{6.85}$$

Next we examine the reaction $\gamma p \to \frac{3}{2}^-$ which can proceed with γp in S-wave or D-wave. The photon couples to $\ell = 0$ giving $j^p = 1^-$ and to $\ell = 2$ giving $j^p = 1^-, 2^-, 3^-$; however, only the 1^- and 2^- states couple with the proton to give $J^P = \frac{3}{2}^-$. Thus, $J^P = \frac{3}{2}^-$ couples to the $M2$ and $E1$ multipoles with amplitudes

$$A^{mp=j^-}_{\gamma p \to \frac{3}{2}^-} = \bar{u}^\mu(P, M) \gamma^\nu \gamma^\alpha P^{(j)}_{\mu\nu\alpha\mu'\nu'\alpha'}(P) L^{(2)\mu'\nu'}(p_{p\gamma}) \epsilon^{\alpha'}(k, m_\gamma) u(p_i, m_i), \tag{6.86}$$

where $j = 1, 2$. We can then generalize this for all $P = (-)^{J-\frac{1}{2}}$ states $(J > \frac{1}{2})$ as

$$A_{\gamma p \to J^P}^{mp=j^p} = \bar{u}^{\mu_1 \mu_2 \dots \mu_{\ell-1}}(P, M)\gamma^{\mu_\ell}\gamma^{\mu_{\ell+1}} P^{(j)}_{\mu_1 \mu_2 \dots \mu_{\ell+1}\nu_1\nu_2\dots\nu_{\ell+1}}(P)L^{(\ell)\nu_1\nu_2\dots\nu_\ell}(p_{p\gamma})\epsilon^{\nu_{\ell+1}}(k, m_\gamma)u(p_i, m_i), \tag{6.87}$$

where $j = J - \frac{1}{2}, J + \frac{1}{2}, p = (-)^{J-\frac{1}{2}}$ and $\ell = J + \frac{1}{2}$.

6.6.3 $\gamma p \to J^P \to p\omega$ **Amplitudes**

Now that we've written the amplitudes for $\gamma p \to J^P$ and $J^P \to p\omega$, we want to combine these to construct $A_{\gamma p \to J^P \to p\omega}$. To do this we first define generic versions of the N^* amplitudes defined in the previous 2 sections:

$$A_{\gamma p \to J^P} \equiv \bar{u}_{\mu_1 \mu_2 \dots \mu_{J-\frac{1}{2}}}(P, M)X_{PROD}^{\nu\mu_1\mu_2\dots\mu_{J-\frac{1}{2}}}\epsilon_\nu(k, m_\gamma)u(p_i, m_i) \tag{6.88a}$$

$$A_{J^P \to p\omega} \equiv \bar{u}(p_f, m_f)\epsilon_\nu^*(q, m_\omega)X_{DECAY}^{\nu\mu_1\mu_2\dots\mu_{J-\frac{1}{2}}}u_{\mu_1\mu_2\dots\mu_{J-\frac{1}{2}}}(P, M), \tag{6.88b}$$

where X_{PROD}, X_{DECAY} depend on the initial and final state quantum numbers respectively. Since the N^* state is an intermediate particle (we can not observe it), its spin projections must be summed over coherently as

$$A_{\gamma p \to J^P \to p\omega} = \sum_M \bar{u}(p_f, m_f)\epsilon_\alpha^*(q, m_\omega)X_{DECAY}^{\alpha\mu_1\mu_2\dots\mu_{J-\frac{1}{2}}}u_{\mu_1\mu_2\dots\mu_{J-\frac{1}{2}}}(P, M)\bar{u}_{\nu_1\nu_2\dots\nu_{J-\frac{1}{2}}}(P, M)$$
$$\times X_{PROD}^{\beta\nu_1\nu_2\dots\nu_{J-\frac{1}{2}}}\epsilon_\beta(k, m_\gamma)u(p_i, m_i)\mathcal{R}(s), \tag{6.89}$$

where $\mathcal{R}(s)$ is the *mass-dependence* of the state. In the simplest case, this would be a constant width Breit-Wigner. In our PWA, we bin the data finely in $\sqrt{s}$ which allows us to treat $\mathcal{R}(s)$ as a constant complex number in each energy bin.

Using (6.39), (6.89) can be rewritten as

$$A_{\gamma p \to J^P \to p\omega} = \bar{u}(p_f, m_f)\epsilon_\alpha^*(q, m_\omega)X_{DECAY}^{\alpha\mu_1\mu_2\dots\mu_{J-\frac{1}{2}}}P^{(J)}_{\mu_1\mu_2\dots\mu_{J-\frac{1}{2}}\nu_1\nu_2\dots\nu_{J-\frac{1}{2}}}(P)$$
$$\times X_{PROD}^{\beta\nu_1\nu_2\dots\nu_{J-\frac{1}{2}}}\epsilon_\beta(k, m_\gamma)u(p_i, m_i)\mathcal{R}(s). \tag{6.90}$$

This is the prescription followed to combine all $\gamma p \to J^P$ amplitudes with $J^P \to p\omega$ amplitudes when constructing $\gamma p \to J^P \to p\omega$ amplitudes.

6.7 Summary

All of our amplitudes are constructed in a covariant framework, removing the *extra* boosts and rotations needed to properly handle final state particles with spin. The covariant ω decay amplitude reduces to the familiar Zemach form in the ω rest frame. Non-resonant amplitudes have been constructed using effective Lagrangians while resonant amplitudes are built using the Rarita-Schwinger formalism.

Chapter 7

Differential Cross Sections and Spin Density Matrix Elements

In the previous chapters, we have discussed all the details involving event selection, acceptance and normalization. We have also detailed the systematic uncertainties arising from each step of our analysis. In this chapter, final measurements for the differential cross section and ω polarization observables will be presented. Any additional analysis procedures required to extract these measurements will be documented in this chapter. The differential cross section measurements will be presented first, followed by the ω spin density matrix elements. This chapter also contains comparisons of our results to all previous measurements in our energy range. Comparisons to various theoretical models will be shown in Chapter 8.

7.1 The Mother of All Fits

A key first step prior to making any of our measurements is running the *Mother of All Fits*, a fit containing all s-channel waves with $J \leq 21/2$ of both parities. The results of this fit are *NOT* interpreted as physics. This fit simply constitutes a (nearly) complete basis which provides us with the best possible description of our data. The fit contains 108 free parameters, the form of which is discussed below.

7.1.1 Partial Wave Amplitudes

The details concerning the form of the s-channel resonant amplitudes are discussed in depth in Section 6.6. In this section, we denote the amplitudes for $\gamma p \to J^P \to p\omega$ as

$$A_{\gamma p \to J^P \to p\omega} = \epsilon_\mu^*(q, m_\omega) A^\mu_{MP,L,S,m_i,m_\gamma,m_f}, \tag{7.1}$$

where q is the momentum of the ω, m_x are the spin projections (along the beam direction) of the particles x, MP denotes the production multipole and L, S denote the orbital angular momentum and spin of the $p\omega$ system. We then incorporate the $\omega \to \pi^+\pi^-\pi^0$ decay and write

$$A_{\gamma p \to J^P \to p\omega \to p\pi^+\pi^-\pi^0} = \omega_\mu(p_{\pi^+}, p_{\pi^-}, p_{\pi^0}) A^\mu_{MP,L,S,m_i,m_\gamma,m_f}, \tag{7.2}$$

where $\omega_\mu(p_{\pi^+}, p_{\pi^-}, p_{\pi^0})$, defined in (6.51), includes the ω decay amplitude and the sum over the ω spin projections.

In this fit, we aren't concerned with representing actual physics. We simply want to provide the fit with enough freedom to properly describe all kinematic distributions (including correlations) in the data. To this end, we chose to write the amplitudes in each $\sqrt{s}$ bin as

$$A_{\gamma p \to J^P \to p\omega \to p\pi^+\pi^-\pi^0} = f_{MP}(\theta_{J^P}) r_{J^P LS} e^{i\phi_{J^P}} \omega_\mu(p_{\pi^+}, p_{\pi^-}, p_{\pi^0}) A^\mu_{MP,L,S,m_i,m_\gamma,m_f}, \tag{7.3}$$

where $r_{J^P LS}$, ϕ_{J^P} and θ_{J^P} are real fit parameters (variable with no limits in each $\sqrt{s}$ bin) and

$$f_{MP}(\theta_{J^P}) = \left\{ \begin{array}{ll} \cos\theta_{J^P}, & \text{for electric multipoles} \\ \sin\theta_{J^P}, & \text{for magnetic multipoles} \end{array} \right\}. \tag{7.4}$$

Thus, each J^P has an independent phase angle and each of its decays has an independent magnitude. The multipoles are handled such that each J^P has an independent ratio of electric to magnetic strengths; however, the sum of the two is bounded to remove the overall scale ambiguity between the production and decay parameters.

The Lorentz invariant intensity is then constructed out of the partial wave amplitudes as

$$|\mathcal{M}(\vec{x}, X)|^2 = \sum_{m_i, m_\gamma, m_f} \Big| \sum_{J^P, MP, LS} A_{\gamma p \to J^P \to p\omega \to p\pi^+\pi^-\pi^0}(\vec{x}, X)\Big|^2, \tag{7.5}$$

where $\vec{x}$ denotes the fit parameters and X is the complete set of kinematics.

7.1.2 Maximum Likelihood Fit

The method used to perform the fit is the extended maximum likelihood method described in Section 5.2. The CERNLIB package MINUIT, discussed in detail in Section 5.4, is used to minimize the negative log likelihood

$$-\ln\mathcal{L} = -\sum_i^n Q_i \ln|\mathcal{M}(\vec{x}, X_i)|^2 + \frac{\mathcal{S}(s)}{N_{raw}} \sum_i^{N_{acc}} |\mathcal{M}(\vec{x}, X_i)|^2, \tag{7.6}$$

originally written in (5.27). In each $\sqrt{s}$ bin, a minimum of five iterations of the fit were run. The iteration with the best likelihood was, in all cases, used to extract the measurements.

7.1.3 Quality Checks

To ensure that the fits provided excellent descriptions of the data, a number of quality checks were performed in each $\sqrt{s}$ bin. First, the description of the ω production angle in the center-of-mass frame (θ_{CM}^ω) was examined. Figure 7.1 shows the agreement between the data and the accepted Monte Carlo weighted by the fit results in two $\sqrt{s}$ bins. The fit is able to reproduce all the features of the data in this angle.

Agreement in the production angle is not sufficient, we also must examine the ω decay angles. Figure 7.2(a) shows the decay angles in the Adair frame (see Appendix A) in various $\cos\theta_{CM}^\omega$ bins from the $\sqrt{s} = 2.005$ GeV bin. It is vitally important for the weighted accepted Monte Carlo to match these distributions. If the fit doesn't properly describe the ω decay angles, then the spin density matrix elements extracted from the fit won't be accurate. Also, the pion distributions from the ω decay affect the integrated acceptance calculation in the production angle. Thus, if the fit fails to describe the ω decay, then the differential cross sections measured for ω production will also be inaccurate. Figure 7.2(b) shows the weighted Monte Carlo decay angles from the same $\sqrt{s}$ bin as Figure 7.2(a). The agreement with the data is very good. Therefore, we conclude that the Mother of All Fits does describe the data in all relevant distributions.

(a)   (b)
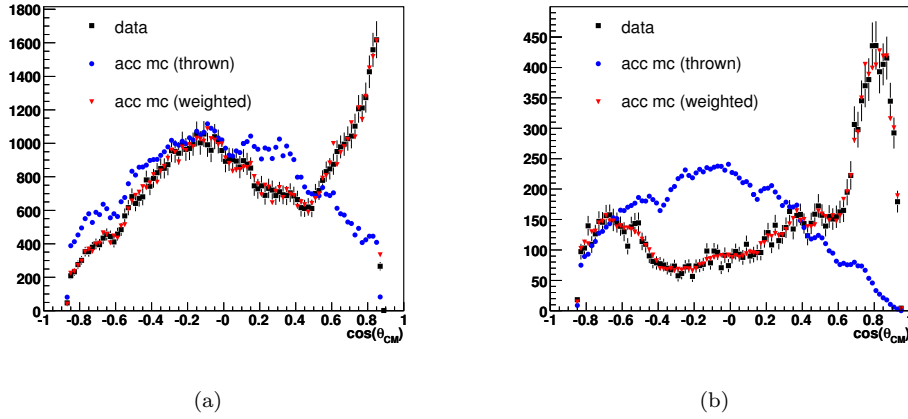
Figure 7.1: Events vs $\cos\theta^{\omega}_{CM}$: Comparisons between data (black squares), accepted phase space Monte Carlo (blue circles) and accepted Monte Carlo weighted by the results from the *Mother* fit (red triangles) for the (a) $\sqrt{s} = 2.005$ GeV bin and (b) $\sqrt{s} = 2.705$ GeV bin. Clearly, the fit results are in excellent agreement with the data.
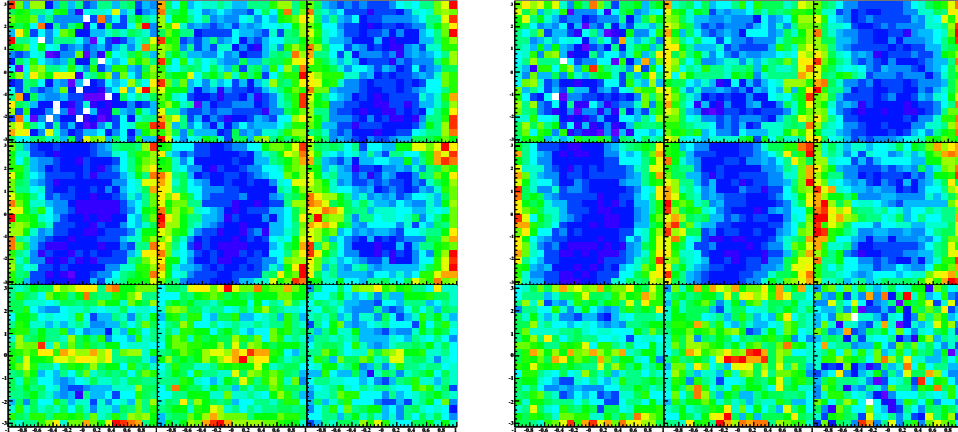
Figure 7.2: ϕ_{Adair} vs $\cos\theta_{Adair}$, from the ω decay, in $\cos\theta^{\omega}_{CM}$ bins from the $\sqrt{s} = 2.005$ GeV bin for (a) data; (b) accepted Monte Carlo weighted by the results of the *Mother* fit. In each plot, the left most bin in the top row represents the backwards direction while the right most bin in the bottom row corresponds to the forward direction ($\cos\theta^{\omega}_{CM}$ increases from top to bottom and from left to right in each row). The agreement between the data and weighted accepted Monte Carlo is excellent.

7.2 Differential Cross Sections

In particle and nuclear physics, the likelihood that an interaction between particles will occur is referred to as the *cross section*. The term originates from the classical picture of (point-like) projectiles incident on an area which includes a solid target. The probability that a single projectile will produce an interaction (assuming a homogeneous solid) is simply the ratio of the cross sectional area of the solid to the total area of the target. In this section, we will present final differential cross section results for the reaction $\gamma p \to p\omega$. The choice of reporting $d\sigma/d\cos\theta_{CM}^{\omega}$, as opposed to the invariants $d\sigma/dt$ and $d\sigma/du$, aids in studying the evolution of the results with respect to center-of-mass energy.

7.2.1 Calculation

Each differential cross section point is extracted using the equation

$$\frac{d\sigma}{d\cos\theta_{CM}^{\omega}} = \left(\frac{A_{target}}{\mathcal{F}(\sqrt{s})\rho_{target}\ell_{target}N_A}\right)\frac{\mathcal{Y}(\sqrt{s},\theta_{CM}^{\omega})}{\Delta\cos\theta_{CM}^{\omega}\eta(\sqrt{s},\theta_{CM}^{\omega})}\frac{1}{BF(\omega\to\pi^+\pi^-\pi^0)}, \tag{7.7}$$

where ρ, ℓ and A are the target density, length and atomic weight respectively, N_A is Avogadro's number, $\mathcal{F}(\sqrt{s})$ is the (corrected) number of photons in each $\sqrt{s}$ bin incident on the target, $\Delta\cos\theta_{CM}^{\omega}$ is the width of each $\cos\theta_{CM}^{\omega}$ bin (for our analysis, this quantity is always 0.1) and $BF \approx 0.891$ is the $\omega \to \pi^+\pi^-\pi^0$ branching fraction. The values used for the *target factors* are listed in Table 7.1. The detected data yield in each $(\sqrt{s}, \theta_{CM}^{\omega})$ bin is obtained as

$$\mathcal{Y}(\sqrt{s},\theta_{CM}^{\omega}) = \sum_i^N Q_i, \tag{7.8}$$

where N is the number of detected events in the bin and Q_i are the Q-values obtained using the signal extraction technique described in Section 3.9. The acceptance in each $(\sqrt{s}, \theta_{CM}^{\omega})$ bin is obtained as

$$\eta(\sqrt{s},\theta_{CM}^{\omega}) = \frac{\sum_i^{N_{acc}} |\mathcal{M}_i|^2}{\sum_j^{N_{raw}} |\mathcal{M}_j|^2}, \tag{7.9}$$

where $N_{acc}(N_{raw})$ are the number of accepted(raw) Monte Carlo events in the bin and the $|\mathcal{M}|^2$ are the event physics weights obtained from the *Mother* fit. Notice that had we used an accurate *physics generator* the $|\mathcal{M}|^2$ factors would have been used to weight the event generation. Had this been done we would have then calculated the acceptance by simply summing the number of accepted and raw events in each bin. The end result, ignoring statistical fluctuations, would have been the same.

Factor	Value	Description
ρ_{target}	0.7177 g/cm^3	Target density (see Section 4.4)
ℓ_{target}	40 cm	Target length [39]
N_A	6.022 $\times 10^{23}$	Avogadro's number
A_{target}	1.00794 $g/mole$	Target atomic weight

Table 7.1: Target factors used for all $d\sigma/d\cos\theta_{CM}^{\omega}$ measurements.

Source	Value	Description
PID	1.3%	Feldman-Cousins signal loss upper limit (Section 3.6)
Normalization	1.8%	Std. dev. of normalized yield vs run (Section 4.6)
Photon Attenuation	0.2%	R. Schumacher flux study [70]
LH2 Density	0.11%	Std. dev. of cryotarget measurement vs run (Section 4.4)
Target Length	0.125%	Reported measurement precision [39]
Acceptance	4-6%	Sector-dependent yield estimate (Section 4.3)
Branching Fraction	0.7%	Reported by PDG

Table 7.2: Systematic errors for all $d\sigma/d\cos\theta^\omega_{CM}$ measurements.

7.2.2 Errors

The statistical errors in each $(\sqrt{s}, \theta^\omega_{CM})$ bin are given as

$$\sigma^2_{\mathcal{Y}} = \mathcal{Y} + (\sum_i^N \sigma_{Q_i})^2 \tag{7.10a}$$

$$\sigma^2_{acc} = N_{acc} \tag{7.10b}$$

$$\sigma^2_{raw} = N_{raw}. \tag{7.10c}$$

The systematic errors applied (which account for possible uncertainties in the normalization and acceptance) are listed in Table 7.2. The numeric values of the errors are given in Appendix B. The plots shown below only contain the statistical errors.

7.2.3 Results

Figures 7.3–7.9 show the final results for our $d\sigma/d\cos\theta^\omega_{CM}$ measurements in each $\sqrt{s}$ bin, the numeric values are given in Appendix B. Notice that no differential cross section measurements are reported in the $\sqrt{s} = 1.955$ GeV, 2.735 GeV and 2.745 GeV bins due to the normalization issues discussed in detail in Section 4.5.3. There are many interesting features present in our measurements. In the next chapter, specifics concerning the processes which could have produced these features will be discussed. In this section, we will simply point out some of these features and provide brief comments pertaining to possible (generic) production mechanisms.

A very prominent forward peak begins to rise just above threshold and continues as the dominant feature up through our highest energies. This type of behavior in a differential cross section typically indicates a strong t-channel contribution. A backwards peak begins to emerge around $\sqrt{s} \sim 2.2$ GeV whose prominence increases as the energy increases (though it is always at least one order of magnitude smaller than the forward peak). This type of behavior typically indicates a strong u-channel contribution.

In the transverse direction there exists evidence for possible resonance contributions. Near threshold, the transverse cross section is mostly flat. Around $\sqrt{s} \sim 1.9$ GeV it begins to develop a *humped* shape, which is indicative of the presence of a resonance with $J > 1/2$. Near $\sqrt{s} \sim 2.1$ GeV, the cross section begins to develop two dips (or three humps, whichever you prefer). This is typical of a $J > 3/2$ resonance contribution. In Chapter 8 a partial wave analysis will be performed to study the production mechanisms. We draw attention to these interesting features in the measurements here to provide motivation for our PWA analysis.
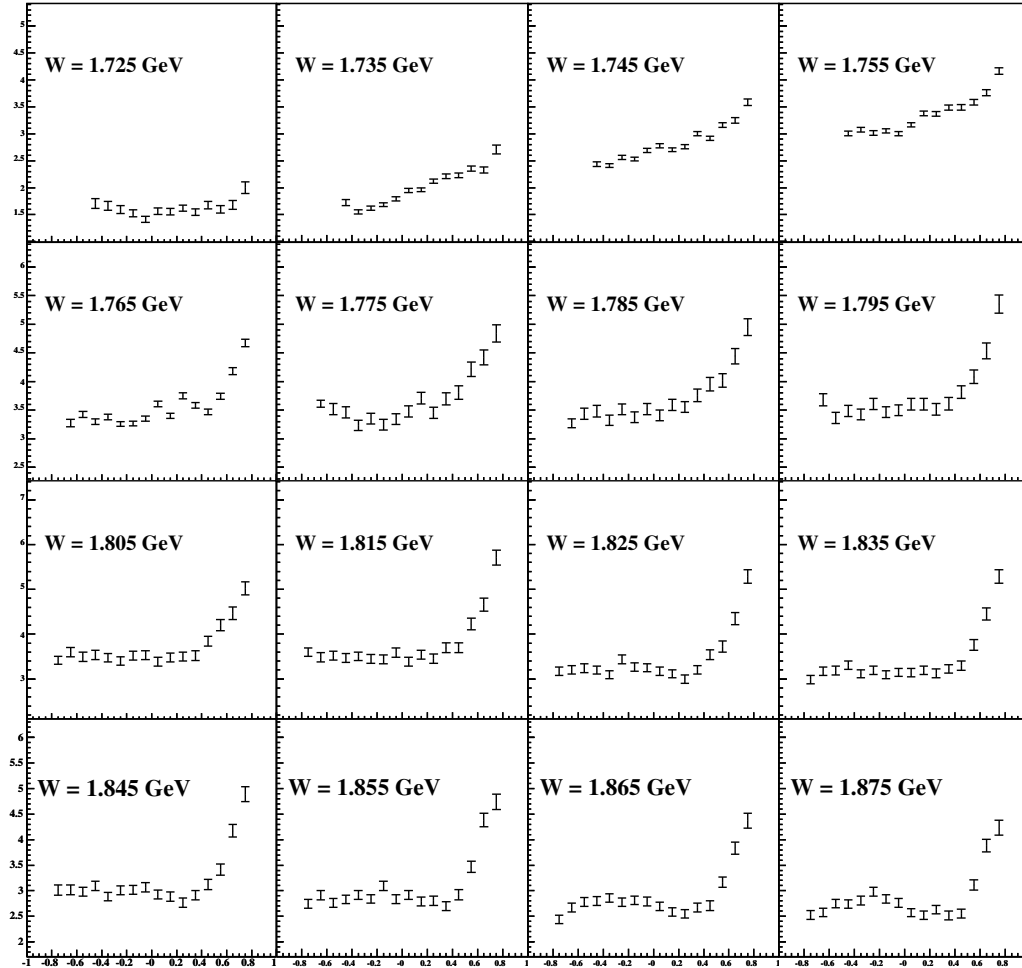
Figure 7.3: $\frac{d\sigma}{d\cos\theta^\omega_{CM}}$ (μb) vs $\cos\theta^\omega_{CM}$: Differential cross section results for bins in the energy range 1.72 GeV $\leq \sqrt{s} < 1.88$ GeV. The centroid of each 10 MeV wide bin is printed on the plot. The error bars do not include systematic uncertainties, these are discussed in the text.
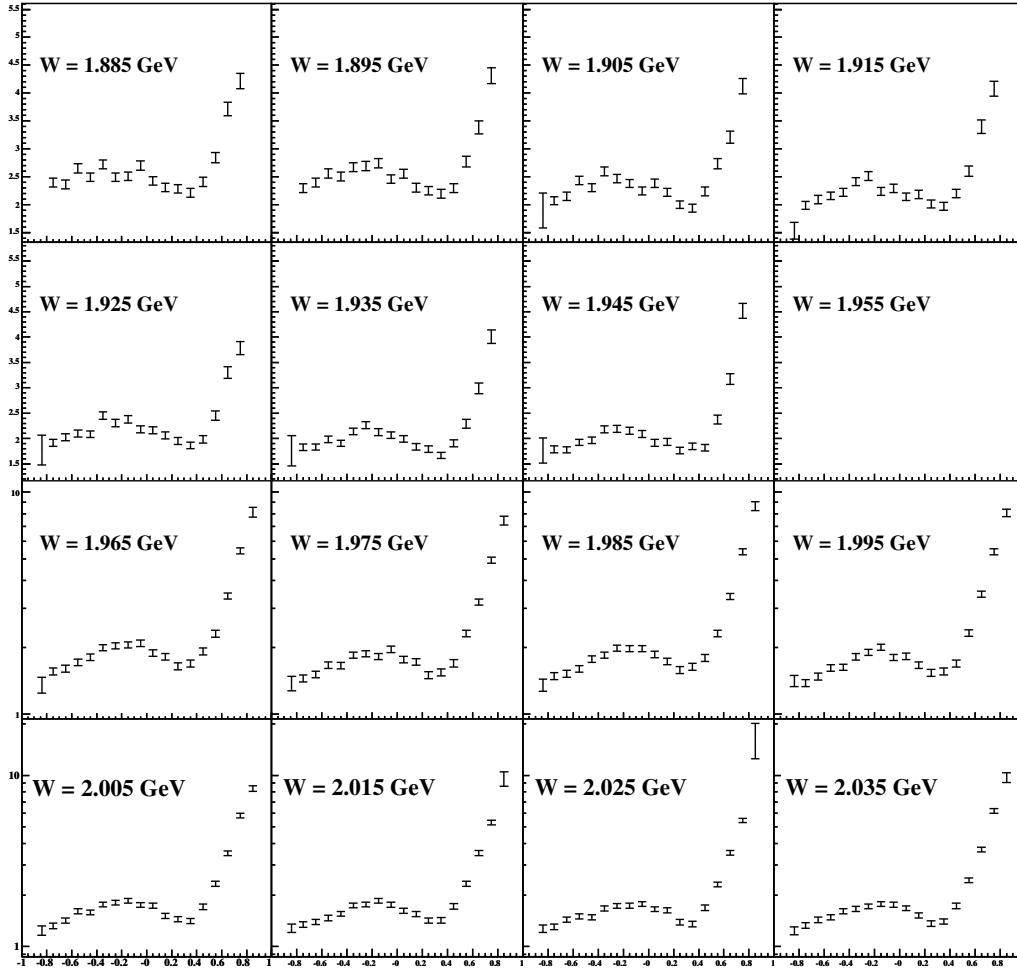
Figure 7.4: $\frac{d\sigma}{d\cos\theta_{CM}^{\omega}}$ (μb) vs $\cos\theta_{CM}^{\omega}$: Differential cross section results for bins in the energy range 1.88 GeV $\leq \sqrt{s} < 2.04$ GeV. The centroid of each 10 MeV wide bin is printed on the plot. The error bars do not include systematic uncertainties, these are discussed in the text.
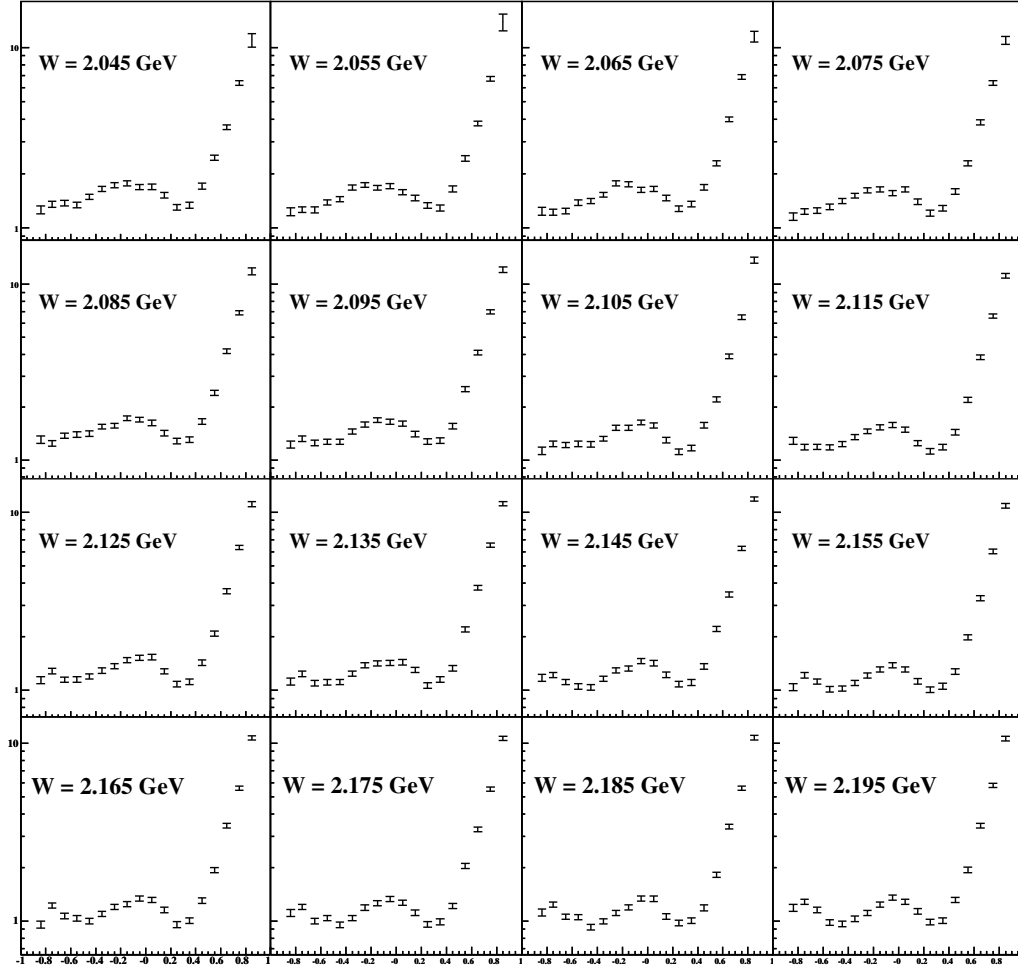
Figure 7.5: $\frac{d\sigma}{d\cos\theta_{CM}^{\omega}}$ (μb) vs $\cos\theta_{CM}^{\omega}$: Differential cross section results for bins in the energy range 2.04 GeV $\leq \sqrt{s} <$ 2.2 GeV. The centroid of each 10 MeV wide bin is printed on the plot. The error bars do not include systematic uncertainties, these are discussed in the text.
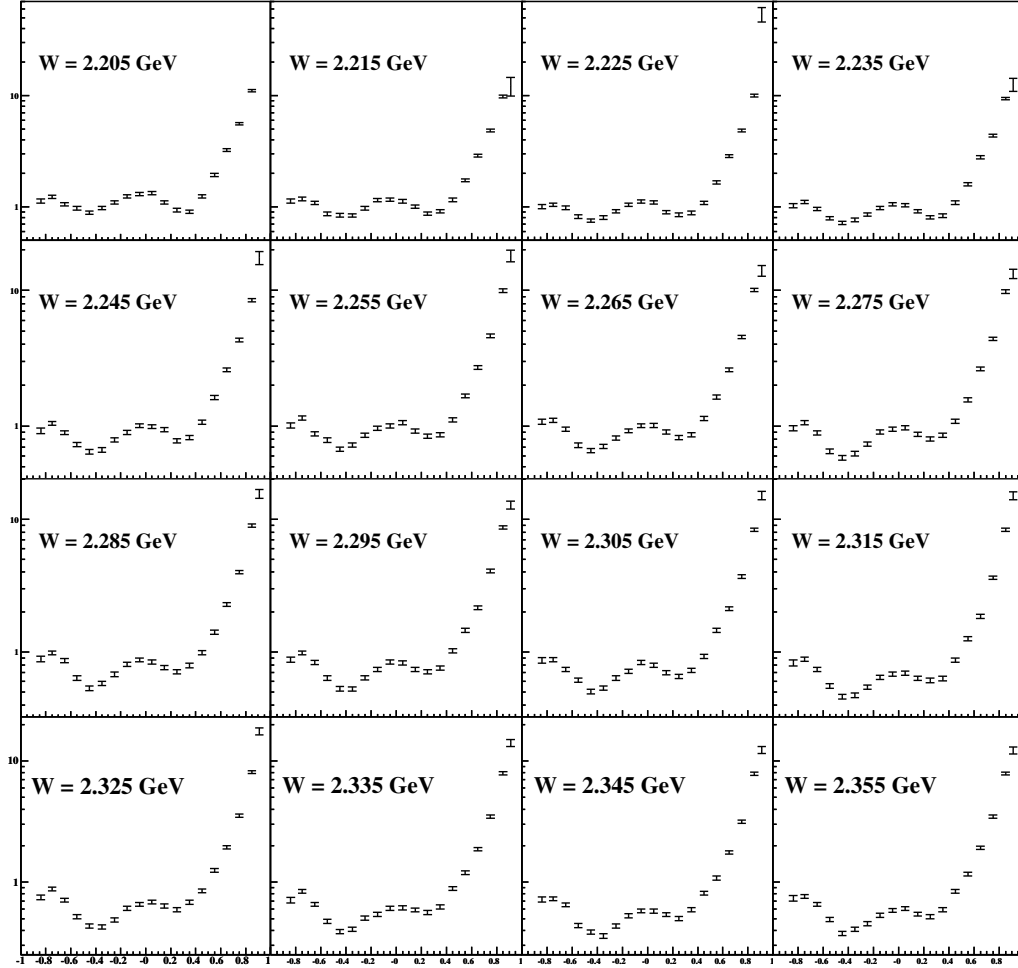
Figure 7.6: $\frac{d\sigma}{d\cos\theta^\omega_{CM}}$ (μb) vs $\cos\theta^\omega_{CM}$: Differential cross section results for bins in the energy range 2.2 GeV $\leq \sqrt{s} < 2.36$ GeV. The centroid of each 10 MeV wide bin is printed on the plot. The error bars do not include systematic uncertainties, these are discussed in the text.
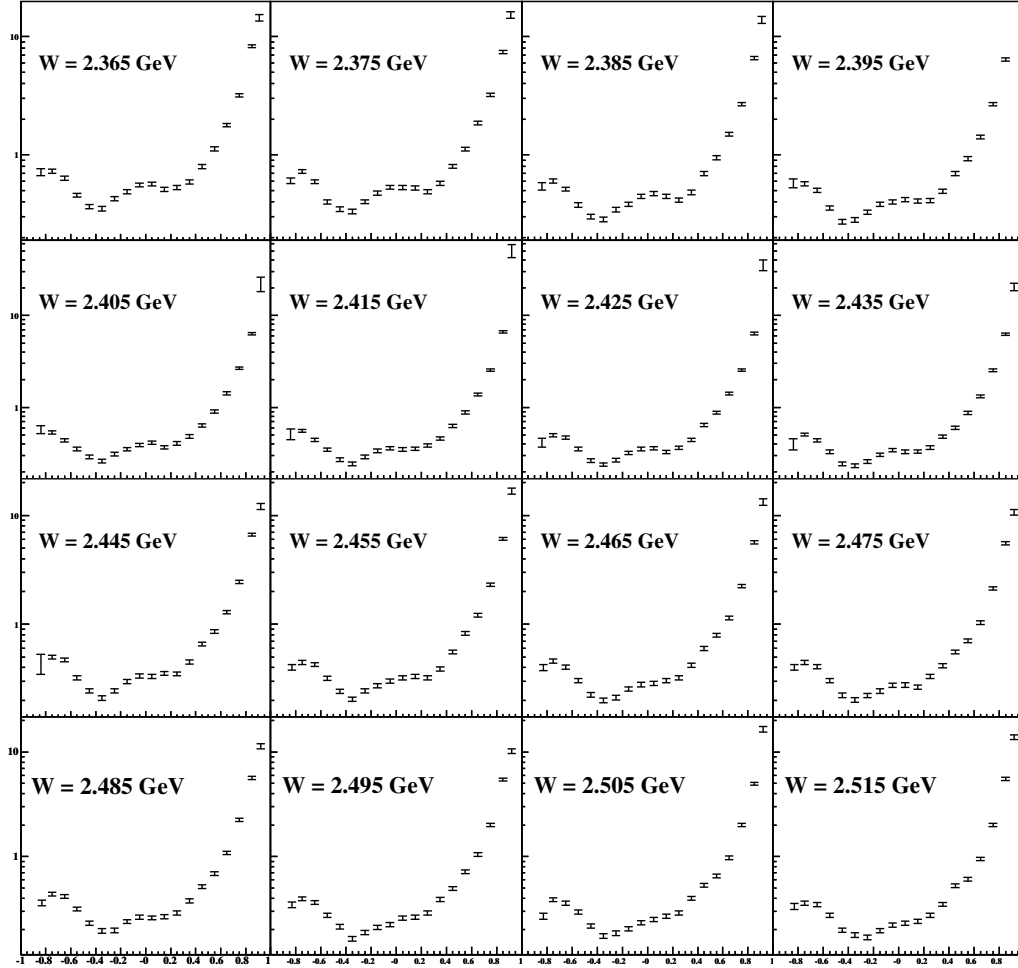
Figure 7.7: $\frac{d\sigma}{d\cos\theta^\omega_{CM}}$ (μb) vs $\cos\theta^\omega_{CM}$: Differential cross section results for bins in the energy range 2.36 GeV $\leq \sqrt{s} < 2.52$ GeV. The centroid of each 10 MeV wide bin is printed on the plot. The error bars do not include systematic uncertainties, these are discussed in the text.
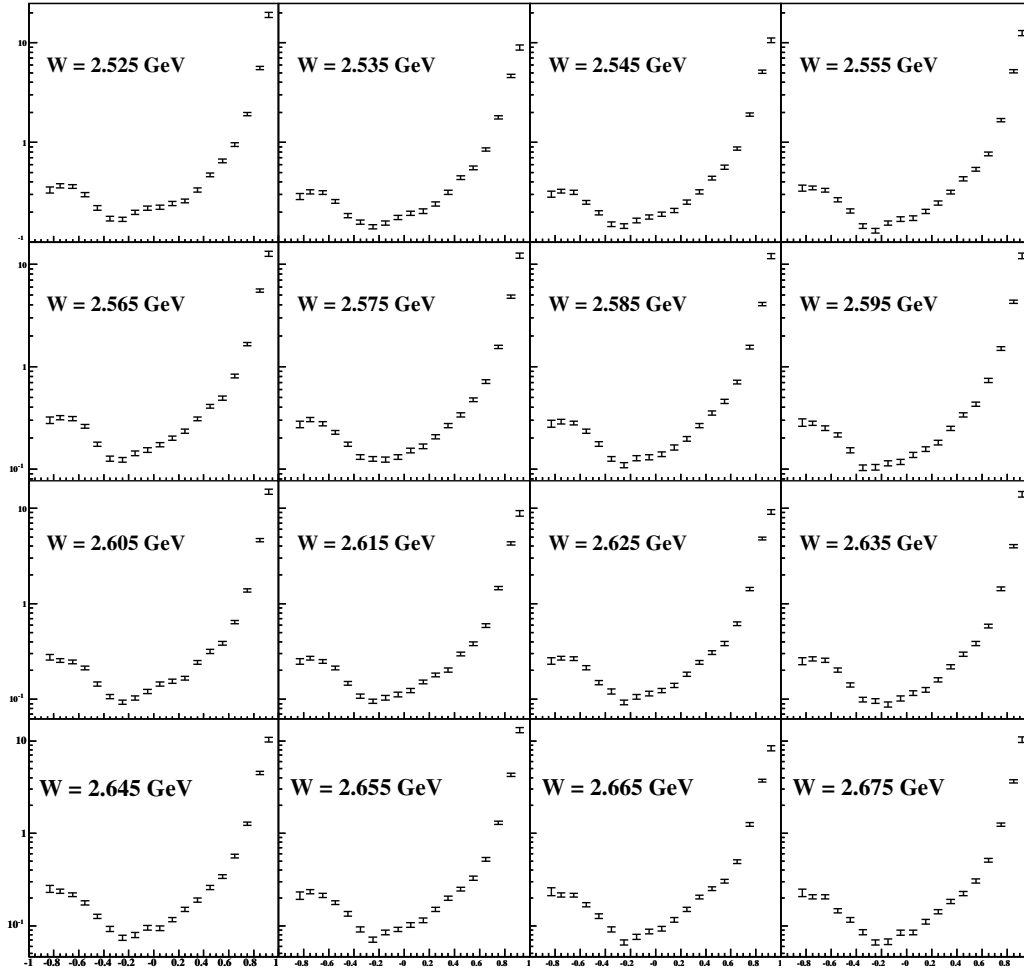
Figure 7.8: $\frac{d\sigma}{d\cos\theta^{\omega}_{CM}}$ (μb) vs $\cos\theta^{\omega}_{CM}$: Differential cross section results for bins in the energy range $2.52\,\text{GeV} \leq \sqrt{s} < 2.68\,\text{GeV}$. The centroid of each 10 MeV wide bin is printed on the plot. The error bars do not include systematic uncertainties, these are discussed in the text.
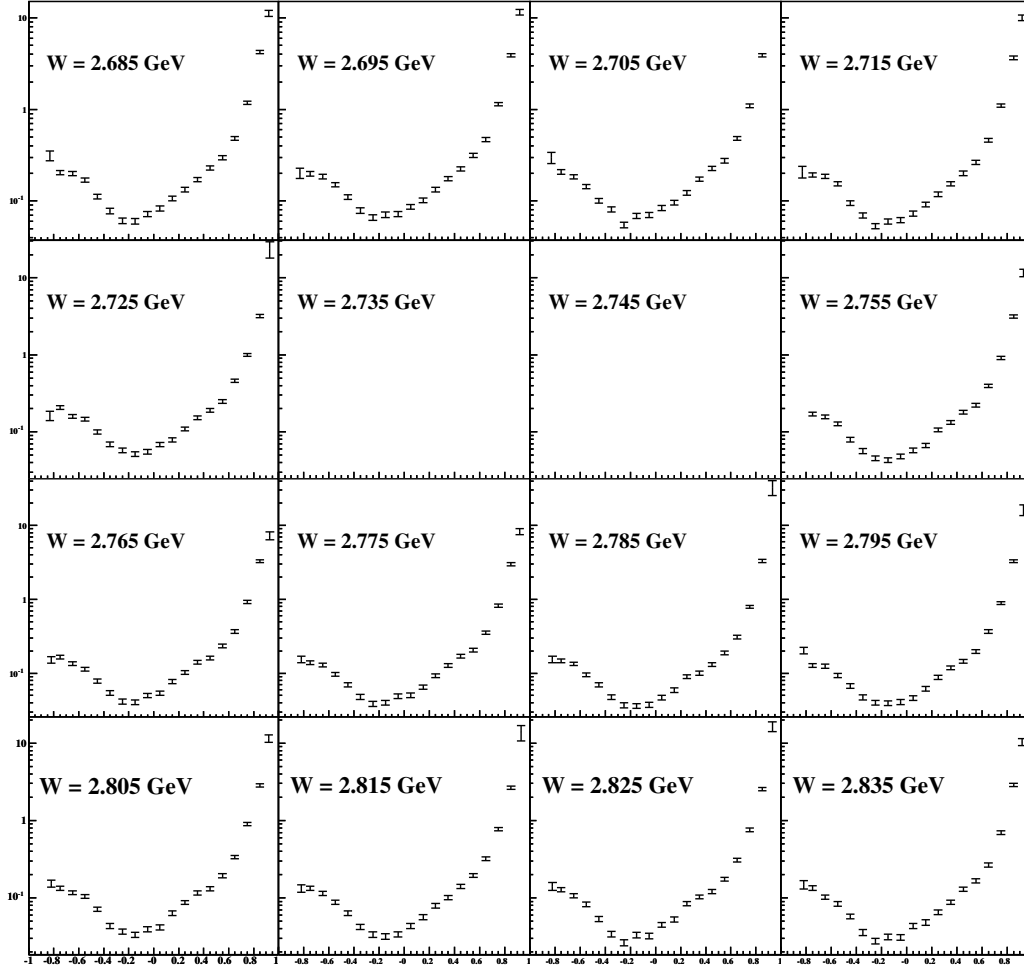
Figure 7.9: $\frac{d\sigma}{d\cos\theta_{CM}^{\omega}}$ (μb) vs $\cos\theta_{CM}^{\omega}$: Differential cross section results for bins in the energy range 2.68 GeV $\leq \sqrt{s} < 2.84$ GeV. The centroid of each 10 MeV wide bin is printed on the plot. The error bars do not include systematic uncertainties, these are discussed in the text.

7.3   Spin Density Matrix Elements

The decay distribution of the ω yields information about its polarization — it is a *self-analyzing* particle. This polarization information can be used to provide insight into the nature of the production amplitudes. Since the ω is a spin-1 particle, its spin density matrix has nine complex elements; however, parity, hermiticity and normalization reduce the number of independent elements (for an unpolarized beam) to four real quantities (of which, three are measurable). Traditionally, these are chosen to be ρ^0_{00}, ρ^0_{1-1} and $Re(\rho^0_{10})$. Since our results cover a large range of energies and angles, we chose the quantization axis to be the photon direction in the overall CM frame — known as the *Adair* frame (see Appendix A).

7.3.1   Calculation

Using the results of the *Mother* fit, it is a straightforward process to project out the spin density matrix elements:

$$\rho^0_{MM'} = \frac{1}{N} \sum_{m_\gamma, m_i, m_f} A^{m_\gamma, m_i, m_f, M}_{\gamma p \to p\omega} A^{*m_\gamma, m_i, m_f, M'}_{\gamma p \to p\omega}, \tag{7.11}$$

where the M, M' refer to the spin projection of the ω (to the $\hat{k}$-axis in the CM frame) and

$$N = \sum_{m_\gamma, m_i, m_f} \sum_M |A^{m_\gamma, m_i, m_f, M}_{\gamma p \to p\omega}|^2, \tag{7.12}$$

is a normalization factor. Measurement of the matrix elements traditionally denoted by $\rho^1_{MM'}, \rho^2_{MM'}$ and $\rho^3_{MM'}$ requires a polarized beam (which was not used during the $g11a$ run period). The spin density matrix elements ($\rho^0_{MM'}$) can be projected out of the *Mother* fit at any $\cos\theta^\omega_{CM}$; however, they only constitute a measurement at angles where we have data. Thus, for this reason (and for convenience) we have chosen to project out these observables at the centroids of the $(\sqrt{s}, \theta^\omega_{CM})$ bins used for the differential cross section measurements.

7.3.2   Statistical Error Estimation

For the near threshold bins, $\sqrt{s} < 1.76$ GeV, the covariance matrix returned by MINUIT from the *Mother* fit was used to obtain the statistical errors on $\rho^0_{MM'}$; however, in some energy bins, this error calculation yielded unphysically large results. The excess number of parameters occasionally led to rather large interferences between waves, causing their contributions to the total amplitude to (virtually) cancel out. In some cases, the MINUIT covariance matrix did not adequately reflect these correlations which resulted in an inaccurate error calculation.

Excluding the near threshold region, the physics changes very little between a 10 MeV wide $\sqrt{s}$ bin and its nearest neighbors. Thus, we can estimate the statistical error on $\rho^0_{MM'}(\sqrt{s}, \theta^\omega_{CM})$ by comparing it to $\rho^0_{MM'}(\sqrt{s} \pm 10MeV, \theta^\omega_{CM})$:

$$\sigma^2(\sqrt{s}, \theta^\omega_{CM}) = \frac{1}{2} \sum_{i=-1}^{1} \left(\rho^0_{MM'}(\sqrt{s} + i \cdot 10MeV, \theta^\omega_{CM}) - \bar{\rho}^0_{MM'}(\sqrt{s}, \theta^\omega_{CM}) \right)^2, \tag{7.13}$$

where $\bar{\rho}^0_{MM'}(\sqrt{s}, \theta^\omega_{CM})$ is the mean value of the three measurements. A smoothing algorithm was then applied to provide a more accurate error estimation. This simply involved setting the statistical error on $\rho^0_{MM'}(\sqrt{s}, \theta^\omega_{CM})$ to be the mean value of the estimated errors at $(\sqrt{s} - 10MeV, \theta^\omega_{CM})$, $(\sqrt{s}, \theta^\omega_{CM})$ and $(\sqrt{s}+10MeV, \theta^\omega_{CM})$. At points where the MINUIT error calculations were reasonable, they agreed very well with our results. Also, the statistical errors obtained using Schilling's method (see Figure 7.11) are in agreement with these calculations.
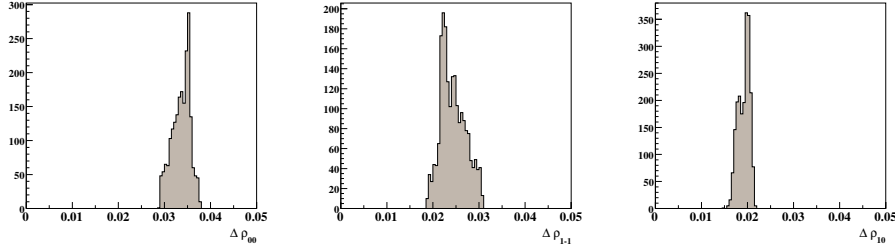
Figure 7.10: Results from the toy model study used to estimate systematic errors for $\rho^0_{MM'}$ — see text for details. (a) $\Delta\rho^0_{00}$ (b) $\Delta\rho^0_{1-1}$ (c) $\Delta Re(\rho^0_{10})$.

7.3.3 Systematic Error Estimation

There is no standard (or rigorous) method for calculating systematic errors on $\rho^0_{MM'}$. We chose to first estimate the maximum possible effect of our acceptance uncertainty (an overestimate of the errors) by distorting the normalized decay distributions W, for each $\rho^0_{MM'}(\sqrt{s}, \theta^\omega_{CM})$ measurement at each $(\theta_{Adair}, \phi_{Adair})$ by

$$\Delta W(\theta_{Adair}, \phi_{Adair}) = \bar{\sigma}_{acc} \frac{\partial W}{\partial \rho^0_{MM'}}(\theta_{Adair}, \phi_{Adair}), \tag{7.14}$$

where $\bar{\sigma}_{acc} = 0.05$ is the (approximate) mean acceptance uncertainty. The distorted distributions were then refit using (7.16) to obtain $\Delta\rho^0_{MM'}$. The results of this study are shown in Figure 7.10. Since $\Delta\rho^0_{MM'}$ are overestimates of the errors, the *ad hoc* choice of (approximately) half their mean values should provide a reasonably conservative estimate for the systematic errors. Thus, we set

$$\sigma_{00} = 0.0175 \tag{7.15a}$$
$$\sigma_{1-1} = 0.0125 \tag{7.15b}$$
$$\sigma_{10} = 0.01. \tag{7.15c}$$

7.3.4 Comparison to Schilling's Method

An important systematic check of our method of extracting the spin density matrix elements, using a nearly complete basis of partial waves, involves comparing our results to those obtained using a more *traditional* method. Previous results (the few that exist) were obtained by binning the data in production angle (or t) and then fitting the data in each bin to Schilling's equation [71]

$$W(\theta_{Adair}, \phi_{Adair}) = \frac{3}{4\pi} \left(\frac{1}{2}(1 - \rho^0_{00}) + \frac{1}{2}(3\rho^0_{00} - 1)\cos^2\theta_{Adair} - \rho^0_{1-1}\sin^2\theta_{Adair}\cos 2\phi_{Adair} \right.$$
$$\left. - \sqrt{2}Re\rho^0_{10}\sin 2\theta_{Adair}\cos\phi_{Adair} \right), \tag{7.16}$$

to extract the spin density matrix elements. Though the methods may be different, both use the properties of a spin-1 particle to extract the polarization information. Thus, both methods should yield the same results. Figure 7.11 shows the comparison of the spin density matrix elements obtained using partial waves (open markers) *vs* Schilling's method (filled markers) in four $\sqrt{s}$ bins evenly distributed over our energy range. The agreement is excellent. From this study, we can conclude that our technique for extracting the polarization information is working properly.
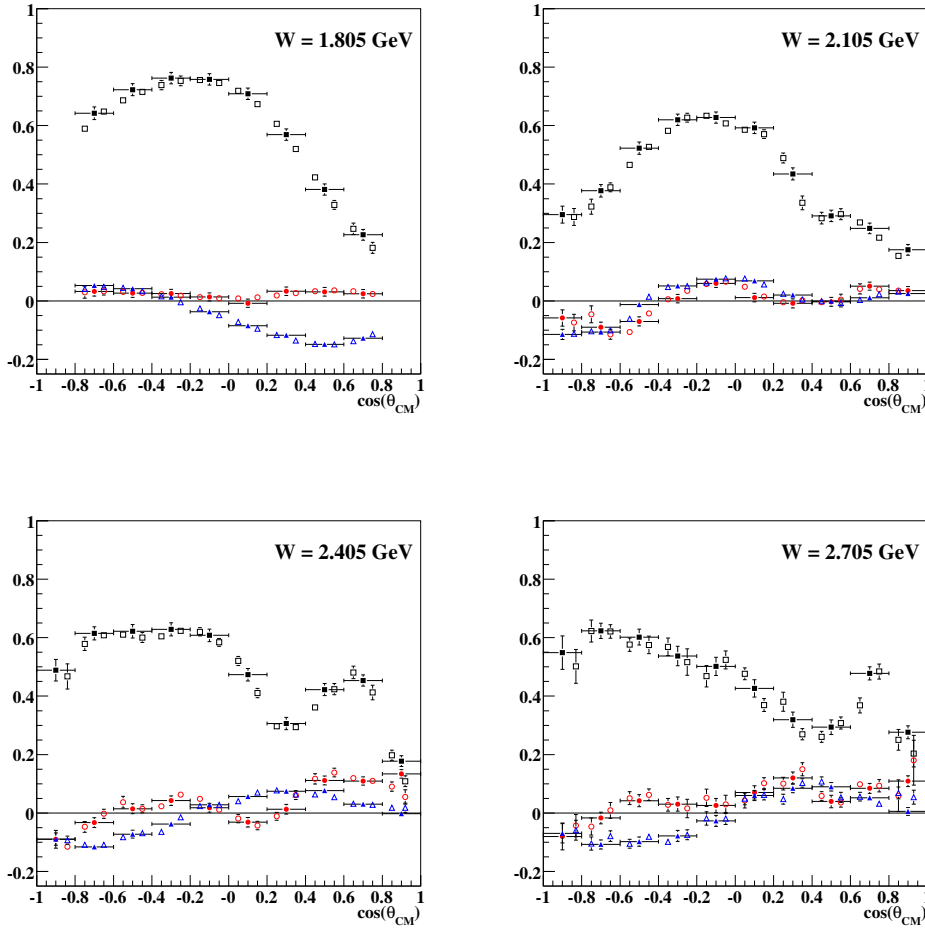
Figure 7.11: Spin density matrix elements, in the Adair frame, vs $\cos\theta^{\omega}_{CM}$: The black squares are ρ^0_{00} obtained from (filled) Schilling's method and from (open) the PWA. The red circles are ρ^0_{1-1} obtained from (filled) Schilling's method and from (open) the PWA. The blue triangles are $Re(\rho^0_{10})$ obtained from (filled) Schilling's method and from (open) the PWA. The agreement is excellent. The error bars on the points obtained using Schilling's method are purely statistical, obtained using the covariance matrix from each independent fit. The agreement between the statistical error bars obtained using Schilling's method and those of Section 7.3.2 provides added confidence in our statistical error calculations.

7.3.5 Results

Figures 7.12 – 7.18 show the final results for our spin density matrix element measurements in each $\sqrt{s}$ bin. Recall that we did not report differential cross section results in the $\sqrt{s} = 1.955$ GeV, 2.735 GeV and 2.745 GeV bins due to *normalization issues*. Since normalization information does not factor into the extraction of $\rho^0_{MM'}$, there is no reason to exclude these bins from the spin density matrix measurements. The quality of the results is very exciting and should provide stringent constraints on future theoretical work on $\gamma p \to p\omega$. As in the previous results section, here we will draw attention to some of the interesting features present in our measurements; however, the detailed studies of the production mechanisms will be carried out in the next chapter.

Near threshold and at forward angles, each of the $\rho^0_{MM'}$ elements shows interesting behavior. It is in this region where the differential cross section develops a strong forward peak, which is indicative of t-channel contributions. The diagonal ρ^0_{00} element decreases sharply as the energy increases, or equivalently, as the forward peak increases in significance. This is typical of spin-0 exchange in t-channel where the ω is forced to carry all of the photon's spin at forward angles. In this same region, the off-diagonal element ρ^0_{1-1} ($Re(\rho^0_{10})$) increases(decreases) as the energy increases. This detailed polarization information will be crucial in determining the spin and parity of the exchanged particle(s) in the t-channel production mechanism.

In the region near threshold and away from the forward angles, the off-diagonal spin density matrix elements are very small while ρ^0_{00} is quite large. It is also interesting to note that, in this region, ρ^0_{00} has a *humped* shape that peaks near $\cos\theta^\omega_{CM} = 0$ at ~ 0.8. Around $\sqrt{s} \sim 1.9$ GeV, the off-diagonal elements begin to deviate from zero and ρ^0_{00} begins to decrease slightly (while maintaining approximately the same shape). For the next ~ 200 MeV, this trend continues with the off-diagonal elements also developing a humped shape to them. Around $\sqrt{s} \sim 2.1$ GeV, the off-diagonal elements begin to flatten out again. The diagonal ρ^0_{00} begins to increase at backwards angles. Over the next 100 MeV, the off-diagonal elements begin to separate near $\cos\theta^\omega_{CM} \sim 0.2$. This *separation* persists until $\sqrt{s} \sim 2.4$ GeV. This angular region is far enough removed from the forward peak that this behavior could be caused by resonance production. Previous analyses [30, 28] which attempted to extract resonance contributions in this energy range did not have access to the polarization information. We will show in the next chapter that including these measurements can drastically affect the extracted resonance contributions.

In this same energy range, starting near $\sqrt{s} \sim 2.1$ GeV, a dip in ρ^0_{00} appears at $\cos\theta^\omega_{CM} \sim 0.4$ which continues to increase in prominence until about $\sqrt{s} \sim 2.5$ GeV. Above this energy, its significance slowly decreases; however, it is still present at our highest energies. This dip is located near where the forward peak (which is typically associated with t-channel contributions) has decreased in significance such that it is approximately the same size as the the cross section in the region $0 < \cos\theta^\omega_{CM} < 0.4$. Thus, it is possible that this dip results from interference between the t-channel and (currently undetermined) larger angle production mechanisms. Understanding this feature of the polarization measurements should lead to greatly improved t-channel models.

Now that we have discussed the forward angle measurements at higher energies, we will turn our attention to the backwards direction. Recall that the differential cross section possessed a peak at these angles which is typically indicative of strong u-channel contributions. By $\sqrt{s} \sim 2.4$ GeV, ρ^0_{00} has become virtually flat for $\cos\theta^\omega_{CM} < 0.4$. It remains this way until $\sqrt{s} \sim 2.7$ GeV. Above this energy, it develops a slope, decreasing as $\cos\theta^\omega_{CM}$ increases. Also near $\sqrt{s} \sim 2.4$ GeV, the off-diagonal elements begin to separate in the backwards direction, with $\rho^0_{1-1} > Re(\rho^0_{10})$. This continues over the rest of our energy range. There are no previous polarization measurements at these angles. Our results will provide the first *real* constraint on u-channel models.
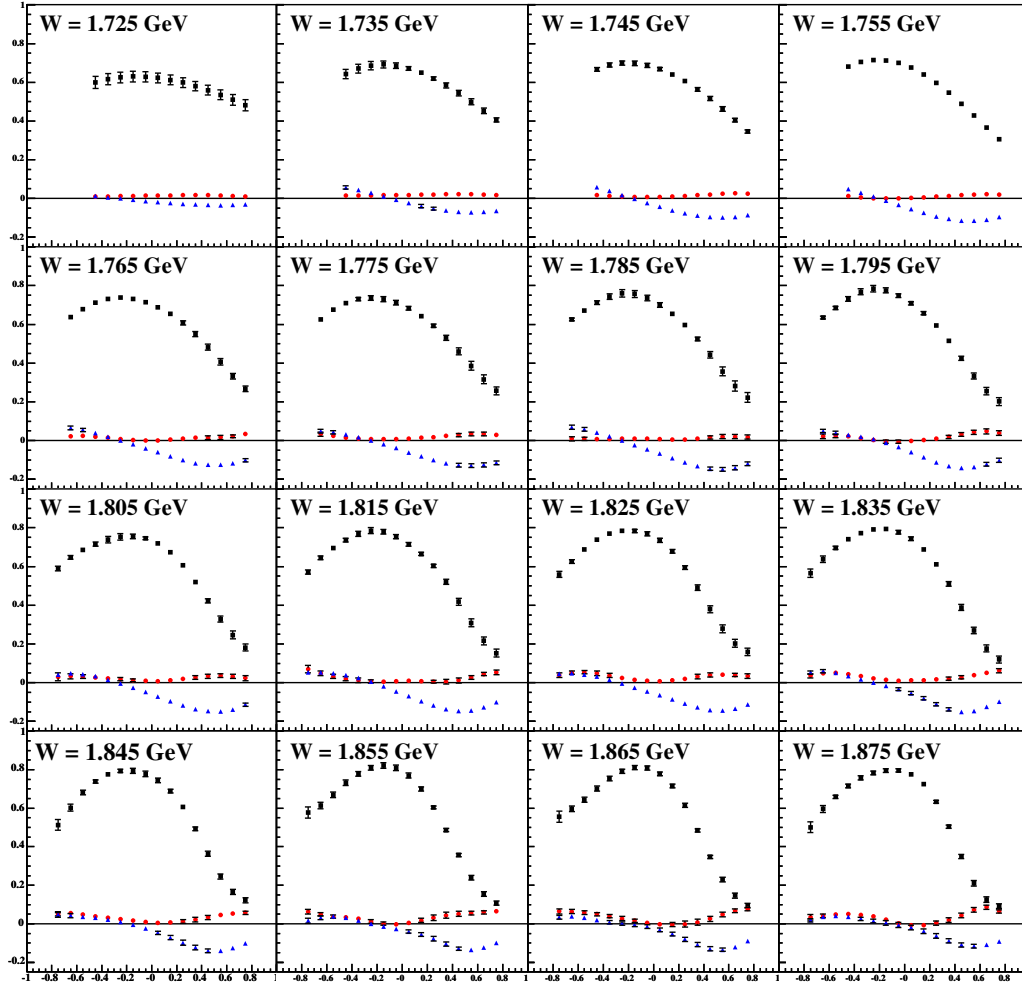
Figure 7.12: $\rho^0_{MM'}$ vs $\cos\theta^\omega_{CM}$: Spin density matrix element measurements, in the Adair frame, for bins in the range 1.72 GeV $\leq \sqrt{s} <$ 1.88 GeV. The black squares are ρ^0_{00}, the red circles are ρ^0_{1-1} and the blue triangles are $Re(\rho^0_{10})$. The centroid of each 10 MeV wide bin is printed on the plot. The error bars do not include systematic uncertainties, these are discussed in the text.
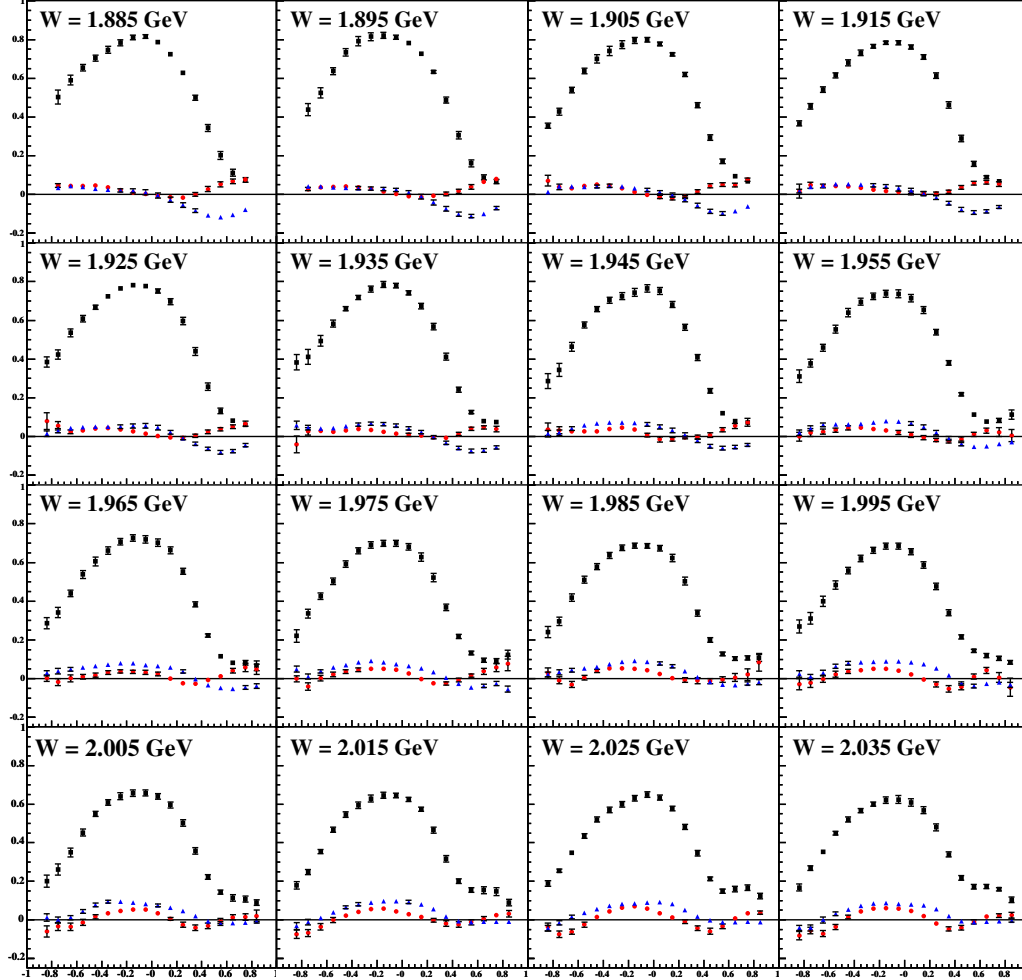
Figure 7.13: $\rho^0_{MM'}$ vs $\cos\theta^\omega_{CM}$: Spin density matrix element measurements, in the Adair frame, for bins in the range 1.88 GeV $\leq \sqrt{s} <$ 2.04 GeV. The black squares are ρ^0_{00}, the red circles are ρ^0_{1-1} and the blue triangles are $Re(\rho^0_{10})$. The centroid of each 10 MeV wide bin is printed on the plot. The error bars do not include systematic uncertainties, these are discussed in the text.
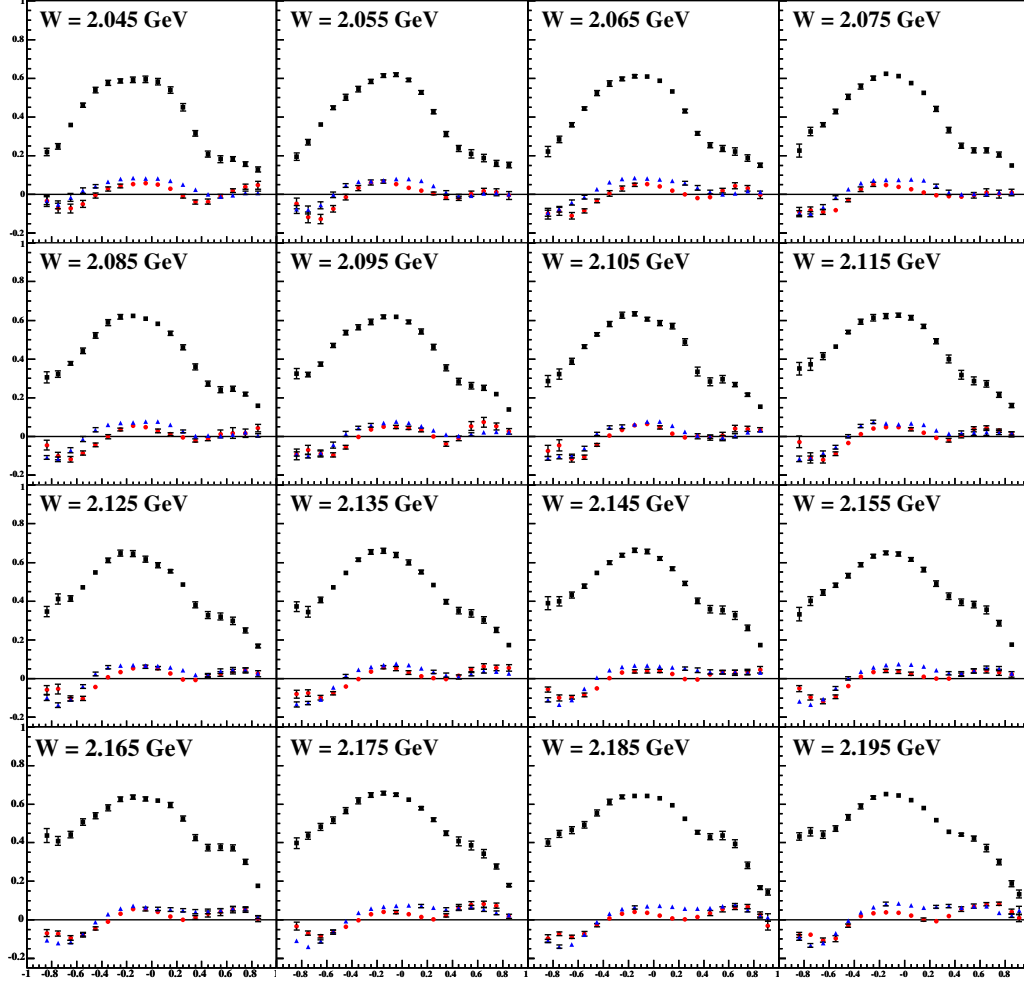
Figure 7.14: $\rho^0_{MM'}$ vs $\cos\theta^\omega_{CM}$: Spin density matrix element measurements, in the Adair frame, for bins in the range 2.04 GeV $\leq \sqrt{s} <$ 2.2 GeV. The black squares are ρ^0_{00}, the red circles are ρ^0_{1-1} and the blue triangles are $Re(\rho^0_{10})$. The centroid of each 10 MeV wide bin is printed on the plot. The error bars do not include systematic uncertainties, these are discussed in the text.
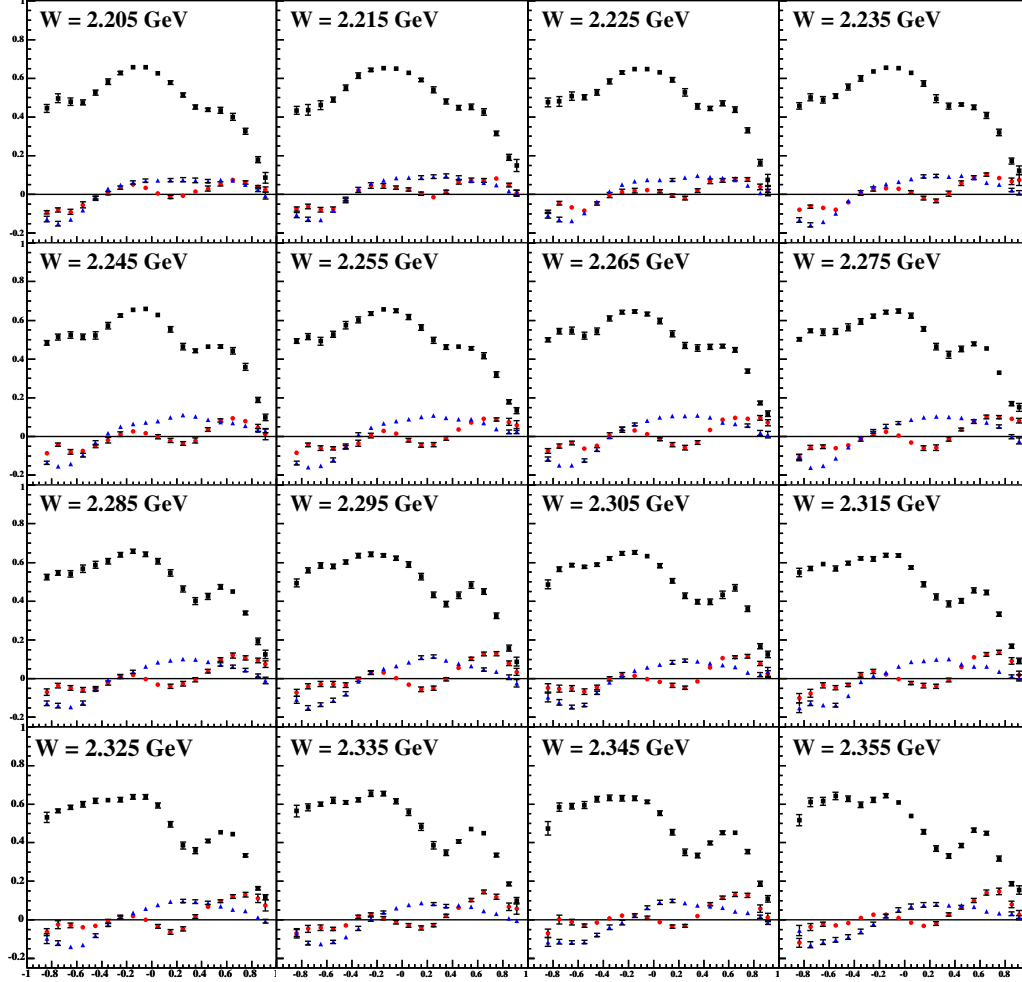
Figure 7.15: $\rho^0_{MM'}$ vs $\cos\theta^\omega_{CM}$: Spin density matrix element measurements, in the Adair frame, for bins in the range 2.2 GeV $\leq \sqrt{s} <$ 2.36 GeV. The black squares are ρ^0_{00}, the red circles are ρ^0_{1-1} and the blue triangles are $Re(\rho^0_{10})$. The centroid of each 10 MeV wide bin is printed on the plot. The error bars do not include systematic uncertainties, these are discussed in the text.
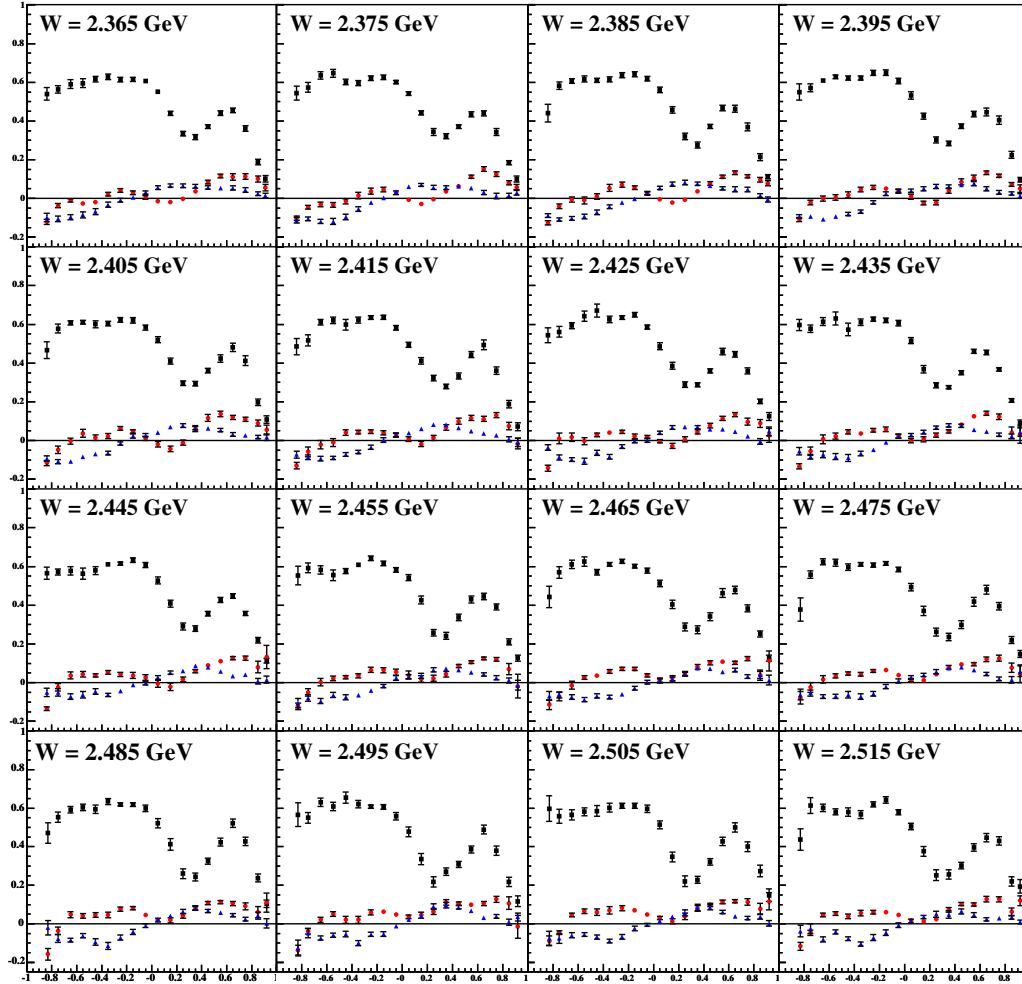
Figure 7.16: $\rho^0_{MM'}$ vs $\cos\theta^\omega_{CM}$: Spin density matrix element measurements, in the Adair frame, for bins in the range 2.36 GeV $\leq \sqrt{s} <$ 2.52 GeV. The black squares are ρ^0_{00}, the red circles are ρ^0_{1-1} and the blue triangles are $Re(\rho^0_{10})$. The centroid of each 10 MeV wide bin is printed on the plot. The error bars do not include systematic uncertainties, these are discussed in the text.
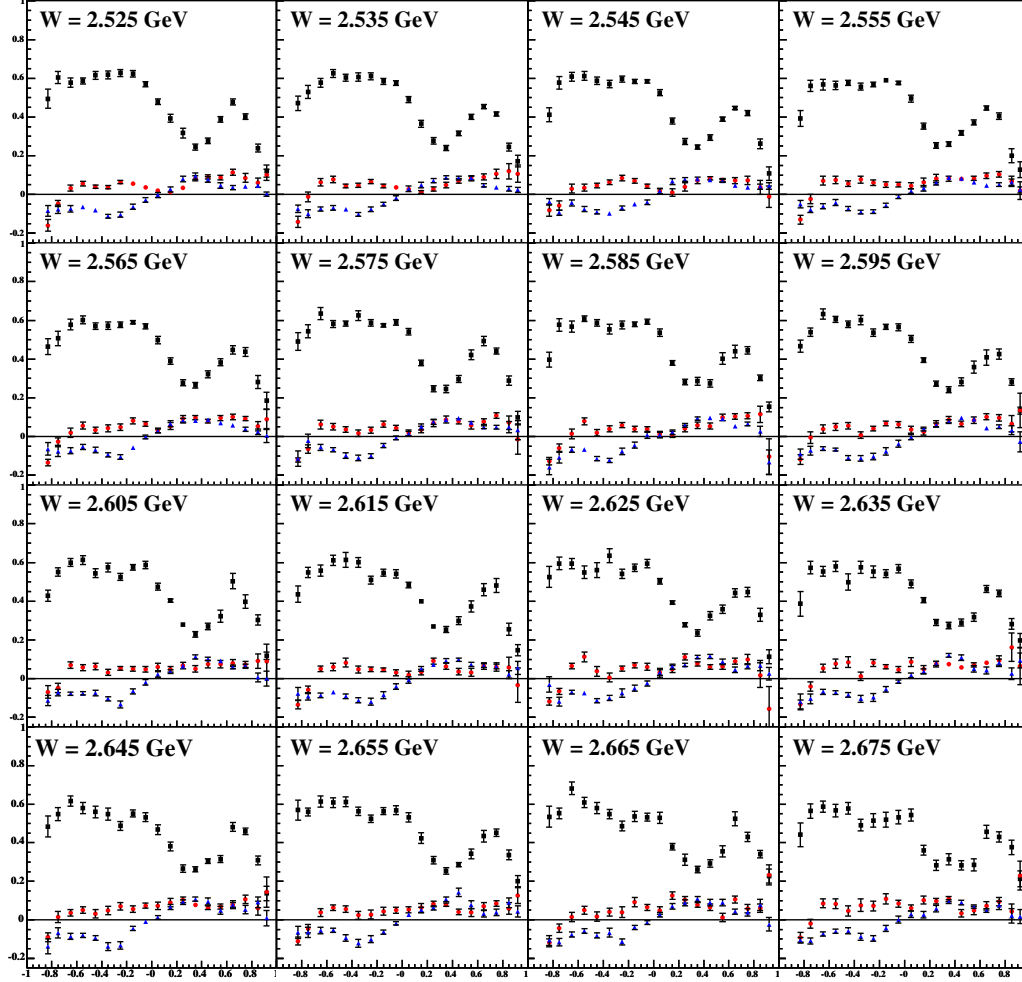
Figure 7.17: $\rho^0_{MM'}$ vs $\cos\theta^\omega_{CM}$: Spin density matrix element measurements, in the Adair frame, for bins in the range 2.52 GeV $\leq \sqrt{s} <$ 2.68 GeV. The black squares are ρ^0_{00}, the red circles are ρ^0_{1-1} and the blue triangles are $Re(\rho^0_{10})$. The centroid of each 10 MeV wide bin is printed on the plot. The error bars do not include systematic uncertainties, these are discussed in the text.
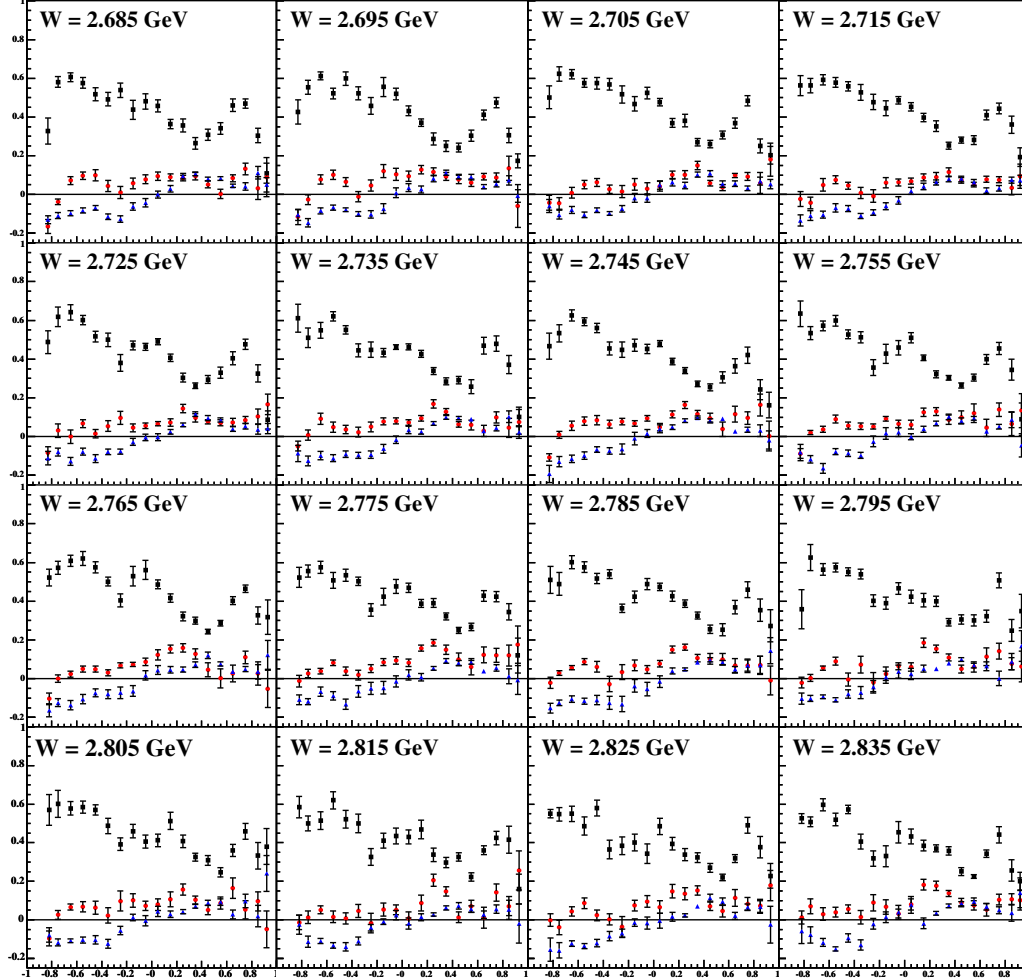
Figure 7.18: $\rho^0_{MM'}$ vs $\cos\theta^\omega_{CM}$: Spin density matrix element measurements, in the Adair frame, for bins in the range 2.68 GeV $\leq \sqrt{s} <$ 2.84 GeV. The black squares are ρ^0_{00}, the red circles are ρ^0_{1-1} and the blue triangles are $Re(\rho^0_{10})$. The centroid of each 10 MeV wide bin is printed on the plot. The error bars do not include systematic uncertainties, these are discussed in the text.

7.4 Comparison to Previous Measurements

In the previous two sections, we presented differential cross section and ω polarization measurements for the reaction $\gamma p \to p\omega$ in the energy range 1.72 GeV $< \sqrt{s} <$ 2.84 GeV. As an important systematic check, we must now compare our results to those obtained by previous experiments. Published differential cross section results exist which overlap most of the measurements made in this work; however, spin density matrix element results are scarce. There are only eight published points below $\sqrt{s} = 2.4$ GeV. Above this energy, the only previous measurements were made at very forward angles. This section presents a detailed comparison of our work with all previous published results which overlap our energy range. In some cases, the number of our energy bins which overlap the previous results make labeling difficult. Therefore, we have adopted a *deep sea* color scheme for our markers; lowest energy results are light blue, becoming darker as the energy increases.

7.4.1 CLAS 2003

In January 2003, the CLAS collaboration (Battaglieri et al [22]) published differential cross section measurements for $\gamma p \to p\omega$ in the energy range 2.624 GeV $\leq \sqrt{s} \leq$ 2.87 GeV. Figure 7.19 shows the comparison between the CLAS 2003 results and our (overlapping) results. Overall, the agreement is fair. It is important to note that the CLAS 2003 result did not report bin centroids (only ranges). Thus, care must be taken when comparing our results to theirs in the forward direction, where the cross section varies rapidly with production angle. In this region, the centroids are most likely located in the forward half of their bins.

There are a few areas where discrepancies are noticeable. Our measurements are systematically higher in the backwards direction by $\sim 25 - 50\%$. As $\sqrt{s}$ increases, it also appears as though our results become systematically lower in the $0 \leq \cos\theta_{CM}^{\omega} \leq 0.5$ region. Even though both of these results were obtained using the CLAS detector, there are some important differences which could account for these discrepancies. The previous CLAS analysis was performed using data from the $g6a$ dataset, for which the center of the target was placed 90 cm farther upstream than for $g11a$. Thus, the detector geometry was quite different in the two datasets. Whether this is the cause of any of the discrepancies we can't say; however, it is possible that this has some effect.

In the previous CLAS analysis, only the proton and π^+ were required to be detected. Thus, it was not possible to extract the spin density matrix elements from their data. The only available polarization measurements in this energy range were made at very forward angles (small $|t|$) [24]. These values were used in their event generator at all production angles — since no other measurements were available; however, our measurements of the spin density matrix elements show that the values are quite different at backward and forward angles. The inaccurate spin density matrix used in the backward direction by the previous CLAS analysis could have led to large errors in the acceptance calculation. This is a possible explanation for the discrepancy between the two measurements in the backwards direction; however, it is unlikely that this can explain the disagreement in the highest energy bin in the $0 \leq \cos\theta_{CM}^{\omega} \leq 0.5$ region (this is not near the holes in the CLAS detector).

We conclude this section by restating that the overall agreement between the two results is good. The disagreement in the backwards direction could be caused by the use of an inaccurate spin density matrix in the previous analysis, leading to errors in the acceptance calculation. The only other noticeable discrepancy is in the $0 \leq \cos\theta_{CM}^{\omega} \leq 0.5$ region and increases with $\sqrt{s}$. In this region, our results show a smooth systematic decrease with increasing energy. The previous results are (nearly) independent of $\sqrt{s}$ here. The smooth systematic fall off of our differential cross section in this region is consistent with *typical* measurements of this type. The source of this discrepancy may never be known; however, we feel confident in our measurements in this region.
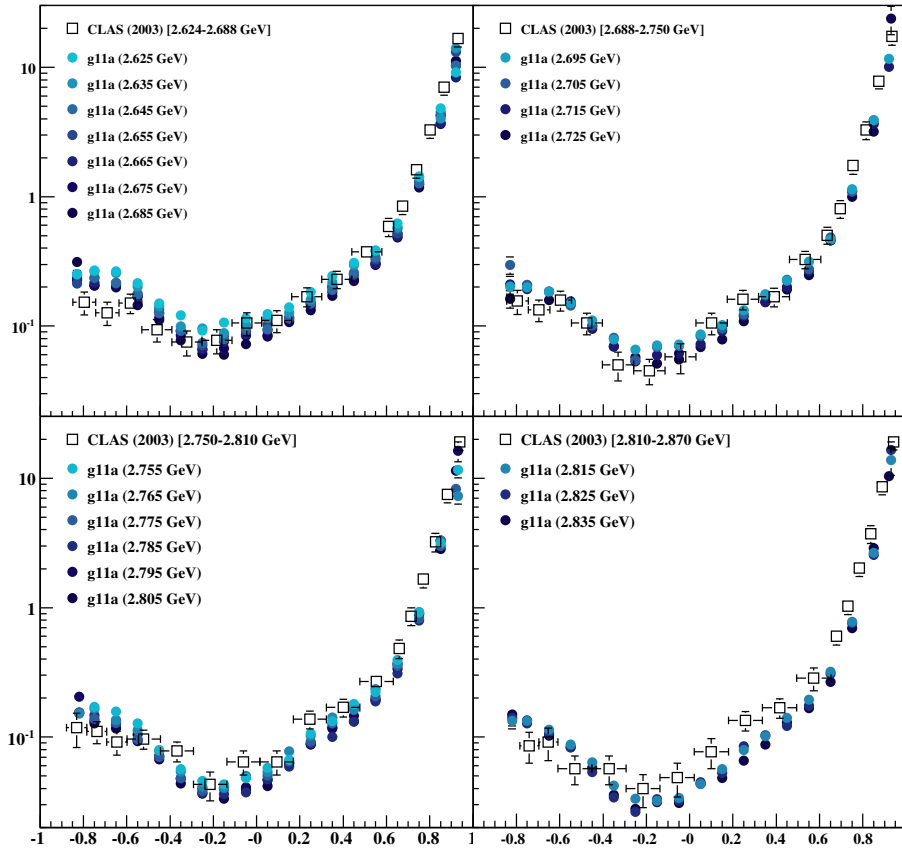
Figure 7.19: $\frac{d\sigma}{d\cos\theta_{CM}^\omega}(\mu b)$ vs $\cos\theta_{CM}^\omega$: Comparison of the CLAS differential cross sections published in 2003 [22] (open squares) with this work (filled circles). The two results are in fair agreement. A more detailed discussion is presented in the text.

7.4.2   SAPHIR 2003

In October 2003, the SAPHIR collaboration (Barth et al [23]) published differential cross section and spin density matrix element measurements for $\gamma p \to p\omega$ in the energy range from threshold up to $\sqrt{s} = 2.4$ GeV. The SAPHIR detector is a large acceptance spectrometer located at the Bonn electron stretcher ring ELSA. The accepted solid angle is $\sim 0.6 \times 4\pi$ Sr — due to pieces of the magnetic poles. Photons are produced from the ELSA electron beam via bremsstrahlung radiation. Their energies are determined using a tagging system, which is also used (along with a photon veto counter) to measure the photon flux. Drift chambers are utilized to track charged particles which are bent in a magnetic field, providing momentum determination and a scintillator wall provides time-of-flight information which is used to determine particle masses.

Differential Cross Sections

Figures 7.20 and 7.21 show the comparisons between the differential cross section results from SAPHIR (open squares) and our analysis (filled circles). It is important to note that the SAPHIR error bars only contain the statistical uncertainties (the systematic errors are described in the paper; however, the wording is fairly cryptic). The overall agreement is good, although there are some discrepancies. The biggest disagreement is in the (first) threshold bin. The cross section rises rapidly near threshold; the SAPHIR result increases by a factor of ~ 3 from the first to the second bin. The low edge of the first SAPHIR bin is 4 MeV lower than our first bin. Thus, it is possible that the rapidly changing cross section coupled with the different bin edges causes this discrepancy.

In almost every energy bin, the backwards most SAPHIR point is much lower than our result. These points are generally also much lower than the next SAPHIR point in the same energy bin. It would appear as though there needs to be a large systematic error bar placed on these points. In the energy range from 1.76 GeV $< \sqrt{s} <$ 1.87 GeV, our results are systematically lower than SAPHIR in the region around $\cos\theta_{CM}^{\omega} \sim 0.5$. In this region, our cross section begins to develop a dip that is not present in the SAPHIR results; however, for $\sqrt{s} > 1.87$ GeV the dip is present in both measurements.

For $\sqrt{s} > 2.1$ GeV, our results are higher than SAPHIR for most points in regions with $\cos\theta_{CM}^{\omega} < 0$. The scatter of the SAPHIR measurements in this region suggests reasonably large systematic uncertainties exist. This would decrease the discrepancy; however, the majority of our points would still be above SAPHIR suggesting a systematic difference between the two sets of measurements in this region.

Spin Density Matrix Elements

Figures 7.22 – 7.24 show the comparison between the spin density matrix element results from SAPHIR (filled squares and triangles) and this work (filled circles). The SAPHIR collaboration published their results in both the Gottfried-Jackson and Helicity frames (see Appendix A), with each measurement constituting an independent fit to the data. Both results can be rotated into the Adair frame (in which our measurements are reported) yielding slightly different (though statistically consistent) results. The SAPHIR measurements, which consist of four energy bins containing two t bins (eight total points), are the only published ω polarization measurements in this energy range. Our results contain ~ 1200 points which overlap the SAPHIR results. This makes a detailed comparison difficult; however, we can say that the SAPHIR results are consistent with our measurements. This comparison illustrates how much of an improvement in precision our spin density matrix element results are over previous measurements.
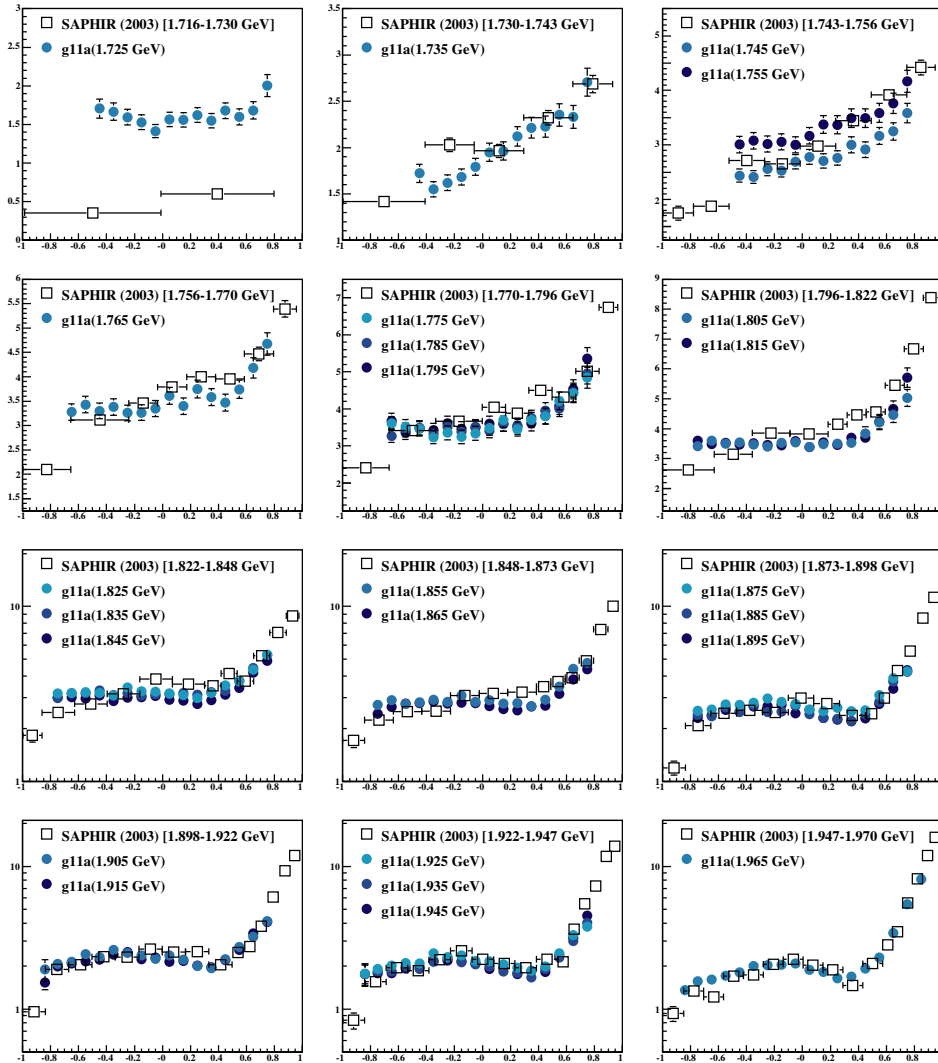
Figure 7.20: $\frac{d\sigma}{d\cos\theta_{CM}^{\omega}}(\mu b)$ vs $\cos\theta_{CM}^{\omega}$: Comparison of the SAPHIR differential cross sections published in 2003 [23] (open squares) with this work (filled circles) for 1.716 GeV $\leq \sqrt{s} <$ 1.97 GeV. The two results are in good agreement — a detailed discussion is presented in the text.
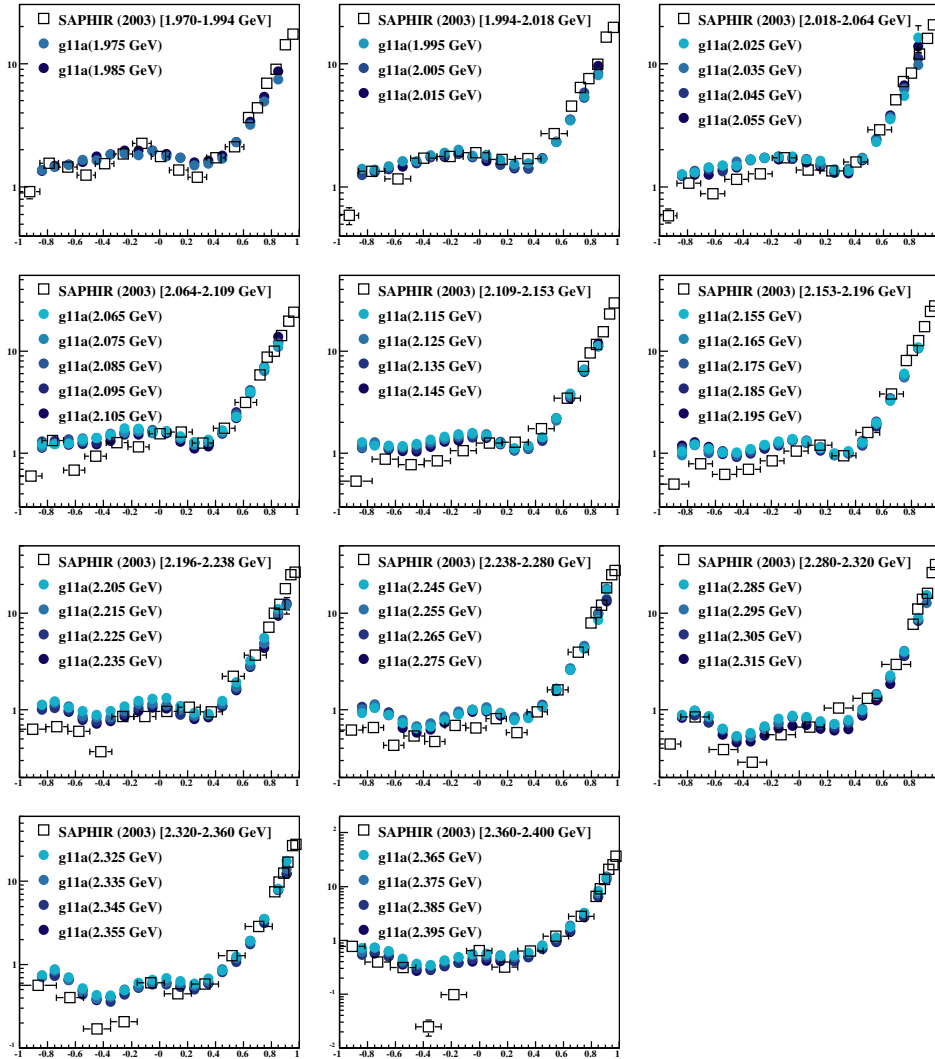
Figure 7.21: $\frac{d\sigma}{d\cos\theta^\omega_{CM}}(\mu b)$ vs $\cos\theta^\omega_{CM}$: Comparison of the SAPHIR differential cross sections published in 2003 [23] (open squares) with this work (filled circles) for 1.97 GeV $\leq \sqrt{s} < 2.4$ GeV. The two results are in good agreement — a detailed discussion is presented in the text.

Figure 7.22: ρ^0_{00} in the Adair frame vs $\cos\theta^\omega_{CM}$: Comparison of the SAPHIR spin density matrix elements published in 2003 [23] (filled squares and triangles) with this work (filled circles). SAPHIR extracted results independently in the Gottfried-Jackson and Helicity frames — both presented here rotated to the Adair frame. The two results are consistent, a more detailed discussion is presented in the text.

Figure 7.23: ρ^0_{1-1} in the Adair frame vs $\cos\theta^\omega_{CM}$: Comparison of the SAPHIR spin density matrix elements published in 2003 [23] (filled squares and triangles) with this work (filled circles). SAPHIR extracted results independently in the Gottfried-Jackson and Helicity frames — both presented here rotated to the Adair frame. The two results are consistent, a more detailed discussion is presented in the text.

Figure 7.24: $Re(\rho^0_{10})$ in the Adair frame vs $\cos\theta^\omega_{CM}$: Comparison of the SAPHIR spin density matrix elements published in 2003 [23] (filled squares and triangles) with this work (filled circles). SAPHIR extracted results independently in the Gottfried-Jackson and Helicity frames — both presented here rotated to the Adair frame. The two results are consistent, a more detailed discussion is presented in the text.

(a)   (b)   (c)

Figure 7.25: $\frac{d\sigma}{d\cos\theta_{CM}^\omega}(\mu b)$ vs $\cos\theta_{CM}^\omega$: Comparison of the Daresbury differential cross sections [25, 26] (open squares) with this work (filled circles) – the two results are in good agreement. The data points in (c) have no error bars (the points were extracted from a PDF image).

7.4.3 Daresbury 1984 and 1977

In 1984 (Barber et al [25]) and 1977 (Clift et al [26]), the LAMP2 group measured differential cross sections and spin density matrix elements using data collected at the NINA electron synchrotron located at Daresbury, Warrington, UK. The detector consists of a tagging system, multi-wire proportional chambers and a lead glass calorimeter. The 1984 measurements were only at very forward angles, while the 1977 results were only at very backwards angles. In both of these regions, the CLAS detector has low acceptance. Thus, our statistical uncertainties are larger here than for the majority of our results.

Differential Cross Sections

Figure 7.25 shows the comparison between the Daresbury differential cross section results — in both the forward and backward regions — and this work. In the forward direction, we have 34 bins which overlap the Daresbury results. The agreement is quite good. At backwards angles, our results are also in good agreement with Daresbury. Recall that it was in this kinematic region where our results disagreed with the previous CLAS publication by $\sim 25-50\%$. We conclude this section by noting that the Daresbury backwards measurements show a *dip* near $\cos\theta_{CM}^\omega \sim -0.95$ (see Figure 7.25(c)). At this energy, this corresponds to the value of u where the non-degenerate Regge nucleon propagator contains a node. Unfortunately, the acceptance of the CLAS detector does not allow us to confirm or deny this feature of the cross section.

Spin Density Matrix Elements

Figures 7.26 and 7.27 show comparisons of spin density matrix element measurements between Daresbury (open squares) and this work (filled circles). The Daresbury results were obtained at forward angles where we (again) note that the low acceptance of the CLAS detector yields our largest statistical uncertainties. The error bars on both measurements are somewhat large, making a detailed comparison difficult; however, the results appear to be consistent for each of the $\rho_{MM'}^0$ results.
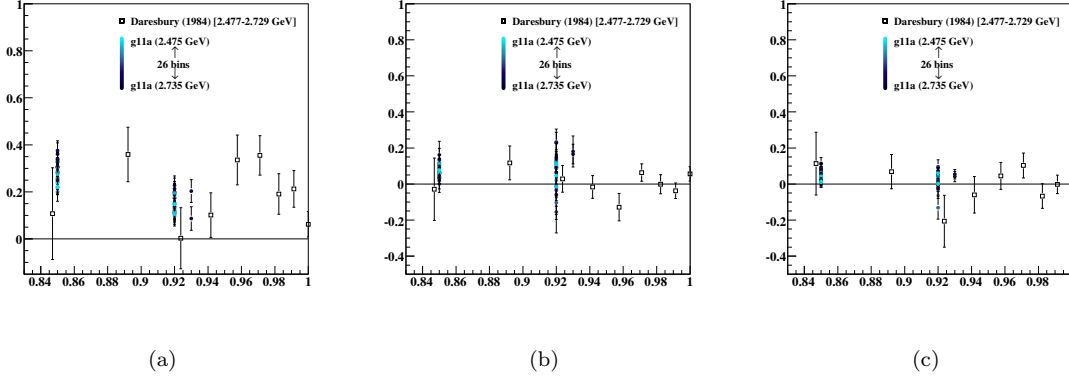
(a)   (b)   (c)

Figure 7.26: $\rho^0_{MM'}$ in the Adair frame vs $\cos\theta^\omega_{CM}$: Comparison of the Daresbury spin density matrix elements [25] (open squares) with this work (filled circles) in the range 2.47 GeV $\leq \sqrt{s} <$ 2.74 GeV for (a) ρ^0_{00} (b) ρ^0_{1-1} (c) $Re(\rho^0_{10})$. The two results are in good agreement.
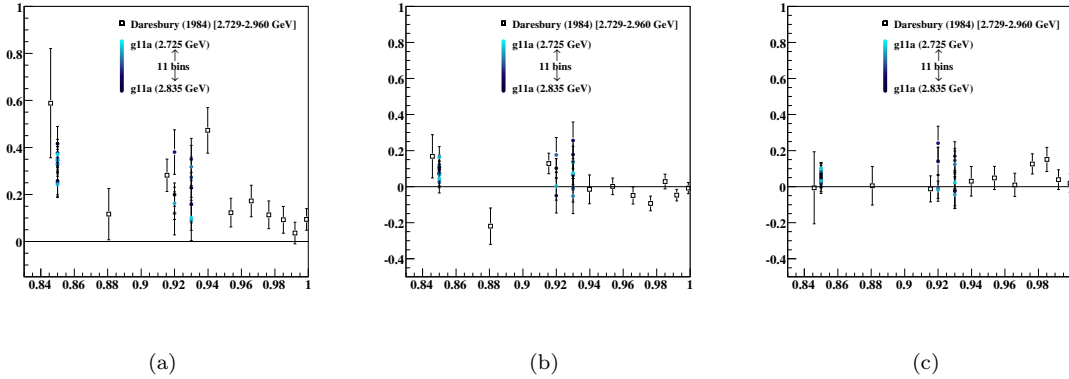
(a)   (b)   (c)

Figure 7.27: $\rho^0_{MM'}$ in the Adair frame vs $\cos\theta^\omega_{CM}$: Comparison of the Daresbury spin density matrix elements [25] (open squares) with this work (filled circles) in the range 2.72 GeV $\leq \sqrt{s} <$ 2.96 GeV for (a) ρ^0_{00} (b) ρ^0_{1-1} (c) $Re(\rho^0_{10})$. The two results are in good agreement.
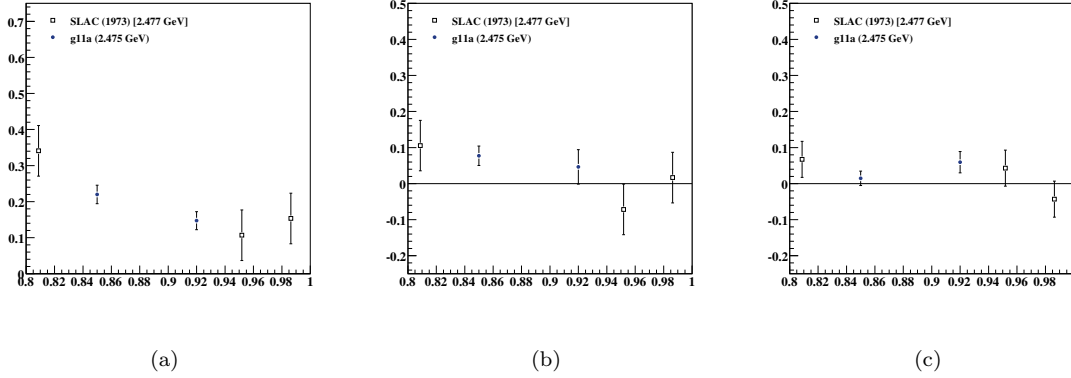
(a)   (b)   (c)

Figure 7.28: $\rho^0_{MM'}$ in the Adair frame vs $\cos\theta^\omega_{CM}$: Comparison of the SLAC spin density matrix elements [24] (open squares) with this work (filled circles) for (a) ρ^0_{00} (b) ρ^0_{1-1} (c) $Re(\rho^0_{10})$. The two results are in good agreement.

7.4.4 SLAC 1973

In 1973, Ballam et al [24] published differential cross section and spin density matrix element measurements at $E_\gamma = 2.8$ GeV using data collected at SLAC. The data were obtained by exposing a hydrogen bubble chamber to monochromatic photons from the SLAC backscattered laser beam. Figure 7.28 shows the comparison of the SLAC spin density matrix measurements — reported only for forward angles — and this work. The two results are in good agreement. Figure 7.29 shows a comparison of the SLAC differential cross section measurements to our results. The error bars on the SLAC results are fairly large; however, we can at least say that their measurements are consistent with ours.
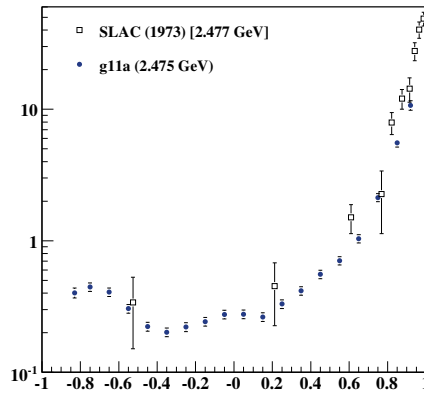
Figure 7.29: $\frac{d\sigma}{d\cos\theta^\omega_{CM}}(\mu b)$ vs $\cos\theta^\omega_{CM}$: Comparison of the SLAC differential cross section published in 1973 (open squares) with this work (filled circles). The two results are in good agreement.

7.5   Summary

We have made differential cross section and spin density matrix element measurements for ~ 20 points in each of 112 $\sqrt{s}$ bins in the energy range 1.72 GeV $< \sqrt{s} <$ 2.84 GeV. These are the most precise measurements ever made at these energies. All of our results are in fair agreement with previous world data, in many regions the agreement is excellent. Our $d\sigma/d\cos\theta^{\omega}_{CM}$ and $\rho^0_{MM'}$ results possess a number of features which could be indicative of resonance production. At higher energies, our differential cross sections have strong forward and backward peaks. These structures are typically modeled as non-resonant t- and u-channel production mechanisms. Our results will place new stringent constraints on available theoretical models. A number of the features present in our measurements have never been observed before. For example, the *dip* in ρ^0_{00} in the forward direction at higher energies. Thus, interpretation of these results is sure to lead to newer (better) models of ω photoproduction in the near future.

Chapter 8

Partial Wave Analysis Results

In the previous chapters, all of the work required to extract differential cross section and spin density matrix elements from the CLAS $g11a$ dataset has been discussed in detail. Now that these measurements are complete, we can use them to gain insight into the $\gamma p \rightarrow p\omega$ production mechanisms which are divided into two categories — resonant and non-resonant. Ultimately, our goal is to extract the resonance contributions. To accomplish this, a good understanding (or model) of the non-resonant processes involved is needed. The beginning of this chapter is devoted to examining how well existing non-resonant models describe our measurements. Next, an event-based partial wave analysis will be performed to determine the dominant J^P contributions. The cross sections and phase motion obtained from this analysis will be used to determine which resonant states, if any, are present in our data.

The technique we will employ to extract the resonant contributions is known as *mass-independent* partial wave analysis. The probability amplitude for an unstable particle to propagate, known as a *propagator*, is a complex function of the particle's energy and momentum. The functional form of the propagator is determined by how the particle interacts with the vacuum. Thus, calculating this quantity involves summing an infinite number of Feynman diagrams. If the state of interest is the only state with a given set of quantum numbers, in a relatively large energy range, then the propagator can be approximated as a constant width Breit-Wigner (see (8.10)). This model reduces the infinite sum of Feynman diagrams to a simple expression involving s and two parameters, known as the mass (m) and width (Γ) of the resonance. If, however, multiple states with the same quantum numbers do exist *close* together, as determined by their widths, then the Breit-Wigner approximation is not valid and a different model must be employed. To avoid this model dependency, we have chosen to bin our data finely in $\sqrt{s}$. In each narrow energy bin, the propagator can be safely approximated as a constant complex number. Utilizing this technique allows us to extract resonance contributions in a model independent way.

8.1 Theoretical Models for Non-Resonant Photoproduction

The *current* theoretical models for non-resonant ω photoproduction were constructed using the only available polarization information — the extreme forward angle data from SLAC [24] and Daresbury [25]. At all other angles, the models are completely unconstrained by polarization measurements. Using the spin density matrix element measurements presented in this work, we can provide the first real test of these models. In this section, we will examine the models of Oh, Titov and Lee [28] and Sibirstev, Tsushima and Krewald [69]. The Feynman diagrams for all exchange mechanisms used in these models are shown in Figure 8.1.
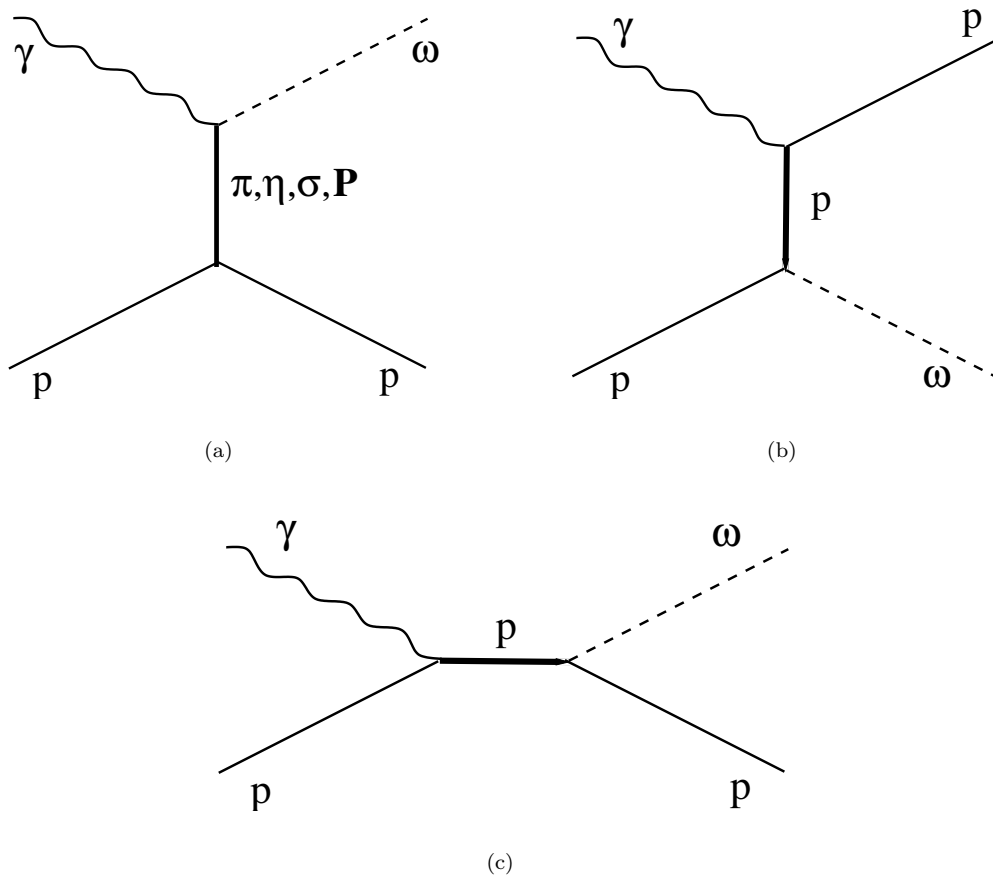
Figure 8.1: Non-resonant Feynman Diagrams: (a) t-channel meson and/or Pomeron exchange. (b) u-channel (crossed) nucleon exchange. (c) s-channel (direct) nucleon exchange.

8.1.1 The Oh, Titov, Lee Model

The model developed by Oh, Titov and Lee [28] (OTL) incorporates pseudoscalar meson, π^0 and η, and Pomeron exchange t-channel processes along with nucleon exchange in both the s- and u-channel. The OTL model also has resonant terms; however, we've excluded them in this comparison. This model was fit to data from SAPHIR [23], SLAC [24] and Daresbury [26].

t-channel

The OTL model incorporates both pseudoscalar meson, π^0 and η, and Pomeron t-channel exchange mechanisms. The pseudoscalar exchange amplitudes are just those of Section 6.5.1, using the parameters listed in Table 8.1. The coupling constant $g_{\pi NN}$ was previously determined by studying πN scattering. The coupling constants $g_{\gamma\pi\omega}$ and $g_{\gamma\eta\omega}$ were locked using the $\omega \to \pi\gamma$ and $\omega \to \eta\gamma$ decay widths respectively. The $g_{\eta NN}$ coupling is not well known due to the lack of backwards angle measurements at moderately high energies for the $p\eta$ final state. The OTL model set this value using $g_{\pi NN}$ and an SU(3) relation. The form factor cutoffs were obtained by fitting the available data. The Pomeron amplitude used by the Oh, Titov and Lee model is discussed in Section 6.5.2. The OTL model follows the work of Donnachie and Landshoff [72] when constructing this amplitude. The parameters used in the Pomeron exchange amplitude (see Section 6.5.2) were determined by fitting all vector meson (ω, ρ and ϕ) total cross sections at high energies.

nucleon exchange

The OTL model also incorporates both direct and crossed nucleon exchange terms. The amplitudes are discussed in Section 6.5.4. The two terms are combined, in this model, according to the simple prescription:

$$A_{nucleon} = F(s, \Lambda_{\omega NN})A^{direct}_{\gamma p \to p\omega} + F(u, \Lambda_{\omega NN})A^{crossed}_{\gamma p \to p\omega}, \tag{8.1}$$

where

$$F(x, \Lambda) = \frac{\Lambda^4}{\Lambda^4 + (x - w_p^2)^2}, \tag{8.2}$$

is a form factor dressing the ωNN vertex and w_P is the mass of the proton. The coupling constant $g_{\omega NN}$ and cut-off $\Lambda_{\omega NN}$ were fit to the existing data, while the *magnetic* coupling κ_ω was set to zero following previous meson exchange models.

Parameter	Value	Obtained From
$g_{\pi NN}$	13.26	πN scattering
$g_{\eta NN}$	3.53	SU(3) relation and $g_{\pi NN}$
$g_{\gamma\pi\omega}$	1.823	$\omega \to \pi\gamma$ decay width
$g_{\gamma\eta\omega}$	0.416	$\omega \to \eta\gamma$ decay width
$\Lambda_{\pi NN}$	0.6	Fit to data
$\Lambda_{\gamma\pi\omega}$	0.7	Fit to data
$\Lambda_{\eta NN}$	1.0	Fit to data
$\Lambda_{\gamma\eta\omega}$	0.9	Fit to data
$g_{\omega NN}$	10.35	Fit to data
κ_ω	0	Value used by previous models
$\Lambda_{\omega NN}$	0.5	Fit to data

Table 8.1: Parameters used in the Oh, Titov and Lee model [28].

Comparison to Our Measurements

Figure 8.2 shows the comparison between the non-resonant terms of the OTL model and our measurements at $\sqrt{s} = 2$ GeV and $\sqrt{s} = 2.8$ GeV. Remember that we are only showing the non-resonant terms from the OTL model, thus we don't expect agreement at all angles. In the lower energy bin, the OTL model does a good job of reproducing the forward cross section and spin density matrix elements. At this energy, the model's forward dependence is dominated by π^0 exchange. We also note that the large angle cross section shows hints of resonance contributions which would interfere with the t-channel terms of the OTL model; thus, we do not expect perfect agreement between the measurements and the OTL model.

In the higher energy bin, the OTL model does a good job of reproducing the forward cross section; however, the forward spin density matrix elements do not match nearly as well as in the lower energy region. The ρ_{00}^0 element rises much faster (with decreasing $\cos\theta_{CM}$) in the data than in the model. Also, the agreement of the $Re(\rho_{10}^0)$ element in the forward direction is not good. In the backwards direction, the only data available when the parameters of this model were fit was the Daresbury measurements [26]. There was no published polarization information in this angular range. Neither the cross section nor the ρ_{00}^0 density matrix element are well reproduced by the non-resonant terms of the OTL model in the backwards direction. It is possible that resonance contributions are significant in the backwards direction. If this is the case, then we would not expect the u-channel OTL terms (by themselves) to provide a good match to our measurements.

Incorporating Our Results

The u-channel terms of the OTL model fail to adequately describe our backwards cross section and polarization measurements. Most models assume the backwards photoproduction of ω mesons to be dominated by u-channel processes. For now, we will proceed under this assumption. When the OTL model was constructed, neither our results nor the previous CLAS results [22], whose cross section measurements are in good agreement with ours, had been published. Using our backwards cross section measurements, $\cos\theta_{CM} < -0.4$, we can refit the OTL u-channel parameters $g_{\omega NN}$ and $\Lambda_{\omega NN}$ by coupling our highest 20 $\sqrt{s}$ bins. Figures 8.3(a) and (b) show the results of this fit in the $\sqrt{s} = 2.8$ GeV bin. This fit provides an excellent description of the backwards cross section; however, the ρ_{00}^0 element of the spin density matrix is still poorly reproduced by the model.

Recall that the OTL model (along with most models) sets $\kappa_\omega = 0$, obtained from previous meson exchange models. The effects of removing this (arbitrary) constraint are shown in Figures 8.3(c) and (d). This fit is the same as described above, but with κ_ω left as a free parameter. The values of the parameters obtained from this fit are listed in Table 8.2. The results of this fit not only provide an excellent description of the backwards cross section, but also of the entire spin density matrix in the backwards direction. It is interesting to note that the value obtained from our fit, $\kappa_\omega = -1.05$, is similar to the Quark Model calculation of Downum et al [73], $\kappa_\omega = -1.5$. Recall that this fit was run under the assumption that the backwards production amplitude is dominated by u-channel processes. It is possible that this is not the case, or that the structure of the OTL nucleon exchange amplitudes are incorrect. Thus, caution should be applied when interpreting these results.

$g_{\omega NN}$	κ_ω	$\Lambda_{\omega NN}$
1.04	-1.05	1.24

Table 8.2: Parameters obtained by fitting the Oh, Titov, Lee model [28] to our backwards data.
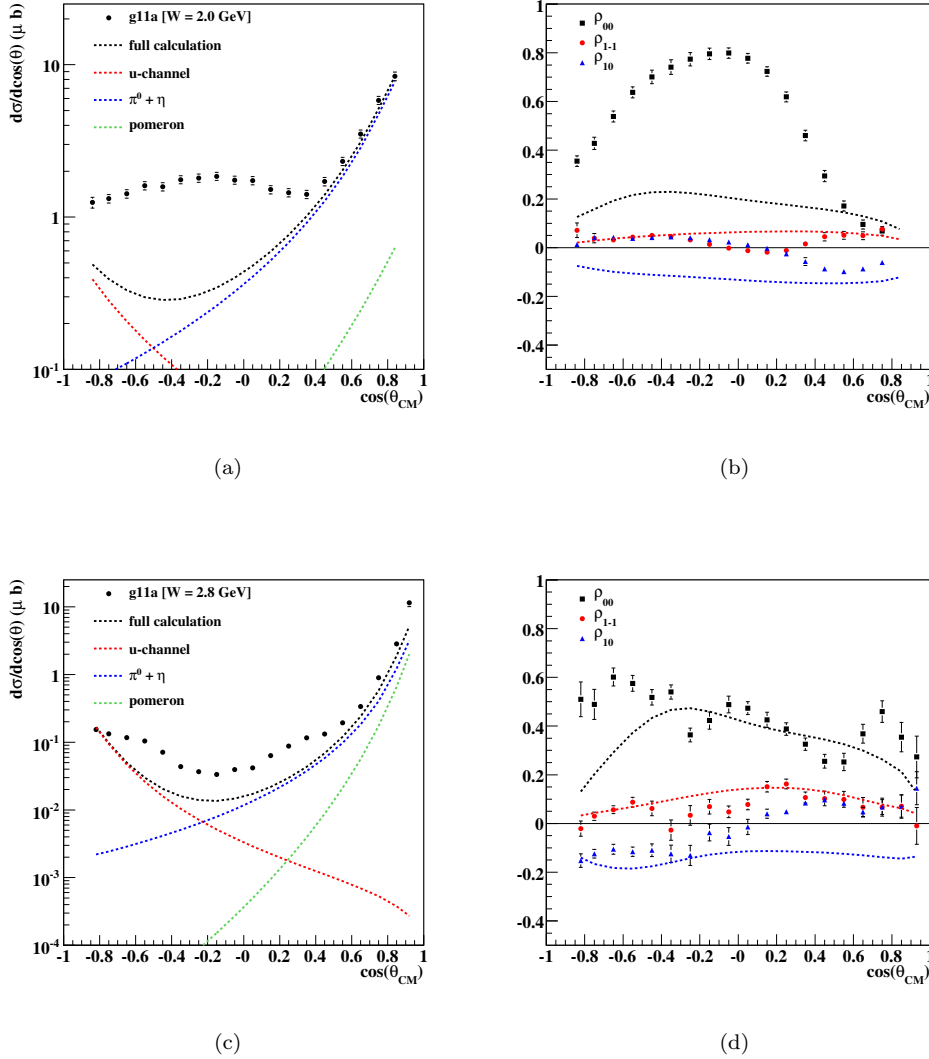
Figure 8.2: Non-resonant terms of the Oh, Titov and Lee model compared to our measurements in the $\sqrt{s} = 2$ GeV bin, (a) and (b), and $\sqrt{s} = 2.8$ GeV bin, (c) and (d). The agreement in the forward direction in the lower energy bin is quite good. At higher energies, the forward cross section is described well; however, the spin density matrix elements are not reproduced well by the model.

(a)

(b)

(c)

(d)
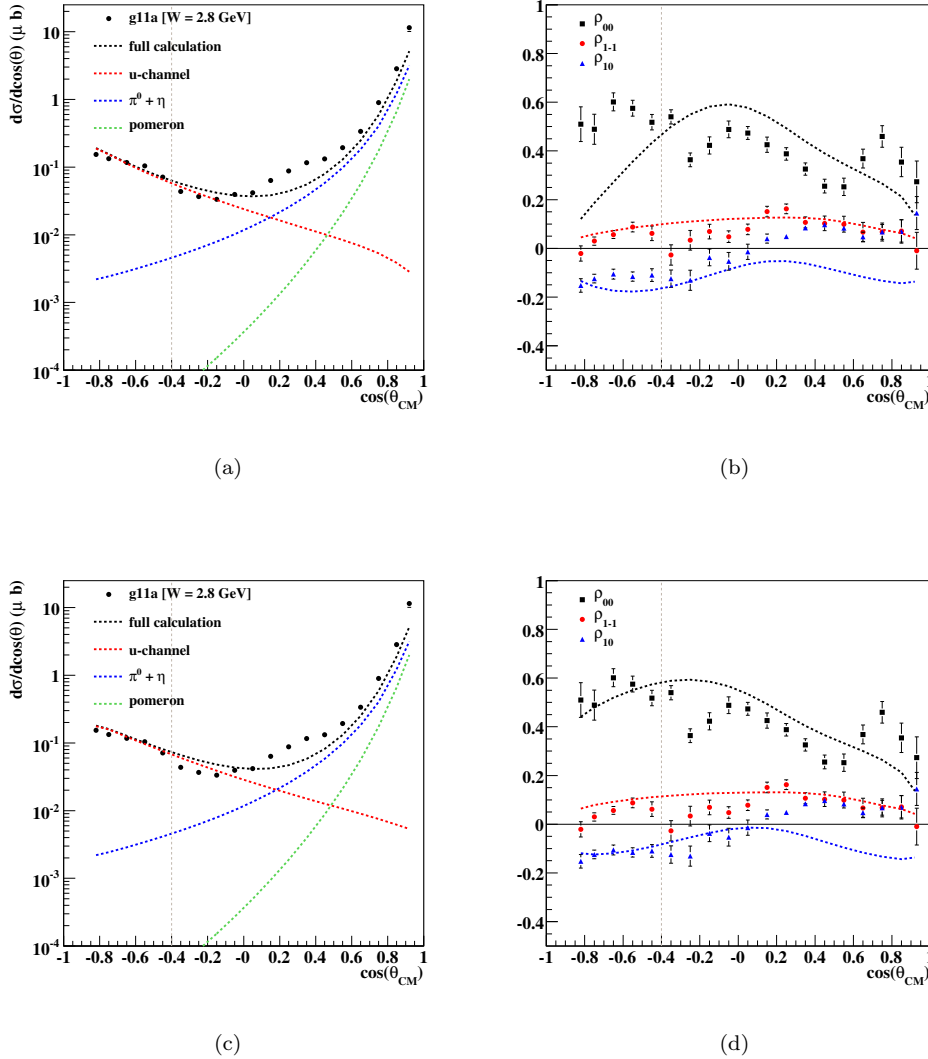
Figure 8.3: Non-resonant terms of the Oh, Titov and Lee model fit to our highest 20 $\sqrt{s}$ bins (shown here for $\sqrt{s}$ = 2.8 GeV). In both fits, only the u-channel parameters are allowed to vary. Plots (a) and (b) were fit to the backwards most five points while enforcing $\kappa_\omega = 0$. The backwards differential cross section is described well; however, agreement with the spin density matrix elements is poor. Plots (c) and (d) were fit allowing κ_ω to vary freely. The agreement with the polarization observables is greatly improved.

8.1.2 The Sibirstev, Tsushima and Krewald Model

The model developed by Sibirstev, Tsushima and Krewald [69] (STK) also incorporates pseudoscalar meson (π^0 and η) and nucleon exchange, both s- and u-channel. The STK model replaces the Pomeron exchange of the OTL model with σ meson exchange in the t-channel. The STK model, which was fit only to higher energy data from SLAC [24] and Daresbury [26], did not incorporate any resonant terms.

t-channel

The pseudoscalar exchange amplitudes (including form factors) are the same as the OTL model. The σ exchange amplitude is discussed in Section 6.5.3. The t-channel parameters of the STK model were obtained using the same methods as the OTL model and the values are very similar. As with the OTL model, the STK model does a good job reproducing the forward cross section but fails to match the forward spin density matrix elements. Thus, swapping the Pomeron for a σ meson is not sufficient to provide a better description of the forward ω polarization.

nucleon exchange

Though both the OTL and STK models incorporate both direct and crossed nucleon exchange, the STK model handles the ωNN vertex quite differently from the OTL model. Motivated by gauge invariance and crossing symmetry, the STK model combines the nucleon exchange terms according to

$$A_{nucleon} = F(s, \Lambda_{\omega NN})F(u, \Lambda_{\omega NN})\left(A_{\gamma p \to p\omega}^{direct} + A_{\gamma p \to p\omega}^{crossed}\right), \tag{8.3}$$

where $F(x, \Lambda)$ takes on the same form as in the OTL model. This model is also able to describe the backwards cross section; however, even with κ_ω free it fails to reproduce the spin density matrix elements in the backwards direction.

8.1.3 Non-Resonant Terms Included in Our PWA

The available non-resonant models do a very good job reproducing our measurements at lower energies. The forward cross section and spin density matrix elements are described well by the OTL model for $\sqrt{s} < 2.1$ GeV, where the dominant contribution is from π^0 exchange in the t-channel. At higher energies, the OTL model adequately reproduces the cross section at forward angles; however, the agreement with the spin density matrix elements is poor in this energy regime. The STK model, which replaces the Pomeron exchange used in the OTL model with σ meson exchange, also fails to reproduce the density matrix elements at these energies.

We have chosen to use the OTL t-channel terms in our PWA. Though the quality of the model is not excellent at our highest energies, our partial wave analysis is mainly interested in the energy regime from threshold up to $\sqrt{s} \sim 2.4$ GeV. The discrepancy between the OTL model and our forward data is still present towards the upper regions of this energy range and is noticeable when comparing the PWA results to our measurements; however, the quality of this non-resonant model should be high enough to allow us to identify any dominant resonance contributions present in our data.

In Section 8.1.1, we found that modifying the parameters of the OTL model provided a good description of the backwards cross section and spin density matrix elements. This modification was performed under the assumption that the backwards production amplitude is dominated by u-channel processes. The validity of this assumption is unclear; however, we can conclude that one of the following must be true: (1) the magnetic coupling at the ωNN vertex is non-zero: $\kappa_\omega \neq 0$; (2) the structure of the nucleon exchange amplitudes used in the OTL and most other models are not

(a)   (b)
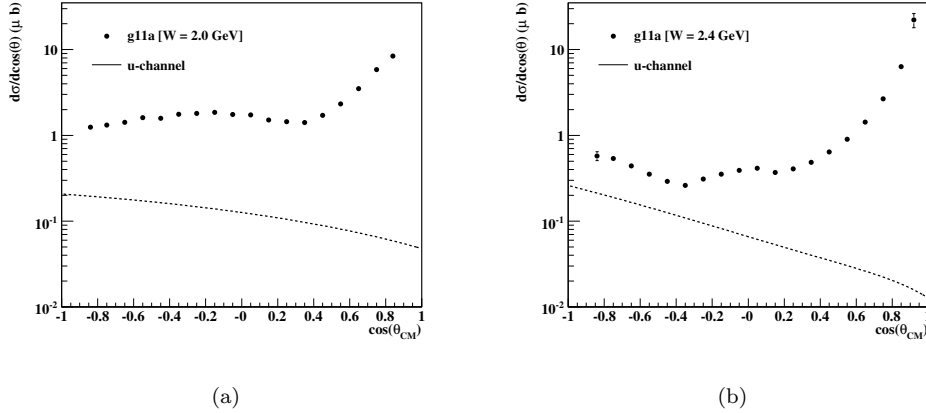
Figure 8.4: The OTL u-channel model, fit to our high energy data, projected down to the lower energy bins, (a) $\sqrt{s} = 2$ GeV and (b) $\sqrt{s} = 2.4$ GeV.

correct descriptions of the u-channel production mechanism; (3) the backward direction production amplitude is not dominated by u-channel processes.

Conclusion (1) contradicts what is used in most meson exchange models, including those where the ω is only an intermediate particle ($\gamma p \rightarrow N\pi$, $\pi N \rightarrow \pi N$, $\gamma p \rightarrow p\eta$, etc.). There are a few possibilities for satisfying conclusion (2). Perhaps a different prescription for restoring gauge invariance, which is broken by adding the form factors to the nucleon exchange amplitudes, could better describe the spin density matrix elements without requiring $\kappa_\omega \neq 0$. Another possibility would be including resonant terms in the u-channel. Conclusion (3) could simply imply the backwards production amplitude at our highest energies is some mixture of u-channel and resonant terms. Regardless of which is true, our confidence in the available u-channel models is low.

At lower energies, $\sqrt{s} < 2$ GeV, there is no hint of any backwards peak in the cross section. Thus, any u-channel contributions should be negligible regardless of which model is employed. At higher energies, there is a backwards peak in the cross section which could be the result of u-channel, resonant or some combination of processes. Figure 8.4 shows the modified OTL u-channel terms (using the parameters listed in Table 8.2) projected down into the energy regime of interest for our PWA. At $\sqrt{s} = 2$ GeV, this model predicts the u-channel contribution to be $\sim 15\%$ at our backwards most angles. By $\sqrt{s} = 2.4$ GeV the predicted u-channel contribution reaches $\sim 30\%$ in the backwards direction. Thus, even at the highest energies we will study with our PWA, this model, obtained via the (extreme) assumption that all of the backwards cross section for $\sqrt{s} > 2.6$ GeV is u-channel, predicts a u-channel contribution which we should be able to ignore when searching for dominant resonant contributions. Based on these arguments, we have chosen to exclude u-channel terms from our PWA. The important question is: *How does the quality of the non-resonant terms affect the resonance parameters?* For the u-channel terms, we will show in Section 8.6 that including these terms does not have a major effect on the extracted resonance contributions.

(a)   (b)
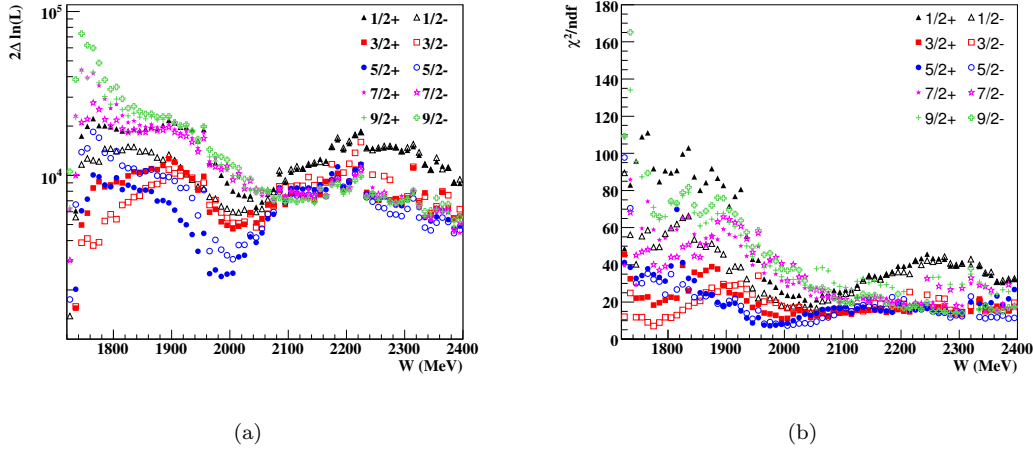
Figure 8.5: Goodness-of-Fit vs center-of-mass energy for fits with locked OTL t-channel and one free s-channel wave. (a) $-2\,(\ln L - \ln L_{mother})$ vs. $W(\mathrm{MeV})$: Likelihood difference between these fits and the *Mother* fit in each $\sqrt{s}$ bin (lower is better) — the *Mother* fit is, of course, better in every bin. (b) χ^2/ndf vs $W(\mathrm{MeV})$: The χ^2 was obtained by comparing projections of $d\sigma/d\cos\theta^\omega_{CM}$ and $\rho^0_{MM'}$ from these fits to the measurements presented in Chapter 7. In both plots, it is clear that the $J^P = 3/2^-$ fit is the best from threshold up to $W \sim 1850$ MeV and the fit with $J^P = 5/2^+$ is the best in the energy range 1850 MeV $< W < 2000$ MeV. A more detailed discussion is presented in the text.

8.2   *s*-channel Scans

In the previous section, we decided to use the Oh, Titov and Lee (OTL) t-channel model, which has no free parameters, and to exclude (for now) any u-channel diagrams. Though this non-resonant model is not perfect, it should be adequate to pursue our current goals — to search for evidence of strong resonance contributions in ω photoproduction. We will begin this pursuit by scanning the desired energy regime, 1.72 GeV $< \sqrt{s} < 2.4$ GeV, using only the OTL t-channel terms and waves from a single spin-parity, J^P. All of the fits described in this section utilize the same resonance fit parameters as the *Mother* fit (see Section 7.1.1). Also, all of the resonance parameters used in these fits are variable, with no constraints, in each $\sqrt{s}$ bin.

8.2.1   OTL t-channel + 1 s-channel Wave

The goal of this scan is to identify (possible) energy ranges where waves of a given J^P perform significantly better than waves of any other spin-parity. This information alone does not constitute evidence of resonance production; however, it can serve as a guide as to which waves are more likely to contribute strongly to ω photoproduction. Figure 8.5 shows comparisons of the goodness-of-fit quantities for all waves with $J \leq 9/2$. From threshold up to $\sqrt{s} \sim 1.85$ GeV, the fit with $J^P = 3/2^-$ is clearly the best. In the energy range 1.85 GeV $< \sqrt{s} < 2$ GeV, the preferred wave is $J^P = 5/2^+$. We reiterate that this information alone is not sufficient to claim conclusive evidence of resonance production. This requires extracting cross sections and phase motion consistent with the presence of resonance states. The results of these fits will simply be used as a road map to help guide our search efforts.

	J^P				
	$1/2^-$	$1/2^+$	$3/2^+$	$5/2^-$	$5/2^+$
Dominant $3/2^-$?	$\checkmark$	$\checkmark$	$\checkmark$	$\checkmark$	$\approx$

Table 8.3: For fits with locked OTL t-channel and a free $3/2^-$ plus one additional J^P in s-channel, the contribution extracted for the $3/2^-$ wave is the bigger of the two s-channel terms for $\sqrt{s} < 1.85$ GeV for all $J^P \neq 5/2^+$. For the $J^P = 5/2^+$ case, the contributions of the two s-channel waves are approximately equal.

8.2.2   OTL t-channel + $3/2^-$ + 1 additional s-channel Wave

In the previous section, we showed that the $J^P = 3/2^-$ wave provided the best single s-channel wave fit for $\sqrt{s} <1.85$ GeV. Now we want to add an additional free s-channel wave to this fit, and again look for energy regions where a specific J^P performs better than the rest. Figures 8.6(a) and (b) show the goodness-of-fit quantities for all additional waves with $J \leq 5/2$ from threshold up to $\sqrt{s} = 2.1$ GeV. The fit with an additional $J^P = 5/2^+$ is clearly the best. In fact, the $\chi^2/ndf \sim 1$ near threshold and is always less than 5 for $\sqrt{s} < 2$ GeV. In the fit with the additional $J^P = 5/2^+$ wave, the contributions extracted for the two s-channel waves are approximately equal in size for $\sqrt{s} < 1.85$ GeV. For all of the other fits, the extracted contribution for the $J^P = 3/2^-$ wave is the bigger of the two s-channel terms in this energy range — this is shown in Table 8.3.

8.2.3   OTL t-channel + $5/2^+$ + 1 additional s-channel Wave

Our initial s-channel scans showed that the $J^P = 5/2^+$ provided the best single s-channel wave fit in the energy range 1.85 GeV $< \sqrt{s} < 2$ GeV. Following the same approach used in the previous section, we now want to add an additional free s-channel wave to this fit. Figures 8.6(c) and (d) show the goodness-of-fit quantities for all additional waves with $J \leq 7/2$ for 1.8 GeV $< \sqrt{s} < 2.2$ GeV. For $\sqrt{s} < 2$ GeV, the fit with an additional $J^P = 3/2^-$ wave is clearly the best — this is simply the result obtained in the previous section. For $\sqrt{s} > 2.1$ GeV, the best fit is obtained when adding the $J^P = 7/2^-$ wave. For all of these fits, the contribution extracted for the $J^P = 5/2^+$ wave is the bigger of the two s-channel terms in the energy range 1.85 GeV $< \sqrt{s} < 2$ GeV — this is shown in Table 8.4.

	J^P						
	$1/2^-$	$1/2^+$	$3/2^+$	$3/2^-$	$5/2^-$	$7/2^-$	$7/2^+$
Dominant $5/2^+$?	$\checkmark$	$\checkmark$	$\checkmark$	$\checkmark$	$\checkmark$	$\checkmark$	$\checkmark$

Table 8.4: For fits with locked OTL t-channel and a free $5/2^+$ plus one additional J^P in s-channel, the extracted contribution for the $5/2^+$ wave is the bigger of the two s-channel terms in the energy range 1.85 GeV $< \sqrt{s} < 2$ GeV for all J^P.
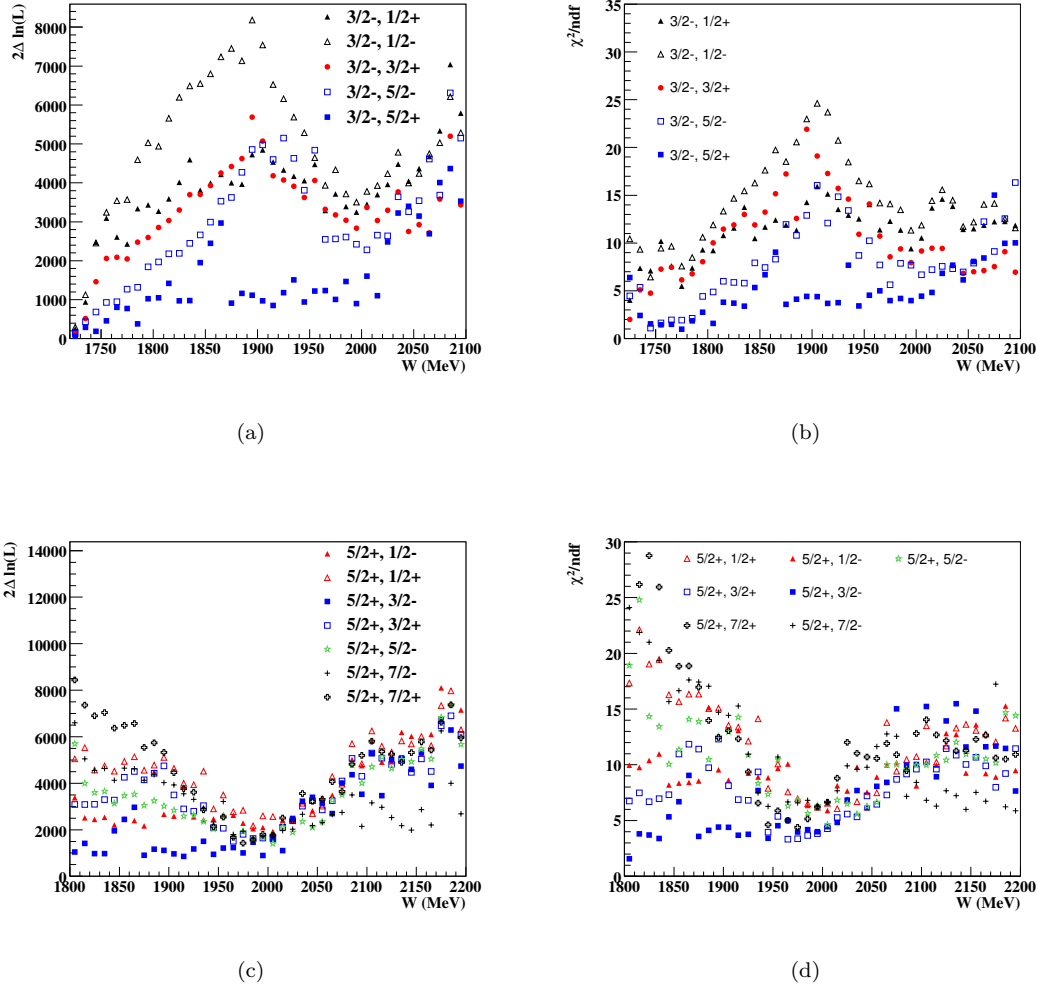
Figure 8.6: Goodness-of-Fit vs center-of-mass energy for fits with locked OTL t-channel and two free s-channel waves. (a) $-2\left(\ln L - \ln L_{mother}\right)$ vs. $W(\text{MeV})$: Likelihood difference between fits with a $3/2^-$ plus another J^P and the *Mother* fit in each $\sqrt{s}$ bin. (b) χ^2/ndf vs $W(\text{MeV})$ for the same fits in (a). The χ^2 was obtained in the same manner used in Figure 8.5. (c) Same as (a) except for fits with a $5/2^+$ plus another J^P. (d) Same as (b) except for fits with a $5/2^+$ plus another J^P.

8.3   Fit I (1.72 GeV $< \sqrt{s} < 2$ GeV)

In the previous section, we found that in the energy range 1.72 GeV $< \sqrt{s} < 2$ GeV the best fit with two s-channel waves is obtained using $J^P = 3/2^-, 5/2^+$. To extract any possible resonance contributions in these waves, we begin by assuming that each J^P is dominated by a single N^* state in this small energy range. This assumption permits us to fix the decay couplings to be independent of the center-of-mass energy $\sqrt{s}$, providing stability in the fits from bin to bin. The preliminary s-channel scans discussed above did not show any strong evidence (multiple bumps in σ) for multiple N^* states in either of the waves used in this fit. We can further justify this assumption by citing the small energy range in which we are fitting.

To implement this physics at fit time, we must make a slight modification to the parameters used in the *Mother* fit:

$$A^{fit}_{\gamma p \to J^P \to p\omega} = g^{J^P}_{LS} f_{MP}(\theta_{J^P}(s)) r_{J^P}(s) e^{i\phi_{J^P}(s)} A_{J^P, MP, L, S, m_i, m_\gamma, m_f}, \tag{8.4}$$

where $g^{J^P}_{LS}$ are the decay coupling constants, $r_{J^P}(s)$ and $\phi_{J^P}(s)$ are the magnitude and phase of the wave's *mass-dependence* and

$$f_{MP}(\theta_{J^P}(s)) = \left\{ \begin{array}{ll} \cos\theta_{J^P}(s), & \text{for electric multipoles} \\ \sin\theta_{J^P}(s), & \text{for magnetic multipoles} \end{array} \right\}, \tag{8.5}$$

handles the multipole production couplings (discussed below). In all fits using these parameters, the starting values were obtained pseudo-randomly in the range $(0, 2\pi)$ for angles and $(-1000, 1000)$ for couplings. No bin tracking was used.

The first step towards extracting resonance contributions is to fit, in parallel, all of the energy bins with $\sqrt{s} < 2$ GeV using the parameters described in (8.4). In this fit, the decay couplings $g^{J^P}_{L,S}$ are forced to be independent of s while all other parameters are free to vary from bin to bin. The results of this fit could be used to extract the cross sections and phase motion; however, there is one more constraint, imposed by the single-state assumption, which can be enforced to improve bin to bin stability.

8.3.1   Multipole Parameters

In Section 6.6.2, we showed that two of the Lorentz invariant amplitudes obtained for each $\gamma p N^*$ vertex are not *angularly-independent*. They only differ by an energy factor and are impossible to distinguish in a single narrow $\sqrt{s}$ bin. Thus, we chose to write our amplitudes using the multipole basis where we ignore the *extra* Lorentz invariant amplitudes. This choice was motivated by our use of the mass-independent PWA fitting technique and not physics. On purely physical grounds, there is no reason to exclude any of these amplitudes.

In terms of our fit parameters, this means that we can not assume that the θ_{J^P}'s are constants; however, we can derive the functional form of their energy dependence using the relation

$$\cos\theta_{J^P}(s) A^{J^P}_E + \sin\theta_{J^P}(s) A^{J^P}_M = \alpha A^{J^P}_1 + \beta A^{J^P}_2 + \gamma A^{J^P}_3, \tag{8.6}$$

where $A^{J^P}_{E(M)}$ are the electric(magnetic) multipole amplitudes used in the fits and $A^{J^P}_i$ are the three Lorentz invariant amplitudes with couplings α, β, γ which are independent of s. For the parity chain $P = (-)^{J-1/2}$, (8.6) can be rewritten as

$$\cos\theta_{J^P}(s) A^{J^P}_E + \sin\theta_{J^P}(s) A^{J^P}_M = \left(\alpha + \frac{\beta}{E^2_{\gamma CM}} \right) A^{J^P}_E + \gamma A^{J^P}_M. \tag{8.7}$$

(a)   (b)
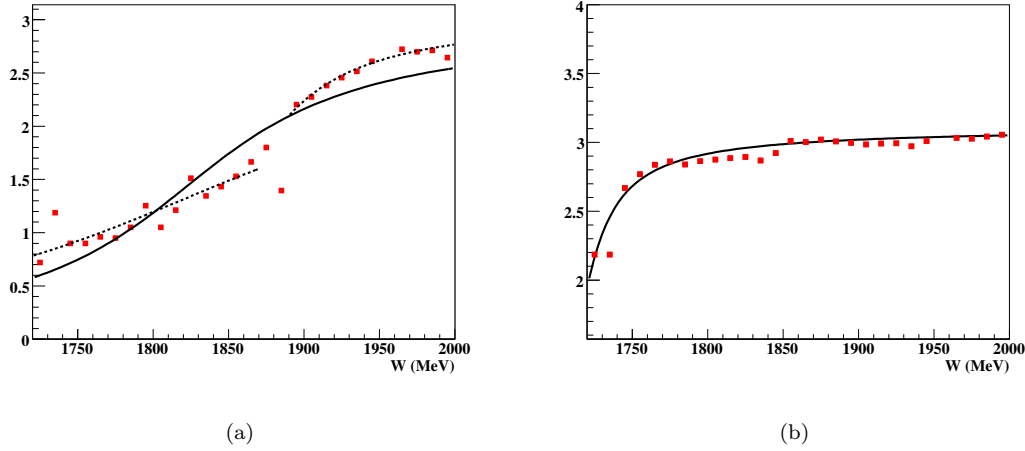
Figure 8.7: Multipole production fit parameters from Fit I: (a) $\theta_{3/2^-}$ vs W(MeV): The lines represent fits to (8.9). The solid line was fit to the entire energy range, while the dotted lines were fit to sub-ranges. See text for details. (b) $\theta_{5/2^+}$ vs W(MeV): Notation the same as in (a).

Thus, the ratio of magnetic to electric couplings is given by

$$\tan\theta_{J^P}(s) = \frac{\gamma}{\alpha + \beta/E^2_{\gamma CM}}, \tag{8.8}$$

which yields

$$\theta_{J^P}(s) = \tan^{-1}\frac{\gamma}{\alpha + \beta/E^2_{\gamma CM}}. \tag{8.9}$$

If our single-state assumption is valid, then the extracted multipole production parameters θ_{J^P} should have the s dependence given in (8.9).

Figure 8.7 shows the values obtained for $\theta_{3/2^-}$ and $\theta_{5/2^+}$ vs $\sqrt{s}$ from the fit discussed at the end of the previous section. The agreement with (8.9) is quite good. For the $3/2^-$ case, the fit over the entire energy range is decent; however, fits to sub-ranges of the energy are much better. Possible explanations include the presence of two resonances or overlap with a process (resonant or non-resonant) not included in the fit. We have seen some evidence for the existence of a second $3/2^-$ state near $\sqrt{s} \sim 2.1$ GeV; however, it is not conclusive. We chose to use the fit to the lower sub-range. It is at these energies where the $3/2^-$ wave was the most significant in the preliminary s-channel scans. The disagreement of the multipole parameters extracted at higher energies with the fit to the lower region (for whatever reason(s)) will have no effect on the conclusions we will draw regarding these waves. For the $5/2^+$ wave, the fit to (8.9) over the entire energy range is in excellent agreement with the values extracted from the PWA fits.

The agreement of the extracted values for θ_{J^P} with (8.9) provides us with preliminary evidence for the presence of resonance contributions. If these waves were simply mocking up some process(es) not included in the fits, then it is unlikely that the multipole production parameters would agree so well with (8.9). Of course, to conclusively prove the existence of resonance contributions we need to examine the cross sections and phase motion of the waves.

8.3.2 Cross Sections and Phase Motion

In the previous sections, we ran a fit coupling all bins with $\sqrt{s} < 2$ GeV to obtain the values of the decay couplings. We then fit the extracted multipole production parameters θ_{JP} to (8.9), which allows us to lock these values in each $\sqrt{s}$ bin. The only remaining variable parameters are $r_{JP}(s)$ and $\phi_{JP}(s)$, which are free to take on any value in each $\sqrt{s}$ bin. Figures 8.8 and 8.9 show the cross sections and phase motion obtained from these fits. The error bars on $\Delta\phi$ are purely statistical, obtained from MINUIT. The error bars on the extracted cross sections include the MINUIT uncertainties, along with the statistical uncertainties related to yield extraction (signal-background separation, see Section 3.9). Systematic uncertainties in the yield extraction and normalization are not included in this plot. Estimating systematic errors in the partial wave analysis technique is discussed in the *Future Work* section at the end of this chapter.

The cross sections extracted for the *s*-channel waves are consistent with either near or sub-threshold resonance states. The PDG lists two states consistent with this hypothesis. The $F_{15}(1680)$ is a very well known **** state. Its Breit-Wigner parameters are quoted as $M_{F_{15}} = 1680 - 1690$ MeV and $\Gamma_{F_{15}} = 120 - 140$ MeV. This state also has a very large **** photo-coupling of $0.21 - 0.32\%$. The $D_{13}(1700)$ is a *** state that is not as well known due to its relatively weak coupling to $N\pi$. Its Breit-Wigner parameters are quoted as $M_{D_{13}} = 1650 - 1750$ MeV and $\Gamma_{D_{13}} = 50 - 150$ MeV. This state is currently listed as having a relatively weak ** photo-coupling of $0.01 - 0.05\%$. At first glance, it would appear that the cross section extracted for the $5/2^+$ wave is too wide to be the $F_{15}(1680)$; however, near threshold this state is suppressed both by phase space and because its lowest orbital angular momentum (in both the initial and final states) is $L = 1$ resulting in (at least) a factor of $E_{CM}^{\gamma} p_{CM}^{\omega}$ in its amplitudes. Therefore, the cross sections extracted for this wave from our PWA are not inconsistent with the $F_{15}(1680)$.

Figure 8.9 shows the phase motion between these two waves in this energy range. The dashed line shows a fit using constant width Breit-Wigner line shapes of the form

$$BW(s) = \frac{m\Gamma}{s - m^2 + im\Gamma}, \tag{8.10}$$

while requiring all of the parameters to be within the limits quoted by the PDG for the $F_{15}(1680)$ and $D_{13}(1700)$. The results obtained were $M_{5/2^+} = 1680$ MeV, $\Gamma_{5/2^+} = 140$ MeV, $M_{3/2^-} = 1750$ MeV and $\Gamma_{3/2^-} = 50$ MeV The agreement is quite good. The only discrepancies are in the first few bins above threshold and in the region near $\sqrt{s} \sim 1.85$ GeV. The $F_{15}(1680)$ Breit-Wigner parameters are very well known; however, there is more uncertainty concerning the $D_{13}(1700)$. The solid line was fit allowing the $3/2^-$ parameters to vary freely, while the $5/2^+$ parameters were still constrained to be within the PDG limits. The fit yielded $M_{3/2^-} = 1754$ MeV and $\Gamma_{3/2^-} = 39$ MeV, which are very close the PDG values.

Allowing the $3/2^-$ parameters to deviate slightly from the PDG values removes the discrepancy near threshold. The only remaining region where the phase motion does not match the $F_{15}(1680)/D_{13}(1700)$ hypothesis is near $\sqrt{s} \sim 1.85$ GeV. There are a number of possible explanations for this. The most likely of which is that a process (resonant or non-resonant) which contributes at these energies is not included in Fit I. If this were the case, the waves included in the fit could deviate from their true parameters in an attempt to account for the missing wave(s). Another possibility is the existence of a second resonance state in either of these partial waves near this energy, which couples weakly to $p\omega$ making it difficult to see in the cross sections but noticeable in the phase motion. At this stage, we can not make any strong statements regarding this discrepancy.

Regardless of the reason for the small discrepancy in the phase motion near $\sqrt{s} \sim 1.85$ GeV, the cross sections and phase motion shown in Figures 8.8 and 8.9 provide very strong evidence for
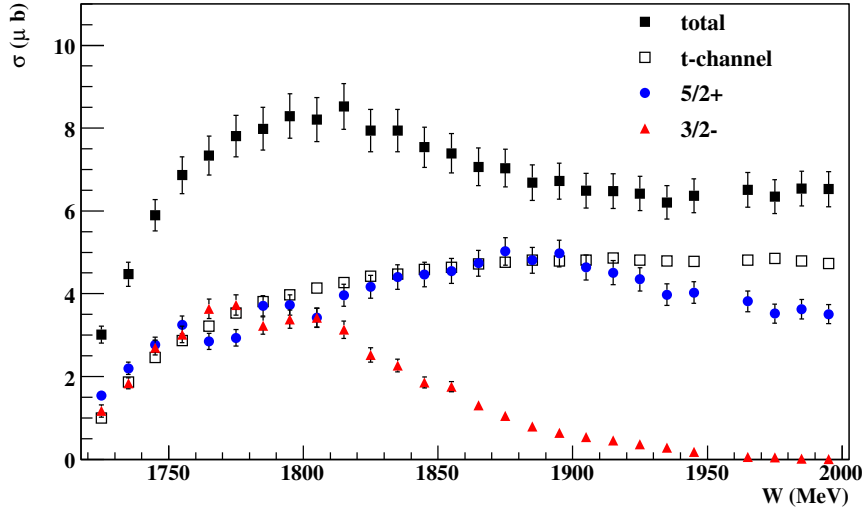
Figure 8.8: Results from Fit I: $\sigma(\mu b)$ vs W(MeV): Cross sections from all of the waves included in the fit (filled squares), only t-channel waves (open squares), only $J^P = 5/2^+$ waves (circles) and only $J^P = 3/2^-$ waves (triangles). The cross sections extracted for both s-channel waves are consistent with near/sub-threshold resonances. The error bars are discussed in the text.
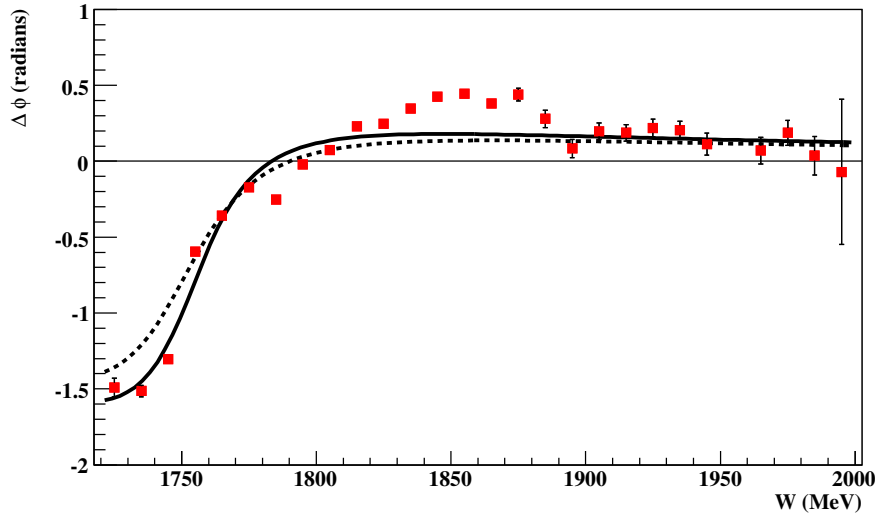
Figure 8.9: Results from Fit I: $\Delta\phi = \phi_{3/2^-} - \phi_{5/2^+}$(radians) vs W(MeV): The dashed line was fit using constant width Breit-Wigner's requiring the parameters to be within the limits quoted by the PDG for the **** $F_{15}(1680)$ and *** $D_{13}(1700)$. The results obtained were $M_{5/2^+} = 1680$ MeV, $\Gamma_{5/2^+} = 140$ MeV, $M_{3/2^-} = 1750$ MeV and $\Gamma_{3/2^-} = 50$ MeV. The solid line was fit allowing the $3/2^-$ parameters to vary freely yielding $M_{3/2^-} = 1754$ MeV and $\Gamma_{3/2^-} = 39$ MeV. The error bars are purely statistical, obtained from MINUIT.

(a)   (b)
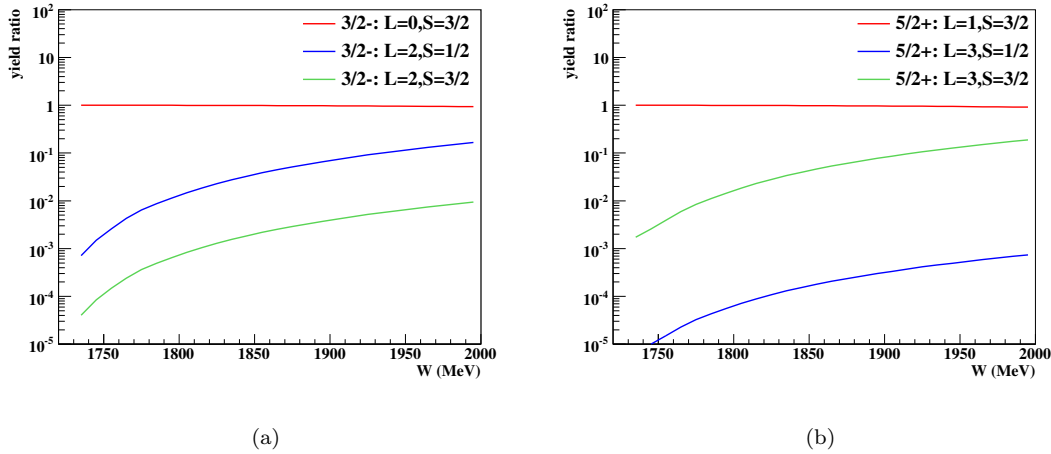
Figure 8.10: L, S Contributions using $g_{LS}^{J^P}$'s from Fit I: (a) $\sigma_{3/2^-}^{LS}/\sigma_{3/2^-}$ vs W(MeV): Ratio of yields obtained from individual LS decay amplitudes to the total yield for $3/2^-$ waves. (b) $\sigma_{5/2^+}^{LS}/\sigma_{5/2^+}$ vs W(MeV): Ratio of yields obtained from individual LS decay amplitudes to the total yield for $5/2^+$ waves.

the presence of contributions from the **** $F_{15}(1680)$ and *** $D_{13}(1700)$ in ω photoproduction. The phase motion is particularly convincing. Recall that the phase parameters, $\phi_{3/2^-}$ and $\phi_{5/2^+}$, were each started pseudo-randomly in the range $(0, 2\pi)$ in each $\sqrt{s}$ bin — no bin tracking was used. Yet the results trace out almost exactly the phase motion expected, using simple constant width Breit-Wigner's, of the PDG $F_{15}(1680)$ and $D_{13}(1700)$ states; thus, we conclude that these states are present in our data.

8.3.3   Validity of Assumptions

Recall that to improve bin to bin stability in the fits, we assumed that each s-channel wave was dominated by a single N^* state. The results of the previous section would seem to validate this. Though it is still possible that multiple states exist and contribute in either (or both) of these waves, the dominant contributions are clearly from the $F_{15}(1680)$ and $D_{13}(1700)$ states. In some models, the width of a resonance is written as a function of both s and L. The mass-dependent parameters, $r_{J^P}(s)$ and $\phi_{J^P}(s)$, used in our fits do not depend on the orbital angular momentum. This raises the question as to whether more freedom is needed in Fit I. Figure 8.10 shows the ratios of the contributions of the various L, S decays to the total contribution for each J^P. Over most of the energy range of Fit I, each J^P is dominated by the decay with the lowest orbital angular momentum; thus, any dependence on L will be safely absorbed into the parameters $r_{J^P}(s)$ and $\phi_{J^P}(s)$. If there is L-dependence in the width of the resonances, it would have a small effect on the resonance parameters extracted by fitting the phase motion in Figure 8.9; however, this would not have any impact on the conclusion that the states which we have observed are the PDG **** $F_{15}(1680)$ and *** $D_{13}(1700)$ resonances.

8.3.4 Comparison to Observables

Fit I is a very simple fit containing only locked Oh, Titov and Lee t-channel, along with $J^P = 3/2^-$ and $J^P = 5/2^+$ s-channel waves. At these energies, the OTL model is dominated by π^0 exchange. In the previous sections, we detailed our approach to extracting the PDG $F_{15}(1680)$ and $D_{13}(1700)$ states. Therefore, the final version of Fit I basically consists of only three tree-level processes. This is almost certainly not all of the physics contributing to ω photoproduction in this energy range. Thus, we would not expect Fit I to provide a perfect description of our data. Before we examine the quality of Fit I, we note that the OTL t-channel terms do a good job describing our forward data in the energy regime of Fit I.

Figure 8.11 shows the physics observables $d\sigma/d\cos\theta_{CM}^\omega$ (differential cross section) and $\rho_{MM'}^0$ (spin density matrix elements) projected out of Fit I compared to our measurements in two $\sqrt{s}$ bins. The agreement is remarkable given the small number of waves present in the fit. In the $\sqrt{s} = 1.8$ GeV bin, the $F_{15}(1680)$ and $D_{13}(1700)$ contributions are approximately equivalent in size. The differential cross section projected out of Fit I intersects the error bars on 15 of the 16 points we measured in this bin, with the only outlier being the backwards most point. The spin density matrix elements are also described excellently by Fit I, especially in the forward direction. There is some slight disagreement with the off-diagonal elements in the backwards direction but this is minor. The three processes included in Fit I provide an excellent description of all available $\gamma p \rightarrow p\omega$ observables at $\sqrt{s} = 1.8$ GeV. It is possible that the small discrepancies in the backwards direction are due to the lack of any u-channel terms in Fit I. This could be investigated further once improved u-channel models are available.

Figure 8.11(c) shows the comparison between our $d\sigma/d\cos\theta_{CM}^\omega$ measurements and the projection obtained from Fit I at $\sqrt{s} = 1.9$ GeV. At this energy, the $D_{13}(1700)$ contribution is very small, leaving mostly just the $F_{15}(1680)$ and t-channel π^0 exchange. The agreement in this bin is not quite as good as in the $\sqrt{s} = 1.8$ GeV bin; however, it is still very good. The Fit I projection intersects the error bars on 15 of the 17 measurements in this bin. As in the lower energy bin, the only discrepancy is in the backwards most points. Figure 8.11(d) shows the comparison between our $\rho_{MM'}^0$ measurements and the projections obtained from Fit I in the $\sqrt{s} = 1.9$ GeV bin. Again, the agreement in this bin is not quite as good as in the $\sqrt{s} = 1.8$ GeV bin, but it is still very good considering the small number of waves used in the fit. As in the lower energy bin, the agreement is good in the forward direction but develops a minor discrepancy in the off-diagonal elements in the backward direction. As noted above, it is possible that these small discrepancies in the backwards direction are due to the lack of any u-channel terms included in Fit I. Improved u-channel models would be required to test this hypothesis.

It would appear that there is some process present in the data which is not included in Fit I. This process becomes more important as the energy increases, leading to the slightly larger discrepancies in the $\sqrt{s} = 1.9$ GeV bin. In Section 8.5, we will offer one possibility for the identity of this process. For now we will focus on how well Fit I reproduces our measurements. This fit represents about the simplest physics model that can be constructed. Though we did not start off by including known PDG resonance states, the fit has clearly extracted them from our data. The end result is that Fit I consists solely of the **** $F_{15}(1680)$ and *** $D_{13}(1700)$ resonant states in s-channel and the Oh, Titov and Lee t-channel model, which in the energy regime of Fit I is dominated by π^0 exchange. These simple tree level processes are able to almost completely reproduce our data for $\sqrt{s} < 2$ GeV. This is a truly remarkable result. We conclude this comparison by noting that the large angle cross section at $\sqrt{s} = 1.8$ GeV is virtually flat. Without polarization information, the production mechanism could have easily been mistaken for a $J = 1/2$ wave. This demonstrates the importance of the spin density matrix element measurements.

(a)

(b)

(c)

(d)
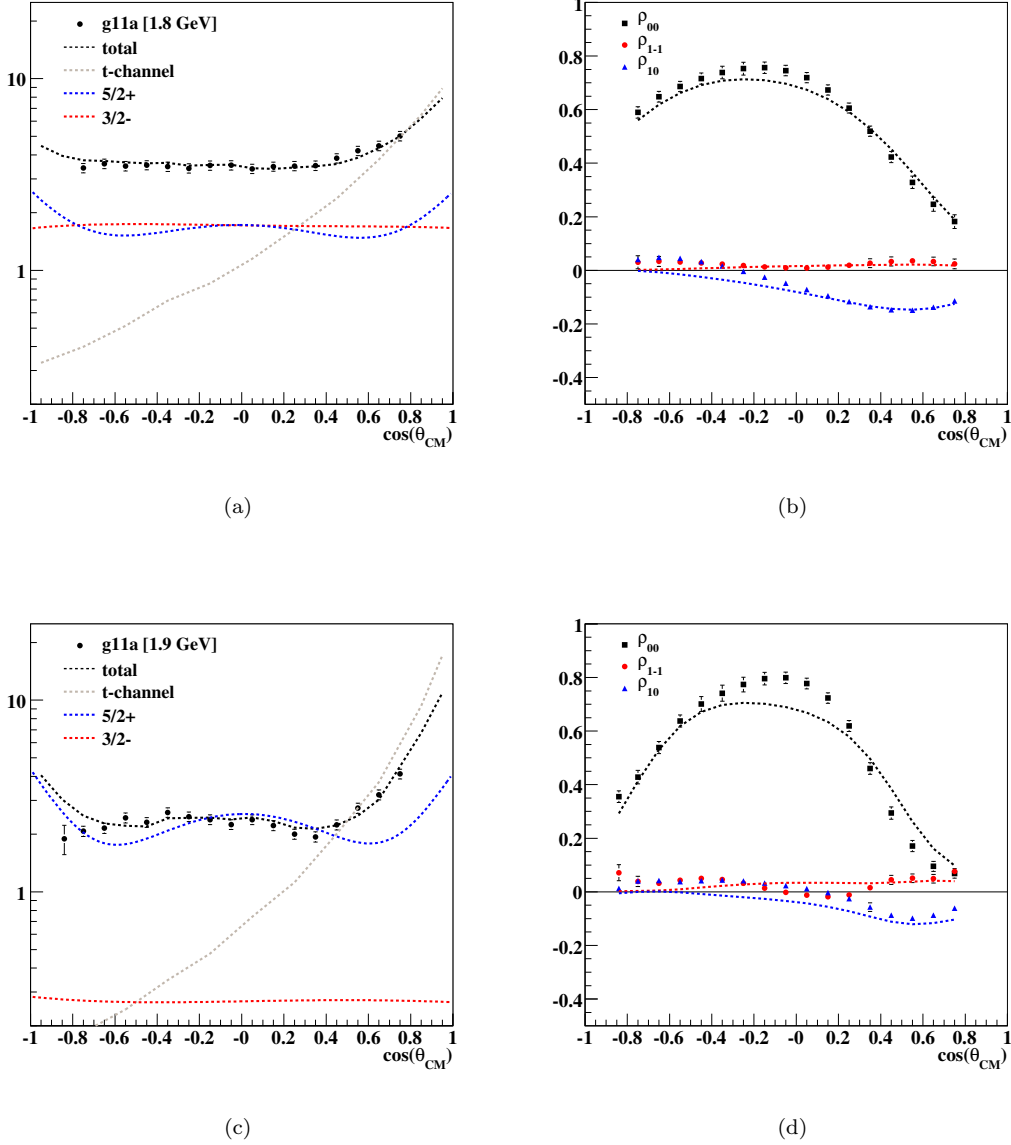
Figure 8.11: Comparisons of Fit I to Observables: (a) $d\sigma/d\cos\theta_{CM}^{\omega}(\mu b)$ vs $\cos\theta_{CM}^{\omega}$: Differential cross sections, projected out of the final version of Fit I, compared to our measurements made in the $\sqrt{s} = 1.8$ GeV bin. (b) $\rho_{MM'}^{0}$ vs $\cos\theta_{CM}^{\omega}$: Spin density matrix elements from Fit I compared to our measurements at $\sqrt{s} = 1.8$ GeV. (c) $d\sigma/d\cos\theta_{CM}^{\omega}(\mu b)$ vs $\cos\theta_{CM}^{\omega}$: Differential cross sections projected out of Fit I compared to our measurements at $\sqrt{s} = 1.9$ GeV. (d) $\rho_{MM'}^{0}$ vs $\cos\theta_{CM}^{\omega}$: Spin density matrix elements projected out of Fit I compared to our measurements at $\sqrt{s} = 1.9$ GeV. Given the small number of waves included in Fit I, the agreement is excellent.
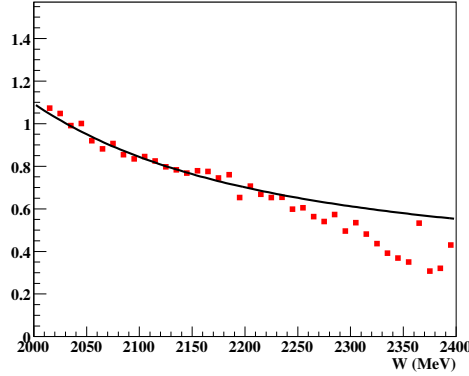
Figure 8.12: $\theta_{7/2^-}$ vs W(MeV): Multipole production parameter extracted for the $J^P = 7/2^-$ wave. The line represents a fit to (8.9).

8.4 Fit II (2 GeV < $\sqrt{s}$ < 2.4 GeV)

We now want to examine the energy range 2 GeV < $\sqrt{s}$ < 2.4 GeV. Our preliminary s-channel scans showed that the best fit with two s-channel waves in this energy range was obtained using $J^P = 5/2^+, 7/2^-$. As in the previous section, we will begin by assuming that each J^P is dominated by a single N^*. Therefore, in this fit we will use the same resonance parameterization used in Fit I. Furthermore, we will assume that the $J^P = 5/2^+$ state is the $F_{15}(1680)$ which was found to dominate the lower energy region examined in Fit I; therefore, the same L, S decay couplings and multipole production parameter used in Fit I, will also be used in this fit for the $J^P = 5/2^+$ wave.

As with Fit I, the first step towards extracting possible resonance contributions was to perform a coupled fit of all of the energy bins with 2 GeV < $\sqrt{s}$ < 2.4 GeV. As stated above, the $J^P = 5/2^+$ decay couplings and multipole production parameters are all locked to the values obtained in Fit I. The $J^P = 7/2^-$ decay couplings are forced to be independent of s, while all other parameters are free to vary from bin to bin. The $7/2^-$ wave belongs to the same parity chain as the $3/2^-$ and $5/2^+$. Thus, if the strength found in the $7/2^-$ wave is from resonance production, the s dependence of its multipole parameter should follow (8.9). Figure 8.12 shows the values obtained for $\theta_{7/2^-}$ vs $\sqrt{s}$ from this fit. The agreement with (8.9) is excellent for $\sqrt{s}$ < 2.25 GeV. Above these energies, our confidence in the non-resonant terms used in Fit II diminishes rapidly. This is a plausible explanation for the $\sqrt{s}$ > 2.25 GeV discrepancy. Overall, the agreement is good and the results of this fit will be used to lock the values of $\theta_{7/2^-}$ in each $\sqrt{s}$ bin in the next stage of Fit II.

8.4.1 Cross Sections and Phase Motion

The only remaining variable parameters are $r_{J^P}(s)$ and $\phi_{J^P}(s)$, which are free to take on any value in each $\sqrt{s}$ bin. Figures 8.13 and 8.14 show the cross sections and phase motion obtained from this fit. As in Fit I, the error bars on $\Delta\phi$ are purely statistical, obtained from MINUIT, while the cross section errors include the MINUIT and yield extraction uncertainties. The cross sections extracted for the $J^P = 5/2^+$ wave are consistent with the tail of the **** $F_{15}(1680)$ state found to dominate most of the energy region in Fit I. The $J^P = 7/2^-$ cross section is indicative of a fairly wide resonant state with a mass around 2.2 GeV. The PDG lists a state consistent with this hypothesis, the $G_{17}(2190)$ with Breit-Wigner parameters $M_{G_{17}} = 2100 - 2200$ GeV and $\Gamma_{G_{17}} = 300 - 700$ MeV. This
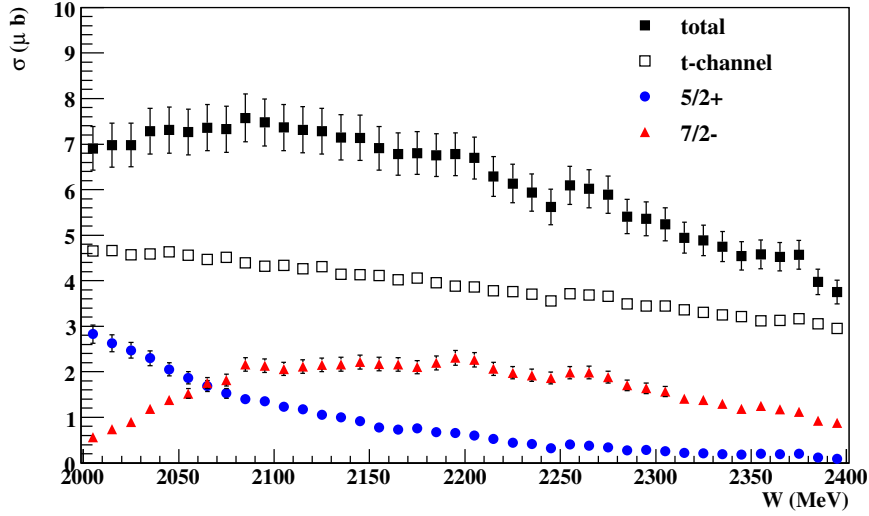
Figure 8.13: Results from Fit II: $\sigma(\mu b)$ vs $W(\text{MeV})$: Cross sections from all of the waves in the fit (filled squares), only t-channel waves (open squares), only $J^P = 5/2^+$ waves (circles) and only $J^P = 7/2^-$ waves (triangles). The cross section extracted for $J^P = 5/2^+$ is consistent with the tail of the $F_{15}(1680)$ state found in Fit I. The $J^P = 7/2^-$ is indicative of a state near 2.2 GeV. The errors are discussed in the text.
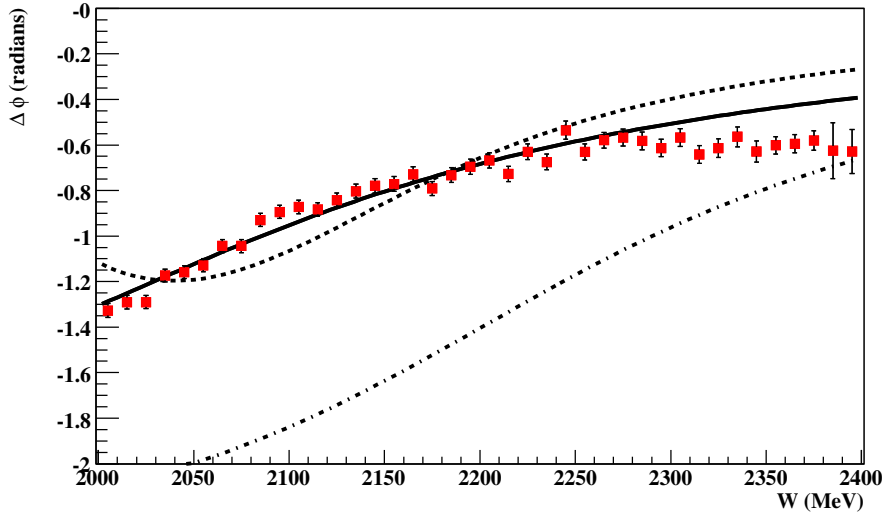
Figure 8.14: Results from Fit II: $\Delta\phi = \phi_{7/2^-} - \phi_{5/2^+}$ (radians) vs $W(\text{MeV})$: The dot-dashed line is the phase motion expected assuming constant width Breit-Wigner's and exactly the PDG parameters for the $F_{15}(1680)$ and $G_{17}(2190)$. The solid line used the $F_{15}(1680)$ PDG parameters but allowed the $7/2^-$ parameters to vary freely yielding $M_{7/2^-} = 1984$ MeV and $\Gamma_{7/2^-} = 468$ MeV. The dashed line forced the $7/2^-$ parameters to be within the PDG limits but allowed the $5/2^+$ parameters to vary yielding $M_{7/2^-} = 2100$ MeV, $\Gamma_{7/2^-} = 300$ MeV, $M_{5/2^+} = 1949$ MeV and $\Gamma_{5/2^+} = 174$ MeV.

state earned its **** rating from studies of $\pi N \to \pi N$ scattering experiments, little else is known about it. The photo-coupling is currently classified as having only a * rating.

Figure 8.14 shows the phase motion between the $5/2^+$ and $7/2^-$ from Fit II. The $F_{15}(1680)$, $G_{17}(2190)$ PDG parameters provide a decent qualitative description of the phase motion; however, the quantitative agreement is poor. Fitting with the $F_{15}(1680)$ PDG parameters locked but allowing the $J^P = 7/2^-$ parameters to vary freely produces a good fit. The width extracted for the $J^P = 7/2^-$ is within the PDG limits for the $G_{17}(2190)$, but the mass is about 100 MeV too low (and also inconsistent with the cross sections extracted for this wave). Fitting using the $G_{17}(2190)$ PDG parameters but allowing the $J^P = 5/2^+$ parameters to vary freely provides a fair description of the phase motion. The parameters extracted for the $J^P = 5/2^+$ are in good agreement with the *missing* $F_{15}(2000)$ state. Interpreting this result is non-trivial. It is possible that there is a second $5/2^+$ state which overlaps the $F_{15}(1680)$. If this is the case, the Breit-Wigner is not a proper description of the phase. The poor quality of the non-resonant terms, at these energies, may also be affecting the phase motion. For now, we can not definitively answer this; however, the behavior of the $J^P = 7/2^-$ cross section, along with the qualitative energy dependence of the phase motion is strong enough evidence to claim that the **** $G_{17}(2190)$ is most likely present in our data.

8.4.2 Validity of Assumptions

The single state assumption appears to be valid for the $7/2^-$ wave. There may be second $5/2^+$ state near 2 GeV. This makes the situation complicated. The single state assumption only applies to the decay and multipole couplings. In Fit I, (8.9) provided a good fit for $\theta_{5/2^+}$ over the entire energy range. Thus, it should still provide a good description of $\theta_{5/2^+}$ for most (if not all) of the energy range of Fit II. The $5/2^+$ decay couplings were fit over the entire energy range of Fit I. If a second state does exist near 2 GeV, then the Fit I decay couplings would incorporate both the $F_{15}(1680)$ and $F_{15}(2000)$ values. The single state assumption may not be valid for the $5/2^+$; however, it should not affect the (modest) claims made from Fit II.

We discussed in Section 8.3.3 that the resonant width may depend on the orbital angular momentum L. The mass dependent parameters used in Fit II, $r_{J^P}(s)$ and $\phi_{J^P}(s)$, did not depend on L. In Fit I, both of the resonant waves were dominated by a single L, S decay due to the proximity to $p\omega$ threshold. We concluded that no additional parameters were required. Figure 8.15 shows the ratio of individual L, S decay contributions to the total contribution for each J^P. At these energies, the $7/2^-$ is dominated by its lowest orbital angular momentum decay; however, the $5/2^+$ has comparable contributions from two separate L, S decays. Thus, it is possible that more freedom is needed in Fit II. We could rerun the fit with the additional parameters, but a model would be required to interpret the results. There is also the possible complication of overlapping $5/2^+$ states, which would also need to be interpreted within a model.

8.4.3 Comparison to Observables

Fit II is a simple fit containing locked OTL t-channel, along with $J^P = 5/2^+$ and $J^P = 7/2^-$ s-channel waves. At these energies, the OTL model is mostly dominated by π^0 exchange; however, at the highest energies in this fit the Pomeron exchange starts to become significant. In the previous sections, we detailed our approach to extracting (most likely) the $F_{15}(1680)$ and $G_{17}(2190)$ states. Therefore, the final version of Fit II is made up of only four tree level processes. In this energy range, there is almost certainly more — possibly a lot more — physics contributing to ω photoproduction. Also, we have shown in Section 8.1.1 that the OTL non-resonant terms do not provide a perfect description of the data at these energies. Because of these facts, we do not expect Fit II to provide as good a description of our data as Fit I.

(a)   (b)
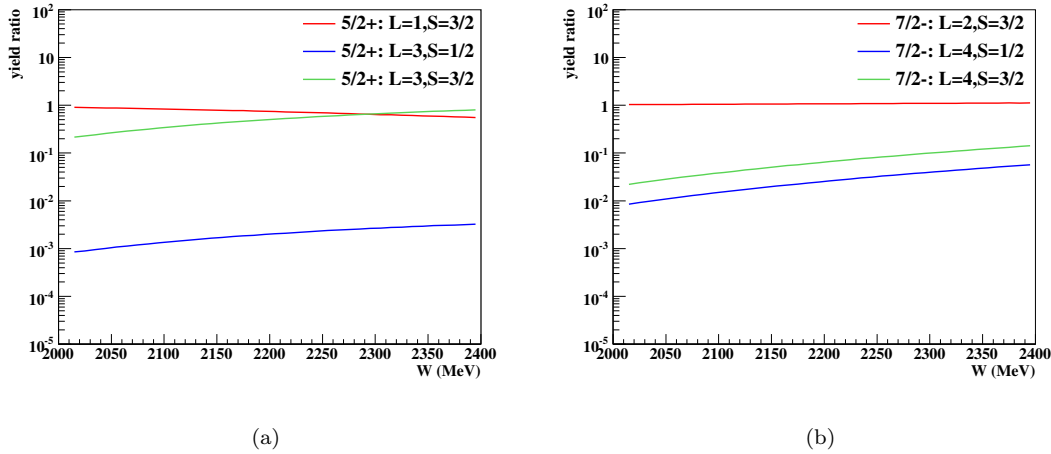
Figure 8.15: L, S Contributions using $g_{LS}^{J^P}$'s from Fit II:: (a) $\sigma_{5/2^+}^{LS}/\sigma_{5/2^+}$ vs $W(\mathrm{MeV})$: Ratio of yields obtained from individual LS decay amplitudes to the total yield for $5/2^+$ waves. (b) $\sigma_{7/2^-}^{LS}/\sigma_{7/2^-}$ vs $W(\mathrm{MeV})$: Same as (a) but for $7/2^-$ waves.

Figure 8.16 shows the observables $d\sigma/d\cos\theta_{CM}^\omega$ and $\rho_{MM'}^0$ projected out of Fit II compared to our measurements in two $\sqrt{s}$ bins. The agreement is good given the small number of waves included in the fit and the concerns regarding the quality of the non-resonant terms. In the $\sqrt{s} = 2.1$ GeV bin, the contributions from the $J^P = 5/2^+$ and $J^P = 7/2^-$ states are approximately the same size. The differential cross section is reproduced quite well. The only real discrepancy is the backwards most point. In this same bin, the spin density matrix elements ρ_{00}^0 and ρ_{1-1}^0 are described reasonably well. The remaining element, $Re(\rho_{10}^0)$, shows some discrepancies in the transverse direction. Overall, Fit II provides reasonably good agreement in this energy bin.

Figure 8.16(c) shows the comparison between our $d\sigma/d\cos\theta_{CM}^\omega$ measurements and the projections obtained from Fit II at $\sqrt{s} = 2.3$ GeV. In this bin, the $J^P = 7/2^-$ contribution is much larger than that of the $J^P = 5/2^+$. The description of the differential cross section is excellent at this energy. Figure 8.16(d) shows the comparison between our $\rho_{MM'}^0$ measurements and the projections obtained from Fit II in the same energy bin. The discrepancies in the forward direction are much larger than in the $\sqrt{s} = 2.1$ GeV bin. This is mostly due to the poor quality of the t-channel model. The off-diagonal elements of the spin density matrix also show fairly poor agreement in the backward direction. This could be caused by the lack of u-channel waves included in Fit II. In the transverse direction, the off-diagonal elements do a fairly decent job describing the data.

Given the small number of waves included in Fit II and the known issues with the non-resonant terms, the fit does a good job reproducing our measurements in this energy range. It is also highly probable that production mechanisms not included in Fit II do contribute to ω photoproduction at these energies. The $J^P = 5/2^+$ wave extracted from Fit II is consistent with the tail of the **** $F_{15}(1680)$ observed at lower energies in Fit I (but may also include a $F_{15}(2000)$ contribution). This fit has also yielded fairly strong, though not conclusive, evidence for the presence of the **** $G_{17}(2190)$. To prove this state contributes to ω photoproduction, and to extract resonance parameters, a better understanding of the non-resonant processes in this energy range is required.

(a)

(b)

(c)

(d)
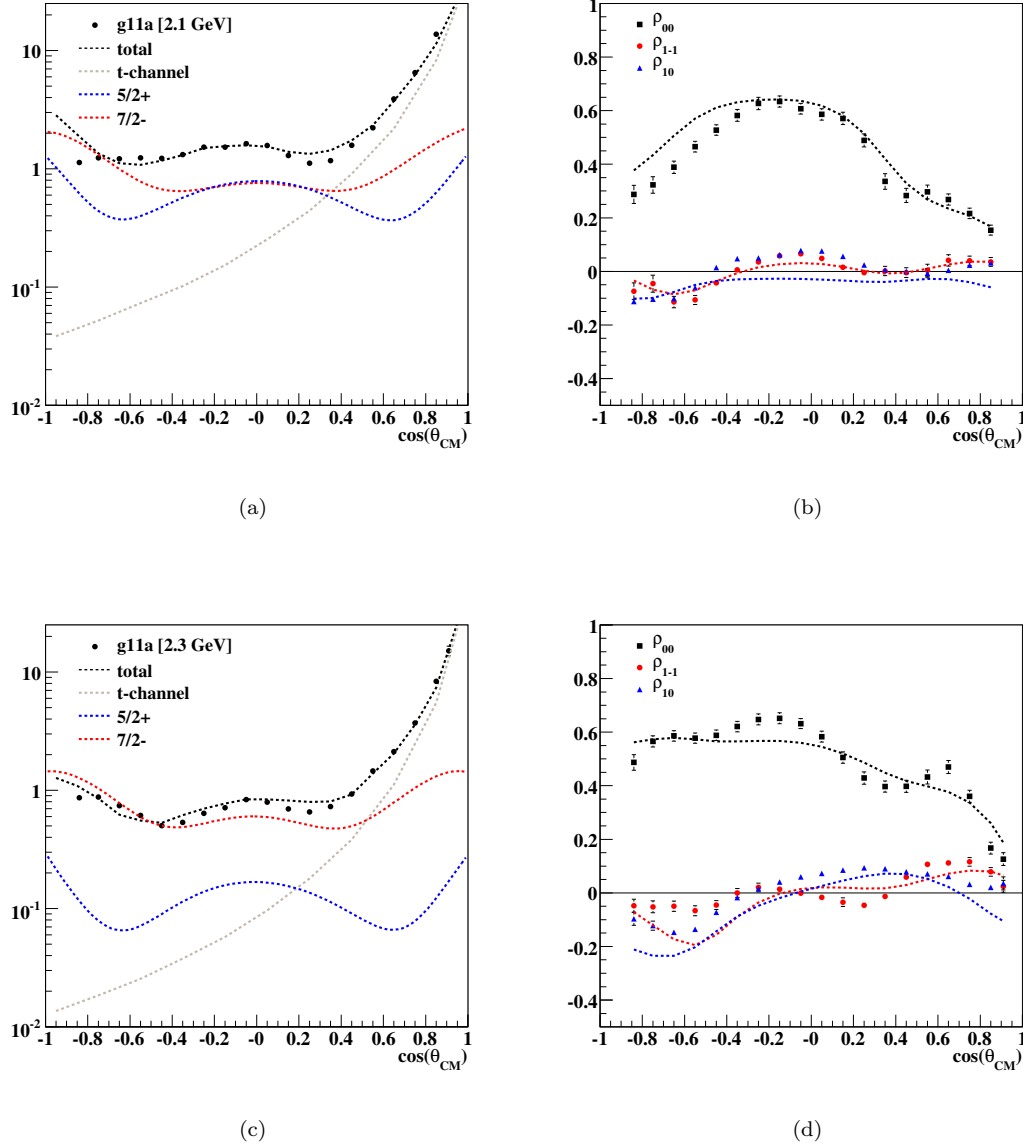
Figure 8.16: Comparisons of Fit II to Observables: (a) $d\sigma/d\cos\theta^\omega_{CM}(\mu b)$ vs $\cos\theta^\omega_{CM}$: Differential cross sections, projected out of the final version of Fit II, compared to our measurements made in the $\sqrt{s} = 2.1$ GeV bin. (b) $\rho^0_{MM'}$ vs $\cos\theta^\omega_{CM}$: Spin density matrix elements from Fit II compared to our measurements at $\sqrt{s} = 2.1$ GeV. (c) $d\sigma/d\cos\theta^\omega_{CM}(\mu b)$ vs $\cos\theta^\omega_{CM}$: Differential cross sections projected out of Fit II compared to our measurements at $\sqrt{s} = 2.3$ GeV. (d) $\rho^0_{MM'}$ vs $\cos\theta^\omega_{CM}$: Spin density matrix elements projected out of Fit II compared to our measurements at $\sqrt{s} = 2.3$ GeV. Given the small number of waves included in Fit II, and the known issues with the non-resonant terms at these energies, the agreement is good.

8.5   Evidence for Additional Resonance States

In the previous sections, the energy ranges 1.72 GeV $< \sqrt{s} <$ 2 GeV and 2 GeV $< \sqrt{s} <$ 2.4 GeV were fit and the dominant resonant contributions were found to come from the $F_{15}(1680)$, $D_{13}(1700)$ and (most likely) the $G_{17}(2190)$. All of these states have either a **** or *** rating from the PDG. One of the motivating factors for undertaking this study was to search for *missing resonances*, states predicted by the Constituent Quark Model (CQM) which have not been seen in other final states. Though the dominant waves extracted so far have all been known resonances, this does not exclude the possibility that other states contribute to ω photoproduction. The CQM calculations [16] predict that there are four resonant states with $J^P = 3/2^+$ near $\sqrt{s} \sim 1.9$ GeV which couple strongly to $p\omega$. In this section, we will attempt to test this prediction.

8.5.1   Fit III (1.72 GeV $< \sqrt{s} <$ 2 GeV)

This fit is simply Fit I with an additional $J^P = 3/2^+$ wave included. The decay couplings $g_{LS}^{J^P}$ and multipole parameters θ_{J^P} from Fit I for the $J^P = 3/2^-, 5/2^+$ states were kept locked. The first step in Fit III was to run a fit coupling all of the bins in the range 1.85 GeV $< \sqrt{s} <$ 1.95 GeV to obtain the decay couplings and multipole parameter for the $J^P = 3/2^+$ wave. We again employed the *single-state* assumption for the $3/2^+$. The CQM predicts four states in this small energy range. If this prediction is accurate, then the single-state assumption would simply result in Fit III using the average decay couplings of the various $J^P = 3/2^+$ resonances. To first order, this approximation should be sufficient.

Figure 8.17 shows the cross sections and phase motion extracted from Fit III. The cross sections of the $J^P = 3/2^-, 5/2^+$ resonant states are nearly identical to what was obtained from Fit I. The cross section of the $J^P = 3/2^+$ wave does show some fairly smooth structure. The phase motion of the $J^P = 3/2^+$ wave, relative to the other two resonant states, is not consistent with a single constant width Breit-Wigner hypothesis for the $3/2^+$. To test whether the phase motion is consistent with the CQM model predictions, we would need to employ a model to handle the propagators of four overlapping states. For now, we can conclude that our data shows evidence for a production mechanism which strongly overlaps the $J^P = 3/2^+$ partial wave. The cross sections and phase motion obtained for this wave are smoothly varying; however, they do not agree well with the hypothesis of a single resonant state.

8.5.2   Limitations of the Model-Independent Technique

Numerous other fits run in the energy bins near $\sqrt{s} \sim 2$ GeV have yielded inconclusive evidence for states of various J^P's. These fits are very similar to Fit III. Generally, smooth structures are found in the extracted cross sections; however, the phase motion is inconsistent with a single resonant state. It is possible that a number of resonant states exist which couple relatively strongly to $p\omega$ at these energies. It is also possible that the smooth cross sections are simply the result of overlap of various partial waves with unaccounted for non-resonant terms. It would appear that we have reached the limits of what our model independent technique can extract from our data.

In the spring of 2007, ω photoproduction data were taken with the CLAS detector using linearly polarized photons. The coherent peak in the photon beam was located in the energy regime discussed above. If there are more resonances which couple to $p\omega$ at these energies, the additional polarization information may help extract them; however, if there truly are multiple overlapping states with the same quantum numbers contributing, then extracting these states in a model independent way may be impossible. More discussion on this topic can be found in the *Future Work* section at the end of this chapter.
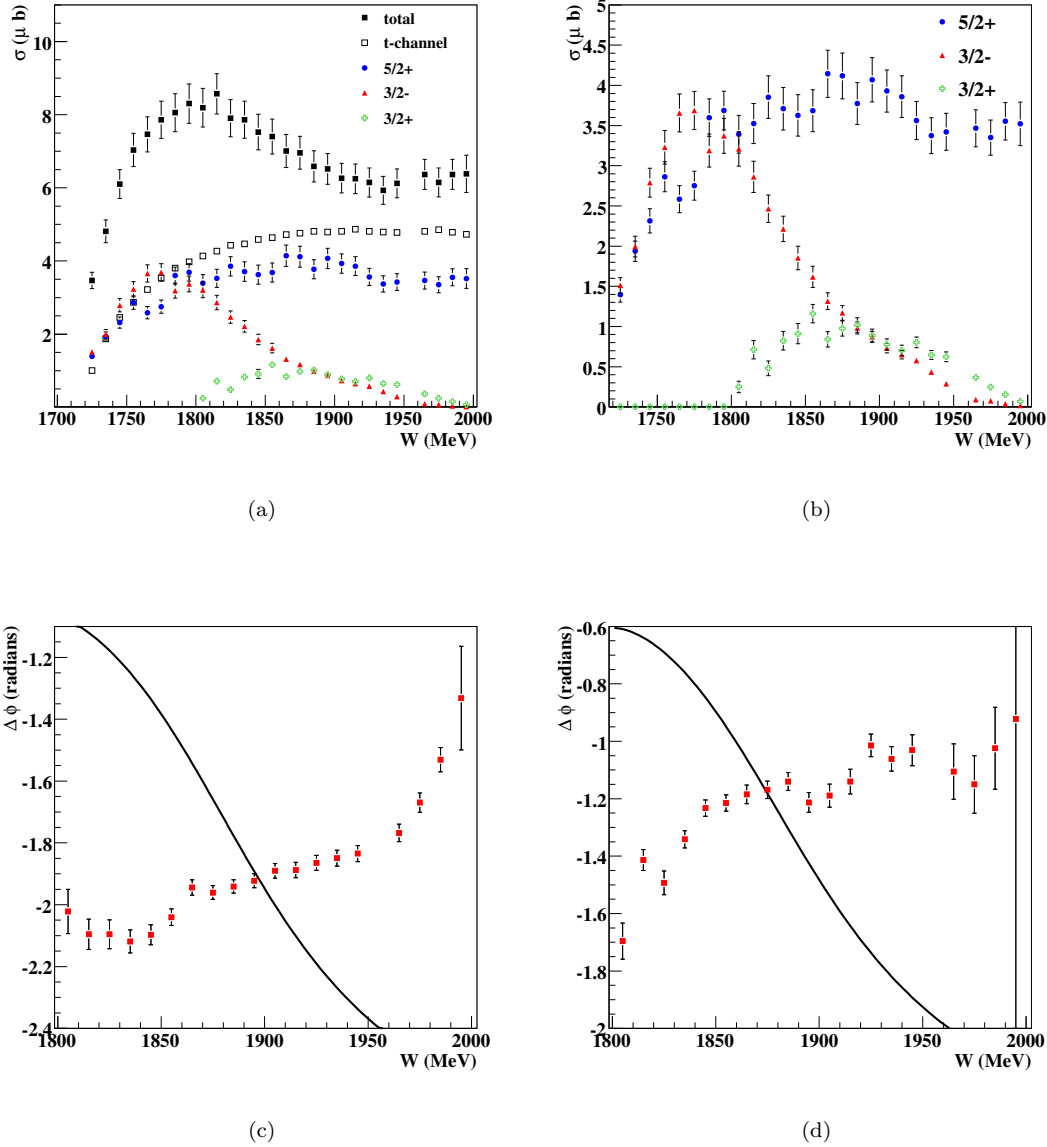
Figure 8.17: Results from Fit III: (a) $\sigma(\mu b)$ vs $W(\text{MeV})$: Cross sections extracted from all of the waves in the fit (filled squares), only t-channel waves (open squares), only $5/2^+$ waves (circles), only $3/2^-$ waves (triangles) and only $3/2^+$ waves (crosses). The errors bars were obtained as in Fit I and II. (b) Same as (a) with only the resonant waves. (c) $\Delta\phi = \phi_{5/2^+} - \phi_{3/2^+}(\text{radians})$ vs $W(\text{MeV})$. (d) $\Delta\phi = \phi_{3/2^-} - \phi_{3/2^+}(\text{radians})$ vs $W(\text{MeV})$. The error bars on both $\Delta\phi$ plots are purely statistical, obtained from MINUIT. The curves show the phase motion expected assuming the $J^P = 3/2^+$ has Breit-Wigner parameters $M_{3/2^+} = 1875$ MeV and $\Gamma_{3/2^+} = 150$ MeV while locking the $J^P = 3/2^-$ and $J^P = 5/2^+$ parameters to be those of the $D_{13}(1700)$ and $F_{15}(1680)$ respectively. The phase motion obtained for the $3/2^+$ is not consistent with a single resonant state.

(a)   (b)
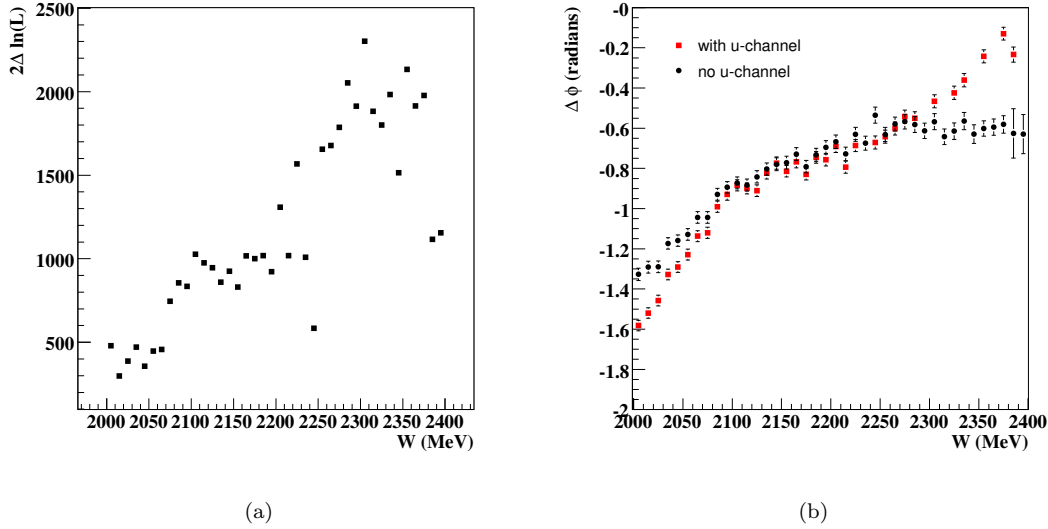
Figure 8.18: Fit II $+u$-channel: (a) $-2(\ln L_u - \ln L_{no-u})$ vs W(MeV): Likelihood difference obtained by adding u-channel terms to Fit II. The fit run without u-channel is better in all energy bins. (b) $\Delta\phi = \phi_{7/2^-} - \phi_{5/2^+}$(radians) vs W(MeV): Phase motion obtained with and without u-channel terms in Fit II. Including u-channel terms only creates discrepancies in the phase motion where one of the s-channel waves has a small contribution to the cross section. The error bars on both phase motion plots are purely statistical, obtained from MINUIT.

8.6   Including u-channel Diagrams

For $\sqrt{s} < 2$ GeV, any u-channel contribution must be small due to the lack of any peak in the backwards cross section. Thus, the conclusions drawn from Fit I are independent of whether or not u-channel terms are included. The same can not be said for the energy regime of Fit II. In Section 8.1.1, we were able to modify the u-channel parameters of the Oh, Titov and Lee model to better describe our highest energy data; however, these amplitudes were not included in our PWA fits due to a lack of confidence in the assumptions used to obtain the parameters.

Figure 8.18(a) shows the likelihood difference obtained by adding the modified OTL u-channel terms to Fit II. The version of the fit run without u-channel amplitudes is better in every $\sqrt{s}$ bin. Perhaps this isn't surprising since the modified OTL terms were obtained assuming the entire backwards production amplitude is u-channel. To obtain a better u-channel model, the OTL parameters should be fit including s-channel waves; however, to simply estimate the effects of neglecting u-channel terms in Fit II, these parameters are sufficient. Figure 8.18(b) shows the phase motion obtained from Fit II with and without u-channel amplitudes. The agreement is very good in the region where both of the s-channel waves have strong contributions to the cross section. It is only in the regions where the cross section of one of the s-channel terms is very small that including u-channel terms leads to a discrepancy in the extracted phase motion. Therefore, the conclusions drawn from Fit II regarding the $J^P = 7/2^-$ state are robust against how the u-channel terms are modeled.

8.7   Conclusions and Future Work

Though much work has been done in the past on ω photoproduction, the lack of detailed polarization measurements in most kinematic regions made it difficult to determine the nature of the production mechanisms. With our spin density matrix measurements, we can provide the first real test of the available theoretical models. We began this chapter by examining non-resonant production mechanisms. At lower energies, there is general agreement that at forward angles the dominant process is t-channel π^0 exchange. Our work provides strong confirmation of this hypothesis. At extremely high energies, ω photoproduction is known to be dominated by diffractive processes. These are generally modeled as Pomeron exchange. The high energy models can be projected down to our energy regime and combined with the π^0 exchange amplitude to obtain a good description of the forward cross section over a fairly large energy range; however, these models do not agree well with our highest energy polarization measurements at forward angles. This suggests that more work needs to be done to understand the forward production mechanisms at intermediate energies.

At our highest energies, the cross section also has a backwards peak. Previous models have described this as u-channel nucleon exchange. There are various prescriptions of this process which have been employed, all of which are capable of reproducing the backwards cross section. To obtain a good description of the spin density matrix elements in the backwards direction, we found that the magnetic coupling at the ωNN vertex κ_ω, must be allowed to vary (previous meson exchange models almost unanimously set this quantity to zero). Implicit in these models is an assumption that the backwards production mechanism, at our highest energies, is dominated by u-channel processes. It is possible that resonance terms play an important role here. More work needs to be done to determine the validity of this assumption. Until then, little confidence should be placed on the values of the u-channel parameters extracted using these models.

The primary goal of our partial wave analysis was to extract the dominant resonance contributions to ω photoproduction. Using the mass-independent technique, we have extracted very strong evidence for the presence of both the **** $F_{15}(1680)$ and *** $D_{13}(1700)$ states in the near-threshold region. The cross sections and phase motion extracted for the $J^P = 3/2^-$ and $J^P = 5/2^+$ partial waves are in excellent agreement with the $F_{15}(1680)/D_{13}(1700)$ hypothesis. It is our conclusion that these PDG states are present in our data. Furthermore, the ability of Fit I, which contains only the $F_{15}(1680)$ and $D_{13}(1700)$ s-channel amplitudes and the π^0 t-channel amplitude, to reproduce both our $d\sigma/d\cos\theta_{CM}^\omega$ and $\rho_{MM'}^0$ measurements for $\sqrt{s} < 2$ GeV is truly remarkable. It is also important to note that the large angle cross section for $\sqrt{s} < 1.85$ GeV is virtually flat. Without polarization information, the production mechanism could easily be mistaken for a $J = 1/2$ wave. This demonstrates the importance of the $\rho_{MM'}^0$ measurements.

At higher energies, we have found fairly strong evidence for the presence of the **** $G_{17}(2190)$ resonance. The cross sections extracted for the $J^P = 7/2^-$ partial wave are in excellent agreement with this hypothesis. The phase motion shows the same qualitative behavior as what would be expected from the $G_{17}(2190)$; however, there are quantitative discrepancies. It is possible that a second $J^P = 5/2^+$ state exists near 2 GeV. This would affect our interpretation of the phase motion. It is also possible that this disagreement is caused by the uncertainties in the non-resonant terms at these energies. Until a better understanding of the non-resonant processes is available, we can only speculate as to whether this is the case. For now, the cross sections and phase motion extracted for the $J^P = 7/2^-$ partial wave provide strong enough evidence to claim that the $G_{17}(2190)$ is most likely present in our data. As for the $F_{15}(2000)$, we do not have sufficient evidence at this time to make any strong claims about this state. If this state is present in our data, a model may be required to extract it.

The dominant resonances found in Fit I and Fit II were all states with either a **** or *** PDG rating. One of the motivating factors for performing this analysis was to search for new resonance states. In Fit III, we presented evidence for contributions from the $J^P = 3/2^+$ partial wave near $\sqrt{s} \sim 1.9$ GeV. The cross sections extracted for this wave are consistent with resonance production. The phase motion is smoothly varying; however, it is not consistent with what would be expected from a single N^* state. The Constituent Quark Model predicts there are four resonant states in this energy regime. Without a model to describe the mass dependence of these overlapping states, we can not confirm or deny whether the phase motion we have extracted is consistent with the CQM calculations. For now, the evidence for the presence of a $J^P = 3/2^+$ resonant state in our data is inconclusive. Similar evidence has been found for a number of other partial waves around $\sqrt{s} \sim 2$ GeV. Using only our unpolarized data, we are unable to make any conclusive statements about these partial waves.

In the spring of 2007, the CLAS collaboration collected ω photoproduction data using linearly polarized photons. The coherent peak of the photon beam is located near $\sqrt{s} \sim 2$ GeV. This additional polarization information could help separate the partial wave contributions at these energies; thus, any strong resonance contributions may be extractable. These measurements should be completed by the end of 2008. Of course, if the CQM is correct and there are multiple overlapping resonant states with the same quantum numbers that couple to γp and $p\omega$ in this energy regime, then it may not be possible to extract these states in a model-independent way. Hopefully, the additional information obtained from the linearly polarized photons used in the new CLAS experiment will be sufficient to remove any ambiguities in extracting the partial wave contributions. If this is the case and if improvements are made to the non-resonant models, then it may be possible to conclusively confirm or deny the CQM predictions.

Our work has also sparked interest from the Excited Baryon Analysis Center (EBAC) — a theory group at Jefferson Lab. EBAC is currently conducting coupled-channel analyses of meson production data. The goal of their work is to extract N^* parameters and to map out the quark-gluon substructure of nucleon resonances. The measurements presented in this thesis will provide a wealth of information for the EBAC theorists to interpret. Though their approach to extracting resonance parameters is very different from ours, the results obtained from our mass-independent partial wave analysis are also useful to EBAC. Our PWA results can provide EBAC with input and guidance for their analyses [74]. In the future, it would also be useful to incorporate the coupled-channel approach used by EBAC into our non-resonant terms to enforce unitarity.

It has been a little less than three years since the $g11a$ data were collected and calibrated by the CLAS collaboration. Since that time, a tremendous amount of work has been done (primarily at JLab, the INFN in Genova, Italy and here at CMU) to ensure that this dataset is of the highest possible quality. We have completed our differential cross section and spin density matrix element measurements using the $g11a$ dataset and are currently moving towards publishing these results. Tremendous progress has been made on our mass-independent partial wave analysis; however, some work still needs to be done prior to publication of this work. The error bars presented in this chapter did not include any systematic uncertainties of the mass-independent PWA technique itself. Studies need to be performed to quantify these uncertainties prior to releasing these results. Also, a final set of fits, similar to Fit III, for other partial waves must be decided upon. This involves determining which J^P contributions are significant enough to warrant confidence that the production amplitude does truly overlap the given wave. No claims of resonance production will be made concerning these partial waves; however, they should prove useful to theorists who can attempt to interpret their meaning. The collective work presented in this thesis will greatly advance the world's understanding of ω photoproduction and, in time, hopefully provide insight into the ever-elusive theory of Quantum Chromodynamics.

Bibliography

[1] M. Williams and C.A. Meyer. *Kinematic Fitting in CLAS*. CLAS Note 2003-017.

[2] S. Stepanyan et al. *Observation of an Exotic S=+1 Baryon in Exclusive Photoproduction from the Deuteron*. Phys. Rev. Lett. **91**, 252001 (2003).

[3] C. Meyer and M. Williams. *Kinematic Fitting The Reacton $\gamma d \to K^+ K^- p(n)$*. CLAS Analysis Note 2004-109.

[4] C. Meyer and M. Williams. *Fitting the g2a Data Set*. CLAS Analysis Note 2004-113.

[5] C.A. Meyer, M. Williams and R. Bradford. *Computing Invariant Masses and Missing Masses*. CLAS Note 2004-008.

[6] B. McKinnon et al. *Search for the θ^+ Pentaquark in the Reaction $\gamma d \to pK^- K^+ n$*. Phys. Rev. Lett. **96**, 212001 (2006).

[7] M. Williams, D. Applegate and C.A. Meyer. *Determining Momentum and Energy Corrections for g1c Using Kinematic Fitting*. CLAS Note 2004-017.

[8] D. Sober, H. Crannell and and F.J. Klein. *The Tagger Energy Scale: Interpreting the CMU Kinematic Fit Results*. CLAS Note 2004-019.

[9] D. Applegate, M. Bellis, Z. Krahn, C. Meyer and M. Williams. *A Detailed Study of the Sources of Systematic Errors in the CLAS g11 Data*. CLAS Note 2006-017.

[10] M. Williams, C.A. Meyer and M. Bellis. *Probabilistic Event Weighting to Separate Signal from Background*. CLAS Note 2007-013.

[11] W.-M. Yao et al. *Review of Particle Physics*. J. Phys. G **33**, 1 (2006).

[12] F. Halzen and A. D. Martin. *Quarks and Leptons*. John Wiley and Sons, New York, 1984.

[13] S. Capstick and W. Roberts. *$N\pi$ decays of baryons in a relativized model*. Phys. Rev. D **47**, 1994-2010 (1993).

[14] D.B. Lichtenberg, L.J. Tassie and P.J. Keleman. *Quark-Diquark Model of Baryons and SU(6)*. Phys. Rev. **167**, 1535-1542 (1968).

[15] R. Koniuk and N. Isgur. *Baryon decays in a quark model with chromodynamics*. Phys. Rev. D **21**, 1868-1886 (1980).

[16] S. Capstick. *Quark models of baryon masses and decays*. nucl-th/0011082 (2000).

[17] J. Bulava, R. Edwards, G. Fleming, K.J. Juge, A.C. Lichtl, N. Mathur, C. Morningstar, D. Richards, S.J. Wallace. *Hadronic Resonances from Lattice QCD*. arXiv:0708.2072v2 (2007).

[18] A.C. Lichtl. Private Communication (2007).

[19] Adam C. Lichtl. *Quantum Operator Design for Lattice Baryon Spectroscopy.* Ph.D. thesis, Carnegie Mellon University, 2006. hep-lat/0609019.

[20] M. Pichowsky, C. Savkli and F. Tabakin. *Polarization observables in vector meson photoproduction.* Phys. Rev. C **53**, 593-610 (1996).

[21] F.J. Klein. Ph.D. Thesis, Bonn Universtiy, 1996

[22] M. Battaglieri et al. *Photoproduction of the ω Meson on the Proton at Large Momentum Transfer.* Phys. Rev. Lett. **90**, 022002 (2003).

[23] J. Barth et al. *Low-energy photoproduction of ω-mesons.* Eur. Phys. J. A **18**, 117 (2003).

[24] J. Ballam et al. *Vector-Meson Production by Polarized Photons at 2.8, 4.7, and 9.3 GeV.* Phys. Rev. D **7**, 3150 (1973).

[25] D.P. Barber et al. *A Study Of The Reactions Gamma P to Omega P And Gamma P to Omega Delta+.* Z. Phys. C **26**, 343 (1984).

[26] R.W. Clift et al. *Observation of a baryon exchange dip and parton effects in backward photoproduction of ω.* Phys. Lett. B**72**, 144 (1977).

[27] Q. Zhao. *Nucleonic resonance excitations with linearly polarized photons in $\gamma p \rightarrow \omega p$.* Phys. Rev. C **63**, 025203 (2001)

[28] Y. Oh, A.I. Titov and T.S.H. Lee. *Nucleon resonances in ω photoproduction.* Phys. Rev. C **63** (2001).

[29] A.I. Titov and T.S.H. Lee. *Effective Lagrangian approach to the ω photoproduction near threshold.* Phys. Rev. C **66**, 015204 (2002)

[30] G. Penner and U. Mosel. *Vector meson production and nucleon resonance analysis in a coupled-channel approach for energies $m_N < \sqrt{s} < 2\,GeV$. II. Photon-induced results.* Phys. Rev. C **66**, 055212 (2002).

[31] V. Shklyar, H. Lenske, U. Mosel, and G. Penner. *Coupled-channel analysis of ω-meson production in πN and γN reactions for c.m. energies up to 2 GeV.* Phys. Rev. C **71**, 055206 (2005).

[32] M. Battaglieri et al. *Spectroscopy of Exotic Baryons with CLAS: Search for ground and first excited states.* CLAS Analysis Proposal PR04-021.

[33] Jefferson Lab. *The JLab Picture Exchange*, `http://www1.jlab.org/ul/jpix`

[34] Jefferson Lab. `http://www.jlab.org/`

[35] B.M. Dumham. *Jefferson Lab, a status report.* Thomas Jefferson National Accelerator Facility, 1997.

[36] S. Gagnon. *Jefferson Lab Site Tour*, `http://education.jlab.org/sitetour/guidedtour05.l.alt.html`

[37] D.I. Sober, et al. *The bremsstrahlung tagged photon beam in Hall B at JLab.* Nucl Inst Meth A **440**, 263 (2000).

[38] Jefferson Lab. *Experimental Hall B*, `http://www.jlab.org/Hall-B/`

[39] S. Christo. *The g11a Target Cell*, `http://www.jlab.org/~christo/g11a_target.html`

[40] Y.G. Sharabian et al. *A new highly segmented start counter for the CLAS detector.* Nucl. Phys. A **556**, 246 (2006).

[41] Alan J. Street et al. *Final site assembly and testing of the superconducting toroidal magnet for the CEBAF Larege Acceptance Spectrometer (CLAS).* IEEE Trans. Mag. **32**, No. 4, 2074 (1996).

[42] M.D. Mestayer et al. *The CLAS drift chamber system.* Nucl Inst Meth A **449**, 81 (2000).

[43] D.S. Carman et al. *The Region One drift chamber for the CLAS spectrometer.* Nucl Inst Meth A **419**, 315 (1998).

[44] Y.M. Qin et al. *Prototype studies and design considerations for the CLAS Region Two drift chambers.* Nucl Inst Meth A **367**, 316 (1995).

[45] F.J. Barbosa, et al. *A drift chamber system for a toroidal detector.* Nucl Inst Meth A **323**, 19 (1992).

[46] E. Smith et al. *The time-of-flight system for CLAS.* Nucl Inst Meth A **432**, 265 (1999).

[47] J. Ball and E. Pasyuk. *Photon Flux Determination Through Sampling of "out-of-time" Hits with the Hall B Photon Tagger.* CLAS Note 2005-002.

[48] M. Battaglieri and R. De Vita. *The g11 Triggers efficiency.* Private Communication (2005).

[49] M. Ungaro, R. De Vita and L. Elouadrhiri. *g11 data processing.* CLAS Note 2005-014.

[50] Siegmund Brandt. *Statistical and Computational Methods in Data Analysis.* North Holland Publishing Company, 1970.

[51] A.G. Frodesen, O. Skjeggestad, and H. Tøfte. *Probablity and Statistics in Particle Physics.* Universitetsforlaget, 1979.

[52] J. McNabb. *Photoproduction of Λ and Σ^0 Hyperons off Protons in the Nucleon Resonance Region using CLAS at Jefferson Lab.* Ph.D. thesis, Carnegie Mellon University, 2002.

[53] E. Pasyuk. *The CLAS ELOSS Package.* Software available via the CLAS CVS repository under `clas/packages/utilities/eloss`.

[54] S. Stepanyan. *Evidence for an Exotic Pentaquark Baryon State $\Theta^+(1530)$, in the $\gamma\, d \rightarrow p\, K^+\, K^-\, n$ reaction.* CLAS Analysis Note 2003-105.

[55] V. Koubarovski. Private Communication.

[56] Donald H. Perkins. *Introduction to High Energy Physics.* 4th Edition, Cambridge University Press, 2000.

[57] G. Feldman and R. Cousins. *Unified approach to the classical statistical analysis of small signals.* Phys. Rev. D **57**, 3873 - 3889 (1998).

[58] M. Holtrop. *GSIM: CLAS GEANT Simulation*, `http://www.physics.unh.edu/maurik/Gsim/gsim_current_code_dev.shtml`

[59] R. Bradford and R.A. Schumacher. *Liquid Hydrogen Density in the G1C CLAS Cryotarget.* CLAS Note 2002-003.

[60] M. Battaglieri and R. De Vita. *Summary of g11 data.* Private Communication (2005).

[61] S.U. Chung. *Formulas for Partial Wave Analysis: Version II.* BNL preprint BNL-QGS-93-05 (1999).

[62] F. James. *MINUIT: Function Minimization and Error Analysis.* CERN Program Library D506 (1998).

[63] R. Fletcher and M.J.D. Powell. *A rapidly converging descent method for minimization.* Comput. J **6**, 163 (1963).

[64] W. Rarita and J. Schwinger. *On a Theory of Particles with Half-Integral Spin.* Phys. Rev. **60**, 61 (1941).

[65] S.U. Chung. *Spin Formalisms.* BNL preprint BNL-QGS-02-0900 (2004).

[66] M.E. Peskin and D.V. Schroeder. *An Introduction to Quantum Field Theory.* Westview Press, 1995.

[67] A.V. Anisovich, E. Klempt, A.V. Sarantsev and U Thoma. *Partial-wave decomposition of pion and photoproduction amplitudes.* Eur. Phys. J A **24**, 111-128 (2005).

[68] Charles Zemach. *Three-Pion Decays of Unstable Particles.* Phys. Rev. B **133**, 1201-1220 (1964).

[69] A. Sibirtsev, K. Tsushima and S. Krewald. *Omega photoproduction beyond the resonance region at small u.* arXiv:nucl-th/0202083.

[70] R. Schumacher. *Photon Attenuation in the CLAS Beam Line.* CLAS Note 2001-010.

[71] K. Schilling, P. Seyboth and G. Wolf. *On The Analysis of Vector-Meson Production By Polarized Photons.* Nucl. Phys. B **15**, 397 (1970).

[72] A. Donnachie and P.V. Landshoff. *Elastic scattering and diffraction dissociation.* Nuclear Physics B **244**, 322-336 (1984).

[73] C. Downum, T. Barnes, J.R. Stone and E.S. Swanson. *Nucleon meson coupling constants and form factors in the quark model.* Phys. Lett. B **638**, 455-460 (2006).

[74] M. Paris. Private Communication (2007).

Appendix A

$\omega \to \pi^+\pi^-\pi^0$ Decay Frames

The same notation first defined in Chapter 5 is also used here. The 4-momentum of the incident photon and ω meson in the overall center-of-mass frame are denoted as k and q respectively. All of our measurements are reported in the Adair frame. In this frame, the z-axis is chosen to be the direction of the photon in the overall CM frame. The y-axis is chosen to be the normal to the production plane. Thus, the coordinate system in the Adair frame is [71]

$$\hat{z} = \hat{k} \tag{A.1a}$$

$$\hat{y} = \frac{\vec{k} \times \vec{q}}{|\vec{k} \times \vec{q}|} \tag{A.1b}$$

$$\hat{x} = \hat{y} \times \hat{z}. \tag{A.1c}$$

The Helicity and Gottfried-Jackson frames differ from the Adair frame only in the choice of the z-axis. In the Helicity frame, the z-axis is chosen to be the direction of the ω in the overall CM frame, $\hat{q}$. In the Gottfried-Jackson system, the z-axis is chosen to be the direction of the photon in the ω rest frame. In all three systems, the decay angles are defined as

$$\cos\theta = \hat{\pi} \cdot \hat{z} \tag{A.2a}$$

$$\cos\phi = \frac{\hat{y} \cdot (\hat{z} \times \hat{\pi})}{|\hat{z} \times \hat{\pi}|} \tag{A.2b}$$

$$\sin\phi = -\frac{\hat{x} \cdot (\hat{z} \times \hat{\pi})}{|\hat{z} \times \hat{\pi}|}, \tag{A.2c}$$

where $\hat{\pi}$ is the normal to the $\omega \to \pi^+\pi^-\pi^0$ decay plane in the ω rest frame. The spin density matrix elements can easily be rotated amongst these three frames using [71]

$$\rho_{MM'}^{0_A} = \sum_{\mu\mu'} d_{M\mu}^1(-\alpha)\rho_{\mu'M'}^{0_B} d_{\mu'M'}^1(\alpha), \tag{A.3}$$

where A and B denote the frames and α is the angle that rotates $\hat{z}_B \to \hat{z}_A$ given by

$$\alpha = \sin^{-1}|\hat{z}_B \times \hat{z}_A|. \tag{A.4}$$

For example, the angle required to rotate the spin density matrix elements from the Helicity frame to the Adair frame is $\alpha = \sin^{-1}\hat{q} \times \hat{k} = -\theta_{CM}^\omega$.

Appendix B

Data Tables

B.1 $\frac{d\sigma}{d\cos\theta_{cm}^{\omega}}$ Measurements

$\sqrt{s}_{min}$ (GeV)	$\sqrt{s}_{max}$ (GeV)	$\cos\theta_{CM}^{\omega}$	$\frac{d\sigma}{d\cos\theta_{CM}^{\omega}}$ (μb)	σ_{stat} (μb)	σ_{sys} (μb)
1.72	1.73	-0.45	1.7069	0.0937	0.0795
1.72	1.73	-0.35	1.6655	0.0819	0.0775
1.72	1.73	-0.25	1.5941	0.0706	0.0742
1.72	1.73	-0.15	1.5279	0.0645	0.0711
1.72	1.73	-0.05	1.4140	0.0567	0.0658
1.72	1.73	0.05	1.5667	0.0596	0.0729
1.72	1.73	0.15	1.5576	0.0580	0.0725
1.72	1.73	0.25	1.6205	0.0596	0.0754
1.72	1.73	0.35	1.5468	0.0591	0.0720
1.72	1.73	0.45	1.6783	0.0669	0.0781
1.72	1.73	0.55	1.5988	0.0704	0.0744
1.72	1.73	0.65	1.6819	0.0805	0.0783
1.72	1.73	0.75	2.0032	0.1084	0.0932
1.73	1.74	-0.45	1.7230	0.0559	0.0805
1.73	1.74	-0.35	1.5503	0.0419	0.0725
1.73	1.74	-0.25	1.6210	0.0384	0.0758
1.73	1.74	-0.15	1.6832	0.0363	0.0787
1.73	1.74	-0.05	1.7931	0.0359	0.0838
1.73	1.74	0.05	1.9501	0.0378	0.0911
1.73	1.74	0.15	1.9636	0.0371	0.0918
1.73	1.74	0.25	2.1222	0.0394	0.0992
1.73	1.74	0.35	2.2134	0.0421	0.1034
1.73	1.74	0.45	2.2277	0.0443	0.1041
1.73	1.74	0.55	2.3546	0.0507	0.1100
1.73	1.74	0.65	2.3319	0.0571	0.1090
1.73	1.74	0.75	2.7077	0.0805	0.1265
1.74	1.75	-0.45	2.4378	0.0424	0.1144
1.74	1.75	-0.35	2.4114	0.0366	0.1131
1.74	1.75	-0.25	2.5621	0.0366	0.1202
1.74	1.75	-0.15	2.5310	0.0351	0.1188
1.74	1.75	-0.05	2.6902	0.0364	0.1262
1.74	1.75	0.05	2.7780	0.0371	0.1304
1.74	1.75	0.15	2.7033	0.0359	0.1268
1.74	1.75	0.25	2.7598	0.0368	0.1295
1.74	1.75	0.35	3.0018	0.0401	0.1409
1.74	1.75	0.45	2.9134	0.0400	0.1367
1.74	1.75	0.55	3.1613	0.0453	0.1483
1.74	1.75	0.65	3.2482	0.0489	0.1524
1.74	1.75	0.75	3.5852	0.0592	0.1682
1.75	1.76	-0.45	3.0056	0.0442	0.1416
1.75	1.76	-0.35	3.0783	0.0431	0.1450
1.75	1.76	-0.25	3.0137	0.0412	0.1420
1.75	1.76	-0.15	3.0554	0.0412	0.1439
1.75	1.76	-0.05	3.0021	0.0400	0.1414
1.75	1.76	0.05	3.1680	0.0416	0.1492
1.75	1.76	0.15	3.3760	0.0445	0.1590
1.75	1.76	0.25	3.3690	0.0444	0.1587
1.75	1.76	0.35	3.4893	0.0463	0.1644

1.75	1.76	0.45	3.4909	0.0480	0.1645
1.75	1.76	0.55	3.5878	0.0519	0.1690
1.75	1.76	0.65	3.7649	0.0540	0.1774
1.75	1.76	0.75	4.1668	0.0615	0.1963
1.76	1.77	-0.65	3.2756	0.0649	0.1549
1.76	1.77	-0.55	3.4274	0.0516	0.1621
1.76	1.77	-0.45	3.3000	0.0476	0.1561
1.76	1.77	-0.35	3.3795	0.0469	0.1599
1.76	1.77	-0.25	3.2579	0.0445	0.1541
1.76	1.77	-0.15	3.2656	0.0440	0.1545
1.76	1.77	-0.05	3.3502	0.0452	0.1585
1.76	1.77	0.05	3.6082	0.0478	0.1707
1.76	1.77	0.15	3.3975	0.0455	0.1607
1.76	1.77	0.25	3.7496	0.0495	0.1774
1.76	1.77	0.35	3.5835	0.0492	0.1695
1.76	1.77	0.45	3.4720	0.0498	0.1642
1.76	1.77	0.55	3.7416	0.0549	0.1770
1.76	1.77	0.65	4.1807	0.0597	0.1977
1.76	1.77	0.75	4.6748	0.0678	0.2211
1.77	1.78	-0.65	3.6086	0.0619	0.1714
1.77	1.78	-0.55	3.5182	0.0941	0.1671
1.77	1.78	-0.45	3.4599	0.1002	0.1643
1.77	1.78	-0.35	3.2359	0.0908	0.1537
1.77	1.78	-0.25	3.3552	0.0934	0.1593
1.77	1.78	-0.15	3.2449	0.0930	0.1541
1.77	1.78	-0.05	3.3421	0.0940	0.1587
1.77	1.78	0.05	3.4801	0.0988	0.1653
1.77	1.78	0.15	3.7074	0.1034	0.1761
1.77	1.78	0.25	3.4544	0.0966	0.1640
1.77	1.78	0.35	3.6982	0.1055	0.1756
1.77	1.78	0.45	3.8049	0.1161	0.1807
1.77	1.78	0.55	4.2141	0.1265	0.2001
1.77	1.78	0.65	4.4180	0.1301	0.2098
1.77	1.78	0.75	4.8395	0.1521	0.2298
1.78	1.79	-0.65	3.2677	0.0781	0.1558
1.78	1.79	-0.55	3.4374	0.0946	0.1639
1.78	1.79	-0.45	3.4816	0.0979	0.1660
1.78	1.79	-0.35	3.3252	0.0911	0.1585
1.78	1.79	-0.25	3.5149	0.0953	0.1676
1.78	1.79	-0.15	3.3772	0.0924	0.1610
1.78	1.79	-0.05	3.5167	0.0955	0.1677
1.78	1.79	0.05	3.4098	0.0943	0.1626
1.78	1.79	0.15	3.5881	0.0981	0.1711
1.78	1.79	0.25	3.5561	0.0958	0.1695
1.78	1.79	0.35	3.7560	0.1084	0.1791
1.78	1.79	0.45	3.9515	0.1173	0.1884
1.78	1.79	0.55	4.0158	0.1170	0.1915
1.78	1.79	0.65	4.4427	0.1314	0.2118
1.78	1.79	0.75	4.9499	0.1494	0.2360
1.79	1.80	-0.65	3.6825	0.1070	0.1763
1.79	1.80	-0.55	3.3620	0.0958	0.1609
1.79	1.80	-0.45	3.4841	0.0966	0.1668
1.79	1.80	-0.35	3.4254	0.0936	0.1640
1.79	1.80	-0.25	3.6095	0.0981	0.1728
1.79	1.80	-0.15	3.4659	0.0956	0.1659
1.79	1.80	-0.05	3.4971	0.0968	0.1674
1.79	1.80	0.05	3.6018	0.1002	0.1724
1.79	1.80	0.15	3.6048	0.0999	0.1725
1.79	1.80	0.25	3.5140	0.0992	0.1682
1.79	1.80	0.35	3.6140	0.1103	0.1730
1.79	1.80	0.45	3.8154	0.1128	0.1826
1.79	1.80	0.55	4.0819	0.1182	0.1954
1.79	1.80	0.65	4.5337	0.1378	0.2170
1.79	1.80	0.75	5.3540	0.1612	0.2563
1.80	1.81	-0.75	3.4162	0.0885	0.1642
1.80	1.81	-0.65	3.5986	0.1066	0.1729
1.80	1.81	-0.55	3.4972	0.1036	0.1681
1.80	1.81	-0.45	3.5376	0.1000	0.1700
1.80	1.81	-0.35	3.4756	0.0971	0.1670
1.80	1.81	-0.25	3.4044	0.0949	0.1636
1.80	1.81	-0.15	3.5235	0.0968	0.1693
1.80	1.81	-0.05	3.5354	0.0973	0.1699
1.80	1.81	0.05	3.3854	0.0950	0.1627
1.80	1.81	0.15	3.4783	0.0974	0.1672
1.80	1.81	0.25	3.5008	0.1011	0.1682
1.80	1.81	0.35	3.5191	0.1099	0.1691

1.80	1.81	0.45	3.8423	0.1123	0.1846
1.80	1.81	0.55	4.2028	0.1254	0.2020
1.80	1.81	0.65	4.4654	0.1403	0.2146
1.80	1.81	0.75	5.0214	0.1491	0.2413
1.81	1.82	-0.75	3.6032	0.0945	0.1738
1.81	1.82	-0.65	3.4868	0.1071	0.1682
1.81	1.82	-0.55	3.5225	0.1016	0.1699
1.81	1.82	-0.45	3.4664	0.0983	0.1672
1.81	1.82	-0.35	3.5058	0.0975	0.1691
1.81	1.82	-0.25	3.4516	0.0970	0.1665
1.81	1.82	-0.15	3.4394	0.0965	0.1659
1.81	1.82	-0.05	3.5882	0.1025	0.1731
1.81	1.82	0.05	3.3858	0.0960	0.1633
1.81	1.82	0.15	3.5382	0.0995	0.1707
1.81	1.82	0.25	3.4542	0.1070	0.1666
1.81	1.82	0.35	3.6974	0.1125	0.1784
1.81	1.82	0.45	3.7014	0.1093	0.1786
1.81	1.82	0.55	4.2293	0.1316	0.2040
1.81	1.82	0.65	4.6602	0.1464	0.2248
1.81	1.82	0.75	5.7089	0.1659	0.2754
1.82	1.83	-0.75	3.1757	0.0923	0.1538
1.82	1.83	-0.65	3.2047	0.0982	0.1552
1.82	1.83	-0.55	3.2415	0.0966	0.1570
1.82	1.83	-0.45	3.1994	0.0912	0.1550
1.82	1.83	-0.35	3.0950	0.0873	0.1499
1.82	1.83	-0.25	3.4372	0.0953	0.1665
1.82	1.83	-0.15	3.2645	0.0923	0.1581
1.82	1.83	-0.05	3.2519	0.0913	0.1575
1.82	1.83	0.05	3.1751	0.0913	0.1538
1.82	1.83	0.15	3.1183	0.0901	0.1510
1.82	1.83	0.25	2.9987	0.0960	0.1452
1.82	1.83	0.35	3.2050	0.0972	0.1552
1.82	1.83	0.45	3.5442	0.1082	0.1717
1.82	1.83	0.55	3.7225	0.1223	0.1803
1.82	1.83	0.65	4.3457	0.1340	0.2105
1.82	1.83	0.75	5.2880	0.1515	0.2561
1.83	1.84	-0.75	2.9857	0.0914	0.1452
1.83	1.84	-0.65	3.1755	0.0959	0.1544
1.83	1.84	-0.55	3.1884	0.0949	0.1550
1.83	1.84	-0.45	3.3064	0.0962	0.1608
1.83	1.84	-0.35	3.1167	0.0891	0.1516
1.83	1.84	-0.25	3.1940	0.0895	0.1553
1.83	1.84	-0.15	3.0919	0.0888	0.1503
1.83	1.84	-0.05	3.1494	0.0919	0.1531
1.83	1.84	0.05	3.1452	0.0917	0.1529
1.83	1.84	0.15	3.1927	0.0967	0.1552
1.83	1.84	0.25	3.1230	0.0985	0.1519
1.83	1.84	0.35	3.2277	0.0963	0.1569
1.83	1.84	0.45	3.2965	0.1032	0.1603
1.83	1.84	0.55	3.7618	0.1216	0.1829
1.83	1.84	0.65	4.4483	0.1351	0.2163
1.83	1.84	0.75	5.2872	0.1522	0.2571
1.84	1.85	-0.75	3.0106	0.0984	0.1470
1.84	1.85	-0.65	3.0173	0.0925	0.1473
1.84	1.85	-0.55	2.9804	0.0893	0.1455
1.84	1.85	-0.45	3.0980	0.0909	0.1512
1.84	1.85	-0.35	2.8837	0.0837	0.1408
1.84	1.85	-0.25	3.0103	0.0860	0.1470
1.84	1.85	-0.15	3.0160	0.0871	0.1472
1.84	1.85	-0.05	3.0710	0.0905	0.1499
1.84	1.85	0.05	2.9223	0.0865	0.1427
1.84	1.85	0.15	2.8855	0.0895	0.1409
1.84	1.85	0.25	2.7661	0.0879	0.1350
1.84	1.85	0.35	2.9133	0.0896	0.1422
1.84	1.85	0.45	3.1227	0.1019	0.1524
1.84	1.85	0.55	3.4136	0.1107	0.1666
1.84	1.85	0.65	4.1730	0.1245	0.2037
1.84	1.85	0.75	4.8874	0.1460	0.2386
1.85	1.86	-0.75	2.7423	0.0892	0.1344
1.85	1.86	-0.65	2.9145	0.0915	0.1428
1.85	1.86	-0.55	2.7623	0.0852	0.1354
1.85	1.86	-0.45	2.8320	0.0833	0.1388
1.85	1.86	-0.35	2.9177	0.0859	0.1430
1.85	1.86	-0.25	2.8394	0.0815	0.1391
1.85	1.86	-0.15	3.0957	0.0894	0.1517
1.85	1.86	-0.05	2.8372	0.0852	0.1390

1.85	1.86	0.05	2.9154	0.0849	0.1429
1.85	1.86	0.15	2.7866	0.0871	0.1366
1.85	1.86	0.25	2.8040	0.0893	0.1374
1.85	1.86	0.35	2.6977	0.0865	0.1322
1.85	1.86	0.45	2.9234	0.0989	0.1433
1.85	1.86	0.55	3.4669	0.1100	0.1699
1.85	1.86	0.65	4.3827	0.1326	0.2148
1.85	1.86	0.75	4.7371	0.1490	0.2321
1.86	1.87	-0.75	2.4385	0.0816	0.1200
1.86	1.87	-0.65	2.6678	0.0878	0.1312
1.86	1.87	-0.55	2.7812	0.0871	0.1368
1.86	1.87	-0.45	2.7967	0.0853	0.1376
1.86	1.87	-0.35	2.8592	0.0836	0.1407
1.86	1.87	-0.25	2.7745	0.0827	0.1365
1.86	1.87	-0.15	2.8108	0.0840	0.1383
1.86	1.87	-0.05	2.7919	0.0848	0.1374
1.86	1.87	0.05	2.6917	0.0819	0.1324
1.86	1.87	0.15	2.5825	0.0840	0.1271
1.86	1.87	0.25	2.5464	0.0820	0.1253
1.86	1.87	0.35	2.6720	0.0895	0.1315
1.86	1.87	0.45	2.7064	0.0922	0.1331
1.86	1.87	0.55	3.1658	0.1018	0.1557
1.86	1.87	0.65	3.8306	0.1172	0.1885
1.86	1.87	0.75	4.3700	0.1462	0.2150
1.87	1.88	-0.75	2.5266	0.0875	0.1248
1.87	1.88	-0.65	2.5764	0.0842	0.1272
1.87	1.88	-0.55	2.7494	0.0838	0.1358
1.87	1.88	-0.45	2.7371	0.0824	0.1352
1.87	1.88	-0.35	2.8060	0.0846	0.1386
1.87	1.88	-0.25	2.9821	0.0897	0.1473
1.87	1.88	-0.15	2.8386	0.0848	0.1402
1.87	1.88	-0.05	2.7596	0.0845	0.1363
1.87	1.88	0.05	2.5713	0.0791	0.1270
1.87	1.88	0.15	2.5215	0.0830	0.1245
1.87	1.88	0.25	2.6328	0.0835	0.1300
1.87	1.88	0.35	2.5137	0.0860	0.1241
1.87	1.88	0.45	2.5499	0.0865	0.1259
1.87	1.88	0.55	3.1143	0.0998	0.1538
1.87	1.88	0.65	3.8797	0.1236	0.1916
1.87	1.88	0.75	4.2360	0.1445	0.2092
1.88	1.89	-0.75	2.3908	0.0801	0.1185
1.88	1.89	-0.65	2.3592	0.0769	0.1170
1.88	1.89	-0.55	2.6497	0.0813	0.1314
1.88	1.89	-0.45	2.4863	0.0753	0.1233
1.88	1.89	-0.35	2.7220	0.0802	0.1350
1.88	1.89	-0.25	2.4911	0.0740	0.1235
1.88	1.89	-0.15	2.5086	0.0761	0.1244
1.88	1.89	-0.05	2.7022	0.0830	0.1340
1.88	1.89	0.05	2.4253	0.0751	0.1202
1.88	1.89	0.15	2.3071	0.0764	0.1144
1.88	1.89	0.25	2.2810	0.0755	0.1131
1.88	1.89	0.35	2.2083	0.0772	0.1095
1.88	1.89	0.45	2.4069	0.0826	0.1193
1.88	1.89	0.55	2.8390	0.0918	0.1408
1.88	1.89	0.65	3.7160	0.1208	0.1842
1.88	1.89	0.75	4.2132	0.1389	0.2089
1.89	1.90	-0.75	2.2966	0.0792	0.1143
1.89	1.90	-0.65	2.3956	0.0787	0.1192
1.89	1.90	-0.55	2.5560	0.0802	0.1272
1.89	1.90	-0.45	2.5028	0.0760	0.1246
1.89	1.90	-0.35	2.6728	0.0799	0.1330
1.89	1.90	-0.25	2.6923	0.0812	0.1340
1.89	1.90	-0.15	2.7383	0.0831	0.1363
1.89	1.90	-0.05	2.4543	0.0760	0.1222
1.89	1.90	0.05	2.5551	0.0804	0.1272
1.89	1.90	0.15	2.3013	0.0764	0.1145
1.89	1.90	0.25	2.2519	0.0751	0.1121
1.89	1.90	0.35	2.1964	0.0790	0.1093
1.89	1.90	0.45	2.2907	0.0797	0.1140
1.89	1.90	0.55	2.7708	0.0942	0.1379
1.89	1.90	0.65	3.3824	0.1169	0.1683
1.89	1.90	0.75	4.3113	0.1398	0.2146
1.90	1.91	-0.84	1.8925	0.3164	0.0946
1.90	1.91	-0.75	2.0713	0.0709	0.1035
1.90	1.91	-0.65	2.1488	0.0740	0.1074
1.90	1.91	-0.55	2.4323	0.0769	0.1215

1.90	1.91	-0.45	2.3046	0.0705	0.1151
1.90	1.91	-0.35	2.5939	0.0780	0.1296
1.90	1.91	-0.25	2.4668	0.0735	0.1232
1.90	1.91	-0.15	2.3792	0.0724	0.1189
1.90	1.91	-0.05	2.2442	0.0708	0.1121
1.90	1.91	0.05	2.3813	0.0751	0.1190
1.90	1.91	0.15	2.2167	0.0726	0.1107
1.90	1.91	0.25	1.9985	0.0675	0.0998
1.90	1.91	0.35	1.9360	0.0706	0.0967
1.90	1.91	0.45	2.2376	0.0777	0.1118
1.90	1.91	0.55	2.7321	0.0954	0.1365
1.90	1.91	0.65	3.2094	0.1112	0.1603
1.90	1.91	0.75	4.1228	0.1339	0.2060
1.91	1.92	-0.84	1.5306	0.1483	0.0768
1.91	1.92	-0.75	1.9862	0.0704	0.0996
1.91	1.92	-0.65	2.0893	0.0714	0.1048
1.91	1.92	-0.55	2.1568	0.0695	0.1082
1.91	1.92	-0.45	2.2189	0.0689	0.1113
1.91	1.92	-0.35	2.4118	0.0730	0.1210
1.91	1.92	-0.25	2.5109	0.0773	0.1259
1.91	1.92	-0.15	2.2362	0.0704	0.1122
1.91	1.92	-0.05	2.2887	0.0722	0.1148
1.91	1.92	0.05	2.1391	0.0692	0.1073
1.91	1.92	0.15	2.1796	0.0730	0.1093
1.91	1.92	0.25	2.0115	0.0702	0.1009
1.91	1.92	0.35	1.9652	0.0711	0.0986
1.91	1.92	0.45	2.1975	0.0774	0.1102
1.91	1.92	0.55	2.5949	0.0920	0.1301
1.91	1.92	0.65	3.3972	0.1183	0.1704
1.91	1.92	0.75	4.0801	0.1343	0.2046
1.92	1.93	-0.84	1.7726	0.2928	0.0892
1.92	1.93	-0.75	1.9135	0.0682	0.0963
1.92	1.93	-0.65	2.0223	0.0691	0.1018
1.92	1.93	-0.55	2.0977	0.0681	0.1056
1.92	1.93	-0.45	2.0824	0.0663	0.1048
1.92	1.93	-0.35	2.4503	0.0751	0.1234
1.92	1.93	-0.25	2.3064	0.0712	0.1161
1.92	1.93	-0.15	2.3796	0.0739	0.1198
1.92	1.93	-0.05	2.1787	0.0693	0.1097
1.92	1.93	0.05	2.1634	0.0720	0.1089
1.92	1.93	0.15	2.0599	0.0704	0.1037
1.92	1.93	0.25	1.9479	0.0682	0.0981
1.92	1.93	0.35	1.8638	0.0677	0.0938
1.92	1.93	0.45	1.9839	0.0712	0.0999
1.92	1.93	0.55	2.4512	0.0899	0.1234
1.92	1.93	0.65	3.2981	0.1158	0.1660
1.92	1.93	0.75	3.7861	0.1270	0.1906
1.93	1.94	-0.84	1.7569	0.2987	0.0888
1.93	1.94	-0.75	1.8260	0.0665	0.0923
1.93	1.94	-0.65	1.8324	0.0629	0.0926
1.93	1.94	-0.55	1.9826	0.0638	0.1002
1.93	1.94	-0.45	1.9040	0.0593	0.0962
1.93	1.94	-0.35	2.1389	0.0655	0.1081
1.93	1.94	-0.25	2.2629	0.0700	0.1144
1.93	1.94	-0.15	2.1288	0.0671	0.1076
1.93	1.94	-0.05	2.0647	0.0662	0.1043
1.93	1.94	0.05	1.9941	0.0675	0.1008
1.93	1.94	0.15	1.8359	0.0628	0.0928
1.93	1.94	0.25	1.7907	0.0642	0.0905
1.93	1.94	0.35	1.6663	0.0607	0.0842
1.93	1.94	0.45	1.9090	0.0679	0.0965
1.93	1.94	0.55	2.2927	0.0849	0.1159
1.93	1.94	0.65	2.9902	0.1034	0.1511
1.93	1.94	0.75	4.0075	0.1334	0.2025
1.94	1.95	-0.84	1.7623	0.2486	0.0894
1.94	1.95	-0.75	1.7858	0.0662	0.0906
1.94	1.95	-0.65	1.7770	0.0639	0.0901
1.94	1.95	-0.55	1.9240	0.0637	0.0976
1.94	1.95	-0.45	1.9663	0.0624	0.0997
1.94	1.95	-0.35	2.1794	0.0689	0.1106
1.94	1.95	-0.25	2.1938	0.0681	0.1113
1.94	1.95	-0.15	2.1573	0.0694	0.1094
1.94	1.95	-0.05	2.0908	0.0683	0.1061
1.94	1.95	0.05	1.9143	0.0655	0.0971
1.94	1.95	0.15	1.9318	0.0658	0.0980
1.94	1.95	0.25	1.7645	0.0631	0.0895

1.94	1.95	0.35	1.8473	0.0674	0.0937
1.94	1.95	0.45	1.8167	0.0663	0.0922
1.94	1.95	0.55	2.3719	0.0882	0.1203
1.94	1.95	0.65	3.1760	0.1069	0.1611
1.94	1.95	0.75	4.5172	0.1443	0.2292
1.95	1.96	-0.84	1.0915	0.0862	0.0556
1.95	1.96	-0.75	1.2419	0.0458	0.0632
1.95	1.96	-0.65	1.3540	0.0476	0.0689
1.95	1.96	-0.55	1.4854	0.0498	0.0756
1.95	1.96	-0.45	1.5410	0.0476	0.0785
1.95	1.96	-0.35	1.5979	0.0492	0.0814
1.95	1.96	-0.25	1.6285	0.0508	0.0829
1.95	1.96	-0.15	1.5920	0.0508	0.0811
1.95	1.96	-0.05	1.6228	0.0518	0.0826
1.95	1.96	0.05	1.5261	0.0509	0.0777
1.95	1.96	0.15	1.4351	0.0491	0.0731
1.95	1.96	0.25	1.3797	0.0495	0.0703
1.95	1.96	0.35	1.3641	0.0489	0.0695
1.95	1.96	0.45	1.5433	0.0562	0.0786
1.95	1.96	0.55	1.8245	0.0675	0.0929
1.95	1.96	0.65	2.5270	0.0838	0.1287
1.95	1.96	0.75	3.9179	0.1231	0.1995
1.95	1.96	0.85	4.6360	0.5605	0.2361
1.96	1.97	-0.84	1.3542	0.1105	0.0692
1.96	1.97	-0.75	1.5607	0.0575	0.0798
1.96	1.97	-0.65	1.6046	0.0565	0.0820
1.96	1.97	-0.55	1.7107	0.0571	0.0874
1.96	1.97	-0.45	1.8040	0.0589	0.0922
1.96	1.97	-0.35	1.9971	0.0622	0.1021
1.96	1.97	-0.25	2.0287	0.0637	0.1037
1.96	1.97	-0.15	2.0504	0.0665	0.1048
1.96	1.97	-0.05	2.0844	0.0677	0.1065
1.96	1.97	0.05	1.8822	0.0639	0.0962
1.96	1.97	0.15	1.8152	0.0624	0.0928
1.96	1.97	0.25	1.6442	0.0599	0.0840
1.96	1.97	0.35	1.6922	0.0610	0.0865
1.96	1.97	0.45	1.9169	0.0696	0.0980
1.96	1.97	0.55	2.3002	0.0829	0.1176
1.96	1.97	0.65	3.4089	0.1106	0.1742
1.96	1.97	0.75	5.4403	0.1664	0.2781
1.96	1.97	0.85	8.1364	0.4241	0.4159
1.97	1.98	-0.84	1.3772	0.1012	0.0707
1.97	1.98	-0.75	1.4484	0.0540	0.0743
1.97	1.98	-0.65	1.5097	0.0535	0.0775
1.97	1.98	-0.55	1.6614	0.0560	0.0852
1.97	1.98	-0.45	1.6528	0.0542	0.0848
1.97	1.98	-0.35	1.8466	0.0581	0.0947
1.97	1.98	-0.25	1.8746	0.0594	0.0962
1.97	1.98	-0.15	1.8170	0.0586	0.0932
1.97	1.98	-0.05	1.9598	0.0635	0.1006
1.97	1.98	0.05	1.7637	0.0600	0.0905
1.97	1.98	0.15	1.7227	0.0594	0.0884
1.97	1.98	0.25	1.5021	0.0540	0.0771
1.97	1.98	0.35	1.5432	0.0560	0.0792
1.97	1.98	0.45	1.6955	0.0623	0.0870
1.97	1.98	0.55	2.3084	0.0814	0.1184
1.97	1.98	0.65	3.1977	0.1038	0.1641
1.97	1.98	0.75	4.9478	0.1558	0.2539
1.97	1.98	0.85	7.4371	0.3413	0.3816
1.98	1.99	-0.84	1.3529	0.0829	0.0697
1.98	1.99	-0.75	1.4856	0.0548	0.0765
1.98	1.99	-0.65	1.5228	0.0536	0.0784
1.98	1.99	-0.55	1.5986	0.0534	0.0823
1.98	1.99	-0.45	1.7707	0.0573	0.0912
1.98	1.99	-0.35	1.8439	0.0579	0.0950
1.98	1.99	-0.25	1.9793	0.0620	0.1019
1.98	1.99	-0.15	1.9729	0.0633	0.1016
1.98	1.99	-0.05	1.9757	0.0636	0.1018
1.98	1.99	0.05	1.8559	0.0627	0.0956
1.98	1.99	0.15	1.7303	0.0596	0.0891
1.98	1.99	0.25	1.5832	0.0573	0.0815
1.98	1.99	0.35	1.6327	0.0582	0.0841
1.98	1.99	0.45	1.7945	0.0665	0.0924
1.98	1.99	0.55	2.3098	0.0807	0.1190
1.98	1.99	0.65	3.3872	0.1086	0.1744
1.98	1.99	0.75	5.3834	0.1683	0.2773

1.98	1.99	0.85	8.6507	0.3973	0.4455
1.99	2.00	-0.84	1.4115	0.0837	0.0730
1.99	2.00	-0.75	1.3815	0.0525	0.0714
1.99	2.00	-0.65	1.4786	0.0521	0.0764
1.99	2.00	-0.55	1.6165	0.0548	0.0836
1.99	2.00	-0.45	1.6249	0.0520	0.0840
1.99	2.00	-0.35	1.8141	0.0576	0.0938
1.99	2.00	-0.25	1.9020	0.0608	0.0983
1.99	2.00	-0.15	2.0038	0.0648	0.1036
1.99	2.00	-0.05	1.8009	0.0591	0.0931
1.99	2.00	0.05	1.8212	0.0607	0.0941
1.99	2.00	0.15	1.6640	0.0567	0.0860
1.99	2.00	0.25	1.5330	0.0554	0.0792
1.99	2.00	0.35	1.5566	0.0568	0.0805
1.99	2.00	0.45	1.6933	0.0623	0.0875
1.99	2.00	0.55	2.3230	0.0811	0.1201
1.99	2.00	0.65	3.4704	0.1116	0.1794
1.99	2.00	0.75	5.3934	0.1722	0.2788
1.99	2.00	0.85	8.0706	0.3203	0.4172
2.00	2.01	-0.84	1.2464	0.0779	0.0647
2.00	2.01	-0.75	1.3205	0.0496	0.0685
2.00	2.01	-0.65	1.4209	0.0513	0.0737
2.00	2.01	-0.55	1.6061	0.0557	0.0833
2.00	2.01	-0.45	1.5826	0.0517	0.0821
2.00	2.01	-0.35	1.7591	0.0558	0.0913
2.00	2.01	-0.25	1.8031	0.0577	0.0936
2.00	2.01	-0.15	1.8518	0.0591	0.0961
2.00	2.01	-0.05	1.7486	0.0567	0.0907
2.00	2.01	0.05	1.7345	0.0590	0.0900
2.00	2.01	0.15	1.5147	0.0526	0.0786
2.00	2.01	0.25	1.4456	0.0521	0.0750
2.00	2.01	0.35	1.4106	0.0512	0.0732
2.00	2.01	0.45	1.7104	0.0645	0.0888
2.00	2.01	0.55	2.3228	0.0799	0.1205
2.00	2.01	0.65	3.5101	0.1119	0.1821
2.00	2.01	0.75	5.8343	0.1830	0.3027
2.00	2.01	0.85	8.3998	0.3151	0.4359
2.01	2.02	-0.84	1.2834	0.0710	0.0668
2.01	2.02	-0.75	1.3439	0.0497	0.0700
2.01	2.02	-0.65	1.3960	0.0501	0.0727
2.01	2.02	-0.55	1.4697	0.0516	0.0765
2.01	2.02	-0.45	1.5556	0.0513	0.0810
2.01	2.02	-0.35	1.7438	0.0547	0.0908
2.01	2.02	-0.25	1.7602	0.0558	0.0917
2.01	2.02	-0.15	1.8561	0.0596	0.0967
2.01	2.02	-0.05	1.7596	0.0576	0.0916
2.01	2.02	0.05	1.6189	0.0551	0.0843
2.01	2.02	0.15	1.5503	0.0537	0.0807
2.01	2.02	0.25	1.4199	0.0518	0.0740
2.01	2.02	0.35	1.4236	0.0518	0.0741
2.01	2.02	0.45	1.7149	0.0638	0.0893
2.01	2.02	0.55	2.3309	0.0789	0.1214
2.01	2.02	0.65	3.5197	0.1122	0.1833
2.01	2.02	0.75	5.3153	0.1638	0.2768
2.01	2.02	0.85	9.5740	0.9453	0.4986
2.02	2.03	-0.84	1.2745	0.0670	0.0666
2.02	2.03	-0.75	1.3066	0.0491	0.0683
2.02	2.03	-0.65	1.4357	0.0510	0.0751
2.02	2.03	-0.55	1.4995	0.0507	0.0784
2.02	2.03	-0.45	1.4866	0.0492	0.0777
2.02	2.03	-0.35	1.6719	0.0537	0.0874
2.02	2.03	-0.25	1.7295	0.0559	0.0904
2.02	2.03	-0.15	1.7359	0.0553	0.0907
2.02	2.03	-0.05	1.7758	0.0582	0.0928
2.02	2.03	0.05	1.6550	0.0558	0.0865
2.02	2.03	0.15	1.6316	0.0562	0.0853
2.02	2.03	0.25	1.3921	0.0504	0.0728
2.02	2.03	0.35	1.3565	0.0496	0.0709
2.02	2.03	0.45	1.6889	0.0626	0.0883
2.02	2.03	0.55	2.3079	0.0784	0.1206
2.02	2.03	0.65	3.5327	0.1132	0.1847
2.02	2.03	0.75	5.4577	0.1664	0.2853
2.02	2.03	0.85	16.3240	3.8523	0.8534
2.03	2.04	-0.84	1.2399	0.0654	0.0651
2.03	2.04	-0.75	1.3305	0.0492	0.0698
2.03	2.04	-0.65	1.4358	0.0517	0.0753

2.03	2.04	-0.55	1.4840	0.0511	0.0779
2.03	2.04	-0.45	1.6106	0.0528	0.0845
2.03	2.04	-0.35	1.6603	0.0537	0.0871
2.03	2.04	-0.25	1.7187	0.0547	0.0902
2.03	2.04	-0.15	1.7753	0.0570	0.0932
2.03	2.04	-0.05	1.7588	0.0572	0.0923
2.03	2.04	0.05	1.6765	0.0562	0.0880
2.03	2.04	0.15	1.5228	0.0532	0.0799
2.03	2.04	0.25	1.3655	0.0496	0.0716
2.03	2.04	0.35	1.4033	0.0515	0.0736
2.03	2.04	0.45	1.7289	0.0632	0.0907
2.03	2.04	0.55	2.4389	0.0816	0.1280
2.03	2.04	0.65	3.6875	0.1178	0.1935
2.03	2.04	0.75	6.2005	0.1877	0.3253
2.03	2.04	0.85	9.7174	0.6345	0.5099
2.04	2.05	-0.84	1.2597	0.0656	0.0663
2.04	2.05	-0.75	1.3546	0.0500	0.0713
2.04	2.05	-0.65	1.3743	0.0494	0.0724
2.04	2.05	-0.55	1.3429	0.0463	0.0707
2.04	2.05	-0.45	1.4879	0.0490	0.0784
2.04	2.05	-0.35	1.6465	0.0530	0.0867
2.04	2.05	-0.25	1.7249	0.0550	0.0908
2.04	2.05	-0.15	1.7674	0.0572	0.0931
2.04	2.05	-0.05	1.6893	0.0544	0.0890
2.04	2.05	0.05	1.6908	0.0572	0.0890
2.04	2.05	0.15	1.5189	0.0528	0.0800
2.04	2.05	0.25	1.3016	0.0484	0.0685
2.04	2.05	0.35	1.3385	0.0493	0.0705
2.04	2.05	0.45	1.7077	0.0634	0.0899
2.04	2.05	0.55	2.4545	0.0815	0.1293
2.04	2.05	0.65	3.6138	0.1131	0.1903
2.04	2.05	0.75	6.3671	0.1855	0.3353
2.04	2.05	0.85	11.0047	0.9435	0.5796
2.05	2.06	-0.84	1.2324	0.0613	0.0651
2.05	2.06	-0.75	1.2650	0.0469	0.0669
2.05	2.06	-0.65	1.2598	0.0455	0.0666
2.05	2.06	-0.55	1.3859	0.0484	0.0733
2.05	2.06	-0.45	1.4444	0.0470	0.0763
2.05	2.06	-0.35	1.6715	0.0545	0.0884
2.05	2.06	-0.25	1.7300	0.0541	0.0914
2.05	2.06	-0.15	1.6706	0.0533	0.0883
2.05	2.06	-0.05	1.7065	0.0559	0.0902
2.05	2.06	0.05	1.5814	0.0532	0.0836
2.05	2.06	0.15	1.4634	0.0508	0.0774
2.05	2.06	0.25	1.3344	0.0485	0.0705
2.05	2.06	0.35	1.2921	0.0482	0.0683
2.05	2.06	0.45	1.6454	0.0609	0.0870
2.05	2.06	0.55	2.4286	0.0807	0.1284
2.05	2.06	0.65	3.7904	0.1211	0.2004
2.05	2.06	0.75	6.6910	0.2001	0.3537
2.05	2.06	0.85	13.8177	1.4916	0.7304
2.06	2.07	-0.84	1.2351	0.0624	0.0655
2.06	2.07	-0.75	1.2223	0.0451	0.0648
2.06	2.07	-0.65	1.2424	0.0447	0.0659
2.06	2.07	-0.55	1.3790	0.0489	0.0732
2.06	2.07	-0.45	1.4107	0.0466	0.0748
2.06	2.07	-0.35	1.5293	0.0483	0.0811
2.06	2.07	-0.25	1.7635	0.0568	0.0936
2.06	2.07	-0.15	1.7420	0.0564	0.0924
2.06	2.07	-0.05	1.6256	0.0525	0.0862
2.06	2.07	0.05	1.6458	0.0547	0.0873
2.06	2.07	0.15	1.4682	0.0507	0.0779
2.06	2.07	0.25	1.2794	0.0463	0.0679
2.06	2.07	0.35	1.3559	0.0499	0.0719
2.06	2.07	0.45	1.6827	0.0620	0.0893
2.06	2.07	0.55	2.2825	0.0766	0.1211
2.06	2.07	0.65	4.0008	0.1261	0.2123
2.06	2.07	0.75	6.8545	0.1993	0.3637
2.06	2.07	0.85	11.4903	0.7653	0.6096
2.07	2.08	-0.84	1.1569	0.0571	0.0616
2.07	2.08	-0.75	1.2318	0.0445	0.0656
2.07	2.08	-0.65	1.2496	0.0442	0.0665
2.07	2.08	-0.55	1.3117	0.0467	0.0698
2.07	2.08	-0.45	1.4100	0.0457	0.0751
2.07	2.08	-0.35	1.5101	0.0486	0.0804
2.07	2.08	-0.25	1.6186	0.0530	0.0862

2.07	2.08	-0.15	1.6330	0.0528	0.0870
2.07	2.08	-0.05	1.5625	0.0505	0.0832
2.07	2.08	0.05	1.6371	0.0549	0.0872
2.07	2.08	0.15	1.4010	0.0491	0.0746
2.07	2.08	0.25	1.2074	0.0444	0.0643
2.07	2.08	0.35	1.2841	0.0470	0.0684
2.07	2.08	0.45	1.5954	0.0586	0.0850
2.07	2.08	0.55	2.2838	0.0752	0.1216
2.07	2.08	0.65	3.8473	0.1216	0.2049
2.07	2.08	0.75	6.3553	0.1873	0.3384
2.07	2.08	0.85	10.9784	0.5484	0.5846
2.08	2.09	-0.84	1.3061	0.0622	0.0698
2.08	2.09	-0.75	1.2462	0.0459	0.0666
2.08	2.09	-0.65	1.3749	0.0487	0.0735
2.08	2.09	-0.55	1.3963	0.0479	0.0746
2.08	2.09	-0.45	1.4132	0.0480	0.0755
2.08	2.09	-0.35	1.5503	0.0508	0.0829
2.08	2.09	-0.25	1.5674	0.0507	0.0838
2.08	2.09	-0.15	1.7282	0.0565	0.0924
2.08	2.09	-0.05	1.7000	0.0545	0.0909
2.08	2.09	0.05	1.6268	0.0551	0.0869
2.08	2.09	0.15	1.4203	0.0503	0.0759
2.08	2.09	0.25	1.2799	0.0472	0.0684
2.08	2.09	0.35	1.3071	0.0486	0.0699
2.08	2.09	0.45	1.6601	0.0608	0.0887
2.08	2.09	0.55	2.4068	0.0821	0.1286
2.08	2.09	0.65	4.1614	0.1305	0.2224
2.08	2.09	0.75	6.8882	0.1993	0.3681
2.08	2.09	0.85	11.8749	0.5336	0.6346
2.09	2.10	-0.84	1.2268	0.0572	0.0658
2.09	2.10	-0.75	1.3213	0.0465	0.0709
2.09	2.10	-0.65	1.2499	0.0441	0.0670
2.09	2.10	-0.55	1.2696	0.0453	0.0681
2.09	2.10	-0.45	1.2700	0.0427	0.0681
2.09	2.10	-0.35	1.4543	0.0478	0.0780
2.09	2.10	-0.25	1.5955	0.0520	0.0856
2.09	2.10	-0.15	1.6876	0.0553	0.0905
2.09	2.10	-0.05	1.6513	0.0540	0.0886
2.09	2.10	0.05	1.6125	0.0538	0.0865
2.09	2.10	0.15	1.4039	0.0486	0.0753
2.09	2.10	0.25	1.2722	0.0453	0.0682
2.09	2.10	0.35	1.2894	0.0482	0.0692
2.09	2.10	0.45	1.5562	0.0572	0.0835
2.09	2.10	0.55	2.5295	0.0850	0.1357
2.09	2.10	0.65	4.0967	0.1258	0.2197
2.09	2.10	0.75	6.9864	0.1983	0.3747
2.09	2.10	0.85	12.1247	0.4657	0.6503
2.10	2.11	-0.84	1.1296	0.0531	0.0608
2.10	2.11	-0.75	1.2376	0.0441	0.0666
2.10	2.11	-0.65	1.2181	0.0427	0.0656
2.10	2.11	-0.55	1.2386	0.0452	0.0667
2.10	2.11	-0.45	1.2283	0.0420	0.0661
2.10	2.11	-0.35	1.3215	0.0425	0.0711
2.10	2.11	-0.25	1.5242	0.0498	0.0821
2.10	2.11	-0.15	1.5259	0.0492	0.0821
2.10	2.11	-0.05	1.6351	0.0533	0.0880
2.10	2.11	0.05	1.5710	0.0525	0.0846
2.10	2.11	0.15	1.2974	0.0452	0.0698
2.10	2.11	0.25	1.1164	0.0411	0.0601
2.10	2.11	0.35	1.1713	0.0447	0.0631
2.10	2.11	0.45	1.5801	0.0576	0.0851
2.10	2.11	0.55	2.2185	0.0739	0.1194
2.10	2.11	0.65	3.8934	0.1211	0.2096
2.10	2.11	0.75	6.5032	0.1825	0.3501
2.10	2.11	0.85	13.7254	0.5572	0.7389
2.11	2.12	-0.84	1.2860	0.0608	0.0695
2.11	2.12	-0.75	1.1854	0.0420	0.0640
2.11	2.12	-0.65	1.1856	0.0403	0.0641
2.11	2.12	-0.55	1.1788	0.0411	0.0637
2.11	2.12	-0.45	1.2316	0.0413	0.0665
2.11	2.12	-0.35	1.3537	0.0449	0.0731
2.11	2.12	-0.25	1.4564	0.0477	0.0787
2.11	2.12	-0.15	1.5382	0.0504	0.0831
2.11	2.12	-0.05	1.5813	0.0525	0.0854
2.11	2.12	0.05	1.4919	0.0502	0.0806
2.11	2.12	0.15	1.2456	0.0433	0.0673

2.11	2.12	0.25	1.1229	0.0408	0.0607
2.11	2.12	0.35	1.1844	0.0444	0.0640
2.11	2.12	0.45	1.4412	0.0536	0.0779
2.11	2.12	0.55	2.2061	0.0750	0.1192
2.11	2.12	0.65	3.8438	0.1198	0.2077
2.11	2.12	0.75	6.5921	0.1839	0.3562
2.11	2.12	0.85	11.1877	0.3421	0.6045
2.12	2.13	-0.84	1.1415	0.0530	0.0619
2.12	2.13	-0.75	1.2837	0.0455	0.0696
2.12	2.13	-0.65	1.1472	0.0397	0.0622
2.12	2.13	-0.55	1.1497	0.0406	0.0623
2.12	2.13	-0.45	1.1969	0.0409	0.0649
2.12	2.13	-0.35	1.2899	0.0434	0.0699
2.12	2.13	-0.25	1.3683	0.0451	0.0742
2.12	2.13	-0.15	1.4727	0.0484	0.0799
2.12	2.13	-0.05	1.5233	0.0506	0.0826
2.12	2.13	0.05	1.5348	0.0522	0.0832
2.12	2.13	0.15	1.2792	0.0447	0.0694
2.12	2.13	0.25	1.0843	0.0399	0.0588
2.12	2.13	0.35	1.1168	0.0427	0.0606
2.12	2.13	0.45	1.4300	0.0520	0.0775
2.12	2.13	0.55	2.0778	0.0690	0.1127
2.12	2.13	0.65	3.6031	0.1151	0.1954
2.12	2.13	0.75	6.3371	0.1807	0.3436
2.12	2.13	0.85	11.1063	0.3386	0.6022
2.13	2.14	-0.84	1.1200	0.0518	0.0609
2.13	2.14	-0.75	1.2352	0.0438	0.0672
2.13	2.14	-0.65	1.0949	0.0383	0.0596
2.13	2.14	-0.55	1.1086	0.0395	0.0603
2.13	2.14	-0.45	1.1124	0.0386	0.0605
2.13	2.14	-0.35	1.2399	0.0415	0.0675
2.13	2.14	-0.25	1.3852	0.0457	0.0754
2.13	2.14	-0.15	1.4178	0.0471	0.0772
2.13	2.14	-0.05	1.4243	0.0475	0.0775
2.13	2.14	0.05	1.4375	0.0487	0.0782
2.13	2.14	0.15	1.3013	0.0455	0.0708
2.13	2.14	0.25	1.0656	0.0384	0.0580
2.13	2.14	0.35	1.1491	0.0432	0.0625
2.13	2.14	0.45	1.3268	0.0483	0.0722
2.13	2.14	0.55	2.1937	0.0737	0.1194
2.13	2.14	0.65	3.7758	0.1163	0.2055
2.13	2.14	0.75	6.5423	0.1845	0.3560
2.13	2.14	0.85	11.1724	0.3184	0.6080
2.14	2.15	-0.84	1.1746	0.0551	0.0642
2.14	2.15	-0.75	1.2195	0.0419	0.0666
2.14	2.15	-0.65	1.1119	0.0388	0.0607
2.14	2.15	-0.55	1.0501	0.0379	0.0574
2.14	2.15	-0.45	1.0377	0.0359	0.0567
2.14	2.15	-0.35	1.1589	0.0387	0.0633
2.14	2.15	-0.25	1.2925	0.0429	0.0706
2.14	2.15	-0.15	1.3281	0.0434	0.0725
2.14	2.15	-0.05	1.4614	0.0474	0.0798
2.14	2.15	0.05	1.4183	0.0489	0.0775
2.14	2.15	0.15	1.2230	0.0428	0.0668
2.14	2.15	0.25	1.0858	0.0396	0.0593
2.14	2.15	0.35	1.1074	0.0424	0.0605
2.14	2.15	0.45	1.3611	0.0503	0.0743
2.14	2.15	0.55	2.2102	0.0744	0.1207
2.14	2.15	0.65	3.4534	0.1076	0.1886
2.14	2.15	0.75	6.2674	0.1757	0.3423
2.14	2.15	0.85	11.8561	0.3379	0.6475
2.15	2.16	-0.84	1.0417	0.0479	0.0571
2.15	2.16	-0.75	1.2133	0.0421	0.0665
2.15	2.16	-0.65	1.1176	0.0381	0.0613
2.15	2.16	-0.55	1.0158	0.0364	0.0557
2.15	2.16	-0.45	1.0215	0.0348	0.0560
2.15	2.16	-0.35	1.1013	0.0374	0.0604
2.15	2.16	-0.25	1.2125	0.0404	0.0665
2.15	2.16	-0.15	1.3116	0.0431	0.0719
2.15	2.16	-0.05	1.3826	0.0457	0.0758
2.15	2.16	0.05	1.3124	0.0437	0.0719
2.15	2.16	0.15	1.1228	0.0403	0.0615
2.15	2.16	0.25	1.0052	0.0366	0.0551
2.15	2.16	0.35	1.0552	0.0397	0.0578
2.15	2.16	0.45	1.2745	0.0465	0.0699
2.15	2.16	0.55	1.9814	0.0667	0.1086

2.15	2.16	0.65	3.2878	0.1009	0.1802
2.15	2.16	0.75	6.0271	0.1666	0.3304
2.15	2.16	0.85	10.8696	0.3022	0.5958
2.16	2.17	-0.84	0.9570	0.0441	0.0526
2.16	2.17	-0.75	1.2237	0.0424	0.0673
2.16	2.17	-0.65	1.0697	0.0376	0.0588
2.16	2.17	-0.55	1.0347	0.0368	0.0569
2.16	2.17	-0.45	1.0001	0.0345	0.0550
2.16	2.17	-0.35	1.0964	0.0374	0.0603
2.16	2.17	-0.25	1.1984	0.0401	0.0659
2.16	2.17	-0.15	1.2481	0.0414	0.0687
2.16	2.17	-0.05	1.3427	0.0443	0.0739
2.16	2.17	0.05	1.3152	0.0446	0.0723
2.16	2.17	0.15	1.1547	0.0405	0.0635
2.16	2.17	0.25	0.9553	0.0352	0.0525
2.16	2.17	0.35	1.0066	0.0384	0.0554
2.16	2.17	0.45	1.3072	0.0472	0.0719
2.16	2.17	0.55	1.9321	0.0662	0.1063
2.16	2.17	0.65	3.4348	0.1053	0.1889
2.16	2.17	0.75	5.5973	0.1546	0.3079
2.16	2.17	0.85	10.6959	0.2941	0.5884
2.17	2.18	-0.84	1.1097	0.0506	0.0613
2.17	2.18	-0.75	1.2004	0.0401	0.0663
2.17	2.18	-0.65	0.9994	0.0351	0.0552
2.17	2.18	-0.55	1.0398	0.0371	0.0574
2.17	2.18	-0.45	0.9513	0.0345	0.0525
2.17	2.18	-0.35	1.0409	0.0359	0.0575
2.17	2.18	-0.25	1.1908	0.0401	0.0657
2.17	2.18	-0.15	1.2608	0.0424	0.0696
2.17	2.18	-0.05	1.3297	0.0443	0.0734
2.17	2.18	0.05	1.2657	0.0430	0.0699
2.17	2.18	0.15	1.1153	0.0389	0.0616
2.17	2.18	0.25	0.9599	0.0357	0.0530
2.17	2.18	0.35	0.9900	0.0371	0.0547
2.17	2.18	0.45	1.2160	0.0435	0.0671
2.17	2.18	0.55	2.0462	0.0682	0.1130
2.17	2.18	0.65	3.2788	0.1004	0.1810
2.17	2.18	0.75	5.5340	0.1544	0.3055
2.17	2.18	0.85	10.6810	0.2929	0.5896
2.18	2.19	-0.84	1.1182	0.0500	0.0620
2.18	2.19	-0.75	1.2387	0.0417	0.0686
2.18	2.19	-0.65	1.0605	0.0361	0.0588
2.18	2.19	-0.55	1.0521	0.0368	0.0583
2.18	2.19	-0.45	0.9231	0.0325	0.0511
2.18	2.19	-0.35	0.9965	0.0342	0.0552
2.18	2.19	-0.25	1.1083	0.0374	0.0614
2.18	2.19	-0.15	1.1920	0.0402	0.0660
2.18	2.19	-0.05	1.3361	0.0440	0.0740
2.18	2.19	0.05	1.3349	0.0458	0.0740
2.18	2.19	0.15	1.0613	0.0370	0.0588
2.18	2.19	0.25	0.9753	0.0356	0.0540
2.18	2.19	0.35	1.0053	0.0372	0.0557
2.18	2.19	0.45	1.1874	0.0434	0.0658
2.18	2.19	0.55	1.8198	0.0619	0.1008
2.18	2.19	0.65	3.3962	0.1042	0.1882
2.18	2.19	0.75	5.5989	0.1572	0.3102
2.18	2.19	0.85	10.7522	0.3022	0.5957
2.19	2.20	-0.84	1.1877	0.0522	0.0660
2.19	2.20	-0.75	1.2805	0.0427	0.0712
2.19	2.20	-0.65	1.1551	0.0397	0.0642
2.19	2.20	-0.55	0.9838	0.0355	0.0547
2.19	2.20	-0.45	0.9645	0.0341	0.0536
2.19	2.20	-0.35	1.0285	0.0360	0.0572
2.19	2.20	-0.25	1.1119	0.0380	0.0618
2.19	2.20	-0.15	1.2387	0.0410	0.0689
2.19	2.20	-0.05	1.3541	0.0460	0.0753
2.19	2.20	0.05	1.2834	0.0448	0.0714
2.19	2.20	0.15	1.1326	0.0405	0.0630
2.19	2.20	0.25	0.9857	0.0357	0.0548
2.19	2.20	0.35	1.0068	0.0376	0.0560
2.19	2.20	0.45	1.3156	0.0472	0.0731
2.19	2.20	0.55	1.9408	0.0652	0.1079
2.19	2.20	0.65	3.4475	0.1072	0.1917
2.19	2.20	0.75	5.8045	0.1644	0.3227
2.19	2.20	0.85	10.6370	0.3009	0.5914
2.20	2.21	-0.84	1.1319	0.0502	0.0632

2.20	2.21	-0.75	1.2296	0.0420	0.0686
2.20	2.21	-0.65	1.0521	0.0362	0.0587
2.20	2.21	-0.55	0.9724	0.0347	0.0543
2.20	2.21	-0.45	0.8850	0.0318	0.0494
2.20	2.21	-0.35	0.9782	0.0344	0.0546
2.20	2.21	-0.25	1.0918	0.0378	0.0609
2.20	2.21	-0.15	1.2409	0.0418	0.0692
2.20	2.21	-0.05	1.3059	0.0439	0.0729
2.20	2.21	0.05	1.3279	0.0448	0.0741
2.20	2.21	0.15	1.0955	0.0382	0.0611
2.20	2.21	0.25	0.9324	0.0345	0.0520
2.20	2.21	0.35	0.9040	0.0339	0.0504
2.20	2.21	0.45	1.2441	0.0446	0.0694
2.20	2.21	0.55	1.9305	0.0658	0.1077
2.20	2.21	0.65	3.2420	0.1013	0.1809
2.20	2.21	0.75	5.5932	0.1562	0.3121
2.20	2.21	0.85	11.0986	0.3035	0.6193
2.21	2.22	-0.84	1.1263	0.0506	0.0631
2.21	2.22	-0.75	1.1790	0.0405	0.0660
2.21	2.22	-0.65	1.0834	0.0367	0.0607
2.21	2.22	-0.55	0.8655	0.0315	0.0485
2.21	2.22	-0.45	0.8395	0.0297	0.0470
2.21	2.22	-0.35	0.8343	0.0293	0.0467
2.21	2.22	-0.25	0.9708	0.0336	0.0544
2.21	2.22	-0.15	1.1524	0.0394	0.0645
2.21	2.22	-0.05	1.1653	0.0388	0.0652
2.21	2.22	0.05	1.1223	0.0388	0.0628
2.21	2.22	0.15	1.0052	0.0356	0.0563
2.21	2.22	0.25	0.8704	0.0313	0.0487
2.21	2.22	0.35	0.9116	0.0337	0.0510
2.21	2.22	0.45	1.1575	0.0409	0.0648
2.21	2.22	0.55	1.7323	0.0573	0.0970
2.21	2.22	0.65	2.8865	0.0902	0.1616
2.21	2.22	0.75	4.8773	0.1382	0.2731
2.21	2.22	0.85	9.8413	0.2690	0.5510
2.21	2.22	0.91	12.2185	2.3177	0.6841
2.22	2.23	-0.84	1.0056	0.0453	0.0565
2.22	2.23	-0.75	1.0455	0.0363	0.0587
2.22	2.23	-0.65	0.9806	0.0339	0.0551
2.22	2.23	-0.55	0.8185	0.0295	0.0460
2.22	2.23	-0.45	0.7535	0.0276	0.0423
2.22	2.23	-0.35	0.7997	0.0286	0.0449
2.22	2.23	-0.25	0.9129	0.0318	0.0513
2.22	2.23	-0.15	1.0411	0.0353	0.0585
2.22	2.23	-0.05	1.1209	0.0375	0.0630
2.22	2.23	0.05	1.0967	0.0379	0.0616
2.22	2.23	0.15	0.8937	0.0320	0.0502
2.22	2.23	0.25	0.8474	0.0306	0.0476
2.22	2.23	0.35	0.8830	0.0333	0.0496
2.22	2.23	0.45	1.0857	0.0392	0.0610
2.22	2.23	0.55	1.6536	0.0561	0.0929
2.22	2.23	0.65	2.8537	0.0887	0.1603
2.22	2.23	0.75	4.8640	0.1395	0.2733
2.22	2.23	0.85	9.9876	0.2806	0.5612
2.22	2.23	0.91	54.0003	7.9192	3.0343
2.23	2.24	-0.84	1.0234	0.0446	0.0577
2.23	2.24	-0.75	1.1037	0.0368	0.0622
2.23	2.24	-0.65	0.9534	0.0322	0.0538
2.23	2.24	-0.55	0.7899	0.0289	0.0445
2.23	2.24	-0.45	0.7164	0.0265	0.0404
2.23	2.24	-0.35	0.7624	0.0274	0.0430
2.23	2.24	-0.25	0.8549	0.0303	0.0482
2.23	2.24	-0.15	0.9724	0.0333	0.0548
2.23	2.24	-0.05	1.0568	0.0356	0.0596
2.23	2.24	0.05	1.0322	0.0353	0.0582
2.23	2.24	0.15	0.9101	0.0324	0.0513
2.23	2.24	0.25	0.8043	0.0294	0.0454
2.23	2.24	0.35	0.8335	0.0310	0.0470
2.23	2.24	0.45	1.0905	0.0389	0.0615
2.23	2.24	0.55	1.6034	0.0539	0.0904
2.23	2.24	0.65	2.7896	0.0874	0.1573
2.23	2.24	0.75	4.3660	0.1264	0.2462
2.23	2.24	0.85	9.4121	0.2623	0.5307
2.23	2.24	0.91	12.6636	1.6938	0.7141
2.24	2.25	-0.84	0.9224	0.0420	0.0522
2.24	2.25	-0.75	1.0461	0.0351	0.0592

2.24	2.25	-0.65	0.8931	0.0306	0.0505
2.24	2.25	-0.55	0.7312	0.0274	0.0414
2.24	2.25	-0.45	0.6460	0.0241	0.0366
2.24	2.25	-0.35	0.6672	0.0241	0.0378
2.24	2.25	-0.25	0.7904	0.0282	0.0447
2.24	2.25	-0.15	0.8983	0.0318	0.0508
2.24	2.25	-0.05	1.0067	0.0345	0.0570
2.24	2.25	0.05	0.9909	0.0344	0.0561
2.24	2.25	0.15	0.9390	0.0331	0.0531
2.24	2.25	0.25	0.7769	0.0281	0.0440
2.24	2.25	0.35	0.8216	0.0298	0.0465
2.24	2.25	0.45	1.0640	0.0383	0.0602
2.24	2.25	0.55	1.6222	0.0548	0.0918
2.24	2.25	0.65	2.5927	0.0810	0.1467
2.24	2.25	0.75	4.3096	0.1239	0.2439
2.24	2.25	0.85	8.4918	0.2378	0.4805
2.24	2.25	0.91	17.3993	1.8950	0.9845
2.25	2.26	-0.84	1.0100	0.0436	0.0574
2.25	2.26	-0.75	1.1439	0.0385	0.0650
2.25	2.26	-0.65	0.8761	0.0307	0.0497
2.25	2.26	-0.55	0.7882	0.0290	0.0448
2.25	2.26	-0.45	0.6759	0.0253	0.0384
2.25	2.26	-0.35	0.7244	0.0262	0.0411
2.25	2.26	-0.25	0.8566	0.0305	0.0486
2.25	2.26	-0.15	0.9629	0.0335	0.0547
2.25	2.26	-0.05	1.0008	0.0345	0.0568
2.25	2.26	0.05	1.0613	0.0370	0.0603
2.25	2.26	0.15	0.9157	0.0323	0.0520
2.25	2.26	0.25	0.8437	0.0310	0.0479
2.25	2.26	0.35	0.8637	0.0321	0.0490
2.25	2.26	0.45	1.1095	0.0390	0.0630
2.25	2.26	0.55	1.6671	0.0569	0.0947
2.25	2.26	0.65	2.7017	0.0851	0.1534
2.25	2.26	0.75	4.6252	0.1335	0.2626
2.25	2.26	0.85	9.9479	0.2829	0.5649
2.25	2.26	0.91	18.0394	1.8084	1.0243
2.26	2.27	-0.84	1.0782	0.0491	0.0614
2.26	2.27	-0.75	1.1022	0.0372	0.0628
2.26	2.27	-0.65	0.9446	0.0333	0.0538
2.26	2.27	-0.55	0.7212	0.0267	0.0411
2.26	2.27	-0.45	0.6583	0.0250	0.0375
2.26	2.27	-0.35	0.7057	0.0259	0.0402
2.26	2.27	-0.25	0.8133	0.0288	0.0463
2.26	2.27	-0.15	0.9218	0.0321	0.0525
2.26	2.27	-0.05	1.0050	0.0341	0.0573
2.26	2.27	0.05	1.0096	0.0354	0.0575
2.26	2.27	0.15	0.9053	0.0320	0.0516
2.26	2.27	0.25	0.8224	0.0301	0.0469
2.26	2.27	0.35	0.8606	0.0318	0.0490
2.26	2.27	0.45	1.1375	0.0411	0.0648
2.26	2.27	0.55	1.6362	0.0551	0.0932
2.26	2.27	0.65	2.5894	0.0835	0.1475
2.26	2.27	0.75	4.5238	0.1317	0.2578
2.26	2.27	0.85	10.0611	0.2895	0.5733
2.26	2.27	0.91	13.9744	1.2428	0.7963
2.27	2.28	-0.84	0.9618	0.0426	0.0550
2.27	2.28	-0.75	1.0566	0.0368	0.0604
2.27	2.28	-0.65	0.8919	0.0310	0.0510
2.27	2.28	-0.55	0.6526	0.0250	0.0373
2.27	2.28	-0.45	0.5832	0.0222	0.0333
2.27	2.28	-0.35	0.6269	0.0234	0.0358
2.27	2.28	-0.25	0.7370	0.0263	0.0421
2.27	2.28	-0.15	0.9034	0.0319	0.0517
2.27	2.28	-0.05	0.9497	0.0326	0.0543
2.27	2.28	0.05	0.9688	0.0333	0.0554
2.27	2.28	0.15	0.8683	0.0313	0.0496
2.27	2.28	0.25	0.8015	0.0293	0.0458
2.27	2.28	0.35	0.8555	0.0317	0.0489
2.27	2.28	0.45	1.0869	0.0387	0.0621
2.27	2.28	0.55	1.5585	0.0538	0.0891
2.27	2.28	0.65	2.6457	0.0843	0.1513
2.27	2.28	0.75	4.3942	0.1281	0.2512
2.27	2.28	0.85	9.8093	0.2837	0.5609
2.27	2.28	0.91	13.2425	1.0394	0.7572
2.28	2.29	-0.84	0.8873	0.0411	0.0509
2.28	2.29	-0.75	0.9843	0.0339	0.0565

2.28	2.29	-0.65	0.8622	0.0302	0.0495
2.28	2.29	-0.55	0.6373	0.0242	0.0366
2.28	2.29	-0.45	0.5345	0.0206	0.0307
2.28	2.29	-0.35	0.5789	0.0217	0.0332
2.28	2.29	-0.25	0.6793	0.0252	0.0390
2.28	2.29	-0.15	0.8085	0.0288	0.0464
2.28	2.29	-0.05	0.8716	0.0304	0.0500
2.28	2.29	0.05	0.8440	0.0300	0.0484
2.28	2.29	0.15	0.7654	0.0273	0.0439
2.28	2.29	0.25	0.7109	0.0262	0.0408
2.28	2.29	0.35	0.7914	0.0298	0.0454
2.28	2.29	0.45	0.9918	0.0358	0.0569
2.28	2.29	0.55	1.4137	0.0485	0.0811
2.28	2.29	0.65	2.2834	0.0721	0.1310
2.28	2.29	0.75	3.9948	0.1181	0.2292
2.28	2.29	0.85	8.9678	0.2592	0.5145
2.28	2.29	0.91	15.5160	1.2012	0.8902
2.29	2.30	-0.84	0.8738	0.0384	0.0503
2.29	2.30	-0.75	0.9851	0.0328	0.0567
2.29	2.30	-0.65	0.8354	0.0288	0.0481
2.29	2.30	-0.55	0.6365	0.0239	0.0366
2.29	2.30	-0.45	0.5290	0.0209	0.0305
2.29	2.30	-0.35	0.5271	0.0200	0.0303
2.29	2.30	-0.25	0.6404	0.0236	0.0369
2.29	2.30	-0.15	0.7407	0.0268	0.0426
2.29	2.30	-0.05	0.8396	0.0297	0.0483
2.29	2.30	0.05	0.8297	0.0296	0.0478
2.29	2.30	0.15	0.7415	0.0266	0.0427
2.29	2.30	0.25	0.7128	0.0262	0.0410
2.29	2.30	0.35	0.7596	0.0283	0.0437
2.29	2.30	0.45	1.0222	0.0371	0.0589
2.29	2.30	0.55	1.4603	0.0514	0.0841
2.29	2.30	0.65	2.1624	0.0716	0.1245
2.29	2.30	0.75	4.0827	0.1203	0.2351
2.29	2.30	0.85	8.6990	0.2502	0.5008
2.29	2.30	0.91	12.8375	0.8890	0.7391
2.30	2.31	-0.84	0.8647	0.0419	0.0500
2.30	2.31	-0.75	0.8769	0.0301	0.0507
2.30	2.31	-0.65	0.7412	0.0260	0.0428
2.30	2.31	-0.55	0.6131	0.0231	0.0354
2.30	2.31	-0.45	0.5034	0.0197	0.0291
2.30	2.31	-0.35	0.5351	0.0206	0.0309
2.30	2.31	-0.25	0.6374	0.0236	0.0368
2.30	2.31	-0.15	0.7135	0.0259	0.0412
2.30	2.31	-0.05	0.8356	0.0293	0.0483
2.30	2.31	0.05	0.7925	0.0289	0.0458
2.30	2.31	0.15	0.6970	0.0259	0.0403
2.30	2.31	0.25	0.6552	0.0246	0.0379
2.30	2.31	0.35	0.7270	0.0270	0.0420
2.30	2.31	0.45	0.9291	0.0334	0.0537
2.30	2.31	0.55	1.4560	0.0504	0.0841
2.30	2.31	0.65	2.1220	0.0685	0.1226
2.30	2.31	0.75	3.7045	0.1112	0.2140
2.30	2.31	0.85	8.3426	0.2415	0.4820
2.30	2.31	0.91	15.1300	1.0754	0.8741
2.31	2.32	-0.84	0.8290	0.0425	0.0481
2.31	2.32	-0.75	0.8815	0.0303	0.0511
2.31	2.32	-0.65	0.7412	0.0261	0.0430
2.31	2.32	-0.55	0.5557	0.0212	0.0322
2.31	2.32	-0.45	0.4597	0.0184	0.0266
2.31	2.32	-0.35	0.4722	0.0186	0.0274
2.31	2.32	-0.25	0.5434	0.0206	0.0315
2.31	2.32	-0.15	0.6450	0.0240	0.0374
2.31	2.32	-0.05	0.6814	0.0248	0.0395
2.31	2.32	0.05	0.6954	0.0259	0.0403
2.31	2.32	0.15	0.6347	0.0238	0.0368
2.31	2.32	0.25	0.6116	0.0235	0.0355
2.31	2.32	0.35	0.6317	0.0244	0.0366
2.31	2.32	0.45	0.8705	0.0327	0.0505
2.31	2.32	0.55	1.2564	0.0446	0.0728
2.31	2.32	0.65	1.8576	0.0622	0.1077
2.31	2.32	0.75	3.6224	0.1106	0.2100
2.31	2.32	0.85	8.3602	0.2414	0.4846
2.31	2.32	0.91	15.0495	0.9912	0.8724
2.32	2.33	-0.84	0.7492	0.0362	0.0436
2.32	2.33	-0.75	0.8781	0.0309	0.0511

2.32	2.33	-0.65	0.7093	0.0255	0.0413
2.32	2.33	-0.55	0.5196	0.0201	0.0302
2.32	2.33	-0.45	0.4339	0.0176	0.0252
2.32	2.33	-0.35	0.4279	0.0171	0.0249
2.32	2.33	-0.25	0.4889	0.0190	0.0284
2.32	2.33	-0.15	0.6090	0.0230	0.0354
2.32	2.33	-0.05	0.6569	0.0238	0.0382
2.32	2.33	0.05	0.6860	0.0252	0.0399
2.32	2.33	0.15	0.6365	0.0236	0.0370
2.32	2.33	0.25	0.5924	0.0228	0.0345
2.32	2.33	0.35	0.6838	0.0265	0.0398
2.32	2.33	0.45	0.8466	0.0317	0.0492
2.32	2.33	0.55	1.2546	0.0452	0.0730
2.32	2.33	0.65	1.9398	0.0639	0.1128
2.32	2.33	0.75	3.5376	0.1061	0.2058
2.32	2.33	0.85	8.1008	0.2377	0.4712
2.32	2.33	0.91	17.6330	1.1891	1.0257
2.33	2.34	-0.84	0.7093	0.0376	0.0414
2.33	2.34	-0.75	0.8394	0.0298	0.0490
2.33	2.34	-0.65	0.6576	0.0238	0.0384
2.33	2.34	-0.55	0.4744	0.0189	0.0277
2.33	2.34	-0.45	0.3905	0.0163	0.0228
2.33	2.34	-0.35	0.4094	0.0166	0.0239
2.33	2.34	-0.25	0.5032	0.0200	0.0294
2.33	2.34	-0.15	0.5430	0.0207	0.0317
2.33	2.34	-0.05	0.6085	0.0229	0.0355
2.33	2.34	0.05	0.6134	0.0227	0.0358
2.33	2.34	0.15	0.5885	0.0220	0.0343
2.33	2.34	0.25	0.5615	0.0216	0.0328
2.33	2.34	0.35	0.6252	0.0241	0.0365
2.33	2.34	0.45	0.8831	0.0323	0.0515
2.33	2.34	0.55	1.1993	0.0439	0.0700
2.33	2.34	0.65	1.8697	0.0636	0.1091
2.33	2.34	0.75	3.4787	0.1077	0.2030
2.33	2.34	0.85	7.9586	0.2453	0.4645
2.33	2.34	0.91	14.0979	0.9370	0.8229
2.34	2.35	-0.84	0.7185	0.0367	0.0421
2.34	2.35	-0.75	0.7281	0.0259	0.0426
2.34	2.35	-0.65	0.6513	0.0237	0.0381
2.34	2.35	-0.55	0.4375	0.0172	0.0256
2.34	2.35	-0.45	0.3872	0.0161	0.0227
2.34	2.35	-0.35	0.3589	0.0146	0.0210
2.34	2.35	-0.25	0.4357	0.0171	0.0255
2.34	2.35	-0.15	0.5284	0.0201	0.0309
2.34	2.35	-0.05	0.5802	0.0216	0.0340
2.34	2.35	0.05	0.5783	0.0222	0.0339
2.34	2.35	0.15	0.5398	0.0207	0.0316
2.34	2.35	0.25	0.5015	0.0196	0.0294
2.34	2.35	0.35	0.5920	0.0232	0.0347
2.34	2.35	0.45	0.8101	0.0306	0.0474
2.34	2.35	0.55	1.0803	0.0400	0.0633
2.34	2.35	0.65	1.7618	0.0588	0.1032
2.34	2.35	0.75	3.1507	0.0986	0.1845
2.34	2.35	0.85	7.8696	0.2367	0.4609
2.34	2.35	0.91	12.3372	0.8371	0.7225
2.35	2.36	-0.84	0.7344	0.0385	0.0432
2.35	2.36	-0.75	0.7591	0.0272	0.0446
2.35	2.36	-0.65	0.6546	0.0240	0.0385
2.35	2.36	-0.55	0.4932	0.0192	0.0290
2.35	2.36	-0.45	0.3770	0.0159	0.0222
2.35	2.36	-0.35	0.4085	0.0166	0.0240
2.35	2.36	-0.25	0.4542	0.0183	0.0267
2.35	2.36	-0.15	0.5309	0.0207	0.0312
2.35	2.36	-0.05	0.5856	0.0217	0.0344
2.35	2.36	0.05	0.6066	0.0229	0.0356
2.35	2.36	0.15	0.5437	0.0208	0.0320
2.35	2.36	0.25	0.5203	0.0202	0.0306
2.35	2.36	0.35	0.5911	0.0231	0.0347
2.35	2.36	0.45	0.8410	0.0313	0.0494
2.35	2.36	0.55	1.1686	0.0425	0.0687
2.35	2.36	0.65	1.9209	0.0648	0.1129
2.35	2.36	0.75	3.4846	0.1088	0.2048
2.35	2.36	0.85	7.8838	0.2339	0.4633
2.35	2.36	0.91	12.2587	0.7900	0.7204
2.36	2.37	-0.84	0.7152	0.0473	0.0422
2.36	2.37	-0.75	0.7272	0.0272	0.0429

2.36	2.37	-0.65	0.6344	0.0238	0.0374
2.36	2.37	-0.55	0.4565	0.0182	0.0269
2.36	2.37	-0.45	0.3659	0.0159	0.0216
2.36	2.37	-0.35	0.3503	0.0149	0.0207
2.36	2.37	-0.25	0.4244	0.0175	0.0250
2.36	2.37	-0.15	0.4898	0.0194	0.0289
2.36	2.37	-0.05	0.5561	0.0214	0.0328
2.36	2.37	0.05	0.5667	0.0220	0.0334
2.36	2.37	0.15	0.5105	0.0205	0.0301
2.36	2.37	0.25	0.5317	0.0213	0.0314
2.36	2.37	0.35	0.5915	0.0238	0.0349
2.36	2.37	0.45	0.7979	0.0309	0.0470
2.36	2.37	0.55	1.1245	0.0427	0.0663
2.36	2.37	0.65	1.7880	0.0614	0.1054
2.36	2.37	0.75	3.2008	0.1005	0.1887
2.36	2.37	0.85	8.2995	0.2454	0.4894
2.36	2.37	0.91	14.4732	0.8853	0.8534
2.37	2.38	-0.84	0.6051	0.0331	0.0358
2.37	2.38	-0.75	0.7247	0.0268	0.0429
2.37	2.38	-0.65	0.5950	0.0220	0.0352
2.37	2.38	-0.55	0.4009	0.0161	0.0237
2.37	2.38	-0.45	0.3469	0.0150	0.0205
2.37	2.38	-0.35	0.3327	0.0143	0.0197
2.37	2.38	-0.25	0.4016	0.0161	0.0238
2.37	2.38	-0.15	0.4763	0.0185	0.0282
2.37	2.38	-0.05	0.5329	0.0206	0.0315
2.37	2.38	0.05	0.5298	0.0204	0.0313
2.37	2.38	0.15	0.5242	0.0206	0.0310
2.37	2.38	0.25	0.4877	0.0195	0.0289
2.37	2.38	0.35	0.5751	0.0227	0.0340
2.37	2.38	0.45	0.8026	0.0302	0.0475
2.37	2.38	0.55	1.1187	0.0421	0.0662
2.37	2.38	0.65	1.8586	0.0636	0.1100
2.37	2.38	0.75	3.2214	0.1037	0.1906
2.37	2.38	0.85	7.4087	0.2199	0.4383
2.37	2.38	0.91	15.2270	0.9718	0.9009
2.38	2.39	-0.84	0.5418	0.0381	0.0322
2.38	2.39	-0.75	0.6001	0.0236	0.0356
2.38	2.39	-0.65	0.5136	0.0202	0.0305
2.38	2.39	-0.55	0.3773	0.0157	0.0224
2.38	2.39	-0.45	0.3014	0.0135	0.0179
2.38	2.39	-0.35	0.2848	0.0128	0.0169
2.38	2.39	-0.25	0.3442	0.0146	0.0204
2.38	2.39	-0.15	0.3826	0.0154	0.0227
2.38	2.39	-0.05	0.4455	0.0177	0.0264
2.38	2.39	0.05	0.4720	0.0191	0.0280
2.38	2.39	0.15	0.4448	0.0180	0.0264
2.38	2.39	0.25	0.4151	0.0171	0.0246
2.38	2.39	0.35	0.4817	0.0198	0.0286
2.38	2.39	0.45	0.6945	0.0276	0.0412
2.38	2.39	0.55	0.9476	0.0362	0.0563
2.38	2.39	0.65	1.4983	0.0527	0.0889
2.38	2.39	0.75	2.6949	0.0867	0.1600
2.38	2.39	0.85	6.5649	0.1990	0.3897
2.38	2.39	0.91	13.8375	0.9251	0.8214
2.39	2.40	-0.84	0.5784	0.0495	0.0345
2.39	2.40	-0.75	0.5682	0.0222	0.0338
2.39	2.40	-0.65	0.5031	0.0197	0.0300
2.39	2.40	-0.55	0.3562	0.0154	0.0212
2.39	2.40	-0.45	0.2714	0.0124	0.0162
2.39	2.40	-0.35	0.2823	0.0128	0.0168
2.39	2.40	-0.25	0.3283	0.0141	0.0196
2.39	2.40	-0.15	0.3818	0.0157	0.0227
2.39	2.40	-0.05	0.4001	0.0163	0.0238
2.39	2.40	0.05	0.4191	0.0173	0.0250
2.39	2.40	0.15	0.4084	0.0169	0.0243
2.39	2.40	0.25	0.4096	0.0170	0.0244
2.39	2.40	0.35	0.4935	0.0203	0.0294
2.39	2.40	0.45	0.6948	0.0278	0.0414
2.39	2.40	0.55	0.9295	0.0359	0.0554
2.39	2.40	0.65	1.4217	0.0521	0.0847
2.39	2.40	0.75	2.6899	0.0880	0.1602
2.39	2.40	0.85	6.3854	0.2005	0.3803
2.40	2.41	-0.84	0.5760	0.0590	0.0344
2.40	2.41	-0.75	0.5380	0.0219	0.0322
2.40	2.41	-0.65	0.4396	0.0180	0.0263

2.40	2.41	-0.55	0.3531	0.0156	0.0211
2.40	2.41	-0.45	0.2913	0.0137	0.0174
2.40	2.41	-0.35	0.2606	0.0119	0.0156
2.40	2.41	-0.25	0.3102	0.0139	0.0185
2.40	2.41	-0.15	0.3520	0.0154	0.0210
2.40	2.41	-0.05	0.3899	0.0166	0.0233
2.40	2.41	0.05	0.4128	0.0173	0.0247
2.40	2.41	0.15	0.3685	0.0156	0.0220
2.40	2.41	0.25	0.4070	0.0174	0.0243
2.40	2.41	0.35	0.4845	0.0205	0.0290
2.40	2.41	0.45	0.6396	0.0261	0.0382
2.40	2.41	0.55	0.9002	0.0360	0.0538
2.40	2.41	0.65	1.4254	0.0517	0.0852
2.40	2.41	0.75	2.6651	0.0877	0.1593
2.40	2.41	0.85	6.3248	0.1963	0.3780
2.40	2.41	0.92	22.1209	3.9442	1.3220
2.41	2.42	-0.84	0.5135	0.0690	0.0308
2.41	2.42	-0.75	0.5576	0.0218	0.0334
2.41	2.42	-0.65	0.4431	0.0177	0.0266
2.41	2.42	-0.55	0.3470	0.0151	0.0208
2.41	2.42	-0.45	0.2700	0.0122	0.0162
2.41	2.42	-0.35	0.2435	0.0114	0.0146
2.41	2.42	-0.25	0.2910	0.0130	0.0174
2.41	2.42	-0.15	0.3372	0.0144	0.0202
2.41	2.42	-0.05	0.3606	0.0148	0.0216
2.41	2.42	0.05	0.3501	0.0150	0.0210
2.41	2.42	0.15	0.3545	0.0149	0.0213
2.41	2.42	0.25	0.3859	0.0166	0.0231
2.41	2.42	0.35	0.4615	0.0192	0.0277
2.41	2.42	0.45	0.6276	0.0252	0.0376
2.41	2.42	0.55	0.8828	0.0346	0.0529
2.41	2.42	0.65	1.3776	0.0500	0.0826
2.41	2.42	0.75	2.5484	0.0846	0.1528
2.41	2.42	0.85	6.6197	0.2136	0.3969
2.41	2.42	0.92	50.5117	8.1777	3.0288
2.42	2.43	-0.84	0.4171	0.0472	0.0251
2.42	2.43	-0.75	0.4965	0.0199	0.0299
2.42	2.43	-0.65	0.4723	0.0187	0.0284
2.42	2.43	-0.55	0.3537	0.0150	0.0213
2.42	2.43	-0.45	0.2651	0.0121	0.0159
2.42	2.43	-0.35	0.2397	0.0109	0.0144
2.42	2.43	-0.25	0.2675	0.0119	0.0161
2.42	2.43	-0.15	0.3197	0.0136	0.0192
2.42	2.43	-0.05	0.3538	0.0148	0.0213
2.42	2.43	0.05	0.3586	0.0151	0.0216
2.42	2.43	0.15	0.3296	0.0139	0.0198
2.42	2.43	0.25	0.3643	0.0153	0.0219
2.42	2.43	0.35	0.4424	0.0183	0.0266
2.42	2.43	0.45	0.6429	0.0254	0.0387
2.42	2.43	0.55	0.8794	0.0343	0.0529
2.42	2.43	0.65	1.4189	0.0512	0.0854
2.42	2.43	0.75	2.5460	0.0844	0.1532
2.42	2.43	0.85	6.3620	0.1961	0.3827
2.42	2.43	0.92	35.2374	4.7528	2.1199
2.43	2.44	-0.84	0.4014	0.0574	0.0242
2.43	2.44	-0.75	0.5080	0.0206	0.0307
2.43	2.44	-0.65	0.4389	0.0176	0.0265
2.43	2.44	-0.55	0.3294	0.0142	0.0199
2.43	2.44	-0.45	0.2430	0.0117	0.0147
2.43	2.44	-0.35	0.2330	0.0110	0.0141
2.43	2.44	-0.25	0.2580	0.0122	0.0156
2.43	2.44	-0.15	0.3065	0.0134	0.0185
2.43	2.44	-0.05	0.3441	0.0147	0.0208
2.43	2.44	0.05	0.3302	0.0144	0.0199
2.43	2.44	0.15	0.3327	0.0145	0.0201
2.43	2.44	0.25	0.3657	0.0159	0.0221
2.43	2.44	0.35	0.4811	0.0203	0.0290
2.43	2.44	0.45	0.6023	0.0249	0.0364
2.43	2.44	0.55	0.8729	0.0355	0.0527
2.43	2.44	0.65	1.3186	0.0498	0.0796
2.43	2.44	0.75	2.5352	0.0879	0.1530
2.43	2.44	0.85	6.2531	0.2017	0.3775
2.43	2.44	0.92	20.4293	1.8774	1.2331
2.44	2.45	-0.84	0.4379	0.0907	0.0265
2.44	2.45	-0.75	0.5004	0.0203	0.0303
2.44	2.45	-0.65	0.4694	0.0186	0.0284

2.44	2.45	-0.55	0.3221	0.0141	0.0195
2.44	2.45	-0.45	0.2439	0.0113	0.0148
2.44	2.45	-0.35	0.2101	0.0099	0.0127
2.44	2.45	-0.25	0.2450	0.0113	0.0148
2.44	2.45	-0.15	0.2963	0.0130	0.0179
2.44	2.45	-0.05	0.3339	0.0142	0.0202
2.44	2.45	0.05	0.3311	0.0144	0.0201
2.44	2.45	0.15	0.3532	0.0150	0.0214
2.44	2.45	0.25	0.3501	0.0151	0.0212
2.44	2.45	0.35	0.4511	0.0191	0.0273
2.44	2.45	0.45	0.6601	0.0265	0.0400
2.44	2.45	0.55	0.8546	0.0343	0.0518
2.44	2.45	0.65	1.2921	0.0484	0.0782
2.44	2.45	0.75	2.4529	0.0836	0.1485
2.44	2.45	0.85	6.6655	0.2118	0.4037
2.44	2.45	0.92	12.0805	0.7576	0.7316
2.45	2.46	-0.83	0.4025	0.0236	0.0245
2.45	2.46	-0.75	0.4456	0.0184	0.0271
2.45	2.46	-0.65	0.4260	0.0170	0.0259
2.45	2.46	-0.55	0.3195	0.0135	0.0194
2.45	2.46	-0.45	0.2423	0.0114	0.0147
2.45	2.46	-0.35	0.2048	0.0096	0.0124
2.45	2.46	-0.25	0.2446	0.0108	0.0149
2.45	2.46	-0.15	0.2731	0.0120	0.0166
2.45	2.46	-0.05	0.3008	0.0129	0.0183
2.45	2.46	0.05	0.3210	0.0140	0.0195
2.45	2.46	0.15	0.3324	0.0141	0.0202
2.45	2.46	0.25	0.3211	0.0139	0.0195
2.45	2.46	0.35	0.3869	0.0166	0.0235
2.45	2.46	0.45	0.5558	0.0229	0.0338
2.45	2.46	0.55	0.8252	0.0323	0.0501
2.45	2.46	0.65	1.2131	0.0452	0.0737
2.45	2.46	0.75	2.3066	0.0777	0.1402
2.45	2.46	0.85	6.0812	0.1914	0.3695
2.45	2.46	0.92	16.6890	1.0844	1.0141
2.46	2.47	-0.83	0.4018	0.0258	0.0245
2.46	2.47	-0.75	0.4574	0.0199	0.0279
2.46	2.47	-0.65	0.4035	0.0172	0.0246
2.46	2.47	-0.55	0.3028	0.0135	0.0185
2.46	2.47	-0.45	0.2240	0.0111	0.0137
2.46	2.47	-0.35	0.1989	0.0100	0.0121
2.46	2.47	-0.25	0.2121	0.0105	0.0129
2.46	2.47	-0.15	0.2546	0.0119	0.0155
2.46	2.47	-0.05	0.2791	0.0126	0.0170
2.46	2.47	0.05	0.2871	0.0130	0.0175
2.46	2.47	0.15	0.3027	0.0135	0.0185
2.46	2.47	0.25	0.3231	0.0143	0.0197
2.46	2.47	0.35	0.4200	0.0178	0.0256
2.46	2.47	0.45	0.5991	0.0249	0.0365
2.46	2.47	0.55	0.7916	0.0326	0.0483
2.46	2.47	0.65	1.1410	0.0434	0.0696
2.46	2.47	0.75	2.2386	0.0783	0.1365
2.46	2.47	0.85	5.6690	0.1849	0.3456
2.46	2.47	0.92	13.2784	0.8854	0.8095
2.47	2.48	-0.83	0.4020	0.0247	0.0246
2.47	2.48	-0.75	0.4454	0.0185	0.0272
2.47	2.48	-0.65	0.4073	0.0168	0.0249
2.47	2.48	-0.55	0.3048	0.0135	0.0186
2.47	2.48	-0.45	0.2227	0.0109	0.0136
2.47	2.48	-0.35	0.2018	0.0095	0.0123
2.47	2.48	-0.25	0.2214	0.0106	0.0135
2.47	2.48	-0.15	0.2427	0.0113	0.0148
2.47	2.48	-0.05	0.2754	0.0123	0.0168
2.47	2.48	0.05	0.2765	0.0125	0.0169
2.47	2.48	0.15	0.2634	0.0119	0.0161
2.47	2.48	0.25	0.3306	0.0144	0.0202
2.47	2.48	0.35	0.4168	0.0176	0.0255
2.47	2.48	0.45	0.5559	0.0228	0.0340
2.47	2.48	0.55	0.7062	0.0284	0.0432
2.47	2.48	0.65	1.0374	0.0403	0.0634
2.47	2.48	0.75	2.1305	0.0753	0.1303
2.47	2.48	0.85	5.5480	0.1865	0.3393
2.47	2.48	0.92	10.7217	0.6224	0.6558
2.48	2.49	-0.83	0.3616	0.0222	0.0222
2.48	2.49	-0.75	0.4385	0.0184	0.0269
2.48	2.49	-0.65	0.4166	0.0171	0.0256

2.48	2.49	-0.55	0.3165	0.0137	0.0194
2.48	2.49	-0.45	0.2304	0.0110	0.0141
2.48	2.49	-0.35	0.1950	0.0094	0.0120
2.48	2.49	-0.25	0.1969	0.0093	0.0121
2.48	2.49	-0.15	0.2392	0.0107	0.0147
2.48	2.49	-0.05	0.2629	0.0118	0.0161
2.48	2.49	0.05	0.2601	0.0117	0.0160
2.48	2.49	0.15	0.2662	0.0120	0.0163
2.48	2.49	0.25	0.2893	0.0129	0.0178
2.48	2.49	0.35	0.3771	0.0163	0.0231
2.48	2.49	0.45	0.5172	0.0216	0.0317
2.48	2.49	0.55	0.6906	0.0281	0.0424
2.48	2.49	0.65	1.0887	0.0411	0.0668
2.48	2.49	0.75	2.2368	0.0801	0.1373
2.48	2.49	0.85	5.6449	0.1869	0.3464
2.48	2.49	0.92	11.3877	0.6259	0.6988
2.49	2.50	-0.83	0.3462	0.0222	0.0213
2.49	2.50	-0.75	0.3962	0.0172	0.0244
2.49	2.50	-0.65	0.3644	0.0155	0.0224
2.49	2.50	-0.55	0.2754	0.0122	0.0170
2.49	2.50	-0.45	0.2143	0.0103	0.0132
2.49	2.50	-0.35	0.1646	0.0083	0.0101
2.49	2.50	-0.25	0.1882	0.0091	0.0116
2.49	2.50	-0.15	0.2103	0.0099	0.0129
2.49	2.50	-0.05	0.2234	0.0103	0.0138
2.49	2.50	0.05	0.2593	0.0119	0.0160
2.49	2.50	0.15	0.2643	0.0121	0.0163
2.49	2.50	0.25	0.2890	0.0131	0.0178
2.49	2.50	0.35	0.3888	0.0170	0.0239
2.49	2.50	0.45	0.4966	0.0211	0.0306
2.49	2.50	0.55	0.7181	0.0295	0.0442
2.49	2.50	0.65	1.0461	0.0408	0.0644
2.49	2.50	0.75	2.0129	0.0712	0.1239
2.49	2.50	0.85	5.4718	0.1759	0.3369
2.49	2.50	0.92	10.2329	0.5413	0.6300
2.50	2.51	-0.83	0.2691	0.0178	0.0166
2.50	2.51	-0.75	0.3879	0.0172	0.0240
2.50	2.51	-0.65	0.3582	0.0157	0.0221
2.50	2.51	-0.55	0.2959	0.0134	0.0183
2.50	2.51	-0.45	0.2168	0.0106	0.0134
2.50	2.51	-0.35	0.1745	0.0088	0.0108
2.50	2.51	-0.25	0.1848	0.0094	0.0114
2.50	2.51	-0.15	0.2039	0.0098	0.0126
2.50	2.51	-0.05	0.2337	0.0106	0.0144
2.50	2.51	0.05	0.2514	0.0113	0.0155
2.50	2.51	0.15	0.2699	0.0121	0.0167
2.50	2.51	0.25	0.2887	0.0127	0.0178
2.50	2.51	0.35	0.4006	0.0172	0.0247
2.50	2.51	0.45	0.5343	0.0224	0.0330
2.50	2.51	0.55	0.6536	0.0267	0.0404
2.50	2.51	0.65	0.9724	0.0374	0.0601
2.50	2.51	0.75	2.0057	0.0708	0.1239
2.50	2.51	0.85	4.9859	0.1616	0.3080
2.50	2.51	0.92	16.4826	0.9919	1.0180
2.51	2.52	-0.83	0.3328	0.0222	0.0206
2.51	2.52	-0.75	0.3591	0.0160	0.0223
2.51	2.52	-0.65	0.3483	0.0151	0.0216
2.51	2.52	-0.55	0.2739	0.0123	0.0170
2.51	2.52	-0.45	0.1982	0.0099	0.0123
2.51	2.52	-0.35	0.1777	0.0089	0.0110
2.51	2.52	-0.25	0.1684	0.0085	0.0104
2.51	2.52	-0.15	0.1960	0.0096	0.0121
2.51	2.52	-0.05	0.2212	0.0103	0.0137
2.51	2.52	0.05	0.2306	0.0108	0.0143
2.51	2.52	0.15	0.2409	0.0114	0.0149
2.51	2.52	0.25	0.2749	0.0121	0.0170
2.51	2.52	0.35	0.3494	0.0151	0.0217
2.51	2.52	0.45	0.5268	0.0220	0.0326
2.51	2.52	0.55	0.6064	0.0254	0.0376
2.51	2.52	0.65	0.9496	0.0372	0.0588
2.51	2.52	0.75	2.0066	0.0721	0.1243
2.51	2.52	0.85	5.5321	0.1857	0.3428
2.51	2.52	0.92	13.8996	0.7295	0.8613
2.52	2.53	-0.83	0.3318	0.0232	0.0206
2.52	2.53	-0.75	0.3670	0.0166	0.0228
2.52	2.53	-0.65	0.3592	0.0156	0.0223

2.52	2.53	-0.55	0.2988	0.0137	0.0186
2.52	2.53	-0.45	0.2200	0.0111	0.0137
2.52	2.53	-0.35	0.1717	0.0087	0.0107
2.52	2.53	-0.25	0.1688	0.0086	0.0105
2.52	2.53	-0.15	0.1990	0.0096	0.0124
2.52	2.53	-0.05	0.2192	0.0105	0.0136
2.52	2.53	0.05	0.2228	0.0106	0.0139
2.52	2.53	0.15	0.2425	0.0117	0.0151
2.52	2.53	0.25	0.2583	0.0122	0.0161
2.52	2.53	0.35	0.3329	0.0149	0.0207
2.52	2.53	0.45	0.4743	0.0206	0.0295
2.52	2.53	0.55	0.6487	0.0277	0.0403
2.52	2.53	0.65	0.9512	0.0381	0.0591
2.52	2.53	0.75	1.9236	0.0711	0.1196
2.52	2.53	0.85	5.5777	0.1841	0.3467
2.52	2.53	0.92	19.0123	1.1532	1.1819
2.53	2.54	-0.83	0.2863	0.0197	0.0179
2.53	2.54	-0.75	0.3190	0.0145	0.0199
2.53	2.54	-0.65	0.3130	0.0136	0.0195
2.53	2.54	-0.55	0.2561	0.0116	0.0160
2.53	2.54	-0.45	0.1840	0.0093	0.0115
2.53	2.54	-0.35	0.1584	0.0081	0.0099
2.53	2.54	-0.25	0.1423	0.0073	0.0089
2.53	2.54	-0.15	0.1554	0.0078	0.0097
2.53	2.54	-0.05	0.1768	0.0087	0.0110
2.53	2.54	0.05	0.1946	0.0094	0.0121
2.53	2.54	0.15	0.2040	0.0099	0.0127
2.53	2.54	0.25	0.2416	0.0111	0.0151
2.53	2.54	0.35	0.3150	0.0140	0.0196
2.53	2.54	0.45	0.4447	0.0193	0.0277
2.53	2.54	0.55	0.5523	0.0235	0.0344
2.53	2.54	0.65	0.8498	0.0339	0.0530
2.53	2.54	0.75	1.7839	0.0636	0.1113
2.53	2.54	0.85	4.6455	0.1563	0.2897
2.53	2.54	0.92	8.9402	0.5006	0.5576
2.54	2.55	-0.83	0.3023	0.0213	0.0189
2.54	2.55	-0.75	0.3234	0.0151	0.0202
2.54	2.55	-0.65	0.3154	0.0141	0.0197
2.54	2.55	-0.55	0.2502	0.0119	0.0157
2.54	2.55	-0.45	0.1959	0.0097	0.0123
2.54	2.55	-0.35	0.1509	0.0081	0.0094
2.54	2.55	-0.25	0.1449	0.0077	0.0091
2.54	2.55	-0.15	0.1647	0.0083	0.0103
2.54	2.55	-0.05	0.1784	0.0087	0.0112
2.54	2.55	0.05	0.1902	0.0091	0.0119
2.54	2.55	0.15	0.2076	0.0099	0.0130
2.54	2.55	0.25	0.2521	0.0116	0.0158
2.54	2.55	0.35	0.3189	0.0144	0.0200
2.54	2.55	0.45	0.4376	0.0193	0.0274
2.54	2.55	0.55	0.5639	0.0245	0.0353
2.54	2.55	0.65	0.8654	0.0352	0.0541
2.54	2.55	0.75	1.8945	0.0726	0.1185
2.54	2.55	0.85	5.1063	0.1818	0.3195
2.54	2.55	0.92	10.5661	0.5901	0.6611
2.55	2.56	-0.83	0.3483	0.0245	0.0219
2.55	2.56	-0.75	0.3491	0.0162	0.0219
2.55	2.56	-0.65	0.3294	0.0144	0.0207
2.55	2.56	-0.55	0.2655	0.0120	0.0167
2.55	2.56	-0.45	0.2050	0.0100	0.0129
2.55	2.56	-0.35	0.1446	0.0075	0.0091
2.55	2.56	-0.25	0.1296	0.0069	0.0081
2.55	2.56	-0.15	0.1548	0.0080	0.0097
2.55	2.56	-0.05	0.1697	0.0086	0.0107
2.55	2.56	0.05	0.1734	0.0088	0.0109
2.55	2.56	0.15	0.2034	0.0098	0.0128
2.55	2.56	0.25	0.2457	0.0113	0.0154
2.55	2.56	0.35	0.3183	0.0141	0.0200
2.55	2.56	0.45	0.4307	0.0189	0.0270
2.55	2.56	0.55	0.5372	0.0234	0.0337
2.55	2.56	0.65	0.7632	0.0319	0.0479
2.55	2.56	0.75	1.6636	0.0639	0.1044
2.55	2.56	0.85	5.1738	0.1813	0.3248
2.55	2.56	0.92	12.5346	0.7140	0.7868
2.56	2.57	-0.83	0.3006	0.0219	0.0189
2.56	2.57	-0.75	0.3175	0.0148	0.0200
2.56	2.57	-0.65	0.3109	0.0141	0.0196

2.56	2.57	-0.55	0.2616	0.0117	0.0165
2.56	2.57	-0.45	0.1748	0.0089	0.0110
2.56	2.57	-0.35	0.1261	0.0068	0.0079
2.56	2.57	-0.25	0.1226	0.0066	0.0077
2.56	2.57	-0.15	0.1418	0.0074	0.0089
2.56	2.57	-0.05	0.1537	0.0079	0.0097
2.56	2.57	0.05	0.1731	0.0086	0.0109
2.56	2.57	0.15	0.2002	0.0094	0.0126
2.56	2.57	0.25	0.2350	0.0110	0.0148
2.56	2.57	0.35	0.3096	0.0139	0.0195
2.56	2.57	0.45	0.4101	0.0181	0.0258
2.56	2.57	0.55	0.4920	0.0219	0.0310
2.56	2.57	0.65	0.8101	0.0331	0.0510
2.56	2.57	0.75	1.6611	0.0599	0.1046
2.56	2.57	0.85	5.5220	0.1945	0.3477
2.56	2.57	0.92	12.6503	0.7213	0.7966
2.57	2.58	-0.83	0.2742	0.0199	0.0173
2.57	2.58	-0.75	0.3044	0.0139	0.0192
2.57	2.58	-0.65	0.2760	0.0126	0.0174
2.57	2.58	-0.55	0.2285	0.0104	0.0144
2.57	2.58	-0.45	0.1748	0.0088	0.0110
2.57	2.58	-0.35	0.1313	0.0071	0.0083
2.57	2.58	-0.25	0.1259	0.0068	0.0080
2.57	2.58	-0.15	0.1237	0.0066	0.0078
2.57	2.58	-0.05	0.1307	0.0069	0.0083
2.57	2.58	0.05	0.1516	0.0079	0.0096
2.57	2.58	0.15	0.1663	0.0086	0.0105
2.57	2.58	0.25	0.2062	0.0100	0.0130
2.57	2.58	0.35	0.2666	0.0124	0.0168
2.57	2.58	0.45	0.3369	0.0156	0.0213
2.57	2.58	0.55	0.4743	0.0216	0.0300
2.57	2.58	0.65	0.7156	0.0307	0.0452
2.57	2.58	0.75	1.5542	0.0594	0.0982
2.57	2.58	0.85	4.8275	0.1710	0.3050
2.57	2.58	0.92	12.1426	0.6698	0.7671
2.58	2.59	-0.83	0.2763	0.0218	0.0175
2.58	2.59	-0.75	0.2900	0.0141	0.0184
2.58	2.59	-0.65	0.2812	0.0132	0.0178
2.58	2.59	-0.55	0.2340	0.0110	0.0148
2.58	2.59	-0.45	0.1764	0.0093	0.0112
2.58	2.59	-0.35	0.1256	0.0072	0.0080
2.58	2.59	-0.25	0.1095	0.0063	0.0069
2.58	2.59	-0.15	0.1278	0.0070	0.0081
2.58	2.59	-0.05	0.1306	0.0072	0.0083
2.58	2.59	0.05	0.1392	0.0076	0.0088
2.58	2.59	0.15	0.1623	0.0087	0.0103
2.58	2.59	0.25	0.1966	0.0099	0.0125
2.58	2.59	0.35	0.2664	0.0127	0.0169
2.58	2.59	0.45	0.3538	0.0167	0.0224
2.58	2.59	0.55	0.4573	0.0209	0.0290
2.58	2.59	0.65	0.7076	0.0302	0.0448
2.58	2.59	0.75	1.5530	0.0599	0.0984
2.58	2.59	0.85	4.0874	0.1512	0.2590
2.58	2.59	0.92	12.0439	0.6856	0.7633
2.59	2.60	-0.83	0.2846	0.0234	0.0181
2.59	2.60	-0.75	0.2807	0.0138	0.0178
2.59	2.60	-0.65	0.2514	0.0125	0.0160
2.59	2.60	-0.55	0.2158	0.0109	0.0137
2.59	2.60	-0.45	0.1521	0.0087	0.0097
2.59	2.60	-0.35	0.1026	0.0064	0.0065
2.59	2.60	-0.25	0.1040	0.0062	0.0066
2.59	2.60	-0.15	0.1142	0.0067	0.0073
2.59	2.60	-0.05	0.1173	0.0069	0.0075
2.59	2.60	0.05	0.1376	0.0077	0.0087
2.59	2.60	0.15	0.1570	0.0085	0.0100
2.59	2.60	0.25	0.1818	0.0093	0.0116
2.59	2.60	0.35	0.2499	0.0121	0.0159
2.59	2.60	0.45	0.3373	0.0164	0.0214
2.59	2.60	0.55	0.4293	0.0210	0.0273
2.59	2.60	0.65	0.7342	0.0318	0.0467
2.59	2.60	0.75	1.5058	0.0592	0.0957
2.59	2.60	0.85	4.3062	0.1579	0.2738
2.59	2.60	0.92	12.1045	0.7036	0.7696
2.60	2.61	-0.83	0.2757	0.0189	0.0176
2.60	2.61	-0.75	0.2545	0.0116	0.0162
2.60	2.61	-0.65	0.2456	0.0109	0.0157

2.60	2.61	-0.55	0.2124	0.0094	0.0135
2.60	2.61	-0.45	0.1446	0.0071	0.0092
2.60	2.61	-0.35	0.1069	0.0058	0.0068
2.60	2.61	-0.25	0.0933	0.0050	0.0060
2.60	2.61	-0.15	0.1036	0.0053	0.0066
2.60	2.61	-0.05	0.1203	0.0062	0.0077
2.60	2.61	0.05	0.1447	0.0070	0.0092
2.60	2.61	0.15	0.1544	0.0075	0.0098
2.60	2.61	0.25	0.1665	0.0081	0.0106
2.60	2.61	0.35	0.2429	0.0107	0.0155
2.60	2.61	0.45	0.3170	0.0143	0.0202
2.60	2.61	0.55	0.3861	0.0169	0.0246
2.60	2.61	0.65	0.6440	0.0272	0.0411
2.60	2.61	0.75	1.3759	0.0555	0.0877
2.60	2.61	0.85	4.6394	0.1766	0.2959
2.60	2.61	0.92	14.8759	0.8642	0.9487
2.61	2.62	-0.83	0.2485	0.0169	0.0159
2.61	2.62	-0.75	0.2685	0.0120	0.0172
2.61	2.62	-0.65	0.2499	0.0107	0.0160
2.61	2.62	-0.55	0.2132	0.0093	0.0136
2.61	2.62	-0.45	0.1468	0.0069	0.0094
2.61	2.62	-0.35	0.1078	0.0056	0.0069
2.61	2.62	-0.25	0.0957	0.0051	0.0061
2.61	2.62	-0.15	0.1039	0.0055	0.0066
2.61	2.62	-0.05	0.1124	0.0058	0.0072
2.61	2.62	0.05	0.1232	0.0063	0.0079
2.61	2.62	0.15	0.1523	0.0073	0.0097
2.61	2.62	0.25	0.1802	0.0085	0.0115
2.61	2.62	0.35	0.2023	0.0093	0.0129
2.61	2.62	0.45	0.2991	0.0137	0.0191
2.61	2.62	0.55	0.3820	0.0174	0.0244
2.61	2.62	0.65	0.5921	0.0266	0.0379
2.61	2.62	0.75	1.4601	0.0616	0.0934
2.61	2.62	0.85	4.2739	0.1736	0.2734
2.61	2.62	0.92	8.8465	0.5604	0.5660
2.62	2.63	-0.83	0.2513	0.0198	0.0161
2.62	2.63	-0.75	0.2691	0.0128	0.0173
2.62	2.63	-0.65	0.2657	0.0122	0.0170
2.62	2.63	-0.55	0.2141	0.0103	0.0137
2.62	2.63	-0.45	0.1490	0.0078	0.0096
2.62	2.63	-0.35	0.1208	0.0069	0.0078
2.62	2.63	-0.25	0.0925	0.0053	0.0059
2.62	2.63	-0.15	0.1063	0.0059	0.0068
2.62	2.63	-0.05	0.1151	0.0063	0.0074
2.62	2.63	0.05	0.1236	0.0066	0.0079
2.62	2.63	0.15	0.1399	0.0076	0.0090
2.62	2.63	0.25	0.1834	0.0091	0.0118
2.62	2.63	0.35	0.2436	0.0116	0.0156
2.62	2.63	0.45	0.3089	0.0147	0.0198
2.62	2.63	0.55	0.3840	0.0181	0.0246
2.62	2.63	0.65	0.6204	0.0281	0.0398
2.62	2.63	0.75	1.4249	0.0572	0.0914
2.62	2.63	0.85	4.8167	0.1848	0.3091
2.62	2.63	0.92	9.1397	0.5325	0.5866
2.63	2.64	-0.83	0.2508	0.0206	0.0161
2.63	2.64	-0.75	0.2658	0.0132	0.0171
2.63	2.64	-0.65	0.2563	0.0123	0.0165
2.63	2.64	-0.55	0.2026	0.0102	0.0130
2.63	2.64	-0.45	0.1413	0.0078	0.0091
2.63	2.64	-0.35	0.0993	0.0058	0.0064
2.63	2.64	-0.25	0.0961	0.0057	0.0062
2.63	2.64	-0.15	0.0879	0.0053	0.0057
2.63	2.64	-0.05	0.1021	0.0058	0.0066
2.63	2.64	0.05	0.1158	0.0066	0.0075
2.63	2.64	0.15	0.1262	0.0071	0.0081
2.63	2.64	0.25	0.1604	0.0085	0.0103
2.63	2.64	0.35	0.2185	0.0105	0.0141
2.63	2.64	0.45	0.2970	0.0145	0.0191
2.63	2.64	0.55	0.3841	0.0189	0.0247
2.63	2.64	0.65	0.5819	0.0268	0.0375
2.63	2.64	0.75	1.4324	0.0598	0.0922
2.63	2.64	0.85	4.0083	0.1521	0.2581
2.63	2.64	0.92	14.0138	0.9401	0.9023
2.64	2.65	-0.83	0.2513	0.0223	0.0162
2.64	2.65	-0.75	0.2373	0.0120	0.0153
2.64	2.65	-0.65	0.2168	0.0107	0.0140

2.64	2.65	-0.55	0.1769	0.0090	0.0114
2.64	2.65	-0.45	0.1261	0.0069	0.0081
2.64	2.65	-0.35	0.0924	0.0055	0.0060
2.64	2.65	-0.25	0.0741	0.0047	0.0048
2.64	2.65	-0.15	0.0793	0.0049	0.0051
2.64	2.65	-0.05	0.0954	0.0055	0.0062
2.64	2.65	0.05	0.0942	0.0056	0.0061
2.64	2.65	0.15	0.1164	0.0065	0.0075
2.64	2.65	0.25	0.1498	0.0078	0.0097
2.64	2.65	0.35	0.1903	0.0098	0.0123
2.64	2.65	0.45	0.2598	0.0130	0.0168
2.64	2.65	0.55	0.3405	0.0169	0.0220
2.64	2.65	0.65	0.5662	0.0263	0.0366
2.64	2.65	0.75	1.2653	0.0515	0.0817
2.64	2.65	0.85	4.5037	0.1831	0.2909
2.64	2.65	0.92	10.3146	0.6251	0.6662
2.65	2.66	-0.83	0.2123	0.0192	0.0138
2.65	2.66	-0.75	0.2344	0.0123	0.0152
2.65	2.66	-0.65	0.2134	0.0108	0.0138
2.65	2.66	-0.55	0.1780	0.0089	0.0115
2.65	2.66	-0.45	0.1347	0.0075	0.0087
2.65	2.66	-0.35	0.0915	0.0056	0.0059
2.65	2.66	-0.25	0.0711	0.0045	0.0046
2.65	2.66	-0.15	0.0846	0.0050	0.0055
2.65	2.66	-0.05	0.0913	0.0053	0.0059
2.65	2.66	0.05	0.1023	0.0059	0.0066
2.65	2.66	0.15	0.1139	0.0065	0.0074
2.65	2.66	0.25	0.1507	0.0078	0.0098
2.65	2.66	0.35	0.1984	0.0099	0.0129
2.65	2.66	0.45	0.2497	0.0123	0.0162
2.65	2.66	0.55	0.3264	0.0162	0.0211
2.65	2.66	0.65	0.5234	0.0238	0.0339
2.65	2.66	0.75	1.3066	0.0542	0.0847
2.65	2.66	0.85	4.2821	0.1666	0.2774
2.65	2.66	0.92	13.1388	0.8041	0.8512
2.66	2.67	-0.83	0.2350	0.0227	0.0153
2.66	2.67	-0.75	0.2156	0.0110	0.0140
2.66	2.67	-0.65	0.2138	0.0105	0.0139
2.66	2.67	-0.55	0.1694	0.0087	0.0110
2.66	2.67	-0.45	0.1269	0.0069	0.0082
2.66	2.67	-0.35	0.0917	0.0057	0.0060
2.66	2.67	-0.25	0.0662	0.0043	0.0043
2.66	2.67	-0.15	0.0760	0.0047	0.0049
2.66	2.67	-0.05	0.0869	0.0051	0.0056
2.66	2.67	0.05	0.0933	0.0054	0.0061
2.66	2.67	0.15	0.1155	0.0064	0.0075
2.66	2.67	0.25	0.1500	0.0077	0.0097
2.66	2.67	0.35	0.2042	0.0102	0.0133
2.66	2.67	0.45	0.2514	0.0126	0.0163
2.66	2.67	0.55	0.3043	0.0148	0.0198
2.66	2.67	0.65	0.4944	0.0226	0.0321
2.66	2.67	0.75	1.2496	0.0525	0.0812
2.66	2.67	0.85	3.7087	0.1430	0.2410
2.66	2.67	0.92	8.3662	0.5374	0.5437
2.67	2.68	-0.83	0.2268	0.0211	0.0148
2.67	2.68	-0.75	0.2066	0.0109	0.0135
2.67	2.68	-0.65	0.2051	0.0104	0.0134
2.67	2.68	-0.55	0.1455	0.0077	0.0095
2.67	2.68	-0.45	0.1159	0.0066	0.0076
2.67	2.68	-0.35	0.0851	0.0054	0.0056
2.67	2.68	-0.25	0.0659	0.0044	0.0043
2.67	2.68	-0.15	0.0671	0.0043	0.0044
2.67	2.68	-0.05	0.0844	0.0052	0.0055
2.67	2.68	0.05	0.0847	0.0052	0.0055
2.67	2.68	0.15	0.1105	0.0065	0.0072
2.67	2.68	0.25	0.1420	0.0077	0.0093
2.67	2.68	0.35	0.1832	0.0093	0.0119
2.67	2.68	0.45	0.2231	0.0113	0.0145
2.67	2.68	0.55	0.3055	0.0157	0.0199
2.67	2.68	0.65	0.5132	0.0239	0.0335
2.67	2.68	0.75	1.2451	0.0530	0.0812
2.67	2.68	0.85	3.6553	0.1454	0.2383
2.67	2.68	0.92	10.3264	0.6656	0.6732
2.68	2.69	-0.83	0.3125	0.0384	0.0204
2.68	2.69	-0.75	0.2050	0.0113	0.0134
2.68	2.69	-0.65	0.1989	0.0104	0.0130

2.68	2.69	-0.55	0.1690	0.0089	0.0111
2.68	2.69	-0.45	0.1114	0.0067	0.0073
2.68	2.69	-0.35	0.0777	0.0054	0.0051
2.68	2.69	-0.25	0.0609	0.0042	0.0040
2.68	2.69	-0.15	0.0603	0.0042	0.0039
2.68	2.69	-0.05	0.0723	0.0046	0.0047
2.68	2.69	0.05	0.0834	0.0053	0.0055
2.68	2.69	0.15	0.1071	0.0064	0.0070
2.68	2.69	0.25	0.1330	0.0074	0.0087
2.68	2.69	0.35	0.1715	0.0091	0.0112
2.68	2.69	0.45	0.2291	0.0122	0.0150
2.68	2.69	0.55	0.2963	0.0155	0.0194
2.68	2.69	0.65	0.4825	0.0241	0.0316
2.68	2.69	0.75	1.1817	0.0512	0.0773
2.68	2.69	0.85	4.2340	0.1818	0.2769
2.68	2.69	0.92	11.2165	0.8296	0.7335
2.69	2.70	-0.83	0.2025	0.0263	0.0133
2.69	2.70	-0.75	0.1986	0.0111	0.0130
2.69	2.70	-0.65	0.1845	0.0102	0.0121
2.69	2.70	-0.55	0.1506	0.0083	0.0099
2.69	2.70	-0.45	0.1106	0.0067	0.0073
2.69	2.70	-0.35	0.0787	0.0053	0.0052
2.69	2.70	-0.25	0.0659	0.0044	0.0043
2.69	2.70	-0.15	0.0707	0.0048	0.0046
2.69	2.70	-0.05	0.0718	0.0046	0.0047
2.69	2.70	0.05	0.0863	0.0053	0.0057
2.69	2.70	0.15	0.1021	0.0062	0.0067
2.69	2.70	0.25	0.1329	0.0075	0.0087
2.69	2.70	0.35	0.1759	0.0095	0.0115
2.69	2.70	0.45	0.2242	0.0119	0.0147
2.69	2.70	0.55	0.3141	0.0163	0.0206
2.69	2.70	0.65	0.4675	0.0235	0.0307
2.69	2.70	0.75	1.1445	0.0504	0.0751
2.69	2.70	0.85	3.9045	0.1634	0.2561
2.69	2.70	0.92	11.5869	0.8079	0.7601
2.70	2.71	-0.83	0.2976	0.0411	0.0196
2.70	2.71	-0.75	0.2079	0.0111	0.0137
2.70	2.71	-0.65	0.1845	0.0095	0.0121
2.70	2.71	-0.55	0.1443	0.0079	0.0095
2.70	2.71	-0.45	0.1011	0.0060	0.0067
2.70	2.71	-0.35	0.0813	0.0053	0.0054
2.70	2.71	-0.25	0.0546	0.0038	0.0036
2.70	2.71	-0.15	0.0687	0.0044	0.0045
2.70	2.71	-0.05	0.0705	0.0044	0.0046
2.70	2.71	0.05	0.0840	0.0050	0.0055
2.70	2.71	0.15	0.0961	0.0057	0.0063
2.70	2.71	0.25	0.1227	0.0068	0.0081
2.70	2.71	0.35	0.1727	0.0091	0.0114
2.70	2.71	0.45	0.2278	0.0120	0.0150
2.70	2.71	0.55	0.2755	0.0148	0.0181
2.70	2.71	0.65	0.4849	0.0235	0.0319
2.70	2.71	0.75	1.0932	0.0483	0.0719
2.70	2.71	0.85	3.8924	0.1644	0.2561
2.71	2.72	-0.83	0.2095	0.0303	0.0138
2.71	2.72	-0.75	0.1929	0.0100	0.0127
2.71	2.72	-0.65	0.1852	0.0094	0.0122
2.71	2.72	-0.55	0.1546	0.0080	0.0102
2.71	2.72	-0.45	0.0950	0.0056	0.0063
2.71	2.72	-0.35	0.0697	0.0046	0.0046
2.71	2.72	-0.25	0.0533	0.0036	0.0035
2.71	2.72	-0.15	0.0596	0.0039	0.0039
2.71	2.72	-0.05	0.0616	0.0040	0.0041
2.71	2.72	0.05	0.0728	0.0045	0.0048
2.71	2.72	0.15	0.0917	0.0054	0.0061
2.71	2.72	0.25	0.1189	0.0067	0.0078
2.71	2.72	0.35	0.1541	0.0082	0.0102
2.71	2.72	0.45	0.2006	0.0108	0.0132
2.71	2.72	0.55	0.2642	0.0140	0.0174
2.71	2.72	0.65	0.4608	0.0219	0.0304
2.71	2.72	0.75	1.1028	0.0499	0.0728
2.71	2.72	0.85	3.6561	0.1536	0.2413
2.71	2.72	0.92	10.0580	0.6873	0.6639
2.72	2.73	-0.83	0.1622	0.0227	0.0107
2.72	2.73	-0.75	0.2070	0.0111	0.0137
2.72	2.73	-0.65	0.1593	0.0087	0.0105
2.72	2.73	-0.55	0.1471	0.0080	0.0097

2.72	2.73	-0.45	0.0997	0.0058	0.0066
2.72	2.73	-0.35	0.0692	0.0048	0.0046
2.72	2.73	-0.25	0.0575	0.0040	0.0038
2.72	2.73	-0.15	0.0514	0.0037	0.0034
2.72	2.73	-0.05	0.0552	0.0037	0.0037
2.72	2.73	0.05	0.0686	0.0044	0.0045
2.72	2.73	0.15	0.0786	0.0049	0.0052
2.72	2.73	0.25	0.1091	0.0062	0.0072
2.72	2.73	0.35	0.1534	0.0083	0.0102
2.72	2.73	0.45	0.1913	0.0104	0.0127
2.72	2.73	0.55	0.2482	0.0134	0.0164
2.72	2.73	0.65	0.4594	0.0229	0.0304
2.72	2.73	0.75	0.9979	0.0465	0.0661
2.72	2.73	0.85	3.1886	0.1379	0.2111
2.72	2.73	0.93	23.7068	5.6487	1.5695
2.73	2.74	-0.83	0.1625	0.0336	0.0108
2.73	2.74	-0.75	0.1468	0.0087	0.0097
2.73	2.74	-0.65	0.1504	0.0082	0.0100
2.73	2.74	-0.55	0.1162	0.0067	0.0077
2.73	2.74	-0.45	0.0790	0.0051	0.0052
2.73	2.74	-0.35	0.0587	0.0042	0.0039
2.73	2.74	-0.25	0.0437	0.0032	0.0029
2.73	2.74	-0.15	0.0456	0.0033	0.0030
2.73	2.74	-0.05	0.0479	0.0033	0.0032
2.73	2.74	0.05	0.0549	0.0037	0.0036
2.73	2.74	0.15	0.0661	0.0045	0.0044
2.73	2.74	0.25	0.0950	0.0056	0.0063
2.73	2.74	0.35	0.1191	0.0066	0.0079
2.73	2.74	0.45	0.1451	0.0086	0.0096
2.73	2.74	0.55	0.2095	0.0119	0.0139
2.73	2.74	0.65	0.2980	0.0166	0.0198
2.73	2.74	0.75	0.7026	0.0335	0.0467
2.73	2.74	0.85	2.5852	0.1222	0.1717
2.73	2.74	0.93	7.1194	1.0041	0.4728
2.74	2.75	-0.75	0.1301	0.0080	0.0087
2.74	2.75	-0.65	0.1083	0.0063	0.0072
2.74	2.75	-0.55	0.0932	0.0056	0.0062
2.74	2.75	-0.45	0.0665	0.0045	0.0044
2.74	2.75	-0.35	0.0400	0.0032	0.0027
2.74	2.75	-0.25	0.0352	0.0028	0.0023
2.74	2.75	-0.15	0.0351	0.0028	0.0023
2.74	2.75	-0.05	0.0377	0.0029	0.0025
2.74	2.75	0.05	0.0455	0.0033	0.0030
2.74	2.75	0.15	0.0595	0.0041	0.0040
2.74	2.75	0.25	0.0725	0.0046	0.0048
2.74	2.75	0.35	0.0949	0.0058	0.0063
2.74	2.75	0.45	0.1240	0.0077	0.0083
2.74	2.75	0.55	0.1567	0.0098	0.0104
2.74	2.75	0.65	0.2714	0.0154	0.0181
2.74	2.75	0.75	0.6371	0.0321	0.0424
2.74	2.75	0.85	2.2678	0.1122	0.1511
2.74	2.75	0.92	4.6272	0.4311	0.3082
2.75	2.76	-0.75	0.1705	0.0096	0.0114
2.75	2.76	-0.65	0.1570	0.0085	0.0105
2.75	2.76	-0.55	0.1276	0.0073	0.0085
2.75	2.76	-0.45	0.0794	0.0050	0.0053
2.75	2.76	-0.35	0.0565	0.0041	0.0038
2.75	2.76	-0.25	0.0456	0.0033	0.0030
2.75	2.76	-0.15	0.0432	0.0031	0.0029
2.75	2.76	-0.05	0.0484	0.0034	0.0032
2.75	2.76	0.05	0.0579	0.0039	0.0039
2.75	2.76	0.15	0.0668	0.0045	0.0045
2.75	2.76	0.25	0.1062	0.0063	0.0071
2.75	2.76	0.35	0.1322	0.0074	0.0088
2.75	2.76	0.45	0.1808	0.0102	0.0121
2.75	2.76	0.55	0.2218	0.0123	0.0148
2.75	2.76	0.65	0.3958	0.0207	0.0264
2.75	2.76	0.75	0.9154	0.0414	0.0612
2.75	2.76	0.85	3.1494	0.1428	0.2104
2.75	2.76	0.93	11.6066	1.3111	0.7755
2.76	2.77	-0.82	0.1516	0.0151	0.0102
2.76	2.77	-0.75	0.1655	0.0096	0.0111
2.76	2.77	-0.65	0.1354	0.0077	0.0091
2.76	2.77	-0.55	0.1132	0.0065	0.0076
2.76	2.77	-0.45	0.0784	0.0050	0.0053
2.76	2.77	-0.35	0.0540	0.0039	0.0036

2.76	2.77	-0.25	0.0415	0.0031	0.0028
2.76	2.77	-0.15	0.0407	0.0030	0.0027
2.76	2.77	-0.05	0.0501	0.0035	0.0034
2.76	2.77	0.05	0.0536	0.0036	0.0036
2.76	2.77	0.15	0.0777	0.0050	0.0052
2.76	2.77	0.25	0.1027	0.0059	0.0069
2.76	2.77	0.35	0.1417	0.0078	0.0095
2.76	2.77	0.45	0.1617	0.0091	0.0108
2.76	2.77	0.55	0.2342	0.0129	0.0157
2.76	2.77	0.65	0.3674	0.0194	0.0246
2.76	2.77	0.75	0.9223	0.0433	0.0618
2.76	2.77	0.85	3.2975	0.1505	0.2210
2.76	2.77	0.93	7.3021	0.8602	0.4894
2.77	2.78	-0.82	0.1548	0.0156	0.0104
2.77	2.78	-0.75	0.1387	0.0082	0.0093
2.77	2.78	-0.65	0.1288	0.0074	0.0087
2.77	2.78	-0.55	0.0964	0.0057	0.0065
2.77	2.78	-0.45	0.0702	0.0047	0.0047
2.77	2.78	-0.35	0.0482	0.0037	0.0032
2.77	2.78	-0.25	0.0386	0.0029	0.0026
2.77	2.78	-0.15	0.0401	0.0030	0.0027
2.77	2.78	-0.05	0.0491	0.0034	0.0033
2.77	2.78	0.05	0.0504	0.0035	0.0034
2.77	2.78	0.15	0.0649	0.0044	0.0044
2.77	2.78	0.25	0.0923	0.0055	0.0062
2.77	2.78	0.35	0.1274	0.0072	0.0086
2.77	2.78	0.45	0.1710	0.0095	0.0115
2.77	2.78	0.55	0.2058	0.0118	0.0138
2.77	2.78	0.65	0.3553	0.0188	0.0239
2.77	2.78	0.75	0.8247	0.0385	0.0554
2.77	2.78	0.85	2.9881	0.1376	0.2009
2.77	2.78	0.92	8.2652	0.7546	0.5556
2.78	2.79	-0.82	0.1541	0.0160	0.0104
2.78	2.79	-0.75	0.1475	0.0087	0.0099
2.78	2.79	-0.65	0.1341	0.0076	0.0090
2.78	2.79	-0.55	0.0952	0.0057	0.0064
2.78	2.79	-0.45	0.0703	0.0046	0.0047
2.78	2.79	-0.35	0.0478	0.0036	0.0032
2.78	2.79	-0.25	0.0370	0.0029	0.0025
2.78	2.79	-0.15	0.0361	0.0028	0.0024
2.78	2.79	-0.05	0.0374	0.0029	0.0025
2.78	2.79	0.05	0.0472	0.0034	0.0032
2.78	2.79	0.15	0.0593	0.0042	0.0040
2.78	2.79	0.25	0.0897	0.0054	0.0060
2.78	2.79	0.35	0.1004	0.0060	0.0068
2.78	2.79	0.45	0.1313	0.0080	0.0089
2.78	2.79	0.55	0.1891	0.0109	0.0128
2.78	2.79	0.65	0.3093	0.0167	0.0209
2.78	2.79	0.75	0.7938	0.0377	0.0535
2.78	2.79	0.85	3.3052	0.1500	0.2229
2.78	2.79	0.93	32.9026	7.5316	2.2185
2.79	2.80	-0.82	0.2043	0.0211	0.0138
2.79	2.80	-0.75	0.1275	0.0081	0.0086
2.79	2.80	-0.65	0.1251	0.0076	0.0085
2.79	2.80	-0.55	0.0932	0.0060	0.0063
2.79	2.80	-0.45	0.0672	0.0048	0.0045
2.79	2.80	-0.35	0.0476	0.0038	0.0032
2.79	2.80	-0.25	0.0401	0.0032	0.0027
2.79	2.80	-0.15	0.0395	0.0031	0.0027
2.79	2.80	-0.05	0.0409	0.0031	0.0028
2.79	2.80	0.05	0.0464	0.0034	0.0031
2.79	2.80	0.15	0.0621	0.0045	0.0042
2.79	2.80	0.25	0.0883	0.0056	0.0060
2.79	2.80	0.35	0.1187	0.0071	0.0080
2.79	2.80	0.45	0.1457	0.0086	0.0099
2.79	2.80	0.55	0.1977	0.0117	0.0134
2.79	2.80	0.65	0.3687	0.0203	0.0249
2.79	2.80	0.75	0.8904	0.0432	0.0602
2.79	2.80	0.85	3.2927	0.1553	0.2227
2.79	2.80	0.93	16.2386	2.6437	1.0982
2.80	2.81	-0.82	0.1536	0.0156	0.0104
2.80	2.81	-0.75	0.1329	0.0080	0.0090
2.80	2.81	-0.65	0.1167	0.0068	0.0079
2.80	2.81	-0.55	0.1045	0.0060	0.0071
2.80	2.81	-0.45	0.0713	0.0046	0.0048
2.80	2.81	-0.35	0.0436	0.0034	0.0030

2.80	2.81	-0.25	0.0366	0.0029	0.0025
2.80	2.81	-0.15	0.0334	0.0026	0.0023
2.80	2.81	-0.05	0.0395	0.0029	0.0027
2.80	2.81	0.05	0.0417	0.0030	0.0028
2.80	2.81	0.15	0.0634	0.0042	0.0043
2.80	2.81	0.25	0.0874	0.0053	0.0059
2.80	2.81	0.35	0.1161	0.0066	0.0079
2.80	2.81	0.45	0.1320	0.0080	0.0090
2.80	2.81	0.55	0.1931	0.0113	0.0131
2.80	2.81	0.65	0.3371	0.0183	0.0229
2.80	2.81	0.75	0.8969	0.0440	0.0608
2.80	2.81	0.85	2.8308	0.1318	0.1920
2.80	2.81	0.92	11.4752	1.1928	0.7784
2.81	2.82	-0.82	0.1331	0.0145	0.0091
2.81	2.82	-0.75	0.1337	0.0083	0.0091
2.81	2.82	-0.65	0.1139	0.0070	0.0078
2.81	2.82	-0.55	0.0875	0.0055	0.0060
2.81	2.82	-0.45	0.0638	0.0044	0.0043
2.81	2.82	-0.35	0.0422	0.0034	0.0029
2.81	2.82	-0.25	0.0335	0.0028	0.0023
2.81	2.82	-0.15	0.0320	0.0026	0.0022
2.81	2.82	-0.05	0.0339	0.0027	0.0023
2.81	2.82	0.05	0.0433	0.0032	0.0029
2.81	2.82	0.15	0.0565	0.0041	0.0038
2.81	2.82	0.25	0.0792	0.0051	0.0054
2.81	2.82	0.35	0.1013	0.0062	0.0069
2.81	2.82	0.45	0.1410	0.0086	0.0096
2.81	2.82	0.55	0.1947	0.0115	0.0132
2.81	2.82	0.65	0.3204	0.0176	0.0218
2.81	2.82	0.75	0.7761	0.0374	0.0528
2.81	2.82	0.85	2.6499	0.1368	0.1803
2.81	2.82	0.93	13.7872	3.0930	0.9380
2.82	2.83	-0.82	0.1408	0.0164	0.0096
2.82	2.83	-0.75	0.1271	0.0079	0.0087
2.82	2.83	-0.65	0.1067	0.0065	0.0073
2.82	2.83	-0.55	0.0828	0.0053	0.0057
2.82	2.83	-0.45	0.0536	0.0039	0.0037
2.82	2.83	-0.35	0.0340	0.0030	0.0023
2.82	2.83	-0.25	0.0263	0.0023	0.0018
2.82	2.83	-0.15	0.0331	0.0027	0.0023
2.82	2.83	-0.05	0.0324	0.0026	0.0022
2.82	2.83	0.05	0.0449	0.0033	0.0031
2.82	2.83	0.15	0.0527	0.0038	0.0036
2.82	2.83	0.25	0.0847	0.0053	0.0058
2.82	2.83	0.35	0.1032	0.0062	0.0070
2.82	2.83	0.45	0.1216	0.0076	0.0083
2.82	2.83	0.55	0.1743	0.0105	0.0119
2.82	2.83	0.65	0.3088	0.0176	0.0211
2.82	2.83	0.75	0.7574	0.0378	0.0517
2.82	2.83	0.85	2.5479	0.1248	0.1739
2.82	2.83	0.93	16.4933	2.4029	1.1255
2.83	2.84	-0.82	0.1491	0.0185	0.0102
2.83	2.84	-0.75	0.1342	0.0085	0.0092
2.83	2.84	-0.65	0.1027	0.0063	0.0070
2.83	2.84	-0.55	0.0839	0.0053	0.0057
2.83	2.84	-0.45	0.0577	0.0041	0.0039
2.83	2.84	-0.35	0.0358	0.0030	0.0025
2.83	2.84	-0.25	0.0278	0.0024	0.0019
2.83	2.84	-0.15	0.0313	0.0026	0.0021
2.83	2.84	-0.05	0.0309	0.0025	0.0021
2.83	2.84	0.05	0.0434	0.0031	0.0030
2.83	2.84	0.15	0.0482	0.0037	0.0033
2.83	2.84	0.25	0.0656	0.0046	0.0045
2.83	2.84	0.35	0.0876	0.0056	0.0060
2.83	2.84	0.45	0.1296	0.0084	0.0089
2.83	2.84	0.55	0.1672	0.0104	0.0114
2.83	2.84	0.65	0.2661	0.0156	0.0182
2.83	2.84	0.75	0.6948	0.0372	0.0476
2.83	2.84	0.85	2.8842	0.1572	0.1974
2.83	2.84	0.92	10.3796	1.0817	0.7104

B.2 $\rho^0_{MM'}$ Measurements

Systematic errors for all measurements: $\sigma^{sys}_{00} = 0.0175$, $\sigma^{sys}_{1-1} = 0.0125$ and $\sigma^{sys}_{10} = 0.010$.

$\sqrt{s}_{min}$ (GeV)	$\sqrt{s}_{max}$ (GeV)	$\cos\theta^\omega_{CM}$	ρ^0_{00}	σ^{stat}_{00}	ρ^0_{1-1}	σ^{stat}_{1-1}	$Re(\rho^0_{10})$	σ^{stat}_{10}
1.72	1.73	-0.45	0.6003	0.0313	0.0095	0.0030	0.0125	0.0063
1.72	1.73	-0.35	0.6156	0.0295	0.0108	0.0030	0.0061	0.0060
1.72	1.73	-0.25	0.6253	0.0280	0.0121	0.0030	-0.0004	0.0056
1.72	1.73	-0.15	0.6295	0.0267	0.0133	0.0030	-0.0069	0.0053
1.72	1.73	-0.05	0.6285	0.0257	0.0143	0.0029	-0.0131	0.0050
1.72	1.73	0.05	0.6227	0.0251	0.0153	0.0028	-0.0188	0.0048
1.72	1.73	0.15	0.6125	0.0247	0.0160	0.0027	-0.0238	0.0046
1.72	1.73	0.25	0.5982	0.0246	0.0165	0.0025	-0.0281	0.0044
1.72	1.73	0.35	0.5803	0.0248	0.0167	0.0024	-0.0314	0.0042
1.72	1.73	0.45	0.5592	0.0253	0.0163	0.0021	-0.0335	0.0041
1.72	1.73	0.55	0.5354	0.0260	0.0154	0.0019	-0.0344	0.0039
1.72	1.73	0.65	0.5092	0.0270	0.0138	0.0016	-0.0337	0.0036
1.72	1.73	0.75	0.4810	0.0282	0.0113	0.0013	-0.0312	0.0033
1.73	1.74	-0.45	0.6424	0.0230	0.0140	0.0040	0.0570	0.0087
1.73	1.74	-0.35	0.6703	0.0230	0.0154	0.0037	0.0449	0.0067
1.73	1.74	-0.25	0.6868	0.0219	0.0162	0.0039	0.0289	0.0047
1.73	1.74	-0.15	0.6919	0.0189	0.0168	0.0041	0.0110	0.0043
1.73	1.74	-0.05	0.6865	0.0145	0.0174	0.0041	-0.0071	0.0058
1.73	1.74	0.05	0.6718	0.0097	0.0181	0.0037	-0.0243	0.0075
1.73	1.74	0.15	0.6490	0.0070	0.0191	0.0031	-0.0395	0.0084
1.73	1.74	0.25	0.6193	0.0088	0.0202	0.0028	-0.0523	0.0083
1.73	1.74	0.35	0.5838	0.0123	0.0214	0.0030	-0.0620	0.0071
1.73	1.74	0.45	0.5435	0.0150	0.0222	0.0037	-0.0684	0.0050
1.73	1.74	0.55	0.4994	0.0157	0.0223	0.0044	-0.0710	0.0032
1.73	1.74	0.65	0.4528	0.0143	0.0210	0.0049	-0.0695	0.0047
1.73	1.74	0.75	0.4051	0.0113	0.0180	0.0047	-0.0633	0.0077
1.74	1.75	-0.45	0.6667	0.0097	0.0177	0.0030	0.0579	0.0066
1.74	1.75	-0.35	0.6891	0.0102	0.0128	0.0027	0.0386	0.0055
1.74	1.75	-0.25	0.6991	0.0118	0.0095	0.0028	0.0181	0.0040
1.74	1.75	-0.15	0.6982	0.0123	0.0077	0.0028	-0.0028	0.0037
1.74	1.75	-0.05	0.6876	0.0110	0.0073	0.0027	-0.0235	0.0050
1.74	1.75	0.05	0.6682	0.0086	0.0082	0.0025	-0.0431	0.0061
1.74	1.75	0.15	0.6408	0.0066	0.0102	0.0027	-0.0609	0.0062
1.74	1.75	0.25	0.6059	0.0072	0.0132	0.0031	-0.0760	0.0053
1.74	1.75	0.35	0.5640	0.0095	0.0169	0.0034	-0.0878	0.0041
1.74	1.75	0.45	0.5157	0.0112	0.0210	0.0032	-0.0953	0.0042
1.74	1.75	0.55	0.4623	0.0114	0.0245	0.0028	-0.0977	0.0053
1.74	1.75	0.65	0.4051	0.0100	0.0264	0.0029	-0.0946	0.0054
1.74	1.75	0.75	0.3466	0.0084	0.0251	0.0038	-0.0853	0.0043
1.75	1.76	-0.45	0.6815	0.0055	0.0125	0.0026	0.0483	0.0027
1.75	1.76	-0.35	0.7047	0.0049	0.0060	0.0024	0.0303	0.0024
1.75	1.76	-0.25	0.7153	0.0044	0.0018	0.0024	0.0099	0.0022
1.75	1.76	-0.15	0.7135	0.0041	-0.0000	0.0024	-0.0117	0.0022
1.75	1.76	-0.05	0.6999	0.0039	0.0003	0.0023	-0.0337	0.0022
1.75	1.76	0.05	0.6754	0.0038	0.0023	0.0023	-0.0551	0.0022
1.75	1.76	0.15	0.6410	0.0038	0.0055	0.0022	-0.0750	0.0021
1.75	1.76	0.25	0.5978	0.0038	0.0095	0.0023	-0.0923	0.0020
1.75	1.76	0.35	0.5468	0.0038	0.0137	0.0025	-0.1057	0.0020
1.75	1.76	0.45	0.4897	0.0038	0.0175	0.0026	-0.1139	0.0020
1.75	1.76	0.55	0.4285	0.0038	0.0204	0.0026	-0.1155	0.0021
1.75	1.76	0.65	0.3660	0.0039	0.0215	0.0026	-0.1094	0.0021
1.75	1.76	0.75	0.3057	0.0042	0.0200	0.0023	-0.0950	0.0024
1.76	1.77	-0.65	0.6387	0.0059	0.0220	0.0065	0.0654	0.0103
1.76	1.77	-0.55	0.6787	0.0035	0.0235	0.0047	0.0552	0.0083
1.76	1.77	-0.45	0.7114	0.0009	0.0194	0.0028	0.0391	0.0048
1.76	1.77	-0.35	0.7316	0.0022	0.0140	0.0022	0.0203	0.0019
1.76	1.77	-0.25	0.7377	0.0039	0.0084	0.0019	0.0007	0.0009
1.76	1.77	-0.15	0.7316	0.0051	0.0034	0.0032	-0.0190	0.0010
1.76	1.77	-0.05	0.7151	0.0055	0.0008	0.0050	-0.0391	0.0013
1.76	1.77	0.05	0.6892	0.0059	0.0017	0.0057	-0.0596	0.0016
1.76	1.77	0.15	0.6536	0.0071	0.0056	0.0058	-0.0803	0.0020
1.76	1.77	0.25	0.6078	0.0099	0.0104	0.0062	-0.1001	0.0022
1.76	1.77	0.35	0.5506	0.0134	0.0139	0.0073	-0.1161	0.0027
1.76	1.77	0.45	0.4823	0.0161	0.0151	0.0092	-0.1251	0.0040
1.76	1.77	0.55	0.4070	0.0169	0.0164	0.0099	-0.1251	0.0058
1.76	1.77	0.65	0.3328	0.0151	0.0227	0.0079	-0.1167	0.0075
1.76	1.77	0.75	0.2677	0.0143	0.0353	0.0069	-0.1014	0.0081
1.77	1.78	-0.65	0.6267	0.0062	0.0331	0.0097	0.0489	0.0104
1.77	1.78	-0.55	0.6763	0.0041	0.0237	0.0068	0.0429	0.0084

1.77	1.78	-0.45	0.7108	0.0047	0.0155	0.0050	0.0325	0.0050
1.77	1.78	-0.35	0.7307	0.0081	0.0100	0.0027	0.0186	0.0019
1.77	1.78	-0.25	0.7366	0.0119	0.0076	0.0025	0.0015	0.0018
1.77	1.78	-0.15	0.7296	0.0132	0.0074	0.0042	-0.0180	0.0028
1.77	1.78	-0.05	0.7113	0.0119	0.0087	0.0055	-0.0390	0.0033
1.77	1.78	0.05	0.6826	0.0093	0.0109	0.0056	-0.0607	0.0038
1.77	1.78	0.15	0.6434	0.0076	0.0141	0.0056	-0.0819	0.0044
1.77	1.78	0.25	0.5928	0.0079	0.0183	0.0060	-0.1011	0.0056
1.77	1.78	0.35	0.5309	0.0127	0.0236	0.0068	-0.1166	0.0073
1.77	1.78	0.45	0.4602	0.0185	0.0292	0.0083	-0.1266	0.0089
1.77	1.78	0.55	0.3862	0.0226	0.0336	0.0096	-0.1297	0.0099
1.77	1.78	0.65	0.3162	0.0234	0.0346	0.0094	-0.1253	0.0101
1.77	1.78	0.75	0.2568	0.0213	0.0303	0.0075	-0.1139	0.0098
1.78	1.79	-0.65	0.6251	0.0078	0.0101	0.0108	0.0684	0.0107
1.78	1.79	-0.55	0.6719	0.0071	0.0094	0.0091	0.0586	0.0090
1.78	1.79	-0.45	0.7127	0.0097	0.0088	0.0062	0.0415	0.0056
1.78	1.79	-0.35	0.7435	0.0153	0.0089	0.0044	0.0212	0.0030
1.78	1.79	-0.25	0.7596	0.0189	0.0102	0.0046	-0.0004	0.0035
1.78	1.79	-0.15	0.7570	0.0183	0.0110	0.0068	-0.0227	0.0053
1.78	1.79	-0.05	0.7361	0.0151	0.0099	0.0075	-0.0452	0.0058
1.78	1.79	0.05	0.7006	0.0116	0.0069	0.0064	-0.0678	0.0052
1.78	1.79	0.15	0.6540	0.0077	0.0047	0.0058	-0.0903	0.0050
1.78	1.79	0.25	0.5959	0.0063	0.0059	0.0063	-0.1121	0.0058
1.78	1.79	0.35	0.5248	0.0092	0.0107	0.0071	-0.1317	0.0073
1.78	1.79	0.45	0.4421	0.0166	0.0165	0.0086	-0.1456	0.0086
1.78	1.79	0.55	0.3566	0.0230	0.0203	0.0108	-0.1494	0.0099
1.78	1.79	0.65	0.2816	0.0259	0.0208	0.0112	-0.1403	0.0102
1.78	1.79	0.75	0.2229	0.0243	0.0184	0.0116	-0.1200	0.0103
1.79	1.80	-0.65	0.6354	0.0079	0.0225	0.0119	0.0497	0.0087
1.79	1.80	-0.55	0.6856	0.0083	0.0248	0.0090	0.0399	0.0083
1.79	1.80	-0.45	0.7316	0.0112	0.0210	0.0077	0.0304	0.0058
1.79	1.80	-0.35	0.7677	0.0156	0.0121	0.0066	0.0198	0.0040
1.79	1.80	-0.25	0.7834	0.0168	0.0021	0.0075	0.0067	0.0051
1.79	1.80	-0.15	0.7754	0.0138	-0.0045	0.0086	-0.0107	0.0070
1.79	1.80	-0.05	0.7486	0.0099	-0.0057	0.0082	-0.0328	0.0074
1.79	1.80	0.05	0.7088	0.0089	-0.0024	0.0066	-0.0588	0.0061
1.79	1.80	0.15	0.6577	0.0082	0.0031	0.0055	-0.0864	0.0045
1.79	1.80	0.25	0.5935	0.0059	0.0099	0.0065	-0.1125	0.0036
1.79	1.80	0.35	0.5148	0.0067	0.0192	0.0083	-0.1327	0.0037
1.79	1.80	0.45	0.4248	0.0103	0.0315	0.0098	-0.1419	0.0049
1.79	1.80	0.55	0.3334	0.0166	0.0434	0.0108	-0.1374	0.0070
1.79	1.80	0.65	0.2550	0.0199	0.0475	0.0121	-0.1218	0.0095
1.79	1.80	0.75	0.2015	0.0204	0.0386	0.0126	-0.1022	0.0106
1.80	1.81	-0.75	0.5894	0.0116	0.0299	0.0208	0.0409	0.0059
1.80	1.81	-0.65	0.6478	0.0095	0.0333	0.0134	0.0486	0.0063
1.80	1.81	-0.55	0.6861	0.0069	0.0312	0.0091	0.0449	0.0053
1.80	1.81	-0.45	0.7155	0.0111	0.0277	0.0077	0.0330	0.0050
1.80	1.81	-0.35	0.7384	0.0159	0.0233	0.0077	0.0160	0.0048
1.80	1.81	-0.25	0.7529	0.0164	0.0180	0.0081	-0.0041	0.0058
1.80	1.81	-0.15	0.7561	0.0121	0.0127	0.0079	-0.0257	0.0066
1.80	1.81	-0.05	0.7456	0.0080	0.0090	0.0066	-0.0483	0.0066
1.80	1.81	0.05	0.7189	0.0074	0.0086	0.0051	-0.0714	0.0059
1.80	1.81	0.15	0.6730	0.0072	0.0120	0.0049	-0.0947	0.0047
1.80	1.81	0.25	0.6058	0.0059	0.0187	0.0075	-0.1169	0.0036
1.80	1.81	0.35	0.5195	0.0070	0.0267	0.0104	-0.1356	0.0029
1.80	1.81	0.45	0.4229	0.0107	0.0332	0.0110	-0.1473	0.0032
1.80	1.81	0.55	0.3285	0.0153	0.0358	0.0094	-0.1487	0.0053
1.80	1.81	0.65	0.2466	0.0197	0.0329	0.0099	-0.1378	0.0075
1.80	1.81	0.75	0.1819	0.0189	0.0241	0.0130	-0.1137	0.0091
1.81	1.82	-0.75	0.5710	0.0114	0.0698	0.0194	0.0530	0.0054
1.81	1.82	-0.65	0.6457	0.0095	0.0487	0.0118	0.0544	0.0045
1.81	1.82	-0.55	0.6943	0.0074	0.0323	0.0107	0.0497	0.0044
1.81	1.82	-0.45	0.7351	0.0096	0.0208	0.0117	0.0400	0.0049
1.81	1.82	-0.35	0.7684	0.0136	0.0122	0.0112	0.0252	0.0054
1.81	1.82	-0.25	0.7853	0.0146	0.0069	0.0089	0.0052	0.0053
1.81	1.82	-0.15	0.7797	0.0129	0.0057	0.0058	-0.0186	0.0048
1.81	1.82	-0.05	0.7537	0.0108	0.0075	0.0033	-0.0442	0.0048
1.81	1.82	0.05	0.7142	0.0099	0.0093	0.0024	-0.0699	0.0050
1.81	1.82	0.15	0.6651	0.0086	0.0084	0.0036	-0.0946	0.0052
1.81	1.82	0.25	0.6029	0.0089	0.0054	0.0079	-0.1174	0.0048
1.81	1.82	0.35	0.5208	0.0130	0.0046	0.0124	-0.1359	0.0043
1.81	1.82	0.45	0.4182	0.0179	0.0117	0.0125	-0.1457	0.0039
1.81	1.82	0.55	0.3093	0.0209	0.0272	0.0088	-0.1427	0.0040
1.81	1.82	0.65	0.2159	0.0207	0.0443	0.0084	-0.1263	0.0060
1.81	1.82	0.75	0.1527	0.0208	0.0537	0.0125	-0.0993	0.0073
1.82	1.83	-0.75	0.5594	0.0147	0.0397	0.0122	0.0471	0.0046

1.82	1.83	-0.65	0.6265	0.0097	0.0518	0.0091	0.0475	0.0053
1.82	1.83	-0.55	0.6890	0.0054	0.0545	0.0091	0.0423	0.0053
1.82	1.83	-0.45	0.7391	0.0042	0.0483	0.0119	0.0306	0.0045
1.82	1.83	-0.35	0.7705	0.0058	0.0370	0.0107	0.0140	0.0052
1.82	1.83	-0.25	0.7843	0.0071	0.0251	0.0078	-0.0051	0.0059
1.82	1.83	-0.15	0.7836	0.0086	0.0154	0.0046	-0.0249	0.0060
1.82	1.83	-0.05	0.7687	0.0101	0.0095	0.0021	-0.0448	0.0063
1.82	1.83	0.05	0.7355	0.0109	0.0083	0.0019	-0.0652	0.0068
1.82	1.83	0.15	0.6782	0.0096	0.0123	0.0036	-0.0861	0.0065
1.82	1.83	0.25	0.5947	0.0100	0.0208	0.0074	-0.1072	0.0060
1.82	1.83	0.35	0.4907	0.0143	0.0314	0.0112	-0.1268	0.0056
1.82	1.83	0.45	0.3796	0.0186	0.0397	0.0112	-0.1409	0.0045
1.82	1.83	0.55	0.2790	0.0207	0.0422	0.0078	-0.1443	0.0037
1.82	1.83	0.65	0.2034	0.0207	0.0394	0.0084	-0.1341	0.0052
1.82	1.83	0.75	0.1589	0.0195	0.0338	0.0127	-0.1116	0.0070
1.83	1.84	-0.75	0.5647	0.0216	0.0355	0.0107	0.0526	0.0088
1.83	1.84	-0.65	0.6376	0.0162	0.0485	0.0039	0.0598	0.0079
1.83	1.84	-0.55	0.6954	0.0084	0.0511	0.0061	0.0508	0.0062
1.83	1.84	-0.45	0.7399	0.0036	0.0446	0.0063	0.0349	0.0043
1.83	1.84	-0.35	0.7723	0.0027	0.0335	0.0053	0.0176	0.0048
1.83	1.84	-0.25	0.7910	0.0054	0.0224	0.0043	0.0010	0.0065
1.83	1.84	-0.15	0.7933	0.0077	0.0145	0.0035	-0.0153	0.0074
1.83	1.84	-0.05	0.7773	0.0091	0.0111	0.0027	-0.0331	0.0078
1.83	1.84	0.05	0.7427	0.0091	0.0115	0.0025	-0.0545	0.0083
1.83	1.84	0.15	0.6886	0.0075	0.0137	0.0039	-0.0807	0.0084
1.83	1.84	0.25	0.6119	0.0076	0.0165	0.0065	-0.1101	0.0084
1.83	1.84	0.35	0.5097	0.0118	0.0203	0.0087	-0.1369	0.0083
1.83	1.84	0.45	0.3886	0.0154	0.0271	0.0085	-0.1514	0.0067
1.83	1.84	0.55	0.2693	0.0172	0.0381	0.0068	-0.1466	0.0046
1.83	1.84	0.65	0.1764	0.0179	0.0515	0.0073	-0.1252	0.0045
1.83	1.84	0.75	0.1202	0.0176	0.0621	0.0103	-0.0971	0.0056
1.84	1.85	-0.75	0.5131	0.0284	0.0501	0.0080	0.0483	0.0134
1.84	1.85	-0.65	0.6026	0.0184	0.0548	0.0069	0.0428	0.0114
1.84	1.85	-0.55	0.6807	0.0124	0.0476	0.0059	0.0361	0.0071
1.84	1.85	-0.45	0.7393	0.0083	0.0388	0.0058	0.0306	0.0047
1.84	1.85	-0.35	0.7761	0.0070	0.0311	0.0051	0.0228	0.0048
1.84	1.85	-0.25	0.7932	0.0089	0.0239	0.0058	0.0105	0.0056
1.84	1.85	-0.15	0.7933	0.0130	0.0165	0.0065	-0.0060	0.0058
1.84	1.85	-0.05	0.7774	0.0146	0.0097	0.0052	-0.0253	0.0065
1.84	1.85	0.05	0.7441	0.0125	0.0058	0.0047	-0.0469	0.0081
1.84	1.85	0.15	0.6890	0.0089	0.0065	0.0069	-0.0714	0.0106
1.84	1.85	0.25	0.6060	0.0074	0.0120	0.0101	-0.0982	0.0125
1.84	1.85	0.35	0.4931	0.0095	0.0213	0.0121	-0.1237	0.0122
1.84	1.85	0.45	0.3632	0.0131	0.0330	0.0109	-0.1398	0.0092
1.84	1.85	0.55	0.2459	0.0137	0.0447	0.0069	-0.1397	0.0049
1.84	1.85	0.65	0.1654	0.0129	0.0537	0.0064	-0.1248	0.0032
1.84	1.85	0.75	0.1223	0.0139	0.0574	0.0082	-0.1007	0.0040
1.85	1.86	-0.75	0.5782	0.0291	0.0622	0.0114	0.0157	0.0131
1.85	1.86	-0.65	0.6140	0.0179	0.0491	0.0080	0.0314	0.0087
1.85	1.86	-0.55	0.6698	0.0148	0.0374	0.0086	0.0382	0.0058
1.85	1.86	-0.45	0.7312	0.0144	0.0344	0.0078	0.0304	0.0059
1.85	1.86	-0.35	0.7792	0.0121	0.0261	0.0074	0.0158	0.0067
1.85	1.86	-0.25	0.8098	0.0124	0.0118	0.0088	0.0003	0.0064
1.85	1.86	-0.15	0.8214	0.0144	0.0003	0.0086	-0.0141	0.0062
1.85	1.86	-0.05	0.8095	0.0153	-0.0019	0.0060	-0.0272	0.0068
1.85	1.86	0.05	0.7694	0.0138	0.0052	0.0063	-0.0403	0.0083
1.85	1.86	0.15	0.7000	0.0110	0.0178	0.0103	-0.0561	0.0102
1.85	1.86	0.25	0.6041	0.0084	0.0318	0.0149	-0.0777	0.0114
1.85	1.86	0.35	0.4864	0.0081	0.0438	0.0159	-0.1046	0.0108
1.85	1.86	0.45	0.3574	0.0085	0.0515	0.0126	-0.1282	0.0084
1.85	1.86	0.55	0.2391	0.0113	0.0556	0.0095	-0.1356	0.0055
1.85	1.86	0.65	0.1540	0.0116	0.0598	0.0080	-0.1232	0.0039
1.85	1.86	0.75	0.1072	0.0102	0.0651	0.0067	-0.0994	0.0036
1.86	1.87	-0.75	0.5555	0.0286	0.0644	0.0130	0.0346	0.0100
1.86	1.87	-0.65	0.5965	0.0152	0.0638	0.0117	0.0391	0.0056
1.86	1.87	-0.55	0.6433	0.0131	0.0578	0.0096	0.0317	0.0052
1.86	1.87	-0.45	0.7017	0.0137	0.0499	0.0080	0.0183	0.0079
1.86	1.87	-0.35	0.7543	0.0123	0.0394	0.0088	0.0076	0.0088
1.86	1.87	-0.25	0.7917	0.0111	0.0275	0.0100	0.0012	0.0085
1.86	1.87	-0.15	0.8109	0.0115	0.0157	0.0084	-0.0052	0.0090
1.86	1.87	-0.05	0.8086	0.0107	0.0055	0.0057	-0.0153	0.0100
1.86	1.87	0.05	0.7787	0.0095	-0.0018	0.0062	-0.0312	0.0104
1.86	1.87	0.15	0.7150	0.0100	-0.0048	0.0109	-0.0532	0.0105
1.86	1.87	0.25	0.6146	0.0106	-0.0018	0.0153	-0.0803	0.0108
1.86	1.87	0.35	0.4847	0.0090	0.0083	0.0154	-0.1085	0.0110
1.86	1.87	0.45	0.3473	0.0084	0.0256	0.0133	-0.1295	0.0103

1.86	1.87	0.55	0.2299	0.0115	0.0477	0.0115	-0.1345	0.0087
1.86	1.87	0.65	0.1465	0.0130	0.0680	0.0100	-0.1206	0.0067
1.86	1.87	0.75	0.0932	0.0119	0.0762	0.0092	-0.0904	0.0064
1.87	1.88	-0.75	0.5005	0.0278	0.0335	0.0136	0.0183	0.0088
1.87	1.88	-0.65	0.5958	0.0185	0.0414	0.0099	0.0360	0.0051
1.87	1.88	-0.55	0.6592	0.0088	0.0494	0.0076	0.0407	0.0048
1.87	1.88	-0.45	0.7154	0.0102	0.0497	0.0056	0.0362	0.0073
1.87	1.88	-0.35	0.7575	0.0109	0.0465	0.0061	0.0262	0.0087
1.87	1.88	-0.25	0.7828	0.0103	0.0377	0.0076	0.0148	0.0098
1.87	1.88	-0.15	0.7953	0.0099	0.0212	0.0060	0.0043	0.0115
1.87	1.88	-0.05	0.7959	0.0083	0.0029	0.0028	-0.0061	0.0129
1.87	1.88	0.05	0.7762	0.0059	-0.0079	0.0036	-0.0193	0.0130
1.87	1.88	0.15	0.7241	0.0067	-0.0065	0.0072	-0.0380	0.0125
1.87	1.88	0.25	0.6331	0.0084	0.0039	0.0104	-0.0624	0.0120
1.87	1.88	0.35	0.5039	0.0085	0.0197	0.0115	-0.0888	0.0114
1.87	1.88	0.45	0.3494	0.0112	0.0434	0.0117	-0.1095	0.0104
1.87	1.88	0.55	0.2097	0.0152	0.0720	0.0124	-0.1162	0.0089
1.87	1.88	0.65	0.1254	0.0151	0.0863	0.0111	-0.1085	0.0076
1.87	1.88	0.75	0.0921	0.0123	0.0649	0.0082	-0.0922	0.0078
1.88	1.89	-0.75	0.5030	0.0369	0.0465	0.0093	0.0346	0.0073
1.88	1.89	-0.65	0.5899	0.0251	0.0439	0.0073	0.0431	0.0043
1.88	1.89	-0.55	0.6537	0.0168	0.0434	0.0047	0.0395	0.0029
1.88	1.89	-0.45	0.7041	0.0152	0.0453	0.0046	0.0301	0.0048
1.88	1.89	-0.35	0.7463	0.0179	0.0375	0.0053	0.0238	0.0072
1.88	1.89	-0.25	0.7835	0.0162	0.0230	0.0059	0.0216	0.0090
1.88	1.89	-0.15	0.8106	0.0126	0.0110	0.0041	0.0190	0.0110
1.88	1.89	-0.05	0.8149	0.0093	0.0027	0.0022	0.0109	0.0127
1.88	1.89	0.05	0.7860	0.0051	-0.0060	0.0025	-0.0050	0.0133
1.88	1.89	0.15	0.7233	0.0030	-0.0147	0.0047	-0.0277	0.0130
1.88	1.89	0.25	0.6290	0.0059	-0.0152	0.0076	-0.0545	0.0119
1.88	1.89	0.35	0.4996	0.0129	0.0007	0.0101	-0.0828	0.0098
1.88	1.89	0.45	0.3434	0.0174	0.0282	0.0128	-0.1067	0.0073
1.88	1.89	0.55	0.2018	0.0208	0.0525	0.0123	-0.1159	0.0061
1.88	1.89	0.65	0.1120	0.0175	0.0681	0.0115	-0.1057	0.0071
1.88	1.89	0.75	0.0754	0.0122	0.0788	0.0071	-0.0789	0.0072
1.89	1.90	-0.75	0.4386	0.0313	0.0283	0.0086	0.0417	0.0043
1.89	1.90	-0.65	0.5247	0.0266	0.0378	0.0054	0.0423	0.0024
1.89	1.90	-0.55	0.6366	0.0174	0.0382	0.0045	0.0377	0.0034
1.89	1.90	-0.45	0.7342	0.0195	0.0405	0.0044	0.0346	0.0061
1.89	1.90	-0.35	0.7908	0.0244	0.0376	0.0050	0.0324	0.0080
1.89	1.90	-0.25	0.8148	0.0212	0.0287	0.0045	0.0311	0.0087
1.89	1.90	-0.15	0.8211	0.0150	0.0162	0.0033	0.0293	0.0085
1.89	1.90	-0.05	0.8117	0.0100	0.0023	0.0031	0.0240	0.0087
1.89	1.90	0.05	0.7816	0.0060	-0.0091	0.0043	0.0110	0.0097
1.89	1.90	0.15	0.7259	0.0046	-0.0127	0.0054	-0.0111	0.0115
1.89	1.90	0.25	0.6331	0.0082	-0.0074	0.0066	-0.0409	0.0128
1.89	1.90	0.35	0.4870	0.0152	0.0030	0.0085	-0.0740	0.0120
1.89	1.90	0.45	0.3065	0.0198	0.0168	0.0114	-0.1016	0.0097
1.89	1.90	0.55	0.1610	0.0184	0.0387	0.0117	-0.1119	0.0081
1.89	1.90	0.65	0.0883	0.0125	0.0657	0.0078	-0.0997	0.0073
1.89	1.90	0.75	0.0660	0.0107	0.0806	0.0067	-0.0702	0.0089
1.90	1.91	-0.84	0.3550	0.0125	0.0713	0.0273	0.0127	0.0021
1.90	1.91	-0.75	0.4282	0.0177	0.0385	0.0144	0.0404	0.0033
1.90	1.91	-0.65	0.5387	0.0145	0.0320	0.0069	0.0426	0.0030
1.90	1.91	-0.55	0.6375	0.0147	0.0436	0.0050	0.0384	0.0059
1.90	1.91	-0.45	0.7008	0.0213	0.0501	0.0048	0.0417	0.0082
1.90	1.91	-0.35	0.7412	0.0242	0.0455	0.0050	0.0442	0.0085
1.90	1.91	-0.25	0.7735	0.0207	0.0316	0.0043	0.0408	0.0078
1.90	1.91	-0.15	0.7955	0.0160	0.0137	0.0042	0.0328	0.0075
1.90	1.91	-0.05	0.7987	0.0128	-0.0017	0.0061	0.0229	0.0080
1.90	1.91	0.05	0.7775	0.0102	-0.0126	0.0090	0.0116	0.0088
1.90	1.91	0.15	0.7234	0.0088	-0.0185	0.0096	-0.0032	0.0100
1.90	1.91	0.25	0.6191	0.0105	-0.0119	0.0082	-0.0255	0.0116
1.90	1.91	0.35	0.4604	0.0132	0.0150	0.0087	-0.0568	0.0125
1.90	1.91	0.45	0.2940	0.0151	0.0447	0.0110	-0.0870	0.0116
1.90	1.91	0.55	0.1709	0.0120	0.0508	0.0102	-0.0988	0.0095
1.90	1.91	0.65	0.0952	0.0062	0.0492	0.0102	-0.0868	0.0076
1.90	1.91	0.75	0.0686	0.0042	0.0767	0.0091	-0.0609	0.0072
1.91	1.92	-0.84	0.3666	0.0129	0.0174	0.0354	0.0171	0.0089
1.91	1.92	-0.75	0.4554	0.0143	0.0479	0.0155	0.0401	0.0039
1.91	1.92	-0.65	0.5413	0.0139	0.0440	0.0084	0.0471	0.0042
1.91	1.92	-0.55	0.6149	0.0128	0.0439	0.0070	0.0525	0.0057
1.91	1.92	-0.45	0.6804	0.0156	0.0418	0.0057	0.0547	0.0060
1.91	1.92	-0.35	0.7317	0.0136	0.0341	0.0056	0.0518	0.0065
1.91	1.92	-0.25	0.7660	0.0099	0.0249	0.0058	0.0473	0.0079
1.91	1.92	-0.15	0.7837	0.0089	0.0171	0.0055	0.0413	0.0104

1.91	1.92	-0.05	0.7834	0.0100	0.0116	0.0068	0.0317	0.0131
1.91	1.92	0.05	0.7613	0.0117	0.0081	0.0092	0.0187	0.0134
1.91	1.92	0.15	0.7098	0.0131	0.0057	0.0101	0.0041	0.0115
1.91	1.92	0.25	0.6141	0.0143	0.0054	0.0085	-0.0156	0.0102
1.91	1.92	0.35	0.4632	0.0169	0.0143	0.0084	-0.0454	0.0104
1.91	1.92	0.45	0.2894	0.0169	0.0367	0.0106	-0.0777	0.0107
1.91	1.92	0.55	0.1577	0.0139	0.0584	0.0098	-0.0936	0.0097
1.91	1.92	0.65	0.0898	0.0081	0.0630	0.0093	-0.0867	0.0083
1.91	1.92	0.75	0.0685	0.0052	0.0536	0.0118	-0.0640	0.0079
1.92	1.93	-0.84	0.3859	0.0263	0.0802	0.0427	0.0152	0.0150
1.92	1.93	-0.75	0.4238	0.0236	0.0566	0.0221	0.0301	0.0109
1.92	1.93	-0.65	0.5359	0.0207	0.0249	0.0094	0.0434	0.0036
1.92	1.93	-0.55	0.6092	0.0171	0.0309	0.0072	0.0491	0.0044
1.92	1.93	-0.45	0.6679	0.0111	0.0419	0.0063	0.0510	0.0056
1.92	1.93	-0.35	0.7239	0.0076	0.0439	0.0052	0.0503	0.0068
1.92	1.93	-0.25	0.7648	0.0075	0.0375	0.0058	0.0514	0.0091
1.92	1.93	-0.15	0.7813	0.0075	0.0262	0.0053	0.0554	0.0112
1.92	1.93	-0.05	0.7763	0.0068	0.0142	0.0043	0.0563	0.0124
1.92	1.93	0.05	0.7516	0.0102	0.0036	0.0069	0.0456	0.0123
1.92	1.93	0.15	0.6968	0.0154	-0.0050	0.0074	0.0218	0.0100
1.92	1.93	0.25	0.5961	0.0194	-0.0070	0.0067	-0.0081	0.0082
1.92	1.93	0.35	0.4399	0.0206	0.0044	0.0080	-0.0369	0.0082
1.92	1.93	0.45	0.2581	0.0194	0.0243	0.0104	-0.0629	0.0091
1.92	1.93	0.55	0.1324	0.0142	0.0379	0.0088	-0.0804	0.0096
1.92	1.93	0.65	0.0812	0.0074	0.0511	0.0087	-0.0750	0.0092
1.92	1.93	0.75	0.0598	0.0063	0.0663	0.0127	-0.0447	0.0087
1.93	1.94	-0.84	0.3840	0.0401	-0.0406	0.0441	0.0585	0.0216
1.93	1.94	-0.75	0.4126	0.0382	0.0272	0.0200	0.0465	0.0123
1.93	1.94	-0.65	0.4944	0.0281	0.0290	0.0066	0.0423	0.0069
1.93	1.94	-0.55	0.5827	0.0181	0.0244	0.0054	0.0449	0.0061
1.93	1.94	-0.45	0.6598	0.0108	0.0330	0.0053	0.0529	0.0073
1.93	1.94	-0.35	0.7189	0.0112	0.0401	0.0050	0.0620	0.0088
1.93	1.94	-0.25	0.7618	0.0157	0.0354	0.0057	0.0670	0.0089
1.93	1.94	-0.15	0.7847	0.0158	0.0238	0.0056	0.0651	0.0085
1.93	1.94	-0.05	0.7790	0.0121	0.0141	0.0064	0.0562	0.0083
1.93	1.94	0.05	0.7413	0.0109	0.0096	0.0086	0.0418	0.0084
1.93	1.94	0.15	0.6735	0.0137	0.0050	0.0078	0.0226	0.0084
1.93	1.94	0.25	0.5673	0.0170	-0.0038	0.0062	-0.0026	0.0080
1.93	1.94	0.35	0.4119	0.0178	-0.0064	0.0074	-0.0326	0.0081
1.93	1.94	0.45	0.2425	0.0140	0.0129	0.0084	-0.0589	0.0090
1.93	1.94	0.55	0.1265	0.0082	0.0407	0.0081	-0.0729	0.0098
1.93	1.94	0.65	0.0804	0.0043	0.0477	0.0089	-0.0724	0.0097
1.93	1.94	0.75	0.0742	0.0054	0.0395	0.0151	-0.0558	0.0092
1.94	1.95	-0.84	0.2867	0.0389	0.0376	0.0318	0.0154	0.0174
1.94	1.95	-0.75	0.3451	0.0333	0.0327	0.0177	0.0204	0.0148
1.94	1.95	-0.65	0.4641	0.0232	0.0275	0.0058	0.0414	0.0093
1.94	1.95	-0.55	0.5767	0.0164	0.0269	0.0061	0.0580	0.0078
1.94	1.95	-0.45	0.6586	0.0139	0.0282	0.0074	0.0679	0.0070
1.94	1.95	-0.35	0.7042	0.0155	0.0381	0.0057	0.0730	0.0065
1.94	1.95	-0.25	0.7245	0.0183	0.0471	0.0056	0.0737	0.0064
1.94	1.95	-0.15	0.7446	0.0199	0.0367	0.0058	0.0708	0.0070
1.94	1.95	-0.05	0.7651	0.0192	0.0077	0.0088	0.0634	0.0088
1.94	1.95	0.05	0.7523	0.0174	-0.0149	0.0126	0.0501	0.0104
1.94	1.95	0.15	0.6819	0.0152	-0.0134	0.0097	0.0319	0.0115
1.94	1.95	0.25	0.5651	0.0155	-0.0043	0.0082	0.0088	0.0117
1.94	1.95	0.35	0.4087	0.0156	-0.0029	0.0103	-0.0215	0.0101
1.94	1.95	0.45	0.2364	0.0114	0.0086	0.0119	-0.0500	0.0092
1.94	1.95	0.55	0.1214	0.0061	0.0352	0.0115	-0.0598	0.0096
1.94	1.95	0.65	0.0795	0.0036	0.0551	0.0138	-0.0541	0.0089
1.94	1.95	0.75	0.0722	0.0054	0.0728	0.0204	-0.0430	0.0078
1.95	1.96	-0.84	0.3114	0.0331	-0.0003	0.0220	0.0200	0.0144
1.95	1.96	-0.75	0.3786	0.0208	0.0210	0.0195	0.0425	0.0122
1.95	1.96	-0.65	0.4589	0.0174	0.0251	0.0135	0.0613	0.0097
1.95	1.96	-0.55	0.5544	0.0199	0.0338	0.0112	0.0642	0.0059
1.95	1.96	-0.45	0.6400	0.0210	0.0442	0.0108	0.0626	0.0043
1.95	1.96	-0.35	0.6958	0.0184	0.0461	0.0076	0.0657	0.0052
1.95	1.96	-0.25	0.7246	0.0162	0.0400	0.0055	0.0731	0.0053
1.95	1.96	-0.15	0.7376	0.0176	0.0313	0.0075	0.0792	0.0055
1.95	1.96	-0.05	0.7373	0.0196	0.0218	0.0110	0.0787	0.0075
1.95	1.96	0.05	0.7146	0.0198	0.0097	0.0128	0.0686	0.0094
1.95	1.96	0.15	0.6533	0.0172	-0.0050	0.0101	0.0485	0.0113
1.95	1.96	0.25	0.5397	0.0148	-0.0185	0.0085	0.0205	0.0118
1.95	1.96	0.35	0.3800	0.0126	-0.0238	0.0093	-0.0110	0.0104
1.95	1.96	0.45	0.2187	0.0089	-0.0132	0.0109	-0.0388	0.0081
1.95	1.96	0.55	0.1130	0.0067	0.0123	0.0107	-0.0530	0.0061
1.95	1.96	0.65	0.0768	0.0048	0.0308	0.0138	-0.0498	0.0063

1.95	1.96	0.75	0.0830	0.0105	0.0225	0.0229	-0.0389	0.0064
1.95	1.96	0.85	0.1138	0.0233	0.0058	0.0307	-0.0291	0.0076
1.96	1.97	-0.84	0.2861	0.0295	0.0030	0.0173	0.0288	0.0136
1.96	1.97	-0.75	0.3414	0.0261	-0.0173	0.0175	0.0398	0.0144
1.96	1.97	-0.65	0.4406	0.0176	0.0021	0.0176	0.0477	0.0096
1.96	1.97	-0.55	0.5381	0.0208	0.0103	0.0119	0.0585	0.0050
1.96	1.97	-0.45	0.6057	0.0223	0.0184	0.0117	0.0655	0.0046
1.96	1.97	-0.35	0.6610	0.0197	0.0316	0.0093	0.0731	0.0065
1.96	1.97	-0.25	0.7068	0.0166	0.0374	0.0079	0.0805	0.0064
1.96	1.97	-0.15	0.7261	0.0171	0.0354	0.0085	0.0795	0.0055
1.96	1.97	-0.05	0.7199	0.0192	0.0327	0.0106	0.0714	0.0051
1.96	1.97	0.05	0.7033	0.0190	0.0246	0.0095	0.0649	0.0059
1.96	1.97	0.15	0.6629	0.0174	0.0016	0.0053	0.0589	0.0072
1.96	1.97	0.25	0.5540	0.0160	-0.0247	0.0056	0.0377	0.0079
1.96	1.97	0.35	0.3834	0.0130	-0.0254	0.0058	-0.0010	0.0076
1.96	1.97	0.45	0.2237	0.0086	-0.0071	0.0042	-0.0334	0.0070
1.96	1.97	0.55	0.1169	0.0070	0.0126	0.0071	-0.0486	0.0067
1.96	1.97	0.65	0.0825	0.0076	0.0413	0.0120	-0.0518	0.0070
1.96	1.97	0.75	0.0828	0.0125	0.0586	0.0221	-0.0461	0.0094
1.96	1.97	0.84	0.0668	0.0244	0.0482	0.0267	-0.0387	0.0120
1.97	1.98	-0.84	0.2207	0.0325	-0.0001	0.0157	0.0496	0.0150
1.97	1.98	-0.75	0.3364	0.0223	-0.0393	0.0193	0.0103	0.0132
1.97	1.98	-0.65	0.4272	0.0168	0.0025	0.0148	0.0382	0.0083
1.97	1.98	-0.55	0.5037	0.0165	0.0228	0.0122	0.0576	0.0041
1.97	1.98	-0.45	0.5920	0.0174	0.0368	0.0094	0.0693	0.0051
1.97	1.98	-0.35	0.6606	0.0166	0.0461	0.0087	0.0846	0.0061
1.97	1.98	-0.25	0.6903	0.0160	0.0500	0.0074	0.0917	0.0059
1.97	1.98	-0.15	0.6988	0.0160	0.0517	0.0073	0.0854	0.0053
1.97	1.98	-0.05	0.6992	0.0160	0.0469	0.0069	0.0742	0.0070
1.97	1.98	0.05	0.6816	0.0169	0.0279	0.0050	0.0645	0.0072
1.97	1.98	0.15	0.6279	0.0206	-0.0013	0.0043	0.0529	0.0067
1.97	1.98	0.25	0.5231	0.0218	-0.0238	0.0072	0.0338	0.0065
1.97	1.98	0.35	0.3680	0.0172	-0.0244	0.0088	0.0053	0.0058
1.97	1.98	0.45	0.2186	0.0114	-0.0063	0.0092	-0.0265	0.0066
1.97	1.98	0.55	0.1329	0.0101	0.0161	0.0094	-0.0446	0.0078
1.97	1.98	0.65	0.0946	0.0106	0.0381	0.0155	-0.0370	0.0090
1.97	1.98	0.75	0.0903	0.0133	0.0590	0.0217	-0.0249	0.0108
1.97	1.98	0.84	0.1241	0.0231	0.0781	0.0376	-0.0538	0.0153
1.98	1.99	-0.84	0.2406	0.0285	0.0290	0.0265	0.0223	0.0123
1.98	1.99	-0.75	0.2968	0.0220	-0.0079	0.0182	0.0330	0.0136
1.98	1.99	-0.65	0.4197	0.0189	-0.0295	0.0159	0.0436	0.0094
1.98	1.99	-0.55	0.5111	0.0184	0.0052	0.0113	0.0531	0.0070
1.98	1.99	-0.45	0.5778	0.0158	0.0406	0.0083	0.0617	0.0068
1.98	1.99	-0.35	0.6373	0.0155	0.0525	0.0056	0.0752	0.0066
1.98	1.99	-0.25	0.6759	0.0148	0.0534	0.0039	0.0874	0.0042
1.98	1.99	-0.15	0.6871	0.0131	0.0518	0.0033	0.0911	0.0042
1.98	1.99	-0.05	0.6854	0.0124	0.0429	0.0041	0.0874	0.0067
1.98	1.99	0.05	0.6733	0.0150	0.0240	0.0039	0.0795	0.0086
1.98	1.99	0.15	0.6226	0.0197	0.0036	0.0051	0.0646	0.0089
1.98	1.99	0.25	0.5032	0.0205	-0.0069	0.0117	0.0386	0.0077
1.98	1.99	0.35	0.3383	0.0168	-0.0101	0.0163	0.0071	0.0065
1.98	1.99	0.45	0.1998	0.0119	-0.0124	0.0138	-0.0175	0.0071
1.98	1.99	0.55	0.1272	0.0097	-0.0049	0.0142	-0.0303	0.0073
1.98	1.99	0.65	0.1045	0.0097	0.0064	0.0194	-0.0327	0.0066
1.98	1.99	0.75	0.1070	0.0110	0.0212	0.0299	-0.0248	0.0089
1.98	1.99	0.84	0.1077	0.0178	0.0847	0.0461	-0.0176	0.0129
1.99	2.00	-0.84	0.2705	0.0335	-0.0284	0.0279	0.0248	0.0172
1.99	2.00	-0.75	0.3111	0.0301	-0.0211	0.0233	0.0091	0.0128
1.99	2.00	-0.65	0.3987	0.0264	-0.0021	0.0173	0.0303	0.0125
1.99	2.00	-0.55	0.4847	0.0218	0.0225	0.0156	0.0640	0.0112
1.99	2.00	-0.45	0.5589	0.0163	0.0374	0.0107	0.0803	0.0095
1.99	2.00	-0.35	0.6208	0.0159	0.0446	0.0072	0.0836	0.0073
1.99	2.00	-0.25	0.6631	0.0158	0.0498	0.0044	0.0861	0.0044
1.99	2.00	-0.15	0.6849	0.0155	0.0506	0.0031	0.0892	0.0031
1.99	2.00	-0.05	0.6854	0.0156	0.0409	0.0047	0.0892	0.0049
1.99	2.00	0.05	0.6562	0.0159	0.0210	0.0056	0.0848	0.0068
1.99	2.00	0.15	0.5874	0.0167	-0.0034	0.0072	0.0750	0.0078
1.99	2.00	0.25	0.4771	0.0173	-0.0293	0.0128	0.0545	0.0074
1.99	2.00	0.35	0.3405	0.0150	-0.0517	0.0171	0.0166	0.0063
1.99	2.00	0.45	0.2166	0.0108	-0.0417	0.0147	-0.0247	0.0081
1.99	2.00	0.55	0.1436	0.0087	0.0112	0.0136	-0.0390	0.0096
1.99	2.00	0.65	0.1193	0.0104	0.0430	0.0154	-0.0268	0.0073
1.99	2.00	0.75	0.1053	0.0107	0.0060	0.0256	-0.0196	0.0067
1.99	2.00	0.84	0.0843	0.0091	-0.0447	0.0466	-0.0317	0.0123
2.00	2.01	-0.84	0.1999	0.0319	-0.0609	0.0283	0.0129	0.0193
2.00	2.01	-0.75	0.2613	0.0283	-0.0345	0.0206	-0.0002	0.0157

2.00	2.01	-0.65	0.3501	0.0231	-0.0356	0.0191	0.0109	0.0112
2.00	2.01	-0.55	0.4531	0.0189	-0.0137	0.0158	0.0434	0.0095
2.00	2.01	-0.45	0.5491	0.0132	0.0161	0.0103	0.0777	0.0100
2.00	2.01	-0.35	0.6095	0.0144	0.0344	0.0070	0.0940	0.0080
2.00	2.01	-0.25	0.6413	0.0180	0.0454	0.0052	0.0945	0.0053
2.00	2.01	-0.15	0.6572	0.0176	0.0535	0.0049	0.0892	0.0043
2.00	2.01	-0.05	0.6576	0.0157	0.0521	0.0058	0.0829	0.0060
2.00	2.01	0.05	0.6400	0.0144	0.0349	0.0065	0.0751	0.0079
2.00	2.01	0.15	0.5959	0.0153	0.0049	0.0079	0.0635	0.0079
2.00	2.01	0.25	0.5029	0.0170	-0.0256	0.0126	0.0454	0.0057
2.00	2.01	0.35	0.3585	0.0167	-0.0403	0.0146	0.0198	0.0051
2.00	2.01	0.45	0.2226	0.0123	-0.0313	0.0141	-0.0064	0.0074
2.00	2.01	0.55	0.1434	0.0109	-0.0068	0.0130	-0.0196	0.0094
2.00	2.01	0.65	0.1141	0.0166	0.0126	0.0130	-0.0172	0.0077
2.00	2.01	0.75	0.1075	0.0158	0.0150	0.0175	-0.0134	0.0068
2.00	2.01	0.84	0.0888	0.0145	0.0203	0.0308	-0.0076	0.0082
2.01	2.02	-0.84	0.1788	0.0190	-0.0753	0.0222	-0.0326	0.0187
2.01	2.02	-0.75	0.2471	0.0131	-0.0682	0.0181	-0.0122	0.0137
2.01	2.02	-0.65	0.3541	0.0113	-0.0370	0.0173	0.0086	0.0069
2.01	2.02	-0.55	0.4666	0.0132	-0.0012	0.0135	0.0379	0.0070
2.01	2.02	-0.45	0.5451	0.0145	0.0222	0.0071	0.0652	0.0080
2.01	2.02	-0.35	0.5944	0.0173	0.0415	0.0047	0.0806	0.0082
2.01	2.02	-0.25	0.6286	0.0179	0.0560	0.0061	0.0896	0.0063
2.01	2.02	-0.15	0.6462	0.0148	0.0568	0.0069	0.0957	0.0057
2.01	2.02	-0.05	0.6451	0.0123	0.0442	0.0067	0.0971	0.0073
2.01	2.02	0.05	0.6250	0.0108	0.0283	0.0064	0.0927	0.0087
2.01	2.02	0.15	0.5731	0.0109	0.0141	0.0066	0.0807	0.0074
2.01	2.02	0.25	0.4657	0.0160	-0.0025	0.0104	0.0549	0.0049
2.01	2.02	0.35	0.3170	0.0173	-0.0203	0.0147	0.0178	0.0024
2.01	2.02	0.45	0.2003	0.0116	-0.0248	0.0142	-0.0076	0.0042
2.01	2.02	0.55	0.1543	0.0118	-0.0131	0.0123	-0.0120	0.0050
2.01	2.02	0.65	0.1538	0.0183	0.0050	0.0108	-0.0102	0.0040
2.01	2.02	0.75	0.1463	0.0215	0.0232	0.0076	-0.0099	0.0029
2.01	2.02	0.85	0.0899	0.0174	0.0320	0.0165	-0.0105	0.0056
2.02	2.03	-0.84	0.1881	0.0145	-0.0370	0.0201	-0.0441	0.0148
2.02	2.03	-0.75	0.2541	0.0083	-0.0744	0.0168	-0.0161	0.0116
2.02	2.03	-0.65	0.3474	0.0078	-0.0628	0.0134	0.0145	0.0091
2.02	2.03	-0.55	0.4356	0.0124	-0.0249	0.0129	0.0368	0.0060
2.02	2.03	-0.45	0.5206	0.0143	0.0157	0.0078	0.0560	0.0067
2.02	2.03	-0.35	0.5695	0.0145	0.0428	0.0044	0.0722	0.0061
2.02	2.03	-0.25	0.5986	0.0148	0.0621	0.0058	0.0809	0.0047
2.02	2.03	-0.15	0.6308	0.0153	0.0704	0.0073	0.0854	0.0047
2.02	2.03	-0.05	0.6507	0.0145	0.0583	0.0064	0.0905	0.0063
2.02	2.03	0.05	0.6336	0.0129	0.0339	0.0069	0.0923	0.0070
2.02	2.03	0.15	0.5782	0.0118	0.0123	0.0069	0.0811	0.0057
2.02	2.03	0.25	0.4832	0.0132	-0.0098	0.0088	0.0515	0.0032
2.02	2.03	0.35	0.3451	0.0140	-0.0433	0.0114	0.0165	0.0025
2.02	2.03	0.45	0.2123	0.0101	-0.0597	0.0150	-0.0032	0.0022
2.02	2.03	0.55	0.1494	0.0105	-0.0337	0.0127	-0.0111	0.0019
2.02	2.03	0.65	0.1591	0.0136	0.0068	0.0072	-0.0115	0.0021
2.02	2.03	0.75	0.1667	0.0144	0.0348	0.0077	-0.0107	0.0040
2.02	2.03	0.85	0.1234	0.0148	0.0368	0.0085	-0.0132	0.0050
2.03	2.04	-0.84	0.1674	0.0182	-0.0816	0.0216	-0.0422	0.0137
2.03	2.04	-0.75	0.2681	0.0128	-0.0547	0.0171	-0.0423	0.0151
2.03	2.04	-0.65	0.3532	0.0073	-0.0720	0.0156	-0.0008	0.0157
2.03	2.04	-0.55	0.4497	0.0105	-0.0370	0.0132	0.0309	0.0103
2.03	2.04	-0.45	0.5205	0.0124	0.0137	0.0099	0.0532	0.0063
2.03	2.04	-0.35	0.5659	0.0111	0.0443	0.0075	0.0714	0.0043
2.03	2.04	-0.25	0.6005	0.0117	0.0568	0.0076	0.0838	0.0038
2.03	2.04	-0.15	0.6218	0.0165	0.0606	0.0065	0.0866	0.0039
2.03	2.04	-0.05	0.6244	0.0205	0.0584	0.0058	0.0830	0.0043
2.03	2.04	0.05	0.6088	0.0199	0.0465	0.0071	0.0796	0.0049
2.03	2.04	0.15	0.5688	0.0180	0.0201	0.0063	0.0750	0.0042
2.03	2.04	0.25	0.4808	0.0182	-0.0186	0.0076	0.0566	0.0042
2.03	2.04	0.35	0.3391	0.0136	-0.0473	0.0106	0.0201	0.0042
2.03	2.04	0.45	0.2171	0.0122	-0.0411	0.0118	-0.0068	0.0033
2.03	2.04	0.55	0.1715	0.0130	-0.0113	0.0107	-0.0112	0.0023
2.03	2.04	0.65	0.1724	0.0104	0.0160	0.0074	-0.0087	0.0048
2.03	2.04	0.75	0.1589	0.0083	0.0221	0.0098	-0.0082	0.0074
2.03	2.04	0.85	0.1048	0.0146	0.0240	0.0135	-0.0043	0.0083
2.04	2.05	-0.84	0.2196	0.0196	-0.0332	0.0297	-0.0324	0.0203
2.04	2.05	-0.75	0.2488	0.0140	-0.0707	0.0248	-0.0533	0.0208
2.04	2.05	-0.65	0.3584	0.0063	-0.0722	0.0235	-0.0150	0.0199
2.04	2.05	-0.55	0.4614	0.0107	-0.0487	0.0190	0.0198	0.0152
2.04	2.05	-0.45	0.5391	0.0145	-0.0046	0.0133	0.0422	0.0087
2.04	2.05	-0.35	0.5768	0.0134	0.0292	0.0108	0.0655	0.0045

2.04	2.05	-0.25	0.5872	0.0109	0.0446	0.0096	0.0811	0.0055
2.04	2.05	-0.15	0.5924	0.0142	0.0526	0.0073	0.0843	0.0050
2.04	2.05	-0.05	0.5955	0.0167	0.0576	0.0041	0.0833	0.0034
2.04	2.05	0.05	0.5823	0.0161	0.0519	0.0066	0.0814	0.0029
2.04	2.05	0.15	0.5392	0.0176	0.0285	0.0075	0.0716	0.0031
2.04	2.05	0.25	0.4504	0.0188	-0.0089	0.0092	0.0504	0.0053
2.04	2.05	0.35	0.3154	0.0150	-0.0386	0.0115	0.0249	0.0072
2.04	2.05	0.45	0.2083	0.0155	-0.0366	0.0122	0.0012	0.0062
2.04	2.05	0.55	0.1828	0.0175	-0.0097	0.0101	-0.0120	0.0047
2.04	2.05	0.65	0.1833	0.0125	0.0200	0.0092	-0.0040	0.0060
2.04	2.05	0.75	0.1569	0.0112	0.0398	0.0133	0.0088	0.0080
2.04	2.05	0.85	0.1287	0.0127	0.0481	0.0206	0.0090	0.0086
2.05	2.06	-0.84	0.1960	0.0187	-0.0464	0.0278	-0.0768	0.0202
2.05	2.06	-0.75	0.2701	0.0148	-0.1173	0.0277	-0.0793	0.0200
2.05	2.06	-0.65	0.3623	0.0071	-0.1276	0.0242	-0.0555	0.0184
2.05	2.06	-0.55	0.4468	0.0096	-0.0747	0.0169	-0.0025	0.0142
2.05	2.06	-0.45	0.5015	0.0154	-0.0134	0.0144	0.0460	0.0088
2.05	2.06	-0.35	0.5445	0.0147	0.0338	0.0135	0.0645	0.0051
2.05	2.06	-0.25	0.5841	0.0107	0.0615	0.0128	0.0687	0.0057
2.05	2.06	-0.15	0.6136	0.0105	0.0671	0.0088	0.0733	0.0056
2.05	2.06	-0.05	0.6192	0.0097	0.0541	0.0062	0.0791	0.0032
2.05	2.06	0.05	0.5914	0.0089	0.0354	0.0061	0.0803	0.0015
2.05	2.06	0.15	0.5275	0.0096	0.0208	0.0061	0.0701	0.0026
2.05	2.06	0.25	0.4266	0.0112	0.0056	0.0083	0.0442	0.0068
2.05	2.06	0.35	0.3121	0.0127	-0.0153	0.0107	0.0101	0.0103
2.05	2.06	0.45	0.2382	0.0153	-0.0189	0.0110	-0.0097	0.0093
2.05	2.06	0.55	0.2099	0.0211	0.0040	0.0125	-0.0065	0.0064
2.05	2.06	0.65	0.1879	0.0192	0.0186	0.0129	0.0059	0.0053
2.05	2.06	0.75	0.1596	0.0154	0.0117	0.0178	0.0090	0.0065
2.05	2.06	0.85	0.1522	0.0140	-0.0049	0.0197	-0.0004	0.0064
2.06	2.07	-0.84	0.2217	0.0266	-0.0982	0.0278	-0.0963	0.0161
2.06	2.07	-0.75	0.2845	0.0174	-0.0863	0.0201	-0.0761	0.0143
2.06	2.07	-0.65	0.3594	0.0104	-0.1090	0.0172	-0.0414	0.0138
2.06	2.07	-0.55	0.4434	0.0085	-0.0836	0.0109	-0.0126	0.0096
2.06	2.07	-0.45	0.5237	0.0133	-0.0326	0.0103	0.0274	0.0071
2.06	2.07	-0.35	0.5725	0.0136	0.0050	0.0141	0.0627	0.0048
2.06	2.07	-0.25	0.5971	0.0097	0.0312	0.0133	0.0800	0.0054
2.06	2.07	-0.15	0.6102	0.0080	0.0501	0.0094	0.0838	0.0053
2.06	2.07	-0.05	0.6095	0.0068	0.0534	0.0072	0.0818	0.0033
2.06	2.07	0.05	0.5867	0.0056	0.0405	0.0074	0.0778	0.0017
2.06	2.07	0.15	0.5310	0.0063	0.0210	0.0054	0.0713	0.0034
2.06	2.07	0.25	0.4306	0.0101	0.0001	0.0051	0.0579	0.0090
2.06	2.07	0.35	0.3158	0.0105	-0.0184	0.0065	0.0346	0.0123
2.06	2.07	0.45	0.2537	0.0136	-0.0136	0.0069	0.0120	0.0093
2.06	2.07	0.55	0.2375	0.0158	0.0199	0.0123	0.0016	0.0050
2.06	2.07	0.65	0.2224	0.0186	0.0449	0.0158	0.0064	0.0040
2.06	2.07	0.75	0.1885	0.0160	0.0330	0.0144	0.0179	0.0049
2.06	2.07	0.85	0.1511	0.0108	-0.0011	0.0192	0.0125	0.0055
2.07	2.08	-0.84	0.2269	0.0346	-0.0908	0.0237	-0.0944	0.0119
2.07	2.08	-0.75	0.3247	0.0221	-0.0814	0.0180	-0.1012	0.0132
2.07	2.08	-0.65	0.3604	0.0105	-0.0897	0.0127	-0.0655	0.0121
2.07	2.08	-0.55	0.4279	0.0124	-0.0799	0.0073	-0.0157	0.0091
2.07	2.08	-0.45	0.5035	0.0130	-0.0292	0.0094	0.0273	0.0061
2.07	2.08	-0.35	0.5576	0.0137	0.0268	0.0127	0.0576	0.0049
2.07	2.08	-0.25	0.6010	0.0113	0.0523	0.0107	0.0727	0.0053
2.07	2.08	-0.15	0.6241	0.0061	0.0494	0.0071	0.0749	0.0044
2.07	2.08	-0.05	0.6116	0.0049	0.0383	0.0067	0.0746	0.0029
2.07	2.08	0.05	0.5748	0.0059	0.0270	0.0073	0.0770	0.0030
2.07	2.08	0.15	0.5238	0.0078	0.0110	0.0067	0.0719	0.0063
2.07	2.08	0.25	0.4420	0.0124	-0.0043	0.0042	0.0439	0.0108
2.07	2.08	0.35	0.3328	0.0150	-0.0089	0.0058	0.0101	0.0111
2.07	2.08	0.45	0.2518	0.0133	-0.0114	0.0050	0.0010	0.0071
2.07	2.08	0.55	0.2271	0.0128	-0.0044	0.0148	0.0034	0.0039
2.07	2.08	0.65	0.2279	0.0141	0.0105	0.0198	0.0041	0.0040
2.07	2.08	0.75	0.2059	0.0130	0.0022	0.0197	0.0096	0.0051
2.07	2.08	0.85	0.1493	0.0077	0.0105	0.0158	0.0104	0.0063
2.08	2.09	-0.84	0.3060	0.0299	-0.0440	0.0241	-0.1078	0.0093
2.08	2.09	-0.75	0.3231	0.0174	-0.1009	0.0196	-0.1170	0.0117
2.08	2.09	-0.65	0.3777	0.0100	-0.1182	0.0144	-0.0703	0.0136
2.08	2.09	-0.55	0.4438	0.0141	-0.0848	0.0101	-0.0134	0.0130
2.08	2.09	-0.45	0.5228	0.0146	-0.0431	0.0100	0.0352	0.0107
2.08	2.09	-0.35	0.5885	0.0149	-0.0005	0.0112	0.0611	0.0077
2.08	2.09	-0.25	0.6186	0.0124	0.0370	0.0081	0.0702	0.0066
2.08	2.09	-0.15	0.6223	0.0074	0.0554	0.0052	0.0739	0.0045
2.08	2.09	-0.05	0.6099	0.0048	0.0489	0.0073	0.0774	0.0022
2.08	2.09	0.05	0.5818	0.0068	0.0299	0.0091	0.0771	0.0036

2.08	2.09	0.15	0.5338	0.0107	0.0127	0.0083	0.0616	0.0062
2.08	2.09	0.25	0.4601	0.0133	-0.0040	0.0068	0.0272	0.0082
2.08	2.09	0.35	0.3609	0.0156	-0.0201	0.0088	0.0036	0.0068
2.08	2.09	0.45	0.2728	0.0133	-0.0119	0.0101	0.0044	0.0038
2.08	2.09	0.55	0.2418	0.0163	0.0134	0.0210	0.0030	0.0052
2.08	2.09	0.65	0.2470	0.0125	0.0179	0.0273	0.0096	0.0068
2.08	2.09	0.75	0.2202	0.0094	0.0182	0.0220	0.0223	0.0066
2.08	2.09	0.85	0.1586	0.0076	0.0437	0.0185	0.0058	0.0083
2.09	2.10	-0.84	0.3248	0.0259	-0.0912	0.0279	-0.0904	0.0107
2.09	2.10	-0.75	0.3209	0.0117	-0.0690	0.0234	-0.1012	0.0100
2.09	2.10	-0.65	0.3742	0.0106	-0.0877	0.0179	-0.0862	0.0135
2.09	2.10	-0.55	0.4701	0.0106	-0.0948	0.0102	-0.0439	0.0155
2.09	2.10	-0.45	0.5369	0.0115	-0.0543	0.0089	0.0132	0.0127
2.09	2.10	-0.35	0.5642	0.0137	-0.0009	0.0069	0.0450	0.0090
2.09	2.10	-0.25	0.5924	0.0138	0.0359	0.0042	0.0587	0.0089
2.09	2.10	-0.15	0.6183	0.0087	0.0500	0.0046	0.0708	0.0044
2.09	2.10	-0.05	0.6192	0.0068	0.0493	0.0079	0.0776	0.0038
2.09	2.10	0.05	0.5920	0.0108	0.0448	0.0091	0.0708	0.0032
2.09	2.10	0.15	0.5426	0.0131	0.0338	0.0092	0.0537	0.0047
2.09	2.10	0.25	0.4621	0.0153	-0.0004	0.0078	0.0325	0.0050
2.09	2.10	0.35	0.3552	0.0167	-0.0379	0.0120	0.0103	0.0038
2.09	2.10	0.45	0.2833	0.0167	-0.0091	0.0116	0.0019	0.0055
2.09	2.10	0.55	0.2628	0.0161	0.0537	0.0226	0.0121	0.0080
2.09	2.10	0.65	0.2515	0.0128	0.0740	0.0250	0.0213	0.0078
2.09	2.10	0.75	0.2186	0.0062	0.0528	0.0182	0.0248	0.0067
2.09	2.10	0.85	0.1412	0.0073	0.0269	0.0136	0.0218	0.0076
2.10	2.11	-0.84	0.2875	0.0288	-0.0738	0.0282	-0.1124	0.0098
2.10	2.11	-0.75	0.3226	0.0258	-0.0457	0.0291	-0.1034	0.0107
2.10	2.11	-0.65	0.3886	0.0153	-0.1144	0.0171	-0.1010	0.0097
2.10	2.11	-0.55	0.4653	0.0097	-0.1064	0.0116	-0.0611	0.0117
2.10	2.11	-0.45	0.5274	0.0085	-0.0426	0.0079	0.0144	0.0089
2.10	2.11	-0.35	0.5822	0.0132	0.0060	0.0057	0.0474	0.0079
2.10	2.11	-0.25	0.6267	0.0152	0.0350	0.0038	0.0506	0.0090
2.10	2.11	-0.15	0.6337	0.0111	0.0581	0.0052	0.0627	0.0069
2.10	2.11	-0.05	0.6072	0.0097	0.0658	0.0078	0.0776	0.0048
2.10	2.11	0.05	0.5859	0.0122	0.0483	0.0085	0.0765	0.0051
2.10	2.11	0.15	0.5707	0.0150	0.0153	0.0071	0.0561	0.0036
2.10	2.11	0.25	0.4889	0.0170	-0.0042	0.0073	0.0242	0.0053
2.10	2.11	0.35	0.3356	0.0233	0.0019	0.0121	0.0047	0.0062
2.10	2.11	0.45	0.2833	0.0202	-0.0046	0.0130	-0.0006	0.0086
2.10	2.11	0.55	0.2967	0.0188	0.0044	0.0187	-0.0069	0.0134
2.10	2.11	0.65	0.2683	0.0115	0.0411	0.0173	0.0038	0.0114
2.10	2.11	0.75	0.2165	0.0086	0.0394	0.0130	0.0229	0.0070
2.10	2.11	0.85	0.1539	0.0069	0.0351	0.0108	0.0319	0.0077
2.11	2.12	-0.84	0.3506	0.0316	-0.0275	0.0295	-0.1152	0.0143
2.11	2.12	-0.75	0.3728	0.0318	-0.1101	0.0259	-0.1112	0.0110
2.11	2.12	-0.65	0.4163	0.0181	-0.1196	0.0166	-0.0862	0.0117
2.11	2.12	-0.55	0.4657	0.0073	-0.0873	0.0097	-0.0540	0.0095
2.11	2.12	-0.45	0.5403	0.0082	-0.0333	0.0071	0.0018	0.0091
2.11	2.12	-0.35	0.5932	0.0139	0.0133	0.0056	0.0553	0.0084
2.11	2.12	-0.25	0.6126	0.0169	0.0404	0.0035	0.0755	0.0086
2.11	2.12	-0.15	0.6214	0.0136	0.0497	0.0053	0.0689	0.0058
2.11	2.12	-0.05	0.6266	0.0117	0.0480	0.0078	0.0641	0.0063
2.11	2.12	0.05	0.6138	0.0125	0.0384	0.0080	0.0672	0.0045
2.11	2.12	0.15	0.5690	0.0106	0.0193	0.0064	0.0595	0.0050
2.11	2.12	0.25	0.4929	0.0134	-0.0070	0.0053	0.0321	0.0060
2.11	2.12	0.35	0.4002	0.0208	-0.0190	0.0101	0.0146	0.0072
2.11	2.12	0.45	0.3186	0.0223	0.0043	0.0099	0.0182	0.0114
2.11	2.12	0.55	0.2874	0.0201	0.0381	0.0135	0.0205	0.0158
2.11	2.12	0.65	0.2719	0.0162	0.0433	0.0120	0.0223	0.0161
2.11	2.12	0.75	0.2164	0.0129	0.0309	0.0092	0.0206	0.0114
2.11	2.12	0.85	0.1599	0.0109	0.0116	0.0132	0.0167	0.0088
2.12	2.13	-0.84	0.3460	0.0263	-0.0577	0.0231	-0.0986	0.0141
2.12	2.13	-0.75	0.4124	0.0267	-0.0529	0.0250	-0.1366	0.0130
2.12	2.13	-0.65	0.4142	0.0141	-0.1014	0.0132	-0.1066	0.0088
2.12	2.13	-0.55	0.4723	0.0041	-0.1024	0.0109	-0.0411	0.0093
2.12	2.13	-0.45	0.5494	0.0065	-0.0431	0.0073	0.0242	0.0091
2.12	2.13	-0.35	0.6114	0.0122	0.0066	0.0049	0.0587	0.0080
2.12	2.13	-0.25	0.6481	0.0160	0.0341	0.0044	0.0689	0.0067
2.12	2.13	-0.15	0.6460	0.0149	0.0527	0.0060	0.0694	0.0042
2.12	2.13	-0.05	0.6171	0.0148	0.0622	0.0089	0.0674	0.0045
2.12	2.13	0.05	0.5868	0.0132	0.0543	0.0092	0.0643	0.0046
2.12	2.13	0.15	0.5549	0.0090	0.0268	0.0076	0.0591	0.0036
2.12	2.13	0.25	0.4862	0.0067	-0.0048	0.0054	0.0439	0.0063
2.12	2.13	0.35	0.3806	0.0155	-0.0061	0.0067	0.0195	0.0072
2.12	2.13	0.45	0.3283	0.0185	0.0143	0.0083	0.0190	0.0082

2.12	2.13	0.55	0.3210	0.0187	0.0239	0.0124	0.0384	0.0115
2.12	2.13	0.65	0.2983	0.0187	0.0359	0.0123	0.0464	0.0123
2.12	2.13	0.75	0.2498	0.0139	0.0434	0.0135	0.0450	0.0102
2.12	2.13	0.85	0.1692	0.0094	0.0265	0.0157	0.0276	0.0071
2.13	2.14	-0.84	0.3728	0.0253	-0.0799	0.0197	-0.1328	0.0131
2.13	2.14	-0.75	0.3455	0.0273	-0.0738	0.0164	-0.1255	0.0086
2.13	2.14	-0.65	0.4070	0.0154	-0.0987	0.0125	-0.1072	0.0057
2.13	2.14	-0.55	0.4705	0.0057	-0.0747	0.0089	-0.0445	0.0059
2.13	2.14	-0.45	0.5452	0.0054	-0.0407	0.0067	0.0145	0.0084
2.13	2.14	-0.35	0.6137	0.0084	-0.0023	0.0051	0.0458	0.0068
2.13	2.14	-0.25	0.6542	0.0119	0.0376	0.0050	0.0598	0.0049
2.13	2.14	-0.15	0.6606	0.0130	0.0587	0.0083	0.0707	0.0029
2.13	2.14	-0.05	0.6384	0.0133	0.0525	0.0100	0.0765	0.0045
2.13	2.14	0.05	0.6000	0.0139	0.0313	0.0100	0.0697	0.0041
2.13	2.14	0.15	0.5516	0.0094	0.0128	0.0077	0.0525	0.0050
2.13	2.14	0.25	0.4825	0.0070	0.0030	0.0044	0.0347	0.0084
2.13	2.14	0.35	0.3979	0.0116	-0.0011	0.0045	0.0180	0.0102
2.13	2.14	0.45	0.3517	0.0168	0.0146	0.0058	0.0096	0.0105
2.13	2.14	0.55	0.3370	0.0191	0.0482	0.0109	0.0236	0.0088
2.13	2.14	0.65	0.3033	0.0162	0.0638	0.0146	0.0388	0.0088
2.13	2.14	0.75	0.2519	0.0124	0.0566	0.0141	0.0369	0.0075
2.13	2.14	0.85	0.1742	0.0044	0.0563	0.0168	0.0273	0.0043
2.14	2.15	-0.84	0.3893	0.0339	-0.0549	0.0132	-0.1089	0.0099
2.14	2.15	-0.75	0.4004	0.0243	-0.0989	0.0158	-0.1331	0.0064
2.14	2.15	-0.65	0.4323	0.0154	-0.0961	0.0099	-0.1105	0.0037
2.14	2.15	-0.55	0.4780	0.0107	-0.0832	0.0095	-0.0535	0.0066
2.14	2.15	-0.45	0.5468	0.0074	-0.0488	0.0061	0.0050	0.0068
2.14	2.15	-0.35	0.5990	0.0098	0.0028	0.0057	0.0433	0.0056
2.14	2.15	-0.25	0.6371	0.0090	0.0313	0.0051	0.0609	0.0029
2.14	2.15	-0.15	0.6628	0.0101	0.0375	0.0086	0.0673	0.0025
2.14	2.15	-0.05	0.6573	0.0126	0.0396	0.0099	0.0670	0.0044
2.14	2.15	0.05	0.6205	0.0095	0.0397	0.0089	0.0627	0.0054
2.14	2.15	0.15	0.5670	0.0100	0.0256	0.0066	0.0578	0.0055
2.14	2.15	0.25	0.4921	0.0106	-0.0013	0.0034	0.0528	0.0080
2.14	2.15	0.35	0.4020	0.0138	-0.0042	0.0039	0.0434	0.0114
2.14	2.15	0.45	0.3586	0.0189	0.0222	0.0048	0.0345	0.0110
2.14	2.15	0.55	0.3546	0.0206	0.0330	0.0090	0.0338	0.0094
2.14	2.15	0.65	0.3263	0.0211	0.0304	0.0135	0.0344	0.0098
2.14	2.15	0.75	0.2615	0.0144	0.0342	0.0141	0.0316	0.0085
2.14	2.15	0.85	0.1733	0.0059	0.0462	0.0168	0.0310	0.0058
2.15	2.16	-0.84	0.3324	0.0349	-0.0511	0.0146	-0.1170	0.0074
2.15	2.16	-0.75	0.4013	0.0229	-0.0968	0.0133	-0.1348	0.0061
2.15	2.16	-0.65	0.4451	0.0138	-0.1166	0.0123	-0.1057	0.0064
2.15	2.16	-0.55	0.4827	0.0107	-0.0935	0.0097	-0.0500	0.0088
2.15	2.16	-0.45	0.5313	0.0117	-0.0382	0.0065	0.0025	0.0088
2.15	2.16	-0.35	0.5893	0.0107	0.0095	0.0064	0.0371	0.0055
2.15	2.16	-0.25	0.6322	0.0100	0.0342	0.0053	0.0579	0.0027
2.15	2.16	-0.15	0.6494	0.0101	0.0408	0.0082	0.0695	0.0026
2.15	2.16	-0.05	0.6437	0.0103	0.0360	0.0095	0.0743	0.0051
2.15	2.16	0.05	0.6161	0.0098	0.0248	0.0084	0.0727	0.0067
2.15	2.16	0.15	0.5636	0.0127	0.0110	0.0054	0.0624	0.0064
2.15	2.16	0.25	0.4912	0.0149	-0.0006	0.0040	0.0444	0.0071
2.15	2.16	0.35	0.4263	0.0161	0.0003	0.0055	0.0282	0.0093
2.15	2.16	0.45	0.3943	0.0172	0.0202	0.0089	0.0261	0.0108
2.15	2.16	0.55	0.3822	0.0167	0.0399	0.0101	0.0404	0.0099
2.15	2.16	0.65	0.3555	0.0199	0.0410	0.0128	0.0558	0.0092
2.15	2.16	0.75	0.2868	0.0151	0.0327	0.0154	0.0513	0.0110
2.15	2.16	0.85	0.1760	0.0063	0.0215	0.0146	0.0278	0.0077
2.16	2.17	-0.84	0.4370	0.0364	-0.0694	0.0186	-0.1075	0.0052
2.16	2.17	-0.75	0.4094	0.0236	-0.0716	0.0132	-0.1220	0.0072
2.16	2.17	-0.65	0.4415	0.0172	-0.0950	0.0125	-0.1150	0.0080
2.16	2.17	-0.55	0.5067	0.0171	-0.0796	0.0100	-0.0746	0.0094
2.16	2.17	-0.45	0.5403	0.0151	-0.0457	0.0087	-0.0123	0.0073
2.16	2.17	-0.35	0.5813	0.0154	-0.0091	0.0070	0.0285	0.0047
2.16	2.17	-0.25	0.6262	0.0113	0.0304	0.0046	0.0583	0.0022
2.16	2.17	-0.15	0.6371	0.0111	0.0546	0.0075	0.0725	0.0029
2.16	2.17	-0.05	0.6272	0.0102	0.0558	0.0094	0.0658	0.0052
2.16	2.17	0.05	0.6185	0.0078	0.0405	0.0079	0.0559	0.0087
2.16	2.17	0.15	0.5957	0.0129	0.0161	0.0050	0.0532	0.0087
2.16	2.17	0.25	0.5253	0.0141	-0.0006	0.0035	0.0491	0.0084
2.16	2.17	0.35	0.4261	0.0155	0.0122	0.0099	0.0418	0.0111
2.16	2.17	0.45	0.3744	0.0162	0.0304	0.0157	0.0430	0.0123
2.16	2.17	0.55	0.3768	0.0166	0.0402	0.0176	0.0476	0.0104
2.16	2.17	0.65	0.3730	0.0161	0.0534	0.0177	0.0573	0.0102
2.16	2.17	0.75	0.3011	0.0124	0.0523	0.0144	0.0548	0.0086
2.16	2.17	0.85	0.1757	0.0056	0.0049	0.0154	0.0140	0.0080

2.17	2.18	-0.84	0.3976	0.0282	-0.0334	0.0208	-0.1078	0.0067
2.17	2.18	-0.75	0.4370	0.0181	-0.0692	0.0115	-0.1395	0.0065
2.17	2.18	-0.65	0.4823	0.0188	-0.0858	0.0081	-0.1122	0.0083
2.17	2.18	-0.55	0.5172	0.0169	-0.0646	0.0106	-0.0605	0.0084
2.17	2.18	-0.45	0.5657	0.0158	-0.0361	0.0069	-0.0074	0.0054
2.17	2.18	-0.35	0.6182	0.0155	-0.0013	0.0076	0.0353	0.0032
2.17	2.18	-0.25	0.6477	0.0116	0.0291	0.0044	0.0574	0.0032
2.17	2.18	-0.15	0.6567	0.0097	0.0416	0.0057	0.0675	0.0045
2.17	2.18	-0.05	0.6492	0.0084	0.0395	0.0079	0.0732	0.0062
2.17	2.18	0.05	0.6226	0.0069	0.0296	0.0075	0.0753	0.0072
2.17	2.18	0.15	0.5788	0.0085	0.0144	0.0052	0.0722	0.0082
2.17	2.18	0.25	0.5192	0.0100	0.0023	0.0041	0.0620	0.0077
2.17	2.18	0.35	0.4497	0.0129	0.0226	0.0081	0.0532	0.0094
2.17	2.18	0.45	0.4073	0.0220	0.0632	0.0159	0.0610	0.0099
2.17	2.18	0.55	0.3858	0.0234	0.0780	0.0170	0.0653	0.0102
2.17	2.18	0.65	0.3435	0.0222	0.0811	0.0149	0.0524	0.0100
2.17	2.18	0.75	0.2769	0.0136	0.0736	0.0128	0.0352	0.0094
2.17	2.18	0.85	0.1798	0.0080	0.0186	0.0108	0.0246	0.0064
2.18	2.19	-0.84	0.4009	0.0184	-0.0959	0.0192	-0.1096	0.0081
2.18	2.19	-0.75	0.4459	0.0191	-0.0726	0.0106	-0.1396	0.0082
2.18	2.19	-0.65	0.4654	0.0182	-0.0884	0.0093	-0.1290	0.0068
2.18	2.19	-0.55	0.4934	0.0164	-0.0730	0.0123	-0.0775	0.0071
2.18	2.19	-0.45	0.5540	0.0162	-0.0278	0.0092	-0.0128	0.0049
2.18	2.19	-0.35	0.6115	0.0148	0.0077	0.0064	0.0323	0.0043
2.18	2.19	-0.25	0.6384	0.0090	0.0311	0.0037	0.0548	0.0059
2.18	2.19	-0.15	0.6436	0.0069	0.0420	0.0042	0.0642	0.0080
2.18	2.19	-0.05	0.6417	0.0069	0.0373	0.0041	0.0700	0.0065
2.18	2.19	0.05	0.6299	0.0055	0.0218	0.0064	0.0722	0.0052
2.18	2.19	0.15	0.5937	0.0070	0.0061	0.0066	0.0666	0.0054
2.18	2.19	0.25	0.5244	0.0051	0.0028	0.0050	0.0579	0.0070
2.18	2.19	0.35	0.4541	0.0088	0.0143	0.0066	0.0570	0.0065
2.18	2.19	0.45	0.4309	0.0163	0.0350	0.0124	0.0606	0.0058
2.18	2.19	0.55	0.4367	0.0219	0.0547	0.0131	0.0711	0.0064
2.18	2.19	0.65	0.3943	0.0207	0.0638	0.0103	0.0763	0.0080
2.18	2.19	0.75	0.2825	0.0164	0.0686	0.0100	0.0502	0.0087
2.18	2.19	0.85	0.1669	0.0091	0.0274	0.0133	0.0188	0.0092
2.18	2.19	0.91	0.1434	0.0159	-0.0308	0.0233	0.0120	0.0186
2.19	2.20	-0.84	0.4321	0.0188	-0.0791	0.0134	-0.0915	0.0137
2.19	2.20	-0.75	0.4574	0.0218	-0.0781	0.0072	-0.1337	0.0095
2.19	2.20	-0.65	0.4423	0.0190	-0.1054	0.0118	-0.1208	0.0067
2.19	2.20	-0.55	0.4737	0.0149	-0.0978	0.0151	-0.0697	0.0063
2.19	2.20	-0.45	0.5321	0.0140	-0.0301	0.0090	-0.0049	0.0059
2.19	2.20	-0.35	0.5893	0.0135	0.0188	0.0067	0.0389	0.0059
2.19	2.20	-0.25	0.6353	0.0086	0.0340	0.0050	0.0659	0.0078
2.19	2.20	-0.15	0.6534	0.0062	0.0376	0.0038	0.0831	0.0098
2.19	2.20	-0.05	0.6446	0.0060	0.0351	0.0038	0.0857	0.0075
2.19	2.20	0.05	0.6204	0.0061	0.0219	0.0070	0.0738	0.0050
2.19	2.20	0.15	0.5804	0.0069	0.0007	0.0083	0.0625	0.0067
2.19	2.20	0.25	0.5162	0.0073	-0.0083	0.0056	0.0676	0.0081
2.19	2.20	0.35	0.4578	0.0067	0.0185	0.0056	0.0715	0.0090
2.19	2.20	0.45	0.4417	0.0079	0.0555	0.0116	0.0637	0.0057
2.19	2.20	0.55	0.4220	0.0140	0.0712	0.0110	0.0708	0.0031
2.19	2.20	0.65	0.3716	0.0196	0.0808	0.0085	0.0701	0.0067
2.19	2.20	0.75	0.2987	0.0146	0.0827	0.0089	0.0354	0.0067
2.19	2.20	0.85	0.1877	0.0160	0.0418	0.0128	0.0209	0.0094
2.19	2.20	0.91	0.1337	0.0203	0.0101	0.0189	0.0482	0.0211
2.20	2.21	-0.84	0.4446	0.0205	-0.0919	0.0092	-0.1272	0.0150
2.20	2.21	-0.75	0.4971	0.0229	-0.0798	0.0106	-0.1517	0.0118
2.20	2.21	-0.65	0.4791	0.0201	-0.0896	0.0132	-0.1279	0.0069
2.20	2.21	-0.55	0.4752	0.0128	-0.0545	0.0157	-0.0802	0.0073
2.20	2.21	-0.45	0.5270	0.0132	-0.0198	0.0112	-0.0159	0.0081
2.20	2.21	-0.35	0.5818	0.0141	0.0063	0.0086	0.0293	0.0074
2.20	2.21	-0.25	0.6277	0.0084	0.0362	0.0084	0.0493	0.0075
2.20	2.21	-0.15	0.6581	0.0059	0.0501	0.0073	0.0625	0.0087
2.20	2.21	-0.05	0.6566	0.0052	0.0352	0.0050	0.0714	0.0083
2.20	2.21	0.05	0.6257	0.0048	0.0061	0.0076	0.0737	0.0074
2.20	2.21	0.15	0.5776	0.0085	-0.0132	0.0083	0.0742	0.0093
2.20	2.21	0.25	0.5132	0.0113	-0.0072	0.0054	0.0759	0.0112
2.20	2.21	0.35	0.4516	0.0109	0.0147	0.0059	0.0719	0.0121
2.20	2.21	0.45	0.4371	0.0094	0.0302	0.0131	0.0685	0.0088
2.20	2.21	0.55	0.4343	0.0148	0.0537	0.0109	0.0754	0.0061
2.20	2.21	0.65	0.4004	0.0183	0.0746	0.0076	0.0726	0.0058
2.20	2.21	0.75	0.3265	0.0156	0.0629	0.0082	0.0522	0.0063
2.20	2.21	0.85	0.1789	0.0155	0.0382	0.0079	0.0259	0.0106
2.20	2.21	0.91	0.0864	0.0278	0.0257	0.0133	-0.0056	0.0178
2.21	2.22	-0.84	0.4336	0.0202	-0.0747	0.0110	-0.1063	0.0144

2.21	2.22	-0.75	0.4366	0.0282	-0.0622	0.0117	-0.1278	0.0117
2.21	2.22	-0.65	0.4611	0.0223	-0.0787	0.0129	-0.1327	0.0073
2.21	2.22	-0.55	0.4896	0.0139	-0.0770	0.0129	-0.0843	0.0078
2.21	2.22	-0.45	0.5505	0.0145	-0.0326	0.0111	-0.0233	0.0086
2.21	2.22	-0.35	0.6139	0.0143	0.0232	0.0133	0.0249	0.0067
2.21	2.22	-0.25	0.6436	0.0092	0.0471	0.0142	0.0552	0.0061
2.21	2.22	-0.15	0.6520	0.0050	0.0440	0.0119	0.0738	0.0071
2.21	2.22	-0.05	0.6487	0.0042	0.0354	0.0079	0.0843	0.0074
2.21	2.22	0.05	0.6282	0.0040	0.0248	0.0084	0.0874	0.0071
2.21	2.22	0.15	0.5909	0.0084	0.0047	0.0090	0.0877	0.0091
2.21	2.22	0.25	0.5403	0.0152	-0.0135	0.0064	0.0920	0.0094
2.21	2.22	0.35	0.4804	0.0129	0.0145	0.0082	0.0957	0.0101
2.21	2.22	0.45	0.4478	0.0111	0.0648	0.0119	0.0858	0.0101
2.21	2.22	0.55	0.4525	0.0139	0.0740	0.0109	0.0704	0.0076
2.21	2.22	0.65	0.4266	0.0176	0.0730	0.0090	0.0604	0.0068
2.21	2.22	0.75	0.3151	0.0125	0.0820	0.0068	0.0479	0.0065
2.21	2.22	0.85	0.1916	0.0165	0.0486	0.0088	0.0185	0.0073
2.21	2.22	0.91	0.1505	0.0315	0.0076	0.0153	0.0084	0.0138
2.22	2.23	-0.84	0.4755	0.0222	-0.0903	0.0085	-0.1070	0.0145
2.22	2.23	-0.75	0.4813	0.0252	-0.0450	0.0108	-0.1294	0.0128
2.22	2.23	-0.65	0.5089	0.0218	-0.0660	0.0076	-0.1361	0.0073
2.22	2.23	-0.55	0.5025	0.0137	-0.0828	0.0071	-0.0962	0.0061
2.22	2.23	-0.45	0.5268	0.0141	-0.0461	0.0081	-0.0375	0.0068
2.22	2.23	-0.35	0.5843	0.0137	-0.0038	0.0129	0.0155	0.0054
2.22	2.23	-0.25	0.6300	0.0079	0.0135	0.0138	0.0501	0.0057
2.22	2.23	-0.15	0.6484	0.0044	0.0190	0.0118	0.0687	0.0078
2.22	2.23	-0.05	0.6474	0.0036	0.0231	0.0076	0.0764	0.0075
2.22	2.23	0.05	0.6295	0.0037	0.0170	0.0085	0.0750	0.0072
2.22	2.23	0.15	0.5921	0.0127	-0.0055	0.0090	0.0752	0.0080
2.22	2.23	0.25	0.5266	0.0187	-0.0190	0.0089	0.0876	0.0074
2.22	2.23	0.35	0.4542	0.0144	0.0209	0.0095	0.0976	0.0066
2.22	2.23	0.45	0.4451	0.0107	0.0679	0.0117	0.0905	0.0067
2.22	2.23	0.55	0.4700	0.0131	0.0738	0.0095	0.0847	0.0070
2.22	2.23	0.65	0.4383	0.0144	0.0789	0.0086	0.0758	0.0071
2.22	2.23	0.75	0.3305	0.0130	0.0779	0.0096	0.0457	0.0056
2.22	2.23	0.85	0.1648	0.0171	0.0396	0.0150	0.0079	0.0077
2.22	2.23	0.91	0.0747	0.0294	0.0174	0.0237	0.0190	0.0092
2.23	2.24	-0.84	0.4580	0.0173	-0.0779	0.0074	-0.1315	0.0118
2.23	2.24	-0.75	0.5011	0.0178	-0.0629	0.0092	-0.1571	0.0105
2.23	2.24	-0.65	0.4880	0.0171	-0.0685	0.0075	-0.1422	0.0061
2.23	2.24	-0.55	0.5081	0.0123	-0.0792	0.0055	-0.0990	0.0061
2.23	2.24	-0.45	0.5549	0.0159	-0.0398	0.0071	-0.0327	0.0050
2.23	2.24	-0.35	0.5994	0.0138	0.0077	0.0124	0.0182	0.0037
2.23	2.24	-0.25	0.6363	0.0074	0.0283	0.0115	0.0426	0.0047
2.23	2.24	-0.15	0.6554	0.0040	0.0326	0.0073	0.0545	0.0070
2.23	2.24	-0.05	0.6530	0.0037	0.0287	0.0070	0.0654	0.0066
2.23	2.24	0.05	0.6277	0.0067	0.0118	0.0089	0.0801	0.0064
2.23	2.24	0.15	0.5718	0.0144	-0.0181	0.0104	0.0939	0.0083
2.23	2.24	0.25	0.4946	0.0198	-0.0331	0.0104	0.0959	0.0087
2.23	2.24	0.35	0.4563	0.0149	0.0047	0.0133	0.0925	0.0065
2.23	2.24	0.45	0.4648	0.0082	0.0579	0.0123	0.0975	0.0056
2.23	2.24	0.55	0.4492	0.0120	0.0873	0.0101	0.0850	0.0067
2.23	2.24	0.65	0.4084	0.0165	0.1032	0.0091	0.0615	0.0063
2.23	2.24	0.75	0.3204	0.0163	0.0858	0.0077	0.0519	0.0075
2.23	2.24	0.85	0.1734	0.0158	0.0674	0.0166	0.0230	0.0083
2.23	2.24	0.91	0.1239	0.0233	0.0755	0.0297	0.0089	0.0102
2.24	2.25	-0.84	0.4830	0.0120	-0.0849	0.0068	-0.1347	0.0080
2.24	2.25	-0.75	0.5147	0.0159	-0.0418	0.0080	-0.1535	0.0058
2.24	2.25	-0.65	0.5243	0.0168	-0.0777	0.0119	-0.1420	0.0058
2.24	2.25	-0.55	0.5154	0.0139	-0.0743	0.0075	-0.0947	0.0096
2.24	2.25	-0.45	0.5231	0.0196	-0.0482	0.0090	-0.0316	0.0101
2.24	2.25	-0.35	0.5716	0.0169	-0.0193	0.0148	0.0176	0.0062
2.24	2.25	-0.25	0.6245	0.0080	0.0129	0.0119	0.0502	0.0051
2.24	2.25	-0.15	0.6548	0.0045	0.0266	0.0062	0.0663	0.0058
2.24	2.25	-0.05	0.6588	0.0062	0.0176	0.0068	0.0720	0.0060
2.24	2.25	0.05	0.6274	0.0075	-0.0007	0.0112	0.0811	0.0056
2.24	2.25	0.15	0.5529	0.0140	-0.0202	0.0111	0.0985	0.0068
2.24	2.25	0.25	0.4654	0.0171	-0.0356	0.0102	0.1120	0.0069
2.24	2.25	0.35	0.4420	0.0093	-0.0199	0.0122	0.1046	0.0065
2.24	2.25	0.45	0.4653	0.0062	0.0360	0.0100	0.0869	0.0062
2.24	2.25	0.55	0.4651	0.0086	0.0840	0.0080	0.0759	0.0065
2.24	2.25	0.65	0.4423	0.0166	0.0946	0.0065	0.0707	0.0064
2.24	2.25	0.75	0.3599	0.0176	0.0807	0.0070	0.0560	0.0070
2.24	2.25	0.85	0.1888	0.0136	0.0459	0.0183	0.0325	0.0090
2.24	2.25	0.91	0.0990	0.0170	0.0126	0.0284	0.0305	0.0097
2.25	2.26	-0.84	0.4940	0.0119	-0.0827	0.0074	-0.1366	0.0087

2.25	2.26	-0.75	0.5161	0.0155	-0.0427	0.0100	-0.1581	0.0057
2.25	2.26	-0.65	0.4923	0.0199	-0.0594	0.0113	-0.1504	0.0062
2.25	2.26	-0.55	0.5281	0.0164	-0.0604	0.0088	-0.1208	0.0117
2.25	2.26	-0.45	0.5759	0.0193	-0.0528	0.0083	-0.0513	0.0126
2.25	2.26	-0.35	0.6026	0.0163	-0.0350	0.0161	0.0101	0.0093
2.25	2.26	-0.25	0.6352	0.0106	0.0058	0.0128	0.0472	0.0064
2.25	2.26	-0.15	0.6569	0.0075	0.0303	0.0054	0.0688	0.0059
2.25	2.26	-0.05	0.6492	0.0099	0.0152	0.0053	0.0797	0.0060
2.25	2.26	0.05	0.6166	0.0134	-0.0191	0.0098	0.0889	0.0058
2.25	2.26	0.15	0.5633	0.0154	-0.0440	0.0117	0.1023	0.0048
2.25	2.26	0.25	0.4976	0.0161	-0.0414	0.0099	0.1091	0.0050
2.25	2.26	0.35	0.4621	0.0122	-0.0081	0.0098	0.0961	0.0056
2.25	2.26	0.45	0.4646	0.0049	0.0363	0.0070	0.0894	0.0064
2.25	2.26	0.55	0.4553	0.0087	0.0739	0.0054	0.0905	0.0068
2.25	2.26	0.65	0.4176	0.0159	0.0912	0.0056	0.0709	0.0062
2.25	2.26	0.75	0.3208	0.0150	0.0878	0.0089	0.0384	0.0076
2.25	2.26	0.85	0.1794	0.0115	0.0758	0.0177	0.0249	0.0092
2.25	2.26	0.91	0.1340	0.0148	0.0576	0.0253	0.0277	0.0138
2.26	2.27	-0.84	0.5001	0.0109	-0.0747	0.0123	-0.1151	0.0110
2.26	2.27	-0.75	0.5437	0.0136	-0.0489	0.0103	-0.1494	0.0075
2.26	2.27	-0.65	0.5468	0.0177	-0.0332	0.0107	-0.1477	0.0039
2.26	2.27	-0.55	0.5206	0.0175	-0.0615	0.0057	-0.1237	0.0080
2.26	2.27	-0.45	0.5436	0.0168	-0.0480	0.0062	-0.0671	0.0095
2.26	2.27	-0.35	0.6103	0.0127	0.0059	0.0147	-0.0024	0.0078
2.26	2.27	-0.25	0.6431	0.0094	0.0343	0.0132	0.0400	0.0092
2.26	2.27	-0.15	0.6452	0.0084	0.0309	0.0064	0.0631	0.0082
2.26	2.27	-0.05	0.6326	0.0105	0.0120	0.0054	0.0815	0.0071
2.26	2.27	0.05	0.5960	0.0142	-0.0138	0.0083	0.0985	0.0065
2.26	2.27	0.15	0.5304	0.0159	-0.0421	0.0104	0.1066	0.0045
2.26	2.27	0.25	0.4696	0.0155	-0.0574	0.0121	0.1057	0.0035
2.26	2.27	0.35	0.4576	0.0170	-0.0310	0.0095	0.1082	0.0048
2.26	2.27	0.45	0.4635	0.0122	0.0331	0.0053	0.0988	0.0064
2.26	2.27	0.55	0.4666	0.0103	0.0882	0.0067	0.0735	0.0064
2.26	2.27	0.65	0.4489	0.0121	0.0976	0.0069	0.0663	0.0059
2.26	2.27	0.75	0.3383	0.0117	0.0923	0.0072	0.0564	0.0085
2.26	2.27	0.85	0.1742	0.0099	0.0968	0.0115	0.0191	0.0130
2.26	2.27	0.91	0.1181	0.0140	0.0715	0.0149	0.0100	0.0166
2.27	2.28	-0.84	0.5018	0.0089	-0.1069	0.0171	-0.1055	0.0121
2.27	2.28	-0.75	0.5462	0.0087	-0.0560	0.0116	-0.1596	0.0078
2.27	2.28	-0.65	0.5397	0.0166	-0.0519	0.0098	-0.1501	0.0060
2.27	2.28	-0.55	0.5427	0.0159	-0.0591	0.0065	-0.1113	0.0062
2.27	2.28	-0.45	0.5640	0.0180	-0.0448	0.0062	-0.0553	0.0075
2.27	2.28	-0.35	0.5945	0.0142	-0.0126	0.0118	-0.0066	0.0072
2.27	2.28	-0.25	0.6219	0.0100	0.0156	0.0116	0.0278	0.0098
2.27	2.28	-0.15	0.6425	0.0092	0.0238	0.0072	0.0516	0.0108
2.27	2.28	-0.05	0.6484	0.0107	0.0057	0.0064	0.0702	0.0081
2.27	2.28	0.05	0.6238	0.0133	-0.0297	0.0075	0.0868	0.0061
2.27	2.28	0.15	0.5558	0.0126	-0.0604	0.0121	0.0993	0.0052
2.27	2.28	0.25	0.4641	0.0161	-0.0571	0.0137	0.1038	0.0043
2.27	2.28	0.35	0.4228	0.0184	-0.0133	0.0104	0.1019	0.0045
2.27	2.28	0.45	0.4527	0.0151	0.0367	0.0080	0.0957	0.0061
2.27	2.28	0.55	0.4796	0.0093	0.0767	0.0095	0.0840	0.0071
2.27	2.28	0.65	0.4549	0.0075	0.1021	0.0099	0.0732	0.0068
2.27	2.28	0.75	0.3300	0.0073	0.0998	0.0087	0.0519	0.0079
2.27	2.28	0.85	0.1695	0.0114	0.0918	0.0069	0.0001	0.0109
2.27	2.28	0.91	0.1509	0.0194	0.0823	0.0115	-0.0231	0.0153
2.28	2.29	-0.84	0.5253	0.0147	-0.0696	0.0163	-0.1268	0.0120
2.28	2.29	-0.75	0.5452	0.0122	-0.0354	0.0127	-0.1388	0.0110
2.28	2.29	-0.65	0.5417	0.0161	-0.0474	0.0126	-0.1465	0.0073
2.28	2.29	-0.55	0.5678	0.0187	-0.0571	0.0121	-0.1256	0.0098
2.28	2.29	-0.45	0.5876	0.0180	-0.0496	0.0092	-0.0562	0.0087
2.28	2.29	-0.35	0.6063	0.0149	-0.0216	0.0109	-0.0064	0.0071
2.28	2.29	-0.25	0.6406	0.0116	0.0111	0.0098	0.0127	0.0093
2.28	2.29	-0.15	0.6575	0.0109	0.0186	0.0072	0.0359	0.0086
2.28	2.29	-0.05	0.6427	0.0120	-0.0026	0.0042	0.0633	0.0052
2.28	2.29	0.05	0.6056	0.0144	-0.0300	0.0068	0.0837	0.0053
2.28	2.29	0.15	0.5471	0.0168	-0.0387	0.0102	0.0950	0.0065
2.28	2.29	0.25	0.4635	0.0150	-0.0258	0.0128	0.1018	0.0060
2.28	2.29	0.35	0.4017	0.0179	-0.0055	0.0102	0.1002	0.0058
2.28	2.29	0.45	0.4252	0.0153	0.0391	0.0089	0.0866	0.0067
2.28	2.29	0.55	0.4737	0.0113	0.0989	0.0107	0.0736	0.0082
2.28	2.29	0.65	0.4507	0.0060	0.1202	0.0127	0.0625	0.0087
2.28	2.29	0.75	0.3393	0.0102	0.1075	0.0111	0.0441	0.0082
2.28	2.29	0.85	0.1926	0.0174	0.0933	0.0119	0.0166	0.0084
2.28	2.29	0.91	0.1253	0.0222	0.0749	0.0163	-0.0090	0.0161
2.29	2.30	-0.84	0.4941	0.0202	-0.0726	0.0172	-0.1086	0.0172

2.29	2.30	-0.75	0.5593	0.0138	-0.0393	0.0127	-0.1503	0.0125
2.29	2.30	-0.65	0.5838	0.0143	-0.0277	0.0130	-0.1338	0.0097
2.29	2.30	-0.55	0.5796	0.0129	-0.0286	0.0153	-0.1117	0.0106
2.29	2.30	-0.45	0.6027	0.0112	-0.0333	0.0111	-0.0778	0.0101
2.29	2.30	-0.35	0.6354	0.0112	-0.0025	0.0105	-0.0148	0.0067
2.29	2.30	-0.25	0.6424	0.0111	0.0317	0.0101	0.0307	0.0083
2.29	2.30	-0.15	0.6369	0.0087	0.0306	0.0072	0.0502	0.0076
2.29	2.30	-0.05	0.6220	0.0107	0.0022	0.0052	0.0645	0.0046
2.29	2.30	0.05	0.5897	0.0135	-0.0317	0.0061	0.0852	0.0061
2.29	2.30	0.15	0.5262	0.0172	-0.0549	0.0109	0.1084	0.0095
2.29	2.30	0.25	0.4323	0.0144	-0.0487	0.0100	0.1142	0.0089
2.29	2.30	0.35	0.3841	0.0144	-0.0025	0.0080	0.0943	0.0059
2.29	2.30	0.45	0.4305	0.0173	0.0565	0.0067	0.0774	0.0050
2.29	2.30	0.55	0.4842	0.0175	0.1028	0.0082	0.0658	0.0060
2.29	2.30	0.65	0.4492	0.0145	0.1287	0.0092	0.0479	0.0079
2.29	2.30	0.75	0.3248	0.0146	0.1296	0.0109	0.0359	0.0063
2.29	2.30	0.85	0.1580	0.0162	0.0791	0.0123	0.0077	0.0118
2.29	2.30	0.91	0.0875	0.0233	0.0351	0.0172	-0.0242	0.0190
2.30	2.31	-0.84	0.4868	0.0228	-0.0482	0.0211	-0.0965	0.0222
2.30	2.31	-0.75	0.5658	0.0113	-0.0519	0.0180	-0.1222	0.0134
2.30	2.31	-0.65	0.5860	0.0091	-0.0502	0.0145	-0.1468	0.0096
2.30	2.31	-0.55	0.5779	0.0079	-0.0666	0.0144	-0.1354	0.0090
2.30	2.31	-0.45	0.5884	0.0090	-0.0451	0.0109	-0.0725	0.0088
2.30	2.31	-0.35	0.6206	0.0092	-0.0005	0.0111	-0.0178	0.0061
2.30	2.31	-0.25	0.6474	0.0101	0.0203	0.0106	0.0156	0.0063
2.30	2.31	-0.15	0.6518	0.0098	0.0138	0.0066	0.0410	0.0066
2.30	2.31	-0.05	0.6318	0.0074	-0.0012	0.0045	0.0594	0.0050
2.30	2.31	0.05	0.5832	0.0111	-0.0165	0.0078	0.0728	0.0072
2.30	2.31	0.15	0.5053	0.0122	-0.0346	0.0103	0.0849	0.0093
2.30	2.31	0.25	0.4286	0.0146	-0.0465	0.0079	0.0935	0.0084
2.30	2.31	0.35	0.3971	0.0115	-0.0130	0.0068	0.0905	0.0057
2.30	2.31	0.45	0.3978	0.0147	0.0592	0.0053	0.0791	0.0046
2.30	2.31	0.55	0.4326	0.0194	0.1062	0.0052	0.0709	0.0046
2.30	2.31	0.65	0.4698	0.0167	0.1116	0.0079	0.0614	0.0056
2.30	2.31	0.75	0.3603	0.0141	0.1160	0.0099	0.0323	0.0061
2.30	2.31	0.85	0.1672	0.0132	0.0785	0.0103	0.0210	0.0103
2.30	2.31	0.91	0.1261	0.0167	0.0243	0.0183	0.0355	0.0225
2.31	2.32	-0.84	0.5484	0.0212	-0.1002	0.0244	-0.1500	0.0256
2.31	2.32	-0.75	0.5698	0.0108	-0.0755	0.0213	-0.1265	0.0113
2.31	2.32	-0.65	0.5927	0.0070	-0.0340	0.0137	-0.1371	0.0053
2.31	2.32	-0.55	0.5684	0.0132	-0.0466	0.0113	-0.1364	0.0085
2.31	2.32	-0.45	0.5966	0.0097	-0.0325	0.0091	-0.0896	0.0062
2.31	2.32	-0.35	0.6213	0.0081	0.0203	0.0125	-0.0156	0.0065
2.31	2.32	-0.25	0.6189	0.0118	0.0386	0.0105	0.0150	0.0054
2.31	2.32	-0.15	0.6379	0.0088	0.0219	0.0068	0.0312	0.0045
2.31	2.32	-0.05	0.6357	0.0080	-0.0025	0.0048	0.0621	0.0039
2.31	2.32	0.05	0.5740	0.0094	-0.0225	0.0080	0.0866	0.0054
2.31	2.32	0.15	0.4880	0.0135	-0.0352	0.0112	0.0924	0.0060
2.31	2.32	0.25	0.4232	0.0155	-0.0388	0.0103	0.1002	0.0068
2.31	2.32	0.35	0.3867	0.0151	-0.0064	0.0089	0.1012	0.0073
2.31	2.32	0.45	0.4023	0.0118	0.0616	0.0065	0.0747	0.0052
2.31	2.32	0.55	0.4559	0.0136	0.1100	0.0058	0.0629	0.0046
2.31	2.32	0.65	0.4457	0.0118	0.1258	0.0095	0.0637	0.0067
2.31	2.32	0.75	0.3332	0.0106	0.1374	0.0109	0.0373	0.0053
2.31	2.32	0.85	0.1686	0.0108	0.0920	0.0175	0.0120	0.0088
2.31	2.32	0.91	0.0920	0.0139	0.0190	0.0209	0.0035	0.0158
2.32	2.33	-0.84	0.5311	0.0260	-0.0640	0.0188	-0.0977	0.0244
2.32	2.33	-0.75	0.5655	0.0096	-0.0253	0.0202	-0.1208	0.0118
2.32	2.33	-0.65	0.5841	0.0112	-0.0288	0.0124	-0.1403	0.0078
2.32	2.33	-0.55	0.5984	0.0144	-0.0390	0.0072	-0.1295	0.0072
2.32	2.33	-0.45	0.6175	0.0122	-0.0317	0.0076	-0.0826	0.0091
2.32	2.33	-0.35	0.6202	0.0079	-0.0081	0.0112	-0.0258	0.0081
2.32	2.33	-0.25	0.6237	0.0126	0.0144	0.0107	0.0119	0.0080
2.32	2.33	-0.15	0.6387	0.0124	0.0193	0.0078	0.0355	0.0052
2.32	2.33	-0.05	0.6379	0.0114	0.0008	0.0067	0.0571	0.0034
2.32	2.33	0.05	0.5935	0.0136	-0.0339	0.0094	0.0782	0.0052
2.32	2.33	0.15	0.4958	0.0151	-0.0632	0.0122	0.0934	0.0056
2.32	2.33	0.25	0.3855	0.0185	-0.0472	0.0108	0.0976	0.0080
2.32	2.33	0.35	0.3595	0.0155	0.0167	0.0090	0.0948	0.0102
2.32	2.33	0.45	0.4089	0.0087	0.0672	0.0077	0.0873	0.0084
2.32	2.33	0.55	0.4543	0.0077	0.0961	0.0079	0.0697	0.0057
2.32	2.33	0.65	0.4438	0.0064	0.1207	0.0098	0.0543	0.0060
2.32	2.33	0.75	0.3336	0.0086	0.1304	0.0122	0.0452	0.0066
2.32	2.33	0.85	0.1631	0.0087	0.1114	0.0209	0.0118	0.0052
2.32	2.33	0.91	0.1182	0.0132	0.0744	0.0284	-0.0071	0.0089
2.33	2.34	-0.84	0.5647	0.0296	-0.0690	0.0191	-0.0698	0.0249

2.33	2.34	-0.75	0.5841	0.0180	-0.0469	0.0187	-0.1214	0.0101
2.33	2.34	-0.65	0.6003	0.0106	-0.0416	0.0138	-0.1251	0.0074
2.33	2.34	-0.55	0.6189	0.0157	-0.0474	0.0093	-0.1141	0.0088
2.33	2.34	-0.45	0.6084	0.0100	-0.0290	0.0077	-0.0905	0.0071
2.33	2.34	-0.35	0.6225	0.0106	0.0159	0.0094	-0.0455	0.0112
2.33	2.34	-0.25	0.6560	0.0148	0.0269	0.0083	0.0040	0.0104
2.33	2.34	-0.15	0.6548	0.0129	0.0081	0.0087	0.0387	0.0080
2.33	2.34	-0.05	0.6155	0.0128	-0.0126	0.0102	0.0597	0.0058
2.33	2.34	0.05	0.5582	0.0171	-0.0292	0.0104	0.0767	0.0065
2.33	2.34	0.15	0.4824	0.0173	-0.0417	0.0111	0.0879	0.0068
2.33	2.34	0.25	0.3876	0.0192	-0.0279	0.0087	0.0820	0.0080
2.33	2.34	0.35	0.3478	0.0139	0.0210	0.0082	0.0711	0.0095
2.33	2.34	0.45	0.4064	0.0087	0.0620	0.0068	0.0741	0.0069
2.33	2.34	0.55	0.4711	0.0078	0.1025	0.0092	0.0674	0.0049
2.33	2.34	0.65	0.4492	0.0058	0.1456	0.0095	0.0456	0.0054
2.33	2.34	0.75	0.3363	0.0096	0.1193	0.0141	0.0309	0.0054
2.33	2.34	0.85	0.1860	0.0092	0.0676	0.0199	0.0064	0.0065
2.33	2.34	0.91	0.0992	0.0165	0.0581	0.0282	-0.0052	0.0069
2.34	2.35	-0.84	0.4745	0.0349	-0.0711	0.0216	-0.1157	0.0233
2.34	2.35	-0.75	0.5842	0.0216	0.0020	0.0233	-0.1135	0.0123
2.34	2.35	-0.65	0.5896	0.0150	-0.0127	0.0144	-0.1180	0.0086
2.34	2.35	-0.55	0.5955	0.0175	-0.0296	0.0087	-0.1158	0.0085
2.34	2.35	-0.45	0.6259	0.0136	-0.0157	0.0064	-0.0786	0.0084
2.34	2.35	-0.35	0.6334	0.0150	0.0064	0.0071	-0.0392	0.0114
2.34	2.35	-0.25	0.6306	0.0147	0.0217	0.0069	-0.0144	0.0113
2.34	2.35	-0.15	0.6312	0.0120	0.0241	0.0075	0.0215	0.0096
2.34	2.35	-0.05	0.6116	0.0085	0.0107	0.0094	0.0629	0.0094
2.34	2.35	0.05	0.5538	0.0119	-0.0130	0.0078	0.0913	0.0106
2.34	2.35	0.15	0.4542	0.0151	-0.0349	0.0087	0.0981	0.0093
2.34	2.35	0.25	0.3499	0.0166	-0.0315	0.0083	0.0874	0.0071
2.34	2.35	0.35	0.3325	0.0121	0.0185	0.0063	0.0755	0.0055
2.34	2.35	0.45	0.3981	0.0097	0.0805	0.0082	0.0710	0.0050
2.34	2.35	0.55	0.4521	0.0089	0.1143	0.0085	0.0620	0.0034
2.34	2.35	0.65	0.4512	0.0070	0.1316	0.0114	0.0440	0.0036
2.34	2.35	0.75	0.3535	0.0107	0.1271	0.0111	0.0356	0.0057
2.34	2.35	0.85	0.1869	0.0125	0.0581	0.0198	0.0160	0.0080
2.34	2.35	0.91	0.1085	0.0169	0.0117	0.0224	-0.0139	0.0113
2.35	2.36	-0.84	0.5176	0.0292	-0.1195	0.0226	-0.0560	0.0259
2.35	2.36	-0.75	0.6109	0.0224	-0.0371	0.0177	-0.1302	0.0156
2.35	2.36	-0.65	0.6152	0.0202	-0.0228	0.0116	-0.1162	0.0115
2.35	2.36	-0.55	0.6426	0.0200	-0.0300	0.0049	-0.1035	0.0127
2.35	2.36	-0.45	0.6281	0.0154	-0.0169	0.0042	-0.0900	0.0127
2.35	2.36	-0.35	0.5961	0.0145	0.0099	0.0061	-0.0612	0.0120
2.35	2.36	-0.25	0.6223	0.0130	0.0268	0.0064	-0.0227	0.0103
2.35	2.36	-0.15	0.6441	0.0105	0.0270	0.0072	0.0187	0.0100
2.35	2.36	-0.05	0.6083	0.0067	0.0103	0.0065	0.0510	0.0118
2.35	2.36	0.05	0.5382	0.0075	-0.0146	0.0053	0.0697	0.0137
2.35	2.36	0.15	0.4576	0.0121	-0.0324	0.0072	0.0783	0.0122
2.35	2.36	0.25	0.3705	0.0146	-0.0186	0.0097	0.0786	0.0098
2.35	2.36	0.35	0.3310	0.0112	0.0270	0.0087	0.0742	0.0077
2.35	2.36	0.45	0.3855	0.0106	0.0657	0.0097	0.0739	0.0067
2.35	2.36	0.55	0.4656	0.0110	0.1001	0.0098	0.0671	0.0067
2.35	2.36	0.65	0.4496	0.0095	0.1408	0.0137	0.0440	0.0063
2.35	2.36	0.75	0.3175	0.0135	0.1478	0.0171	0.0334	0.0074
2.35	2.36	0.85	0.1864	0.0111	0.0800	0.0167	0.0312	0.0098
2.35	2.36	0.91	0.1543	0.0224	0.0276	0.0211	0.0109	0.0113
2.36	2.37	-0.84	0.5403	0.0329	-0.1207	0.0142	-0.0974	0.0214
2.36	2.37	-0.75	0.5633	0.0191	-0.0373	0.0107	-0.1052	0.0140
2.36	2.37	-0.65	0.5901	0.0227	-0.0094	0.0080	-0.0966	0.0134
2.36	2.37	-0.55	0.5952	0.0235	-0.0252	0.0061	-0.0838	0.0157
2.36	2.37	-0.45	0.6170	0.0147	-0.0180	0.0056	-0.0678	0.0147
2.36	2.37	-0.35	0.6289	0.0145	0.0219	0.0089	-0.0321	0.0127
2.36	2.37	-0.25	0.6144	0.0115	0.0416	0.0104	-0.0085	0.0090
2.36	2.37	-0.15	0.6141	0.0105	0.0294	0.0092	0.0066	0.0076
2.36	2.37	-0.05	0.6067	0.0073	0.0053	0.0088	0.0309	0.0090
2.36	2.37	0.05	0.5510	0.0076	-0.0149	0.0063	0.0556	0.0092
2.36	2.37	0.15	0.4400	0.0107	-0.0194	0.0068	0.0663	0.0089
2.36	2.37	0.25	0.3347	0.0129	-0.0012	0.0078	0.0656	0.0100
2.36	2.37	0.35	0.3174	0.0135	0.0361	0.0070	0.0636	0.0092
2.36	2.37	0.45	0.3715	0.0091	0.0843	0.0089	0.0570	0.0079
2.36	2.37	0.55	0.4400	0.0125	0.1158	0.0102	0.0525	0.0073
2.36	2.37	0.65	0.4545	0.0122	0.1115	0.0162	0.0543	0.0107
2.36	2.37	0.75	0.3617	0.0137	0.1138	0.0147	0.0434	0.0119
2.36	2.37	0.85	0.1885	0.0143	0.1005	0.0156	0.0240	0.0092
2.36	2.37	0.91	0.1024	0.0169	0.0560	0.0159	0.0149	0.0125
2.37	2.38	-0.84	0.5447	0.0360	-0.1011	0.0102	-0.1118	0.0138

2.37	2.38	-0.75	0.5738	0.0243	-0.0453	0.0097	-0.1054	0.0096
2.37	2.38	-0.65	0.6351	0.0193	-0.0309	0.0114	-0.1184	0.0104
2.37	2.38	-0.55	0.6468	0.0199	-0.0324	0.0125	-0.1190	0.0154
2.37	2.38	-0.45	0.6026	0.0144	-0.0143	0.0132	-0.0953	0.0141
2.37	2.38	-0.35	0.5962	0.0134	0.0148	0.0161	-0.0538	0.0122
2.37	2.38	-0.25	0.6204	0.0120	0.0379	0.0153	-0.0208	0.0061
2.37	2.38	-0.15	0.6254	0.0123	0.0452	0.0120	0.0041	0.0071
2.37	2.38	-0.05	0.6009	0.0089	0.0287	0.0099	0.0332	0.0056
2.37	2.38	0.05	0.5415	0.0098	-0.0056	0.0074	0.0616	0.0059
2.37	2.38	0.15	0.4421	0.0112	-0.0276	0.0047	0.0705	0.0080
2.37	2.38	0.25	0.3434	0.0170	-0.0042	0.0052	0.0571	0.0103
2.37	2.38	0.35	0.3214	0.0136	0.0359	0.0040	0.0552	0.0096
2.37	2.38	0.45	0.3712	0.0105	0.0641	0.0069	0.0643	0.0054
2.37	2.38	0.55	0.4345	0.0129	0.1117	0.0087	0.0544	0.0077
2.37	2.38	0.65	0.4394	0.0125	0.1516	0.0122	0.0308	0.0108
2.37	2.38	0.75	0.3432	0.0187	0.1261	0.0122	0.0124	0.0137
2.37	2.38	0.85	0.1846	0.0117	0.0804	0.0107	0.0155	0.0110
2.37	2.38	0.91	0.0999	0.0152	0.0590	0.0135	0.0287	0.0121
2.38	2.39	-0.84	0.4411	0.0456	-0.1255	0.0118	-0.0881	0.0089
2.38	2.39	-0.75	0.5823	0.0196	-0.0395	0.0120	-0.1085	0.0081
2.38	2.39	-0.65	0.6062	0.0122	-0.0052	0.0129	-0.1019	0.0094
2.38	2.39	-0.55	0.6170	0.0151	-0.0101	0.0175	-0.0937	0.0119
2.38	2.39	-0.45	0.6099	0.0112	0.0100	0.0151	-0.0714	0.0121
2.38	2.39	-0.35	0.6146	0.0124	0.0539	0.0182	-0.0423	0.0100
2.38	2.39	-0.25	0.6365	0.0128	0.0708	0.0135	-0.0219	0.0076
2.38	2.39	-0.15	0.6421	0.0129	0.0562	0.0088	-0.0006	0.0077
2.38	2.39	-0.05	0.6176	0.0123	0.0274	0.0087	0.0270	0.0083
2.38	2.39	0.05	0.5605	0.0139	-0.0031	0.0073	0.0547	0.0086
2.38	2.39	0.15	0.4573	0.0169	-0.0208	0.0074	0.0750	0.0109
2.38	2.39	0.25	0.3211	0.0168	-0.0066	0.0050	0.0821	0.0119
2.38	2.39	0.35	0.2755	0.0161	0.0363	0.0072	0.0759	0.0090
2.38	2.39	0.45	0.3719	0.0101	0.0767	0.0093	0.0648	0.0068
2.38	2.39	0.55	0.4670	0.0142	0.1119	0.0087	0.0531	0.0081
2.38	2.39	0.65	0.4629	0.0181	0.1320	0.0095	0.0475	0.0125
2.38	2.39	0.75	0.3690	0.0200	0.1148	0.0079	0.0458	0.0123
2.38	2.39	0.85	0.2135	0.0179	0.0970	0.0111	0.0146	0.0102
2.38	2.39	0.91	0.1123	0.0108	0.0782	0.0132	-0.0051	0.0131
2.39	2.40	-0.84	0.5498	0.0417	-0.1082	0.0114	-0.0931	0.0091
2.39	2.40	-0.75	0.5716	0.0204	-0.0204	0.0115	-0.0926	0.0071
2.39	2.40	-0.65	0.6088	0.0066	0.0000	0.0137	-0.1066	0.0072
2.39	2.40	-0.55	0.6282	0.0090	0.0047	0.0147	-0.0923	0.0070
2.39	2.40	-0.45	0.6217	0.0102	0.0181	0.0152	-0.0801	0.0087
2.39	2.40	-0.35	0.6218	0.0111	0.0458	0.0121	-0.0672	0.0081
2.39	2.40	-0.25	0.6483	0.0127	0.0569	0.0104	-0.0208	0.0085
2.39	2.40	-0.15	0.6500	0.0146	0.0505	0.0069	0.0245	0.0102
2.39	2.40	-0.05	0.6067	0.0151	0.0357	0.0095	0.0402	0.0086
2.39	2.40	0.05	0.5316	0.0191	0.0093	0.0125	0.0399	0.0081
2.39	2.40	0.15	0.4253	0.0163	-0.0240	0.0101	0.0503	0.0109
2.39	2.40	0.25	0.3030	0.0159	-0.0218	0.0123	0.0629	0.0109
2.39	2.40	0.35	0.2852	0.0120	0.0391	0.0119	0.0611	0.0086
2.39	2.40	0.45	0.3732	0.0120	0.0851	0.0157	0.0693	0.0060
2.39	2.40	0.55	0.4363	0.0149	0.1067	0.0130	0.0765	0.0108
2.39	2.40	0.65	0.4458	0.0200	0.1337	0.0100	0.0507	0.0105
2.39	2.40	0.75	0.4044	0.0226	0.1168	0.0081	0.0325	0.0090
2.39	2.40	0.85	0.2255	0.0171	0.0728	0.0104	0.0260	0.0086
2.39	2.40	0.92	0.0974	0.0122	0.0514	0.0201	0.0129	0.0123
2.40	2.41	-0.84	0.4674	0.0432	-0.1153	0.0130	-0.0929	0.0139
2.40	2.41	-0.75	0.5786	0.0229	-0.0474	0.0185	-0.1088	0.0109
2.40	2.41	-0.65	0.6084	0.0108	-0.0025	0.0154	-0.1087	0.0073
2.40	2.41	-0.55	0.6106	0.0096	0.0372	0.0200	-0.0829	0.0075
2.40	2.41	-0.45	0.6005	0.0169	0.0144	0.0140	-0.0686	0.0052
2.40	2.41	-0.35	0.6044	0.0113	0.0228	0.0127	-0.0646	0.0095
2.40	2.41	-0.25	0.6230	0.0116	0.0631	0.0087	-0.0146	0.0082
2.40	2.41	-0.15	0.6201	0.0142	0.0483	0.0087	0.0238	0.0114
2.40	2.41	-0.05	0.5842	0.0134	0.0116	0.0110	0.0280	0.0085
2.40	2.41	0.05	0.5202	0.0159	-0.0192	0.0140	0.0407	0.0051
2.40	2.41	0.15	0.4103	0.0158	-0.0429	0.0145	0.0703	0.0078
2.40	2.41	0.25	0.2970	0.0118	-0.0111	0.0134	0.0772	0.0094
2.40	2.41	0.35	0.2942	0.0116	0.0617	0.0150	0.0634	0.0084
2.40	2.41	0.45	0.3615	0.0121	0.1169	0.0176	0.0636	0.0073
2.40	2.41	0.55	0.4238	0.0192	0.1384	0.0147	0.0544	0.0092
2.40	2.41	0.65	0.4810	0.0212	0.1197	0.0113	0.0322	0.0091
2.40	2.41	0.75	0.4125	0.0250	0.1100	0.0103	0.0281	0.0069
2.40	2.41	0.85	0.1974	0.0175	0.0903	0.0161	0.0181	0.0088
2.40	2.41	0.92	0.1088	0.0183	0.0551	0.0248	0.0180	0.0162
2.41	2.42	-0.84	0.4852	0.0426	-0.1291	0.0168	-0.0722	0.0180

2.41	2.42	-0.75	0.5182	0.0288	-0.0583	0.0256	-0.0862	0.0126
2.41	2.42	-0.65	0.6108	0.0138	-0.0209	0.0227	-0.0929	0.0111
2.41	2.42	-0.55	0.6206	0.0174	-0.0098	0.0200	-0.0891	0.0084
2.41	2.42	-0.45	0.5984	0.0268	0.0419	0.0147	-0.0712	0.0099
2.41	2.42	-0.35	0.6228	0.0158	0.0442	0.0103	-0.0584	0.0091
2.41	2.42	-0.25	0.6355	0.0101	0.0471	0.0093	-0.0344	0.0113
2.41	2.42	-0.15	0.6369	0.0106	0.0395	0.0109	0.0034	0.0117
2.41	2.42	-0.05	0.5821	0.0121	0.0286	0.0107	0.0298	0.0103
2.41	2.42	0.05	0.4941	0.0137	0.0082	0.0115	0.0401	0.0057
2.41	2.42	0.15	0.4116	0.0159	-0.0174	0.0140	0.0604	0.0069
2.41	2.42	0.25	0.3225	0.0146	0.0140	0.0135	0.0826	0.0077
2.41	2.42	0.35	0.2796	0.0111	0.0673	0.0144	0.0818	0.0074
2.41	2.42	0.45	0.3329	0.0152	0.1002	0.0147	0.0653	0.0064
2.41	2.42	0.55	0.4435	0.0159	0.1161	0.0133	0.0480	0.0075
2.41	2.42	0.65	0.4945	0.0251	0.1122	0.0135	0.0376	0.0061
2.41	2.42	0.75	0.3618	0.0191	0.1311	0.0129	0.0259	0.0056
2.41	2.42	0.85	0.1877	0.0190	0.0758	0.0189	0.0070	0.0129
2.41	2.42	0.92	0.0721	0.0201	-0.0154	0.0274	-0.0091	0.0214
2.42	2.43	-0.84	0.5433	0.0384	-0.1414	0.0157	-0.0357	0.0146
2.42	2.43	-0.75	0.5614	0.0274	0.0111	0.0271	-0.0867	0.0133
2.42	2.43	-0.65	0.5935	0.0161	0.0177	0.0222	-0.0977	0.0102
2.42	2.43	-0.55	0.6423	0.0265	-0.0030	0.0187	-0.1062	0.0148
2.42	2.43	-0.45	0.6720	0.0335	0.0302	0.0099	-0.0624	0.0132
2.42	2.43	-0.35	0.6260	0.0169	0.0414	0.0072	-0.0836	0.0119
2.42	2.43	-0.25	0.6355	0.0088	0.0457	0.0081	-0.0302	0.0095
2.42	2.43	-0.15	0.6487	0.0120	0.0229	0.0115	-0.0029	0.0097
2.42	2.43	-0.05	0.5864	0.0113	0.0176	0.0085	0.0014	0.0114
2.42	2.43	0.05	0.4868	0.0177	-0.0036	0.0090	0.0408	0.0084
2.42	2.43	0.15	0.3861	0.0183	-0.0272	0.0131	0.0684	0.0092
2.42	2.43	0.25	0.2891	0.0138	0.0062	0.0130	0.0713	0.0078
2.42	2.43	0.35	0.2887	0.0111	0.0443	0.0112	0.0698	0.0084
2.42	2.43	0.45	0.3600	0.0102	0.0773	0.0112	0.0572	0.0077
2.42	2.43	0.55	0.4599	0.0174	0.1142	0.0107	0.0587	0.0056
2.42	2.43	0.65	0.4445	0.0143	0.1340	0.0112	0.0473	0.0057
2.42	2.43	0.75	0.3590	0.0156	0.0976	0.0181	0.0226	0.0067
2.42	2.43	0.85	0.2029	0.0116	0.0885	0.0206	-0.0034	0.0144
2.42	2.43	0.92	0.1250	0.0207	0.0277	0.0366	0.0483	0.0227
2.43	2.44	-0.84	0.5974	0.0286	-0.1330	0.0126	-0.0544	0.0196
2.43	2.44	-0.75	0.5776	0.0191	-0.0546	0.0217	-0.0839	0.0129
2.43	2.44	-0.65	0.6140	0.0201	0.0067	0.0221	-0.0713	0.0170
2.43	2.44	-0.55	0.6298	0.0338	0.0231	0.0151	-0.0824	0.0166
2.43	2.44	-0.45	0.5730	0.0323	0.0443	0.0109	-0.0894	0.0183
2.43	2.44	-0.35	0.6112	0.0167	0.0370	0.0070	-0.0670	0.0114
2.43	2.44	-0.25	0.6271	0.0102	0.0537	0.0096	-0.0474	0.0074
2.43	2.44	-0.15	0.6206	0.0117	0.0576	0.0118	-0.0092	0.0074
2.43	2.44	-0.05	0.6062	0.0148	0.0213	0.0095	0.0224	0.0109
2.43	2.44	0.05	0.5161	0.0163	-0.0015	0.0111	0.0292	0.0084
2.43	2.44	0.15	0.3684	0.0191	0.0067	0.0138	0.0428	0.0096
2.43	2.44	0.25	0.2859	0.0135	0.0282	0.0108	0.0671	0.0080
2.43	2.44	0.35	0.2747	0.0084	0.0476	0.0091	0.0786	0.0081
2.43	2.44	0.45	0.3514	0.0108	0.0822	0.0073	0.0771	0.0082
2.43	2.44	0.55	0.4607	0.0112	0.1250	0.0071	0.0549	0.0059
2.43	2.44	0.65	0.4540	0.0122	0.1408	0.0107	0.0456	0.0058
2.43	2.44	0.75	0.3682	0.0082	0.1232	0.0140	0.0298	0.0081
2.43	2.44	0.85	0.2079	0.0097	0.0404	0.0295	0.0219	0.0119
2.43	2.44	0.92	0.0892	0.0181	0.0330	0.0472	0.0439	0.0227
2.44	2.45	-0.84	0.5652	0.0320	-0.1344	0.0096	-0.0495	0.0215
2.44	2.45	-0.75	0.5719	0.0148	-0.0235	0.0198	-0.0506	0.0193
2.44	2.45	-0.65	0.5773	0.0217	0.0374	0.0178	-0.0710	0.0143
2.44	2.45	-0.55	0.5623	0.0292	0.0435	0.0147	-0.0627	0.0168
2.44	2.45	-0.45	0.5791	0.0210	0.0371	0.0085	-0.0447	0.0148
2.44	2.45	-0.35	0.6113	0.0056	0.0538	0.0101	-0.0631	0.0090
2.44	2.45	-0.25	0.6150	0.0093	0.0429	0.0114	-0.0422	0.0058
2.44	2.45	-0.15	0.6327	0.0131	0.0374	0.0158	-0.0115	0.0070
2.44	2.45	-0.05	0.6079	0.0127	0.0268	0.0151	-0.0022	0.0095
2.44	2.45	0.05	0.5277	0.0186	-0.0055	0.0176	0.0269	0.0087
2.44	2.45	0.15	0.4083	0.0185	-0.0205	0.0187	0.0517	0.0090
2.44	2.45	0.25	0.2911	0.0178	0.0167	0.0122	0.0595	0.0073
2.44	2.45	0.35	0.2797	0.0151	0.0599	0.0087	0.0870	0.0070
2.44	2.45	0.45	0.3565	0.0126	0.0886	0.0071	0.0805	0.0075
2.44	2.45	0.55	0.4273	0.0143	0.1109	0.0062	0.0579	0.0042
2.44	2.45	0.65	0.4477	0.0129	0.1271	0.0084	0.0348	0.0078
2.44	2.45	0.75	0.3569	0.0104	0.1273	0.0106	0.0410	0.0076
2.44	2.45	0.85	0.2184	0.0145	0.0809	0.0298	0.0080	0.0148
2.44	2.45	0.92	0.1139	0.0125	0.1333	0.0599	0.0160	0.0173
2.45	2.46	-0.83	0.5536	0.0479	-0.1223	0.0161	-0.1047	0.0240

2.45	2.46	-0.75	0.5926	0.0252	-0.0501	0.0201	-0.0787	0.0172
2.45	2.46	-0.65	0.5823	0.0222	0.0032	0.0190	-0.0952	0.0136
2.45	2.46	-0.55	0.5551	0.0283	0.0216	0.0123	-0.0633	0.0133
2.45	2.46	-0.45	0.5761	0.0123	0.0282	0.0092	-0.0745	0.0130
2.45	2.46	-0.35	0.6086	0.0044	0.0361	0.0108	-0.0649	0.0078
2.45	2.46	-0.25	0.6414	0.0122	0.0664	0.0124	-0.0405	0.0078
2.45	2.46	-0.15	0.6167	0.0123	0.0644	0.0130	-0.0170	0.0084
2.45	2.46	-0.05	0.5826	0.0126	0.0546	0.0163	0.0237	0.0117
2.45	2.46	0.05	0.5423	0.0159	0.0395	0.0202	0.0308	0.0112
2.45	2.46	0.15	0.4272	0.0207	0.0199	0.0178	0.0352	0.0121
2.45	2.46	0.25	0.2586	0.0169	0.0231	0.0154	0.0666	0.0103
2.45	2.46	0.35	0.2413	0.0179	0.0447	0.0144	0.0734	0.0067
2.45	2.46	0.45	0.3380	0.0166	0.0864	0.0082	0.0656	0.0065
2.45	2.46	0.55	0.4307	0.0181	0.1064	0.0082	0.0525	0.0071
2.45	2.46	0.65	0.4449	0.0163	0.1255	0.0079	0.0430	0.0089
2.45	2.46	0.75	0.3914	0.0165	0.1200	0.0092	0.0254	0.0111
2.45	2.46	0.85	0.2104	0.0150	0.0701	0.0297	0.0120	0.0129
2.45	2.46	0.92	0.1268	0.0152	-0.0179	0.0615	-0.0129	0.0246
2.46	2.47	-0.83	0.4430	0.0552	-0.1136	0.0244	-0.0689	0.0226
2.46	2.47	-0.75	0.5698	0.0297	-0.0713	0.0221	-0.0629	0.0150
2.46	2.47	-0.65	0.6111	0.0224	-0.0130	0.0203	-0.0742	0.0117
2.46	2.47	-0.55	0.6257	0.0248	0.0270	0.0099	-0.0874	0.0117
2.46	2.47	-0.45	0.5712	0.0146	0.0376	0.0076	-0.0684	0.0113
2.46	2.47	-0.35	0.6114	0.0096	0.0587	0.0093	-0.0743	0.0103
2.46	2.47	-0.25	0.6264	0.0101	0.0716	0.0088	-0.0594	0.0078
2.46	2.47	-0.15	0.6015	0.0107	0.0709	0.0089	-0.0279	0.0092
2.46	2.47	-0.05	0.5787	0.0125	0.0378	0.0092	0.0029	0.0103
2.46	2.47	0.05	0.5133	0.0171	0.0140	0.0113	0.0094	0.0109
2.46	2.47	0.15	0.4047	0.0208	0.0238	0.0127	0.0166	0.0132
2.46	2.47	0.25	0.2882	0.0198	0.0464	0.0115	0.0447	0.0089
2.46	2.47	0.35	0.2734	0.0200	0.0812	0.0122	0.0749	0.0058
2.46	2.47	0.45	0.3408	0.0196	0.1029	0.0103	0.0715	0.0057
2.46	2.47	0.55	0.4630	0.0222	0.1076	0.0075	0.0562	0.0068
2.46	2.47	0.65	0.4790	0.0185	0.1029	0.0089	0.0656	0.0106
2.46	2.47	0.75	0.3833	0.0178	0.1243	0.0118	0.0314	0.0097
2.46	2.47	0.85	0.2523	0.0156	0.0391	0.0260	0.0403	0.0183
2.46	2.47	0.92	0.1259	0.0156	0.1127	0.0512	0.0136	0.0246
2.47	2.48	-0.83	0.3781	0.0598	-0.0782	0.0324	-0.0608	0.0287
2.47	2.48	-0.75	0.5590	0.0189	-0.0242	0.0253	-0.0534	0.0146
2.47	2.48	-0.65	0.6240	0.0157	0.0172	0.0187	-0.0714	0.0104
2.47	2.48	-0.55	0.6198	0.0178	0.0349	0.0114	-0.0703	0.0111
2.47	2.48	-0.45	0.5973	0.0173	0.0469	0.0088	-0.0621	0.0165
2.47	2.48	-0.35	0.6111	0.0102	0.0436	0.0094	-0.0718	0.0152
2.47	2.48	-0.25	0.6070	0.0114	0.0608	0.0081	-0.0573	0.0125
2.47	2.48	-0.15	0.6155	0.0089	0.0648	0.0069	-0.0200	0.0103
2.47	2.48	-0.05	0.5848	0.0118	0.0387	0.0060	0.0098	0.0106
2.47	2.48	0.05	0.4942	0.0191	0.0130	0.0081	0.0265	0.0094
2.47	2.48	0.15	0.3699	0.0241	0.0125	0.0070	0.0401	0.0091
2.47	2.48	0.25	0.2620	0.0200	0.0433	0.0067	0.0562	0.0108
2.47	2.48	0.35	0.2359	0.0191	0.0808	0.0095	0.0740	0.0061
2.47	2.48	0.45	0.2993	0.0204	0.0949	0.0063	0.0797	0.0060
2.47	2.48	0.55	0.4176	0.0228	0.0957	0.0080	0.0656	0.0068
2.47	2.48	0.65	0.4804	0.0229	0.1203	0.0116	0.0454	0.0085
2.47	2.48	0.75	0.3945	0.0187	0.1267	0.0145	0.0191	0.0099
2.47	2.48	0.85	0.2200	0.0187	0.0772	0.0240	0.0147	0.0172
2.47	2.48	0.92	0.1473	0.0179	0.0465	0.0460	0.0593	0.0277
2.48	2.49	-0.83	0.4705	0.0531	-0.1583	0.0313	-0.0200	0.0370
2.48	2.49	-0.75	0.5524	0.0265	-0.0369	0.0191	-0.0772	0.0207
2.48	2.49	-0.65	0.5917	0.0164	0.0478	0.0156	-0.0849	0.0096
2.48	2.49	-0.55	0.6043	0.0177	0.0404	0.0118	-0.0621	0.0103
2.48	2.49	-0.45	0.5948	0.0211	0.0456	0.0122	-0.0945	0.0175
2.48	2.49	-0.35	0.6347	0.0165	0.0450	0.0142	-0.1147	0.0179
2.48	2.49	-0.25	0.6196	0.0081	0.0768	0.0108	-0.0718	0.0129
2.48	2.49	-0.15	0.6188	0.0099	0.0816	0.0085	-0.0418	0.0129
2.48	2.49	-0.05	0.5997	0.0169	0.0448	0.0065	-0.0100	0.0093
2.48	2.49	0.05	0.5230	0.0243	0.0200	0.0092	0.0216	0.0057
2.48	2.49	0.15	0.4125	0.0302	0.0181	0.0129	0.0415	0.0076
2.48	2.49	0.25	0.2598	0.0243	0.0416	0.0124	0.0633	0.0112
2.48	2.49	0.35	0.2430	0.0197	0.0825	0.0107	0.0788	0.0099
2.48	2.49	0.45	0.3253	0.0164	0.1080	0.0089	0.0672	0.0084
2.48	2.49	0.55	0.4239	0.0207	0.1126	0.0083	0.0586	0.0060
2.48	2.49	0.65	0.5222	0.0218	0.1059	0.0108	0.0452	0.0079
2.48	2.49	0.75	0.4274	0.0209	0.0911	0.0182	0.0233	0.0098
2.48	2.49	0.85	0.2378	0.0205	0.0604	0.0299	0.0431	0.0181
2.48	2.49	0.92	0.1047	0.0193	0.1097	0.0494	0.0024	0.0240
2.49	2.50	-0.83	0.5662	0.0622	-0.1366	0.0265	-0.1261	0.0416

2.49	2.50	-0.75	0.5500	0.0284	-0.0387	0.0136	-0.0492	0.0243
2.49	2.50	-0.65	0.6309	0.0210	0.0211	0.0127	-0.0740	0.0101
2.49	2.50	-0.55	0.6091	0.0218	0.0509	0.0126	-0.0592	0.0105
2.49	2.50	-0.45	0.6546	0.0288	0.0210	0.0181	-0.0528	0.0143
2.49	2.50	-0.35	0.6212	0.0198	0.0206	0.0190	-0.1003	0.0144
2.49	2.50	-0.25	0.6083	0.0081	0.0584	0.0137	-0.0553	0.0108
2.49	2.50	-0.15	0.6070	0.0121	0.0631	0.0076	-0.0538	0.0120
2.49	2.50	-0.05	0.5577	0.0188	0.0477	0.0050	-0.0130	0.0079
2.49	2.50	0.05	0.4776	0.0261	0.0363	0.0100	0.0222	0.0036
2.49	2.50	0.15	0.3357	0.0297	0.0449	0.0151	0.0402	0.0055
2.49	2.50	0.25	0.2170	0.0263	0.0631	0.0159	0.0893	0.0135
2.49	2.50	0.35	0.2707	0.0189	0.1108	0.0145	0.0958	0.0145
2.49	2.50	0.45	0.3081	0.0154	0.1054	0.0082	0.0852	0.0090
2.49	2.50	0.55	0.3858	0.0183	0.0985	0.0074	0.0667	0.0073
2.49	2.50	0.65	0.4883	0.0229	0.1058	0.0106	0.0325	0.0065
2.49	2.50	0.75	0.3800	0.0238	0.1277	0.0155	0.0379	0.0093
2.49	2.50	0.85	0.2171	0.0237	0.1068	0.0324	0.0091	0.0156
2.49	2.50	0.92	0.1164	0.0282	-0.0150	0.0593	0.0353	0.0209
2.50	2.51	-0.83	0.5975	0.0664	-0.0889	0.0250	-0.0749	0.0367
2.50	2.51	-0.75	0.5583	0.0370	-0.0465	0.0096	-0.0753	0.0251
2.50	2.51	-0.65	0.5665	0.0266	0.0461	0.0098	-0.0595	0.0139
2.50	2.51	-0.55	0.5812	0.0217	0.0657	0.0122	-0.0548	0.0096
2.50	2.51	-0.45	0.5856	0.0283	0.0598	0.0168	-0.0689	0.0114
2.50	2.51	-0.35	0.6023	0.0234	0.0694	0.0195	-0.0895	0.0107
2.50	2.51	-0.25	0.6134	0.0131	0.0812	0.0131	-0.0686	0.0120
2.50	2.51	-0.15	0.6133	0.0132	0.0695	0.0068	-0.0244	0.0124
2.50	2.51	-0.05	0.5969	0.0190	0.0485	0.0048	-0.0048	0.0081
2.50	2.51	0.05	0.5138	0.0202	0.0305	0.0092	0.0155	0.0051
2.50	2.51	0.15	0.3472	0.0248	0.0125	0.0134	0.0355	0.0074
2.50	2.51	0.25	0.2209	0.0270	0.0385	0.0160	0.0568	0.0162
2.50	2.51	0.35	0.2281	0.0174	0.0808	0.0133	0.0833	0.0182
2.50	2.51	0.45	0.3219	0.0170	0.0982	0.0086	0.0856	0.0138
2.50	2.51	0.55	0.4275	0.0207	0.1136	0.0090	0.0614	0.0087
2.50	2.51	0.65	0.4998	0.0237	0.1170	0.0084	0.0388	0.0075
2.50	2.51	0.75	0.4002	0.0251	0.1130	0.0164	0.0294	0.0083
2.50	2.51	0.85	0.2741	0.0305	0.0775	0.0281	0.0372	0.0124
2.50	2.51	0.92	0.1484	0.0328	0.1171	0.0458	0.0018	0.0140
2.51	2.52	-0.83	0.4385	0.0556	-0.1161	0.0205	-0.0378	0.0305
2.51	2.52	-0.75	0.6136	0.0418	-0.0466	0.0136	-0.0251	0.0256
2.51	2.52	-0.65	0.6010	0.0194	0.0456	0.0088	-0.0816	0.0135
2.51	2.52	-0.55	0.5809	0.0159	0.0536	0.0095	-0.0416	0.0106
2.51	2.52	-0.45	0.5803	0.0215	0.0387	0.0114	-0.0776	0.0089
2.51	2.52	-0.35	0.5669	0.0213	0.0553	0.0147	-0.1050	0.0102
2.51	2.52	-0.25	0.6197	0.0126	0.0609	0.0097	-0.0715	0.0154
2.51	2.52	-0.15	0.6435	0.0172	0.0607	0.0074	-0.0456	0.0151
2.51	2.52	-0.05	0.5789	0.0142	0.0466	0.0053	-0.0069	0.0113
2.51	2.52	0.05	0.5046	0.0173	0.0157	0.0060	0.0138	0.0098
2.51	2.52	0.15	0.3762	0.0251	0.0118	0.0069	0.0351	0.0091
2.51	2.52	0.25	0.2524	0.0278	0.0240	0.0077	0.0501	0.0163
2.51	2.52	0.35	0.2563	0.0232	0.0719	0.0115	0.0482	0.0201
2.51	2.52	0.45	0.3023	0.0174	0.1020	0.0089	0.0645	0.0133
2.51	2.52	0.55	0.3961	0.0196	0.1002	0.0086	0.0458	0.0121
2.51	2.52	0.65	0.4467	0.0216	0.1289	0.0146	0.0239	0.0086
2.51	2.52	0.75	0.4295	0.0219	0.1268	0.0134	0.0290	0.0064
2.51	2.52	0.85	0.2199	0.0253	0.0625	0.0192	0.0328	0.0081
2.51	2.52	0.92	0.1945	0.0354	0.1196	0.0262	0.0093	0.0097
2.52	2.53	-0.83	0.4936	0.0492	-0.1601	0.0299	-0.0836	0.0276
2.52	2.53	-0.75	0.6047	0.0311	-0.0467	0.0162	-0.0761	0.0217
2.52	2.53	-0.65	0.5775	0.0239	0.0328	0.0149	-0.0733	0.0172
2.52	2.53	-0.55	0.5872	0.0156	0.0552	0.0119	-0.0648	0.0077
2.52	2.53	-0.45	0.6149	0.0201	0.0394	0.0082	-0.0809	0.0071
2.52	2.53	-0.35	0.6179	0.0209	0.0373	0.0087	-0.1128	0.0091
2.52	2.53	-0.25	0.6276	0.0177	0.0634	0.0086	-0.1039	0.0139
2.52	2.53	-0.15	0.6235	0.0163	0.0569	0.0074	-0.0630	0.0127
2.52	2.53	-0.05	0.5700	0.0136	0.0373	0.0058	-0.0272	0.0118
2.52	2.53	0.05	0.4794	0.0146	0.0211	0.0047	-0.0028	0.0131
2.52	2.53	0.15	0.3937	0.0194	0.0119	0.0025	0.0260	0.0139
2.52	2.53	0.25	0.3172	0.0257	0.0338	0.0073	0.0795	0.0145
2.52	2.53	0.35	0.2457	0.0157	0.0833	0.0125	0.0947	0.0164
2.52	2.53	0.45	0.2773	0.0153	0.0907	0.0116	0.0774	0.0148
2.52	2.53	0.55	0.3884	0.0140	0.0874	0.0128	0.0460	0.0146
2.52	2.53	0.65	0.4774	0.0159	0.1148	0.0156	0.0358	0.0109
2.52	2.53	0.75	0.4019	0.0138	0.0852	0.0225	0.0409	0.0071
2.52	2.53	0.85	0.2394	0.0208	0.0608	0.0230	0.0453	0.0078
2.52	2.53	0.92	0.1211	0.0306	0.1019	0.0297	0.0024	0.0111
2.53	2.54	-0.83	0.4709	0.0372	-0.1411	0.0299	-0.0730	0.0194

2.53	2.54	-0.75	0.5294	0.0338	-0.0121	0.0254	-0.1000	0.0207
2.53	2.54	-0.65	0.5765	0.0221	0.0632	0.0201	-0.0748	0.0110
2.53	2.54	-0.55	0.6247	0.0214	0.0778	0.0161	-0.0691	0.0125
2.53	2.54	-0.45	0.6038	0.0178	0.0438	0.0094	-0.0757	0.0063
2.53	2.54	-0.35	0.6072	0.0215	0.0475	0.0103	-0.1029	0.0090
2.53	2.54	-0.25	0.6102	0.0187	0.0661	0.0106	-0.0760	0.0121
2.53	2.54	-0.15	0.5845	0.0158	0.0439	0.0102	-0.0507	0.0097
2.53	2.54	-0.05	0.5755	0.0126	0.0369	0.0069	-0.0190	0.0119
2.53	2.54	0.05	0.4905	0.0153	0.0266	0.0056	0.0305	0.0145
2.53	2.54	0.15	0.3654	0.0180	0.0128	0.0082	0.0497	0.0143
2.53	2.54	0.25	0.2775	0.0176	0.0281	0.0116	0.0713	0.0113
2.53	2.54	0.35	0.2395	0.0132	0.0483	0.0139	0.0884	0.0091
2.53	2.54	0.45	0.3159	0.0127	0.0705	0.0115	0.0857	0.0095
2.53	2.54	0.55	0.4013	0.0129	0.0849	0.0105	0.0842	0.0129
2.53	2.54	0.65	0.4535	0.0107	0.0900	0.0157	0.0475	0.0082
2.53	2.54	0.75	0.4154	0.0119	0.1071	0.0241	0.0356	0.0065
2.53	2.54	0.85	0.2454	0.0202	0.1198	0.0402	0.0301	0.0114
2.53	2.54	0.92	0.1725	0.0292	0.1073	0.0448	0.0238	0.0129
2.54	2.55	-0.83	0.4119	0.0362	-0.0805	0.0318	-0.0384	0.0163
2.54	2.55	-0.75	0.5774	0.0323	-0.0572	0.0239	-0.0942	0.0134
2.54	2.55	-0.65	0.6081	0.0235	0.0298	0.0229	-0.0437	0.0155
2.54	2.55	-0.55	0.6122	0.0225	0.0354	0.0187	-0.0752	0.0129
2.54	2.55	-0.45	0.5875	0.0189	0.0466	0.0120	-0.0895	0.0101
2.54	2.55	-0.35	0.5703	0.0189	0.0632	0.0127	-0.0967	0.0072
2.54	2.55	-0.25	0.5957	0.0161	0.0843	0.0140	-0.0697	0.0110
2.54	2.55	-0.15	0.5835	0.0112	0.0710	0.0125	-0.0503	0.0077
2.54	2.55	-0.05	0.5839	0.0082	0.0428	0.0099	-0.0403	0.0114
2.54	2.55	0.05	0.5250	0.0154	0.0175	0.0137	0.0167	0.0128
2.54	2.55	0.15	0.3796	0.0158	0.0107	0.0200	0.0670	0.0152
2.54	2.55	0.25	0.2734	0.0150	0.0399	0.0217	0.0786	0.0096
2.54	2.55	0.35	0.2447	0.0104	0.0726	0.0165	0.0811	0.0056
2.54	2.55	0.45	0.2932	0.0148	0.0836	0.0085	0.0756	0.0062
2.54	2.55	0.55	0.3891	0.0098	0.0744	0.0086	0.0705	0.0081
2.54	2.55	0.65	0.4462	0.0088	0.0717	0.0150	0.0471	0.0066
2.54	2.55	0.75	0.4201	0.0140	0.0736	0.0212	0.0361	0.0075
2.54	2.55	0.85	0.2623	0.0256	0.0375	0.0357	0.0408	0.0130
2.54	2.55	0.92	0.1078	0.0349	-0.0104	0.0553	0.0444	0.0173
2.55	2.56	-0.83	0.3923	0.0415	-0.1303	0.0220	-0.0495	0.0186
2.55	2.56	-0.75	0.5605	0.0293	-0.0238	0.0243	-0.0778	0.0161
2.55	2.56	-0.65	0.5673	0.0283	0.0707	0.0229	-0.0612	0.0133
2.55	2.56	-0.55	0.5630	0.0217	0.0756	0.0191	-0.0416	0.0148
2.55	2.56	-0.45	0.5768	0.0127	0.0563	0.0136	-0.0734	0.0111
2.55	2.56	-0.35	0.5571	0.0185	0.0764	0.0181	-0.0901	0.0098
2.55	2.56	-0.25	0.5683	0.0113	0.0608	0.0153	-0.0881	0.0086
2.55	2.56	-0.15	0.5897	0.0075	0.0518	0.0147	-0.0561	0.0104
2.55	2.56	-0.05	0.5759	0.0086	0.0518	0.0115	-0.0119	0.0102
2.55	2.56	0.05	0.4949	0.0175	0.0446	0.0157	0.0173	0.0125
2.55	2.56	0.15	0.3527	0.0164	0.0622	0.0222	0.0313	0.0150
2.55	2.56	0.25	0.2523	0.0147	0.0819	0.0214	0.0597	0.0114
2.55	2.56	0.35	0.2597	0.0121	0.0820	0.0136	0.0864	0.0056
2.55	2.56	0.45	0.3176	0.0124	0.0789	0.0066	0.0819	0.0051
2.55	2.56	0.55	0.3717	0.0133	0.0829	0.0108	0.0623	0.0067
2.55	2.56	0.65	0.4465	0.0113	0.0970	0.0137	0.0471	0.0051
2.55	2.56	0.75	0.4047	0.0175	0.1044	0.0147	0.0516	0.0100
2.55	2.56	0.85	0.1998	0.0361	0.0671	0.0266	0.0634	0.0166
2.55	2.56	0.92	0.1283	0.0400	0.0202	0.0453	0.0241	0.0161
2.56	2.57	-0.83	0.4645	0.0411	-0.1347	0.0167	-0.0633	0.0315
2.56	2.57	-0.75	0.5074	0.0371	-0.0267	0.0192	-0.0768	0.0256
2.56	2.57	-0.65	0.5781	0.0280	0.0201	0.0232	-0.0737	0.0157
2.56	2.57	-0.55	0.6027	0.0206	0.0564	0.0175	-0.0528	0.0127
2.56	2.57	-0.45	0.5702	0.0159	0.0331	0.0150	-0.0694	0.0145
2.56	2.57	-0.35	0.5731	0.0193	0.0427	0.0173	-0.0935	0.0107
2.56	2.57	-0.25	0.5771	0.0146	0.0485	0.0179	-0.1053	0.0120
2.56	2.57	-0.15	0.5899	0.0081	0.0817	0.0151	-0.0579	0.0064
2.56	2.57	-0.05	0.5692	0.0132	0.0648	0.0124	-0.0012	0.0094
2.56	2.57	0.05	0.4992	0.0192	0.0320	0.0118	0.0287	0.0096
2.56	2.57	0.15	0.3901	0.0173	0.0545	0.0170	0.0666	0.0160
2.56	2.57	0.25	0.2774	0.0157	0.0926	0.0170	0.0829	0.0116
2.56	2.57	0.35	0.2658	0.0141	0.0973	0.0104	0.0812	0.0063
2.56	2.57	0.45	0.3218	0.0178	0.0799	0.0089	0.0867	0.0054
2.56	2.57	0.55	0.3837	0.0188	0.0960	0.0132	0.0713	0.0068
2.56	2.57	0.65	0.4477	0.0205	0.1012	0.0142	0.0578	0.0058
2.56	2.57	0.75	0.4370	0.0233	0.0926	0.0111	0.0382	0.0108
2.56	2.57	0.85	0.2813	0.0335	0.0540	0.0235	0.0254	0.0145
2.56	2.57	0.92	0.1851	0.0444	0.0906	0.0529	0.0056	0.0352
2.57	2.58	-0.83	0.4914	0.0459	-0.1207	0.0098	-0.1147	0.0397

2.57	2.58	-0.75	0.5442	0.0333	-0.0641	0.0220	-0.0221	0.0347
2.57	2.58	-0.65	0.6347	0.0317	0.0630	0.0228	-0.0559	0.0151
2.57	2.58	-0.55	0.5816	0.0187	0.0512	0.0160	-0.0677	0.0107
2.57	2.58	-0.45	0.5837	0.0140	0.0368	0.0135	-0.0982	0.0139
2.57	2.58	-0.35	0.6246	0.0245	0.0179	0.0162	-0.1104	0.0141
2.57	2.58	-0.25	0.5867	0.0172	0.0331	0.0150	-0.1003	0.0124
2.57	2.58	-0.15	0.5743	0.0083	0.0640	0.0156	-0.0457	0.0112
2.57	2.58	-0.05	0.5904	0.0141	0.0442	0.0135	-0.0067	0.0107
2.57	2.58	0.05	0.5419	0.0176	0.0204	0.0139	0.0145	0.0113
2.57	2.58	0.15	0.3808	0.0151	0.0376	0.0167	0.0504	0.0155
2.57	2.58	0.25	0.2473	0.0157	0.0712	0.0190	0.0757	0.0125
2.57	2.58	0.35	0.2457	0.0194	0.0882	0.0173	0.0878	0.0072
2.57	2.58	0.45	0.2972	0.0174	0.0789	0.0142	0.0955	0.0060
2.57	2.58	0.55	0.4223	0.0260	0.0582	0.0183	0.0732	0.0072
2.57	2.58	0.65	0.4929	0.0243	0.0772	0.0148	0.0490	0.0079
2.57	2.58	0.75	0.4414	0.0149	0.1094	0.0141	0.0492	0.0095
2.57	2.58	0.85	0.2894	0.0240	0.0720	0.0347	0.0486	0.0290
2.57	2.58	0.92	0.0982	0.0319	-0.0147	0.0756	0.0333	0.0496
2.58	2.59	-0.83	0.3969	0.0384	-0.1269	0.0190	-0.1579	0.0396
2.58	2.59	-0.75	0.5764	0.0322	-0.0599	0.0223	-0.1066	0.0291
2.58	2.59	-0.65	0.5682	0.0283	0.0139	0.0258	-0.0673	0.0130
2.58	2.59	-0.55	0.6082	0.0148	0.0794	0.0179	-0.0676	0.0056
2.58	2.59	-0.45	0.5873	0.0173	0.0205	0.0165	-0.1137	0.0119
2.58	2.59	-0.35	0.5538	0.0255	0.0398	0.0157	-0.1226	0.0108
2.58	2.59	-0.25	0.5770	0.0204	0.0589	0.0134	-0.0755	0.0169
2.58	2.59	-0.15	0.5796	0.0125	0.0394	0.0151	-0.0443	0.0161
2.58	2.59	-0.05	0.5929	0.0139	0.0392	0.0129	0.0075	0.0159
2.58	2.59	0.05	0.5365	0.0196	0.0118	0.0144	0.0074	0.0139
2.58	2.59	0.15	0.3806	0.0127	0.0113	0.0163	0.0225	0.0127
2.58	2.59	0.25	0.2821	0.0148	0.0411	0.0174	0.0580	0.0095
2.58	2.59	0.35	0.2858	0.0208	0.0578	0.0172	0.0934	0.0084
2.58	2.59	0.45	0.2752	0.0195	0.0543	0.0150	0.0963	0.0055
2.58	2.59	0.55	0.4032	0.0292	0.0986	0.0164	0.0910	0.0054
2.58	2.59	0.65	0.4395	0.0325	0.1035	0.0139	0.0533	0.0072
2.58	2.59	0.75	0.4456	0.0184	0.1073	0.0151	0.0657	0.0096
2.58	2.59	0.85	0.3033	0.0146	0.1149	0.0419	0.0275	0.0260
2.58	2.59	0.92	0.1540	0.0253	-0.1033	0.0927	-0.1314	0.0631
2.59	2.60	-0.83	0.4676	0.0311	-0.1184	0.0248	-0.0903	0.0266
2.59	2.60	-0.75	0.5390	0.0227	-0.0047	0.0299	-0.0722	0.0231
2.59	2.60	-0.65	0.6333	0.0261	0.0393	0.0224	-0.0628	0.0099
2.59	2.60	-0.55	0.6056	0.0155	0.0500	0.0175	-0.0668	0.0079
2.59	2.60	-0.45	0.5798	0.0177	0.0565	0.0174	-0.1101	0.0125
2.59	2.60	-0.35	0.6017	0.0251	0.0070	0.0172	-0.1117	0.0142
2.59	2.60	-0.25	0.5361	0.0196	0.0414	0.0118	-0.1020	0.0170
2.59	2.60	-0.15	0.5673	0.0138	0.0671	0.0121	-0.0773	0.0191
2.59	2.60	-0.05	0.5651	0.0181	0.0622	0.0156	-0.0369	0.0173
2.59	2.60	0.05	0.5046	0.0185	0.0355	0.0176	-0.0031	0.0139
2.59	2.60	0.15	0.3952	0.0119	0.0244	0.0166	0.0390	0.0094
2.59	2.60	0.25	0.2733	0.0137	0.0647	0.0166	0.0611	0.0089
2.59	2.60	0.35	0.2417	0.0156	0.0880	0.0161	0.0775	0.0101
2.59	2.60	0.45	0.2827	0.0206	0.0653	0.0147	0.0967	0.0052
2.59	2.60	0.55	0.3595	0.0309	0.0842	0.0166	0.0890	0.0064
2.59	2.60	0.65	0.4082	0.0407	0.1025	0.0152	0.0441	0.0069
2.59	2.60	0.75	0.4261	0.0275	0.0968	0.0161	0.0505	0.0097
2.59	2.60	0.85	0.2821	0.0178	0.0662	0.0426	0.0323	0.0233
2.59	2.60	0.92	0.1343	0.0185	0.1352	0.0897	-0.0267	0.0522
2.60	2.61	-0.83	0.4279	0.0292	-0.0685	0.0320	-0.1119	0.0260
2.60	2.61	-0.75	0.5513	0.0220	-0.0476	0.0230	-0.0709	0.0168
2.60	2.61	-0.65	0.5995	0.0204	0.0695	0.0172	-0.0768	0.0086
2.60	2.61	-0.55	0.6129	0.0230	0.0576	0.0161	-0.0760	0.0085
2.60	2.61	-0.45	0.5446	0.0224	0.0624	0.0170	-0.0743	0.0137
2.60	2.61	-0.35	0.5742	0.0236	0.0321	0.0158	-0.1035	0.0107
2.60	2.61	-0.25	0.5254	0.0174	0.0528	0.0098	-0.1323	0.0176
2.60	2.61	-0.15	0.5757	0.0147	0.0504	0.0117	-0.0655	0.0142
2.60	2.61	-0.05	0.5872	0.0193	0.0480	0.0148	-0.0179	0.0143
2.60	2.61	0.05	0.4749	0.0174	0.0612	0.0190	0.0228	0.0139
2.60	2.61	0.15	0.4037	0.0082	0.0482	0.0148	0.0365	0.0103
2.60	2.61	0.25	0.2784	0.0061	0.0681	0.0163	0.0644	0.0076
2.60	2.61	0.35	0.2284	0.0149	0.0518	0.0169	0.1130	0.0110
2.60	2.61	0.45	0.2695	0.0177	0.0750	0.0191	0.1027	0.0085
2.60	2.61	0.55	0.3223	0.0312	0.0753	0.0199	0.0911	0.0070
2.60	2.61	0.65	0.5036	0.0393	0.0809	0.0180	0.0599	0.0096
2.60	2.61	0.75	0.3983	0.0359	0.0720	0.0183	0.0671	0.0089
2.60	2.61	0.85	0.3035	0.0262	0.0907	0.0367	0.0066	0.0219
2.60	2.61	0.92	0.1177	0.0190	0.0894	0.0884	0.0006	0.0380
2.61	2.62	-0.83	0.4366	0.0429	-0.1343	0.0216	-0.0775	0.0318

2.61	2.62	-0.75	0.5476	0.0265	-0.0571	0.0186	-0.0907	0.0196
2.61	2.62	-0.65	0.5590	0.0287	0.0509	0.0146	-0.0856	0.0114
2.61	2.62	-0.55	0.6109	0.0257	0.0596	0.0192	-0.0693	0.0076
2.61	2.62	-0.45	0.6131	0.0388	0.0827	0.0231	-0.0909	0.0124
2.61	2.62	-0.35	0.6003	0.0256	0.0484	0.0180	-0.1116	0.0134
2.61	2.62	-0.25	0.5091	0.0196	0.0482	0.0121	-0.1185	0.0183
2.61	2.62	-0.15	0.5470	0.0182	0.0463	0.0105	-0.0844	0.0176
2.61	2.62	-0.05	0.5411	0.0216	0.0313	0.0158	-0.0402	0.0149
2.61	2.62	0.05	0.4847	0.0144	0.0194	0.0203	-0.0071	0.0161
2.61	2.62	0.15	0.4005	0.0069	0.0348	0.0143	0.0511	0.0115
2.61	2.62	0.25	0.2697	0.0076	0.0910	0.0150	0.0715	0.0075
2.61	2.62	0.35	0.2535	0.0155	0.0636	0.0158	0.0928	0.0111
2.61	2.62	0.45	0.2992	0.0200	0.0369	0.0173	0.0986	0.0081
2.61	2.62	0.55	0.3736	0.0281	0.0328	0.0203	0.0735	0.0112
2.61	2.62	0.65	0.4597	0.0315	0.0656	0.0170	0.0672	0.0093
2.61	2.62	0.75	0.4814	0.0350	0.0609	0.0214	0.0632	0.0126
2.61	2.62	0.85	0.2558	0.0319	0.0575	0.0539	0.0216	0.0201
2.61	2.62	0.92	0.1478	0.0284	-0.0339	0.0890	0.0558	0.0340
2.62	2.63	-0.83	0.5257	0.0549	-0.1182	0.0194	-0.0298	0.0394
2.62	2.63	-0.75	0.5951	0.0331	-0.0650	0.0157	-0.1183	0.0237
2.62	2.63	-0.65	0.5938	0.0258	0.0660	0.0145	-0.0688	0.0091
2.62	2.63	-0.55	0.5491	0.0327	0.1129	0.0249	-0.0734	0.0070
2.62	2.63	-0.45	0.5606	0.0378	0.0378	0.0257	-0.1131	0.0115
2.62	2.63	-0.35	0.6353	0.0369	0.0060	0.0223	-0.0993	0.0141
2.62	2.63	-0.25	0.5406	0.0238	0.0522	0.0141	-0.0745	0.0214
2.62	2.63	-0.15	0.5719	0.0191	0.0696	0.0128	-0.0490	0.0153
2.62	2.63	-0.05	0.5941	0.0222	0.0607	0.0180	-0.0246	0.0140
2.62	2.63	0.05	0.5021	0.0144	0.0306	0.0218	0.0314	0.0150
2.62	2.63	0.15	0.3935	0.0086	0.0498	0.0188	0.0625	0.0129
2.62	2.63	0.25	0.2785	0.0107	0.1117	0.0150	0.0712	0.0089
2.62	2.63	0.35	0.2365	0.0161	0.0765	0.0103	0.1116	0.0087
2.62	2.63	0.45	0.3250	0.0224	0.0610	0.0125	0.1149	0.0118
2.62	2.63	0.55	0.3577	0.0216	0.0634	0.0144	0.0876	0.0141
2.62	2.63	0.65	0.4433	0.0224	0.0906	0.0145	0.0469	0.0142
2.62	2.63	0.75	0.4471	0.0244	0.0985	0.0266	0.0650	0.0129
2.62	2.63	0.85	0.3299	0.0326	0.0183	0.0630	0.0682	0.0270
2.62	2.63	0.92	0.1130	0.0354	-0.1552	0.1155	0.0260	0.0332
2.63	2.64	-0.83	0.3867	0.0642	-0.1328	0.0233	-0.1197	0.0415
2.63	2.64	-0.75	0.5735	0.0324	-0.0407	0.0247	-0.1038	0.0260
2.63	2.64	-0.65	0.5543	0.0258	0.0545	0.0211	-0.0672	0.0135
2.63	2.64	-0.55	0.5799	0.0262	0.0773	0.0233	-0.0714	0.0091
2.63	2.64	-0.45	0.4991	0.0422	0.0850	0.0274	-0.0845	0.0122
2.63	2.64	-0.35	0.5752	0.0316	0.0133	0.0215	-0.1038	0.0177
2.63	2.64	-0.25	0.5525	0.0298	0.0820	0.0182	-0.0966	0.0195
2.63	2.64	-0.15	0.5426	0.0214	0.0617	0.0112	-0.0550	0.0140
2.63	2.64	-0.05	0.5681	0.0221	0.0469	0.0156	-0.0145	0.0079
2.63	2.64	0.05	0.4906	0.0202	0.0862	0.0236	0.0168	0.0119
2.63	2.64	0.15	0.4054	0.0138	0.0474	0.0202	0.0377	0.0125
2.63	2.64	0.25	0.2907	0.0154	0.0749	0.0155	0.0782	0.0102
2.63	2.64	0.35	0.2748	0.0161	0.0754	0.0063	0.1198	0.0096
2.63	2.64	0.45	0.2894	0.0179	0.0572	0.0064	0.1092	0.0141
2.63	2.64	0.55	0.3175	0.0210	0.0711	0.0104	0.0515	0.0170
2.63	2.64	0.65	0.4628	0.0173	0.0823	0.0070	0.0429	0.0184
2.63	2.64	0.75	0.4396	0.0169	0.0939	0.0235	0.0814	0.0196
2.63	2.64	0.85	0.2824	0.0282	0.1623	0.0738	0.0261	0.0308
2.63	2.64	0.92	0.1969	0.0362	0.0642	0.0953	0.0943	0.0388
2.64	2.65	-0.83	0.4844	0.0546	-0.0897	0.0230	-0.1375	0.0382
2.64	2.65	-0.75	0.5484	0.0337	0.0143	0.0280	-0.0677	0.0260
2.64	2.65	-0.65	0.6154	0.0267	0.0358	0.0171	-0.0869	0.0156
2.64	2.65	-0.55	0.5799	0.0284	0.0504	0.0179	-0.0802	0.0107
2.64	2.65	-0.45	0.5595	0.0296	0.0309	0.0215	-0.0946	0.0116
2.64	2.65	-0.35	0.5485	0.0313	0.0480	0.0217	-0.1382	0.0203
2.64	2.65	-0.25	0.4875	0.0225	0.0701	0.0185	-0.1328	0.0184
2.64	2.65	-0.15	0.5519	0.0186	0.0563	0.0168	-0.0450	0.0102
2.64	2.65	-0.05	0.5324	0.0230	0.0731	0.0130	-0.0104	0.0065
2.64	2.65	0.05	0.4684	0.0253	0.0726	0.0188	0.0121	0.0088
2.64	2.65	0.15	0.3809	0.0224	0.0890	0.0217	0.0661	0.0125
2.64	2.65	0.25	0.2655	0.0186	0.1041	0.0141	0.0914	0.0126
2.64	2.65	0.35	0.2621	0.0135	0.0767	0.0060	0.1074	0.0109
2.64	2.65	0.45	0.3045	0.0127	0.0624	0.0096	0.0953	0.0175
2.64	2.65	0.55	0.3153	0.0186	0.0681	0.0137	0.0493	0.0214
2.64	2.65	0.65	0.4814	0.0225	0.0780	0.0119	0.0782	0.0211
2.64	2.65	0.75	0.4589	0.0170	0.1060	0.0211	0.0536	0.0211
2.64	2.65	0.85	0.3086	0.0227	0.0604	0.0373	0.0906	0.0283
2.64	2.65	0.92	0.1371	0.0380	0.1443	0.0784	0.0087	0.0397
2.65	2.66	-0.83	0.5698	0.0516	-0.1103	0.0213	-0.0658	0.0314

2.65	2.66	-0.75	0.5595	0.0212	-0.0461	0.0220	-0.0651	0.0261
2.65	2.66	-0.65	0.6150	0.0290	0.0380	0.0202	-0.0552	0.0173
2.65	2.66	-0.55	0.6078	0.0244	0.0626	0.0140	-0.0543	0.0107
2.65	2.66	-0.45	0.6124	0.0257	0.0557	0.0173	-0.0938	0.0167
2.65	2.66	-0.35	0.5641	0.0217	0.0232	0.0197	-0.1221	0.0213
2.65	2.66	-0.25	0.5237	0.0193	0.0277	0.0222	-0.1005	0.0191
2.65	2.66	-0.15	0.5639	0.0179	0.0438	0.0202	-0.0638	0.0110
2.65	2.66	-0.05	0.5685	0.0225	0.0498	0.0163	-0.0188	0.0080
2.65	2.66	0.05	0.5308	0.0242	0.0528	0.0160	0.0262	0.0064
2.65	2.66	0.15	0.4231	0.0279	0.0620	0.0223	0.0499	0.0143
2.65	2.66	0.25	0.3094	0.0187	0.0812	0.0146	0.0618	0.0118
2.65	2.66	0.35	0.2528	0.0170	0.0783	0.0093	0.1058	0.0125
2.65	2.66	0.45	0.2862	0.0098	0.0401	0.0142	0.1429	0.0214
2.65	2.66	0.55	0.3427	0.0254	0.0374	0.0197	0.0780	0.0202
2.65	2.66	0.65	0.4346	0.0302	0.0707	0.0192	0.0317	0.0173
2.65	2.66	0.75	0.4520	0.0199	0.0853	0.0144	0.0385	0.0167
2.65	2.66	0.85	0.3361	0.0254	0.0590	0.0302	0.0882	0.0245
2.65	2.66	0.92	0.2006	0.0281	0.1259	0.0401	0.0436	0.0295
2.66	2.67	-0.83	0.5343	0.0546	-0.1191	0.0202	-0.1069	0.0252
2.66	2.67	-0.75	0.5530	0.0282	-0.0432	0.0221	-0.1163	0.0191
2.66	2.67	-0.65	0.6827	0.0337	0.0140	0.0236	-0.0764	0.0142
2.66	2.67	-0.55	0.6093	0.0262	0.0497	0.0208	-0.0577	0.0121
2.66	2.67	-0.45	0.5797	0.0287	0.0172	0.0249	-0.0812	0.0138
2.66	2.67	-0.35	0.5479	0.0237	0.0405	0.0203	-0.0667	0.0235
2.66	2.67	-0.25	0.4863	0.0256	0.0395	0.0270	-0.1145	0.0163
2.66	2.67	-0.15	0.5362	0.0261	0.0922	0.0248	-0.0396	0.0114
2.66	2.67	-0.05	0.5322	0.0204	0.0641	0.0157	-0.0149	0.0102
2.66	2.67	0.05	0.5297	0.0286	0.0480	0.0186	0.0272	0.0117
2.66	2.67	0.15	0.3794	0.0180	0.1256	0.0202	0.0700	0.0150
2.66	2.67	0.25	0.3117	0.0286	0.1044	0.0170	0.0878	0.0163
2.66	2.67	0.35	0.2608	0.0177	0.0775	0.0124	0.1083	0.0130
2.66	2.67	0.45	0.2920	0.0195	0.0645	0.0166	0.0890	0.0168
2.66	2.67	0.55	0.3551	0.0292	0.0110	0.0218	0.0896	0.0164
2.66	2.67	0.65	0.5246	0.0359	0.1054	0.0185	0.0424	0.0136
2.66	2.67	0.75	0.4303	0.0237	0.0583	0.0217	0.0377	0.0191
2.66	2.67	0.85	0.3407	0.0202	0.0603	0.0207	0.0771	0.0290
2.66	2.67	0.92	0.2271	0.0364	0.2329	0.0523	-0.0240	0.0353
2.67	2.68	-0.83	0.4418	0.0613	-0.0911	0.0254	-0.1059	0.0138
2.67	2.68	-0.75	0.5650	0.0375	-0.0205	0.0221	-0.1094	0.0160
2.67	2.68	-0.65	0.5874	0.0297	0.0849	0.0232	-0.0726	0.0109
2.67	2.68	-0.55	0.5673	0.0323	0.0828	0.0260	-0.0596	0.0107
2.67	2.68	-0.45	0.5784	0.0303	0.0468	0.0264	-0.0569	0.0159
2.67	2.68	-0.35	0.4914	0.0299	0.0753	0.0324	-0.0876	0.0186
2.67	2.68	-0.25	0.5157	0.0346	0.0718	0.0257	-0.0968	0.0153
2.67	2.68	-0.15	0.5189	0.0383	0.1076	0.0266	-0.0448	0.0153
2.67	2.68	-0.05	0.5318	0.0352	0.0838	0.0180	0.0009	0.0177
2.67	2.68	0.05	0.5438	0.0304	0.0607	0.0158	0.0291	0.0165
2.67	2.68	0.15	0.3611	0.0260	0.1026	0.0210	0.0257	0.0169
2.67	2.68	0.25	0.2838	0.0265	0.0956	0.0145	0.0580	0.0172
2.67	2.68	0.35	0.3141	0.0293	0.1083	0.0135	0.0935	0.0100
2.67	2.68	0.45	0.2828	0.0236	0.0331	0.0189	0.0884	0.0123
2.67	2.68	0.55	0.2856	0.0308	0.0492	0.0216	0.0683	0.0080
2.67	2.68	0.65	0.4568	0.0344	0.0725	0.0217	0.0483	0.0094
2.67	2.68	0.75	0.4308	0.0266	0.0940	0.0221	0.0752	0.0217
2.67	2.68	0.85	0.3760	0.0372	0.0430	0.0398	0.0207	0.0372
2.67	2.68	0.92	0.2133	0.0415	0.2286	0.0751	0.0162	0.0365
2.68	2.69	-0.83	0.3278	0.0664	-0.1654	0.0365	-0.1300	0.0213
2.68	2.69	-0.75	0.5810	0.0272	-0.0382	0.0150	-0.1091	0.0149
2.68	2.69	-0.65	0.6060	0.0227	0.0724	0.0201	-0.0970	0.0135
2.68	2.69	-0.55	0.5758	0.0276	0.0965	0.0189	-0.0826	0.0135
2.68	2.69	-0.45	0.5177	0.0332	0.0998	0.0286	-0.0691	0.0109
2.68	2.69	-0.35	0.4920	0.0345	0.0439	0.0298	-0.1146	0.0147
2.68	2.69	-0.25	0.5385	0.0376	0.0109	0.0315	-0.1268	0.0171
2.68	2.69	-0.15	0.4372	0.0486	0.0575	0.0283	-0.0623	0.0199
2.68	2.69	-0.05	0.4813	0.0396	0.0784	0.0227	-0.0429	0.0218
2.68	2.69	0.05	0.4574	0.0318	0.0951	0.0214	0.0003	0.0181
2.68	2.69	0.15	0.3640	0.0238	0.0885	0.0189	0.0305	0.0167
2.68	2.69	0.25	0.3563	0.0331	0.0841	0.0143	0.0936	0.0147
2.68	2.69	0.35	0.2641	0.0297	0.0948	0.0190	0.1070	0.0095
2.68	2.69	0.45	0.3088	0.0287	0.0520	0.0180	0.0802	0.0091
2.68	2.69	0.55	0.3416	0.0296	0.0024	0.0235	0.0818	0.0101
2.68	2.69	0.65	0.4606	0.0329	0.0841	0.0178	0.0442	0.0086
2.68	2.69	0.75	0.4696	0.0246	0.1324	0.0305	0.0412	0.0198
2.68	2.69	0.85	0.3041	0.0370	0.0329	0.0584	0.1124	0.0325
2.68	2.69	0.92	0.1093	0.0516	0.0888	0.1009	0.0501	0.0366
2.69	2.70	-0.83	0.4258	0.0629	-0.1155	0.0395	-0.1055	0.0278

2.69	2.70	-0.75	0.5545	0.0359	-0.0269	0.0258	-0.1460	0.0225
2.69	2.70	-0.65	0.6116	0.0202	0.0778	0.0233	-0.0841	0.0154
2.69	2.70	-0.55	0.5212	0.0286	0.1008	0.0242	-0.0671	0.0136
2.69	2.70	-0.45	0.5986	0.0348	0.0646	0.0229	-0.0784	0.0098
2.69	2.70	-0.35	0.5218	0.0331	-0.0113	0.0264	-0.0998	0.0124
2.69	2.70	-0.25	0.4571	0.0428	0.0464	0.0288	-0.1023	0.0189
2.69	2.70	-0.15	0.5553	0.0490	0.1213	0.0332	-0.0735	0.0249
2.69	2.70	-0.05	0.5190	0.0308	0.1032	0.0311	0.0089	0.0256
2.69	2.70	0.05	0.4319	0.0261	0.0942	0.0265	0.0349	0.0210
2.69	2.70	0.15	0.3718	0.0193	0.1276	0.0212	0.0264	0.0179
2.69	2.70	0.25	0.2867	0.0304	0.1168	0.0198	0.0818	0.0168
2.69	2.70	0.35	0.2500	0.0275	0.0929	0.0198	0.1124	0.0139
2.69	2.70	0.45	0.2421	0.0237	0.0769	0.0213	0.0925	0.0117
2.69	2.70	0.55	0.3028	0.0288	0.0614	0.0187	0.0895	0.0141
2.69	2.70	0.65	0.4108	0.0254	0.0926	0.0163	0.0403	0.0120
2.69	2.70	0.75	0.4744	0.0260	0.0874	0.0236	0.0541	0.0147
2.69	2.70	0.85	0.3050	0.0366	0.1355	0.0616	0.0723	0.0237
2.69	2.70	0.92	0.1742	0.0366	-0.0593	0.1099	-0.0074	0.0324
2.70	2.71	-0.83	0.5018	0.0581	-0.0430	0.0380	-0.0588	0.0339
2.70	2.71	-0.75	0.6225	0.0376	-0.0461	0.0295	-0.1043	0.0226
2.70	2.71	-0.65	0.6213	0.0234	0.0091	0.0270	-0.0789	0.0182
2.70	2.71	-0.55	0.5760	0.0226	0.0509	0.0221	-0.1053	0.0153
2.70	2.71	-0.45	0.5752	0.0300	0.0626	0.0200	-0.0808	0.0119
2.70	2.71	-0.35	0.5685	0.0299	0.0280	0.0218	-0.0984	0.0100
2.70	2.71	-0.25	0.5165	0.0452	0.0158	0.0316	-0.0743	0.0172
2.70	2.71	-0.15	0.4681	0.0369	0.0522	0.0296	-0.0185	0.0228
2.70	2.71	-0.05	0.5238	0.0310	0.0298	0.0310	-0.0186	0.0206
2.70	2.71	0.05	0.4765	0.0201	0.0426	0.0254	0.0493	0.0210
2.70	2.71	0.15	0.3695	0.0221	0.1018	0.0188	0.0624	0.0178
2.70	2.71	0.25	0.3806	0.0325	0.1005	0.0217	0.0474	0.0169
2.70	2.71	0.35	0.2696	0.0194	0.1500	0.0223	0.1028	0.0143
2.70	2.71	0.45	0.2607	0.0190	0.0583	0.0148	0.1079	0.0156
2.70	2.71	0.55	0.3079	0.0205	0.0361	0.0159	0.0534	0.0172
2.70	2.71	0.65	0.3681	0.0256	0.0981	0.0104	0.0559	0.0150
2.70	2.71	0.75	0.4841	0.0258	0.0932	0.0210	0.0318	0.0112
2.70	2.71	0.85	0.2504	0.0357	0.0590	0.0543	0.0689	0.0203
2.70	2.71	0.93	0.2032	0.0456	0.1803	0.0852	0.0544	0.0238
2.71	2.72	-0.83	0.5624	0.0509	-0.0225	0.0387	-0.1343	0.0290
2.71	2.72	-0.75	0.5628	0.0377	-0.0434	0.0301	-0.1090	0.0250
2.71	2.72	-0.65	0.5921	0.0266	0.0497	0.0328	-0.1040	0.0175
2.71	2.72	-0.55	0.5784	0.0245	0.0759	0.0204	-0.0698	0.0214
2.71	2.72	-0.45	0.5583	0.0243	0.0452	0.0171	-0.0730	0.0159
2.71	2.72	-0.35	0.5265	0.0404	0.0087	0.0288	-0.1109	0.0139
2.71	2.72	-0.25	0.4771	0.0398	-0.0079	0.0329	-0.0928	0.0142
2.71	2.72	-0.15	0.4455	0.0383	0.0615	0.0268	-0.0605	0.0186
2.71	2.72	-0.05	0.4855	0.0195	0.0630	0.0179	-0.0301	0.0188
2.71	2.72	0.05	0.4529	0.0221	0.0691	0.0151	0.0183	0.0183
2.71	2.72	0.15	0.3984	0.0216	0.0883	0.0180	0.0416	0.0161
2.71	2.72	0.25	0.3522	0.0280	0.0894	0.0250	0.0630	0.0133
2.71	2.72	0.35	0.2522	0.0184	0.1149	0.0221	0.0797	0.0152
2.71	2.72	0.45	0.2809	0.0153	0.0723	0.0140	0.0795	0.0145
2.71	2.72	0.55	0.2819	0.0228	0.0515	0.0124	0.0621	0.0163
2.71	2.72	0.65	0.4099	0.0257	0.0784	0.0152	0.0209	0.0146
2.71	2.72	0.75	0.4439	0.0282	0.0756	0.0155	0.0322	0.0145
2.71	2.72	0.85	0.3605	0.0443	0.0345	0.0358	0.0741	0.0167
2.71	2.72	0.92	0.1929	0.0484	0.0953	0.0624	0.0731	0.0259
2.72	2.73	-0.83	0.4880	0.0586	-0.0840	0.0324	-0.1114	0.0352
2.72	2.73	-0.75	0.6173	0.0505	0.0311	0.0344	-0.0795	0.0212
2.72	2.73	-0.65	0.6413	0.0392	-0.0004	0.0343	-0.1274	0.0200
2.72	2.73	-0.55	0.6014	0.0236	0.0673	0.0207	-0.0780	0.0186
2.72	2.73	-0.45	0.5166	0.0277	0.0151	0.0224	-0.1126	0.0203
2.72	2.73	-0.35	0.4994	0.0354	0.0543	0.0270	-0.0793	0.0144
2.72	2.73	-0.25	0.3803	0.0439	0.0957	0.0338	-0.0773	0.0137
2.72	2.73	-0.15	0.4709	0.0236	0.0452	0.0213	-0.0279	0.0181
2.72	2.73	-0.05	0.4638	0.0175	0.0557	0.0140	-0.0044	0.0159
2.72	2.73	0.05	0.4901	0.0159	0.0662	0.0109	-0.0025	0.0179
2.72	2.73	0.15	0.4076	0.0196	0.0727	0.0182	0.0250	0.0128
2.72	2.73	0.25	0.3041	0.0231	0.1449	0.0219	0.0605	0.0101
2.72	2.73	0.35	0.2621	0.0139	0.0973	0.0211	0.1158	0.0120
2.72	2.73	0.45	0.2943	0.0200	0.0766	0.0115	0.0954	0.0127
2.72	2.73	0.55	0.3300	0.0281	0.0708	0.0154	0.0849	0.0107
2.72	2.73	0.65	0.4045	0.0337	0.0739	0.0210	0.0400	0.0119
2.72	2.73	0.75	0.4764	0.0269	0.0859	0.0184	0.0527	0.0147
2.72	2.73	0.85	0.3256	0.0447	0.1034	0.0382	0.0371	0.0256
2.72	2.73	0.93	0.0864	0.0467	0.1660	0.0530	0.0411	0.0261
2.73	2.74	-0.83	0.6123	0.0720	-0.0494	0.0256	-0.0871	0.0422

2.73	2.74	-0.75	0.5096	0.0505	0.0079	0.0267	-0.1252	0.0253
2.73	2.74	-0.65	0.5485	0.0413	0.0918	0.0297	-0.0976	0.0218
2.73	2.74	-0.55	0.6209	0.0246	0.0488	0.0265	-0.1114	0.0187
2.73	2.74	-0.45	0.5515	0.0211	0.0361	0.0222	-0.0911	0.0167
2.73	2.74	-0.35	0.4454	0.0338	0.0233	0.0247	-0.0957	0.0155
2.73	2.74	-0.25	0.4487	0.0387	0.0506	0.0256	-0.0927	0.0191
2.73	2.74	-0.15	0.4335	0.0221	0.0786	0.0176	-0.0628	0.0235
2.73	2.74	-0.05	0.4614	0.0118	0.0804	0.0153	-0.0165	0.0200
2.73	2.74	0.05	0.4630	0.0163	0.0727	0.0137	0.0339	0.0186
2.73	2.74	0.15	0.4269	0.0175	0.0954	0.0145	0.0254	0.0137
2.73	2.74	0.25	0.3386	0.0172	0.1682	0.0221	0.0680	0.0093
2.73	2.74	0.35	0.2853	0.0174	0.1286	0.0161	0.0984	0.0097
2.73	2.74	0.45	0.2920	0.0195	0.0636	0.0149	0.0960	0.0078
2.73	2.74	0.55	0.2580	0.0352	0.0600	0.0255	0.0892	0.0071
2.73	2.74	0.65	0.4694	0.0426	0.0297	0.0280	0.0284	0.0062
2.73	2.74	0.75	0.4798	0.0403	0.0996	0.0291	0.0431	0.0147
2.73	2.74	0.85	0.3715	0.0464	0.0453	0.0497	0.1027	0.0297
2.73	2.74	0.93	0.1009	0.0508	0.0755	0.0636	0.0229	0.0323
2.74	2.75	-0.83	0.4675	0.0670	-0.1073	0.0190	-0.1925	0.0451
2.74	2.75	-0.75	0.5338	0.0445	0.0093	0.0173	-0.1290	0.0270
2.74	2.75	-0.65	0.6260	0.0293	0.0568	0.0238	-0.1148	0.0191
2.74	2.75	-0.55	0.5937	0.0201	0.0792	0.0218	-0.0972	0.0189
2.74	2.75	-0.45	0.5608	0.0231	0.0838	0.0240	-0.0670	0.0151
2.74	2.75	-0.35	0.4544	0.0332	0.0641	0.0197	-0.0736	0.0168
2.74	2.75	-0.25	0.4483	0.0398	0.0771	0.0167	-0.0645	0.0255
2.74	2.75	-0.15	0.4726	0.0310	0.0678	0.0143	-0.0095	0.0327
2.74	2.75	-0.05	0.4533	0.0238	0.0945	0.0147	0.0157	0.0207
2.74	2.75	0.05	0.4802	0.0154	0.0485	0.0189	0.0398	0.0205
2.74	2.75	0.15	0.3880	0.0173	0.1148	0.0179	0.0489	0.0122
2.74	2.75	0.25	0.3400	0.0152	0.1631	0.0175	0.0817	0.0101
2.74	2.75	0.35	0.2722	0.0148	0.1159	0.0195	0.0977	0.0089
2.74	2.75	0.45	0.2544	0.0190	0.0952	0.0256	0.0830	0.0085
2.74	2.75	0.55	0.3059	0.0295	0.0387	0.0370	0.0926	0.0051
2.74	2.75	0.65	0.3642	0.0370	0.1163	0.0406	0.0259	0.0049
2.74	2.75	0.75	0.4203	0.0417	0.0959	0.0325	0.0355	0.0127
2.74	2.75	0.85	0.2423	0.0516	0.1638	0.0566	0.0318	0.0300
2.74	2.75	0.92	0.1627	0.0663	0.0031	0.0767	-0.0175	0.0479
2.75	2.76	-0.83	0.6341	0.0654	-0.0875	0.0247	-0.0820	0.0416
2.75	2.76	-0.75	0.5349	0.0334	0.0204	0.0114	-0.1180	0.0191
2.75	2.76	-0.65	0.5717	0.0249	0.0377	0.0166	-0.1632	0.0255
2.75	2.76	-0.55	0.5981	0.0284	0.0904	0.0197	-0.0778	0.0158
2.75	2.76	-0.45	0.5278	0.0226	0.0571	0.0179	-0.0858	0.0160
2.75	2.76	-0.35	0.5119	0.0286	0.0529	0.0172	-0.0973	0.0154
2.75	2.76	-0.25	0.3563	0.0418	0.0521	0.0134	-0.0247	0.0274
2.75	2.76	-0.15	0.4275	0.0484	0.0920	0.0125	0.0165	0.0306
2.75	2.76	-0.05	0.4592	0.0374	0.0652	0.0194	0.0230	0.0223
2.75	2.76	0.05	0.5100	0.0270	0.0618	0.0236	-0.0008	0.0159
2.75	2.76	0.15	0.4065	0.0147	0.1255	0.0221	0.0380	0.0162
2.75	2.76	0.25	0.3224	0.0182	0.1293	0.0215	0.0675	0.0115
2.75	2.76	0.35	0.3036	0.0130	0.0880	0.0239	0.1019	0.0145
2.75	2.76	0.45	0.2639	0.0135	0.0996	0.0320	0.0805	0.0159
2.75	2.76	0.55	0.3045	0.0176	0.1202	0.0477	0.0935	0.0098
2.75	2.76	0.65	0.3988	0.0248	0.0452	0.0454	0.0274	0.0064
2.75	2.76	0.75	0.4549	0.0302	0.1390	0.0356	0.0511	0.0114
2.75	2.76	0.85	0.3454	0.0549	0.0657	0.0598	0.0875	0.0411
2.75	2.76	0.93	0.0894	0.0838	0.1345	0.0885	-0.0450	0.0609
2.76	2.77	-0.82	0.5221	0.0437	-0.1038	0.0309	-0.1628	0.0326
2.76	2.77	-0.75	0.5716	0.0338	0.0013	0.0193	-0.1235	0.0205
2.76	2.77	-0.65	0.6093	0.0289	0.0235	0.0153	-0.1365	0.0251
2.76	2.77	-0.55	0.6213	0.0358	0.0500	0.0161	-0.1055	0.0246
2.76	2.77	-0.45	0.5755	0.0292	0.0493	0.0155	-0.0729	0.0202
2.76	2.77	-0.35	0.5015	0.0224	0.0306	0.0167	-0.0797	0.0229
2.76	2.77	-0.25	0.4045	0.0331	0.0683	0.0133	-0.0724	0.0299
2.76	2.77	-0.15	0.5292	0.0510	0.0729	0.0110	-0.0637	0.0282
2.76	2.77	-0.05	0.5617	0.0485	0.0862	0.0190	0.0173	0.0250
2.76	2.77	0.05	0.4865	0.0228	0.1232	0.0256	0.0449	0.0238
2.76	2.77	0.15	0.4157	0.0215	0.1532	0.0200	0.0466	0.0162
2.76	2.77	0.25	0.3218	0.0230	0.1583	0.0218	0.0468	0.0134
2.76	2.77	0.35	0.2995	0.0186	0.1272	0.0262	0.0732	0.0146
2.76	2.77	0.45	0.2436	0.0114	0.0470	0.0362	0.1205	0.0178
2.76	2.77	0.55	0.2872	0.0145	0.0018	0.0501	0.0760	0.0105
2.76	2.77	0.65	0.4030	0.0213	0.0267	0.0441	0.0365	0.0061
2.76	2.77	0.75	0.4647	0.0187	0.1106	0.0326	0.0493	0.0133
2.76	2.77	0.85	0.3264	0.0452	0.0265	0.0601	0.0355	0.0380
2.76	2.77	0.93	0.3181	0.0890	-0.0521	0.0964	0.1230	0.0746
2.77	2.78	-0.82	0.5225	0.0517	-0.0118	0.0302	-0.1083	0.0251

2.77	2.78	-0.75	0.5554	0.0311	0.0270	0.0221	-0.1183	0.0163
2.77	2.78	-0.65	0.5756	0.0317	0.0391	0.0141	-0.0673	0.0242
2.77	2.78	-0.55	0.5075	0.0407	0.0819	0.0148	-0.0881	0.0214
2.77	2.78	-0.45	0.5342	0.0303	0.0385	0.0210	-0.1322	0.0265
2.77	2.78	-0.35	0.5029	0.0209	0.0193	0.0253	-0.0653	0.0302
2.77	2.78	-0.25	0.3557	0.0325	0.0517	0.0204	-0.0498	0.0318
2.77	2.78	-0.15	0.4238	0.0426	0.0849	0.0181	-0.0468	0.0323
2.77	2.78	-0.05	0.4761	0.0365	0.0935	0.0191	-0.0151	0.0288
2.77	2.78	0.05	0.4694	0.0246	0.0833	0.0192	0.0199	0.0261
2.77	2.78	0.15	0.3883	0.0200	0.1578	0.0158	0.0071	0.0197
2.77	2.78	0.25	0.3909	0.0237	0.1851	0.0166	0.0542	0.0095
2.77	2.78	0.35	0.3217	0.0179	0.1495	0.0244	0.0919	0.0109
2.77	2.78	0.45	0.2501	0.0157	0.0995	0.0323	0.0803	0.0135
2.77	2.78	0.55	0.2671	0.0193	0.0612	0.0420	0.0835	0.0096
2.77	2.78	0.65	0.4276	0.0275	0.1233	0.0415	0.0399	0.0077
2.77	2.78	0.75	0.4236	0.0260	0.1210	0.0354	0.0566	0.0165
2.77	2.78	0.85	0.3455	0.0421	0.1202	0.0540	0.0126	0.0395
2.77	2.78	0.92	0.1196	0.0899	0.1759	0.0958	-0.0069	0.0736
2.78	2.79	-0.82	0.5100	0.0691	-0.0209	0.0287	-0.1521	0.0262
2.78	2.79	-0.75	0.4890	0.0593	0.0298	0.0118	-0.1243	0.0146
2.78	2.79	-0.65	0.6014	0.0327	0.0565	0.0102	-0.1056	0.0176
2.78	2.79	-0.55	0.5752	0.0276	0.0874	0.0159	-0.1157	0.0160
2.78	2.79	-0.45	0.5180	0.0266	0.0616	0.0273	-0.1101	0.0240
2.78	2.79	-0.35	0.5400	0.0231	-0.0272	0.0398	-0.1246	0.0340
2.78	2.79	-0.25	0.3634	0.0226	0.0333	0.0383	-0.1306	0.0400
2.78	2.79	-0.15	0.4226	0.0305	0.0689	0.0272	-0.0374	0.0328
2.78	2.79	-0.05	0.4881	0.0295	0.0479	0.0205	-0.0534	0.0352
2.78	2.79	0.05	0.4737	0.0199	0.0777	0.0177	-0.0143	0.0298
2.78	2.79	0.15	0.4255	0.0260	0.1507	0.0179	0.0399	0.0160
2.78	2.79	0.25	0.3878	0.0185	0.1623	0.0154	0.0487	0.0082
2.78	2.79	0.35	0.3256	0.0177	0.1070	0.0188	0.0839	0.0072
2.78	2.79	0.45	0.2556	0.0218	0.1027	0.0273	0.0974	0.0106
2.78	2.79	0.55	0.2525	0.0310	0.0991	0.0301	0.0836	0.0098
2.78	2.79	0.65	0.3684	0.0348	0.0667	0.0377	0.0475	0.0163
2.78	2.79	0.75	0.4592	0.0407	0.0672	0.0345	0.0675	0.0291
2.78	2.79	0.85	0.3546	0.0576	0.0713	0.0437	0.0696	0.0468
2.78	2.79	0.93	0.2733	0.0837	-0.0097	0.0744	0.1449	0.0667
2.79	2.80	-0.82	0.3585	0.1001	-0.0209	0.0276	-0.1026	0.0290
2.79	2.80	-0.75	0.6265	0.0674	0.0038	0.0179	-0.1019	0.0152
2.79	2.80	-0.65	0.5634	0.0301	0.0546	0.0099	-0.0933	0.0107
2.79	2.80	-0.55	0.5741	0.0228	0.0904	0.0198	-0.1089	0.0119
2.79	2.80	-0.45	0.5522	0.0207	-0.0035	0.0337	-0.0790	0.0221
2.79	2.80	-0.35	0.5396	0.0250	0.0723	0.0439	-0.0716	0.0309
2.79	2.80	-0.25	0.4032	0.0306	-0.0178	0.0494	-0.0416	0.0326
2.79	2.80	-0.15	0.3897	0.0308	0.0256	0.0353	0.0073	0.0320
2.79	2.80	-0.05	0.4659	0.0303	0.0644	0.0187	0.0367	0.0337
2.79	2.80	0.05	0.4229	0.0340	0.0607	0.0223	0.0248	0.0280
2.79	2.80	0.15	0.4045	0.0348	0.1859	0.0250	0.0515	0.0177
2.79	2.80	0.25	0.4001	0.0264	0.1542	0.0185	0.0515	0.0077
2.79	2.80	0.35	0.2921	0.0191	0.1097	0.0171	0.0791	0.0067
2.79	2.80	0.45	0.3052	0.0241	0.0503	0.0209	0.0997	0.0098
2.79	2.80	0.55	0.3009	0.0298	0.0609	0.0268	0.0678	0.0128
2.79	2.80	0.65	0.3224	0.0313	0.1140	0.0451	0.0651	0.0229
2.79	2.80	0.75	0.5074	0.0384	0.1426	0.0401	0.0017	0.0374
2.79	2.80	0.85	0.2488	0.0562	0.0783	0.0314	0.0875	0.0417
2.79	2.80	0.93	0.3494	0.0870	0.0620	0.0794	0.1694	0.0791
2.80	2.81	-0.82	0.5702	0.0799	-0.0977	0.0385	-0.0792	0.0376
2.80	2.81	-0.75	0.6015	0.0701	0.0255	0.0227	-0.1176	0.0188
2.80	2.81	-0.65	0.5780	0.0350	0.0661	0.0149	-0.1079	0.0098
2.80	2.81	-0.55	0.5841	0.0313	0.0680	0.0261	-0.1046	0.0156
2.80	2.81	-0.45	0.5698	0.0266	0.0625	0.0331	-0.1037	0.0217
2.80	2.81	-0.35	0.4877	0.0397	0.0227	0.0396	-0.1239	0.0234
2.80	2.81	-0.25	0.3919	0.0323	0.0969	0.0518	-0.0557	0.0218
2.80	2.81	-0.15	0.4600	0.0350	0.1011	0.0354	0.0117	0.0164
2.80	2.81	-0.05	0.4058	0.0328	0.0719	0.0240	-0.0052	0.0262
2.80	2.81	0.05	0.4125	0.0328	0.0791	0.0298	0.0437	0.0272
2.80	2.81	0.15	0.5133	0.0440	0.1066	0.0380	0.0281	0.0167
2.80	2.81	0.25	0.4076	0.0324	0.1563	0.0291	0.0421	0.0110
2.80	2.81	0.35	0.3261	0.0206	0.1030	0.0211	0.0705	0.0093
2.80	2.81	0.45	0.3083	0.0257	0.0513	0.0239	0.0874	0.0135
2.80	2.81	0.55	0.2470	0.0237	0.0875	0.0309	0.0913	0.0173
2.80	2.81	0.65	0.3598	0.0306	0.1644	0.0541	0.0280	0.0221
2.80	2.81	0.75	0.4594	0.0417	0.0521	0.0473	0.0977	0.0351
2.80	2.81	0.85	0.3323	0.0686	0.0959	0.0492	0.0188	0.0556
2.80	2.81	0.92	0.3804	0.0930	-0.0494	0.0957	0.2413	0.0930
2.81	2.82	-0.82	0.5848	0.0560	-0.0134	0.0365	-0.0245	0.0493

2.81	2.82	-0.75	0.5004	0.0383	0.0121	0.0326	-0.1132	0.0296
2.81	2.82	-0.65	0.5144	0.0452	0.0514	0.0203	-0.1101	0.0135
2.81	2.82	-0.55	0.6200	0.0452	0.0154	0.0303	-0.1327	0.0140
2.81	2.82	-0.45	0.5216	0.0463	0.0067	0.0296	-0.1410	0.0221
2.81	2.82	-0.35	0.5009	0.0478	0.0461	0.0341	-0.1109	0.0207
2.81	2.82	-0.25	0.3257	0.0441	-0.0176	0.0505	-0.0408	0.0163
2.81	2.82	-0.15	0.4100	0.0389	0.0524	0.0335	-0.0093	0.0151
2.81	2.82	-0.05	0.4349	0.0411	0.0519	0.0254	0.0239	0.0236
2.81	2.82	0.05	0.4298	0.0370	0.0066	0.0336	-0.0195	0.0294
2.81	2.82	0.15	0.4687	0.0479	0.0874	0.0412	0.0135	0.0179
2.81	2.82	0.25	0.3374	0.0348	0.2054	0.0318	0.0269	0.0081
2.81	2.82	0.35	0.2976	0.0267	0.1475	0.0250	0.0617	0.0101
2.81	2.82	0.45	0.3260	0.0220	0.0124	0.0281	0.0731	0.0164
2.81	2.82	0.55	0.2216	0.0222	0.0695	0.0317	0.0559	0.0173
2.81	2.82	0.65	0.3609	0.0233	0.0113	0.0549	0.0266	0.0189
2.81	2.82	0.75	0.4241	0.0352	0.1415	0.0439	0.0558	0.0212
2.81	2.82	0.85	0.4159	0.0710	0.0711	0.0504	0.0521	0.0499
2.81	2.82	0.93	0.1588	0.0775	0.2564	0.1012	-0.0200	0.1014
2.82	2.83	-0.82	0.5508	0.0223	-0.0022	0.0324	-0.1541	0.0600
2.82	2.83	-0.75	0.5474	0.0348	-0.0392	0.0379	-0.1588	0.0395
2.82	2.83	-0.65	0.5504	0.0400	0.0437	0.0247	-0.1243	0.0143
2.82	2.83	-0.55	0.4860	0.0472	0.0863	0.0284	-0.1359	0.0137
2.82	2.83	-0.45	0.5798	0.0415	0.0231	0.0271	-0.1204	0.0187
2.82	2.83	-0.35	0.3646	0.0483	0.0021	0.0291	-0.0848	0.0247
2.82	2.83	-0.25	0.3835	0.0462	-0.0367	0.0525	-0.0700	0.0224
2.82	2.83	-0.15	0.4008	0.0440	0.0740	0.0281	-0.0146	0.0205
2.82	2.83	-0.05	0.3433	0.0517	0.0952	0.0297	-0.0165	0.0312
2.82	2.83	0.05	0.4853	0.0423	0.0660	0.0333	-0.0052	0.0385
2.82	2.83	0.15	0.3943	0.0326	0.1483	0.0354	0.0157	0.0219
2.82	2.83	0.25	0.3375	0.0318	0.1347	0.0314	0.0231	0.0094
2.82	2.83	0.35	0.3229	0.0257	0.1525	0.0243	0.0707	0.0077
2.82	2.83	0.45	0.2697	0.0228	0.0705	0.0214	0.1141	0.0183
2.82	2.83	0.55	0.2203	0.0163	0.0449	0.0301	0.0942	0.0181
2.82	2.83	0.65	0.3178	0.0203	0.1140	0.0438	0.0205	0.0183
2.82	2.83	0.75	0.4908	0.0415	0.0822	0.0328	0.0649	0.0161
2.82	2.83	0.85	0.3761	0.0556	0.0719	0.0334	0.0670	0.0328
2.82	2.83	0.93	0.2283	0.0628	0.1776	0.0774	-0.0252	0.0945
2.83	2.84	-0.82	0.5261	0.0248	0.0121	0.0333	-0.0590	0.0639
2.83	2.84	-0.75	0.5086	0.0257	0.0696	0.0380	-0.0776	0.0425
2.83	2.84	-0.65	0.5964	0.0313	0.0292	0.0329	-0.1176	0.0200
2.83	2.84	-0.55	0.5202	0.0329	0.0396	0.0256	-0.1513	0.0110
2.83	2.84	-0.45	0.5724	0.0226	0.0556	0.0222	-0.0944	0.0212
2.83	2.84	-0.35	0.4059	0.0375	0.0134	0.0357	-0.1306	0.0271
2.83	2.84	-0.25	0.3187	0.0401	0.0890	0.0425	-0.0208	0.0280
2.83	2.84	-0.15	0.3303	0.0543	0.0666	0.0374	0.0139	0.0273
2.83	2.84	-0.05	0.4536	0.0560	0.0320	0.0229	0.0386	0.0366
2.83	2.84	0.05	0.4328	0.0383	0.0790	0.0290	0.0780	0.0437
2.83	2.84	0.15	0.3849	0.0283	0.1818	0.0275	-0.0188	0.0274
2.83	2.84	0.25	0.3705	0.0184	0.1763	0.0249	0.0331	0.0094
2.83	2.84	0.35	0.3576	0.0229	0.1371	0.0154	0.0724	0.0088
2.83	2.84	0.45	0.2506	0.0201	0.0894	0.0214	0.0840	0.0111
2.83	2.84	0.55	0.2247	0.0093	0.0749	0.0235	0.0951	0.0193
2.83	2.84	0.65	0.3436	0.0195	0.0524	0.0331	0.0669	0.0172
2.83	2.84	0.75	0.4412	0.0430	0.1047	0.0286	0.0506	0.0182
2.83	2.84	0.85	0.2571	0.0556	0.1075	0.0287	0.0350	0.0412
2.83	2.84	0.92	0.1995	0.0465	0.1024	0.0518	0.1393	0.0775